

*OPERANDO* METHODS FOR ATOMIC-SCALE MECHANISTIC  
UNDERSTANDING OF INTERFACIAL ELECTROCATALYSIS

A Dissertation

Presented to the Faculty of the Graduate School

of Cornell University

In Partial Fulfillment of the Requirements for the Degree of

Doctor of Philosophy

by

Yao Yang

August 2021

© 2021 Yao Yang

# *OPERANDO* METHODS FOR ATOMIC-SCALE MECHANISTIC UNDERSTANDING OF INTERFACIAL ELECTROCATALYSIS

Yao Yang, Ph. D.

Cornell University 2021

## **Abstract**

Electrocatalysis has been the cornerstone for enhancing energy efficiency, minimizing environmental impacts and carbon emissions, and enabling a more sustainable way of meeting global energy needs. Elucidating the structure and reaction mechanisms of electrocatalysts at electrode-electrolyte interfaces is fundamental for advancing renewable energy technologies, including fuel cells, and water electrolyzers, among others. One of the fundamental challenges in electrocatalysis is understanding how to activate and sustain electrocatalytic activity, under operating conditions, for extended time periods, which calls for the use of *in situ/operando* methods.

This thesis first introduces the design and understanding of electrocatalysts for alkaline fuel cells since they enable the use of non-precious metals to catalyze the sluggish oxygen reduction reaction (ORR) at the cathode. Metal oxide-based ORR electrocatalysts, synthesized by a hydrothermal method, in particular, Mn-Co spinel nanoparticles, have demonstrated over 1 W/cm<sup>2</sup> benchmark peak power density with a Pt-based anode and a record 200 mW/cm<sup>2</sup> with a Ni-based anode for a completely non-precious metal-containing alkaline fuel cell, in membrane electrode assembly (MEA) measurements. Analytical scanning transmission electron microscopy (STEM) has been extensively employed to resolve the heterogeneous crystal structures and chemical environments at the atomic scale. *Operando* X-ray absorption spectroscopy (XAS)

methods revealed that the superior performance of Mn-Co spinels in low humidity, relative to Pt, originates from synergistic effects in which the Mn sites bind O<sub>2</sub> while the Co sites activate H<sub>2</sub>O to facilitate the proton-coupled electron transfer process. Moving beyond oxides, we have developed nitride-core oxide-shell Co<sub>4</sub>N/C and Pd-based alloys as ORR electrocatalysts for high-power alkaline fuel cells.

The second part of this thesis focuses on *operando* studies of electrochemical interfaces. *In situ* heating STEM and heating X-ray diffraction were used to track the dynamic order–disorder phase transition of Pt<sub>3</sub>Co intermetallic ORR catalysts during annealing and quantify the degree of ordering as a key structural factor for long-term MEA durability. This thesis then presents the efforts to tackle a grand challenge in physical chemistry: understanding and spatially resolving the electrochemical double layer (EDL) at electrolyte/nanocrystal electrode interfaces. Preliminary studies, with heavy halide anion and/or alkali cations as chemical probes, while promising, have yet to provide compelling evidences of potential-dependent changes of ionic distributions. However, the pursuit of these EDL studies led to the unexpected observation of cathodic corrosion, an enigmatic electrochemical process in which noble metal electrodes corrode under sufficiently reducing potentials. I employed *operando* EC-STEM to reveal that cathodic corrosion at solid-liquid-gas interfaces yields significantly higher levels of structural degradation for nanocrystals than bulk electrodes. The dynamic evolution of morphology, composition, and structural information was retrieved by analytical and 4D-STEM. Such microscopic studies can provide unprecedented insights into the structural evolution of nanoscale electrocatalysts during electrochemical reactions under highly reducing potentials, such as CO<sub>2</sub> and N<sub>2</sub> reduction.

## BIOGRAPHICAL SKETCH

Yao Yang 杨尧

Yao grew up in a farmland in Henan province in the central part of China, which is the birthplace of Chinese civilization. He picked up plenty of hands-on experiences as a kid, including the left-handed habit to handle tools when he helped his father, Xiao-Jun Yang, the only electrician for a village of ~3000 people. After failing to pass the entrance exam for high school in the local county and persuaded by his mother, Xiao-Qing Fan, he spent one more year in middle school and polished his skills in chemistry, mathematics and physics. After three-rounds of competitions in 2008, he won an entrance ticket to the best high school in Henan province, Henan Experimental High School. Its specially designed physical sciences classes revolutionized his view about the outside world, and its chemistry lab stimulated his imagination about how to make things and how such processes, affect their properties.

In 2011, Yao attended Wuhan University (WHU) in Hubei province, which has beautiful cherry blossoms in the spring as well as an endless rainy season. He received a B.S. with Honors in 2015. He was enlightened by the life of a chemist, Linus Pauling when reading his biography, *Force of Nature* by Thomas Hager, and decided to explore a world full of chemistry with hands-on experiments in research labs. He joined Prof. Lin Zhuang's lab and received one-to-one guidance from Prof. Li Xiao. In Zhuang's lab, Yao spent three and a half years cultivating his mind with their world-class electrochemistry expertise and deep insights about fuel cell electrocatalysis. Yao's B.S. thesis was entitled "Studies on Oxygen Cathode Catalysts of Li/Air Batteries", which earned the First-Class Scholarship of Creative Research (6 out of 8000 senior students), established by WHU former president, Prof. Daoyu Liu, who is also a chemist and devoted education reformer.

In 2015, Yao joined Prof. Héctor Abruña's group and was later introduced to Prof. Francis DiSalvo in the Department of Chemistry and Chemical Biology at Cornell University. Yao was co-advised by Prof. David Muller in the School of Applied & Engineering Physics. Here at Cornell, the gap, among electrochemistry, materials design, and electron microscopy, which seems impossible to fill, was gradually bridged by his nearly daily discussions with those three fearless pioneers in their fields. In 2021, he completed his wonderful six-year PhD journey at Cornell with the privilege of having worked with a "Dream Team", Profs. Abruña, Muller and DiSalvo. He then received the prestigious Miller postdoctoral fellowship (2021-2024) working with Prof. Peidong Yang at UC Berkeley for CO<sub>2</sub> reduction electrocatalysis. His achievements, during his PhD study, include the Wentink Award (Highest Graduate Award in Dept. of Chem., 2020), Harvard Rowland Fellowship Finalist (2019), Chinese Government Award for Outstanding Self-Financed Students Abroad (2020), Cornell High-Energy Synchrotron Source (CHESS) Student Research Award (2020), Microscopy Society of America (MSA) Student Poster Award (2019) and Howard Neal Wachter Memorial Prize (Awarded to the best 3rd-year PhD in Physical Chemistry at Cornell, 2018).

He defines his own future academic career as "*Operando* Methods for Interfacial Electrocatalysis", carrying on the legacy of Prof. Abruña's iconic *operando* spirit and will devote his life to developing *operando* TEM and X-ray methods for elucidating electrocatalytic processes.

Dedicated to my persevering mother and optimistic father

and my PhD committee

Héctor D. Abruña (Chairperson)

David A. Muller (Co-Advisor)

Francis J. DiSalvo (Committee Member)

## ACKNOWLEDGMENTS

First and foremost, I am grateful to my PhD advisor, Prof. Héctor Abruña (a.k.a Boss). I first met Prof. Abruña when he visited Prof. Zhuang's lab at Wuhan University in 2012. Astonished as a sophomore, I was too nervous to speak out and introduce myself during the 10 min when he was in student's office. At that time, joining his group at Cornell was simply "mission impossible" to me since I was worried about the financial cost even for applying to PhD programs in the U.S. In addition, the last undergraduate from WHU that joined the dreamful Dept. of Chem. at Cornell was in 2004. Why am I the chosen one? As time went by and my confidence about electrochemistry and English grew, I pushed myself out of my "comfort zone" and went on a journey, full of adventure, at Cornell in 2015. I am grateful to Boss that he didn't mind my anxiety and eyes looking down at my shoes during our first meeting one week after I arrived at Cornell. I am grateful to Boss that he didn't mind that I jumped up and down when I was told "Yes, you are in", in the kitchen, where he often drinks espresso.

During the past five years, I have absorbed knowledge, scientific maturity and more importantly the enthusiasm and optimism towards life from Boss. I am grateful, particularly as an international student, for his efforts in revising dozens of manuscripts, proposals, emails and fellowship applications. His office is always open to everyone and our meetings varied from 3 times per day to 1 time per week. I won't forget the encouragement from Boss in late midnight in his office when things didn't work as hoped. Words like "Don't let those failures get to you, or define who you are. Never doubt yourself" helped me go through the disappointments, charge myself and look forward to the great opportunities ahead. Of course, I won't forget that Boss showed me how to tie a tie, how to fix any parts of a bike and how to appreciate the great chemistry of wine. Above all, I am mostly grateful for his unreserved support, sympathy and trust for students, which set a true role model for being a mentor.

Boss introduced me to Prof. David Muller in October 2015. During our first meeting, I still remember the moment when I was struggling to explain the electron diffraction of lithium peroxide in reciprocal space from my undergraduate research. I feel truly blessed to receive weekly, if not daily, research guidance from David. The discussions with David have gradually shaped my mind from an electrochemist with intuition to more like an electron microscopist with a solid background in physics. I feel fortunate to have witnessed the development of EMPAD, in his group, during the past 5 years and appreciate the hard work behind the “Guinness world record” of the highest-resolution electron microscope. His unparalleled creativity and deep insights in physics and broad knowledge of chemistry and materials science have shown me what a true pioneer looks like and also how to effectively communicate with non-specialists out of my field. With his guidance, I will focus on the quest for a better understanding of interfacial catalysis with *operando* EC-STEM.

Much of the guidance in materials design and synthesis came from the chemical equations Prof. Francis DiSalvo (Frank) wrote on the blackboard in his office. Through discussions with Frank, I gradually realized what they meant as inorganic chemists, or better, as solid-state chemists. Modern solid-state chemistry is empowered by advanced X-ray, TEM and other characterization techniques. As Priestley Medalist, Tobin Marks once noted, “Chemists make things, that with deep knowledge and skill we create the stuff that dreams are made of”. I feel fortunate to have had the chance to sit down with Frank, to go through manuscripts, sentence by sentence, and to be cautious when claiming priority of new materials. Perhaps more importantly, I learned from Frank how to be a good lab manager and better understand human behavior from the book “Misbehaving” I borrowed from his desk. I learned from Frank how to enjoy a life-work balance and appreciate the beauty of natural environment in Ithaca (of course, many kinds of lovely and delicious fishes).

I want to thank all my amazing labmates in the Abruña group (we now have a group jacket to show off). In particular, I want to thank Yin, a synthetic master with whom we have co-authored more than 10 papers, including 2 PNAS and 5 JACS papers, and Yu-Tsun, an electron diffraction expert for my finest PhD work above all; the first *in situ* electrochemical liquid-cell 4D-STEM study. I am grateful to my many wonderful collaborators: Dong and Luxi, who introduced Abruña group to me and collaborated on NMC battery projects, which opened my eyes to commercial applications of LIBs; Rui for his contributions in nitride and MEA projects; Hongsen, Mahdi and Matej, the “Post-doc Golden Triangle” often with critical comments in group meeting; Xinyao for her help in Pt single crystals; Jeesoo for being my awesome lab, class and office mate; Zhen, Barnaby, Megan, Elliot, Yimo, Celesta, *etc.* in the Muller group as my first-class microscopy tutors; Mick and John for their great care for the electron microscopes; Xin from the Brock group with great X-ray expertise; Gary from the van Dover Group as “my diligent sputtering guy”; Profs. Suntivich and Schlom, Ding-Yuan and Hanjong for the help in MBE project; Anu from General Motors for MEA tests.

I feel proud to use my six-year research to acknowledge Profs. Li Xiao and Lin Zhuang at WHU as few PhD students would continue to collaborate with their undergraduate advisors after leaving. It was Prof. Li Xiao who provided the financial support for my PhD applications and strongly recommended me to pursue a completely new field of electron microscopy rather than follow the conservative path to study Li-S batteries after my undergraduate research in Li-Air batteries. She taught me how to perform rigorous electrochemical measurements, in person when she was a visiting scholar at Cornell in 2015. It was Prof. Lin Zhuang, a world-class electrochemist with deep insights, who guided me into the world of renewable energy materials in 2011 and initiated the fruitful collaborations on Co-Mn spinel oxides in 2017. I especially thank Qihao, Hanqing from Zhuang group at WHU for their generous help in constructing the

first operational MEA testing platform at Cornell and Yunfei for the two-year collaboration on Ni-Mn-Co alkaline fuel cells. Of course, I need to thank Zhifei from the Mallouk group at UPenn for designing the low-cost automated spray coating system. I am grateful to Prof. Deli Wang, Jing and Weiping at HUST for their catalyst samples.

Over the six-year PhD work at Cornell, I have experienced and benefited from the interdisciplinary and collaborative environment under the Center for Alkaline Based Energy Solution (CABES). We have written the 17,3000-word-long landmark Chemical Reviews with Cheyenne from the Coates group among 49 authors in total. I am fortunate to have close collaborations with Prof. Mavrikakis and his students, Roberto and Ellen. I feel joyful when talking about chemistry with Profs. Mallouk, Suntivich and Zelenay.

Life at Cornell is not just about research. Among my many wonderful friends, I want to especially thank Adnan for those encouraging words when biking, and Zhifei for chats whenever needed. They helped me survive the anxious and stressful time from May to December in 2020 when I was waiting for any post-doc offers. I spent some great time with Ting-Wei, Junteng, Srinath, Keith, Paden, Sean and Omar at Pi farm, appreciating the great chemistry of beer and wine. Weijia is my best skiing buddy, who pushed me up to the terrifying ~1500 m Whiteface peak and kept me alive. Finally, my life has been blessed with the unreserved support of my parents for my academic dream and I appreciate my sister, Jie, for staying close to my parents. She is the best.

I have distilled my research to a story of “*Operando* Methods in Electrocatalysis” through the collaborations among electrochemistry from Prof. Abruña, solid-state chemistry from Prof. DiSalvo and advanced STEM from Prof. Muller. I hope you all enjoy the journey when navigating through this thesis.

## TABLE OF CONTENTS

ABSTRACT.....	i
BIOGRAPHICAL SKETCH.....	iii
DEDICATION.....	v
ACKNOWLEDGEMENTS.....	vi
LIST OF FIGURES.....	xvii
LIST OF TABLES.....	xxiv
LIST OF ABBREVIATIONS.....	xxv
CHAPTER 1	
<b>Thesis Overview</b> .....	1
<b>Introduction</b> .....	5
1.1 A New Era of Hydrogen Energy.....	5
1.2 Development of Hydrogen Fuel Cell Technologies.....	8
1.3 Primary Challenges of Proton Exchange Membrane Fuel Cells.....	9
1.4 Alkaline Fuel Cells.....	15
1.5 ORR Electrocatalysis in Acidic Media.....	17
1.5.1 Single-Crystal ORR Electrocatalysts in Acidic Media.....	18
1.5.2 Nanoscale ORR Electrocatalysts in Acidic Media.....	32
1.6 ORR Electrocatalysis in Alkaline Media.....	35
1.6.1 Single-Crystal ORR Electrocatalysts in Alkaline Media.....	35
1.6.2 Nanoscale ORR Electrocatalysts in Alkaline Media.....	38
1.7 Analytical and <i>Operando/In Situ</i> Scanning Transmission Electron Microscopy.....	41
1.8 References.....	44

## **PART I Designing and Understanding Non-Precious ORR Electrocatalysts**

### **CHAPTER 2**

#### **Spinel Oxides as Non-Precious Oxygen Reduction Electrocatalysts**

<b>for Alkaline Fuel Cells.....</b>	<b>49</b>
2.1 Introduction.....	49
2.2 Experimental Methods.....	50
2.3 Hydrothermal Synthesis of 15 Types of Spinel Oxides.....	56
2.4 RDE Measurements of ORR Activity and CV Analysis.....	58
2.5 RRDE Measurements of ORR Selectivity.....	63
2.6 Powder XAS Structural Analysis.....	65
2.7 Atomic-Scale STEM Imaging.....	66
2.8 EELS Mapping and Valence Analysis of Single Nanoparticles.....	68
2.9 Catalysis Durability and Degradation Mechanisms.....	75
2.10 Conclusions.....	79
2.11 References.....	79

### **CHAPTER 3**

#### **Activity Enhancement of Co-Mn Spinel Oxides Guided by STEM-EELS.....**

3.1 Introduction.....	83
3.2 Fine Tuning of Spinel Oxide Surface Compositions by Aging Temperatures.....	84
3.3 STEM-EELS and XRD Studies of Chemical Compositions and Structures.....	85
3.4 RDE and MEA Measurements of MCS Catalysts.....	87
3.5 Structural and Surface Analysis of MCS Catalysts.....	88
3.6 Proposed Synergistic Reaction Mechanism.....	94
3.7 Conclusions.....	97
3.8 References.....	98

## CHAPTER 4

<b>High-Loading Composition-Tolerant Co-Mn Spinel Oxides with MEA Performance beyond 1 W/cm<sup>2</sup> in Anion Exchange Membrane Fuel Cells.....</b>	<b>99</b>
4.1 Introduction.....	99
4.2 Experimental Methods.....	102
4.3 Crystal Structure Studies of Co-Mn Oxides at Various Loadings.....	103
4.4 Porosity and Conductivity Studies of Co-Mn Oxides.....	105
4.5 RDE Measurements of Co-Mn Oxides at Various Loadings.....	107
4.6 MEA Measurements of Co-Mn Oxides at Various Loadings and Fuel Cell Test Conditions.....	108
4.7 Conclusions.....	114
4.8 References.....	114

## CHAPTER 5

<b><i>Operando</i> X-ray Absorption Spectroscopy Investigation of Synergistic Reaction Mechanism of Spinel Oxide Catalysts.....</b>	<b>118</b>
5.1 Introduction.....	118
5.2 Experimental Methods.....	119
5.3 Device Design and Methodology for <i>Operando</i> XAS measurements.....	121
5.4 <i>Operando</i> XANES of Mn-Co Oxides under Steady State.....	125
5.5 <i>Operando</i> XANES of Mn-Co Oxides under Non-Steady State.....	130
5.6 Design Trimetallic Mn-Co-Fe Oxides with Improved Durability.....	133
5.7 <i>Operando</i> XANES of Trimetallic Mn-Co-Fe Oxides under Steady State.....	143
5.8 <i>Operando</i> XANES of Trimetallic Mn-Co-Fe Oxides under Non-Steady State.....	151
5.9 Conclusions.....	155
5.10 References.....	156

## CHAPTER 6

<b>Non-Precious ORR Electrocatalysts Beyond Spinel Oxides.....</b>	<b>158</b>
6.1 Introduction.....	158
6.2 Experimental Methods.....	160
6.3 Rock-Salt-Type $\text{MnCo}_2\text{O}_3/\text{C}$ derived from $\text{MnCo}_2\text{O}_4/\text{C}$ .....	161
6.4 Porosity and Microstructure of $\text{MnCo}_2\text{O}_3/\text{C}$ .....	166
6.5 ORR Activity and Durability of $\text{MnCo}_2\text{O}_3/\text{C}$ .....	171
6.6 Conclusions of $\text{MnCo}_2\text{O}_3/\text{C}$ Work.....	174
6.7 Synthesis of a Family of Cobalt Nitrides ( $\text{Co}_2\text{N}/\text{C}$ , $\text{Co}_3\text{N}/\text{C}$ and $\text{Co}_4\text{N}/\text{C}$ ).....	176
6.8 STEM-EELS Mapping of $\text{Co}_4\text{N}/\text{C}$ with Nitride Core and Oxide Shell.....	178
6.9 Surface-Sensitive XPS Analysis of $\text{Co}_4\text{N}/\text{C}$ .....	180
6.10 ORR Activity and Durability of $\text{Co}_4\text{N}/\text{C}$ and Identification of Active Sites..	182
6.11 <i>Operando</i> XAS Studies of the Stability of Cobalt Nitrides under Oxidation Potentials.....	184
6.12 Conclusions.....	187
6.13 References.....	188

## CHAPTER 7

<b>High-Throughput Combinatorial Studies of Palladium-based Oxygen Reduction Electrocatalysts for Alkaline Fuel Cells.....</b>	<b>190</b>
7.1 Introduction.....	190
7.2 Experimental section.....	193
7.3 Magnetron Sputtering of Pd-M thin-film electrodes (M: Cu, Ni, Co, Fe, Mn)...	197
7.4 Chemical Composition and Surface Morphology of Pd-M Thin-Film Alloys...	199
7.5 Crystal Structure of Pd-Based Thin-Film Alloys.....	205

7.6 ORR Activity of Pd-Based Thin-Film Alloys.....	213
7.7 Synthesis of the Nanoparticle Form of Pd <sub>50</sub> Cu <sub>50</sub> , the Optimal Composition from Thin-Film Studies.....	219
7.8 Microstructure and Chemical Composition of Pd <sub>50</sub> Cu <sub>50</sub> Nanoparticles.....	221
7.9 ORR Activity and Durability of PdCu Nanoparticles.....	224
7.10 Conclusions.....	228
7.11 References.....	228

**PART II *Operando/In Situ* Electrochemical STEM (EC-STEM) for Mechanistic Understanding of Electrochemical Reactions at Interfaces**

CHAPTER 8

**Revealing the Atomic Ordering of Binary Intermetallics Using *In Situ* Heating STEM and XRD.....**

8.1 Introduction.....	231
8.2 Experimental Methods.....	236
8.3 <i>In Situ</i> Heating Synchrotron-Based X-ray Diffraction.....	240
8.4 <i>In Situ</i> Heating STEM Imaging.....	251
8.5 Atomic-Scale <i>Ex Situ</i> HAADF-STEM Imaging.....	255
8.6 Correlation of the Degree of Ordering to Catalyst Durability.....	256
8.7 STEM-EDX Analysis of Pt and Co Contents of Individual Pt <sub>3</sub> Co Nanoparticles as a Function of Particle Size.....	259
8.8 Activity and Durability Evaluation of Pt <sub>3</sub> Co/C in Practical MEAs.....	262
8.9 Conclusions.....	264
8.10 References.....	265

## CHAPTER 9

<b><i>Operando</i> EC-STEM to Resolve the Electrochemical Double Layer at Solid/Liquid Interfaces.....</b>	<b>270</b>
9.1 Introduction.....	270
9.2 Resolving Ionic Distributions at Charged Interfaces with Halide Probes.....	271
9.3 Resolving Ionic Distributions at Charged Interfaces with Alkali Cation Probes.....	278
9.4 Conclusions.....	279
9.5 References.....	282

## CHAPTER 10

<b>Elucidating Cathodic Corrosion Mechanisms with <i>Operando</i> Electrochemical Transmission Electron Microscopy.....</b>	<b>283</b>
10.1 Introduction.....	283
10.2 Experimental Methods.....	286
10.3 Cathodic Corrosion of Pt(111) and Au Nanocubes on poly-Pt Electrode.....	289
10.4 <i>Operando/In Situ</i> Electrochemical Liquid-Cell STEM (EC-STEM) Studies of Dynamic Structural Evolution during Cathodic Corrosion.....	297
10.5 Cathodic Corrosion for the synthesis of Au-Pt bimetallic NPs.....	311
10.6 Proposed Cathodic Corrosion Mechanisms.....	314
10.7 Conclusions.....	317
10.8 References.....	318

## CHAPTER 11

<b>Conclusions.....</b>	<b>322</b>
11.1 Summary.....	322

11.2 Future Work.....	325
11.2.1 Elucidating the ORR mechanism on MBE-grown oxides.....	325
11.2.2 Spatially resolved local crystal structures of metal oxide nanocrystals.....	329
11.2.3 MEA measurements with long-term tests in H <sub>2</sub> -Air mode.....	332
11.3 References.....	336
11.4 Publications and Patents during PhD Studies.....	337

## **APPENDIX**

A. Testing Protocols for RDE Measurements.....	340
B. Testing Protocols for MEA Measurements.....	350
C. Testing Protocols for <i>Operando/In Situ</i> Liquid Cell STEM.....	360

## LIST OF FIGURES

<b>Figure 1.1</b> Map of alternative energy storage methods.....	6
<b>Figure 1.2</b> Schematic of hydrogen energy system.....	7
<b>Figure 1.3</b> Schematic of a proton exchange membrane fuel cell.....	10
<b>Figure 1.4</b> 2018 PEMFC Stack Cost Breakdown.....	10
<b>Figure 1.5</b> Progress in lowering cost for light-duty fuel cell vehicles.....	11
<b>Figure 1.6</b> Spider map of U.S. DOE target of components in fuel cell development....	12
<b>Figure 1.7</b> Simplified degradation mechanisms of nanoparticle catalysts on carbon supports after fuel cell tests.....	13
<b>Figure 1.8</b> Comparison of PEMFC and AEMFC.....	16
<b>Figure 1.9</b> Performance enhancement of AEMFCs over the past decade.....	17
<b>Figure 1.10</b> General mechanisms proposed for the OR in acid and base.....	20
<b>Figure 1.11</b> CV profiles of Pt(111) at 50 mV/s in 0.1 M HClO <sub>4</sub> .....	22
<b>Figure 1.12</b> <i>In situ</i> Raman study of Pt single crystals in acidic media.....	23
<b>Figure 1.13</b> ORR polarization profiles of three low-index Pt single crystals.....	24
<b>Figure 1.14</b> Experimental setup for preparing single-crystal Pt with controlled terraces and steps and Unit stereographic triangle of fcc-type single crystals.....	25
<b>Figure 1.15</b> ORR activity of high-index Pt with stepped surface in acidic media.....	26
<b>Figure 1.16</b> ORR activity of stepped Pt surfaces and interfacial water structures.....	27
<b>Figure 1.17</b> ORR Activity of Pt <sub>3</sub> M with surface Pt layer.....	31
<b>Figure 1.18</b> Activity and stability of octahedral PtNi alloys.....	35
<b>Figure 1.19</b> ORR activities of single-crystal precious metals in alkaline media.....	36
<b>Figure 1.20</b> ORR activities of Pt monolayer on single-crystal substrates in base.....	36
<b>Figure 1.21</b> ORR activities of metal-containing N-doped carbon Catalysts .....	39
<b>Figure 1.22</b> Schematic and examples of STEM-EELS elemental analysis.....	42
<b>Figure 1.23</b> Schematic of <i>operando/in situ</i> S/TEM in liquid/gas phase.....	43
<b>Figure 2.1</b> Hydrothermal synthesis method of 15 types of AB <sub>2</sub> O <sub>4</sub> /C.....	51
<b>Figure 2.2</b> Color changes when a diluted NH <sub>3</sub> solution was added to the aqueous metal precursor solutions.....	51
<b>Figure 2.3</b> Powder XRD patterns of AB <sub>2</sub> O <sub>4</sub> /C.....	56
<b>Figure 2.4</b> Crystal model of Co <sub>3</sub> O <sub>4</sub> (Co <sup>II</sup> Co <sup>III</sup> O <sub>4</sub> ) with a cubic spinel structure.....	57
<b>Figure 2.5</b> ORR activity of AB <sub>2</sub> O <sub>4</sub> /C spinel electrocatalysts.....	59
<b>Figure 2.6</b> CV profiles of monometallic oxides and selected bimetallic oxides.....	61
<b>Figure 2.7</b> Quantifying charge from CV profiles of MnCo <sub>2</sub> O <sub>4</sub> /C.....	62
<b>Figure 2.8</b> Tafel plots of Pt/C, MnCo <sub>2</sub> O <sub>4</sub> /C and CoMn <sub>2</sub> O <sub>4</sub> /C.....	62
<b>Figure 2.9</b> RRDE profiles of Pt/C at a mass loading of 25 μg/cm <sup>2</sup> on GC.....	63
<b>Figure 2.10</b> ORR selectivity of CoMn <sub>2</sub> O <sub>4</sub> /C at various mass loadings.....	64
<b>Figure 2.11</b> Powder XANES spectra of spinel MnCo <sub>2</sub> O <sub>4</sub> /C and CoMn <sub>2</sub> O <sub>4</sub> /C.....	66
<b>Figure 2.12</b> HAADF-STEM images of spinel MnCo <sub>2</sub> O <sub>4</sub> /C and CoMn <sub>2</sub> O <sub>4</sub> /C.....	67
<b>Figure 2.13</b> Core-loss EELS spectra of MnCo <sub>2</sub> O <sub>4</sub> /C, CoMn <sub>2</sub> O <sub>4</sub> /C and CoFe <sub>2</sub> O <sub>4</sub> /C.....	69

<b>Figure 2.14</b>	EELS elemental mapping of MnCo <sub>2</sub> O <sub>4</sub> /C, CoMn <sub>2</sub> O <sub>4</sub> /C and CoFe <sub>2</sub> O <sub>4</sub> /C.	69
<b>Figure 2.15</b>	STEM-EELS analysis of a single-crystal MnCo <sub>2</sub> O <sub>4</sub> spinel nanoparticle.	70
<b>Figure 2.16</b>	ELNES spectra of Co and Mn oxide references.	72
<b>Figure 2.17</b>	ELNES spectra of the core-shell MnCo <sub>2</sub> O <sub>4</sub> /C.	73
<b>Figure 2.18</b>	ELNES spectra of O K-edge of Co and Mn oxide references.	75
<b>Figure 2.19</b>	Durability tests of MnCo <sub>2</sub> O <sub>4</sub> /C and CoMn <sub>2</sub> O <sub>4</sub> /C.	76
<b>Figure 2.20</b>	Quantitative TEM-EDX analysis of MnCo <sub>2</sub> O <sub>4</sub> /C and CoMn <sub>2</sub> O <sub>4</sub> /C.	77
<b>Figure 2.21</b>	EELS mapping of MnCo <sub>2</sub> O <sub>4</sub> /C after 10,000 CV cycles.	78
<b>Figure 2.22</b>	EELS mapping of CoMn <sub>2</sub> O <sub>4</sub> /C after 10,000 CV cycles.	78
<b>Figure 3.1</b>	Hydrothermal synthesis of Mn <sub>1.5</sub> Co <sub>1.5</sub> O <sub>4</sub> /C (MCS).	84
<b>Figure 3.2</b>	Correlations of ORR activities of Co <sub>1.5</sub> Mn <sub>1.5</sub> O <sub>4</sub> /C, surface compositions based on EELS and overall crystal structures based on synchrotron XRD.	85
<b>Figure 3.3</b>	Performance of Mn-Co spinel (MCS) catalysts towards the ORR.	88
<b>Figure 3.4</b>	Structural characterization of MCS catalysts.	91
<b>Figure 3.5</b>	Surface analyses of MCS catalysts.	92
<b>Figure 3.6</b>	Mechanistic analysis of MCS-catalyzed ORR.	94
<b>Figure 4.1</b>	Powder XRD patterns of MnCo <sub>2</sub> O <sub>4</sub> and CoMn <sub>2</sub> O <sub>4</sub> nanoparticles with 40, 60 and 80 wt.% metal oxide loadings.	103
<b>Figure 4.2</b>	HAADF-STEM image of MnCo <sub>2</sub> O <sub>4</sub> with 40 wt.% oxide loading.	105
<b>Figure 4.3</b>	Two-point conductivity measurements.	106
<b>Figure 4.4</b>	ORR polarization profiles of MnCo <sub>2</sub> O <sub>4</sub> and CoMn <sub>2</sub> O <sub>4</sub> .	107
<b>Figure 4.5</b>	MEA measurements of AEMFCs using Co-Mn spinel oxides.	109
<b>Figure 4.6</b>	MEA measurements of Pt/C in APEFCs.	111
<b>Figure 4.7</b>	Cross-sectioned SEM images of the catalyst coated membrane.	112
<b>Figure 4.8</b>	MEA measurements of CoMn <sub>2</sub> O <sub>4</sub> at different operating conditions.	113
<b>Figure 5.1</b>	Schematic of the <i>operando</i> XAS electrochemical cell.	121
<b>Figure 5.2</b>	<i>Operando</i> electrochemical cell for XAS experiments.	122
<b>Figure 5.3</b>	SEM image of Co <sub>1.5</sub> Mn <sub>1.5</sub> O <sub>4</sub> /C on carbon paper.	123
<b>Figure 5.4</b>	CV of Co <sub>1.5</sub> Mn <sub>1.5</sub> O <sub>4</sub> /C in the <i>operando</i> electrochemical cell.	124
<b>Figure 5.5</b>	Control Experiment for CV of catalysts with X-ray beam off/on.	124
<b>Figure 5.6</b>	<i>Operando</i> XANES of the Mn K-edge at various applied potentials.	126
<b>Figure 5.7</b>	Valence analysis of Mn K-edge at 0.4 V vs. RHE.	127
<b>Figure 5.8</b>	<i>Operando</i> XANES of the Co K-edge at various applied potentials.	129
<b>Figure 5.7</b>	Valence analysis of Mn K-edge at 0.4 V vs. RHE.	129
<b>Figure 5.10</b>	Periodic changes in the relative X-ray intensities 7722.5 eV (Co K-edge) and 6553.0 eV (Mn K-edge) as a function of the cyclic potential sweep.	131
<b>Figure 5.11</b>	XRD patterns of as-synthesized MCF cubic spinel nanoparticles.	134
<b>Figure 5.12</b>	Atomic-scale HAADF-STEM images of MCF-0.8.	136
<b>Figure 5.13</b>	EELS elemental maps of MCF-0.8.	137

<b>Figure 5.14</b> Electrocatalytic properties of as-synthesized MCF nanoparticles.....	139
<b>Figure 5.15</b> EDX spectra of MCF-0.8 before and after electrochemical cycles.....	141
<b>Figure 5.16</b> <i>Operando</i> XANES of the Mn, Co and Fe K-edges of MCF-0.8.....	145
<b>Figure 5.17</b> Valence analysis of Mn K-edge at 1.2 V vs. RHE.....	147
<b>Figure 5.18</b> <i>Operando</i> EXAFS of Mn (A) and Co (B) at various potentials.....	148
<b>Figure 5.19</b> <i>Operando</i> EXAFS of Fe at a series of the applied potential.....	150
<b>Figure 5.20</b> Periodic changes of the relative X-ray intensities ( $\ln(I_1/I_2)$ ) at 6553 eV (Mn K-edge), 7225 eV (Co K-edge) and 7131 eV (Fe K-edge).....	154
<b>Figure 6.1</b> XRD patterns of CoO/C synthesized from Co <sub>3</sub> O <sub>4</sub> under NH <sub>3</sub> .....	162
<b>Figure 6.2</b> Crystal structures of spinel-type Co <sub>3</sub> O <sub>4</sub> and rock-salt-type CoO.....	163
<b>Figure 6.3</b> XRD, STEM and BET tests of MnCo <sub>2</sub> O <sub>3</sub> /C.....	164
<b>Figure 6.4</b> EDX, EELS and XPS spectra of MnCo <sub>2</sub> O <sub>3</sub> /C.....	165
<b>Figure 6.5</b> A collection of STEM images of MnCo <sub>2</sub> O <sub>3</sub> /C nanoparticles (NPs).....	165
<b>Figure 6.6</b> BET tests of MnCo <sub>2</sub> O <sub>4</sub> and MnCo <sub>2</sub> O <sub>3</sub> without KB carbon support.....	166
<b>Figure 6.7</b> Atomic-scale HAADF-STEM image of rock-salt-type MnCo <sub>2</sub> O <sub>3</sub> /C.....	167
<b>Figure 6.8</b> STEM-EELS elemental mapping and ELNES of MnCo <sub>2</sub> O <sub>3</sub> /C.....	167
<b>Figure 6.9</b> STEM-EELS analysis of MnCo <sub>2</sub> O <sub>3</sub> /C.....	168
<b>Figure 6.10</b> ELNES spectra of MnCo <sub>2</sub> O <sub>3</sub> /C at five different regions.....	169
<b>Figure 6.11</b> ELNES spectra of Oxygen K-edge of MnCo <sub>2</sub> O <sub>3</sub> /C.....	171
<b>Figure 6.12</b> ORR polarization profiles of MnCo <sub>2</sub> O <sub>4</sub> /C, MnCo <sub>2</sub> O <sub>3</sub> /C and Pt/C.....	172
<b>Figure 6.13</b> Tafel plots of MnCo <sub>2</sub> O <sub>3</sub> /C, MnCo <sub>2</sub> O <sub>4</sub> /C and Pt/C.....	173
<b>Figure 6.14</b> ORR profiles before and after the accelerated ageing protocol.....	174
<b>Figure 6.15</b> Table of Contents of this MnCo <sub>2</sub> O <sub>3</sub> /C work with CABES logo.....	175
<b>Figure 6.16</b> Crystal structure analysis of as-synthesized Co <sub>x</sub> N/C (x = 2, 3, 4).....	177
<b>Figure 6.17</b> XRD patterns of samples treated in NH <sub>3</sub> under different temperatures.....	178
<b>Figure 6.18</b> EELS spectrum of Co <sub>4</sub> N/C.....	179
<b>Figure 6.19</b> STEM-EELS of the nitride-core and oxide-shell of Co <sub>4</sub> N/C.....	179
<b>Figure 6.20</b> XPS spectra for Co <sub>4</sub> N.....	181
<b>Figure 6.21</b> Evaluation of ORR activity of Co <sub>x</sub> N/C.....	182
<b>Figure 6.22</b> ORR polarization profiles of Co <sub>4</sub> N/C.....	183
<b>Figure 6.23</b> <i>Operando</i> XAS studies of the stability of cobalt nitrides under electrochemical conditions.....	186
<b>Figure 7.1</b> Methodology for the preparation and activity evaluation of thin-film electrodes.....	198
<b>Figure 7.2</b> Elemental quantification of Pd-Cu thin-films.....	200
<b>Figure 7.3</b> SEM images of Pd-rich Pd <sub>77</sub> Cu <sub>23</sub> and Cu-rich Pd <sub>22</sub> Cu <sub>78</sub> .....	201
<b>Figure 7.4</b> SEM image and the corresponding EDX elemental maps.....	203
<b>Figure 7.5</b> Elemental quantification of Pd-Co thin-film electrodes.....	204
<b>Figure 7.6</b> Relative atomic contents of Pd-Ni and Pd-Fe thin films.....	205
<b>Figure 7.7</b> XRD patterns of 9 Pd-Cu thin films.....	206
<b>Figure 7.8</b> Summary of XRD patterns of Pd-M alloys (M: Cu, Ni, Co and Fe).....	207
<b>Figure 7.9</b> Linear relation of calculated lattice parameters and relative Pd at.% in Pd-M thin films, following the predication of Vegard's law.....	208

<b>Figure 7.10</b>	XRD patterns of Pd-Mn thin films.....	210
<b>Figure 7.11</b>	Phase diagrams of Pd-Ni, Pd-Cu, Pd-Co and Pd-Fe.....	212
<b>Figure 7.12</b>	Phase diagrams of Pd-Mn, Pd-Cr, Pd-CV and Pd-Ti.....	212
<b>Figure 7.13</b>	ORR polarization profiles of Pd-Cu and Pd-Co thin films.....	214
<b>Figure 7.14</b>	CV profiles of 3 types of Pd-Cu films.....	215
<b>Figure 7.15</b>	CV profiles of Pd-rich Pd-Co films and Co-rich Pd-Co films.....	216
<b>Figure 7.16</b>	ORR polarization profiles of Pd-Fe and Pd-Ni thin films.....	217
<b>Figure 7.17</b>	CV profiles of Pd-Fe and Pd-Ni films.....	218
<b>Figure 7.18</b>	Synthesis of Pd/C and PdCu/C using Pd and Cu chloride or nitrate.....	219
<b>Figure 7.19</b>	XRD patterns of PdCu and Pd nanoparticles.....	220
<b>Figure 7.20</b>	XRD patterns of a variety of mixed phased of Pd-Cu disordered alloys...	221
<b>Figure 7.21</b>	S/TEM images of PdCu nanoparticles supported on carbon.....	223
<b>Figure 7.22</b>	STEM-EELS image of a PdCu nanoparticle.....	224
<b>Figure 7.23</b>	ORR activity of PdCu/C and Pd/C.....	225
<b>Figure 7.24</b>	Pourbaix diagram of Cu at 25°C.....	226
<b>Figure 7.25</b>	Durability tests of PdCu/C for 100,000 potential cycles.....	227
<b>Figure 7.26</b>	CO stripping measurements of PdCu/C before/after 100,000 cycles....	227
<b>Figure 8.1</b>	Schematic of the home-made device for the <i>in situ</i> heating XRD.....	242
<b>Figure 8.2</b>	Temperature calibration of the <i>in situ</i> heating stage (Si substrate).....	242
<b>Figure 8.3</b>	<i>In situ</i> heating XRD of Pt <sub>3</sub> Co/C annealed at various temperatures.....	244
<b>Figure 8.4</b>	Powder XRD patterns of Pt <sub>3</sub> Co/C annealed at various temperatures.....	245
<b>Figure 8.5</b>	Measured d-spacings of Pt <sub>3</sub> Co/C (A) after 2 h annealing at various temperatures and (B) at different annealing times at 750 °C.....	247
<b>Figure 8.6</b>	Simulation results for the SROP and LROP as a function of temperature for bulk and spherical NPs with 2.9 and 5.2 nm.....	249
<b>Figure 8.7</b>	<i>In situ</i> heating XRD patterns of Pt <sub>3</sub> Co/C.....	250
<b>Figure 8.8</b>	XRD patterns of Pt <sub>3</sub> Co after annealing at 715 °C for 2 h, and after cooling down to room temperature.....	251
<b>Figure 8.9</b>	<i>In situ</i> heating STEM enabling tracking of the morphological changes of Pt <sub>3</sub> Co/C annealed at 750°C.....	252
<b>Figure 8.10</b>	Atomic-scale <i>ex situ</i> HAADF-STEM images of Pt <sub>3</sub> Co/C.....	256
<b>Figure 8.11</b>	Calculated ECSA, mass-specific activity (MA) and surface-specific activity (SA) at 0.9V vs. RHE of Pt <sub>3</sub> Co/C before and after stability tests.....	258
<b>Figure 8.12</b>	Quantitative EDX Analysis of Pt and Co contents of individual Pt <sub>3</sub> Co NPs as a function of particle size.....	260
<b>Figure 8.13</b>	Theoretical Calculation of Pt/Co mole ratio from a given particle size and shell thickness and comparison to STEM-EDX results.....	261
<b>Figure 8.14</b>	MEA performance comparison of disordered and annealed Pt <sub>3</sub> Co/C before and after stability testing.....	263
<b>Figure 9.1</b>	(A) Potential profile through the electrochemical double layer (B) Schematics of ionic distributions at charged interfaces in non-adsorbing electrolytes.....	271
<b>Figure 9.2</b>	STEM images of 1mM NaBr near a carbon WE under applied potentials..	274

<b>Figure 9.3</b> STEM images of Au nanocubes in 1mM NaBr near a carbon WE under applied potentials.....	274
<b>Figure 9.4</b> STEM images of 1mM NaI near a polycrystalline Pt working electrode (WE) under applied potentials.....	276
<b>Figure 9.5</b> STEM images showing beam-induced damage in 1mM CsI without applied potentials.....	276
<b>Figure 9.6</b> STEM images showing beam-induced damage in 1mM CsBr without applied potentials.....	276
<b>Figure 9.7</b> STEM images of a thin-liquid 1 mM CsClO <sub>4</sub> near poly-Pt WE after triggering a H <sub>2</sub> bubble by scanning potentials to -1.2 V vs. Pt.....	277
<b>Figure 9.8</b> STEM images of a thin-liquid 1 mM CsClO <sub>4</sub> near Au nanocubes attached to poly-Pt WE after triggering a H <sub>2</sub> bubble.....	280
<b>Figure 9.9.</b> STEM images of thin liquid/gas interfaces after generating H <sub>2</sub> bubble....	281
<b>Figure 10.1.</b> Cathodic corrosion of Pt(111) and Au nanocubes on poly-Pt electrode..	290
<b>Figure 10.2.</b> CV profiles of (111), (110) and (100) planes of single-crystal Pt.....	291
<b>Figure 10.3.</b> CV profiles of Pt(111) in Ar-sat. 0.1M HClO <sub>4</sub> before and after cathodic corrosion in 0.1 M NaOH .....	292
<b>Figure 10.4.</b> SEM images of Pt(111) before and after cathodic corrosion.....	293
<b>Figure 10.5.</b> CV profiles of Pt(111) in Ar-sat. 0.1M HClO <sub>4</sub> before and after cathodic corrosion in 0.05 M CsClO <sub>4</sub> . .....	293
<b>Figure 10.6 (a)</b> Charge integral of the PtO <sub>x</sub> reduction peaks and AuO <sub>x</sub> reduction peaks of Au cubes on Pt film after cathodic corrosion. ....	296
<b>Figure 10.7.</b> <i>Operando/in situ</i> electrochemical liquid-cell STEM (EC-STEM) studies of cathodic corrosion.....	299
<b>Figure 10.8.</b> Potential calibration of the reference electrode of Electrochemical liquid-cell chips.....	300
<b>Figure 10.9.</b> STEM images of Pt working electrode (WE) in thin liquid.....	301
<b>Figure 10.10.</b> CV profiles of Au cubes on the Pt WE in 1 mM CsClO <sub>4</sub> .....	302
<b>Figure 10.11.</b> <i>Operando</i> EC-STEM studies of dynamic morphological changes during cathodic corrosion.....	303
<b>Figure 10.12.</b> STEM images of a snapshot of the cathodic corrosion of Au cubes (~100 nm reactants) and the generation and repulsion of numerous small NPs (20-50 nm)...	305
<b>Figure 10.13.</b> <i>In situ</i> scanning electron nanodiffraction (SEND) of reacted Au nanocubes and Au-Pt NPs in thin liquid. ....	307
<b>Figure 10.14.</b> SEND analysis of nanoparticles after the cathodic corrosion of Au nanocubes on Pt film in CsClO <sub>4</sub> at -3 V vs. RHE. ....	308
<b>Figure 10.15.</b> <i>Ex situ</i> STEM-EDX mapping and quantitative analysis in H <sub>2</sub> gas cell..	309
<b>Figure 10.16</b> <i>Ex situ</i> STEM-EELS analysis of Au-Pt alloy NPs generated from Au cubes on the Pt WE after cathodic corrosion reaction in the H <sub>2</sub> gas cell.....	310
<b>Figure 10.17</b> <i>Ex situ</i> STEM-EELS analysis of Au-Pt alloy NPs generated from Au cubes on the Pt WE after cathodic corrosion reaction in the H <sub>2</sub> dry cell.....	310
<b>Figure 10.18</b> Cathodic corrosion for the synthesis of Au-Pt bimetallic NPs.....	312

<b>Figure 10.19.</b> CV profiles of Au and Pt wires in Ar-sat. 0.1 M HClO <sub>4</sub> at 50 mV/s before and after cathodic corrosion in 10 M KOH with an AC square-wave potential.....	313
<b>Figure 10.20</b> Schematic of proposed cathodic corrosion mechanisms.....	315
<b>Figure 10.21</b> Phase diagram of Au and Pt.....	315
<b>Figure 11.1</b> Customized RDE holder for MBE-grown single-crystal oxides.....	326
<b>Figure 11.2</b> ORR activity and stability of various Co-doped Fe <sub>3</sub> O <sub>4</sub> (100) and LaNiO <sub>3</sub> (100) single crystals grown by molecular beam epitaxy.....	327
<b>Figure 11.3</b> ORR activity of LaNiO <sub>3</sub> , LaMnO <sub>3</sub> , LaCoO <sub>3</sub> nanoparticles.....	328
<b>Figure 11.4</b> Proposed structures of layered epitaxial LaMO <sub>3</sub> films.....	329
<b>Figure 11.5</b> Preliminary lattice map from NBED of MnCo <sub>2</sub> O <sub>4</sub> NPs using EMPAD...	331
<b>Figure 11.8</b> Timeline of the progress of MEA studies at Cornell.....	332
<b>Figure 11.9</b> MEA performance of Pt and Mn-Co spinel as cathode catalysts.....	333
<b>Figure 11.10</b> MEA performance of a completely non-precious AEMFC with Ni@CN <sub>x</sub> anode and Mn-Co spinel cathode.....	334
<b>Figure A.1</b> RDE measurements of Pt/C and Co <sub>4</sub> N/C in alkaline media.....	342
<b>Figure A.2</b> CV and RDE measurements of Pt/C with Nafion or QAPPT ionomers and different catalyst-to-ionomer ratios.....	343
<b>Figure A.3</b> Three-electrode RDE setup.....	345
<b>Figure A.4</b> Potentials of various reference electrodes.....	346
<b>Figure A.5</b> ORR profiles of Pt/C in 1M KOH and the definition of half-wave potential.....	348
<b>Figure B.1</b> Schematic of MEA components.....	351
<b>Figure B.2</b> Home-made automated air spray system modified from a 3D printer.....	353
<b>Figure B.3</b> I-V and I-P curves of four MEA trials.....	353
<b>Figure B.4</b> CCM with AEM (4 cm <sup>2</sup> ) and MEA setup.....	354
<b>Figure B.5</b> Open circuit voltage and cell temperature as a function of time in MEA...	356
<b>Figure B.6</b> Cell performance with initial break-in procedure.....	357
<b>Figure B.7</b> Performance loss break-down in an early study of PEMFCs.....	359
<b>Figure C.1</b> Protochips open cell with electrochemical chip in 0.1 M HClO <sub>4</sub> .....	361
<b>Figure C.2</b> CV profiles of bare carbon WE and Pt/C on chip in the open cell.....	362
<b>Figure C.3</b> (A) <i>In Situ</i> liquid-cell TEM setup in F-20 STEM.....	364
<b>Figure C.4</b> Relative chip positions in TEM and the summary of chip dimensions.....	365

## LIST OF TABLES

<b>Table 4.1</b> Literature survey on performance of APEFC/AEFMCs .....	101
<b>Table 4.2</b> PPD summary of MnCo <sub>2</sub> O <sub>4</sub> /C with different oxide loadings.....	110
<b>Table 4.2</b> PPD summary of CoMn <sub>2</sub> O <sub>4</sub> /C with different oxide loadings.....	110
<b>Table 5.1</b> EDX quantitative analysis of MCF_0.8 catalysts.....	142
<b>Table 5.2</b> More accurate EDX quantitative analysis of MCF_0.8 catalysts before and after electrochemical cycles after considering the overlap between Mn K $\beta$ and Fe K $\alpha$ and between Fe K $\beta$ and Co K $\alpha$ .....	143
<b>Table 6.1</b> Literature Summary of metal nitrides and oxynitrides as ORR catalysts for alkaline fuel cells.....	183
<b>Table 7.1</b> Sputtering power of Pd, 3d metal and Ti guns.....	193
<b>Table 7.2</b> Summary of lattice parameters of Pd and 3d metals.....	209
<b>Table 9.1</b> Literature survey of ordered nanoparticle catalysts.....	234
<b>Table A.1</b> ECSA, E <sub>1/2</sub> , MA and SA of Pt/C with Nafion and QAPPT ionomers with different catalyst to ionomer ratios.....	344
<b>Table A.2.</b> Summary of benchmark MA and SA of Pt/C from RDE tests in acidic and alkaline media.....	349

## LIST OF ABBREVIATIONS

AEMFC, alkaline/anion exchange membrane fuel cell  
AST, accelerated stability tests  
APEFC, alkaline polymer electrolyte fuel cell  
BET, Brunauer–Emmett–Teller  
BF, bright field  
BOL, beginning-of-life  
CCM, catalyst coated membrane  
CE, counter electrode  
CV, cyclic voltammetry  
DFT, density functional theory  
DOE, Department of Energy  
 $E_{1/2}$ , half-wave potential  
ECSA, electrochemical surface area  
EC-STEM, electrochemical scanning transmission electron microscopy  
EDL, electrochemical double layer  
EDX, energy-dispersive X-ray spectroscopy  
EELS, electron energy loss spectroscopy  
ELNES, electron energy-loss near-edge structure  
EOL, end-of-life  
EMPAD, electron microscope pixel array detector  
EXAFS, extended X-ray absorption fine structure  
FCC, face-centered cubic  
FCV, fuel cell powered vehicle  
HAADF, high-angle annular dark-field  
HOR, hydrogen oxidation reaction  
HSC, high surface area (carbon)  
HR-TEM, high-resolution transmission electron microscopy  
 $I_d$ , diffusion limiting current density  
 $I_k$ , kinetic current density  
ICP-AES, inductively coupled plasma atomic emission spectroscopy  
GDE, gas diffusion electrode  
LCF, linear combination fitting  
LCPL, linear combination power law equation  
LROP, long-range order parameter  
LCPL, linear combination of power laws  
MA, mass-specific activity  
MBE, molecular beam epitaxy  
MCF, Mn-promoting/doping cobalt ferrite  
MCS, Mn-Co spinel  
MD, molecular dynamics (simulation)  
MEA, membrane electrode assembly  
MOF, metal-organic-framework  
NBED, nanobeam electron diffraction

N-C or CN<sub>x</sub>, nitrogen-doped carbon  
OER, oxygen evolution reaction  
ORR, oxygen reduction reaction  
ODPT, order-disorder phase transition  
PAFC, phosphoric acid fuel cell  
PCA, principal component analysis  
PCET, proton-coupled electron transfer (process)  
PEMFC, proton exchange membrane fuel cell  
PFSA, perfluorosulfonic acid  
PGM, precious-group-metal  
PPD, peak power density  
PSD, particle size distribution  
QAPPT, quaternary ammonium polypiperidine  
RHE, reversible hydrogen electrode  
RDE, rotating disk electrode  
RRDE, rotating ring disk electrode  
RE, reference electrode  
SA, area-specific activity  
SAED, selected area electron diffraction  
SOFC, solid oxide fuel cell  
SROP, short-range order parameter  
SEM, scanning electron microscopy  
S/TEM, scanning/transmission electron microscopy  
SSA, specific surface area  
UHV, ultrahigh vacuum  
WE, working electrode  
XAS, X-ray absorption spectroscopy  
XRD, X-ray diffraction  
XPS, X-ray photoelectron spectroscopy  
M-N-C, Metal-containing nitrogen-doped carbon  
XANES, X-ray absorption near edge structure  
ZIF, zeolitic imidazolate framework

## CHAPTER 1

### Thesis Overview

This thesis focuses on the design and understanding of non-precious ORR electrocatalysts for alkaline fuel cells, in particular, 3d metal oxides. We prepared 15 different  $AB_2O_4/C$  spinel nanoparticles with well-controlled octahedral morphology and particle sizes through a facile hydrothermal synthesis (A: Mn, Fe, Co, Ni, and Cu, and B: Mn, Fe, and Co) ([Chapter 2](#)). The three most active ORR electrocatalysts were  $MnCo_2O_4/C$ ,  $CoMn_2O_4/C$ , and  $CoFe_2O_4/C$ . The most active,  $MnCo_2O_4/C$ , was shown to have a unique Co-Mn core-shell structure. Electron energy loss spectroscopy (EELS) probed the heterogeneous electronic structure at the single-nanoparticle level, and indicated that the Co in the core is predominantly  $Co^{2.7+}$  while in the shell, it is mainly  $Co^{2+}$ . Mn-Co spinel oxides achieved a benchmark peak power density (PPD) of 1.2  $W/cm^2$  at 2.5  $A/cm^2$  in membrane electrode assembly (MEA) measurements in  $H_2-O_2$  mode at 80 °C, which is comparable to that of state-of-the-art Pt/C ( $\sim 1.5 W/cm^2$ ) and the highest MEA performance for non-precious ORR catalysts compared to reported values to date ([Chapters 3 and 4](#)).

The superior ORR activity of Mn-Co spinel oxides, relative to  $Mn_3O_4/C$  and  $Co_3O_4/C$ , suggested an underlying synergistic mechanism between Mn and Co. We developed an *operando* XAS method, with a home-made electrochemical cell, which enabled the tracking of Co and Mn electronic structures with a 3mV potential resolution. Valences changed simultaneously/synchronously and exhibited periodic patterns that tracked the cyclic potential sweeps, providing compelling evidence for the synergistic reaction mechanism, i.e. Co and Mn serving as co-active sites for the ORR ([Chapter 5](#)).

With additional comprehensive examination of Mn-Co catalysts using *in situ* FTIR, XPS analysis, DFT and MD simulations, we were able to identify that Mn prefers to bind O<sub>2</sub> while Co prefers to bind and activate H<sub>2</sub>O, which may explain that Mn-Co spinels even outperform Pt/C cathodes under a more realistic lower relative humidity (e.g. 50% RH) conditions ([Chapter 3](#)). Aiming for not only active but also durable ORR electrocatalysts, we developed Mn-Co-Fe (MCF) trimetallic spinel oxides with enhanced catalyst durability. *Operando* XAS studies showed the periodic conversion between Mn(III, IV)/Co(III) and Mn(II, III)/Co(II) as well as the essentially constant oxidation state of Fe during the CV. This suggested that Mn and Co serve as the synergistic co-active sites to catalyze the ORR, ostensibly resulting in the high activity, while Fe works to maintain the integrity of the spinel structure ([Chapter 5](#)).

Moving beyond spinel oxides, we developed rock-salt-type MnCo<sub>2</sub>O<sub>3</sub>/C through mild reduction of MnCo<sub>2</sub>O<sub>4</sub>/C under ammonia at controlled temperatures, which showed enhanced ORR activity towards the ORR ([Chapter 6](#)). In-depth electron microscopic and spectroscopic investigations indicated that MnCo<sub>2</sub>O<sub>3</sub>/C predominantly has Mn(II) and Co(II) and can be written as MnO(CoO)<sub>2</sub>/C and charge transfer between Co and Mn occurs locally. In an effort to overcome the intrinsic low conductivity of metal oxide nanoparticles, we designed a novel family of cobalt nitrides, among which Co<sub>4</sub>N/C exhibited an 8-fold improvement in mass activity at 0.85 V, when compared to Co<sub>3</sub>O<sub>4</sub>/C. The superior performance was ascribed to the formation of a conductive nitride core surrounded by a naturally formed thin oxide shell (~2 nm). The conductive nitride core effectively mitigated the low conductivity of the metal oxide, and the thin oxide shell on the surface provided active sites for the ORR ([Chapter 6](#)).

The strategies to design non-Pt PGM catalysts, in particular Pd-based alloys, are highly valuable since Pd is the only transition metal with ORR activity comparable to Pt in alkaline media. Pd-based alloys can diversify the catalyst candidates for AEMFC applications demanding very high current and power densities, instead of solely relying on Pt-based ORR electrocatalysts as in PEMFCs. We developed a combinatorial approach, using magnetron sputtering, to prepare ~40 types of Pd-M (M=Fe, Co, Ni and Cu) thin-film electrodes with well-defined compositions and structures as a fast method for assessing their ORR activity (Chapter 7). Pd<sub>50</sub>Cu<sub>50</sub> was identified as the most promising composition for the ORR and employed as a target for nanoparticle synthesis. PdCu/C exhibited a mass-specific activity 3 times that of Pd/C and a remarkable durability with 13 mV negative shifts in the half-wave potential after 100,000 cycles.

The second part of this thesis focuses on the *operando* studies of electrochemical interfaces. In Chapter 8, we present a comprehensive quantitative study of the dynamic order-disorder phase transition of Pt<sub>3</sub>Co nanoparticle intermetallic ORR fuel cell electrocatalysts, during post-synthesis annealing. We employed *in situ* synchrotron-based X-ray diffraction (XRD) and *in situ* STEM to study the phase transition and morphological and structural changes during real-time annealing. *In situ* XRD revealed the impact of annealing/cooling conditions on the degree of ordering, particle size and lattice strain. *In situ* heating STEM enabled visualization of nanoparticle migration and growth and quantified size distribution and surface areas of nanoparticles using an automated algorithm. We find that a higher degree of ordering leads to more active and durable electrocatalysts. The annealed Pt<sub>3</sub>Co/C with an optimal degree of ordering exhibited significantly enhanced durability, relative to the disordered counterpart, in

practical MEA measurements.

In [Chapter 9](#), this thesis presents preliminary progress on employing *operando* EC-STEM to tackle a fundamental challenge in electrochemistry; resolving the electrochemical double layer at electrode/electrolyte interfaces with an emphasis on nanocrystal electrode surfaces. Criteria for chemical probes and *operando* EC-STEM methodology have been discussed in detail. Among five candidates, NaBr, NaI and CsClO<sub>4</sub>, with heavy anions or cations, exhibited no significant changes in ionic distribution at charged interfaces, which is possible due to the inherently low electrolyte concentration (mM-level) to maintain a reasonably wide EDL (> 10 nm). Those other candidates, CsBr and CsI, with both heavy cations and anions, were shown to experience beam-induced damage at relatively low beam doses. While other *operando* methods may provide additional opportunities, the investigation of the EDL at nm-scale led to the microscopic observation of cathodic corrosion ([Chapter 10](#)). The highly kinetically driven corrosion process is evidenced by the successive anisotropic transition from stable Pt(111) bulk single-crystal surfaces evolving to energetically less stable (100) and (110) steps. Furthermore, the cathodic corrosion of Au nanocubes on bulk Pt electrodes led to the unexpected formation of thermodynamically immiscible Au-Pt alloy nanoparticles.

Finally, [Chapter 11](#) concludes this thesis and highlights several research projects as future work.

## Introduction

### 1.1 A New Era of Hydrogen Energy

One of the grand challenges of our time is how to meet the increasing global energy needs in a sustainable and environmentally responsible way. While the use of fossil fuels has greatly improved our standard of living, it has also caused detrimental environmental consequences associated with their extraction and combustion (pollution and carbon emissions causing global warming).<sup>1</sup> Shifting the energy landscape from fossil fuels to renewable energy technologies will play a key role in tackling complex environmental and economic issues. One of the most promising approach to lower carbon emission is to develop the hydrogen energy.

Hydrogen gas has one of the highest energy densities (120 MJ/kg) of any fuel, making it a clean and efficient energy carrier to store and distribute significant amounts of energy (Fig. 1.1).<sup>2</sup> Hydrogen is mostly produced from fossil fuels, which often raises concerns about energy security and reliability of the supply. Traditionally, reforming gas from natural gas/coal provides the majority of hydrogen for chemical industries. Hydrogen is also generated as a large quantities as a byproduct during chemical production, such as in the “chlor-alkali process” (electrolysis of salt water to produce chlorine, hydrogen gas and sodium hydroxide). Thus, any analysis of hydrogen as clean fuel must consider the way in which it is produced.

Water electrolysis is a cost-competitive technology to produce hydrogen at large scale with potentially zero carbon emissions when integrated with renewable electricity. Water electrolysis can use excess renewable electricity to generate clean hydrogen, which shows the potential to balance the mismatch between intermittent wind and solar

energy and stable requirements in existing electricity grids. For example, 1-2 MW proton-exchange membrane (PEM) water electrolyzers have been commercially available from Proton OnSite.<sup>2,3</sup> With a size of a shipping container (12 m long), they can serve as building blocks to meet the energy storage demands of MW or even GW-scale wind and solar power plants.

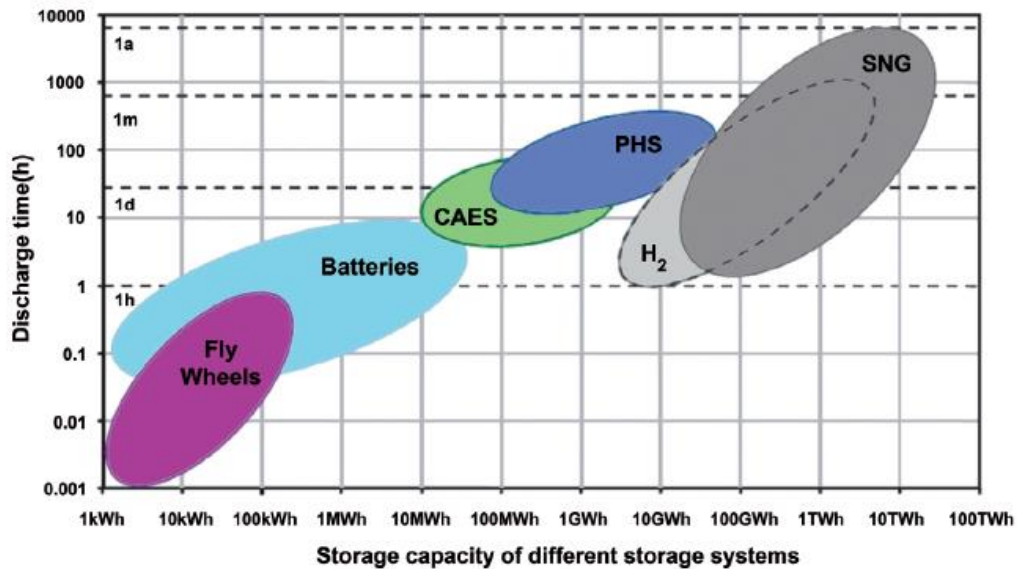


**Figure 1.1** Map of alternative energy storage methods. CAES = compressed air energy storage, PHS = pumped hydroelectric storage, SNG = substitute natural gas. Reproduced from Ref. 2. Copyright 2013 Elsevier.

Hydrogen can be easily stored using existing technologies in pressurized tanks, liquefied at low temperatures or stored in porous or hydride materials. The renewably generated hydrogen can serve as a versatile and scalable energy carrier, bridging power generation and applications in transportation and industry (Fig. 1.2).<sup>4</sup> In particular, hydrogen can be utilized to power fuel cell vehicles (FCVs), which can dramatically reduce the use of fossil fuels in transportation. At a larger scale, hydrogen can tremendously lower carbon emissions tremendously in industries, such as power generation, ammonia production plants, oil refining industries, semiconductor

processing, etc.

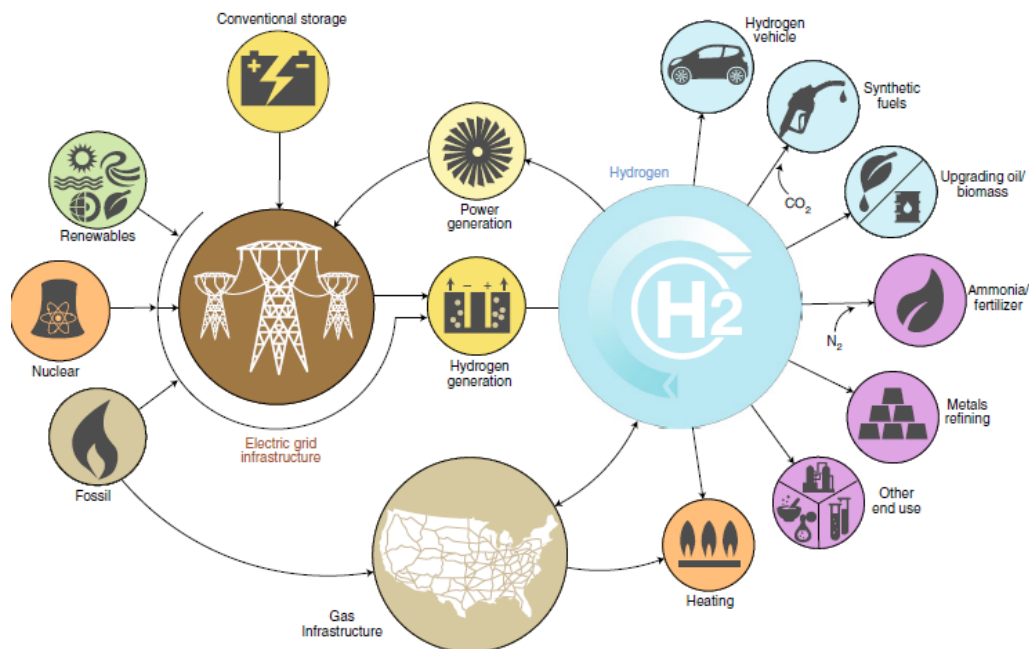


**Figure 1.2** Schematic of Hydrogen Energy System. Hydrogen has the potential in the energy system, as a clean, efficient energy carrier and is comparable to electrical grid and natural gas systems. Reproduced from Ref. 4. Copyright 2012 ECS.

While there have been significant advances in production, storage and utilization of hydrogen, they are accompanied by challenging problems yet to be resolved. The price of  $H_2$  produced from water electrolyzers is about \$5/kg, significantly higher than that from reforming gas (~\$2/kg). In addition, the cost of precious metal catalysts (Ru or Ir) for the oxygen evolution reaction (OER) increases the overall cost of PEM electrolyzers. One solution is to develop alkaline exchange membrane water electrolyzer, which would enable the use of non-precious OER catalysts (e.g., Ni-Fe). In order to develop large-scale cost-competitive hydrogen energy infrastructure, we need to engage partners among scientific research in academia, technological developments in industry, and policy support from government leaders. With all of those efforts combined, a new era of hydrogen energy is on the horizon.

## **1.2 Development of Hydrogen Fuel Cell Technologies**

Renewably generated hydrogen can be most efficiently used for power generation in a hydrogen fuel cell. Fuel cells are electrochemical devices that convert chemical energy directly into electricity with zero carbon emission and water as the only product. Hydrogen fuel cells are not limited by the Carnot cycle and can deliver a practical energy conversion efficiency of 65% or higher, which is more than twice as high as the efficiency of internal combustion engines (~ 25%) and many other power systems.

Although fuel cells were first demonstrated by Sir William Grove in 1839, they were not practically useful until a century later when alkaline fuel cells (AFCs) were invented by Francis Thomas Bacon in 1932. A 5 kW AFC stack, using Ni to overcome electrode corrosion in concentrated KOH, was constructed in 1959 with an operating efficiency of 60%. Since then, AFCs have been used by NASA, in the mid-1960s, as power generators for Apollo missions and Space Shuttle programs, using pure hydrogen and oxygen. However, when alkaline fuel cells are operated with air for daily automotive applications, KOH solutions react with CO<sub>2</sub> and produce carbonates, which can precipitate and block the porous electrodes and lower the ionic conductivity of the electrolyte, causing a detrimental performance drop. Proton exchange membrane fuel cells (PEMFCs) were developed later by William Grubb and Leonard Niedrach at General Electric in the 1960s and used briefly for the NASA Gemini program. However, water-management issues in PEMs made them less reliable and, therefore, less competitive than AFCs. AFCs were thus used by NASA as the primary power system through the 1990s. Several critical innovations, particularly Nafion membranes discovered by Walther Grot at DuPont, low Pt loadings in Pt-based alloys and thin-film

membrane electrode assemblies (MEAs), dramatically lowered the cost and improved the reliability of PEMFCs.<sup>6</sup> The compact configuration of PEMFCs enables a small cell volume, light weight and CO<sub>2</sub>-tolerance offer PEMFCs great advantages over AFCs; especially for EV applications.

PEMFCs inherently require a significant amount of scarce and expensive Pt-based electrocatalysts to facilitate the sluggish oxygen reduction reaction (ORR) while only a minimal amount of Pt is required to catalyze the fast HOR in acid. As an alternative, anion exchange membrane fuel cells (AEMFCs) have drawn increasing attention since they enable the use of non-precious group metal (PGM) electrocatalysts and AEMs can effectively mitigate the carbonate precipitation issue of KOH solutions. Non-precious ORR electrocatalysts, such as 3d metals or metal oxides, perovskites and metal-containing N-doped carbon, are attractive for their low cost, promising activity, and durability. However, AEMFCs also face another challenge; the rate of the HOR on Pt is two orders of magnitude slower in alkaline media than in acidic media, leading to a significantly higher Pt loading requirement at the anode. Thus, low-Pt and eventually non-PGM HOR electrocatalysts must be developed in order to enable the implementation of high-performance alkaline fuel cells at large scale and low cost.

### **1.3 Primary Challenges of Proton Exchange Membrane Fuel Cells**

[Fig. 1.3](#) shows a schematic of a PEMFC in which H<sub>2</sub> is oxidized at the anode and O<sub>2</sub> in air is reduced at the cathode with protons and water transferring through the PEM. After decades of development, PEMFCs have been established as a commercially viable technology for powering electric vehicles (EVs).<sup>5-7</sup> Since 2015, Toyota, General Motors, and other automobile manufacturers, have begun to supply the market with

limited quantities of fuel cell EV (global FCV production in 2019 was ~10,000 units).

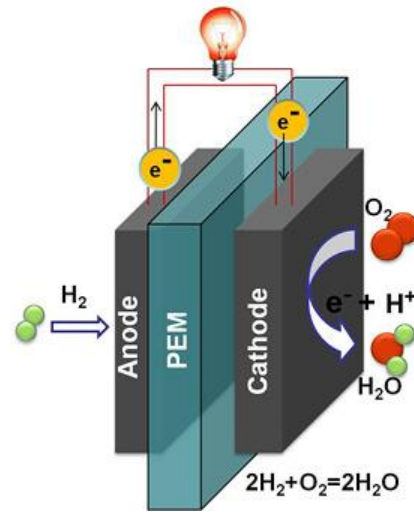


**Figure 1.3** Schematic of a proton exchange membrane fuel cell. Hydrogen at the anode and oxygen from air at the cathode react and produce electricity, water and some heat.

However, PEMFCs rely on a large amount of expensive Pt-based electrocatalysts to facilitate the sluggish oxygen reduction reaction (ORR) at the cathode. The catalyst cost is projected to be the largest single component (up to 40%) of the total cost of a PEMFC stack.<sup>7</sup> (Fig. 1.4)

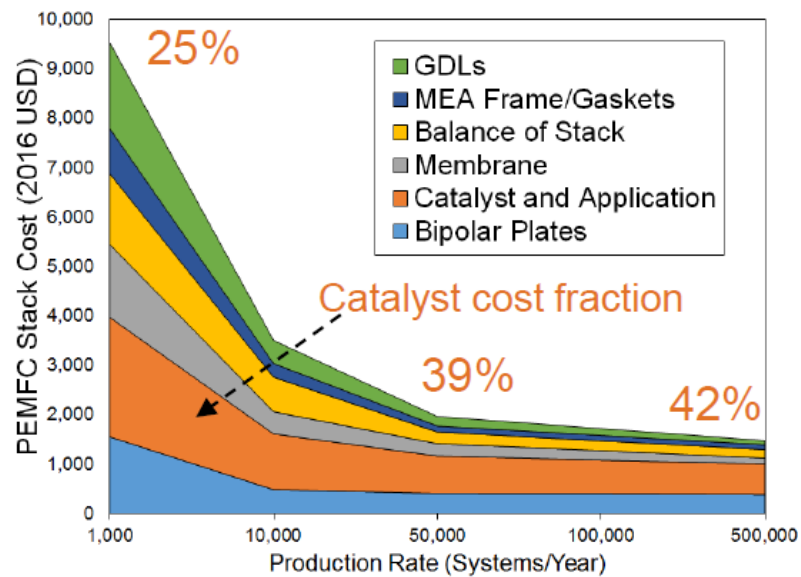


**Figure 1.4** 2018 PEMFC Stack Cost Breakdown. PEMFC stack cost as a function of production rate. Data reproduced from Ref. 7, 2019 U.S. DOE Fuel Cell R&D Overview.

Given the high price and scarcity of Pt, lowering its loading without compromising catalytic activity or durability, has remained as the central question of most electrocatalyst research for PEMFCs. Pt loading at the cathode has dropped significantly from 0.4 to about 0.1 mg<sub>Pt</sub>/cm<sup>2</sup> over the past decade. For example, Pt<sub>3</sub>Co catalysts, recently developed at Cornell and tested at GM, demonstrated a PEMFC performance of mass activity of >0.44 A/mg<sub>Pt</sub> and a power density of >8 kW/g<sub>Pt</sub> with Pt loadings of 0.1 and 0.025 mg/cm<sup>2</sup> in the cathode and anode, respectively).<sup>8</sup> This would project the use of 8-10 g Pt per light-duty vehicle (80 kW power), similar to that in catalytic converters in gasoline powered vehicles today, and a system cost of around \$50/kW<sub>net</sub>. The ultimate goal is to achieve \$30/kW<sub>net</sub> for light-duty vehicles at a large production scale (Fig 1.5).

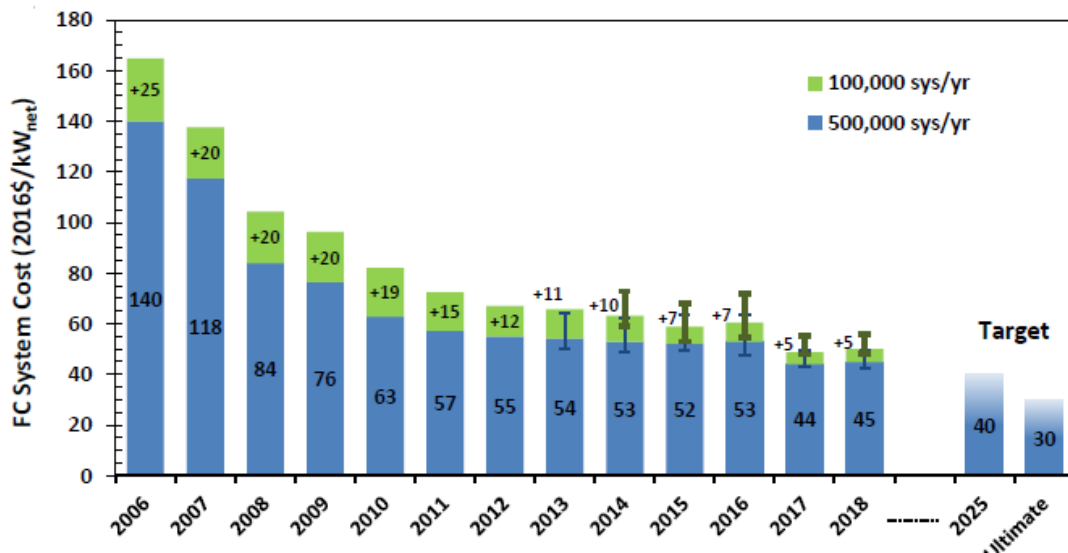


**Figure 1.5** Progress in lowering cost for light-duty fuel cell vehicles. The key driving force has been lowering the Pt loading at the oxygen cathode in PEMFCs. Reproduced from Ref. 7.

Improving catalyst durability and lowering catalyst cost are two of DOE's primary challenges for the commercialization of PEMFCs (Fig. 1.6). While there have been a variety of promising Pt-based ORR catalysts reported, few of them are able to deliver the required long-term durability in MEA measurements. The preliminary durability target, recommended by the U.S DOE, is less than 10% loss in mass activity (MA) at 0.9 V after accelerated stability tests (AST) of 30,000 trapezoidal voltage cycles between 0.6 and 0.95 V. Our ordered Pt<sub>3</sub>Co/C was able to achieve a 5% loss in MA under such test conditions.<sup>8</sup> However there is still a long way to go to meet the ambitious durability target of <10% performance loss after 8,000 h of automotive drive cycles set by the DOE.

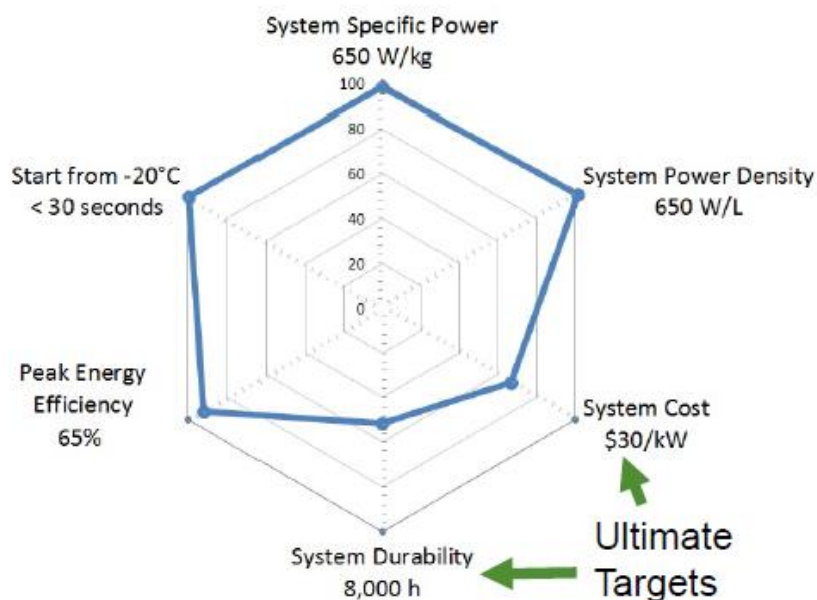


**Figure 1.6** Spider map of U.S. DOE target of multiple components in fuel cell developments. Durability and cost are the primary challenges to fuel cell commercialization. Reproduced from Ref. 7.

In order to improve catalyst durability, we need to gain a comprehensive understanding of the structure/composition of catalysts, catalyst-support interactions

and the impact of fuel cell operating conditions. Most of the Pt or Pt-based catalysts are in nanoparticle (NP) form and dispersed on porous carbon supports, so as to maximize the number of active sites on the surface. Such a configuration can be kinetically unstable under aggressive fuel cell conditions with the catalyst experiencing degradation in the form of loss of electrochemical surface area (ECSA) and thus overall performance. Common degradation mechanisms include, but are not limited to, platinum dissolution, Ostwald ripening, particle coalescence/agglomeration, particle detachment and corrosion of the carbon support (Fig. 1.7).<sup>9</sup>

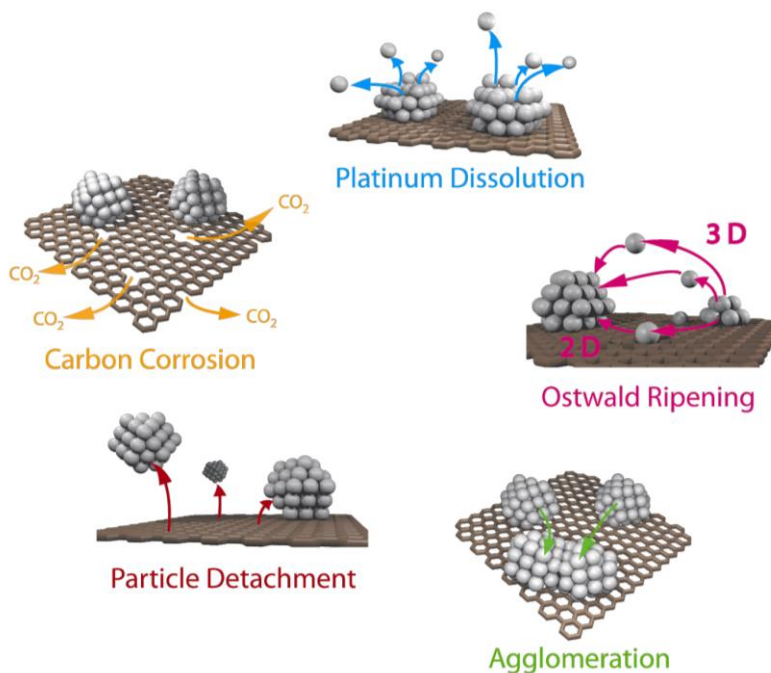


**Figure 1.7** Simplified degradation mechanisms of nanoparticle catalysts on carbon supports after fuel cell tests. Reproduced from Ref. 9. Copyright 2014 Beilstein Institute for the Advancement of Chemical Sciences.

Platinum can dissolve and redeposit in the membrane during PEMFC operation due to the reduction with  $H_2$  gas at the anode.<sup>10,11</sup> Small Pt-based NPs are particularly vulnerable at high cell voltages and often dissolve and redeposit on larger Pt-based NPs,

a process often referred to as Ostwald ripening.<sup>12,13</sup> Another degradation mechanism, particle coalescence/agglomeration, can take place during high-temperature annealing processes during synthesis (Chapter 8) or electrochemical tests.<sup>14,15</sup> Two nearby Pt NPs can migrate and merge into one larger NP, causing a loss of ECSA. Sometimes, particle detachment can happen in which entire Pt NPs detach from the carbon supports due to a weakening particle-support interactions.<sup>16,17</sup>

Carbon corrosion has played an important role (yet often neglected) in catalyst degradation mechanisms and can indirectly lower the ECSA of Pt-based NPs. Carbon corrosion can be unfortunately catalyzed by existing Pt-based NPs and cause detrimental structural changes in both supports and catalysts.<sup>18,19</sup> Carbon corrosion weakens the catalyst-support interaction and facilitate particle movement, coalescence and eventually detachment. It results in the loss of the micro- and mesoporous structure of carbon and hinders the mass transport of reactants.<sup>20</sup> Carbon corrodes in an environment of high relative humidity and oxygen at high cell voltages and forms more hydrophilic oxygenated functional groups, which may cause flooding and slow down the transport of oxygen to the catalyst surface.<sup>14</sup> In some cases, carbon oxidative corrosion can generate carbon monoxide and poison Pt active sites.

Finding alternatives to carbon is challenging since few materials can provide similar electronic conductivity, porosity, high surface areas and chemical stability in strong acidic media under oxidizing potentials. To mitigate carbon corrosion and enhance carbon-catalyst interactions, non-carbon materials, such as nitrides, carbides, and oxides of early transitional metals (Ti, V, W), have been reported to show promising resistance to corrosion under fuel cell operating conditions.<sup>9</sup> Despite promising reports of

enhanced durability, these non-carbon materials will need to provide porous structures to support highly dispersed small Pt-based NPs, in order to deliver comparable activity to catalysts with carbon supports before any serious consideration in practical fuel cell applications.

Although our present knowledge of catalyst degradation has focused on Pt-based NPs in acid, the strategies described here have proved to be useful for a variety of different electrocatalysts. In the following chapters, metal oxides, nitrides, Pd-based catalysts in alkaline media have shown different levels of activity and stability depending on the structures and compositions of the catalysts and applied durability test protocols.

#### **1.4 Alkaline Fuel Cells**

In comparison to PEMFCs, which primarily depend on Pt-based electrocatalysts, alkaline fuel cells have drawn increasing attention because they can enable the use of non-precious metal electrocatalysts. Non-precious catalysts, such as 3d metals or metal oxides, perovskites and metal-containing N-doped carbon, are attractive for their low cost, promising activity and durability. The recent development of anion exchange membranes (AEM) with high ionic conductivity and stability, revived the aging alkaline fuel cell landscape (Fig. 1.8). Various naming schemes have been employed to describe alkaline fuel cell technologies, such as anion exchange membrane fuel cells (AEMFCs), alkaline anion exchange membrane fuel cells (AAEMFCs), alkaline membrane fuel cells (AMFCs), alkaline polymer electrolyte fuel cells (APEFCs) and hydroxide exchange membrane fuel cells (HEMFCs). In this review, the term, AEMFCs, was chosen to be parallel to PEMFCs and convey the possibility to employ both hydroxide and carbonate conducting devices.

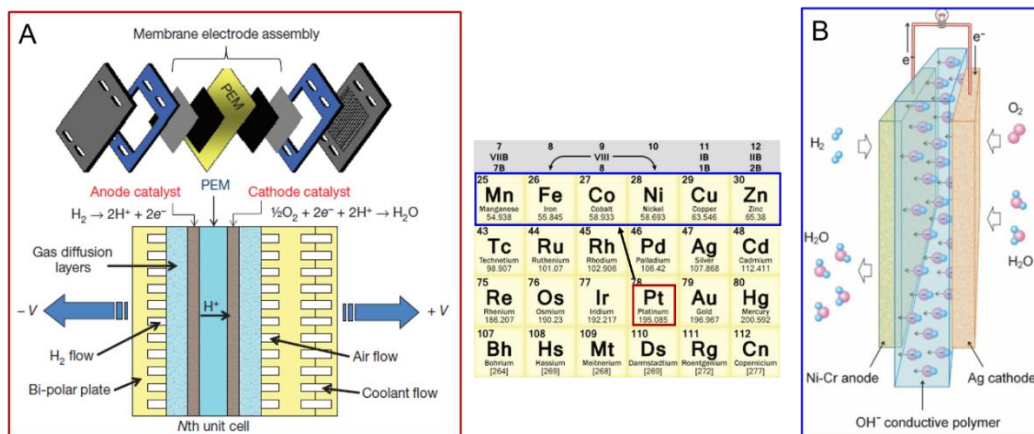


**Figure 1.8** Comparison of PEMFC (A) and AEMFC (B). PEMFC predominantly use Pt-based catalysts while AEMFCs enable the use of low-cost 3d metal catalysts. (A) is reproduced from Ref. 5 Copyright 2012 Springer Nature. (B) is reproduced from 21 Copyright 2008 NAS.

The first MEA performance of an AEMFC was reported by Zhuang et al to have a peak power density of only  $50 \text{ mW/cm}^2$  in 2008,<sup>21</sup> using a Ag cathode, Ni-Cr anode and a quaternary ammonium polysulphone (QAPS) membrane (Fig. 1.9A). After 10-years of continuous development in this community, we have recently achieved an MEA performance of  $1.2 \text{ W/cm}^2$  using a non-precious Co-Mn spinel oxide cathode, Pt-Ru anode and a quaternary ammonium polypiperidine (QAPPT) membrane (Fig. 1.9B, details in Chapter 5). The >20-fold performance enhancement arises, in part, from key advances in developing highly conductive and durable alkaline/anion exchange membranes (AEMs)/ionomers, non-precious ORR/HOR electrocatalysts, and optimization of MEA fabrication and testing protocols. AEMFCs can now achieve a comparable initial performance, using non-precious ORR catalysts, to state-of-the-art PEMFCs using Pt-based catalysts.

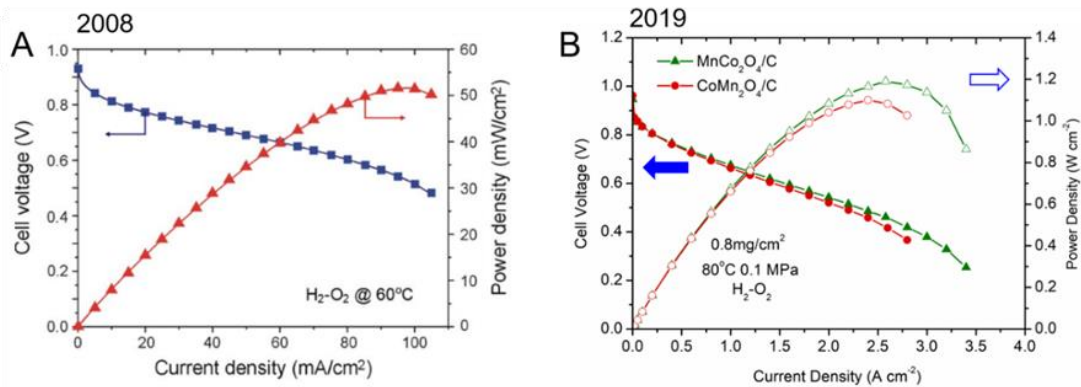


**Figure 1.9** Performance enhancement of AEMFCs over the past decade. (A) MEA results using a Ag cathode (1mg/cm<sup>2</sup>), a Ni-Cr anode (Ni loading: 5mg/cm<sup>2</sup>) and a QAPS membrane.<sup>21</sup> (B) MEA results using a Co-Mn spinel oxide cathode (oxide loading: 0.8 mg/cm<sup>2</sup>), a Pt-Ru anode (Pt loading, 0.25 mg/cm<sup>2</sup>) and a QAPPT membrane. (A) is reproduced from <sup>21</sup> Copyright 2018 NAS.

Practical FCEVs necessitate achieving not only a high initial performance, but also long-term durability during MEA operation in air. While non-precious ORR catalysts will bring new possibilities to fuel cell technologies, it is pivotal to assess the stability of non-precious catalysts and AEMs in high pH environments during fuel cell operation. Deconvolving the stability of catalysts and AEMs can be challenging given that catalysts can generate hydrogen peroxide which can damage membranes while the degraded membrane can partially block active catalytic sites. Since there was no mobile OH<sup>-</sup> anions in AEMs, the impact of CO<sub>2</sub> on AEMFCs is much less than in traditional AFCs. However, CO<sub>2</sub> in air can still noticeably decrease the AEMFC performance and this is an active area to study.

### 1.5 ORR Electrocatalysis in Acidic Media

The oxygen reduction reaction (ORR) at the cathode has a thermodynamic potential of 1.23 V (vs. RHE), however, even the most active monometallic catalyst, Pt, exhibits an overpotential of about 300 mV. Thus, the catalyst development of fuel cells has

primarily focused on the oxygen cathode. This section starts with a fundamental understanding of the ORR mainly using Pt single crystals and then highlights strategies for designing nanoparticle catalysts.

### 1.5.1 Single-Crystal ORR Electrocatalysts in Acidic Media

General ORR mechanisms in acid and base are summarized in [Fig. 1.10](#). Early studies of ORR mechanisms focused on acidic media, in part motivated by the development of PEMFCs. Early studies often used sulfuric or perchlorate acids since they are easier to purify than phosphoric acid. In acidic environments,  $O_2$  can be either reduced completely to  $H_2O$  via a  $4e^-$  process or partially to  $H_2O_2$  via a  $2e^-$  process.<sup>22</sup> Both processes often occur concomitantly as competing reactions and determine the catalyst selectivity. The undesirably formed peroxide results in a lower energy density and can degrade the polymer membrane in fuel cells. The first elemental step involves the adsorption of molecular  $O_2$  ( $O_2^*$ , reaction 1a) on the catalyst surface ([Fig. 1.10](#)). Traditionally, the adsorption energy of  $O_2$  or  $O$  ( $\Delta G_O$ ) has been proposed as the preliminary descriptor to explain the volcano-type correlation of ORR activity for different metal surfaces.<sup>23</sup> An intermediate  $\Delta G_O$  is expected to result in an optimal ORR activity, based on the Sabatier principle, and the scaling relationships between  $\Delta G_O$  and  $\Delta G_{OH}$ , since too weak oxygen adsorption impedes the kinetics of the first step, while too strong an oxygen adsorption hinders the later removal of OH species. However, one should keep in mind that the volcano plots cannot predict the potential-dependent reaction rate, RDSs or the significant effects of the electrolyte environment. In order to elucidate the complex nature of ORR mechanisms, it is highly desirable to couple spectroscopic and electrochemical studies.

Adsorbed  $O_2^*$ , generated in step (a), can be converted into  $HO_2^*$  (superoxide) via three different path ways: (b) a concerted proton-coupled electron transfer process (PCET); (c-d): a decoupled electron transfer process forming  $O_2^{\cdot-}$  (anion radical) followed by a fast protonation; (j, i): a fast surface chemical reaction with coadsorbed  $H_2O^*$  generating another  $*OH$  followed by a fast irreversible electron transfer process ( $C_s^{fast}E_1^{irrev}$ ).<sup>24</sup>  $HO_2^*$  is the central ORR intermediate in acidic media with a soluble nature and short lifetime. It has remained elusive until the very recent development of *in situ* surface-enhanced vibrational spectroscopy (Fig. 1.12). The subsequent reactions of  $HO_2^*$  split at a bifurcation point: (e-g) a chemical process to  $*OH$  and  $O^*$  followed by the conversion of  $O^*$  to  $*OH$ ; (f-h) a PCET process to  $H_2O_2$  (peroxide) followed by the O-O breaking process to form two  $*OH$ . The final step is an irreversible PCET process of  $*OH$  and conversion to  $H_2O$ . Among those multiple O-containing species,  $O_2^{\cdot-}$ ,  $HO_2^*$  and  $H_2O_2^*$  have the potential to diffuse into solution and establish an ad/desorption equilibrium with the corresponding soluble species (k, l and m). In particular,  $HO_2$  can disproportionate into  $H_2O_2$  and  $O_2$  (n), and  $H_2O_2$  can go through a similar process to produce  $H_2O$  and  $O_2$  (o). Neither process involves electron transfer and thus will cause a loss of faradaic efficiency in the overall ORR.

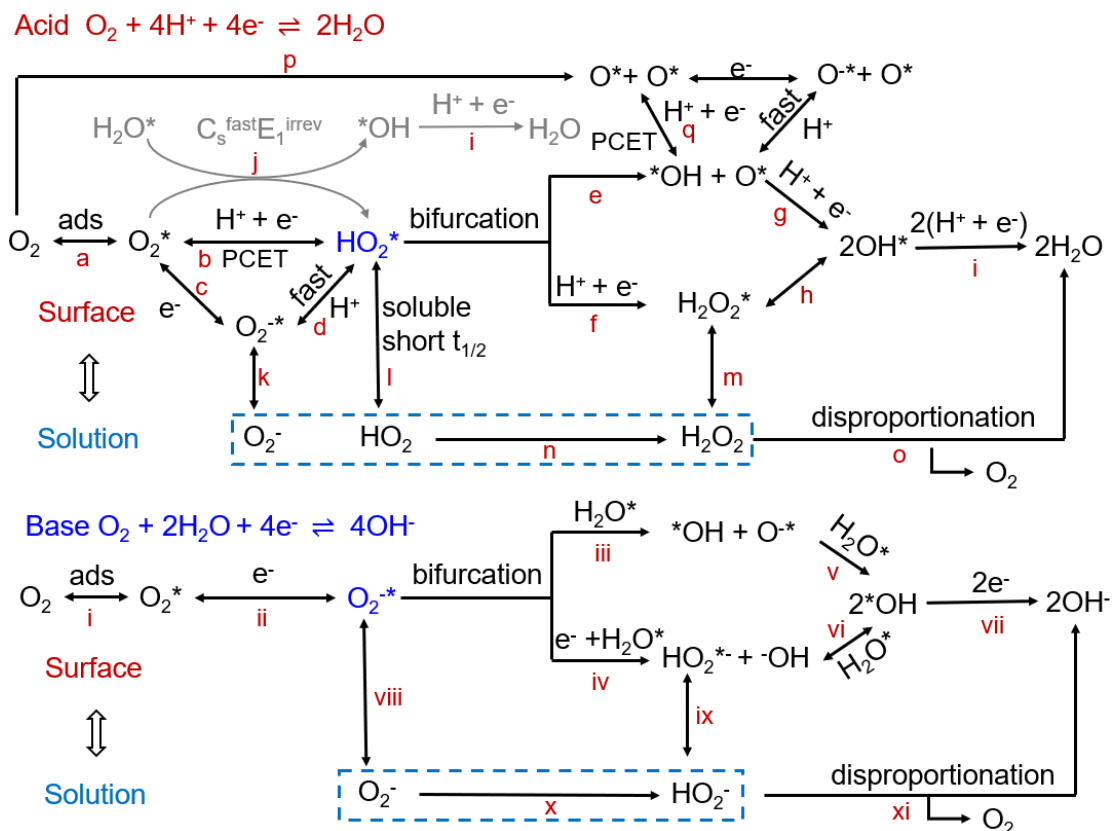


**Figure 1.10** General mechanisms proposed for the oxygen reduction reaction (ORR) in acid and base. Reaction pathways have been established based on extensive studies on Pt surfaces and may be applicable for other types of catalysts. A superscript \* by an intermediate indicates a reaction intermediate adsorbed on the electrocatalytic surface.  $C_s^{fast}E_1^{irrev}$  in acid represents a fast surface chemical reaction preceding an irreversible one-electron transfer process. PCET stands for proton-coupled electron transfer process.  $H_2O$  serves as the proton donor in alkaline media. Reaction pathways originating from step “a” and “p” are the associative and dissociative pathways of the ORR, respectively. Details of the ORR mechanisms can be found in our recent *Chemical Reviews*, “Electrocatalysis in Alkaline Media and Alkaline Membrane Based Energy Technologies”.

Although the ORR mechanism in base is not as well understood as in acid, similar reaction pathways have been proposed and are summarized in [Figure 1.10](#) (lower part). In proton-deficient alkaline environments,  $O_2$  is reduced to  $OH^-$  via a  $4e^-$  process or to  $HO_2^-$  via a  $2e^-$  process. It is important to note that  $H_2O$  is the dominant proton donor for the PCET in base while  $H^+$  ( $H_3O^+$ ) is the dominant proton donor in acidic media.

Equally importantly,  $\text{H}_2\text{O}$  is a reactant in base while  $\text{H}_2\text{O}$  is a reaction product in acid, which leads to a fundamental difference in water management in AEMFCs vs. PEMFCs. In contrast to acidic environments,  $\text{O}_2^{*\cdot}$  (superoxide anion radical) and  $\text{HO}_2^-$  (superoxide anion) are the dominant species in base, considering that the pKa values of  $\text{HO}_2$  and  $\text{H}_2\text{O}_2$  are 4.7 and 11.6, respectively. In weak base (pH=8~11), a significant amount of  $\text{H}_2\text{O}_2$  will co-exist with  $\text{HO}_2^-$ .  $\text{O}_2^{*\cdot}$  can go through a similar bifurcation process to form  $^*\text{OH}$  by either chemical (iii, v) or electrochemical processes (iv, vi). During the ORR, the interfacial pH can be dramatically different from the bulk pH in weak acid (pH = 3~6) or base (pH = 8~11) without sufficient buffer capacity, since  $\text{H}^+$  is constantly consumed or  $\text{OH}^-$  is constantly produced. The interfacial pH can also be well controlled to be close to the bulk pH value with buffer solutions with weak or no specific adsorption of anions such as fluoride to reliably study the effect of pH on the ORR activity of Pt.<sup>25</sup>

The coverage of oxygen-containing species has been proposed to play an important role in the ORR mechanism. CV profiles of Pt reveals the growth process of adsorbed oxygen-containing species,  $\text{OOH}_{\text{ads}}$ ,  $\text{OH}_{\text{ads}}$ ,  $\text{O}_{\text{ads}}$ ,  $\text{H}_2\text{O}_{\text{ads}}$  and  $\text{H}_2\text{O}_{2\text{ads}}$  (Fig. 1.11). In the CV profile of Pt(111), hydrogen adsorption ( $\text{H}_{\text{ads}}$ ) is responsible for pseudo-capacitive current between 0.05 and 0.35 V (region I) while the formation of  $\text{OH}_{\text{ads}}$  and  $\text{O}_{\text{ads}}$  occurs at potentials of ~0.6-0.8 and 0.8-1.15 V (regions II and III), respectively. Initially, at potentials of ~0.6-0.8 V, a stable water layer ( $\text{H}_2\text{O}_{\text{ads}}$ ) converts into a  $\text{H}_2\text{O}_{\text{ads}}/\text{OH}_{\text{ads}}$  mixed layer with a total surface coverage equal to  $2/3(\theta_{\text{H}_2\text{O}} + \theta_{\text{OH}})$ .<sup>22</sup> The symmetrical “butterfly” feature in region II suggests a fast and reversible OH adsorption. At potentials higher than 0.8V,  $\text{OH}_{\text{ads}}$  slowly converts into  $\text{O}_{\text{ads}}$  and the surface is covered

with  $\text{H}_2\text{O}_{\text{ads}}/\text{OH}_{\text{ads}}/\text{O}_{\text{ads}}$  mixed layer. At potentials higher than 1.15V,  $\text{O}_{\text{ads}}$  converts into Pt oxide species and destroys the well-ordered Pt(111) surface.

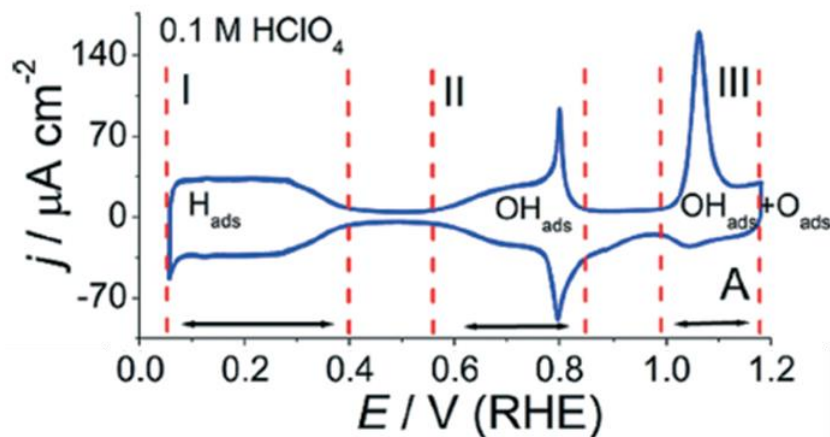


**Figure 1.11** CV profiles of Pt(111) at 50 mV/s in 0.1 M  $\text{HClO}_4$ . Reproduced from Ref. 22. Copyright 2014 RSC.

In early studies, Adzic and Markovic proposed the reduction of  $\text{OH}_{\text{ads}}$  and  $\text{O}_{\text{ads}}$  as the main bottleneck of the ORR mechanism, since  $\text{OH}_{\text{ads}}$  can block active sites for adsorption of  $\text{O}_2$  and other intermediates.<sup>26</sup> However, Feliu et al. studied a variety of low-index and stepped Pt single crystal surfaces and found no clear correlation between the ORR activity and a OH coverage descriptor, the coverage of O-containing species coverage calculated from the integral charges from CVs.<sup>22</sup> Besides of the coverage of O-containing species, the nature of adsorbed species, interfacial water structure and electrode surface charge may significantly impact electrocatalytic activity.

Spectroscopic evidence of reaction intermediates can provide valuable information to identify the key structural factors and rate-determining steps. Recently, Li and Feliu et al. reported on an *in situ* surface-enhanced Raman study of Pt single crystals in  $\text{HClO}_4$ . It provided clear evidence of  $\text{OOH}$  adsorbed on Pt(111) and  $\text{OH}$  adsorbed on Pt(100) and (110) surfaces (Fig. 1.12).<sup>27</sup> DFT calculations supported that  $\text{OOH}^*$  dissociation on

Pt(111) has a larger energy barrier than on Pt(100) and thus it is more stable as a reaction intermediate to emerge in Raman spectra. They further examined the reaction intermediates on high-index stepped Pt. Pt(211) and (311), with (111) terraces/(100) steps and (100) terraces/(111) steps, showed the co-existence of both OH\* and OOH\*, which is consistent with the co-existence of (100) and (111) but with a weaker interaction of OOH\* on stepped surfaces, relative to Pt(111).<sup>28</sup>

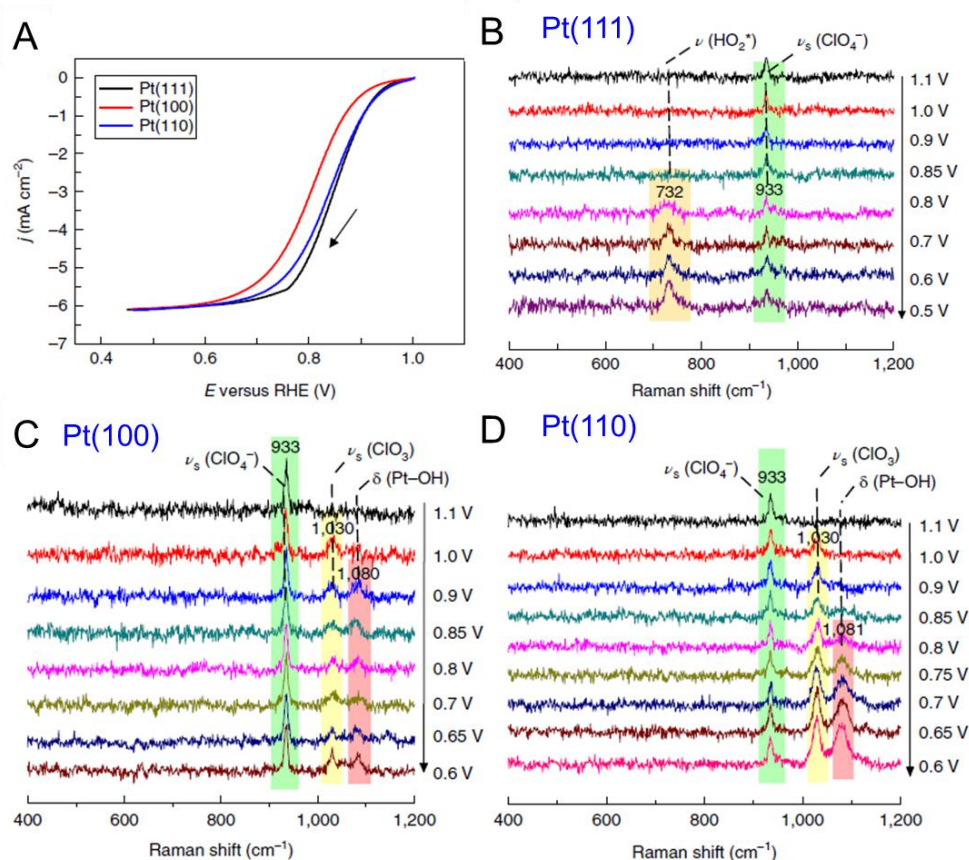


**Figure 1.12** *In situ* Raman study of Pt single crystals in acidic media. (A) ORR polarization profiles of three basal-plane Pt single crystals in O<sub>2</sub>-sat. 0.1M HClO<sub>4</sub> at 1600 rpm and 50 mV/s. (B-D) *In situ* Raman spectra of Pt (111), (100) and (110), respectively, at applied potentials from 1.1 to 0.6 V vs. RHE. Reproduced from 27. Copyright 2019 Springer Nature.

Pt single crystals, prepared by the flame annealing technique (Clavilier method)<sup>29</sup>

and regulating the cut angle,<sup>30</sup> have profoundly shaped the atomic and molecular-level understanding of electrochemical reaction mechanisms, especially the ORR. In nonadsorbing acid, such as HClO<sub>4</sub>, Markvoic et al. reported that the ORR activities of low-index Pt single crystals increased in the order of Pt(100) < Pt(111) ≈ Pt(110) (Fig. 1.13A).<sup>31</sup> In adsorbing acid, such as H<sub>2</sub>SO<sub>4</sub>, ORR activities increased in the opposite order, Pt(111) ≪ Pt(100) < Pt(110), which was due to the specific adsorption of SO<sub>4</sub><sup>2-</sup>/HSO<sub>4</sub><sup>2-</sup> with a strongly inhibitory effect on Pt(111) (Fig. 1.13B).<sup>32</sup> Overall, the three low-index planes of Pt showed lower ORR activity in H<sub>2</sub>SO<sub>4</sub> than in HClO<sub>4</sub>. Additionally, Hoshi et al. reported that the ORR activity of low-index Pd single crystals followed the order of Pd(110) < Pd(111) < Pd(100), which is opposite to Pt in HClO<sub>4</sub>.<sup>33</sup>

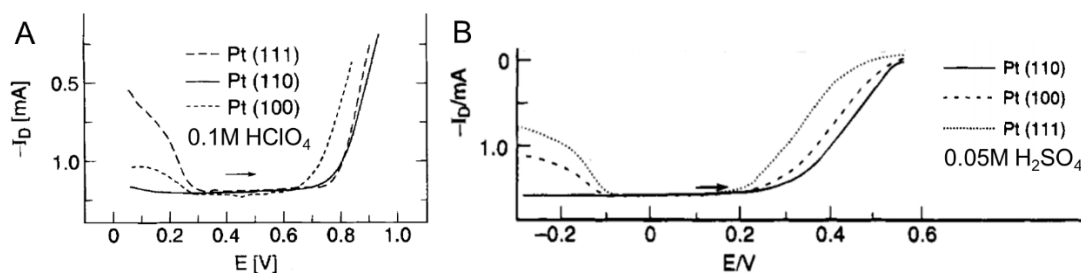


**Figure 1.13** (A) ORR polarization profiles of three low-index Pt single crystals in O<sub>2</sub>-sat. 0.1 M HClO<sub>4</sub> at 900 rpm and 50 mV/s. (B) ORR profiles of Pt in O<sub>2</sub>-sat. 0.05 M H<sub>2</sub>SO<sub>4</sub> at 1600 rpm and 50 mV/s. Reproduced from Refs. 31 and 32. Copyright 1997 ECS and 1995 ACS.

In order to extrapolate these results obtained in low-index basal planes to realistic nanoparticle catalysts, the surface of which often have steps and defects, it is important to study high-index Pt with tunable step density, which can be precisely controlled by orienting and cutting low-index Pt (Fig. 1.14).<sup>29</sup>

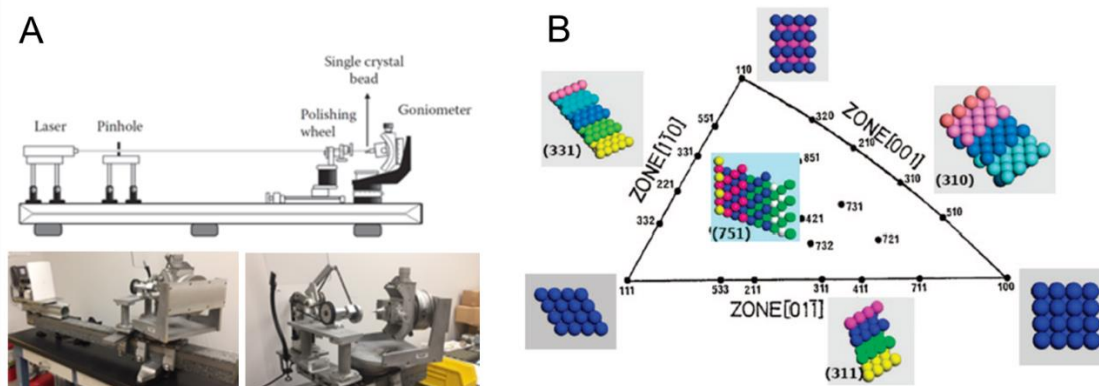


**Figure 1.14** (A) Experimental setup for preparing single-crystal Pt with controlled terraces and steps. (B) Unit stereographic triangle of fcc-type single crystals.

Feliu et al. have systematically studied single-crystal Pt with (111) terraces/(100) steps (noted as  $[n(111 \times 100)]$ ) and (100) terraces/(111) steps (noted as  $[n(100 \times 111)]$ ) (Fig. 1.15A).<sup>34</sup> Both types of stepped Pt surfaces in either HClO<sub>4</sub> or H<sub>2</sub>SO<sub>4</sub> exhibited higher activity at higher step densities. Pt(211) showed the highest activity among stepped Pt with (111) terraces and (100) steps, which was due to the highest step density ((211) or (422) =  $[3(111) \times (100)]$ ). Pt(15,13,13) had lowest step density ( $[14(111) \times (100)]$ ) and thus lowest activity. Similarly, Pt (311) with its highest step density ( $2(100) \times (111)$ ) showed the highest activity among stepped Pt with (100) terraces and (111) steps.

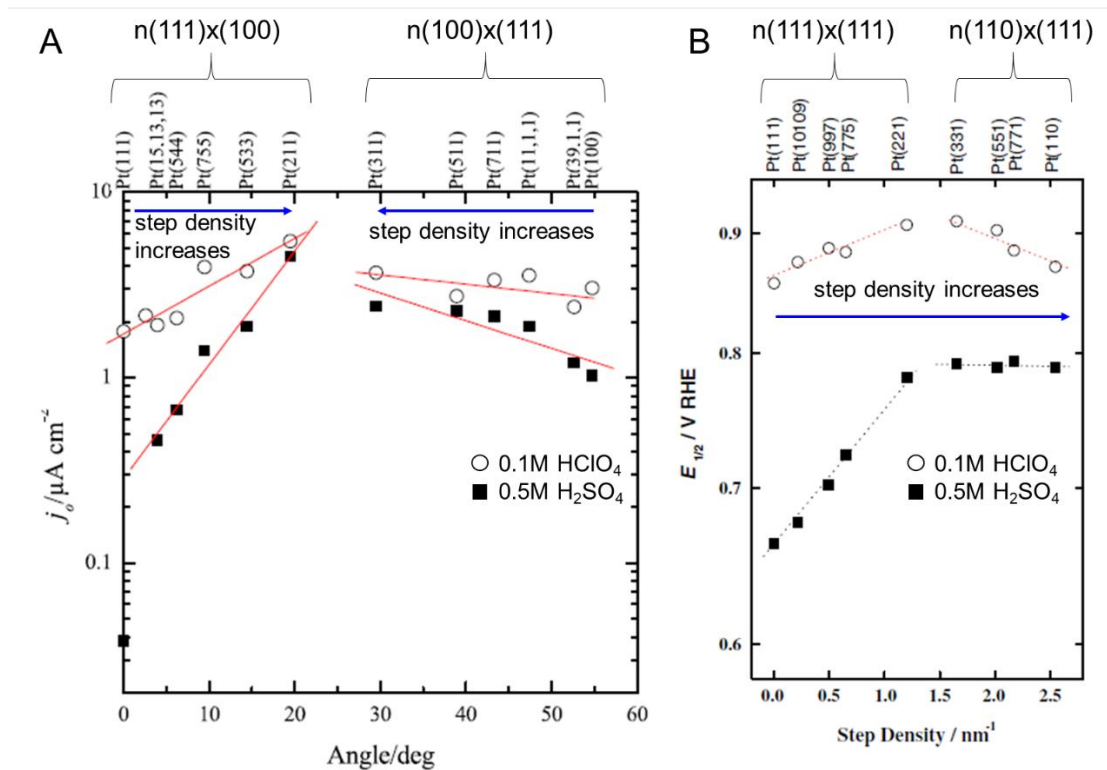


**Figure 1.15** ORR activity of high-index Pt with stepped surface in acidic media. (A) Plot of exchange current density,  $j_0$ , versus the angle of the surface with respect to the Pt(111) surface.<sup>30</sup> (B) Plot of half-wave potential,  $E_{1/2}$ , versus step density.<sup>34</sup>

High-index Pt with (111) steps and (111) and (110) terraces are shown in Fig. 1.15B.<sup>34,35</sup> In H<sub>2</sub>SO<sub>4</sub>, stepped Pt[n(111)×(111)] exhibited an increased activity as the step density increased from Pt(111) to Pt(221). In contrast, the activity of stepped Pt[n(110)×(111)] showed no change in activity as the step density increased from Pt(331) to Pt(110). This unexpected result was ascribed to the fact that one [110] terrace naturally has two atoms in the (111) terrace and one in the (111) step, so that Pt[n(110)×(111)] can be regarded as a mono/bi-atomic (111) terraces separated by (111) steps. Thus, there is no room for bisulfate to form ordered adsorption layers and thus has no blocking effect towards O<sub>2</sub> adsorption, which explains why the activity of Pt[n(110)×(111)] has no structure dependence. In HClO<sub>4</sub>, Pt (221) and (331) have

medium step density and stepped structures of  $[4(111)\times(111)]$  and  $[2(110)\times(111)]$ , respectively, which showed higher ORR activity than either Pt(111) or Pt(110). This was due to the combined effects of both increasing step density (a positive factor) and increasing the inhibitory effects of OH adsorption and oxide formation on (110) domains (a negative factor).

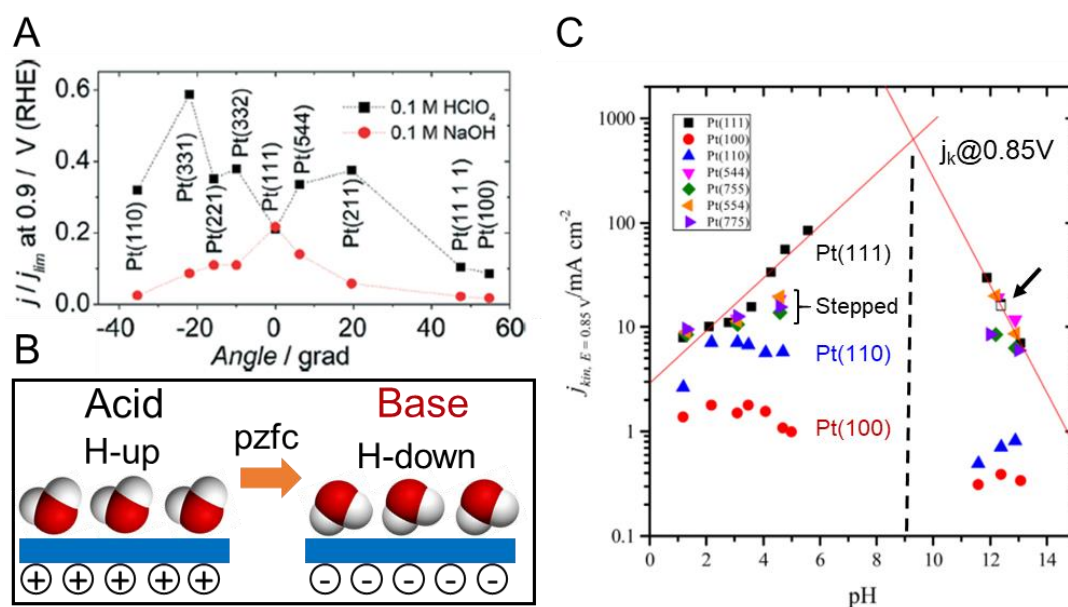


**Figure 1.16** ORR activity of stepped Pt surfaces and interfacial water structures. (A) Normalized ORR current,  $j/j_{lim}$  at 0.9 V during the positive-going scan on Pt single crystals in acid and base at 50 mV/s as a function of the angle of the surface normal to the (111) direction. (B) Simplified schematic of water orientation at a charged Pt(111) surface. Given the potential of zero free charge (pzfc) of Pt(111) at 0.28 V vs. SHE, the Pt(111) surface contains positive charges in acid and negative ones in base, respectively, under typical fuel cell operation potentials (0.7-1.0 V vs. RHE), which leads to preferential H-up and H-down water configurations in acid and base, respectively. (C) Activity plots of the kinetic current density,  $j_k$ , at 0.85 V vs. RHE on Pt single crystals as a function of pH, which were measured by the RDE in O<sub>2</sub>-sat. NaF/HClO<sub>4</sub> and NaF/NaOH buffer solution at 50 mV/s and 2500 rpm. The straight lines correspond to pH-dependent activity of Pt(111) and the dashed line indicates the optimal activity of Pt occurs at pH of ~9. Open square corresponds to Pt(111) in a NaOH/NaF mixture. (A) is reproduced from ref. 22 Copyright 2014 RSC. (C) is reproduced from ref. 38 Copyright 2017 Elsevier.

Fig. 1.16 presents a comprehensive summary of ORR activities of different stepped and low-index Pt surfaces in acid and base.<sup>22</sup> In acid, it is well established that the ORR activity increases with higher step density and stepped Pt surfaces are much more active than the three low-index planes (black profile, Fig. 1.16A). Those observations in model electrodes have stimulated extensive efforts to prepare Pt-based shape-controlled ORR NP electrocatalysts with high index facets. Theoretical simulations ascribed the higher ORR activity on the stepped surfaces to the lower OH adsorption energies and smaller coordination numbers on (110) or (100) steps.<sup>36</sup> The (110) basal plane, despite having the highest step density as [2(111)×(111)], showed a lower activity than other stepped surfaces [n(111)×(111) or (n-1)(111)×(110)] (n > 2), which was ascribed to too weak OH and O adsorption energies. However, such thermodynamic approaches with  $\Delta G_{\text{OHads}}$ , failed to explain the significant difference in ORR activity trends between acid and base. Specifically, Pt(111) exhibits the highest ORR activity, when compared to all stepped surfaces in base and the addition of (110) or (100) steps next to (111) terraces only caused a monotonic activity decay (red profile, Fig. 1.16A). Structural factors, such as the coverage of O-containing species and pztc, have also not resulted in satisfying explanations for the differences between acid and base.<sup>22</sup> It is possible, and likely, that other significant changes in the near-surface environment have yet to be considered. For example, on Pt(111), the interfacial water structure in acid and base can be fundamentally different (Fig. 1.16B). The potential of zero free charge (pzfc) of Pt(111) is 0.28 V vs SHE and pH-independent, which is closely related to the water orientation on surfaces. Under typical ORR conditions (0.7-1.0 V vs. RHE), the ORR occurs over the range of 0.64~0.94 V vs. SHE in 0.1 M acid (e.g. HClO<sub>4</sub>) but over -0.07~0.23 V vs.

SHE in 0.1 M base (e.g. NaOH). Thus, a Pt(111) surface will carry a positive net charge in acid and induce an H-up O-down water orientation while it will exhibit a negative net charge in base and form an H-down O-up water configuration. A similar argument is also applicable to explain the much lower HOR activity in base given the much more rigid water network in base, relative to acid.<sup>37</sup> In summary, besides traditional thermodynamic considerations of O species adsorption, the interfacial water-surface interaction and water-water H-bonded network offer another perspective to better rationalize the activity difference of stepped Pt surfaces in acid and base.

The pH-effects on the ORR activity of Pt have been thoroughly investigated on various stepped surfaces in acid and base with NaF as buffer, with little to no specific anion adsorption (Fig. 1.16C).<sup>38</sup> The kinetic current density,  $j_k$ , at 0.85 V (surface-specific activity, SA) was extracted from ORR polarization profiles based on the Koutecký-Levich equation ( $1/j_m = 1/j_k + 1/j_{lim}$  where  $j_m$  is the measured current density). The ORR activity of Pt(111) exhibited a linear correlation in both acid and base with a maximum activity predicted at a pH of ~9 (dashed line in Fig. 1.16C). It was proposed that the ORR activity of Pt(111) could achieve a maximum value when the onset potential of the ORR (~1.0 V vs. RHE), which is pH-independent vs. RHE, is close to its pzc value (0.28 V vs. SHE) which is pH-independent vs. SHE. When those two values are equal, the interfacial water layer has the highest degree of disorder when the ORR occurs, which allows solution species to repel water most easily and adsorb with the lowest energy barrier for reorientating water. This argument would predict an optimal pH of ~11, and the difference from experimental observation (optimal pH at ~9) is likely because, in base, the pzc of Pt(111) is within the OH<sub>ads</sub> region and the ORR

kinetics are also influenced by the OH adsorption process.<sup>22</sup> In contrast to Pt(111), the ORR activities of Pt(100) and (110) are largely pH-insensitive (blue and red dots in Fig. 1.16C). This was rationalized by the fact that Pt(111) has a relatively weak OH adsorption over the normal ORR potential window of 0.7~1.0 V vs. RHE and OH<sub>ads</sub> on Pt(111) tends to desorb completely at  $E < 0.7$  V. However, Pt(100) and (110) have a relatively stronger OH adsorption and OH only begins to desorb at  $E < 0.3-0.5$  V. Thus, the ORR activities of Pt(100) and Pt(110) are mainly dictated by OH adsorption processes and much less influenced by the interfacial water structure. At  $\text{pH} < 7$ , stepped Pt(544), (755) ( $n=9, 6, n(111)\times(100)$ ) has an ORR activities that lies in between Pt(111) and Pt(100) and Pt(554), (775) ( $n=9, 6, n(111)\times(110)$ ) showed activity in between Pt(111) and Pt(110). At  $\text{pH} > 7$ , all stepped Pt surfaces followed the same trend as Pt(111) since Pt(111) is much more active than Pt(100) or (110) and largely determines the ORR activity. There is no data reported for pH values from 7 to 10 due to the strong anion specific adsorption on Pt in that pH range, such as carbonate or phosphate, which complicates the interpretation of ORR profiles. In summary, catalyst surface structures (step symmetry and density), environment (pH, surface water, cation/anion) and temperature have significant impacts on H/OH adsorption and ORR/HOR activities.

Tuning ORR activity requires a rational understanding of the interaction between catalyst surface and reaction intermediates. Early catalyst studies have attempted to correlate ORR activities to electronic structures (d-band vacancies or d-band center), oxygen adsorption energy ( $\Delta G_{\text{Oads}}$ ), or Pt-Pt bond distance (lattice strain), etc. Appleby et al. first reported that the ORR activities of precious metals showed a volcano-type relation with latent heat and d-band vacancies.<sup>39</sup> Nørskov et al. used DFT calculations

to show that Pt has the highest ORR among all metals and located on the top of the volcano plot of activity as a function of oxygen adsorption energy.<sup>40</sup> The location of Pt in the volcano plot is slightly off from the peak point by 0.2 eV, suggesting that weakening oxygen adsorption energy can potentially enhance its ORR activity. Markovic et al. reported that Pt<sub>3</sub>M formed alloys with 3d metals with Pt as topmost layer after annealing processes (Fig. 1.17A).<sup>41</sup> Such structures used 3d metals to cause lattice contraction and weaken the oxygen adsorption (expressed as a downshift of d-band center). ORR activity of Pt<sub>3</sub>M outperformed Pt and showed a volcano plot as a function of d-band centers. They further reported that Pt<sub>3</sub>Ni(111) with Pt monolayer on the surface exhibited an ORR activity 10 times better than Pt(111), which was ascribed to the proper downshift of d-band center.(Fig. 1.17B).<sup>42</sup>

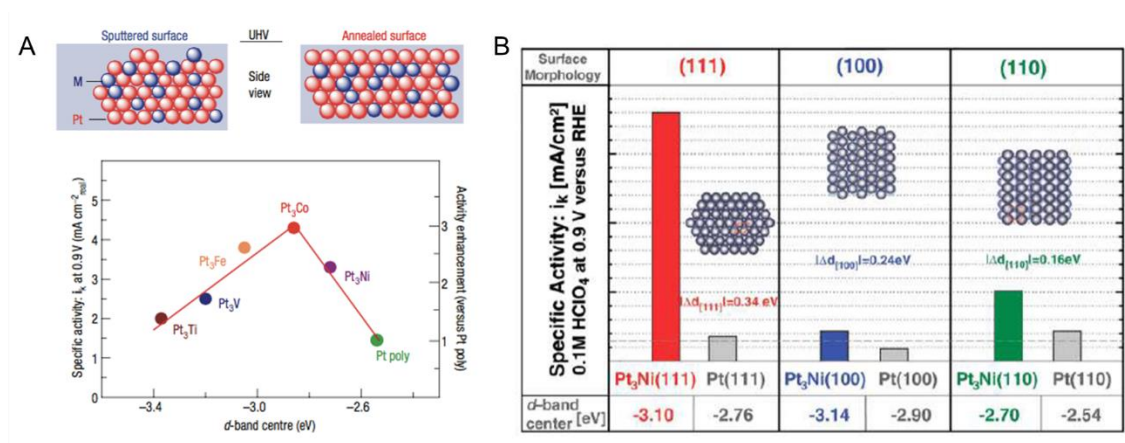


**Figure 1.17** ORR activities of Pt<sub>3</sub>M with surface Pt layer. (A) Volcano plot of ORR activity of Pt<sub>3</sub>M as a function of d-band center. (B) ORR Activity of Pt<sub>3</sub>Ni and Pt with different basal planes and the correlation to d-band center. (A) is reproduced from ref. 41 Copyright 2007 Springer Nature (B) is reproduced from ref. 41 AAAS.

In summary, the proposed volcano plots imply a simplified structure-activity correlation for the complex ORR mechanism. Optimal structural factors may exist, such as the adsorption energy of oxygen ( $\Delta G_{O_{ads}}$ ), from the viewpoint of the Sabatier

principle. There exist scaling relationships between adsorption energies of reactive and intermediate species ( $\Delta G_{\text{Oads}}$  and  $\Delta G_{\text{OHads}}$ ). Tuning  $\Delta G_{\text{Oads}}$  in the complex ORR mechanism may modify not just the  $\text{O}_{\text{ads}}$  or  $\text{OH}_{\text{ads}}$  reduction kinetics but other intermediate reaction steps. In order to fully understanding the ORR mechanism, we need to consider multiple structural factors at the same time, such as the nature of absorbed species and their coverage, structure of surface water and its dissociation, electrode potential and local surface charge.

### **1.5.2 Nanoscale ORR Catalysts in Acidic Media**

From a material-synthesis-by-design perspective, there are virtually unlimited possibilities of ORR electrocatalysts in nanoparticle (NP) forms. Sizes, morphologies, compositions and structures can all be fine tuned to design new materials with the hope of achieving high ORR activities with long-term durability. However, in this field with enormous numbers of catalyst candidates, few have demonstrated realistic MEA performances in PEMFCs. We have to critically evaluate the information when a literature report claims “great ORR catalysts”. This section will introduce several representative examples to highlight the design criteria of ORR electrocatalysts.

Following the guide of volcano plots, Pt-3d metal alloys have been extensively investigated since the incorporation of 3d metals can cause lattice contraction and weaken the adsorption energy of oxygen.  $\text{Pt}_3\text{Co}$  and  $\text{Pt}_3\text{Ni}$  have emerged as the two most promising catalyst candidates (Fig. 1.17A), with significantly higher ORR activities than Pt and promising long-term durability. Pt-based alloys, with higher fractions of Co or other 3d metals, such as  $\text{Pt}_{50}\text{Co}_{50}$ , suffer from severe Co leaching and membrane contamination in acidic media and remain questionable for practical PEMFCs

applications.

As-synthesized Pt<sub>3</sub>Co/C nanoparticle catalysts are often disordered alloys after low-temperature synthesis but can be converted into ordered intermetallic phases upon high-temperature thermal treatment.<sup>43</sup> Our previous work showed that Pt<sub>3</sub>Co ordered intermetallics had a 2-3 atomic-layer-thick Pt shell on the surface and exhibited significantly higher ORR activity and durability than the Pt<sub>3</sub>Co disordered counterparts. The enhanced durability was attributed to the Pt-rich shell suppressing Co leaching and stable intermetallic Pt<sub>3</sub>Co core. Recently, after close examination of XRD data of Pt<sub>3</sub>M alloys in the literature, we found that Pt<sub>3</sub>M disordered alloys are often partially converted to ordered intermetallics (Chapter 8).<sup>8</sup> We employed *in situ* heating synchrotron-based XRD and *in situ* heating TEM to quantify the degree of ordering, and found that the annealed Pt<sub>3</sub>Co/C intermetallics, with an optimal degree of ordering, exhibited significantly enhanced durability in MEA tests, relative to the disordered counterpart.

Following Stamenkovic's report on the extraordinary ORR activity of single-crystal Pt<sub>3</sub>Ni (111)<sup>42</sup> (Fig. 1.17B), researchers have worked on the synthesis of monodisperse octahedral nanoparticles with shape-controlled {111}-bounded facets.<sup>44-47</sup> General methods involve the reduction of Pt and Ni acetylacetonate (acac) precursors in organic solvents with the addition of CO and/or surfactants of oleic acid (OA) and oleylamine (OAm). Pt<sub>3</sub>Ni NPs with various morphologies have been reported, including octahedrons, cubes, truncated octahedrons and nanoframes. Octahedral Pt<sub>3</sub>Ni NPs exhibited much higher ORR activity than cubic Pt<sub>3</sub>Ni or polycrystalline Pt/C (Figs. 1.18A-B).<sup>44,45</sup> Similarly, Pt<sub>3</sub>Ni nanoframes were synthesized by chemically dealloying

Ni-rich PtNi alloys and were claimed to achieve over a 20 times enhancement, of both mass and specific activity, relative to Pt/C.<sup>46</sup> Ni-rich PtNi alloys could also form concave octahedral particles after electrochemical dealloying (Fig. 1.18C).<sup>47</sup> However, the stability of facet-controlled octahedral Pt<sub>3</sub>Ni NPs or other Ni-rich PtNi alloys remains questionable even during short-term fuel cell operation at high current densities. As shown in Fig. 1.18D, octahedral PtNi NPs lost their distinct shapes after only one-day of MEA tests.<sup>48</sup> Given that facet-controlled morphology is critical for maintaining high activity, it is understandable why sustainable high MEA performance has not been achieved with octahedral PtNi catalysts. This structural instability is possibly due to the leaching of Ni and the weak interaction between octahedral PtNi particles and carbon supports since PtNi nanoparticles are often loaded on carbon after solvothermal synthesis.

Despite numerous reports on octahedral Pt<sub>3</sub>Ni and Ni-rich PtNi nanoparticles, their structural instability, synthetic complexity and limited batch size have precluded their commercial viability for PEMFCs. major automotive companies, such as GM and Toyota, have adapted Pt<sub>3</sub>Co ordered intermetallics (Chapter 8) or Pt-Co alloys with a small fraction of Co as the practical ORR electrocatalyst for their PEMFC stacks since the impregnation-reduction method is facile to scale up and yield Pt<sub>3</sub>Co NPs in close contact with the carbon support.<sup>8,43</sup>

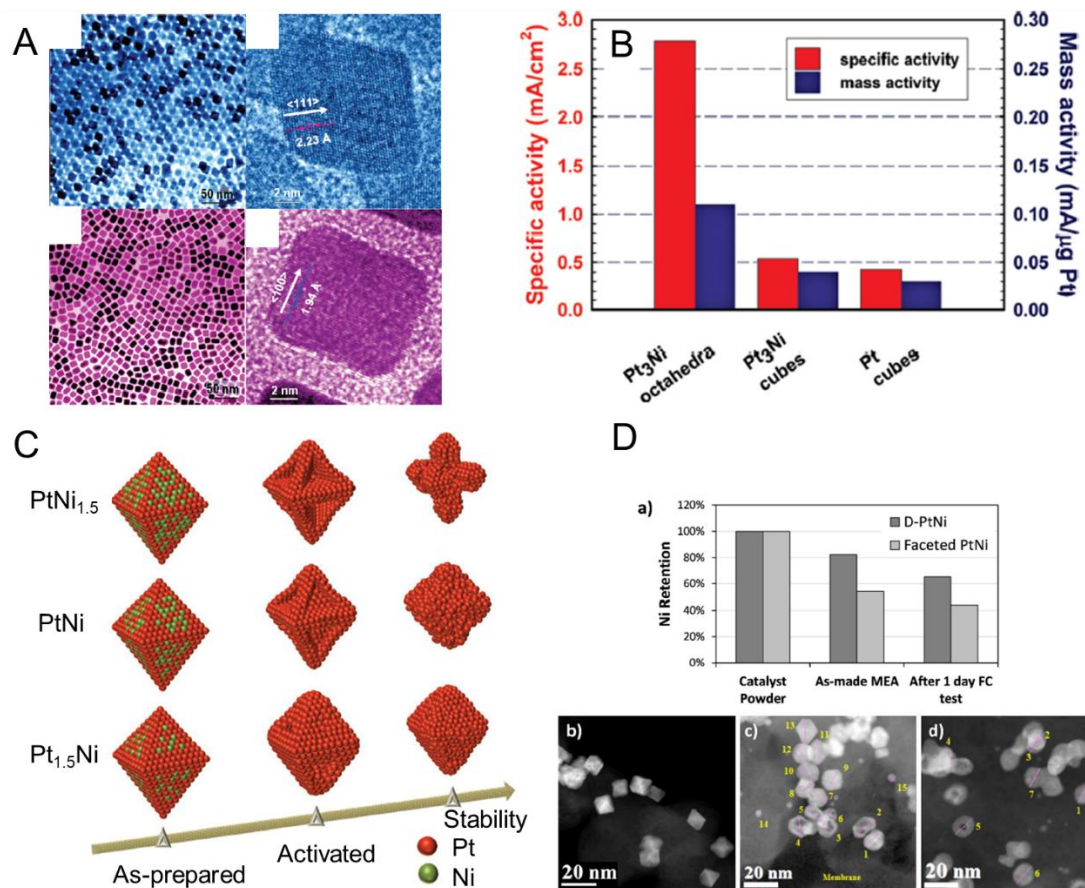


**Figure 1.18** Activity and stability of octahedral PtNi alloys. (A) TEM images of Pt<sub>3</sub>Ni octahedrons and cubes. (B) Surface-specific activity and Mass-specific activity at 0.9 V. (C) Structural evolution of Pt-Ni octahedral alloys through electrochemical dealloying (D) (a) Ni retention of disordered and octahedral PtNi at different stages of life. (b) as-prepared octahedral PtNi catalysts, (c) as-made MEA and (d) after 1 day of MEA tests. (A, B, D) are reproduced from ref. 44, 45, 48, respectively, Copyright 2010-2016 ACS. (C) is reproduced from ref. 47 Springer Nature.

## 1.6 ORR Electrocatalysis in Alkaline Media

### 1.6.2 ORR Mechanism of Single-Crystal Electrocatalysts in Alkaline Media

Although the ORR mechanism is less well understood in alkaline media, relative to acidic media, early studies on single-crystal metals have provided us with valuable insights about the ORR mechanism in base. Markvoic et al. investigated the ORR activities of Pt, Au and Ag single crystals in alkaline media.<sup>49-51</sup> ORR activities of Pt

single crystals increased in the order of Pt(100) < Pt(110) < Pt(111), which is similar to the order in 0.1M HClO<sub>4</sub> but with a larger difference between Pt(110) and Pt(111) (Fig. 1.19A). ORR activity of Au and Ag followed the trends of Au(111) < Au(110) << Au(100) and Ag(100) < Ag(111) < Ag(110), respectively (Figs. 1.19B-C).<sup>50,51</sup> Studies by Feliu et al. showed that Au(111) predominantly generates peroxide via the 2e<sup>-</sup> process.<sup>53</sup> In comparison, Au(100) shows a high selectivity for the 4e<sup>-</sup> ORR at potentials above -0.2 V vs. SHE and a transition to 2e<sup>-</sup> at potentials below -0.2 V vs. SHE in alkaline media, which was ascribed to the existence of a negative charge density on the metal surface that inhibits further reduction of HO<sub>2</sub><sup>-</sup>.

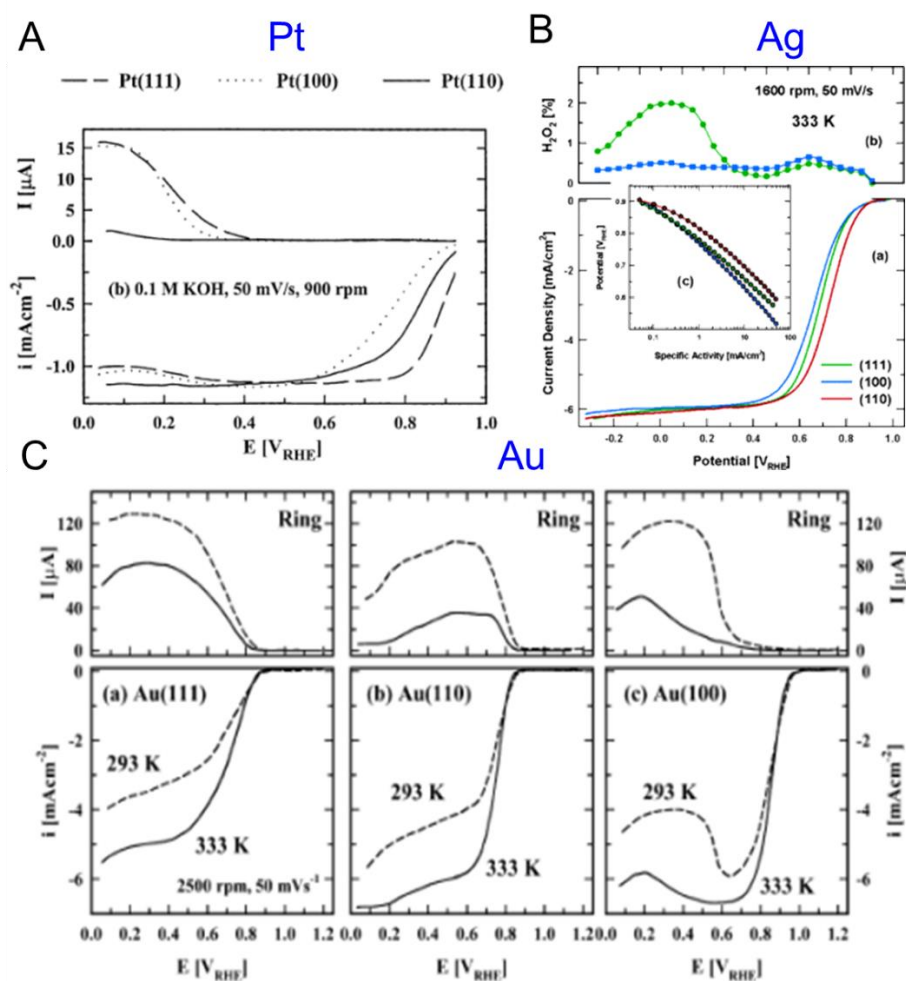


**Figure 1.19** ORR Activities of single-crystal precious metals in alkaline media. (A-C), ORR polarization profiles of Pt, Ag, Au with (111), (100) and (110) facets at 50mV/s and 1600rpm in 0.1M KOH. (A) is reproduced from ref. 49 Copyright 2003 RSC. (B) is reproduced from ref. 50 Copyright 2002 Elsevier. (C) is reproduced from ref. 51 Copyright 2006 ACS.

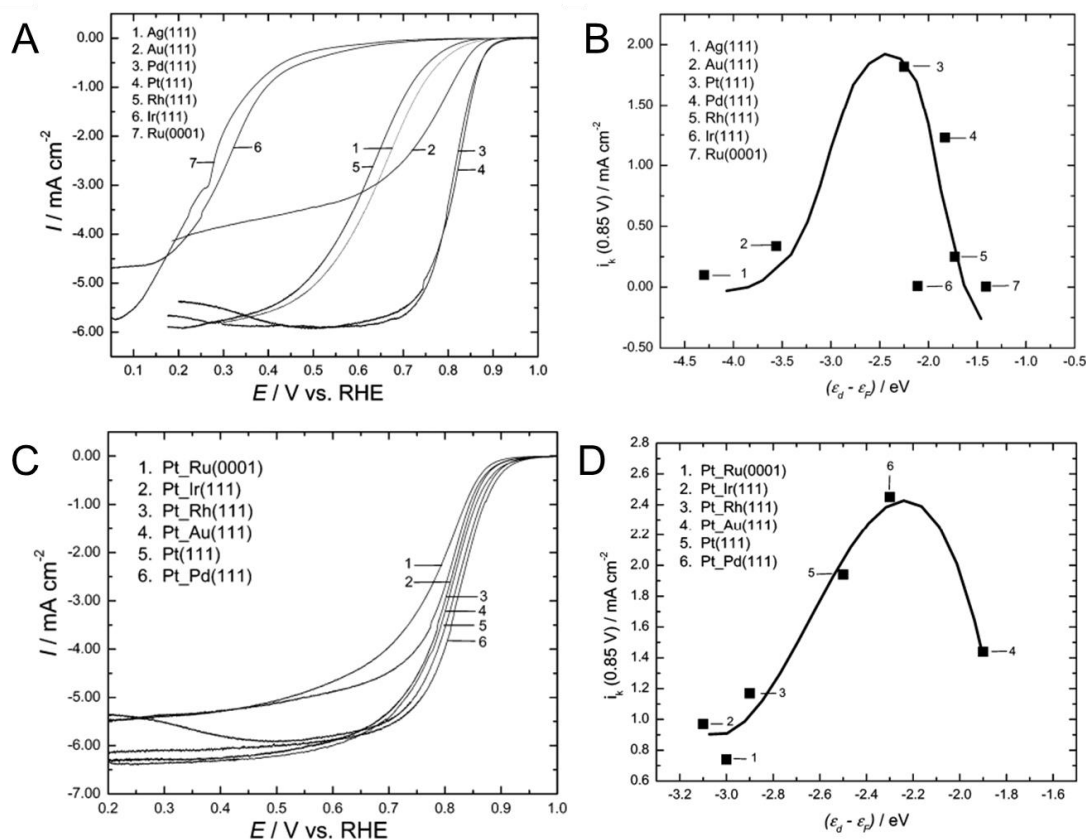


**Figure 1.20** ORR activities of Pt monolayer on single-crystal substrates in base. (A-B) ORR polarization profiles of different metal single crystals in 0.1M KOH at 1600rpm and 5mV/s and correlation of kinetic current at 0.8V to calculated metal d-band center. (C) ORR activity of Pt monolayers on different metal single crystal substrates in 0.1M KOH as a function of calculated metal d-band center. 54 (D) ORR activity of Pt monolayer on different metal substrates in 0.1M HClO<sub>4</sub> and the activation energies for O<sub>2</sub> dissociation (filled circles) and for OH formation (open circles), as a function of the calculated binding energy of atomic oxygen (BE<sub>O</sub>). Labels: 1. Pt/Ru(0001) 2. Pt/Ir(111) 3. Pt/Rh(111) 4. Pt/Au(111) 5. Pt(111) 6. Pt/Pd(111). 55 (A-C) are reproduced from ref. 54 Copyright 2007 ACS. (D) is reproduced from ref. 55 Copyright 2005 Wiley.

Adzic et al. studied a variety of single-crystal metals and reported the following

activity order in alkaline media: Pt(111)  $\approx$  Pd(111) > Au(111) > Ag(111) > Rh(111) > Ir(111) > Ru(111) (Figs. 1.20A-B).<sup>54</sup> ORR activities exhibited a volcano-type dependence on the d-band center of the metals with Pt as the most active element. Pd exhibited ORR activity as high as Pt in alkaline media, in contrast to its low ORR activity in acidic media. For Pt monolayers deposited on different metals using galvanic displacement of Cu, the ORR activity in base followed the order: Pt\_Pd(111) > Pt(111) > Pt\_Au(111) > Pt\_Rh(111) > Pt\_Ir(111) > Pt\_Ru(0001), which exhibited a volcano correlation of ORR activity vs. d-band center (Fig. 1.20C), a trend similar to their ORR activities in acidic media. Mavrikakis and Adzic showed that, for those Pt<sub>ML</sub> on single-crystal substrates, the activation energy of O<sub>2</sub> dissociation (filled circles) decreased while that of O-H formation (open circles) increased at a more negative (stronger) oxygen binding energy (Fig. 1.20D).<sup>55</sup> The highest ORR activity of Pt<sub>ML</sub> on a Pd (111) substrate in acidic media was ascribed to the combination of optimal properties that facilitate O<sub>2</sub> adsorption to dissociate the O-O bond, while also promoting the rapid hydrogenation of Pt-O, as indicated by the crossing of two E<sub>a</sub> trend lines (Figure 1.20D). Given the similar values of the d-band center between Pt and Pt<sub>ML</sub>/Pd, other factors, such as interfacial water structures, could also contribute to the considerable activity enhancement of Pt<sub>ML</sub>/Pd. Additional *in situ* XANES suggested that Pt<sub>ML</sub>/Pd had a lower OH coverage and a more positive OH adsorption peak, relative to Pt, which is consistent with a weaker OH adsorption energy as predicted by simulations.<sup>56</sup>

### 1.6.2 Nanoscale ORR Electrocatalysts in Alkaline Media

Most of Pt-based catalysts developed for PEMFCs are also active for the ORR in alkaline media. 3d-metal-rich Pt-M alloys are more stable in alkaline media since the inevitable leaching problems in acidic media are largely suppressed at high pH environments. However, the main motivation of alkaline fuel cells is to find non-

precious alternatives to Pt. Over the past decade, a variety of non-precious electrocatalysts have been explored, such as metal-containing nitrogen-doped carbons (M-N-C, M is often Fe or Co), perovskites, and transition metal oxides and nitrides. Early studies of M-N-C were inspired by the structure of Fe porphyrin in hemoglobin for carrying oxygen in blood. In the 1960s, Jasinski et al. reported the first Co Phthalocyanine (CoPc) molecular electrocatalysts for the ORR (Fig. 1.21A).<sup>57</sup> Later, Yeager et al. reported the first heterogeneous Fe-N-C ORR catalysts synthesized from polyacrylonitrile (PAN) through heat treatment (Fig. 1.21B).<sup>58</sup>

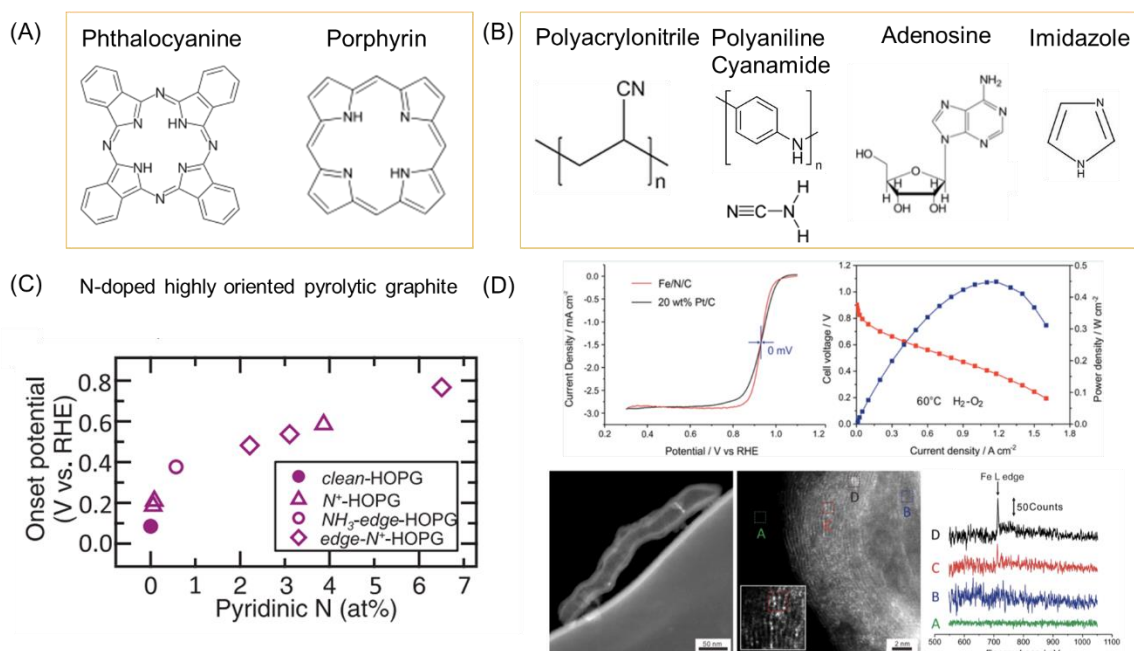


**Figure 1.21** ORR activities of metal-containing N-doped carbon (M-N-C) catalysts. (A) Organic ligands for early ORR molecular electrocatalysts. (B) Common N-containing organic precursors for synthesizing M-N-C. (C) ORR activity (onset potential) as a function of pyridinic N contents in N-doped highly oriented pyrolytic graphite (HOPG) (D) RDE and MEA measurements of Fe/N/C synthesized from adenosine and comparison to Pt. ADF-STEM images of Fe/N/C show atomically dispersed Fe atoms and EELS spectra confirming the existence of Fe atoms. (C) is reproduced from ref. 62 Copyright 2017 AAAS. (D) is reproduced from ref. 63 Copyright by the authors

Several important factors govern the ORR performance of Fe-N-C catalysts, such as Fe and N contents, porosity of carbon supports and coordination environments of N

around Fe (e.g., pyridinic, pyrrolic, quaternary or graphitic N). Fig 1.21C presents ORR activity trends, in terms of onset potential, with a higher content of pyridinic N in N-doped highly oriented pyrolytic graphite (HOPG) yielding higher activity, suggesting that the pyridinic N atoms could be the possible active sites for the ORR.<sup>62</sup> It has not been possible to resolve the active sites directly until the recent advance of STEM and EELS techniques. We recently showed that Fe-N-C, derived from adenosine, achieved an ORR activity comparable to Pt/C in RDE measurements and a peak power density (PPD) of 450 mW/cm<sup>2</sup> in MEA measurements, which is the highest reported performance for M-N-C in AEMFCs up to date (Fig. 1.21D).<sup>63</sup> STEM images and EELS elemental maps clearly showed the existence of single Fe atoms (indicated by the bright spots on the carbon support) and spectroscopic evidence of the presence of Fe. Despite numerous reports of Fe-N-C as active ORR catalysts in RDE measurements from various precursors,<sup>64,65</sup> preliminary MEA measurements while encouraging, lag behind the state-of-the-art Pt/C cathodes with PPDs of around 1-1.5 W/cm<sup>2</sup>. This is primarily due to the intrinsically low density of active sites (N contents is generally 1-5 at.%) and slow mass transport, as a result of the very high loading of carbon (1-2 mg/cm<sup>2</sup>) and thus thick catalyst layers. AEMFCs with Fe-N-C cathodes may not satisfy the requirement of high volumetric energy density of electric vehicles but could be valuable for other medium-to-low power applications such as backup or stationary power.

Perovskites (e.g., LaMO<sub>3</sub>, M can be Co, Ni, Mn, etc.) have been reported to be active catalysts for the ORR but with inferior activity (half-wave potential below 0.75 V vs. reversible hydrogen electrode), likely due to their poor electronic conductivity and/or the μm-sized large grains after thermal treatment at 1000 °C or above for achieving single phases.<sup>66-67</sup> Thus, the key for improving ORR activities of perovskites is to achieve small particle sizes through low-temperature hydrothermal synthesis of certain compositions with intrinsically high conductivity (e.g. LaNiO<sub>3</sub>, which is briefly

discussed in [Section 11.2.1](#)). As a comparison, 3d metal oxides, especially with spinel phases, have attracted increasing attention as ORR electrocatalysts due to their high activity, high density of active sites, stable structure and low cost.<sup>68-69</sup> Detailed studies of 3d metal oxides and nitrides will be covered as part of the main stories of this thesis from [Chapter 2 to 7](#).

### **1.7 Analytical and *Operando/In Situ* Scanning Transmission Electron Microscopy**

The development and application of aberration-corrected scanning/transmission electron microscopes (S/TEM), equipped with electron energy loss spectroscopy (EELS) and energy dispersive X-ray spectroscopy (EDX), has offered invaluable complementary insights for establishing structure/composition-reactivity/durability correlations of electrocatalysts at a microscopic level. STEM with EELS and EDX can provide sub-Ångström spatial resolution with a tremendous amount of morphological/compositional information and electronic structure of the electrocatalysts. STEM-based characterizations have emerged as an indispensable tool for advancing our understanding of fuel cell electrocatalysts and their dynamic evolution during electrochemical reactions at the nm and atomic scales.<sup>70</sup> As shown in [Fig. 1.22](#), STEM images exhibited the structures of Pt-Fe ordered intermetallics at the atomic-scale and EELS elemental mapping showed a PdFe core with a 2-3 atomic-layer Pd-rich shell to mitigate the leaching of Fe for enhanced catalyst durability. S/TEM has been widely used to capture the morphological, chemical and crystal structures of individual nanoparticle catalysts, which is often missed in bulk X-ray analysis, leading to the discovery of novel nanomaterials and to a more rational design of catalysts. In particular, identical-location TEM (IL-TEM), can probe the facet and shape evolution

and catalyst degradation mechanisms at the same regions before and after electrochemical tests.<sup>71</sup>

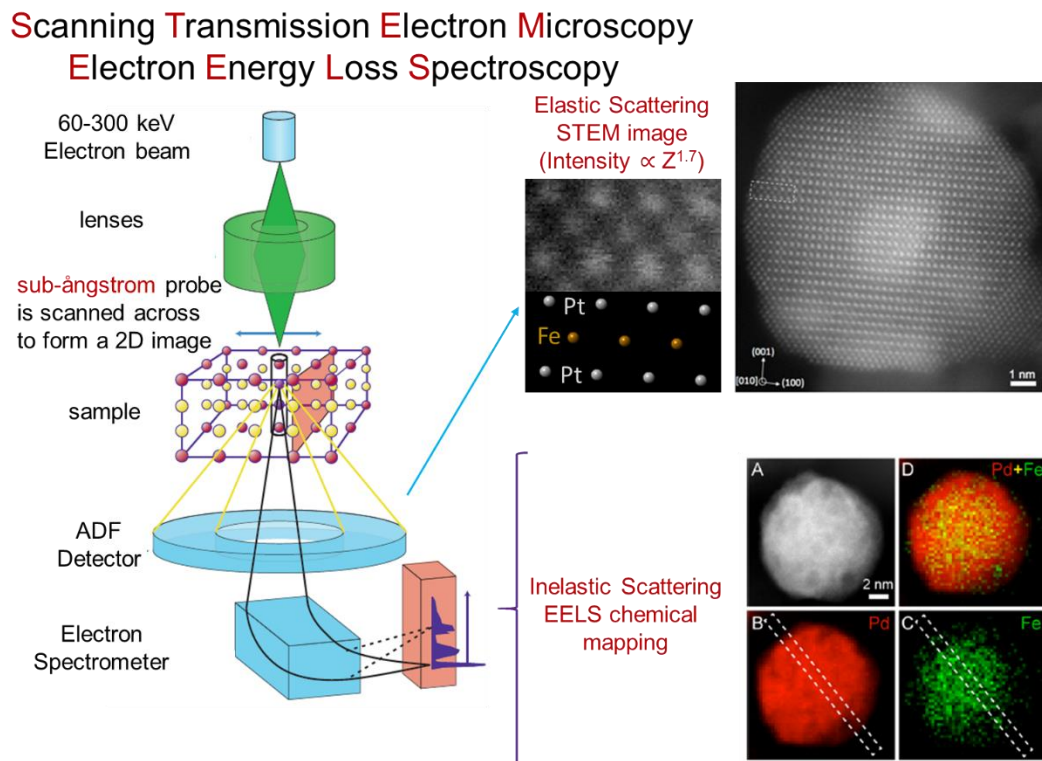
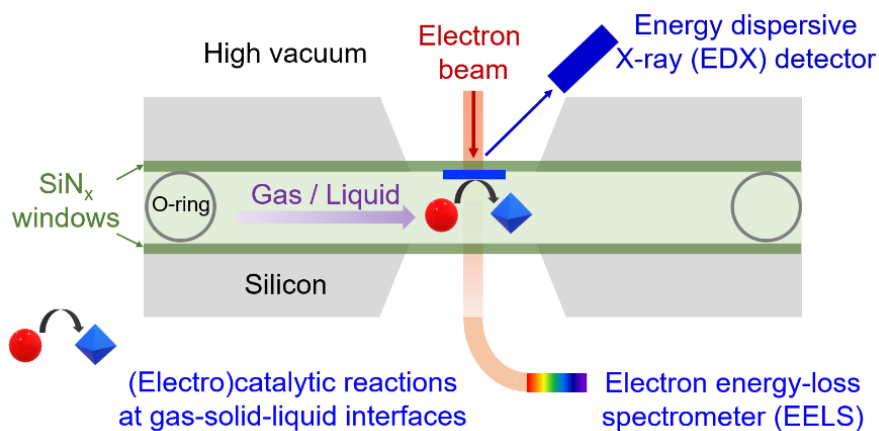


**Figure 1.22** Schematic and examples of STEM-EELS elemental analysis.

While TEM has been instrumental in the development of solid-state electrocatalysts, conventional TEM operates under high vacuum conditions ( $\sim 10^{-10}$  bar) and is incompatible for the study of materials in liquids and/or gases. Recent advances in TEM instrumentation and microchips, with thin, but robust, electron-transparent windows,<sup>72</sup> have enabled *operando/in situ* electrochemical liquid-cell STEM (EC-STEM) with nm and even atomic-scale spatial resolution in realistic electrolytes under operating conditions (Fig. 1.23). The environmental TEM enables the *in situ* study of the dynamical behavior of nanomaterials at high temperatures and pressures up to atmospheric pressure. *In situ* heating TEM can yield new information and insights on

the thermal stability of Pt-based catalysts, surface reconstructions and elemental distribution of Pt-based catalysts, We recently employed *in situ* heating STEM, together with *in situ* heating XRD, to quantify the degree of ordering in Pt<sub>3</sub>Co nanoparticles, and study the (order/disorder) phase transition and morphological changes during high-T



annealing (Chapter 8).

**Figure 1.23** Schematic of in situ S/TEM with EELS/EDX in liquid/gas phase

The majority of chemical reactions, particularly electrochemical process, occur at the electrode-electrolyte interface in solution phase. *In situ* liquid cell TEM is well positioned to provide unique insights on the interfacial electrocatalytic process with nm-scale or higher resolution, composition and chemical bonding information. The electrochemical liquid-cell TEM work was pioneered by Ross *et al.* who employed a home-made liquid cell with a two-electrode system to perform TEM studies of Cu electrodeposition.<sup>73,74</sup> Recently, *in situ* liquid-cell S/TEM have been used to investigate the durability of nanoparticle fuel cell catalysts during potential cycles,<sup>75,76</sup> discharge mechanisms of electrode materials in lithium ion batteries,<sup>77-80</sup> and structural evolution of electrocatalysts during CO<sub>2</sub> reduction.<sup>81-83</sup> Liquid cell TEM has been widely used to study beam-induced growth and corrosion of Pt, Pd or Au-based NPs,<sup>84-85</sup> However, it

should be noted that, the electron beam has served as an active reactant to grow or corrode nanoparticles and has made the reaction mechanisms significantly different from regular (electro)chemical processes. Although liquid-cell TEM has been extensively employed to study chemical phenomena, very few studies have demonstrated reliable electrochemical results in liquid-cell TEM, which can be faithfully compared to standard electrochemical measurements. In [Chapters 9-10](#), we place particular emphasis on *in situ* liquid-cell TEM studies to reliably quantify electrochemical processes and discuss the major challenges facing rigorous electrochemical measurements in liquid-cell TEM. Preliminary progress and testing protocols of *in situ* EC-STEM will be discussed in APPENDIX B.

### 1.8 References:

1. Abruña, H. D.; Energy in the Age of Sustainability. *J. Chem. Edu.* **2013**, 90, 141.
2. Schiller, M. Hydrogen Energy Storage: The Holy Grail for Renewable Energy Grid Integration. *Fuel Cells Bulletin*, **2013**, 12-15.
3. Pivovar, B. Catalysts for Fuel Cell Transportation and Hydrogen Related Uses. *Nat. Catal.* **2019**, 2, 562.
4. Ayers, K. E.; Dalton, L. T.; Anderson, E. B. Efficient Generation of High Energy Density Fuel from Water. *ECS Transactions*, **2012**, 41, 27.
5. Debe, M.; Electrocatalyst Approaches and Challenges for Automotive Fuel Cells. *Nature*. **2012**, 486, 43.
6. Gasteiger, H. A., Kocha, S. S., Somali, B. & Wagner, F. T. Activity Benchmarks and Requirements for Pt, Pt-alloy, and non-Pt Oxygen Reduction Catalysts for PEMFCs. *Appl. Catal., B*. **2005**, 56, 9-35.
7. Papageorgopoulos D, 2019 Annual Merit Review and Peer Evaluation Meeting in Fuel Cells Program Area. U.S. Department of Energy, Washington, DC.
8. Xiong, Y.; Yang, Y.; Joress, H.; Padgett, E.; Gupta, U.; Yarlagaadda, V.; Agyeman-Budu, D. N.; Huang, X.; Moylan, T. E.; Zeng, R.; Kongkanand, A.; Escobedo, F. A.; Brock, J. D.; DiSalvo, F. J.; Muller, D. A.; Abruña, H. D. Revealing the Atomic Ordering of Binary Intermetallics Using *in situ* Heating Techniques at Multilength Scales. *Proc. Natl. Acad. Sci.* **2019**, 116, 1974–1983.
9. Meier, J. C. et al. Mayrhofer, K. J. Design criteria for stable Pt/C fuel cell catalysts. *Beilstein J. Nanotechnol.* **2014**, 5, 44–67.
10. Ferreira, P. J.; La O', G. J.; Shao-Horn, Y.; Morgan, D.; Makharia, R.; Kocha, S.; Gasteiger, H. A. Instability of Pt/C Electrocatalysts in Proton Exchange Membrane Fuel Cells A Mechanistic Investigation *J. Electrochem. Soc.* **2005**, 152, A2256.

11. Shao-Horn, Y.; Ferreira, P. J.; La O', G. J.; Morgan, D.; Gasteiger, H.; Makharia, R. Coarsening of Pt Nanoparticles in Proton Exchange Membrane Fuel Cells upon Potential Cycling. *ECS Trans.* **2006**, 1, 185.
12. Sheng, W.; Chen, S.; Vescovo, E.; Shao-Horn, Y. Size Influence on the Oxygen Reduction Reaction Activity and Instability of Supported Pt Nanoparticles. *J. Electrochem. Soc.* **2012**, 159, B96.
13. Shao-Horn, Y.; Sheng, W. C.; Chen, S.; Ferreira, P. J.; Holby, E. F.; Morgan, D. Instability of Supported Platinum Nanoparticles in Low-Temperature Fuel Cells. *Top. Catal.* **2007**, 46, 285.
14. Mench, M. M.; Kumbur, E. C.; Veziroglu, T. N. Polymer Electrolyte Fuel Cell Degradation; Academic Press: Amsterdam, The Netherlands, 2012.
15. Schlögl, K.; Mayrhofer, K. J. J.; Hanzlik, M.; Arenz, M. Identical-Location TEM Investigations of Pt/C Electrocatalyst Degradation at Elevated Temperatures. *J. Electroanal. Chem.* **2011**, 662, 355.
16. Mayrhofer, K. J. J.; Meier, J. C.; Ashton, S. J.; Wiberg, G. K. H.; Kraus, F.; Hanzlik, M.; Arenz, M. Fuel Cell Catalyst Degradation on the Nanoscale. *Electrochem. Commun.* **2008**, 10, 1144.
17. Mayrhofer, K. J. J.; Ashton, S. J.; Meier, J. C.; Wiberg, G. K. H.; Hanzlik, M.; Arenz, M. Non-Destructive Transmission Electron Microscopy Study of Catalyst Degradation Under Electrochemical Treatment. *J. Power Sources* **2008**, 185, 734.
18. Yaguchi, T.; Kanemura, T.; Shimizu, T.; Imamura, D.; Watabe, A.; Kamino, T. Development of a Technique for In Situ High Temperature TEM Observation of Catalysts in a Highly Moisturized Air Atmosphere. *J. Electron Microsc.* **2012**, 61, 199.
19. Linse, N.; Gubler, L.; Scherer, G. G.; Wokaun, A. The Effect of Platinum on Carbon Corrosion Behavior in Polymer Electrolyte Fuel Cells. *Electrochim. Acta* **2011**, 56, 7541.
20. Schulenburg, H.; Schwanitz, B.; Linse, N.; Scherer, G. G.; Wokaun, A.; Krbanjevic, J.; Grothausmann, R.; Manke, I. 3D Imaging of Catalyst Support Corrosion in Polymer Electrolyte Fuel Cells. *J. Phys. Chem. C* **2011**, 115, 14236.
21. Lu S.; Pan J.; Huang A.; Zhuang L.; Lu J. Alkaline Polymer Electrolyte Fuel Cells Completely Free from Noble Metal Catalysts. *Proc. Natl. Acad. Sci.* **2008**, 105, 20611.
22. Gomez-Marin, A. M.; Rizo, R.; Feliu, J. M. Oxygen Reduction Reaction at Pt Single Crystals: A Critical Review. *Catal. Sci. Technol.* **2014**, 4, 1685
23. Norskov, J. et al. Origin of the Overpotential for Oxygen Reduction at a Fuel Cell Cathode. *J. Phys. Chem. B* **2004**, 108, 17886.
24. Gómez-Marín, A.M.; Feliu, J. M.; Ticianelli, E. Oxygen Reduction on Platinum Surfaces in Acid Media: Experimental Evidence of a CECE/DISP Initial Reaction Path. *ACS Catal.* **2019**, 9, 2238-2251.
25. Briega-Martos, V.; Herrero, E.; Feliu, J. M. Effect of pH and Water Structure on the Oxygen Reduction Reaction on Platinum Electrodes. *Electrochim. Acta* **2017**, 241, 497-509.
26. Wang, J. X.; Markovic, N. M.; Adzic, R. R. Kinetic Analysis of Oxygen Reduction on Pt(111) in Acid Solutions: Intrinsic Kinetic Parameters and Anion Adsorption Effect. *J. Phys. Chem. B* **2004**, 108, 13, 4127.
27. Dong, J.-C. et al. Feliu, J. M.; Tian, Z.-Q.; Li, J. In situ Raman Spectroscopic Evidence for Oxygen Reduction Reaction Intermediates at Platinum Single-Crystal Surfaces. *Nat. Energy.* **2019**, 4, 60.
28. Dong, J.-C. et al. Direct In Situ Raman Spectroscopic Evidence of Oxygen Reduction Reaction Intermediates at High-Index Pt(hkl) Surfaces. *J. Am. Chem. Soc.* **2020**, 142, 715-719.
29. Clavilier, J.; Faure, R.; Guinet, G.; Durand, R. Preparation of monocrystalline Pt microelectrodes and electrochemical study of the plane surfaces cut in the direction of the

- {111} and {110} planes. *J. Electroanal. Chem.* **1980**, 107, 205.
30. Macia, M.; Campina, J. M.; Herrero, E.; Feliu, J. On the Kinetics of Oxygen Reduction on Platinum Stepped Surfaces in Acidic Media. *J. Electroanal. Chem.* **2004**, 564, 141.
  31. Markvoic, N. M.; Gasteiger, H. A.; Ross, P. N. Kinetics of Oxygen Reduction on Pt(hkl) Electrodes: Implications for the Crystallite Size Effect with supported Pt Electrocatalysts. *J. Electrochem. Soc.* **1997**, 144, 1591-1597.
  32. Markvoic, N. M.; Gasteiger, H. A.; Ross, P. N. Oxygen Reduction on Platinum Low-Index Single-Crystal Surfaces in Sulfuric Acid Solution: Rotating Ring-Pt(hkl) Disk Studies. *J. Phys. Chem.* **1995**, 99, 3411.
  33. Kondo, S.; Nakamura, M.; Norihito M.; Hoshi, N. Hoshi, Active Sites for the Oxygen Reduction Reaction on the Low and High Index Planes of Palladium. *J. Phys. Chem. Soc.* **2009**, 113, 12625.
  34. Kuzume, A.; Herrero, E.; Feliu, J. M. Oxygen Reduction on Stepped Platinum Surfaces in Acidic Media. *J. Electroanal. Chem.* **2007**, 599, 333.
  35. Rizo, R.; Herrero, E.; Feliu, J. M. Oxygen Reduction Reaction on Stepped Platinum Surfaces in Alkaline Media. *Phys. Chem. Chem. Phys.* **2013**, 15, 15416.
  36. Calle-Vallejo, F.; Pohl, M. D.; Reinisch, D.; Loffreda, D.; Sautet, P.; Bandarenka, A. S. Why Conclusions from Platinum Model Surfaces do not Necessarily Lead to Enhanced Nanoparticle Catalysts for the Oxygen Reduction Reaction. *Chem. Sci.* **2017**, 8, 2283-2289.
  37. Ledezma-Yanez, I.; Wallace, W. D. Z.; Sebastián-Pascual, P.; Climent, V.; Feliu, J. M.; Koper, M. T. M. Interfacial Water Reorganization as a PH-Dependent Descriptor of the Hydrogen Evolution Rate on Platinum Electrodes. *Nat. Energy* **2017**, 2, 17031.
  38. Briega-Martos, V.; Herrero, E.; Feliu, J. M. Effect of pH and Water Structure on the Oxygen Reduction Reaction on Platinum Electrodes. *Electrochim. Acta* **2017**, 241, 497-509.
  39. Appleby A. J. Electrocatalysis and Fuel Cells. *Catalysis Reviews*, **1971**, 4, 221-244.
  40. Greeley, J.; Norskov, J. et al. Alloys of Platinum and Early Transition Metals as Oxygen Reduction Electrocatalysts. *Nat. Chem.* **2009**, 1, 552.
  41. Stamenkovic, V.; Markovic N. M. et al. Trends in Electrocatalysis on Extended and Nanoscale Pt-Bimetallic Alloy Surfaces. *Nat. Mat.* **2007**, 6, 241
  42. Stamenkovic, V.; Markovic, N. M. et al. Improved Oxygen Reduction Activity on Pt<sub>3</sub>Ni(111) via Increased Surface Site Availability. *Science*, **2007**, 315, 493.
  43. Wang, D.; Xin, H. L.; Hovden, R.; Wang, H.; Yu, Y.; Muller, D. A.; DiSalvo, F. J.; Abruña, H. D. Structurally Ordered Intermetallic Platinum-Cobalt Core-Shell Nanoparticles with Enhanced Activity and Stability as Oxygen Reduction Electrocatalysts. *Nat. Mater.* **2013**, 12, 81-87.
  44. Zhang, J.; Yang, H.; Fang, J.; Zou, S. Synthesis and Oxygen Reduction Activity of Shape-Controlled Pt<sub>3</sub>Ni Nanopolyhedra. *Nano Lett.* **2010**, 10, 638-644.
  45. Wu, Y.; Cai, S.; Wang, D.; He, W.; Li, Y. Syntheses of Water-Soluble Octahedral, Truncated Octahedral, and Cubic Pt-Ni Nanocrystals and Their Structure-Activity Study in Model Hydrogenation Reactions. *J. Am. Chem. Soc.* **2012**, 134, 8975-8981.
  46. Chen, C. et al. Stamenkovic, V. R. Highly Crystalline Multimetallic Nanoframes with Three-Dimensional Electrocatalytic Surfaces. *Science* **2014**, 343, 1339-1343.
  47. Cui, C.; Gan, L.; Heggen, M.; Rudi, S.; Strasser, P. Compositional Segregation in Shaped Pt Alloy Nanoparticles and Their Structural Behaviour During Electrocatalysis. *Nat. Mater.* **2013**, 12, 765-771.
  48. Kongkanand, A.; Mathias, M. F. The Priority and Challenge of High-Power Performance of Low-Platinum Proton-Exchange Membrane Fuel Cells. *J. Phys. Chem. C* **2016**, 7, 1127-1137.
  49. Schmidt T. J.; Stamenkovic V.; Ross P. N.; Marković N. M. Temperature Dependent Surface Electrochemistry on Pt Single Crystals in Alkaline Electrolyte Part 3. The Oxygen

- Reduction Reaction. *Phys. Chem. Chem. Phys.* **2003**, *5*, 400-406.
50. Schmidt T. J.; Stamenkovic V.; Arenz M.; Marković N. M.; Ross P. N. Oxygen Electrocatalysis in Alkaline Electrolyte: Pt (hkl), Au (hkl) and the Effect of Pd-Modification. *Electrochim. Acta*, **2002**, *47*, 3765-3776.
  51. Blizanac B. B.; Ross P. N.; Marković N. M. Oxygen Reduction on Silver Low-Index Single-Crystal Surfaces in Alkaline Solution: Rotating Ring Disk Ag (hkl) Studies. *J. Phys. Chem. B* **2006**, *110*, 4735-4741.
  52. Prieto, A.; Feliu, J. M. et al. The Role of Anions in Oxygen Reduction in Neutral and Basic Media on Gold Single-Crystal Electrodes. *J. Solid State Electrochem.* **2003**, *7*, 599-606.
  53. Rizo, R.; Herrero, E.; Feliu, J. M. Oxygen Reduction Reaction on Stepped Platinum Surfaces in Alkaline Media. *Phys. Chem. Chem. Phys.* **2013**, *15*, 15416.
  54. Lima, F.; Zhang, J.; Shao, M.; Sasaki, K.; Vukmirovic, M.; Ticianelli, E.; Adzic, R. Catalytic Activity–d-Band Center Correlation for the O<sub>2</sub> Reduction Reaction on Platinum in Alkaline Solutions. *J. Phys. Chem. C* **2007**, *111*, 404-410.
  55. Zhang, J.; Vukmirovic, M.; Xu, Y.; Mavrikakis, M.; Adzic, R. R. Controlling the Catalytic of Platinum-Monolayer Electrocatalysts for Oxygen Reduction with Different Substrates. *Angew. Chem. Int. Ed.* **2005**, *44*, 2132-2135.
  56. Zhang, J.; Mo, Y.; Vukmirovic, M. B.; Klie, R.; Sasaki, K.; Adzic, R. R. Platinum Monolayer Electrocatalysts for O<sub>2</sub> Reduction: Pt Monolayer on Pd(111) and on Carbon-Supported Pd Nanoparticles. *J. Phys. Chem. B* **2004**, *108*, 10955-10964.
  57. Jasinski, R. A New Fuel Cell Cathode Catalyst. *Nature* **1964**, *201*, 1212-1213.
  58. Gupta, S.; Tryk, D.; Bae, I.; Aldred, W.; Yeager, E. Heat-Treated Polyacrylonitrile-Based Catalysts for Oxygen Electroreduction. *J. Appl. Electrochem.* **1989**, *19*, 19-27.
  59. Lefevre, M.; Proietti, E.; Jaouen, F.; Dodelet, J.-P. Iron-Based Catalysts with Improved Oxygen Reduction Activity in Polymer Electrolyte Fuel Cells. *Science* **2009**, *324*, 71-74.
  60. Zitolo A. et al. Jaouen, F. Identification of Catalytic Sites for Oxygen Reduction in Iron- and Nitrogen-Doped Graphene Materials *Nat. Mater.* **2015**, *14*, 937-942.
  61. Chung, H. T.; Cullen, D. A.; Higgins, D.; Sneed, B. T.; Holby, E. F.; More, K. L.; Zelenay, P. Direct Atomic-Level Insight into the Active Sites of a High-Performance PGM-Free ORR Catalyst. *Science* **2017**, *357*, 479-484.
  62. Guo, D.; Nakamura, K. Active Sites of Nitrogen-Doped Carbon Materials for Oxygen Reduction Reaction Clarified Using Model Catalysts. *Science* **2016**, *351*, 361-365.
  63. Ren, H.; Wang, Y.; Yang, Y.; Tang, X.; Peng, Y.; Peng, H.; Xiao, L.; Lu, J.; Abruña, H. D.; Zhuang, L. Fe/N/C Nanotubes with Atomic Fe Sites: A Highly Active Cathode Catalyst for Alkaline Polymer Electrolyte Fuel Cells. *ACS Catal.* **2017**, *7*, 6485-6492.
  64. Xiong, Y.; Yang, Y.; DiSalvo, F. J.; Abruña, H. D. Metal-Organic-Framework-Derived Co-Fe Bimetallic Oxygen Reduction Electrocatalyst for Alkaline Fuel Cells. *J. Am. Chem. Soc.* **2019**, *141*, 10744-10750.
  65. Xia, B.; Wang, X. et al. A Metal-Organic-Framework-Derived Bifunctional Oxygen Catalyst. *Nat. Energy* **2016**, *1*, 15006.
  66. Suntivich, J.; Gasteiger, H. A.; Yabuuchi, N.; Nakanishi, H.; Goodenough, J.; Shao-Horn, Y. Design Principles for Oxygen-Reduction Activity on Perovskite Oxide Catalysts for Fuel Cells and Metal–Air Batteries. *Nature Chem.* **2011**, *3*, 647-647.
  67. Suntivich, J.; Gasteiger, H. A.; Goodenough, J.; Shao-Horn, Y. A Perovskite Oxide Optimized for Oxygen Evolution Catalysis from Molecular Orbital Principles. *Science* **2011**, *334*, 1383-1385.
  68. Wang, Y.; Yang, Y.; Jia, S.; Wang, X.; Lyu, K.; Peng, Y.; Zheng, H.; Wei, X.; Ren, H.; Xiao, L.; Wang, J.; Muller, D. A.; Abruña, H. D.; Hwang, B. J.; Lu, J.; Zhuang, L. Synergistic Mn-Co Catalyst Outperforms Pt on High-Rate Oxygen Reduction Reaction for Alkaline Polymer Electrolyte Fuel Cells. *Nat. Commun.* **2019**, *10*, 1506.

69. Yang, Y.; Peng, H.; Xiong, Y.; Li, Q.; Lu, J.; Xiao, L.; DiSalvo, F.; Zhuang, L.; Abruña H. High-Loading Composition-Tolerant Co-Mn Spinel Oxides with Performance beyond 1 W/cm<sup>2</sup> in Alkaline Polymer Electrolyte Fuel Cells. *ACS Energy Lett.* **2019**, *4*, 1251-1257.
70. Muller, D. A. Structure and Bonding at the Atomic Scale by Scanning Transmission Electron Microscopy *Nat. Mater.* **2009**, *8*, 263-270.
71. Arán-Ais, R. M. et al. Abruña, H. D. Identical Location Transmission Electron Microscopy Imaging of Site-Selective Pt Nanocatalysts: Electrochemical Activation and Surface Disorder. *J. Am. Chem. Soc.* **2015**, *137*, 14992-14998.
72. Ross, F. M. Opportunities and Challenges in Liquid Cell Electron Microscopy. *Science.* **2015**, *350*, aaa9886.
73. Williamson, M.; Tromp, R.; Vereecken, P.; Hull, R.; Ross, F. Dynamic Microscopy of Nanoscale Cluster Growth at the Solid-Liquid Interface. *Nat. Mater.* **2003**, *2*, 532-536.
74. de Jonge, N.; Ross, F. M. Electron Microscopy of Specimens in Liquid. *Nat. Nanotech.* **2011**, *6*, 695-704.
75. Beermann, V.; E. Holtz, M.; Padgett, E.; Araujo, J. F. de; A. Muller, D.; Strasser, P. Real-Time Imaging of Activation and Degradation of Carbon Supported Octahedral Pt-Ni Alloy Fuel Cell Catalysts at the Nanoscale Using in Situ Electrochemical Liquid Cell STEM. *Energy Environ. Sci.* **2019**, *12*, 2476-2485.
76. Zhu, G.-Z.; Prabhudev, S.; Yang, J.; Gabardo, C. M.; Botton, G. A.; Solemani, L. In Situ Liquid Cell TEM Study of Morphological Evolution and Degradation of Pt-Fe Nanocatalysts During Potential Cycling. *J. Phys. Chem. C* **2014**, *118*, 22111-22119.
77. Holtz, M.; Yu, Y.; Gunceler, D.; Gao, J.; Sundararaman, R.; Schwarz, K. A.; Arias, T. A.; Abruña, H. D.; Muller D. A. Nanoscale Imaging of Lithium Ion Distribution during *In Situ* Operation of Battery Electrode and Electrolyte. *Nano Lett.* **2014**, *14*, 1453-1439.
78. Sacci, R. L.; Black, J. M.; Balke, N.; Dudney, N. J.; More, K. L.; Unocic, R. R. Nanoscale Imaging of Fundamental Li Battery Chemistry: Solid-Electrolyte Interphase Formation and Preferential Growth of Lithium Metal Nanoclusters. *Nano Lett.* **2015**, *15*, 2011-2018.
79. Yang, C.; Chen, M. et al. Direct Observations of the Formation and Redox-Mediator-Assisted Decomposition of Li<sub>2</sub>O<sub>2</sub> in a Liquid-Cell Li-O<sub>2</sub> Microbattery by Scanning Transmission Electron Microscopy. *Adv. Mater.* **2017**, *29*, 1-7.
80. Lutz, L.; Dachraoui, W.; Demortière, A.; Johnson, L. R.; Bruce, P. G.; Grimaud, A.; Tarascon, J.-M. Operando Monitoring of the Solution-Mediated Discharge and Charge Processes in a Na-O<sub>2</sub> Battery Using Liquid-Electrochemical Transmission Electron Microscopy. *Nano Lett.* **2018**, *18*, 1280-1289.
81. Aran-Ais, R. M.; Rizo, R.; Grosse, P.; Algara-Siller, G.; Dembele, K.; Plodinec, M.; Lunkenbein, T.; Chee, S. W.; Cuenya, B. R. Imaging Electrochemically Synthesized Cu<sub>2</sub>O Cubes and Their Morphological Evolution under Conditions Relevant To CO<sub>2</sub> Electroreduction. *Nat. Commun.* **2020**, *11*, 3489.
82. Li, Y.; Kim, D.; Louisia, S.; Xie, C.; Kong, Q.; Yu, S.; Lin, T.; Aloni, S.; Fakra, S.; Yang, P. Electrochemically Scrambled Nanocrystals are Catalytically Active for CO<sub>2</sub>-To-Multicarbon. *Proc. Natl. Acad. Sci.* **2020**, *117*, 9194-9201.
83. Vavra, J.; Buonsanti, R. Real-time Monitoring Reveals Dissolution/Redeposition Mechanism in Copper Nanocatalysts during the Initial Stages of the CO<sub>2</sub> Reduction Reaction. *Angew. Chem. Int. Ed.* **2021**, *60*, 1347-1354.
84. Hermannsdorfer, de Jonge, N.; Verch, A. Electron Beam Induced Chemistry of Gold Nanoparticles in Saline Solution. *Chem. Commun.* **2015**, *51*, 16393-16396.
85. Liao, H.-G.; Zhrebetsky, D.; Xin, H.; Czarnik, C.; Ercius, P.; Elmlund, H.; Pan, M.; Wang, L.-W.; Zheng, H. Facet Development during Platinum Nanocube Growth. *Science* **2014**, *345*, 916-919.

## CHAPTER 2

### Spinel Oxides as Non-Precious Oxygen Reduction Electrocatalysts for Alkaline Fuel Cells\*

#### 2.1 Introduction

As high-efficiency energy conversion devices, proton exchange membrane fuel cells (PEMFCs) have been recognized as a crucial technology for powering electric vehicles.<sup>1-4</sup> However, PEMFCs rely on increasing the amount of expensive Pt-based electrocatalysts to facilitate the sluggish ORR at the cathode. The catalyst cost is projected to be the largest single component (up to 40%) of the total cost of a PEMFC.<sup>5</sup> Numerous past studies have been devoted to designing Pt-based alloy catalysts to partially replace the Pt with less expensive metals.<sup>6-9</sup> However, the DOE target for total Pt loading of  $\sim 0.1 \text{ g}_{\text{Pt}}/\text{kW}$  has yet to be achieved.<sup>10</sup> As an alternative, anion exchange membrane fuel cells (AEMFCs) have drawn increasing attention, because they enable the use of non-precious metal electrocatalysts, which are stable in alkaline media.<sup>11,12</sup> To facilitate the ORR kinetics in alkaline media, research efforts have been devoted to searching for electrocatalysts, including precious metal-based alloys,<sup>13,14</sup> nitrogen-doped carbons,<sup>15,17</sup> perovskites<sup>18</sup> and transition metal oxides.<sup>19</sup> 3d transition metal oxides with the spinel structure are a novel family of ORR electrocatalysts in alkaline fuel cells, due to their high activity, long-term durability and low cost. 3d Metal oxides have been intensively studied as electrocatalysts for the ORR/OER in alkaline media. Cobalt oxides and manganese oxides have been reported to be effective electrocatalysts

---

\*Reproduced with permission from the following publication:

**Yao Yang**, Yin Xiong, Megan E. Holtz, Xinran Feng, Rui Zeng, Francis J. DiSalvo, David Muller, Héctor Abruña. Octahedral Spinel Electrocatalysts for Alkaline Fuel Cells. *Proc. Natl. Acad. Sci.* **2019**, 116, 244425-24432. Copyright © NAS.

for the ORR.<sup>20-21</sup> Furthermore, Co-based bimetallic oxides have been reported to exhibit enhanced activities for the ORR in alkaline media.<sup>22-30</sup> In spite of numerous studies of 3d metal oxide electrocatalysts, the electrocatalytic mechanism remains poorly understood.<sup>13,19</sup> One of the larger challenges is that their ORR activities depend on the synthetic methods employed by different research groups, and therefore different particle sizes, morphology as well as surface and crystal structures of the nanoscale electrocatalysts. These factors are formidable to control simultaneously and complicate the understanding of the intrinsic activities of these electrocatalysts. In this chapter, we reported on a family of 15 different  $AB_2O_4$  spinels as ORR electrocatalysts with well-controlled particle size and morphology. We systematically investigated their ORR activity and selectivity and established correlations with the structure and local chemical environment, using macroscopic-level XAS and microscopic-level STEM-EELS.

## 2.2 Experimental Methods

**Synthesis:** A class of 15 types of  $AB_2O_4/C$ , A=Mn,Fe,Co,Ni,Cu and B=Mn,Fe,Co, was synthesized using a facile hydrothermal method (Fig. 2.1).

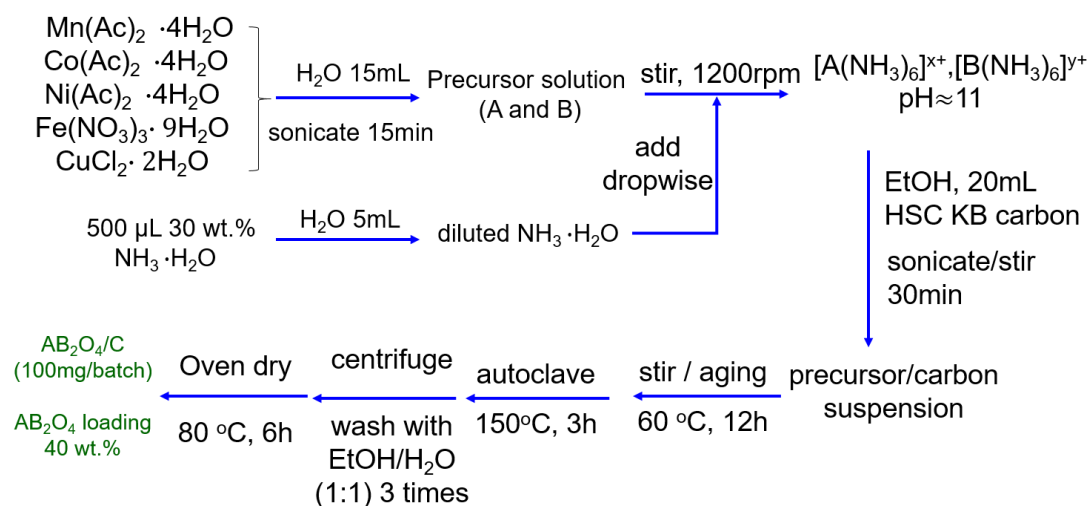


**Figure 2.1.** Hydrothermal synthesis method of 15 types of  $AB_2O_4/C$  where A can be Mn, Co, Ni, Fe and Cu and B can be Mn, Co and Fe. Ketjen black (KB) EC300J is a high-surface-area carbon (HSC-KB) with a Brunauer-Emmett-Teller (BET) surface area of  $800 \text{ m}^2/\text{g}$ .

Metal precursors, including  $Mn(Ac)_2 \cdot 4H_2O$ ,  $Ni(Ac)_2 \cdot 4H_2O$ ,  $Co(Ac)_2 \cdot 4H_2O$ ,  $Fe(NO_3)_2 \cdot 9H_2O$  and  $CuCl_2 \cdot 2H_2O$ , were dissolved in 15 mL deionized (DI) water based on the target stoichiometry of A and B elements and sonicated for 15 min. 500  $\mu\text{L}$  concentrated  $NH_3 \cdot H_2O$  were diluted in 5 mL DI water and added into the metal precursor solution dropwise under vigorous stirring at 1200 rpm. The pH of the formed metal- $NH_3$  complex solution was tested to be around 11 (Figure 2.2). Ethanol (20 mL) was added to the metal- $NH_3$  complex solution to adjust the solvent polarity and for better dispersion of the high-surface-area carbon Ketjen Black (HSC KB) which was added later. The volume ratio of ethanol to  $H_2O$  was controlled to be 1:1.

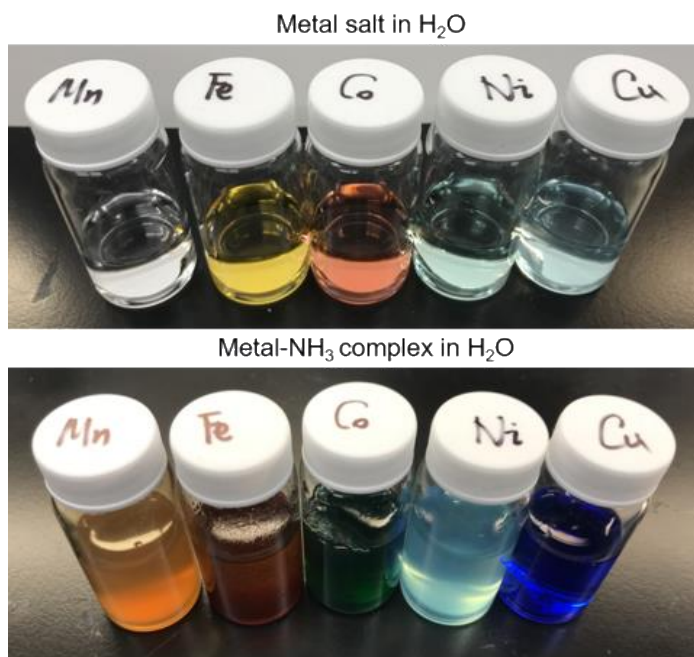


**Figure 2.2.** Color changes when a diluted  $NH_3$  solution was added to the aqueous metal precursor solutions. This simple Metal- $NH_3$  coordination chemistry is a useful visual guide for monitoring the reaction progress.

The resulting suspension/solution with HSC KB was kept under stirring at 1200 rpm and 60 °C for 12 h. The solution was then transferred to a 50 mL autoclave for hydrothermal reaction at 150 °C for 3h and the inner pressure in the autoclave was estimated to be about 30 atm. In general, the pH and ethanol/H<sub>2</sub>O volume ratio in the solvent controlled the precipitation rate of metal hydroxides, and therefore influenced the final metal oxide particle size, morphology and distribution on the carbon substrate. AB<sub>2</sub>O<sub>4</sub> supported on carbon was separated from the residual solution using a centrifuge at 6000 rpm and washed with EtOH/H<sub>2</sub>O (vol. 1:1) three times and dried in an oven at 80 °C for 6h. AB<sub>2</sub>O<sub>4</sub>/C (40 wt.%) could be synthesized in 100 mg batches and such a facile method has the potential to be scaled up. Fe(NO<sub>3</sub>)<sub>3</sub>·9H<sub>2</sub>O was used because Fe(Ac)<sub>2</sub> often led to the formation of Fe<sub>2</sub>O<sub>3</sub> impurities. CuCl<sub>2</sub> was used because Cu(Ac)<sub>2</sub> often led to the formation of CuO impurities. Mn(Ac)<sub>2</sub> and CuCl<sub>2</sub> were added later to the [Co(NH<sub>3</sub>)<sub>6</sub>]<sup>2+</sup> or [Fe(NH<sub>3</sub>)<sub>6</sub>]<sup>3+</sup> to maintain the cubic structures of ACo<sub>2</sub>O<sub>4</sub> and AFe<sub>2</sub>O<sub>4</sub> (A=Mn or Cu) to mitigate the Jahn-Teller distortion of Mn and Cu. Metal precursors for all other bimetallic oxides were added at the same time.

**X-ray Characterizations:** The crystal structure of all the synthesized NPs was examined by powder X-ray diffraction (XRD) using a Rigaku Ultima IV Diffractometer. Diffraction patterns were collected at a scan rate of 2 °/min in 0.02° steps from 20° to 80°. Mn, Co and Fe K-edge X-ray absorption near edge structure (XANES) spectra were acquired at the F-3 and C-1 beamlines of the Cornell High Energy Synchrotron Source (CHESS) from 150 eV below the metal edge out to k=12 using nitrogen filled ion chambers. XANES spectra were calibrated using metal foils and analyzed using the ATHENA software package. Raman spectra were acquired using

a RENISHAW inVia spectrometer with a 532 nm green laser.

**Electron Microscopy and Spectroscopy:** Scanning transmission electron microscopy (STEM) images and elemental electron energy loss spectroscopy (EELS) maps were acquired on a fifth-order aberration-corrected STEM (Cornell Nion UltraSTEM) operated at 100 keV with a beam convergence semi-angle of 30 mrad. Sub-Ångström spatial resolution is achievable under such operating conditions. STEM images were processed using Richard-Lucy deconvolution (3 iterations). EELS spectral images were acquired with a 0.25 eV/channel energy dispersion (energy resolution, 1.0 eV) in a Gatan spectrometer with a size of 100~200 pixels and an acquisition time of 10-20 ms/pixel. The Mn, Co and Fe elemental maps were extracted using their sharp  $L_3$  edges from EELS spectrum images and processed using principal component analysis (PCA, 3 components) and the linear combination of power law (LCPL) to subtract the background, in ImageJ software. Fine EELS spectra with an energy resolution down to 0.5 eV were used to investigate the electron-loss near-edge structure (ELNES). Metal oxide references, including CoO, MnO,  $Co_3O_4$ ,  $Mn_3O_4$ , CoOOH and  $Mn_2O_3$ , were pure chemical reagents (A.R.) with average particle sizes of about 50 nm. CoOOH instead of  $Co_2O_3$  was used as reference for  $Co^{3+}$  since  $Co_2O_3$  is a chemically unstable compound. Beam damage was routinely examined before and after the acquisition of EELS spectrum images (200×200 pixels, 10 ms/pixel). ELNES spectra were aligned by calibrating the high-loss (core-loss) spectrum against the low-loss (zero loss peak, ZLP) spectrum pixel by pixel (acquisition time: 10 ms/pixel) in dual EELS mode. Spectra alignment were performed using customized MATLAB code and ZLP was routinely examined to be precisely at  $0.0 \pm 0.1$  eV to ensure the accuracy of the peak position

for metal L edges and oxygen K edges. Beam damage of reference oxides was routinely examined before and after EELS mapping. TEM-EDX spectra were collected in a FEI Tecnai F-20 electron microscope equipped with an Oxford X-Max detector. The projected crystal models were generated using Crystal Maker software based on standard XRD database.

**Electrochemical Characterizations (RDE):** 5.0 mg AB<sub>2</sub>O<sub>4</sub>/C (40 wt.%) and Pt/C (20 wt.%) catalysts were mixed with 1.0 mL 0.05 wt% Nafion /ethanol solution and subsequently sonicated for approximately 30 minutes to form homogenous catalyst inks. 10  $\mu$ L of the resulting AB<sub>2</sub>O<sub>4</sub>/C catalyst ink was loaded onto a glassy carbon (GC) electrode (diameter, 5 mm) as the working electrode (WE), achieving a metal oxide loading of 0.1 mg/cm<sup>2</sup>, followed by thermal evaporation of the solvent under infrared light. Similarly, 5  $\mu$ L of a Pt/C catalyst ink were loaded on a GC electrode to achieve a loading of 25  $\mu$ g/cm<sup>2</sup>, a common value for comparison in fuel cell tests. Ag/AgCl in saturated KCl solution served as the reference electrode (RE) and a large-surface-area graphite rod was used as the counter electrode (CE). The potential difference between Ag/AgCl in saturated KCl and a reversible hydrogen electrode (RHE) in 1M KOH was calculated to be 1.0258 V based on the Nernst equation. To avoid any potential contamination of precious metal for the measurements on non-precious AB<sub>2</sub>O<sub>4</sub>/C, the three-neck electrochemical cell was washed using aqua regia (HCl+HNO<sub>3</sub>) and followed by rinsing thoroughly (3X) using ultrapure water. Electrochemical measurements were performed on a Solartron potentiostat. ORR measurements were carried on with a rotating disk electrode (RDE, Pine Instruments) in oxygen-saturated 1M KOH solution at room temperature (23 °C). Reproducible experiments suggested

that the relative error in  $E_{1/2}$  was within  $\pm 3$  mV. The MA was calculated by normalizing the kinetic current, extracted from the Koutecky-Levich equation, to the mass loading of the metal oxide.

**Cyclic voltammetry:** CV profiles were obtained at 10 mV/s in Ar-saturated 1M KOH. ORR polarization profiles were obtained at 5 mV/s and 1600 rpm after 10 CV cycles from 0.1 to 1.2 V vs. the reversible hydrogen electrode (RHE) at 10 mV/s to clean the surface and activate the catalyst. The capacitive background currents in CV profiles, measured in Ar-saturated 1M KOH solution (5mV/s, 0.3-1.1 V) were subtracted from the raw ORR data. ORR profiles were then obtained and plotted with metal oxide loadings of 0.1, 0.25, 0.5 and 1.0 mg/cm<sup>2</sup>. Durability tests were carried out by potential cycling from 0.6 V to 1.0 V at 100 mV/s for 10,000 cycles. The ORR profiles after 10,000 cycles were measured in a fresh 1M KOH solution to avoid potential contamination from metal species in the solution.

**RRDE Measurements:** The ORR reaction in alkaline media involves a main reaction of a 4e<sup>-</sup> process to H<sub>2</sub>O and a side reaction of 2a e<sup>-</sup> process to H<sub>2</sub>O<sub>2</sub>. Rotating ring-disk electrode RRDE voltammetry (Pine Instruments) was employed to detect the H<sub>2</sub>O<sub>2</sub> generated at the disk during the oxygen reduction process. The RRDE with a GC disk (0.2475 cm<sup>2</sup>) and a Pt ring (0.1866 cm<sup>2</sup>) was calibrated to have a collection efficiency of 37% using 10 mM K<sub>3</sub>Fe(CN)<sub>6</sub> with 0.1 M K<sub>2</sub>SO<sub>4</sub> supporting electrolyte. RRDE measurements were performed in 1 M KOH at 1600 rpm and 5 mV/s and the ring potential was held at 1.3 V vs. RHE to be sufficiently high to oxidize any H<sub>2</sub>O<sub>2</sub> generated at the disk. The H<sub>2</sub>O<sub>2</sub> yield and electron number were calculated through the following equations at which N<sub>o</sub>=37%:

$$\text{H}_2\text{O}_2 \text{ Yield} = \frac{2I_{\text{R}}/N_0}{(I_{\text{R}}/N_0)+I_{\text{D}}} \times 100\%; \text{ electron number} = \frac{4I_{\text{D}}}{(I_{\text{R}}/N_0)+I_{\text{D}}}$$

### 2.3 Hydrothermal Synthesis of 15 Types of Spinel Oxides

A family of 15 different spinel metal oxides,  $\text{AB}_2\text{O}_4$ , (A: Mn, Fe, Co, Ni, and Cu, and B: Mn, Fe, and Co), were synthesized using a facile hydrothermal method (Fig. 2.1). Briefly, one or two metal precursors were dissolved in water and reacted with ammonium hydroxide to form coordination compounds with  $\text{NH}_3$  ligands. Monometallic or bimetallic hydroxides gradually precipitated from the solution through aging processes, at controlled temperatures, with selected solvents. The metal hydroxides subsequently formed metal oxide nanoparticles, supported on high-surface-area carbon Ketjen black (HSC KB) with a mass loading of 40%, upon reaction in an autoclave at a mild temperature (150 °C) under a modest pressure of about 30 bar. Using powder X-ray diffraction (XRD), the resulting products were found to be single-phase spinels (Fig. 2.3).

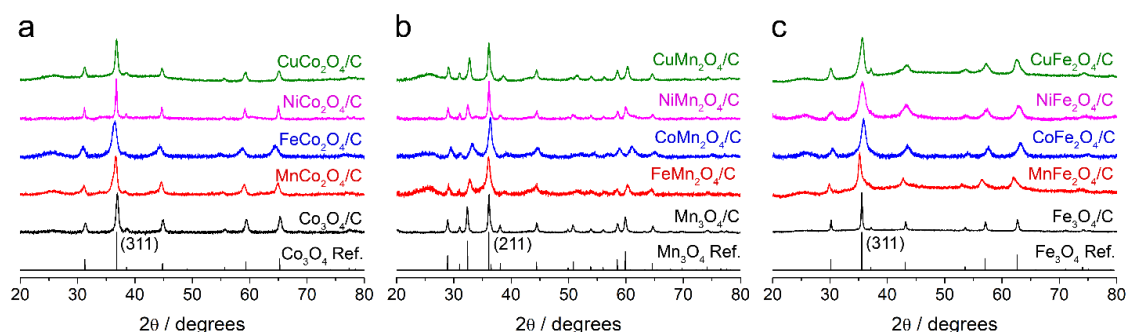


**Figure 2.3.** Powder XRD patterns of  $\text{AB}_2\text{O}_4/\text{C}$  (A: Mn, Fe, Co, Ni, Cu, B: Mn, Fe, Co).  $\text{Co}_3\text{O}_4$ ,  $\text{Mn}_3\text{O}_4$  and  $\text{Fe}_3\text{O}_4$  reference patterns are based on PDFs # 01-076-1802, 01-080-0382 and 01-077-1545, respectively.  $\text{ACo}_2\text{O}_4/\text{C}$ ,  $\text{AMn}_2\text{O}_4/\text{C}$  and  $\text{AFe}_2\text{O}_4/\text{C}$  were found to be cubic spinel, tetragonal spinel and reverse cubic spinel structures, respectively.

The Co-based spinel family ( $\text{ACo}_2\text{O}_4$ ) has a regular cubic spinel structure in which the A atoms occupy the tetrahedral sites while Co atoms occupy the octahedral sites (Fig.

2.4).  $ACo_2O_4/C$  ( $A = Mn, Fe, Ni$  and  $Cu$ ) exhibited similar XRD patterns as  $Co_3O_4/C$ , with (311) as the strongest peak (Fig. 2.3a). The XRD patterns indicated that they all adopt the cubic spinel structure. XRD patterns of  $MnCo_2O_4/C$  and  $FeCo_2O_4/C$  exhibited a slight shift of the (311) reflections to lower angles, relative to  $Co_3O_4/C$ , which is likely due to the lattice expansion upon replacing  $Co$  with  $Fe/Mn$ , as expected from the larger

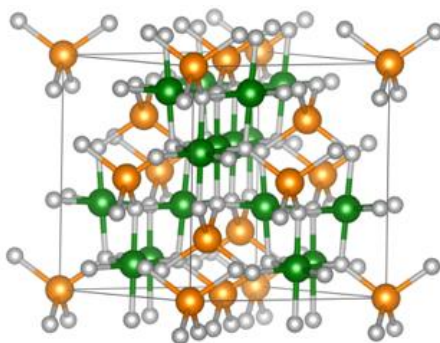


**Figure 2.4.** Crystal model of  $Co_3O_4$  ( $Co^{II}Co_2^{III}O_4$ ) with a cubic spinel structure where  $a=b=c=8.072 \text{ \AA}$  and  $\alpha=\beta=\gamma=90^\circ$ . In the regular cubic spinel structure of  $CoCo_2O_4$  ( $AB_2O_4$ ),  $Co^{II}$  atoms (orange) occupy the tetrahedral sites while  $Co^{III}$  atoms (green) occupy the octahedral sites (oxygen atoms are in grey). 3D crystal model was built based on  $Co_3O_4$  (PDF # 01-076-1802) through the VESTA software.

cationic radii of  $Mn$  and  $Fe$  relative to  $Co$ .<sup>31</sup> In contrast to  $Co_3O_4$ , the  $Mn$ -based spinel family ( $AMn_2O_4$ ) had a tetragonal spinel structure (Fig. 2.3b), due to the Jahn-Teller distortion.<sup>32</sup> The XRD patterns of  $AMn_2O_4/C$  exhibited more diffraction peaks at around  $30^\circ$  and  $60^\circ$ , when compared to  $ACo_2O_4/C$ , indicating a decrease in crystal symmetry (Fig. 2.3b). The XRD patterns of the  $Fe$ -based spinel family, ( $AFe_2O_4/C$ ), on the other hand, adopt a cubic inverse spinel structure, where all of the  $A$  atoms and half of the  $Fe$  atoms occupy octahedral sites, while the other half of the  $Fe$  atoms occupy the tetrahedral sites. The XRD patterns of  $AFe_2O_4/C$  ( $A=Mn, Co, Ni$  and  $Cu$ ) suggest a cubic spinel structure, similar to that of  $Fe_3O_4/C$  (Fig. 2.3c). When compared to  $Fe_3O_4/C$ ,  $AFe_2O_4/C$  exhibited intriguing peak shifts of the (311) reflections: a shift to

$2\theta$  values in the case of  $\text{MnFe}_2\text{O}_4/\text{C}$  and a shift higher  $2\theta$  values for  $\text{CoFe}_2\text{O}_4/\text{C}$ ,  $\text{NiFe}_2\text{O}_4/\text{C}$  and  $\text{CuFe}_2\text{O}_4/\text{C}$ . These observations likely originate from the fact that relative to Fe, Mn has a larger atomic radius while Co, Ni and Cu have smaller radii, causing lattice expansions and contractions, respectively.  $\text{ACo}_2\text{O}_4/\text{C}$  exhibited an average domain size of around 15 nm except for  $\text{NiCo}_2\text{O}_4/\text{C}$ , which had a size of 30 nm.  $\text{AFe}_2\text{O}_4$  exhibited an average domain size of around 12 nm except for  $\text{Fe}_3\text{O}_4/\text{C}$  which had a size of 30 nm.  $\text{AMn}_2\text{O}_4$  had an average domain size of around 12 nm when A were Co and Fe, and a size of around 25 nm when A are Mn, Ni and Cu.

#### **2.4 RDE Measurement of ORR Activity and CV Analysis**

With the crystal structures of  $\text{AB}_2\text{O}_4/\text{C}$  confirmed by XRD, the ORR activities of  $\text{AB}_2\text{O}_4/\text{C}$  were preliminarily evaluated using the rotating-disk electrode (RDE) technique. The ORR polarization profile for Pt/C exhibited a half-wave potential ( $E_{1/2}$ ) of 0.890 V vs. the reversible hydrogen electrode (RHE), a benchmark activity value for Pt in 1M KOH (dashed lines in [Figs. 2.5a-c](#)). The ORR polarization profiles of  $\text{ACo}_2\text{O}_4/\text{C}$  in [Fig. 2.5a](#) suggest that  $\text{ACo}_2\text{O}_4/\text{C}$  reach a transport limited current,  $I_d$ , close to that of Pt/C, indicating that the main reaction product is water, as is the case on Pt.

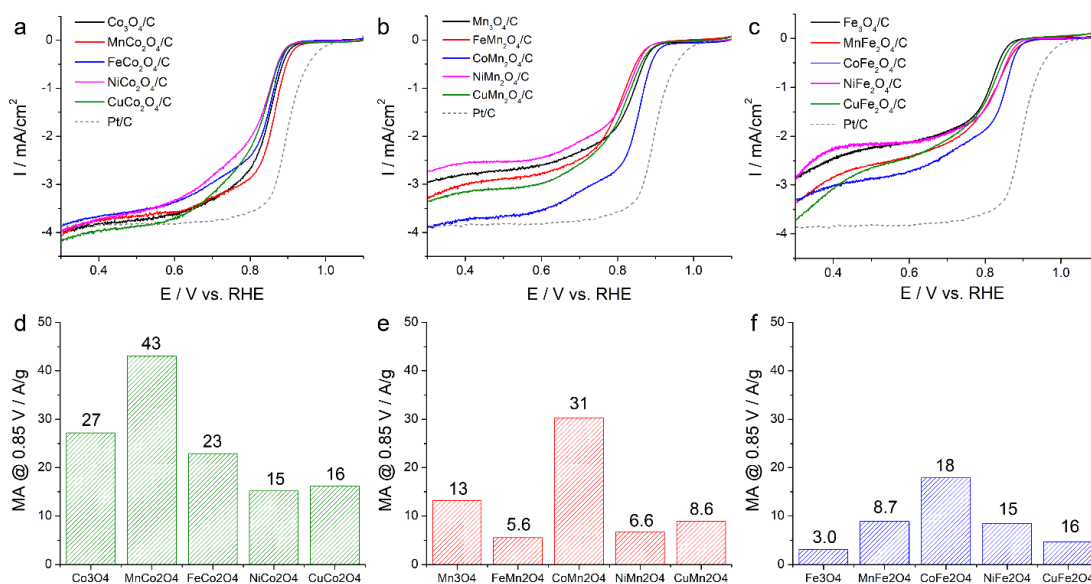


**Figure 2.5.** ORR activity of AB<sub>2</sub>O<sub>4</sub>/C spinel electrocatalysts. (a-c) ORR polarization profiles of 15 different AB<sub>2</sub>O<sub>4</sub>/C in O<sub>2</sub>-saturated 1M KOH at 1600 rpm and a scan rate of 5 mV/s. Mass loading of metal oxides and Pt: 0.1 mg/cm<sup>2</sup> and 25 μg/cm<sup>2</sup>, respectively. (d-f) Mass-specific activity (MA) of AB<sub>2</sub>O<sub>4</sub>/C at 0.85 V vs. RHE, which was calculated by normalizing the kinetic current to the mass loading of the metal oxide. MnCo<sub>2</sub>O<sub>4</sub>/C, CoMn<sub>2</sub>O<sub>4</sub>/C and CoFe<sub>2</sub>O<sub>4</sub>/C were found to be the three most active ORR electrocatalysts.

It should be noted that, based on the Levich equation, the  $I_d$  for the 4e<sup>-</sup> reduction of oxygen in 0.1 M oxygen saturated KOH or HClO<sub>4</sub> should be -5.5 mA/cm<sup>2</sup> at 1600 rpm. Since the O<sub>2</sub> solubility in 1M KOH (as used in the present work) at 25 °C and 1 atm is  $8.42 \times 10^{-4}$  mol/L, which is 70% of its value in 0.1 M KOH ( $1.21 \times 10^{-3}$  mol/L),<sup>33</sup> the  $I_d$  for the 4e<sup>-</sup> reduction of oxygen in 1M KOH will be correspondingly lower with a value of -3.8 mA/cm<sup>2</sup> at 1600rpm. Among the five types of AC<sub>2</sub>O<sub>4</sub>/C catalysts, MnCo<sub>2</sub>O<sub>4</sub>/C clearly stands out as the most active candidate in the Co-based spinel family with an  $E_{1/2}$  value of 0.855 V vs. RHE. The mass-specific activity (MA) at 0.85 V was employed as a metric value to partially evaluate the initial electrocatalytic activity. As shown in Fig. 2.5d, the MA at 0.85 V of MnCo<sub>2</sub>O<sub>4</sub> (43 A/g) was about 1.5 times as high as that of monometallic Co<sub>3</sub>O<sub>4</sub>/C (27 A/g), and over two-times, relative to

$ACo_2O_4/C$  (A=Fe, Ni and Cu), respectively. For the Mn-based spinel family, ORR polarization profiles of  $AMn_2O_4/C$  demonstrate that  $CoMn_2O_4/C$  has significant ORR activity with an  $E_{1/2}$  value of 0.844 V, when compared to that of the monometallic  $Mn_3O_4/C$  (black curve). However, the  $AMn_2O_4/C$  materials involving Fe, Ni and Cu exhibited a decrease in activity (Fig. 2.5b). The MA at 0.85 V of  $CoMn_2O_4/C$  (31 A/g) was 2.5 times as high as that of monometallic  $Mn_3O_4/C$  (13 A/g), and over three times higher than other  $AMn_2O_4/C$  involving Fe, Ni and Cu (Fig. 2.5e). Finally, the ORR polarization profiles of the Fe-based spinel family,  $AFe_2O_4/C$ , exhibited an overall lower activity, relative to the Co-based and Mn-based spinel families.  $I_d$  values of  $AFe_2O_4/C$  were noticeably lower than that of Pt/C, indicating that a significant amount of peroxide formed (Fig. 2.5c). Among the Fe-based spinels, the most active,  $CoFe_2O_4/C$ , had a MA value (18 A/g) twice as large as those of  $MnFe_2O_4/C$  (8.7 A/g) and  $NiFe_2O_4/C$  (8.7 A/g) and over a four-fold increase, relative to  $Fe_3O_4/C$  and  $CuFe_2O_4/C$  (Fig. 2.5f). It is worth pointing out that ferrous ( $Fe^{2+}$ ) ions are actually used as the catalyst in Fenton's reagent to generate radicals that decompose organic compounds, which, in the present context, would also damage the polymer membrane in fuel cells.

In summary,  $MnCo_2O_4/C$ ,  $CoMn_2O_4/C$ , and  $CoFe_2O_4/C$  have been demonstrated to be the three most active candidates among the 15 types of  $AB_2O_4/C$  spinels.  $MnCo_2O_4$  was selected as an example to test the impact of the carbon substrate on the activity.

Cyclic voltammetric (CV) profiles of mono/bimetallic oxides were compared to reveal more information about the active redox couples for catalyzing the ORR (Fig. 2.6).  $Co_3O_4/C$  exhibits two oxidation peaks at 1.08, 0.93 V and one reduction peak at

0.68 V (there is a hint of a second reduction peak at about 0.4 V but the large double layer precludes a more detailed analysis) while  $\text{Mn}_3\text{O}_4/\text{C}$  exhibits one active redox couple at 1.10/0.64 V. The lack of noticeable redox couples for  $\text{Fe}_3\text{O}_4/\text{C}$  from 0.2 to 1.3 V explains why  $\text{Fe}_3\text{O}_4/\text{C}$  shows much lower ORR activity than  $\text{Co}_3\text{O}_4/\text{C}$  and  $\text{Mn}_3\text{O}_4/\text{C}$ .

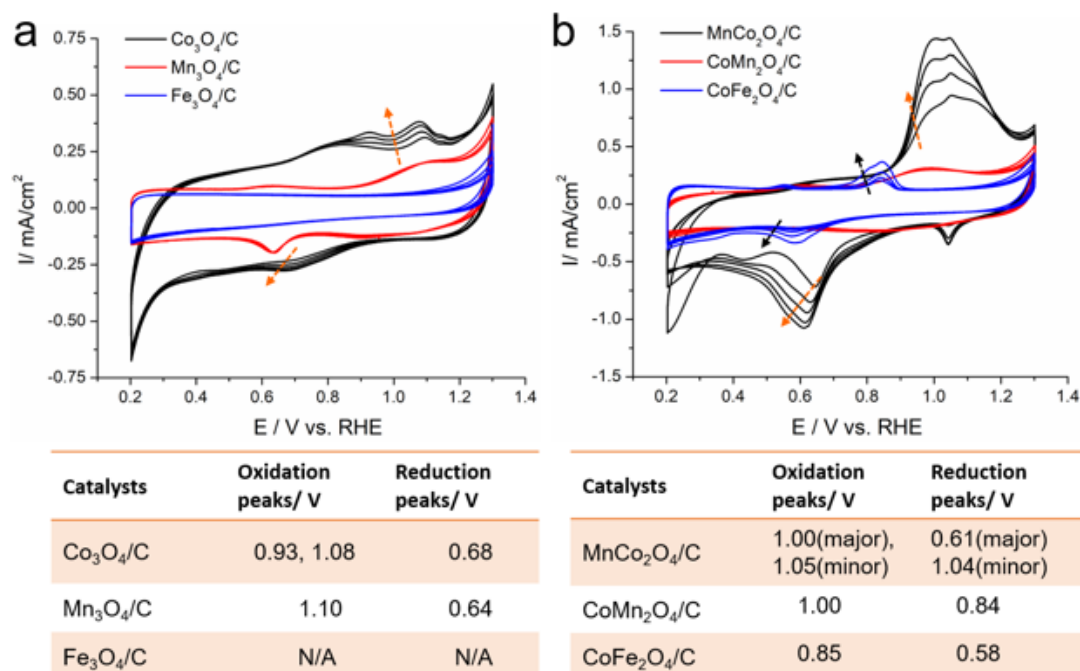


**Figure 2.6** CV profiles (initial four cycles) of monometallic oxides ( $\text{Co}_3\text{O}_4/\text{C}$ ,  $\text{Mn}_2\text{O}_4/\text{C}$ ,  $\text{Fe}_3\text{O}_4/\text{C}$ ) and selected bimetallic oxides ( $\text{MnCo}_2\text{O}_4/\text{C}$ ,  $\text{CoMn}_2\text{O}_4/\text{C}$ ,  $\text{CoFe}_2\text{O}_4/\text{C}$ ) at a scan rate of 10 mV/s at metal oxide loading of 0.1 mg/cm<sup>2</sup> in 1M KOH. Dashed arrows indicate the gradual evolution of redox peaks in the CV profiles. The tables list the oxidation and reduction peak positions.

Among those,  $\text{MnCo}_2\text{O}_4/\text{C}$  exhibited a larger redox current than  $\text{CoMn}_2\text{O}_4/\text{C}$  and  $\text{CoFe}_2\text{O}_4/\text{C}$ , and a pronounced minor redox couple at 1.05/1.04 V. Detailed analysis of the CV profiles suggests that this minor redox couple comes from monolayer species on the surface with a highly reversible reaction process (Fig. 2.7), which may partially explain the highest initial activity of  $\text{MnCo}_2\text{O}_4$  among all  $\text{AB}_2\text{O}_4/\text{C}$  materials.

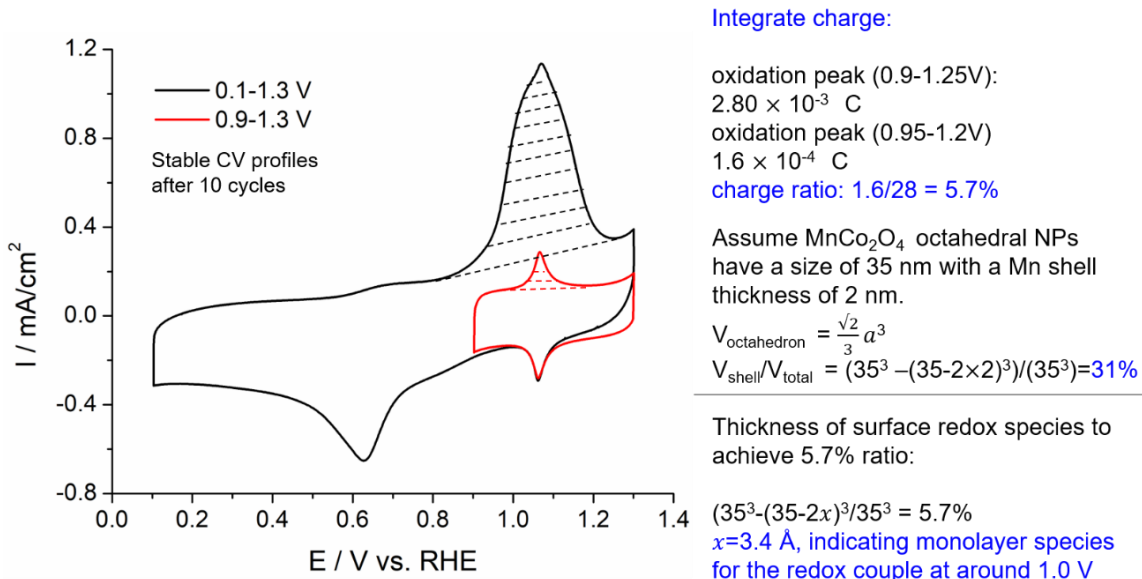


**Figure 2.7.** CV profiles of  $\text{MnCo}_2\text{O}_4/\text{C}$  after ten continuous cycles at a scan rate of 10mV/s in 1M KOH. Charge ratio of the minor peak at 1.05 V to the major peak was calculated to be around 5.7: 100, indicating monolayer species on the surface with a highly reversible reaction process (oxidation/reduction potential of the minor peak is 1.05/1.04 V, with a  $\Delta E_p$  of  $\sim 10$  mV). The coulometric charge of oxidation peaks was integrated as marked by the shadowed areas in CV profiles.

$\text{MnCo}_2\text{O}_4/\text{C}$  and  $\text{CoMn}_2\text{O}_4/\text{C}$  exhibited smaller Tafel slopes of 46 and 49 mV/dec, respectively, relative to Pt/C (66 mV/dec), suggesting a smaller overpotential to achieve the same kinetic current change (Fig. 2.8).

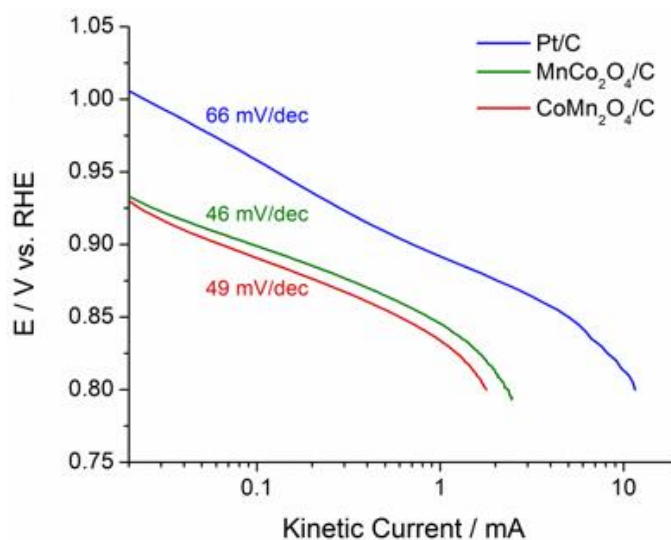


**Figure 2.8** Tafel plots and slopes of Pt/C,  $\text{MnCo}_2\text{O}_4$  and  $\text{CoMn}_2\text{O}_4$ .

## 2.5 RRDE Measurements of ORR Selectivity

After studying the ORR activity of  $\text{AB}_2\text{O}_4/\text{C}$  and corresponding redox couples, the catalyst selectivity was further investigated using the rotating ring-disk electrode (RRDE) technique. The ORR selectivity ( $\text{H}_2\text{O}$  vs  $\text{H}_2\text{O}_2$ ) of Pt/C was first examined using a GC-disk and Pt-ring RRDE, with the ring potential held at 1.3 V vs. RHE to oxidize any peroxide generated at the GC disk.<sup>34</sup> As shown in Fig. 2.9 Pt/C exhibits a potential-dependent  $\text{H}_2\text{O}_2$  yield of 2%~5% and an electron transfer number of 3.98-3.90.

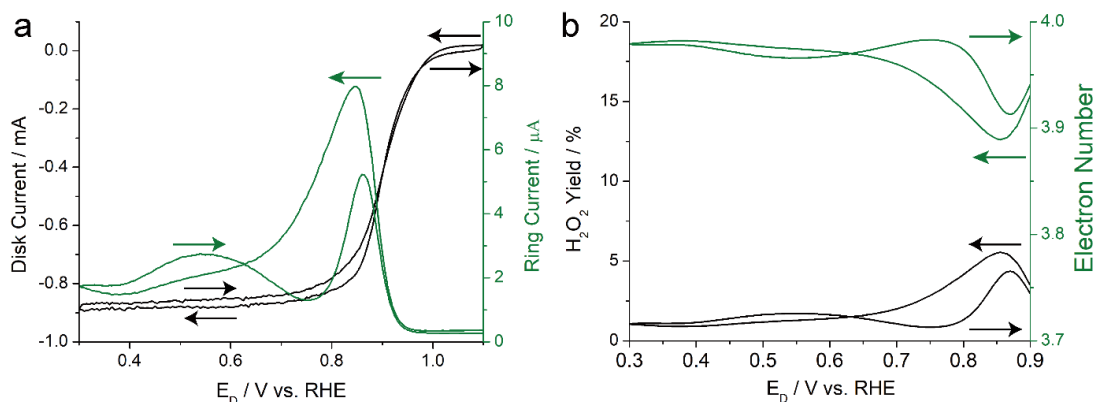


**Figure 2.9** RRDE profiles of Pt/C at a mass loading of  $25 \mu\text{g}/\text{cm}^2$  on GC. (a) disk and ring currents measured in  $\text{O}_2$ -saturated  $1\text{M KOH}_{(\text{aq})}$  at 1600 rpm and a scan rate of 5 mV/s. The ring potential,  $E_R$  was held at 1.3 V vs. RHE to be sufficiently high to oxidize the generated  $\text{H}_2\text{O}_2$  (b)  $\text{H}_2\text{O}_2$  yield and electron number were calculated based on the ring and disk currents.

RRDE profiles of  $\text{CoMn}_2\text{O}_4/\text{C}$  exhibited a peak ring current of  $\sim 35 \mu\text{A}$ , larger than that of Pt/C ( $\sim 8 \mu\text{A}$ ), indicating a larger fraction of peroxide formation.  $\text{H}_2\text{O}_2$  yield and electron transfer number were calculated to be around 20% and 3.6, respectively. Inspired by previous studies on the impact of loading of Fe-N-C catalysts on  $\text{H}_2\text{O}_2$  formation,<sup>35-38</sup> RRDE profiles of  $\text{CoMn}_2\text{O}_4/\text{C}$  at various loadings were measured. When the metal oxide loading was increased from 0.1 to  $0.5 \text{ mg}/\text{cm}^2$ , a significant

improvement in ORR activity was observed with the  $E_{1/2}$  shifting positively by 30 mV from 0.86 V at 0.1 mg/cm<sup>2</sup> to 0.89 V at 0.5 mg/cm<sup>2</sup>. This last value is essentially the same as the measured benchmark value of Pt/C (0.89 V) (Fig. 2.10a).

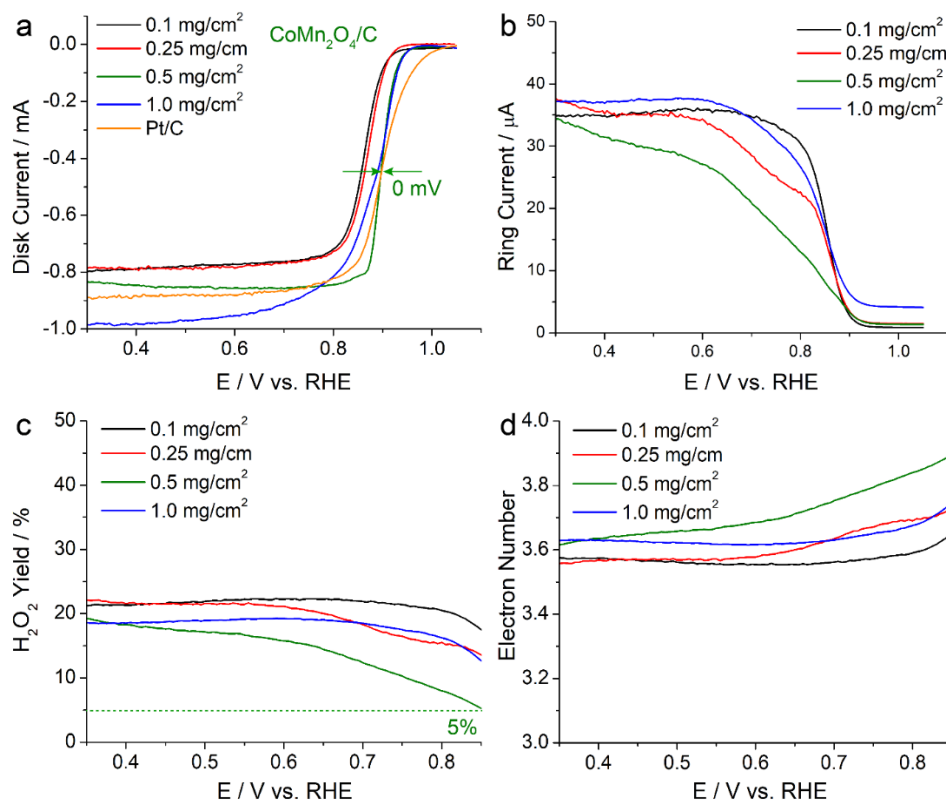


**Figure 2.10. ORR selectivity of CoMn<sub>2</sub>O<sub>4</sub>/C at various mass loadings of metal oxides.** (a-b) RRDE profiles of disk and ring currents measured on a GC-disk and Pt-ring RRDE in O<sub>2</sub>-saturated 1M KOH at 1600 rpm and a scan rate of 5 mV/s. Ring potential was held at 1.3 V vs. RHE to oxidize the H<sub>2</sub>O<sub>2</sub> generated at the disk. (c-d) H<sub>2</sub>O<sub>2</sub> yields and electron numbers calculated based on ring and disk currents. CoMn<sub>2</sub>O<sub>4</sub>/C at an optimal loading of 0.5 mg/cm<sup>2</sup> achieved a  $E_{1/2}$  value of 0.89 V, equal to the Pt/C, and a H<sub>2</sub>O<sub>2</sub> yield down to 5% at 0.85 V, comparable to Pt/C.

The ring current dropped noticeably at higher loadings and the H<sub>2</sub>O<sub>2</sub> yield at 0.9 V decreased from 18% at 0.1 mg/cm<sup>2</sup> to 12.5% at 0.25 mg/cm<sup>2</sup>, and finally to as low as 5% at 0.5 mg/cm<sup>2</sup> (Figs. 2.10b-c). The electron transfer number at 0.9 V increased from 3.65 at 0.1 mg/cm<sup>2</sup> to as high as 3.9 at 0.5 mg/cm<sup>2</sup> (Fig. 2.10d). A similar

improvement was also observed for  $\text{MnCo}_2\text{O}_4/\text{C}$  (Fig. S12 in this work, Yang, PNAS, 2019). The peroxide yield of Co-Mn oxides in alkaline media was comparable to previous reports on similar catalysts.<sup>39</sup> At an ultrahigh loading level of  $1.0 \text{ mg}_{\text{metal oxide}}/\text{cm}^2$ , the ORR polarization profile of  $\text{CoMn}_2\text{O}_4$  in the mass transport-controlled region ( $E < 0.8 \text{ V}$ ) no longer followed the typical diffusion-limited characteristic, indicating significant mass transport limitations arising from the very thick catalyst layer. Therefore, we propose that metal oxides, at higher loading, can provide a higher number of active sites and a sufficiently thick catalyst layer to decompose a significant portion of the electrogenerated  $\text{H}_2\text{O}_2$  before it escapes from the catalyst layer into solution. The high loadings of Co-Mn oxides are critical in practical membrane-electrode assembly (MEA) measurements for a high peak power density of  $> 1 \text{ W}/\text{cm}^2$ , as we reported, in detail, in our recent work.<sup>25,26</sup>

## 2.6 Powder XAS Structural Analysis

In order to establish why  $\text{MnCo}_2\text{O}_4/\text{C}$ ,  $\text{CoMn}_2\text{O}_4/\text{C}$  and  $\text{CoFe}_2\text{O}_4$  stand out as the three most active electrocatalysts toward the ORR, thorough investigations of the morphology, crystal structure and local chemical environment were carried out employing macroscopic-level XAS and microscopic-level STEM-EELS. The Mn XANES spectra in Fig. 2.11a indicate that gradually increasing the Co contents in Mn-based spinels, from  $\text{Mn}_3\text{O}_4/\text{C}$  to  $\text{CoMn}_2\text{O}_4/\text{C}$  and  $\text{MnCo}_2\text{O}_4/\text{C}$ , leads to a progressive positive shift of the Mn edge energy, indicating a higher Mn valence state and charge transfer from Mn to Co. Symmetrically, a gradual increase in the Mn contents in Co-based spinels, from  $\text{Co}_3\text{O}_4/\text{C}$  to  $\text{MnCo}_2\text{O}_4/\text{C}$  and  $\text{CoMn}_2\text{O}_4/\text{C}$ , results in a negative shift in the Co edge energy, again suggesting a lower Co valence state and charge transfer

from Mn to Co (Fig. 2.11b). This local interaction indicates that Mn and Co have mutually altered their electronic structures, which may explain the fact that both  $\text{MnCo}_2\text{O}_4/\text{C}$  and  $\text{CoMn}_2\text{O}_4/\text{C}$  exhibit significantly enhanced ORR activity, relative to their monometallic oxide counterparts,  $\text{Mn}_3\text{O}_4/\text{C}$  and  $\text{Co}_3\text{O}_4/\text{C}$ , respectively.

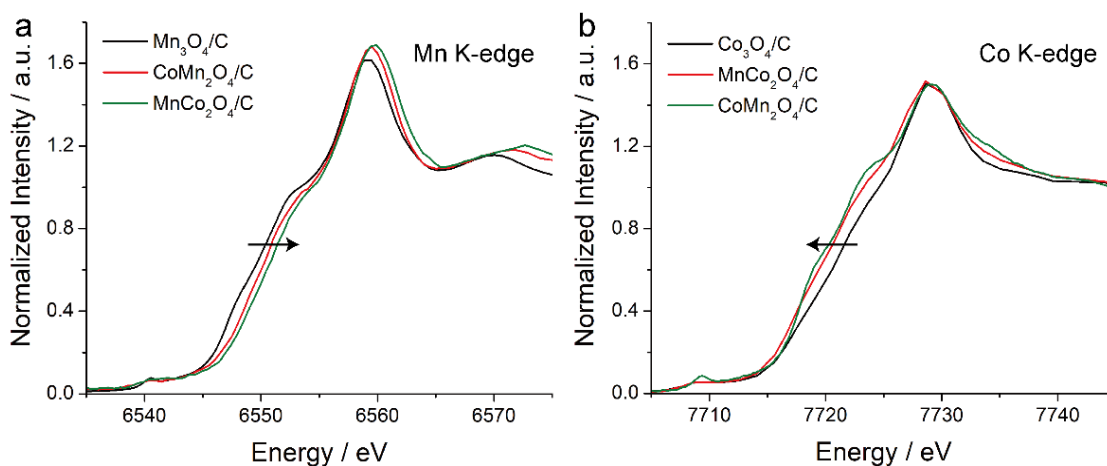


**Figure 2.11 Powder XANES spectra of spinel  $\text{MnCo}_2\text{O}_4/\text{C}$  and  $\text{CoMn}_2\text{O}_4/\text{C}$ .** (a-b) XANES spectra of Mn and Co K-edges of  $\text{Mn}_3\text{O}_4/\text{C}$ ,  $\text{CoMn}_2\text{O}_4/\text{C}$ ,  $\text{MnCo}_2\text{O}_4/\text{C}$  and  $\text{Co}_3\text{O}_4/\text{C}$ , respectively. Black arrows indicate the positive and negative shift in the edge energy of Mn and Co, respectively.

## 2.7 Atomic-scale STEM Imaging

The morphology and microstructure of  $\text{MnCo}_2\text{O}_4/\text{C}$  and  $\text{CoMn}_2\text{O}_4$  were examined using an aberration-corrected STEM. Figs. 2.12a-b exhibit the well-defined octahedral morphology of  $\text{MnCo}_2\text{O}_4$  nanoparticles. The STEM image intensity varies at different regions of the  $\text{MnCo}_2\text{O}_4$  nanoparticles (Fig. 2.12a), indicating the possible existence of nm-scale pores or channels on the surface or inside the metal oxide nanoparticle, which may expose the inner part of the metal oxide to  $\text{O}_2$  molecules.<sup>40,41</sup> The particle size distribution (PSD) histogram of  $\sim 200$   $\text{MnCo}_2\text{O}_4$  nanoparticles indicates an average particle size of 35 nm. The majority of the  $\text{MnCo}_2\text{O}_4$  nanoparticles appear to have multiple subdomains since the domain size, calculated from XRD, was 15 nm.

CoMn<sub>2</sub>O<sub>4</sub>/C nanoparticles were found to have similar octahedral morphology and multiple subdomains.

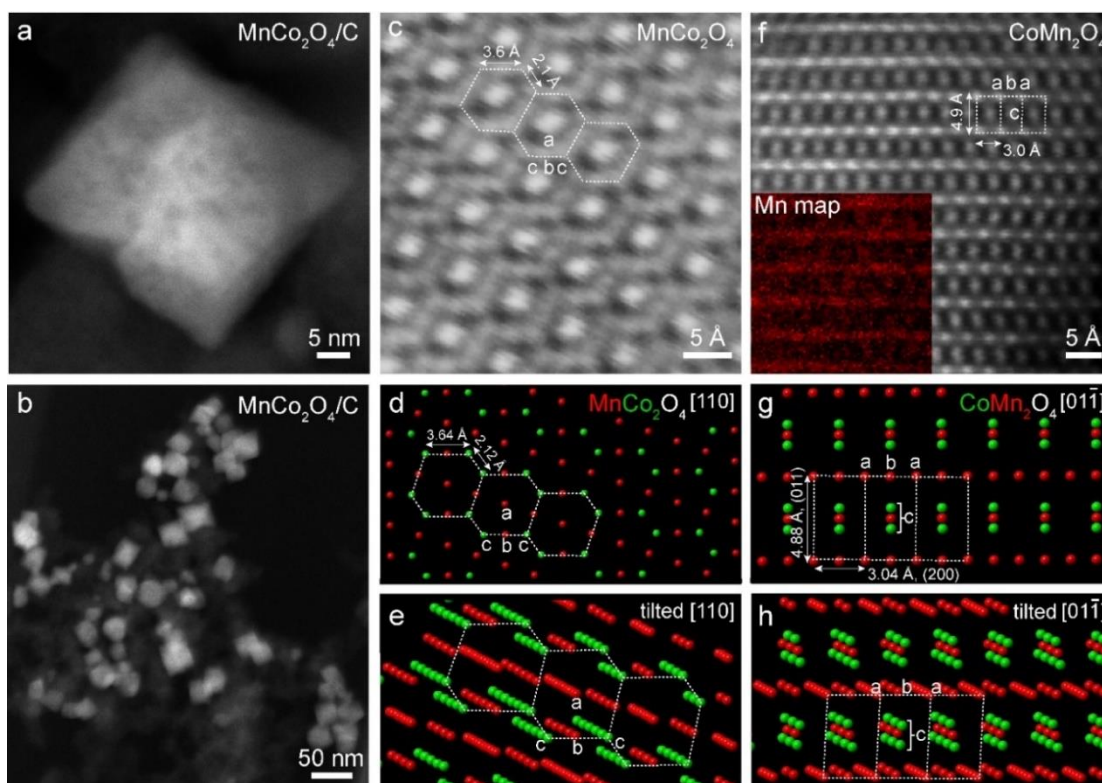


**Figure 2.12** HAADF-STEM images of spinel MnCo<sub>2</sub>O<sub>4</sub>/C and CoMn<sub>2</sub>O<sub>4</sub>/C. (a-b) Octahedral MnCo<sub>2</sub>O<sub>4</sub> nanoparticles with an average particle size of 35 nm supported on HSC KB carbon. (c-e) Atomic-scale STEM image of MnCo<sub>2</sub>O<sub>4</sub> and the corresponding crystal model projected on the [110] zone axis. Atom columns **a** exhibit brighter intensity than **b** and **c** due to the higher atom density, as shown in the tilted crystal model in (e). (f) Atomic-scale STEM image of CoMn<sub>2</sub>O<sub>4</sub> on the [01 $\bar{1}$ ] zone axis. Inset, atomic-scale EELS elemental mapping of Mn showing the characteristic layered structure in spinel. (g-h) Crystal model of CoMn<sub>2</sub>O<sub>4</sub> corresponding to the image in (f) with two perpendicular lattice planes of (011) and (200). Atom columns **a** exhibit higher intensity than **b** due to the higher atom density, as shown in the tilted crystal model in (h).

Furthermore, atomic-scale HAADF-STEM images of MnCo<sub>2</sub>O<sub>4</sub> clearly show the spinel structure on the [110] zone axis (Fig. 2.12c). MnCo<sub>2</sub>O<sub>4</sub> exhibits hexagonal repeating unit cells, as indicated by the dashed boxes with two d-spacings of 3.6 and 2.1 Å (Fig. 2.12c), which match well with the theoretical values (3.64 and 2.12 Å), based

on the crystal model of  $\text{MnCo}_2\text{O}_4$  (PDF # 01-084-0482). The atomic columns, labelled **b** and **c**, on the side of the  $\text{MnCo}_2\text{O}_4$  unit cell in Fig. 2.12c, show a lower intensity than that of atomic columns, labelled **a**, at the center. The intensity variation comes from the fact that atomic columns, **a**, have a higher atom density than those of **b** and **c**, based on the tilted  $[110]$  zone axis (Fig. 2.12e). Atomic-scale STEM images of  $\text{CoMn}_2\text{O}_4$  exhibit the characteristic layered structure on the  $[01\bar{1}]$  zone axis of a tetragonal spinel (Fig. 2.12f). Two d-spacings of 4.9 and 3.0 Å, which were perpendicular to each other, matched well with the theoretical values (4.88 and 3.04 Å), respectively, based on the crystal model of  $\text{CoMn}_2\text{O}_4$  (PDF # 01-077-0471) (Figs. 2.12f-g). Atomic-scale electron energy loss spectroscopy (EELS) of the Mn  $L_2$  edge provides evidence of the layered structure on the  $[01\bar{1}]$  zone axis (Fig. 2.12f, inset). It is of particular interest to observe, in Fig. 2.12f, that atomic columns, **b**, on the side, show a lower intensity than atomic columns, **a**, at the corner. This image intensity variation also originates from the fact that atomic columns, **b**, exhibit a lower atom density than atomic columns, **a**, based on the tilted  $[01\bar{1}]$  zone axis in Fig. 2.12h. A similar layered structure was observed for  $\text{MnCo}_2\text{O}_4$  on a different  $[11\bar{2}]$  zone axis.

## 2.8 EELS Elemental Mapping and Valence Analysis of Single Nanoparticles

The chemical composition of selected metal oxides was then investigated using electron energy loss spectroscopy (EELS). EELS elemental maps were extracted from the sharp Mn, Co and Fe  $L_3$  edges of the core-loss EELS spectra (Fig. 2.14).

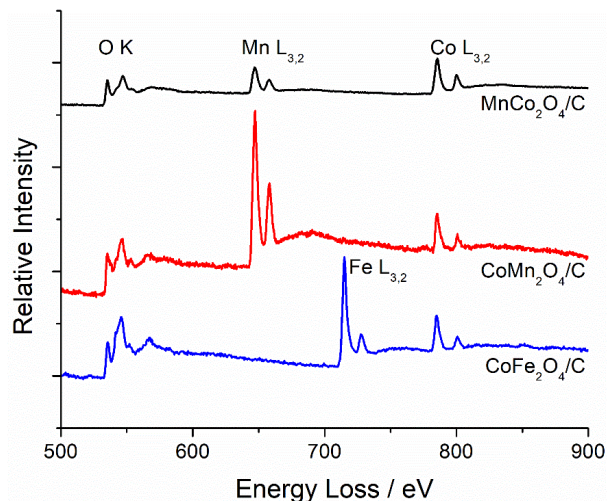


**Figure 2.13** Core-loss EELS spectra of  $\text{MnCo}_2\text{O}_4/\text{C}$ ,  $\text{CoMn}_2\text{O}_4/\text{C}$  and  $\text{CoFe}_2\text{O}_4/\text{C}$  with oxygen K edges and metal  $L_{3,2}$  edges after removing the background using linear combination of power laws (LCPL). Spectra intensity was normalized to the Co  $L_3$  edges. Metal  $L_3$  edges were employed to process metal EELS elemental maps after using principal component analysis (PCA) to deconvolve the signal from the noise.

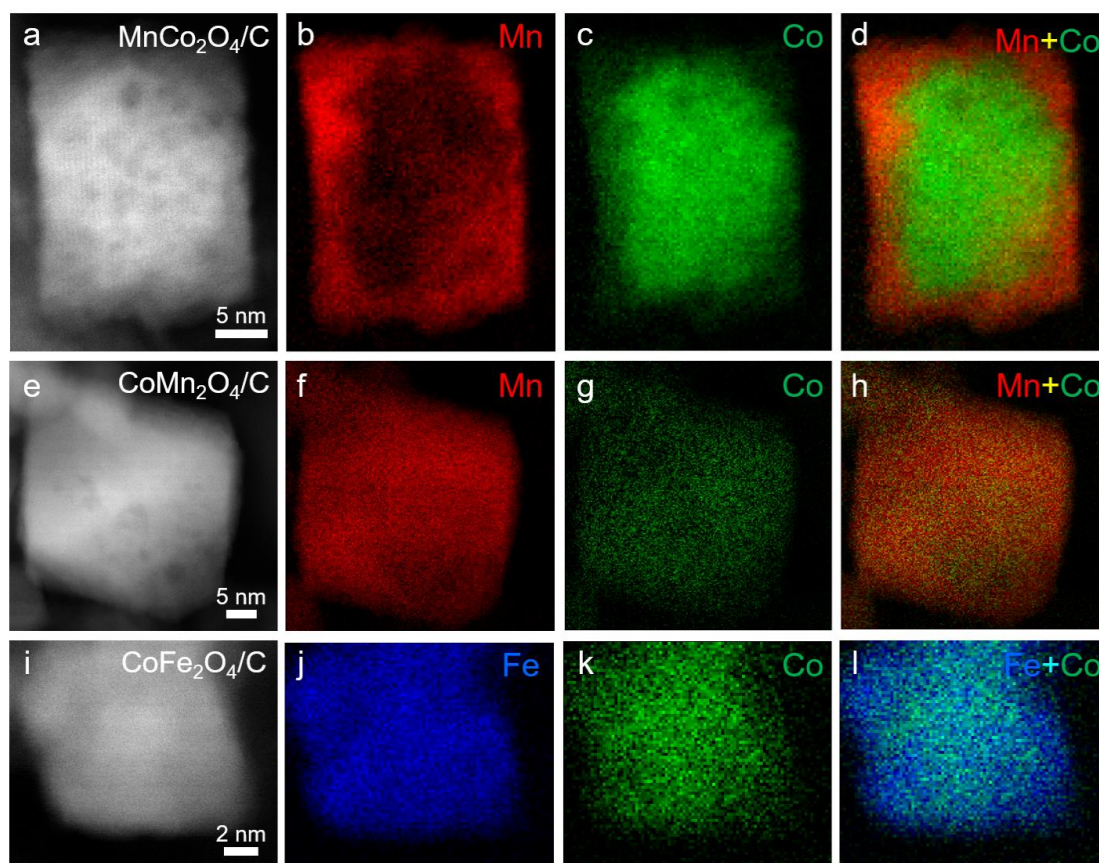


**Figure 2.14** EELS elemental mapping of  $\text{MnCo}_2\text{O}_4/\text{C}$ ,  $\text{CoMn}_2\text{O}_4/\text{C}$  and  $\text{CoFe}_2\text{O}_4/\text{C}$ . (a-d) STEM image of  $\text{MnCo}_2\text{O}_4/\text{C}$  and the corresponding EELS elemental maps of Mn

and Co. Composite map in (d) exhibits a Co-Mn core-shell structure with a 2-4 nm Mn shell. (e-l) STEM images of  $\text{CoMn}_2\text{O}_4/\text{C}$  (e) and  $\text{CoFe}_2\text{O}_4$  (i), respectively and the corresponding EELS elemental maps of Mn-Co (f-h) and Fe-Co (j-l), respectively. Composite maps of Mn vs. Co in (h) and Fe vs. Co in (l) suggest relatively homogenous distributions of Mn with Co and Fe with Co, respectively.

Figs. 2.15a-c present an octahedral  $\text{MnCo}_2\text{O}_4$  nanoparticle with the corresponding EELS elemental maps of Mn (red) and Co (green). The composite map of Mn vs. Co of  $\text{MnCo}_2\text{O}_4$  exhibits a core-shell structure with 2-4 nm Mn-shell on the surface (Fig. 2.15d). We observed that  $\text{CoMn}_2\text{O}_4/\text{C}$  (Figs. 2.15e-h) and  $\text{CoFe}_2\text{O}_4/\text{C}$  (Figs. 2.15i-l) have a relatively homogenous elemental distribution of Co vs. Mn and Co vs. Fe, respectively. Atomic-scale STEM-EELS of  $\text{MnCo}_2\text{O}_4$  suggests smooth elemental gradients from a Co-rich core to a Mn-shell without a distinct boundary (Fig. 2.16).

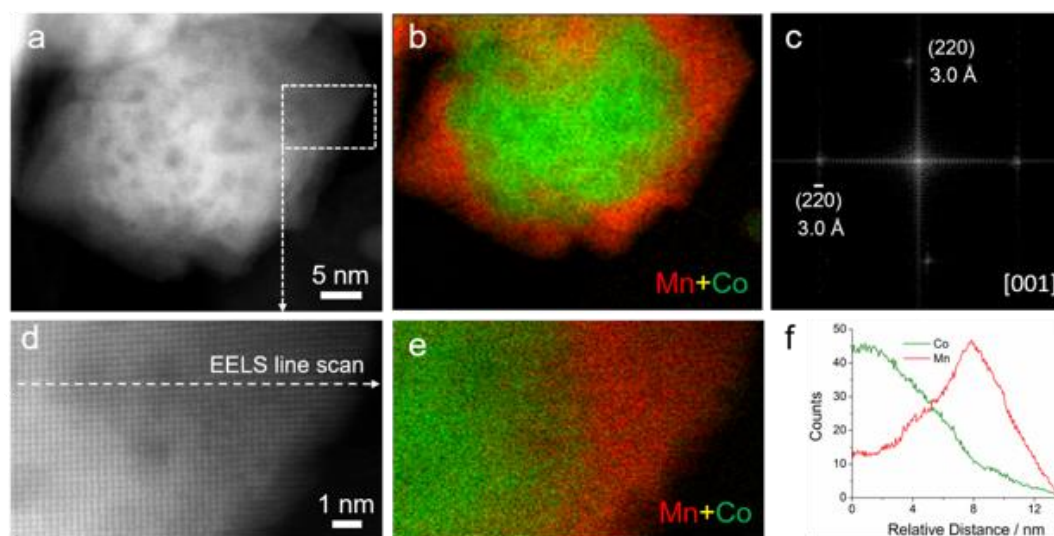


**Figure 2.15** STEM-EELS analysis of a single-crystal  $\text{MnCo}_2\text{O}_4$  spinel nanoparticle. (a) HAADF-STEM image of one  $\text{MnCo}_2\text{O}_4$  nanoparticle. (b) EELS elemental composite map of Co vs. Mn showing that the nanoparticle has a Co-Mn core-shell structure. (c) Fourier transform (FT) of the lattice image in (a) clearly demonstrates that this nanoparticle is a single crystal with  $\{200\}$  d-spacings on the  $[001]$  zone axis (c-direction of the unit cell). (d) Magnified STEM image from the dashed box in (a) showing the lattice with a square symmetry on the  $[001]$  zone axis. (e) Atomic-scale EELS elemental map of Co vs. Mn, corresponding to the image in (d), exhibits a smooth transition in

relative elemental concentration of Co and Mn from core to shell, with an ångstrom-level spatial resolution ( $5\times 5$  pixels per unit cell ( $3\times 3$  Å)). (f) EELS line profiles, along the direction of the dashed line in (d), again demonstrating the gradual decrease/increase in Co/Mn concentration from core to shell. Mn concentration eventually decreases to zero due to the smaller sample thickness near the edge of the nanoparticle.

This helps corroborate the previous CV analysis of the minor redox couple of  $\text{MnCo}_2\text{O}_4/\text{C}$  (Fig. 2.7), as the STEM-EELS mapping of  $\text{MnCo}_2\text{O}_4$  further suggests that the monolayer species on the surface is Mn-rich, which may serve as a key structural factor for the pronounced ORR activity of  $\text{MnCo}_2\text{O}_4$ .

To gain a detailed description of the local electronic structure of  $\text{MnCo}_2\text{O}_4/\text{C}$ , we performed fine structure EELS investigations with high energy resolution. We employed the energy-loss near-edge structure (ELNES) that reflects the density of unfilled states (unfilled DOS) above the Fermi level ( $E_F$ ), which is particularly sensitive to the local atomic environment, such as valence state, chemical bonding and coordination (predominantly nearest-neighbor).<sup>42</sup> Measurements of the fine structure can help us understand the electronic structure of the catalysts and ultimately establish its correlation with electrocatalytic performance. 3d transitional metals normally have sharp L edges in core-loss spectra (Fig. 2.15), which can be further divided into an  $L_2$  edge ( $2p^{1/2}$  to  $3d^{3/2}$  transition) and a stronger  $L_3$  edge ( $2p^{3/2}$  to  $3d^{3/2}3d^{5/2}$  transition). In this work, ELNES spectra with an energy resolution of 0.5 eV were first calibrated against the simultaneously acquired zero loss peak (ZLP) and then employed to fingerprint the catalyst structure.

We further investigated the core-shell structure of  $\text{MnCo}_2\text{O}_4$  to see how the compositional changes across the nanoparticle affect the local binding of both Mn and Co using ELNES. We first obtained reference ELNES spectra for Co and Mn in 2+,

2.67+, and 3+ valence states (Fig. 2.16) using CoO (MnO), Co<sub>3</sub>O<sub>4</sub> (Mn<sub>3</sub>O<sub>4</sub>), and CoOOH (Mn<sub>2</sub>O<sub>3</sub>), respectively. The edges progressively shift to higher energy values for higher valence states, due to the larger energy loss for ejecting electrons from metal p orbitals at higher metal valence states. Larger L<sub>3</sub> to L<sub>2</sub> intensity ratios at higher metal valence states also indicate more covalent metal-oxygen bonds.<sup>43</sup> Co<sub>3</sub>O<sub>4</sub> and Mn<sub>3</sub>O<sub>4</sub> (II,III) appear to have ELNES spectra between +2 and +3 valence states, and the spectra can be reproduced from linear combinations of CoO, MnO (II) and CoOOH, Mn<sub>2</sub>O<sub>3</sub> (III), respectively.<sup>39</sup>

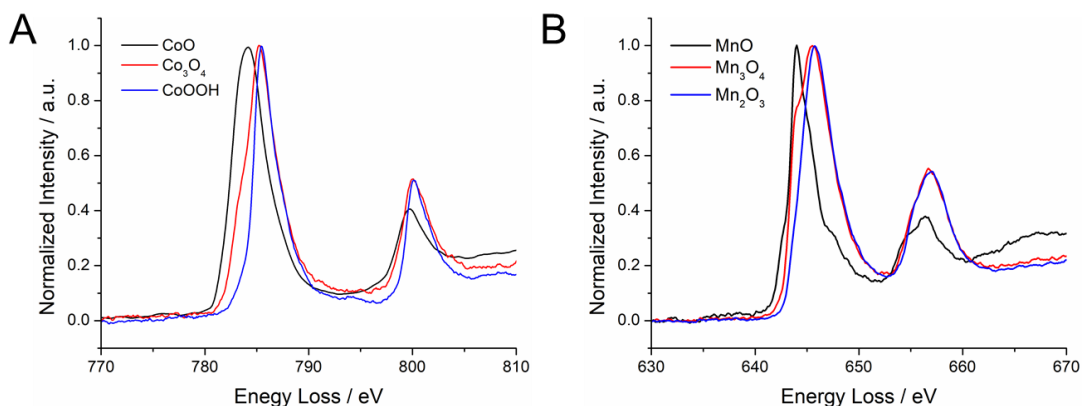


**Figure 2.16** (a) ELNES spectra of Co oxide (A) and Mn oxide (B) oxide references with an energy resolution of 0.5 eV.

Once the reference spectra were obtained, we compared them to the ELNES of the MnCo<sub>2</sub>O<sub>4</sub> core-shell structure. Shell sections at the four corners were labeled as S-1, S-2, S-3 and S-4 (Figs. 2.17a-b). ELNES spectra of Co and Mn in the shell exhibited similar features among the four different shell locations (S-1, S-2, S-3 and S-4), suggesting that all shell sections likely have a uniform chemical bonding environment of Co (Figs. 2.17e) as well as Mn.

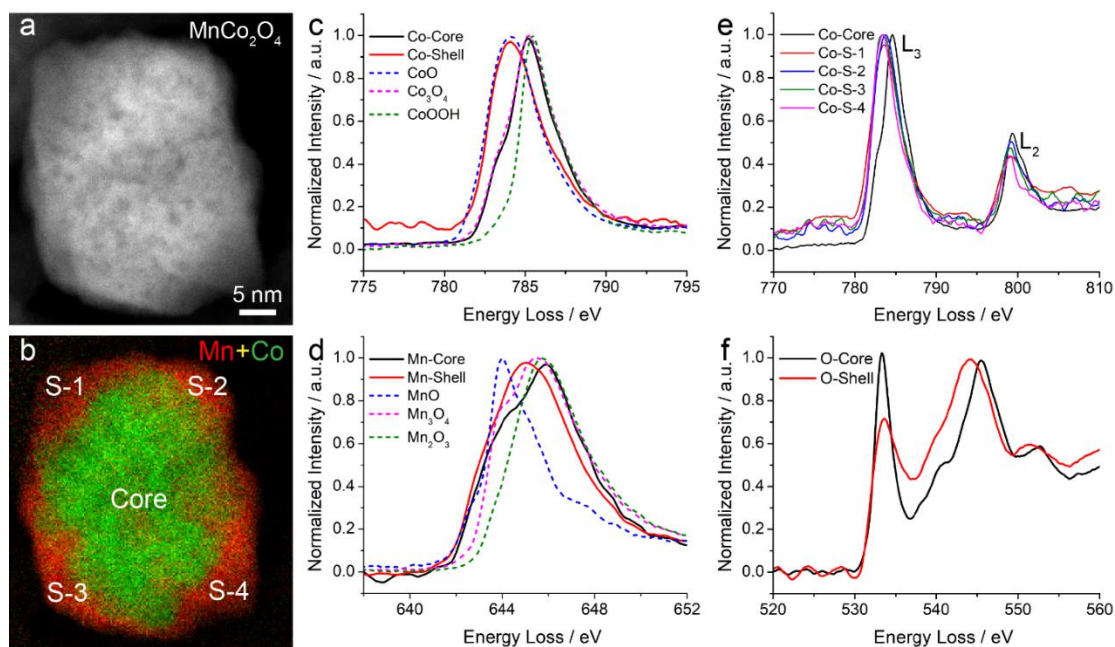


**Figure 2.17** Electron energy-loss near-edge structure (ELNES) of the core-shell  $\text{MnCo}_2\text{O}_4/\text{C}$  with an energy resolution of 0.5 eV. (a-b) STEM image and EELS elemental map of one  $\text{MnCo}_2\text{O}_4$  nanoparticle with a Mn-rich shell. Four different regions on the shell for further analysis were labeled as S-1, S-2, S-3 and S-4, respectively. (c) Comparison of average ELNES spectra of Co in the core and shell with standard Co oxide references. Co at the core clearly has a major contribution from  $\text{Co}_3\text{O}_4$  (II,III) while Co at the shell is  $\text{Co}^{2+}$  resembling the feature of CoO (II) reference. (d) Comparison of average ELNES spectra of Mn in the core and shell with standard Mn oxide references. Mn ELNES spectra, with a higher valence in the core than in the shell, exhibit broader features than Co, indicating a less-ordered nearest neighbor environment. (e) ELNES spectra of Co in the core and shell shows the similar features of Co  $L_{2,3}$  edges among S-1~4, which indicates the relatively uniform local chemical environment of Co at the shell. (f) ELNES average spectra of oxygen K-edge in the core and shell corresponding to the nanoparticle. The higher first-to-second peak ratio of ELNES spectrum in the core indicates a higher metal valence and metal-oxygen bond covalency. Similar ELNES features of the core and shell suggests they possibly share the same spinel structure.

The ELNES spectrum of the Co  $L_3$  edge in the core resembles the features of  $\text{Co}_3\text{O}_4$  (II,III), indicating Co in the core is predominantly cubic spinel, and  $\text{Co}^{2+}$  in the core occupies the tetrahedral sites while  $\text{Co}^{3+}$  in the core occupies half of the octahedral sites (Fig. 2.17c). In contrast, Co in the shell appears (convincingly) to be  $\text{Co}^{2+}$ , resembling

the feature of the CoO (II) reference (Fig. 2.17c). Furthermore, ELNES spectra of the Mn L<sub>3</sub> edge indicate that Mn in the core has a larger contribution from higher Mn valence, when compared to Mn in the shell (Fig. 2.17d). Mn L<sub>3</sub> edges, at both core and shell, are much broader than the Mn oxide references, indicating a less-ordered nearest-neighbor oxygen coordination environment, and a lower crystal symmetry, likely caused by a Jahn-Teller distortion of Mn<sup>3+</sup>[3d<sup>4</sup>].<sup>44</sup> In summary, both Co and Mn have lower metal valences in the shell, suggesting that the shell may have more oxygen vacancies. Compared with the core, where Co occupies both tetrahedral and octahedral sites, Co in the shell prefers to stay in the tetrahedral sites as it is present mainly as Co<sup>2+</sup>. As a comparison, Mn in the shell occupies both tetrahedral and octahedral sites.

Besides the metal L edges, the oxygen K-edge can also provide valuable complementary information about the chemical bonding of the metal center.<sup>45</sup> The first and second peaks in the ELNES spectra of the O K-edge represent the joint density of states between the O-2p and the partially filled transition metal 3d bands and empty 4s,p bands, respectively (Fig. 2.17f). Oxygen in the core exhibits a higher energy second peak, relative to O in the shell, which normally indicates that the metal center in the core has a higher valence.<sup>45</sup> This positive shift agrees with the ELNES spectra of Mn oxide references where the second peak gradually shifts to higher energies as the Mn valence increases from MnO (+2) to Mn<sub>3</sub>O<sub>4</sub> (+2.67) and Mn<sub>2</sub>O<sub>3</sub> (+3) (Fig. 2.18a). Additionally, a larger first-to-second peak ratio in the core indicates that the metal center has a higher metal valence, meaning a higher DOS of unfilled 3d bands available for mixing with the O 2p bands and typically a higher metal covalency. This can also be clearly observed in the ELNES spectra of Co oxide references where CoOOH (+3) and

$\text{Co}_3\text{O}_4(+2.67)$  have larger first-to-second peak ratios than  $\text{CoO} (+2)$  (Fig. 2.18b).

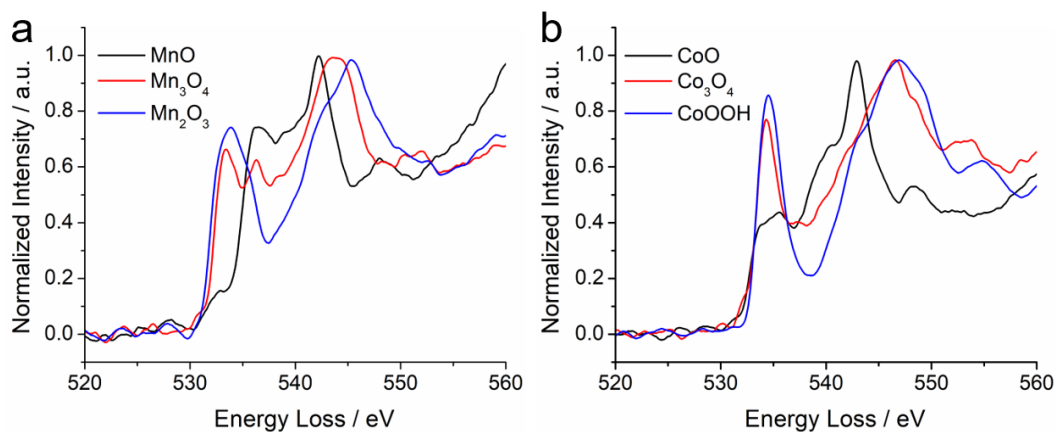


**Figure 2.18** (a) ELNES average spectra of O K-edge of  $\text{CoO}$ ,  $\text{Co}_3\text{O}_4$  and  $\text{CoOOH}$  references. (b) ELNES average spectra of O K-edge  $\text{MnO}$  to  $\text{Mn}_3\text{O}_4$  and  $\text{Mn}_2\text{O}_3$  references.

## 2.9 Catalysis Durability and Degradation Mechanism

Finally, with the intent of developing a Pt-free cathode for AEMFCs, non-precious ORR electrocatalysts need to not only exhibit high initial ORR activity, but also achieve long term durability.<sup>4-5</sup> As shown in Fig. 2.19,  $\text{MnCo}_2\text{O}_4/\text{C}$  and  $\text{CoMn}_2\text{O}_4/\text{C}$  exhibited an activity decay comparable to  $\text{Pt}/\text{C}$ , in terms of the negative shift in the  $E_{1/2}$ . The ORR activity decrease was partially ascribed to the loss of electrochemical surface area, as evidenced by the lower redox peak current after 10,000 CV cycles. Particle aggregation of both  $\text{MnCo}_2\text{O}_4/\text{C}$  and  $\text{CoMn}_2\text{O}_4/\text{C}$  was observed from STEM images of catalysts after 10,000 cycles, which was consistent with the surface area loss in CV profiles.

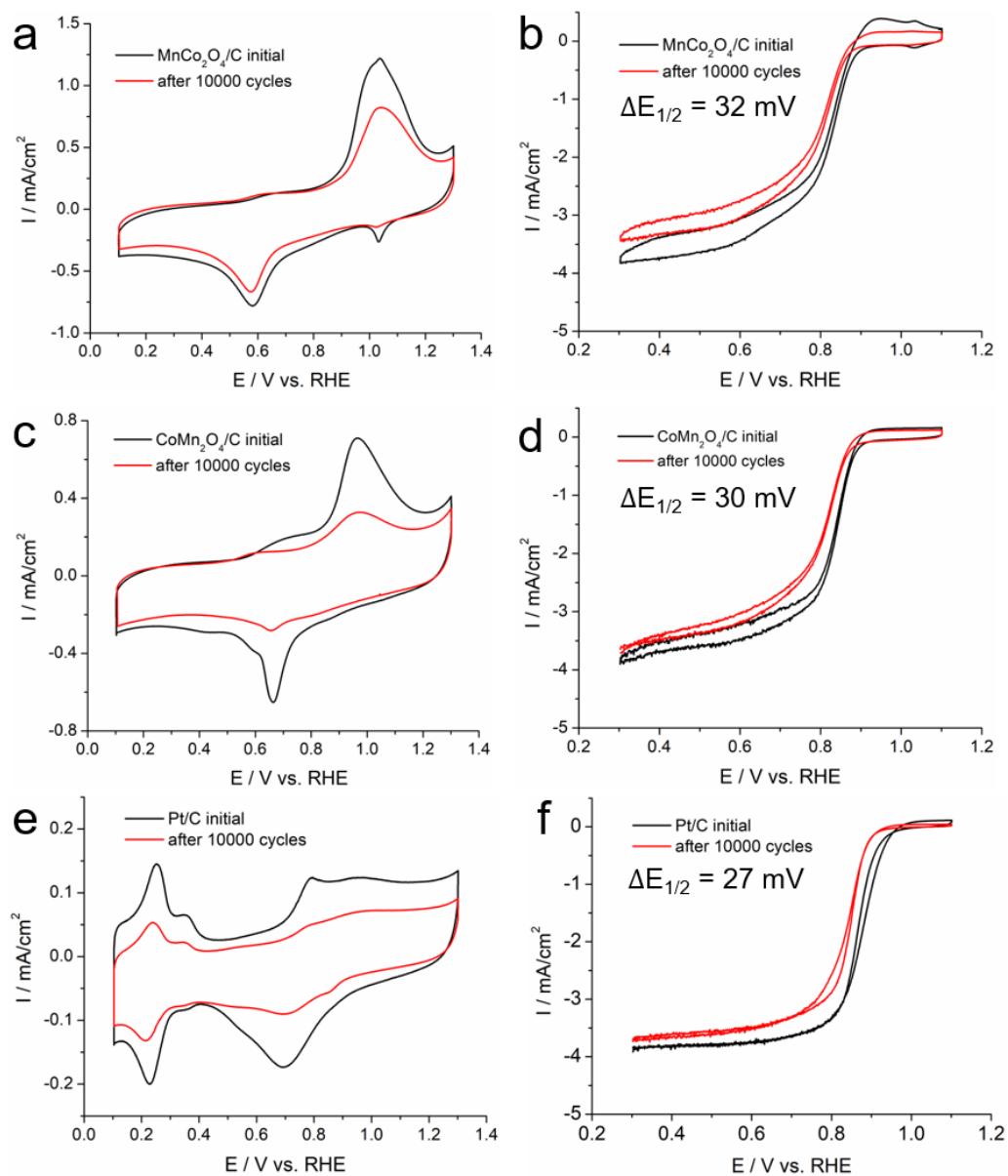


**Figure 2.19** Durability tests of MnCo<sub>2</sub>O<sub>4</sub>/C and CoMn<sub>2</sub>O<sub>4</sub>/C. CV and ORR profiles before and after the accelerated aging protocol: continuous 10,000 cycles at a scan rate of 100 mV/s from 0.6 to 1.0 V vs. RHE in O<sub>2</sub>-saturated 1M KOH. Metal oxide and Pt loadings were controlled to be 0.1 mg/cm<sup>2</sup> and 25 μg/cm<sup>2</sup>, respectively. Measurements after aging protocol were performed in fresh 1M KOH solution to avoid the influence of possible contamination from the aging solution species.

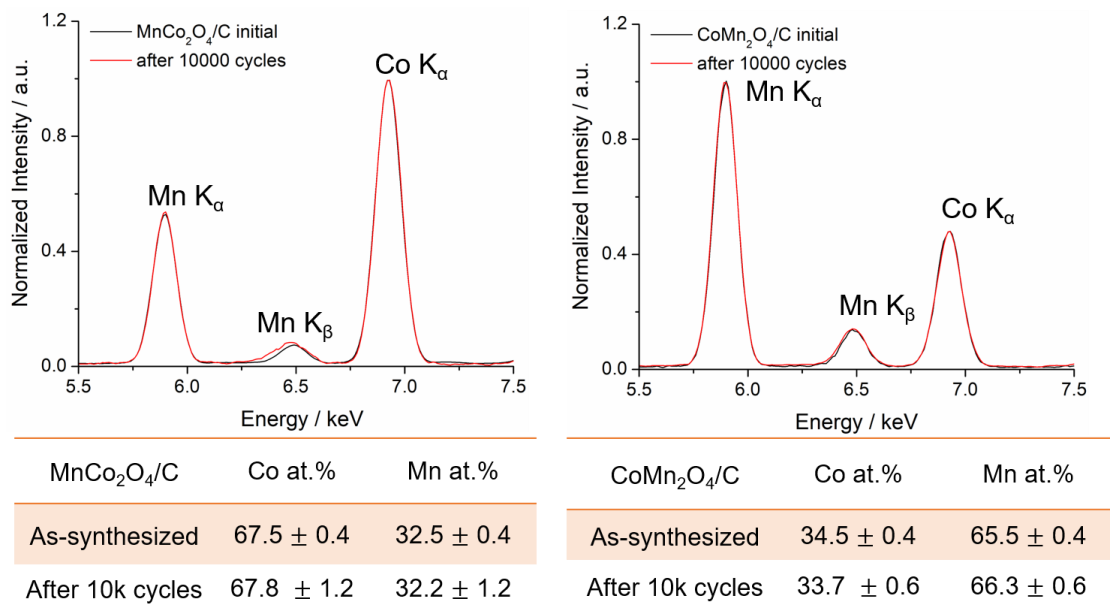


**Figure 2.20** Quantitative TEM-EDX analysis of the relative elemental contents of MnCo<sub>2</sub>O<sub>4</sub>/C and CoMn<sub>2</sub>O<sub>4</sub>/C before and after 10,000 cycles in durability tests. Relative atomic ratios of Co and Mn were calculated by integrating Co and Mn K<sub>α</sub> edges in EDX spectra and applying the Cliff-Lorimer equation. It should be noted that the quantitative results shown here are average values from more than five different regions in TEM grids and the relative errors are defined as one standard deviation (S<sub>d</sub>).

Interestingly, from the TEM-EDX quantitative analysis, the relative contents of Mn and Co were virtually the same before and after CV cycles, indicating a relative stable elemental distribution through long-term cycling (Fig. 2.20). Furthermore, EELS maps of catalysts after durability testing suggest that MnCo<sub>2</sub>O<sub>4</sub>/C still preserves the Co-Mn core-shell structure although with a thinner Mn-shell (Fig. 2.21), while CoMn<sub>2</sub>O<sub>4</sub>/C after 10,000 cycles exhibits the similar uniform distribution of Co and Mn as the initial state (Fig. 2.22). The aforementioned structural investigation provides us with a microscopic picture of the catalyst evolution during durability tests.

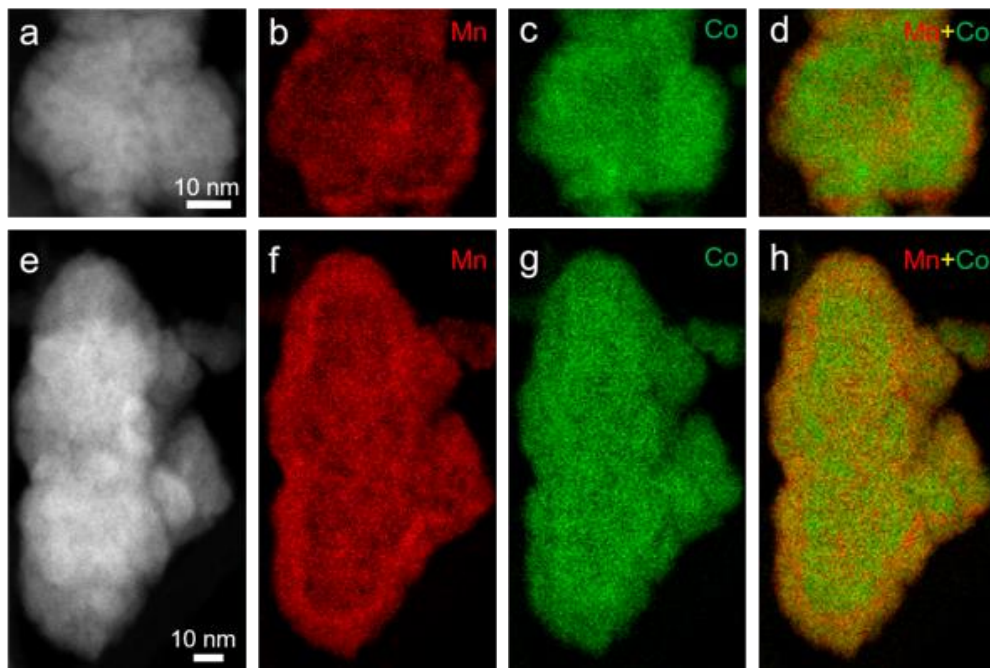


**Figure 2.21** STEM-EELS mapping of  $\text{MnCo}_2\text{O}_4/\text{C}$  after 10,000 CV cycles in durability tests. STEM images and EELS maps of one  $\text{MnCo}_2\text{O}_4$  particle in (a-d) and 4-5 aggregated  $\text{MnCo}_2\text{O}_4$  nanoparticles in (e-h) exhibit a thinner Mn shell, when compared to the initial  $\text{MnCo}_2\text{O}_4$  nanoparticles in [Figs. 2.17](#).

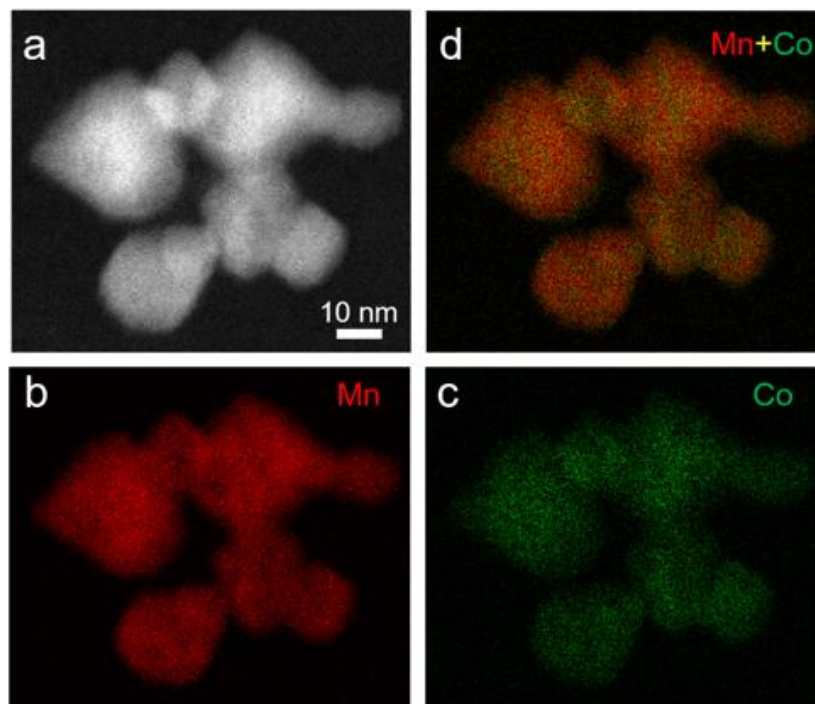


**Figure 2.22** EELS elemental mapping of  $\text{CoMn}_2\text{O}_4/\text{C}$  after 10,000 CV cycles in durability tests, showing a relatively homogenous distribution of Mn vs. Co.

## 2.10 Conclusion

In summary, we report on a systematic study of 15 different  $AB_2O_4/C$  spinel nanoparticles with well-controlled octahedral morphology. The three most active ORR electrocatalysts were  $MnCo_2O_4/C$ ,  $CoMn_2O_4/C$  and  $CoFe_2O_4/C$ .  $CoMn_2O_4/C$  exhibited a half-wave potential of 0.89 V in 1M KOH, equal to the benchmark activity of Pt/C, which was ascribed to charge transfer between Co and Mn, as evidenced by X-ray absorption spectroscopy. Scanning transmission electron microscopy (STEM) provided atomic-scale, spatially-resolved images, and high-energy-resolution electron-loss near-edge structure (ELNES) enabled fingerprinting the local chemical environment around the active sites. The most active  $MnCo_2O_4/C$  was shown to have a unique Co-Mn core-shell structure. ELNES spectra indicate that the Co in the core is predominantly  $Co^{2.7+}$  while in the shell, it is mainly  $Co^{2+}$ . Broader Mn ELNES spectra indicate less-ordered nearest oxygen neighbors. Co in the shell occupies mainly tetrahedral sites, which are likely candidates as the active sites for the ORR. The methodology of using analytical electron microscopy and spectroscopy in this work can enable researchers in the broad catalyst community to understand and design electrocatalysts with atomic-scale precision. This in-depth structural investigation will offer insightful strategies for material design and developments in the renewable energy community, in general, and in fuel cells, in particular.

## 2.11 References

1. Wang L.; Zeng Z.; Gao W.; Maxson T.; Raciti D.; Giroux M.; Pan X.; Wang C.; Greeley J. Tunable Intrinsic Strain in Two-Dimensional Transition Metal Electrocatalysts. *Science* **2019**, 363, 870-874.
2. Stamenkovic, V. R., Strmcnik, D., Lopes, P. P. & Markovic, N. M. Energy and Fuels from Electrochemical Interfaces. *Nat. Mater.* **2017**, 16, 57-69.

3. Xiong, Y.; Yang, Y.; Joress, H.; Padgett, E.; Gupta, U.; Yarlagadda, V.; Agyeman-Budu, D. N.; Huang, X.; Moylan, T. E.; Zeng, R.; Kongkanand, A.; Escobedo, F. A.; Brock, J. D.; DiSalvo, F. J.; Muller, D. A.; Abruña, H. D. Revealing the Atomic Ordering of Binary Intermetallics Using In Situ Heating Techniques at Multilength Scales. *Proc. Natl. Acad. Sci. U.S.A.* **2019**, 116, 1974-1983.
4. Gasteiger, H. A., Kocha, S. S., Somali, B. & Wagner, F. T. Activity Benchmarks and Requirements for Pt, Pt-alloy, and non-Pt Oxygen Reduction Catalysts for PEMFCs. *Appl. Catal., B.* **2005**, 56, 9-35.
5. Papageorgopoulos D, 2017 Annual Merit Review and Peer Evaluation Meeting in Fuel Cells Program Area. U.S. Department of Energy, Washington, DC, **2017**.
6. Wang, D.; Xin, H. L.; Hovden, R.; Wang, H.; Yu, Y.; Muller, D. A.; DiSalvo, F. J.; Abruña, H. D. Structurally Ordered Intermetallic Platinum-Cobalt Core-Shell Nanoparticles with Enhanced Activity and Stability as Oxygen Reduction Electrocatalysts. *Nat. Mater.* **2013**, 12, 81-87.
7. Xiong, Y.; Yang, Y.; DiSalvo, F. J.; Abruña, H. D. Pt-Decorated Composition-Tunable Pd-Fe@Pd/C Core-Shell Nanoparticles with Enhanced Electrocatalytic Activity toward the Oxygen Reduction Reaction. *J. Am. Chem. Soc.* **2018**, 140, 7248-7255.
8. Xiong, Y.; Xiao, L.; Yang, Y.; DiSalvo, F. J.; Abruña, H. D. High-Loading Intermetallic Pt<sub>3</sub>Co/C Core-Shell Nanoparticles as Enhanced Activity Electrocatalysts toward the Oxygen Reduction Reaction (ORR). *Chem. Mater.* **2018**, 30, 1532-1539.
9. Wang, G.; Huang, B.; Xiao, L.; Ren, Z.; Chen, H.; Wang, D.; Abruña, H. D.; Lu, J.; Zhuang, L. Pt Skin on AuCu Intermetallic Substrate: A Strategy to Maximize Pt Utilization for Fuel Cells *J. Am. Chem. Soc.* **2014**, 136, 9643-9649.
10. Groger, O.; Gasteiger, H. A.; Suchsland, J.-P. Review—Electromobility: Batteries or Fuel Cells? *J. Electrochem. Soc.* **2015**, 162, A2605-2622.
11. Lu, S.; Pan, J.; Huang, A.; Zhuang, L.; Lu, J. Alkaline Polymer Electrolyte Fuel Cells Completely Free from Noble Metal Catalysts *Proc. Natl. Acad. Sci. U. S. A.* **2008**, 105, 20611-20614.
12. Yang, Y.; Wang, Y.; Xiong, Y.; Huang, X.; Shen, L.; Huang, R.; Wang, H.; Pastore, J. P.; Yu, S.-H.; Xiao, L.; Brock, J. D.; Zhuang, L.; Abruña, H. D. In Situ X-ray Absorption Spectroscopy of a Synergistic Co-Mn Oxide Catalyst for the Oxygen Reduction Reaction. *J. Am. Chem. Soc.* **2019**, 141, 1463-1466.
13. Ge, X.; Sumboja, A.; Wu, D.; An, T.; Li, B.; Goh, F. W. T.; Hor, T. S. A.; Zong, Y.; Liu, Z. Oxygen Reduction in Alkaline Media: From Mechanisms to Recent Advances of Catalysts *ACS Catal.* **2015**, 5, 4643-4667.
14. Ren, H.; Wang, Y.; Yang, Y.; Tang, X.; Peng, Y.; Peng, H.; Xiao, L.; Lu, J.; Abruña, H. D.; Zhuang, L. Fe/N/C Nanotubes with Atomic Fe Sites: A Highly Active Cathode Catalyst for Alkaline Polymer Electrolyte Fuel Cells. *ACS Catal.* **2017**, 7, 6485-6492.
15. Chung, H. T.; Cullen, D. A.; Higgins, D.; Sneed, B. T.; Holby, E. F.; More, K. L.; Zelenay, P. Direct Atomic-Level Insight into the Active Sites of a High-Performance PGM-Free ORR Catalyst. *Science* **2017**, 357, 479-484.
16. Suntivich, J.; Gasteiger, H. A.; Yabuuchi, N.; Nakanishi, H.; Goodenough, J.; Shao-Horn, Y. Design Principles for Oxygen-Reduction Activity on Perovskite Oxide Catalysts for Fuel Cells and Metal-Air Batteries. *Nat. Chem.* **2011**, 3, 647-647.
17. Zhao, Q.; Yan, Z.; Chen, C.; Chen, J. Spinels: Controlled Preparation, Oxygen Reduction/Evolution Reaction Application, and Beyond. *Chem. Rev.* **2017**, 117, 10121-10211.

18. Liang, Y.; Li, Y.; Wang, H.; Zhou, J.; Wang, J.; Regier, T.; Dai, H. Co<sub>3</sub>O<sub>4</sub> Nanocrystals on Graphene as a Synergistic Catalyst for Oxygen Reduction Reaction. *Nat. Mater.* **2011**, *10*, 780-786.
19. Meng, Y.; Song, W.; Huang, H.; Ren, Z.; Chen, S.; Suib, S. Structure–Property Relationship of Bifunctional MnO<sub>2</sub> Nanostructures: Highly Efficient, Ultra-Stable Electrochemical Water Oxidation and Oxygen Reduction Reaction Catalysts Identified in Alkaline Media *J. Am. Chem. Soc.*, **2014**, *136*, 11452-11464.
20. Liang, Y.; Wang, H.; Zhou, J.; Li, Y.; Wang, J.; Regier, T.; Dai, H. Covalent Hybrid of Spinel Manganese–Cobalt Oxide and Graphene as Advanced Oxygen Reduction Electrocatalysts *J. Am. Chem. Soc.* **2012**, *134*, 3517-3523.
21. Li, C.; Han, X.; Cheng, F.; Hu, Y.; Chen, C.; Chen, J. Phase and Composition Controllable Synthesis of Cobalt Manganese Spinel Nanoparticles towards Efficient Oxygen Electrocatalysis *Nat. Commun.* **2015**, *6*, 7345.
22. Wei, C.; Feng, Z.; Scherer, G.; Barber, J.; Shao-Horn, Y.; Xu, Z. Cations in Octahedral Sites: A Descriptor for Oxygen Electrocatalysis on Transition-Metal Spinels. *Adv. Mater.* **2017**, *29*, 1606800.
23. Wang, Y.; Yang, Y.; Jia, S.; Wang, X.; Lyu, K.; Peng, Y.; Zheng, H.; Wei, X.; Ren, H.; Xiao, L.; Wang, J.; Muller, D. A.; Abruña, H. D.; Hwang, B. J.; Lu, J.; Zhuang, L. Synergistic Mn–Co Catalyst Outperforms Pt on High-Rate Oxygen Reduction for Alkaline Polymer Electrolyte Fuel Cells. *Nat Commun.* **2019**, *10*, 1506.
24. Indra, A.; Menezes, P.; Sahraie, N.; Bergmann, A.; Das, C.; Tallarida, M.; Schmeißer, D.; Strasser, P.; Driess, M. Unification of Catalytic Water Oxidation and Oxygen Reduction Reactions: Amorphous Beat Crystalline Cobalt Iron Oxides. *J. Am. Chem. Soc.* **2014**, *136*, 17530-17536.
25. Wan, L.; Zang, G.; Wang, X.; Zhou, L.; Li, T.; Zhou, Q. Tiny Crystalline Grain Nanocrystal NiCo<sub>2</sub>O<sub>4</sub>/N-doped Graphene Composite for Efficient Oxygen Reduction Reaction. *J. Power Sources.* **2017**, *345*, 41-49.
26. Ning, R.; Tian, J.; Asiri, A.; Qusti, A.; Al-Youbi, A.; Sun, X. Spinel CuCo<sub>2</sub>O<sub>4</sub> Nanoparticles Supported on N-Doped Reduced Graphene Oxide: A Highly Active and Stable Hybrid Electrocatalyst for the Oxygen Reduction Reaction. *Langmuir* **2013**, *29*, 13146-13151.
27. Cao, B.; Veith, G.; Diaz, R.; Liu, J.; Stach, E.; Adzic, R.; Khalifah, P. Cobalt Molybdenum Oxynitrides: Synthesis, Structural Characterization, and Catalytic Activity for the Oxygen Reduction Reaction. *Angew. Chem. In. Ed.* **2013**, *52*, 10753-10757.
28. Shannon, R. D. Revised Effective Ionic Radii and Systematic Studies of Interatomic Distances in Halides and Chalcogenides. *Acta Cryst.* **1976**, *A32*, 751-767.
29. Shoemaker, D. P.; Li, J.; Seshadri, R. Unraveling Atomic Positions in an Oxide Spinel with Two Jahn–Teller Ions: Local Structure Investigation of CuMn<sub>2</sub>O<sub>4</sub>, *J. Am. Chem. Soc.* **2009**, *131*, 11450–11457.
30. Paulus, U. A.; Schmidt, T. J.; Gasteiger, H. A.; Behm, R. J. Oxygen Reduction on a High-Surface Area Pt/Vulcan Carbon Catalyst: A Thin-Film Rotating Ring-Disk Electrode Study. *J. Electroanal. Chem.* **2001**, *495*, 134-145.
31. Bonakdarpour, A.; Lefevre, M.; Yang, R.; Jaouen, F.; Dahn, T.; Dodelet, J.-P.; Dahn, J. R. Impact of Loading in RRDE Experiments on Fe–N–C Catalysts: Two- or Four-Electron Oxygen Reduction? *Electrochem. Solid State Lett.* **2008**, *11*, B105-B108.
32. Jaouen, F.; Dodelet, J.-P. O<sub>2</sub> Reduction Mechanism on Non-Noble Metal Catalysts for PEM Fuel Cells. Part I: Experimental Rates of O<sub>2</sub> Electroreduction, H<sub>2</sub>O<sub>2</sub> Electroreduction, and H<sub>2</sub>O<sub>2</sub> Disproportionation. *J. Phys. Chem. C* **2009**, *113*, 15422–15432.

33. Zhang, G.; Wei, Q.; Yang, X.; Tavares, A.; Sun, S. RRDE Experiments on Noble-Metal and Noble-Metal-Free Catalysts: Impact of Loading on the Activity and Selectivity of Oxygen Reduction Reaction in Alkaline Solution. *Appl. Catal., B.* **2017**, 206, 115–126.
34. Rojas-Carbonell, S.; Artyushkova, K.; Serov, A.; Santoro, C.; Matanovic, I.; Atanassov, P. Effect of pH on the Activity of Platinum Group Metal-Free Catalysts in Oxygen Reduction Reaction. *ACS Catal.* **2018**, 8, 3041–3053.
35. Padgett, E.; Andrejevic, N.; Liu, Z.; Kongkanand, A.; Gu, W.; Moriyama, K.; Jiang, Y.; Kumaraguru, S.; Moylan, T. E.; Kukreja, R.; Muller, D. A. Connecting Fuel Cell Catalyst Nanostructure and Accessibility Using Quantitative Cryo-STEM Tomography. *J. Electrochem. Soc.*, **2018**, 165, F173-F180.
36. Wang, D.; Yu, Y.; Xin, H. L.; Hovden, R.; Ercius, P.; Mundy, J. A.; Chen, H.; Richard, J. H.; Muller, D. A.; DiSalvo, F. J.; Abruña, H. D. Tuning Oxygen Reduction Reaction Activity via Controllable Dealloying: A Model Study of Ordered Cu<sub>3</sub>Pt/C Intermetallic Nanocatalysts. *Nano Lett.* **2012**, 12, 5230-5238.
37. Williams, D. B.; Carter, C. B. Transmission Electron Microscopy: A Textbook for Materials Science (2<sup>nd</sup> Edition). Springer: New York, **2009**, p741.
38. Garvie, L. A. J.; Craven, A. J. High-resolution Parallel Electron Energy-loss Spectroscopy of Mn L<sub>2,3</sub>-Edges in Inorganic Manganese Compounds. *Phys. Chem. Minerals* **1994**, 21, 191-206.
39. de Groot F. M. F.; Fuggle J. C.; Thole B.T.; Sawatzky G. A.; 2p X-ray Absorption of 3d Transition-Metal Compounds: An Atomic Multiplet Description Including the Crystal Field. *Phys. Rev. B* **1990**, 42, 5459-5468.
40. de Groot F. M. F.; Grioni M.; Fuggle J. C.; Ghijsen J.; Sawatzky G. A.; Peterson H. Oxygen 1s X-ray-Absorption Edges of Transition-Metal Oxides. *Phys. Rev. B* **1989**, 40, 5715-5723.

## CHAPTER 3

### Activity Enhancement of Co-Mn Spinel Oxides Guided by STEM-EELS\*<sup>†</sup>

#### 3.1 Introduction

After previous comprehensive investigations of a variety of spinel oxide catalysts,  $AB_2O_4/C$ , Co-Mn bimetallic oxides were found to be the most promising catalyst for the ORR in alkaline media. From a perspective of material design, the rich and complex structures and compositions of Co-Mn spinel oxides need to be further explored and controlled more precisely in order to optimize the catalytic activity. Since the surface composition of electrocatalysts mainly determines the catalytic activity, this chapter will focus on how to fine tune of surface composition and better understanding of the structure-activity correlation of metal oxide electrocatalysts for the ORR. STEM imaging and EELS elemental mapping serve as powerful tools to guide the hydrothermal synthesis and verify the microstructure and local compositions of Co-Mn spinel oxides at the atomic scale. Other spectroscopic techniques and theoretical calculations have been used to identify the potential active sites and reaction path. Experimental details should be referred to the following publication.

---

\*Reproduced and modified with permission from the following publication

Ying Wang, **Yao Yang**, Shuangfeng Jia, Xiaoming Wang, Kangjie Lyu, Yanqiu Peng, He Zheng, Xing Wei, Huan Ren, Li Xiao, Jianbo Wang, David Muller, Héctor Abruña, Bing Joe Hwang, Juntao Lu, Lin Zhuang, Synergistic Mn-Co Catalyst Outperforms Pt on High-Rate Oxygen Reduction for Alkaline Polymer Electrolyte Fuel Cells. *Nat. Commun.* 2019, 10, 1506. Copyright © Springer Nature.

<sup>†</sup>Author Contributions: Y.W. synthesized the materials and conducted the electrochemical measurements; Y.Y. performed the STEM-EELS and XAS measurements and analysis with the help of S.J., H.Z. and X.-m.W. K.L. performed MD simulations; Y.P. performed polyelectrolyte synthesis; X.W. performed FTIR measurements; H.R. performed complementary experiments; J.W., D.A.M., B.J.H., and J.L. performed the analysis of experimental data; L.X., H.D.A., and L.Z. supervised the work and wrote the paper.

### 3.2 Fine Tuning of Spinel Oxide Surface Compositions by Aging Temperatures

In a typical synthesis of  $\text{Mn}_{1.5}\text{Co}_{1.5}\text{O}_4$  spinel (MCS) catalyst supported on carbon black,  $\text{Co}(\text{OAc})_2 \cdot 4\text{H}_2\text{O}$  (63.5 mg) and Vulcan XC-72 (preheated at  $110^\circ\text{C}$  in air, 60.0mg) were added to ultrapure water (30 mL). After ultrasonic blending for 15 min, 0.5 mL of  $\text{NH}_3 \cdot \text{H}_2\text{O}$  was added under magnetic stirring, followed by the addition of  $\text{Mn}(\text{OAc})_2 \cdot 4\text{H}_2\text{O}$  aqueous solution (62.5 mg dissolved in 5 mL water). The mixture was aged at a controlled temperature under magnetic stirring for 2h. After that, the suspension was ultrasonically blended for 10 min, and then transferred to a 40 mL Teflon autoclave for hydrothermal reaction at  $150^\circ\text{C}$  for 3h. The resulting product was collected by centrifugation and washed with water, then freeze dried under vacuum. To ensure a homogeneous distribution of Co and Mn in MCS, the aging temperature must be set to  $60^\circ\text{C}$ . To prepare MCS with Mn segregation on the surface (denoted as Mn-rich MCS), the aging temperature was set to  $40^\circ\text{C}$ ; while to prepare Co-segregated samples (Co-rich MCS), the aging temperature was set to  $80^\circ\text{C}$  before the addition of  $\text{Mn}(\text{OAc})_2$  aqueous solution. (Fig. 3.1)

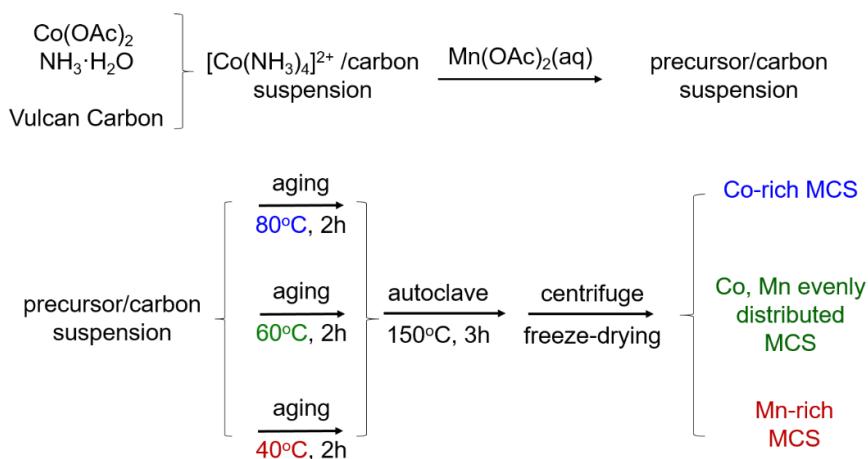


**Figure 3.1.** Hydrothermal synthesis of  $\text{Mn}_{1.5}\text{Co}_{1.5}\text{O}_4/\text{C}$  (MCS) with controlled aging temperatures.

### 3.3 STEM-EELS and XRD Investigations of Chemical Compositions and Structures

The chemical compositions of MCS catalysts were examined using HAADF-STEM images and EELS elemental mapping. MCS catalysts, at a low aging temperature of 40 °C, exhibited a Mn-rich shell with a thickness of 2-3 nm on the surface, based on the composite EELS elemental map in Fig. 3.2. At an intermediate aging temperature of 60 °C, Mn and Co distributed homogeneously on the surface while at a high aging temperature of 80 °C, MCS catalysts clearly showed a Co-rich Shell with a thickness of 2-3 nm on the surface. Those distinct surface chemical compositions are unambiguously verified by STEM-EELS analysis and highlights the importance of precious control of aging temperatures.

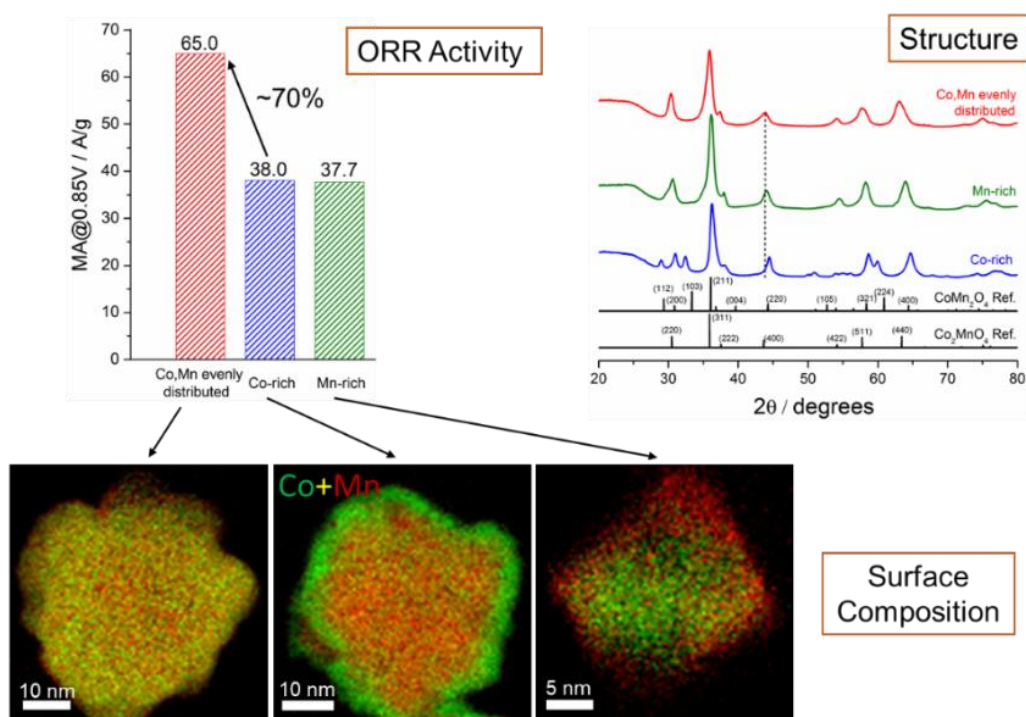


**Figure 3.2** Correlations of ORR activities of Co<sub>1.5</sub>Mn<sub>1.5</sub>O<sub>4</sub>/C, surface compositions based on EELS and overall crystal structures based on synchrotron XRD.

We rationalizes the surface segregation at different temperatures based on the different solubility of  $\text{Mn}(\text{OH})_2$  and  $\text{Co}(\text{OH})_2$ . At 25 °C,  $\text{Mn}(\text{OH})_2$  has a solubility of  $4 \times 10^{-5}$  mol/L while  $\text{Co}(\text{OH})_2$  has a smaller solubility of  $4 \times 10^{-7}$  mol/L.<sup>1-2</sup> At a relatively low temperature of 40 °C, Mn(II) in solution possibly precipitates more slowly than Co(II) given the higher solubility of  $\text{Mn}(\text{OH})_2$ , which leads to a final Mn-rich surface composition. Increasing temperatures to 60 and 80 °C probably gradually slows down the precipitate rate of  $\text{Co}(\text{OH})_2$ , relative to that of  $\text{Mn}(\text{OH})_2$ , resulting in a homogeneous and Co-rich surface composition, respectively. Further fine tuning of Co/Mn-shell thickness and local compositions is potentially achievable by adjusting the concentration of metal precursors and  $\text{NH}_3$ , solvent type and volume, and heating temperature and time in autoclave.

The crystal structure of MCS with different compositions were examined by synchrotron-based XRD (Fig. 3.2, top right). MCS, with a homogenous distribution of Co and Mn, exhibited a cubic spinel structure (green line), resembling the feature of cubic  $\text{MnCo}_2\text{O}_4$ . MCS catalysts, with Mn-rich surface (i.e., Co-rich core), exhibited a cubic structure (red line), like cubic  $\text{MnCo}_2\text{O}_4$ . The relative positive shift of (400) peak in Mn-rich MCS, relative to homogenous MCS, was ascribed to the lattice contraction caused by larger amount of smaller Co atoms in the core region. As a comparison, MCS catalysts with Co-rich surface (i.e., Mn-rich core) showed a tetragonal structure (blue line) like tetragonal  $\text{CoMn}_2\text{O}_4$  reference. The distinct differences in structures between Mn-rich and Co-rich MCS indicates that the relative composition in the core region largely determines the overall crystal structure.

After thorough structural examinations, the ORR activity of MCS catalysts with different compositions were evaluated in RDE measurements in 1M KOH. Homogenous MCS (Co and Mn evenly distributed on the surface) showed an half-wave potential of 0.862 V vs. RHE, significantly higher than that of Co-rich MCS (0.851 V) and Mn-rich MCS (0.850 V) (Fig. 3.2, top left). The mass-specific activity (MA) at 0.85V showed about 70% enhancement from Co-rich or Mn-rich MCS to homogenous MCS catalysts. In summary, with precise control of surface composition guided by STEM-EELS analysis, the ORR activity of Co-Mn spinel oxides was optimized when Co and Mn are mixed homogeneously at the atomic-scale on the surface.

### 3.4 RDE and MEA Measurements of MCS Catalysts

To evaluate the catalyst performance for practical applications, one needs to carry membrane electrode assembly (MEA) tests. The RDE experimental conditions are distinctly different from those in an alkaline polymer electrolyte fuel cell (APEFC), where the electrode is fed with humidified gas, and the catalyst surface is under a humid atmosphere rather than in contact with an ocean of aqueous solution, as is the case under RDE conditions. Thus, it is not surprising that good-performing electrocatalysts in RDE tests can often exhibit poor performance under fuel-cell operation. Moreover, and much to our surprise, the Mn-Co spinel catalyst (denoted hereafter as MCS) reported in this work, exhibited moderate activity in RDE tests, but outstanding APEFC performance. Fig. 3.3A presents typical RDE profiles for the ORR catalyzed by Pt and MCS in 1.0 M KOH solution. A negative shift of 50 mV in the half-wave potential clearly indicates that the ORR occurs at a lower rate on MCS than on Pt, and this trend does not change with potential as evidenced in the Tafel plots (Fig. 3.3A, inset). Such an observation

would usually lead to the conclusion that the MCS would not be a good choice as ORR electrocatalyst for APEFCs. However, the fuel cell tests tell a different, and most unexpected, story (Fig. 3.3B). An APEFC with a Pt-Ru anode and a Pt cathode, exhibiting a peak power density (PPD) of  $1 \text{ W/cm}^2$ , is a benchmark of current APEFC research.<sup>3,4</sup> Upon replacing the Pt cathode with our MCS cathode, the cell performance underwent a slight loss at low current densities, but, as the current density increased, it kept increasing in a steady fashion, reaching a higher PPD of  $1.1 \text{ W/cm}^2$ , a performance metric never previously achieved in APEFCs with a non-precious metal cathode catalyst.

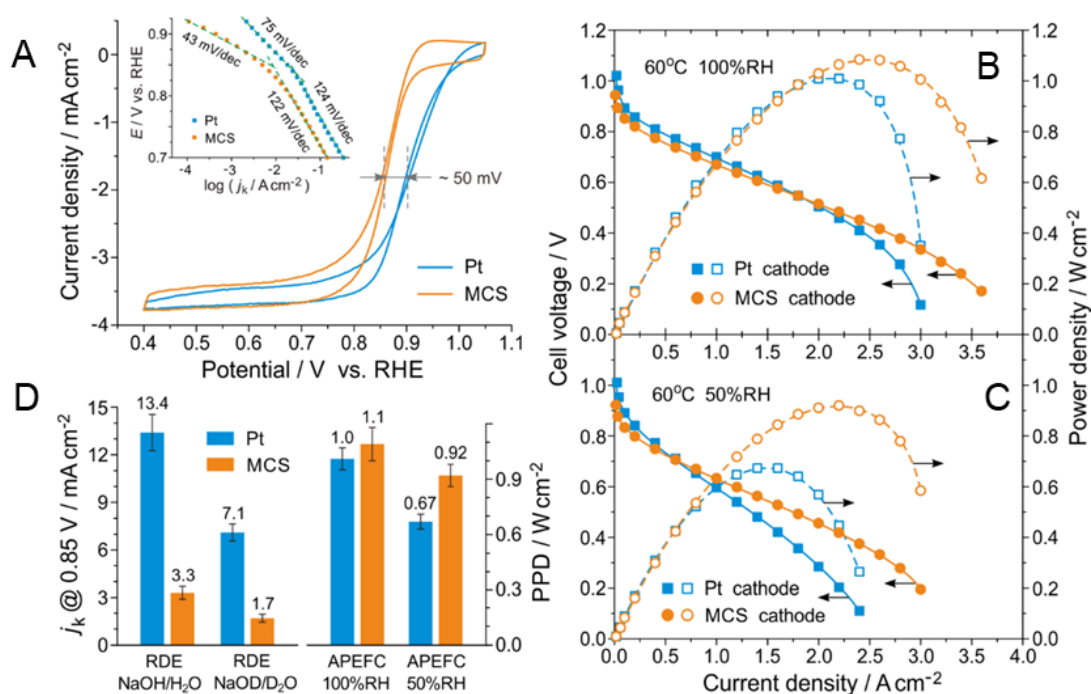


**Figure 3.3** Performance of the Mn-Co spinel (MCS) catalyst towards the oxygen reduction reaction (ORR), relative to a commercial Pt catalyst. (A) Rotating disk electrode (RDE) measurements in  $\text{O}_2$ -saturated KOH solution (1 mol/L) using 40 wt% Pt/C (Johnson Matthey,  $50 \mu\text{g}_{\text{Pt}}/\text{cm}^2$ ) and 40 wt% MCS/C ( $72 \mu\text{g}_{\text{metal}}/\text{cm}^2$ ), respectively, at 1600 rpm and 5 mV/s. Inset: Tafel plots. (B-C) Alkaline polymer electrolyte fuel cell (APEFC) tests with  $\text{H}_2$  and  $\text{O}_2$  at different relative humidities (RH). Anode catalyst: 60 wt% Pt-Ru/C (Johnson Matthey,  $0.4 \text{ mg}_{\text{metal}}/\text{cm}^2$ ). Cathode catalyst: 60 wt% Pt/C (Johnson Matthey,  $0.4 \text{ mg}_{\text{Pt}}/\text{cm}^2$ ) or 40 wt% MCS/C with an optimized loading of  $0.58 \text{ mg}_{\text{metal}}/\text{cm}^2$ . Alkaline polymer electrolyte: aQAPS-S<sub>8</sub> membrane (35  $\mu\text{m}$  in thickness)

and *a*QAPS-S<sub>14</sub> ionomer (20 wt% in electrode)<sup>4</sup>. Operation temperature = 60°C. Backpressure = 0.1 MPa. (D) Performance comparison: Kinetic current densities ( $j_k$ ) at 0.85 V, calculated from the RDE data recorded in 1 mol/L NaOH/H<sub>2</sub>O and 1 mol/L NaOD/D<sub>2</sub>O, and the peak power density (PPD) resulting from APEFC tests.

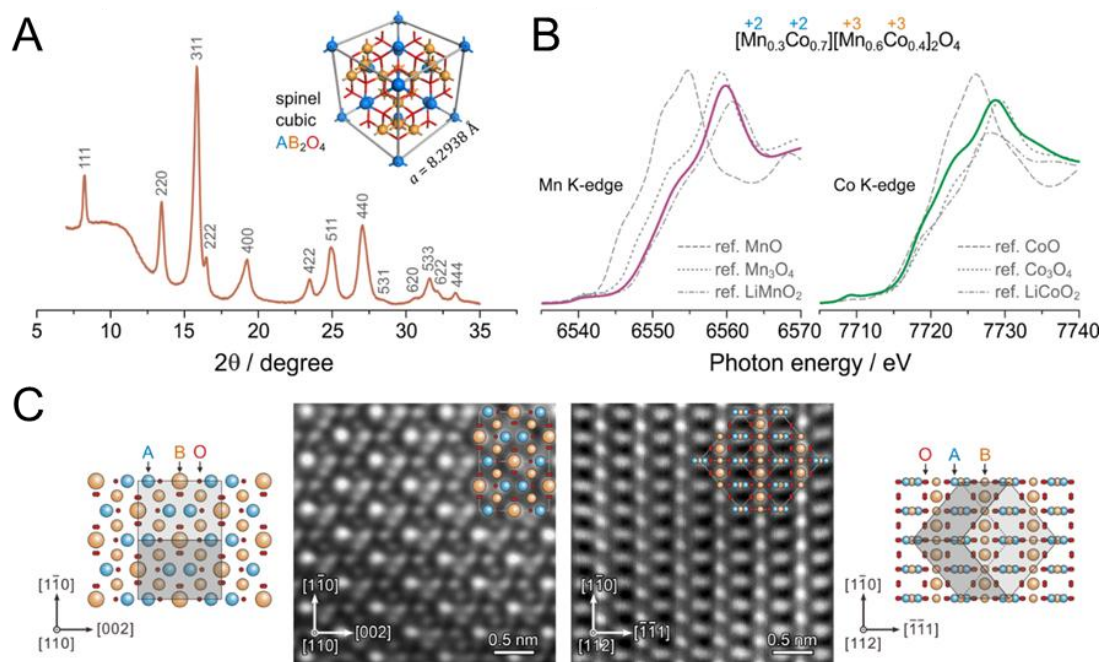
Moreover, the MCS cathode dramatically outperforms the Pt cathode at low relative humidity (RH) over a wider range of current densities. As illustrated in Fig. 3.3C, when the humidity was lowered to 50% RH, a significant drop in cell performance was observed for the Pt cathode, with the PPD decreasing by one third to 0.67 W/cm<sup>2</sup>. However, for the MCS cathode, the PPD remained virtually unchanged at 0.92 W/cm<sup>2</sup>. The ability to work at low RH is a unique advantage for APEFC cathodes, where water (which is a reactant; *vide-infra*) is often depleted, particularly when the cell is operated at high current densities.<sup>5</sup> It should be noted that the Pt cathode has been well optimized to reach its maximum performance, the observed superiority of the MCS cathode, at high current densities and low humidity, is not due to a structural effect of the electrodes. In fact, the Pt cathode is thinner in the catalyst layer, which possesses lower electrical resistance than the MCS cathode. Since the operation conditions (gas backpressure, flow rate, etc.) are the same for both electrodes, the mass transport should not be particular to the thinner Pt cathode. The obvious difference in the water/humidity dependence of the cathode performance are ascribed to a certain catalyst-water interaction.

Fig. 3.3D summarizes the activity comparison between Pt and MCS under different experimental conditions in RDE and fuel-cell tests. While Pt is superior, over the MCS, under water-rich conditions, it becomes inferior at low water content. This suggests the presence of an effect, on the ORR catalytic activity, that is sensitive to the water content and works oppositely on Pt and MCS. In APEFCs, H<sub>2</sub>O is not only necessary for ionic conduction, but is also a reactant in the ORR.

Proton transfer processes in this reaction are as crucial as the electron transfer events themselves,<sup>6,7</sup> as evidenced (via H/D isotope effects) by the significant diminution of the kinetics of the ORR in NaOD/D<sub>2</sub>O solution (Fig. 3.7D). Thus, the ORR will be highly sensitive to the amount, and state, of H<sub>2</sub>O just above the catalyst surface,<sup>8,9</sup> especially when H<sub>2</sub>O is a minority species in the gaseous phase. The high catalytic activity of MCS toward the ORR at low H<sub>2</sub>O content suggests the presence of a special affinity for H<sub>2</sub>O, in addition to the appropriate interactions with O<sub>2</sub>.

### 3.5 Structural and Surface Analysis of MCS Catalysts

In an effort to unveil the origin of these effects, in-depth characterization of the structure and surface properties was carried out. Synchrotron X-ray diffraction (XRD, Fig. 3.4A) clearly indicates the presence of the cubic spinel structure (AB<sub>2</sub>O<sub>4</sub>) with a lattice constant  $a = 8.2938 \text{ \AA}$ . The formal valence of Mn and Co in the MCS sample exhibiting optimal ORR performance (nominally Mn<sub>1.5</sub>Co<sub>1.5</sub>O<sub>4</sub>) were analyzed using X-ray absorption near edge structure (XANES, Fig. 3.4B), which yielded values of +2.76 and +2.56, respectively. The stoichiometry of the spinel (AB<sub>2</sub>O<sub>4</sub>) was thus determined to be [Mn<sub>0.3</sub>Co<sub>0.7</sub>][Mn<sub>0.6</sub>Co<sub>0.4</sub>]<sub>2</sub>O<sub>4</sub>, indicating that while Co is distributed almost uniformly at the tetrahedral (A) and octahedral (B) sites of the spinel lattice, Mn is enriched at the B site. The elemental ratio of Mn/Co is 3/2 at the catalytically active B site.<sup>10</sup> The high-angle annular dark-field STEM images (HAADF-STEM, Fig. 3.4C), taken on the [110] and [112] zone axes, provide atomic views of the arrangement of metal ions inside the MCS lattice. The high-contrast patterns match well the lattice model reconstructed based on the above-determined stoichiometry.



**Figure 3.4** Structural characterization of the MCS catalyst exhibiting optimal ORR performance. (A) Synchrotron X-ray diffraction (XRD) pattern, identifying the spinel cubic crystal structure with a lattice constant  $a = 8.2938 \text{ \AA}$  (inset). The raised baseline at around  $10^\circ$  is due to the carbon black support of the MCS. (B) X-ray absorption near edge structure (XANES) spectra. The K-edge absorptions of Mn and Co were collected, each with three reference samples. The formal valences of Mn and Co were determined to be +2.76 and +2.56, respectively, corresponding to a stoichiometry of  $[\text{Mn}_{0.3}\text{Co}_{0.7}][\text{Mn}_{0.6}\text{Co}_{0.4}]_2\text{O}_4$ . (C) High-angle annular dark-field images from scanning transmission electron microscopy (HAADF-STEM) images of the MCS lattice, taken on zone axes of  $[110]$  and  $[112]$ . Models of lattice projection are provided, with a unit cell embedded in the picture, to interpret the atomic resolution images.

In an attempt to distinguish the functionality of the Mn sites and Co sites on the spinel surface, we deliberately prepared MCS samples with Mn-segregated and Co-segregated surfaces, denoted as Mn-MCS and Co-MCS, respectively. The success in controlling surface segregation was ascertained by elemental mapping using electron energy loss spectroscopy (Fig. 3.5A, inset), as discussed before. Samples were then characterized with X-ray photoelectron spectroscopy (XPS) to identify the oxygen-containing surface species (Fig. 3a). In addition to  $\text{O}^{2-}$  that constitutes the spinel,  $\text{OH}_{\text{ads}}$

and  $\text{H}_2\text{O}_{\text{ads}}$  were identified by their distinct chemical shifts.<sup>11,12</sup> While Mn segregation resulted in an enhancement in the  $\text{O}^{2-}$  component and a diminution of  $\text{H}_2\text{O}_{\text{ads}}$ , Co segregation caused a reversal effect with a clear increase in the  $\text{H}_2\text{O}_{\text{ads}}$  component. These results suggest that the actual MCS surface consists mainly of Mn-OH/Mn-O and Co-OH/Co-OH<sub>2</sub>, in agreement with the zeta-potential analysis in solutions of varying pH. As shown in Fig. 3.5B, the potential of zero charge (PZC) of MCS appears at pH = 5.5, and shifts to pH = 8.5 upon Co segregation, and to pH = 3.3 upon Mn segregation. These observations suggest that the Co sites interact weakly with O, and tend to be positively charged, likely as Co-OH<sub>2</sub><sup>δ+</sup>, while the Mn sites have a strong affinity for O, and tend to be negatively charged, likely as Mn-O<sup>δ-</sup>.

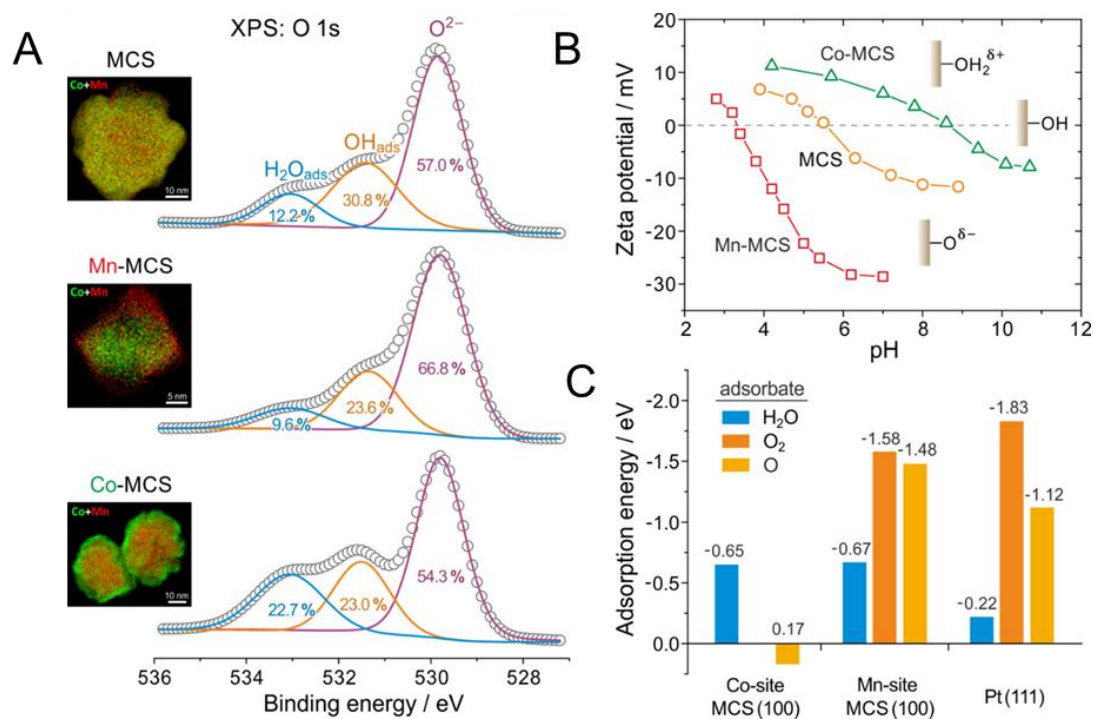


**Figure 3.5.** Surface analyses of the MCS catalysts. (A) Oxygen 1s spectra of X-ray photoelectron spectroscopy (XPS) for MCS and two reference samples with Mn or Co enriched on the surface (denoted as Mn-MCS and Co-MCS, respectively). Insets are electron energy loss spectroscopy (EELS) mapping for these samples (also see figs.

S11–S13). Spectral deconvolution identified three distinct chemical environments of O, corresponding to those of  $\text{H}_2\text{O}_{\text{ads}}$ ,  $\text{OH}_{\text{ads}}$ , and  $\text{O}^{2-}$ <sup>26,27</sup>. (B) Zeta potential measurements for MCS, Mn-MCS, and Co-MCS particles dispersed in solutions of different pH. (C) Density functional theory (DFT) calculated adsorption energies for  $\text{H}_2\text{O}$ ,  $\text{O}_2$ , and O on the Mn and Co sites of the MCS (100) surface, in comparison to those on Pt (111). No stable adsorption structure was found for  $\text{O}_2$  on the Co site of MCS (100). See tables S1–S6 for supplementary data of DFT calculations. The adsorption energy of O was defined relative to half the energy of  $\text{O}_2$ , such that negative values indicate a spontaneous dissociation of  $\text{O}_2$  on the surface.

The above experimental observations of the surface character of the MCS are in qualitative agreement with density functional theory (DFT) calculations (Fig. 3.5C). The Mn sites on MCS are highly active for binding both  $\text{O}_2$  and  $\text{H}_2\text{O}$ , but the Mn- $\text{O}_2$  interaction is stronger than the Mn- $\text{OH}_2$  interaction, suggesting that the Mn sites prefer to bind  $\text{O}_2$  over  $\text{H}_2\text{O}$  when the MCS is exposed to humid air. In contrast, the Co sites have a notable affinity for  $\text{H}_2\text{O}$  but appear not to bind  $\text{O}_2$  by itself (given that  $\text{O}_2$  can adsorb at the bridge sites between Mn and Co atoms). Hence, when the MCS cathode is exposed to humid  $\text{O}_2$ , the Mn sites and Co sites on the surface bind different adsorbates, preferentially yielding Mn- $\text{O}_2$  and Co- $\text{OH}_2$ , respectively.

The DFT calculations can also provide an assessment of the capability of breaking the O-O bond at a catalytic site. Specifically, the adsorption energy of an O atom is calculated relative to half the energy of  $\text{O}_2$ , such that negative values designate a thermodynamically spontaneous dissociation of  $\text{O}_2$ . As presented in Fig. 3.5c, the dissociation of  $\text{O}_2$  is energetically highly favorable on the Mn site, but disfavored (albeit slightly) on the Co site. One can thus conclude that the MCS possesses a synergistic surface for ORR catalysis, with the Mn sites binding and cleaving  $\text{O}_2$ , and the Co sites enriching and activating  $\text{H}_2\text{O}$ , so as to facilitate the proton-couple electron transfer

processes of the oxygen reduction reaction in fuel cell.

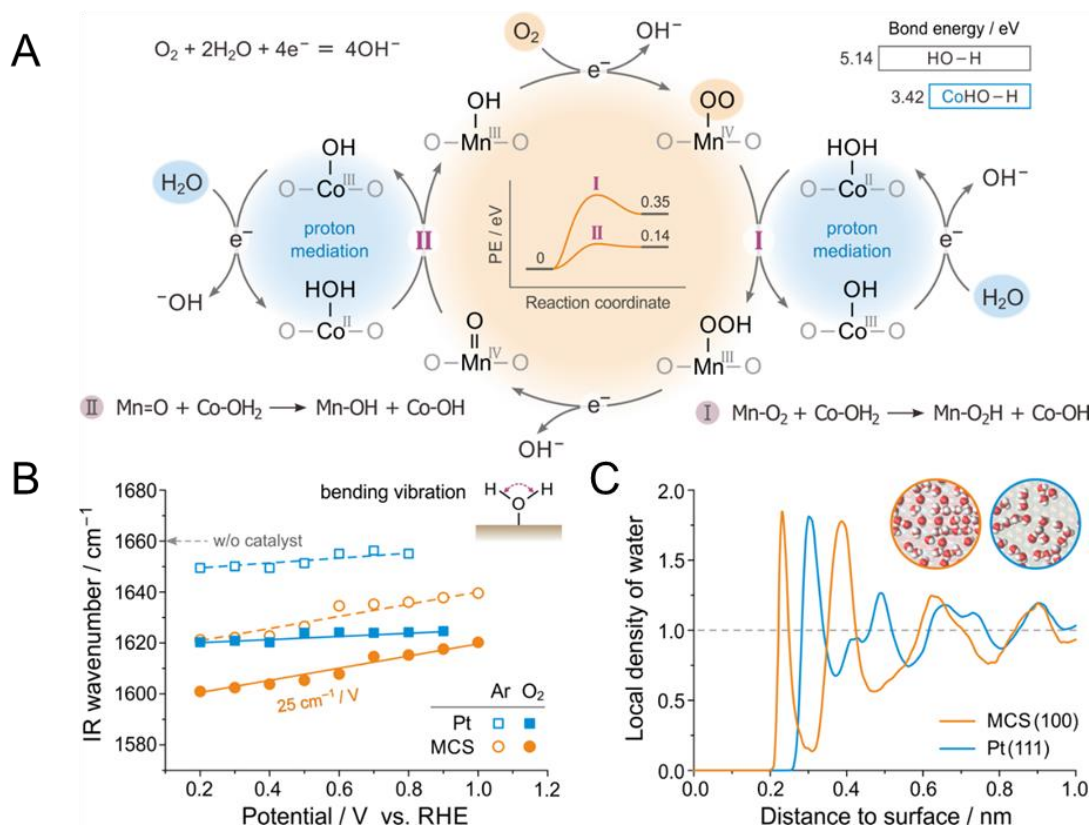


**Figure 3.6.** Mechanistic analysis of the MCS-catalyzed ORR. (A) Schematic illustration of the proposed synergistic mechanism of ORR on MCS, featuring the dissociative reduction of  $O_2$  at the Mn site, the proton mediation by the Co site, and the surface proton transfer in between (reactions I and II). Inset central: DFT-calculated energy barriers for reactions I & II on MCS (100) (See tables S7–S8 for details). Inset upper-right: DFT-calculated bond energies of O–H in  $H_2O$  and  $Co-OH_2$ . (B) Results of *in-situ* attenuated total reflection Fourier transform infrared (ATR-FTIR) studies for MCS and Pt electrodes in Ar or  $O_2$  saturated KOH solutions. See fig. S14 for relevant FTIR spectra. The IR signals of interest were from the bending vibration of  $H_2O$  (inset). The Stark effect (wavenumber shift with potential) is a measure of the  $H_2O$  adsorption on the surface. (C) Local density of water on MCS (100) and Pt (111) surfaces at 300 K, obtained from atomistic molecular dynamics (MD) simulations. Inset: Snapshots of water molecules in a surface layer up to 0.3 nm thick.

### 3.6 Proposed Synergistic Reaction Mechanism

The proposed synergistic mechanism of the MCS-catalyzed ORR is illustrated,

stepwise, in Fig. 3.6A. Assuming that Mn-OH and Co-OH represent the initial states, the O<sub>2</sub> is preferentially bound to the Mn site to yield Mn-O<sub>2</sub>, along with a 1e<sup>-</sup> reduction to produce OH<sup>-</sup>. H<sub>2</sub>O is preferentially bound to the Co site, as Co-OH<sub>2</sub>, also with a 1e<sup>-</sup> reduction to generate OH<sup>-</sup>. A surface proton transfer (reaction I) can then occur from the Co-OH<sub>2</sub> to the proximate Mn-O<sub>2</sub>, leading to a regenerated Co-OH and a Mn-OOH species that is followed by a 1e<sup>-</sup> reduction to produce Mn=O and OH<sup>-</sup>. The Mn=O can take the second proton, transferred from Co-OH<sub>2</sub>, to regenerate the Mn-OH (reaction II). The extraordinary feature of this mechanism includes the proton mediation by the turnover of Co-OH/Co-OH<sub>2</sub> and the surface proton transfer between the proximate Co and Mn sites. On the one hand, based on DFT calculations, the O-H bond energy decreases from 5.14 eV to 3.42 eV when the H<sub>2</sub>O is bound to the Co site (Fig. 3.6A, upper-right inset). On the other hand, the energy barriers for reaction I and II are small (Fig. 3.6A, central inset). We believe that these energetic features are fundamental to the H<sub>2</sub>O activation and proton-transferred reduction of O<sub>2</sub> on MCS.

To ascertain the involvement of surface H<sub>2</sub>O in the MCS-catalyzed ORR, *in-situ* attenuated total reflection Fourier transform infrared spectroscopy (ATR-FTIR) was employed to detect the subtle changes in the H<sub>2</sub>O vibrations on Pt and MCS surfaces under electrochemical conditions (Fig. 3.6B). The H<sub>2</sub>O bending vibration,  $\delta(\text{HOH})$ , turns out to be at higher wavenumbers on Pt than on MCS, indicating that the Pt-H<sub>2</sub>O interaction is weaker than the MCS-H<sub>2</sub>O interaction.<sup>13</sup> Even more compelling evidence for the strong adsorption of H<sub>2</sub>O on the MCS surface is provided by the Stark effect, namely, a significant potential-dependent shift in the  $\delta(\text{HOH})$  wavenumber of 25 cm<sup>-1</sup>/V. In contrast, such a Stark effect is negligible on a Pt surface. These experimental

observations are consistent with the DFT calculations (Fig. 3.5C) that show that the adsorption energy of H<sub>2</sub>O on Pt (111) is only one third of that on MCS (100).

Additional valuable information was provided by *in-situ* ATR-FTIR experiments, showing that the  $\delta(\text{HOH})$  wavenumber decreased on both Pt and MCS when the atmosphere was switched from Ar to O<sub>2</sub> (Fig. 3.6B). This can only be ascribed to the additional interaction between the surface H<sub>2</sub>O and the surface oxygen species, providing unambiguous evidence for the involvement of surface H<sub>2</sub>O in the ORR. Moreover, the  $\delta(\text{HOH})$  Stark effect remained unchanged on MCS during the ORR, indicating that the surface H<sub>2</sub>O has not been repelled by the co-adsorption of O<sub>2</sub>; whereas the originally weak Stark effect of  $\delta(\text{HOH})$  on Pt could barely be observed during the ORR, suggesting that the H<sub>2</sub>O is likely to be further away from the Pt surface when covered by oxygen species. The identification of the different functionalities of the Mn sites and Co sites, and the direct observation of the involvement of surface H<sub>2</sub>O in the MCS-catalyzed ORR, provide strong support for the synergistic mechanism (Fig. 3.6A). The above computational and experimental observations clearly establish the superior activity of MCS over Pt for the ORR under conditions of high current density and low humidity. The lower ORR activity of MCS in RDE tests is also understandable. In O<sub>2</sub> saturated KOH solutions, the molar ratio of H<sub>2</sub>O/O<sub>2</sub> is over 10<sup>4</sup>, so that the hydrophilic MCS surface is dominated by H<sub>2</sub>O,<sup>14,15</sup> despite the oxophilicity of the Mn sites. Molecular dynamics (MD) simulations (Fig. 3.6C) show that liquid water can wet the MCS surface with a proximity of 0.23 nm, in comparison to 0.3 nm on a Pt surface. Thus, there is more space for O<sub>2</sub> adsorption on a Pt surface than on an MCS surface under water-flooding conditions.

### 3.7 Conclusion

Although MCS-like materials were used as ORR catalysts in the literature,<sup>16-18</sup> the cell performance has not reached such a high level as reported in this work, and the mechanistic understanding has been vague. Here we report on a Mn-Co spinel catalyst that, when employed as the cathode in an APEFC, can deliver greater power, at high current densities, than a Pt cathode. The power density of an APEFC employing such a Mn-Co cathode reached 1.1 W/cm<sup>2</sup> at 2.5 A/cm<sup>2</sup> at 60°C. Moreover, this catalyst works much better than Pt at low humidity. In-depth characterization revealed that the remarkable performance of this Mn-Co catalyst originates from synergistic effects in which the Mn sites bind O<sub>2</sub>, and the Co sites, in close proximity, activate H<sub>2</sub>O so as to facilitate the proton-coupled electron transfer processes of oxygen reduction. Such an electrocatalytic synergy is pivotal to the high rate of the ORR, particularly under water depletion/low humidity conditions. Our findings represent not only the discovery of a practical, high-performance non-precious metal catalyst for APEFCs, but also reveal a new strategy for the ORR catalyst design. In addition to the electronic effects that have often been used and/or invoked to tune the reactivity of solid surfaces toward O<sub>2</sub>,<sup>19,20</sup> designing synergistic surfaces that can activate H<sub>2</sub>O and facilitate proton transfer processes is also pivotal for ORR catalysts, in particular for metal oxides working in alkaline media, where both O<sub>2</sub> and H<sub>2</sub>O are reactants.

### 3.8 References

1. Fox, R. K.; Swinehart, D. F.; Garrett, A. B. The equilibria of Manganese Hydroxide,  $\text{Mn}(\text{OH})_2$ , in Solutions of Hydrochloric Acid and Sodium Hydroxide. *J. Am. Chem. Soc.* **1941**, 63, 1779-1782.
2. Gayer, K. H.; Garrett, A. B. The Solubility of Cobalt Hydroxide,  $\text{Co}(\text{OH})_2$ , in Solutions of Hydrochloric Acid and Sodium Hydroxide at 25°. *J. Am. Chem. Soc.* **1950**, 72, 3921-3923.
3. Wang, Y. *et al.* Pt-Ru Catalyzed Hydrogen Oxidation In Alkaline Media: Oxophilic Effect Or Electronic Effect? *Energy Environ. Sci.* **2015**, 8, 177-181.
4. Ponce-González, J. *et al.* High performance aliphatic-heterocyclic benzyl-quaternary ammonium radiation-grafted anion-exchange membranes. *Energy Environ. Sci.* **2016**, 9, 3724-3735.
5. Dekel, D. R., Rasin, I. G., Page, M. & Brandon, S. Steady state and transient simulation of anion exchange membrane fuel cells. *J. Power Sources* **2018**, 375, 191-204.
6. Tse, E. C. M. *et al.* Proton transfer dynamics control the mechanism of  $\text{O}_2$  reduction by a non-precious metal electrocatalyst. *Nat. Mater.* **2016**, 15, 754-759.
7. Hammes-Schiffer, S. & Stuchebrukhov, A. A. Theory of coupled electron and proton transfer reactions. *Chem. Rev.* **2010**, 110, 6939-6960.
8. Lu, F. *et al.* Surface proton transfer promotes four-electron oxygen reduction on gold nanocrystal surfaces in alkaline solution. *J. Am. Chem. Soc.* **2017**, 139, 7310-7317.
9. Staszak-Jirkovský, J. *et al.* Water as a promoter and catalyst for dioxygen electrochemistry in aqueous and organic media. *ACS Catal.* **2015**, 5, 6600-6607.
10. Wei, C. *et al.* Cations in octahedral sites: A descriptor for oxygen electrocatalysis on transition-metal spinels. *Adv. Mater.* **2017**, 29, 1606800.
11. Nesbitt, H. W. & Banerjee, D. Interpretation of XPS Mn(2p) spectra of Mn oxyhydroxides and constraints on the mechanism of  $\text{MnO}_2$  precipitation. *Am. Mineral.* **1998**, 83, 303-315.
12. Kurbatov, G., Darque-Ceretti, E. & Aucouturier, M. Characterization of hydroxylated oxide film on iron surfaces and its acid-base properties using XPS. *Surf. Interface Anal.* **1992**, 18, 811-820.
13. Ataka, K., Yotsuyanagi, T. & Osawa, M. Potential-dependent reorientation of water molecules at an electrode/electrolyte interface studied by surface-enhanced infrared absorption spectroscopy. *J. Phys. Chem.* **1996**, 100, 10664-10672.
14. Thiel, P. A. & Madey, T. E. The interaction of water with solid surfaces: fundamental aspects. *Surf. Sci. Rep.* **1987**, 7, 211-385.
15. Mu, R. T., Zhao, Z. J., Dohnálek, Z. & Gong, J. L. Structural motifs of water on metal oxide surfaces. *Chem. Soc. Rev.* **2017**, 46, 1785-1806.
16. Cheng, F. Y. *et al.* Rapid room-temperature synthesis of nanocrystalline spinels as oxygen reduction and evolution electrocatalysts. *Nat. Chem.* **2011**, 3, 79-84.
17. Hong, W. T. *et al.* Toward the rational design of non-precious transition metal oxides for oxygen electrocatalysis. *Energy Environ. Sci.* **2015**, 8, 1404-1427.
18. Li, C. *et al.* Phase and composition controllable synthesis of cobalt manganese spinel nanoparticles towards efficient oxygen electrocatalysis. *Nat. Commun.* **2015**, 6, 7345.
19. Huang, B., Xiao, L., Lu, J. T. & Zhuang, L. Spatially resolved quantification of the surface reactivity of solid catalysts. *Angew. Chem. Int. Ed.* **2016**, 55, 6239-6243.
20. Seh, Z. W. *et al.* Combining theory and experiment in electrocatalysis: insights into materials design. *Science* **2017**, 355, 4998-5009.

## CHAPTER 4

### High-Loading Composition-Tolerant Co-Mn Spinel Oxides with MEA Performance beyond 1 W/cm<sup>2</sup> in Alkaline/Anion Exchange Membrane Fuel Cells\*,†

#### 4.1 Introduction

Hydrogen fuel cells have been recognized as a critical renewable energy technology, especially for powering electric vehicles (EVs).<sup>1-3</sup> Despite the tremendous effort in lowering Pt loading in the cathode of proton-exchange membrane fuel cells (PEMFCs), a significant amount of Pt (>0.2 g<sub>Pt</sub>/kW) is still necessary to provide a power density of >1 W/cm<sup>2</sup> at ≥ 0.65 V and the catalyst cost accounts for more than one-third of a PEMFC stack cost.<sup>4-8</sup> Alternatively, alkaline polymer electrolyte fuel cells (APEFCs) or anion-exchange membrane fuel cells (AEMFCs), in principle, enable the use non-precious metals or metal oxides as stable ORR electrocatalysts.<sup>9-19</sup>

During the development of PEMFCs and APEFCs or Alkaline/Anion Exchange Membrane Fuel Cells (AEMFCs), the RDE has been widely used, in research laboratories, to screen electrocatalysts and evaluate their activity/durability. For example, RDE measurements showed a rather good quantitative agreement with MEA tests for the benchmark activities of Pt/C in PEMFCs.<sup>3</sup>

---

\*Reproduced and modified with permission from the following publication  
**Yao Yang**, Hanqing Peng, Yin Xiong, Qihao Li, Juntao Lu, Li Xiao, Francis J. DiSalvo, Lin Zhuang, Héctor Abruña. High-loading Composition-Tolerant Co-Mn Spinel Oxides with Performance beyond 1W/cm<sup>2</sup> in Alkaline Polymer Electrolyte Fuel Cells.  
*ACS Energy Lett.* 2019, 4, 1251. © ACS

†**Yao Yang**, Héctor Abruña, Lin Zhuang, Hanqing Peng, Li Xiao, Cobalt-Manganese Spinel Oxide Catalysts. U.S. Patent Pending, No. 62/818.843, Filed Date: March 15, 2019.

However, RDE and MEA measurements have significant differences in terms of the test conditions, water management, mass transport mechanism, etc. For instance, although the spectacular ORR activity of shape-controlled Pt-based alloy catalysts, up to a factor of 20 relative to Pt/C, was reported from RDE measurements,<sup>25-29</sup> those reports have not translated into realistic MEA results in PEMFCs. Only after one-day of MEA testing, octahedral PtNi catalysts exhibited a loss of their distinct shapes and leached out a significant amount of Ni, contaminating the membrane.<sup>4</sup> In other RDE studies, it was shown that 1-3 atomic-layers of Pt on the surface of Pt-based alloys yielded the highest ORR activity under acidic conditions.<sup>8,29-31</sup> However, MEA results in PEMFCs suggested that 4-7 atomic layers of Pt were required to effectively mitigate the transition metal leaching problem, while still being thin enough to maintain the lattice strain for enhanced activities.<sup>32-34</sup> In our previous study on  $\text{Co}_{1.5}\text{Mn}_{1.5}\text{O}_4/\text{C}$  for APEFCs (Chapter 3), only modest activity was observed from RDE measurements. However, a high power density in MEA measurements, surpassing that of Pt/C at lower relative humidity, was achieved through optimizing the surface composition.<sup>18</sup> The RDE-MEA correlation/discrepancy show it is important to include MEA tests in early-stage catalyst development, in addition to RDE measurements for catalyst screening.

In this work, we reported on Mn-Co spinel oxide electrocatalysts as the oxygen cathode in practical MEA tests in APEFCs.  $\text{MnCo}_2\text{O}_4/\text{C}$  (80 wt.%) exhibited a peak power density of  $1.2 \text{ W/cm}^2$ , a benchmark value compared to the state-of-art non-precious cathodes using N-doped carbon ( $< 0.5 \text{ W/cm}^2$ ),<sup>15,35-38</sup> and 3d metal oxides ( $0.5\text{-}1 \text{ W/cm}^2$ ).<sup>18,19</sup> With further optimization on MEA components, we predict that Co-Mn oxides could eventually achieve or surpass the performance of precious metal

cathodes (e.g., Pt, Pd and Ag-based catalysts) in APEFCs (1.0-1.5 W/cm<sup>2</sup>).<sup>13,14,39-44</sup> The

MEA measurements in literatures were summarized in Table 4.1.

Cathode Catalysts <sup>[Ref]</sup>	Cathode Loading (mg/cm <sup>2</sup> )	Anode / PGM loading (mg/cm <sup>2</sup> )	Membrane /ionomer	T <sub>cell</sub> / °C	Gas type	P <sub>back</sub> / MPa (Ca/An)	RH (%) (Ca/An)	PPD / W/cm <sup>2</sup>
<b>MnCo<sub>2</sub>O<sub>4</sub>/C</b> <b>This work</b>	metal oxides, 0.8	0.4	QAPPT	80 60 60	H <sub>2</sub> /O <sub>2</sub>	0.1/0.1 0.1/0.1 0	100/100	1.2 1.0 0.92
<b>CoMn<sub>2</sub>O<sub>4</sub>/C</b> <b>This work</b>	metal oxides, 0.8	0.4	QAPPT	80	H <sub>2</sub> /O <sub>2</sub>	0.1/0.1	100/100	1.1
N-C-CoO <sub>x</sub> <sup>[19]</sup>	2.4	0.1	LDPE-BP MA/ETFE	65	H <sub>2</sub> /O <sub>2</sub> H <sub>2</sub> /Air	0.1/0.1 0.08/0.12	N/A	0.73 0.55
N-C-CoO <sub>x</sub> <sup>[19]</sup>	2.4	0.7	LDPE-BP MA/ETFE	65	H <sub>2</sub> /O <sub>2</sub> H <sub>2</sub> /Air	0.1/0.1 0.08/0.12	N/A	1.05 0.66
Co <sub>1.5</sub> Mn <sub>1.5</sub> O <sub>4</sub> /C <sup>[18]</sup>	metal oxides,0.8	0.4	αQAPS-S <sub>8</sub>	60	H <sub>2</sub> /O <sub>2</sub>	0.1/0.1	100/100 50/50	1.1 0.67
Fe/N/C nanotubes <sup>[15]</sup>	2.0	0.4	αQAPS-S <sub>14</sub>	60	H <sub>2</sub> /O <sub>2</sub>	0.1/0.1	100/100	0.45
N-doped Carbon <sup>[35]</sup>	1.0	0.6	ETFE- BTMA/ ETFE	60	H <sub>2</sub> /O <sub>2</sub>	0/0	83/83	0.7
Fe-N-C <sup>[36]</sup>	3.5	0.2	Tokuyama A201	70	H <sub>2</sub> /O <sub>2</sub>	0.14/0.14	100/100	0.225
Fe-N/C <sup>[37]</sup>	2.0	0.5	VTLC-PET	80	H <sub>2</sub> /O <sub>2</sub>	N/A	100/100	0.38
g-CN-CNF <sup>[38]</sup>	2.0	0.1	Tokuyama A201	50	H <sub>2</sub> /O <sub>2</sub>	0.05/0.05	100/100	0.171
<b>Pt/C</b> <b>This work</b>	0.4	Pt/C, 0.4	QAPPT	80 80 60 60	H <sub>2</sub> /O <sub>2</sub> H <sub>2</sub> /Air H <sub>2</sub> /O <sub>2</sub> H <sub>2</sub> /O <sub>2</sub>	0.1/0.1 0.1/0.1 0.1/0.1 0/0	100/100 100/100 100/100 100/100	1.5 1.0 1.3 1.0
Pt/C <sup>[18]</sup>	0.4	0.4	αQAPS-S <sub>8</sub>	60	H <sub>2</sub> /O <sub>2</sub>	0.1/0.1	100/100 50/50	1.0 0.67
Pt/C <sup>[41]</sup>	0.4	0.6	LDPE- AEM	80	H <sub>2</sub> /O <sub>2</sub> H <sub>2</sub> /Air	0/0	100/100	1.45 0.63
Pt/C <sup>[42]</sup>	0.6	0.75	TPN/FLN- 55	80	H <sub>2</sub> /O <sub>2</sub>	0.285/0.285	100/100	1.46
PdCu/C <sup>[13]</sup>	0.6	Pd- CeO <sub>2</sub> /C,0.4	ETFE- BTMA	70 60	H <sub>2</sub> /O <sub>2</sub>	0.1/0.2	39/35	1.0 0.83
Ag/C <sup>[41]</sup>	0.8	0.6	LDPE- AEM	80	H <sub>2</sub> /O <sub>2</sub>	0/0	100/100	0.90
Ag/C <sup>[43]</sup>	1.0	0.6	EFTE- AEM	70	H <sub>2</sub> /O <sub>2</sub> H <sub>2</sub> /Air	0/0	84/84	1.11 0.70

Ag/C <sup>[14]</sup>	0.86	0.4	LDPE15- AEM /ETFE	80	H <sub>2</sub> /O <sub>2</sub> H <sub>2</sub> /Air	0/0	92/92	1.62 0.85
----------------------	------	-----	-------------------------	----	---	-----	-------	--------------

**Table 4.1.** Literature survey on APEFC measurements. PGM refers to Pt group metals, including Pt, Ru, Rh, Pd, Ir and Os. PtRu/C was used as the anode catalyst unless otherwise noted. PPD refers to peak power density. The reference number in the main text was used here.

## 4.2 Experimental Methods

Hydrothermal synthesis, structural characterization and electrochemical measurements adapted same procedures as Chapter 2. High-surface-area carbon Ketjen Black (HSC KB) was weighted to achieve target metal oxide loadings of 40, 60 and 80 wt.% in the catalyst/carbon composites. Catalyst synthesis could be achieved at the gram-level per batch with desirable single phase and controllable particle size, showing the potential for large-scale production.

**Membrane-electrode assembly (MEA) tests:** The alkaline polymer electrolyte (APE) and ionomer binder used in fuel cells were both quaternary ammonium poly(N-methyl-piperidine-co-p-terphenyl) (QAPPT) with an ion-exchange capacity (IEC) of 2.58 mmol/g. Synthesis details of QAPPT can be found in our previous report.<sup>40</sup> The catalyst ink was prepared by mixing PtRu/C (60%w/w in metal content) or Co-Mn oxides/C with ionomer binder (catalyst:ionomer = 4:1 wt./wt.), dispersed with n-propanol and ultrasonicated for half an hour. The ink was then sprayed on the QAPPT membrane (Cl<sup>-</sup> form, 30 ± 3 μm in dry state), forming a catalyst-coated membrane (CCM) with an electrode area of 4 cm<sup>2</sup>. The metal loading of PtRu in the anode was 0.4 mg/cm<sup>2</sup>. Next, the prepared CCM was soaked in 1 M KOH for 24 h at 55°C to exchange Cl<sup>-</sup> with OH<sup>-</sup>, and washed with distilled water before fuel cell tests to remove the excess KOH. The resulting CCM was positioned between two pieces of Teflon-treated carbon

paper (AvCarb GDS3250) to make the membrane electrode assembly (MEA) *in situ*: no hot-pressing was required. H<sub>2</sub>/O<sub>2</sub> single cell APEFCs were tested using an 850E Multi Range fuel cell test station (Scribner Associates, USA) in a galvanic mode at 60°C or 80°C. H<sub>2</sub> and O<sub>2</sub> were fully humidified at 60°C or 80°C (100% RH) and fed with a flow rate 1000 mL/min and a backpressure of either 0 or 0.1 MPa symmetrically on both sides. The fuel cell was briefly activated at a constant current and then the cell voltage at a series of current density was recorded.

### 4.3 Crystal Structure Studies of Co-Mn Oxides at Various Oxide Loadings

MnCo<sub>2</sub>O<sub>4</sub> and CoMn<sub>2</sub>O<sub>4</sub> nanoparticles (NPs) were synthesized using a facile hydrothermal method, as described in Chapter 2. Crystal structures of MnCo<sub>2</sub>O<sub>4</sub>/C and CoMn<sub>2</sub>O<sub>4</sub>/C were examined using powder X-ray diffraction (XRD) (Figure 4.1).

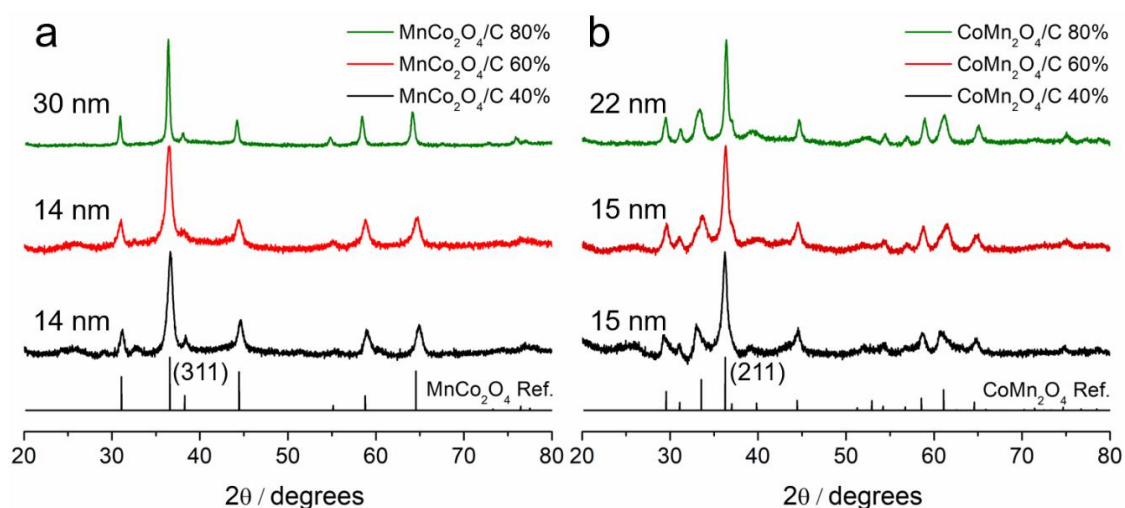


**Figure 4.1.** (a) Powder XRD patterns of MnCo<sub>2</sub>O<sub>4</sub> and (b) CoMn<sub>2</sub>O<sub>4</sub> nanoparticles with 40, 60 and 80 wt.% metal oxide loadings on high-surface-area carbon Ketjen Black (HSC KB), compared to XRD references of spinel-type MnCo<sub>2</sub>O<sub>4</sub> and CoMn<sub>2</sub>O<sub>4</sub>. Domain sizes of MnCo<sub>2</sub>O<sub>4</sub> and CoMn<sub>2</sub>O<sub>4</sub> nanoparticles are listed on the left side of the XRD patterns.

MnCo<sub>2</sub>O<sub>4</sub>/C with metal oxide loadings of 40, 60 and 80 wt.% all exhibited single-phase

cubic spinel structures when compared to the  $\text{MnCo}_2\text{O}_4$  reference (Figure 4.1a). Such a high loading of 80 wt.% has not been reported before for the oxygen cathode in hydrogen fuel cells although it is a common value used for fabricating the metal oxide cathodes in Li-ion batteries.<sup>45</sup> Average domain sizes of 40, 60, 80 wt.%  $\text{MnCo}_2\text{O}_4/\text{C}$  were calculated to be 14, 14 and 30 nm, respectively, using the major (311) peak based on the Scherrer equation. Larger domain sizes of 80 wt.%, relative to 40 and 60 wt.%, suggested that nanocrystals could grow into a larger size at a higher coverage of metal oxides on carbon. As a comparison,  $\text{CoMn}_2\text{O}_4/\text{C}$ , with various metal oxide loadings, showed a single-phase tetragonal spinel structures due to the strong Jahn-Teller effect of Mn (Figure 4.1b). The domain size of 80 wt.%  $\text{CoMn}_2\text{O}_4/\text{C}$  was calculated to be 22 nm using the (211) major diffraction peak (PDF # 01-077-0471), which was slightly larger than those at 40 and 60 wt.% (15 nm).

The microstructure of Co-Mn NPs supported on HSC KB was examined using aberration-corrected high-angle annular dark-field (HAADF) scanning transmission electron microscopy (STEM) imaging. As shown in Figure 4.2a,  $\text{MnCo}_2\text{O}_4$  NPs (40 wt.%) with an octahedral morphology were well embedded in the carbon matrix. Particle size distribution (PSD) histograms exhibited an average size of 35 nm (Figure 4.2b), indicating the majority of the  $\text{MnCo}_2\text{O}_4$  NPs have several sub-domains, given the XRD domain size of 14 nm. Atomic-scale STEM image further showed the internal structure of individual  $\text{MnCo}_2\text{O}_4$  NPs. As shown in Figures 4.2c, single-crystal  $\text{MnCo}_2\text{O}_4$  particles showed lattice d-spacings of 2.9 Å, which matched the theoretical value, 2.93 Å, of  $\text{MnCo}_2\text{O}_4$  (220) reflection (PDF # 01-084-0482). Since STEM image intensity is proportional to atomic number and relative atomic density, the variation in

image contrast suggests the existence of nm-sized pores.

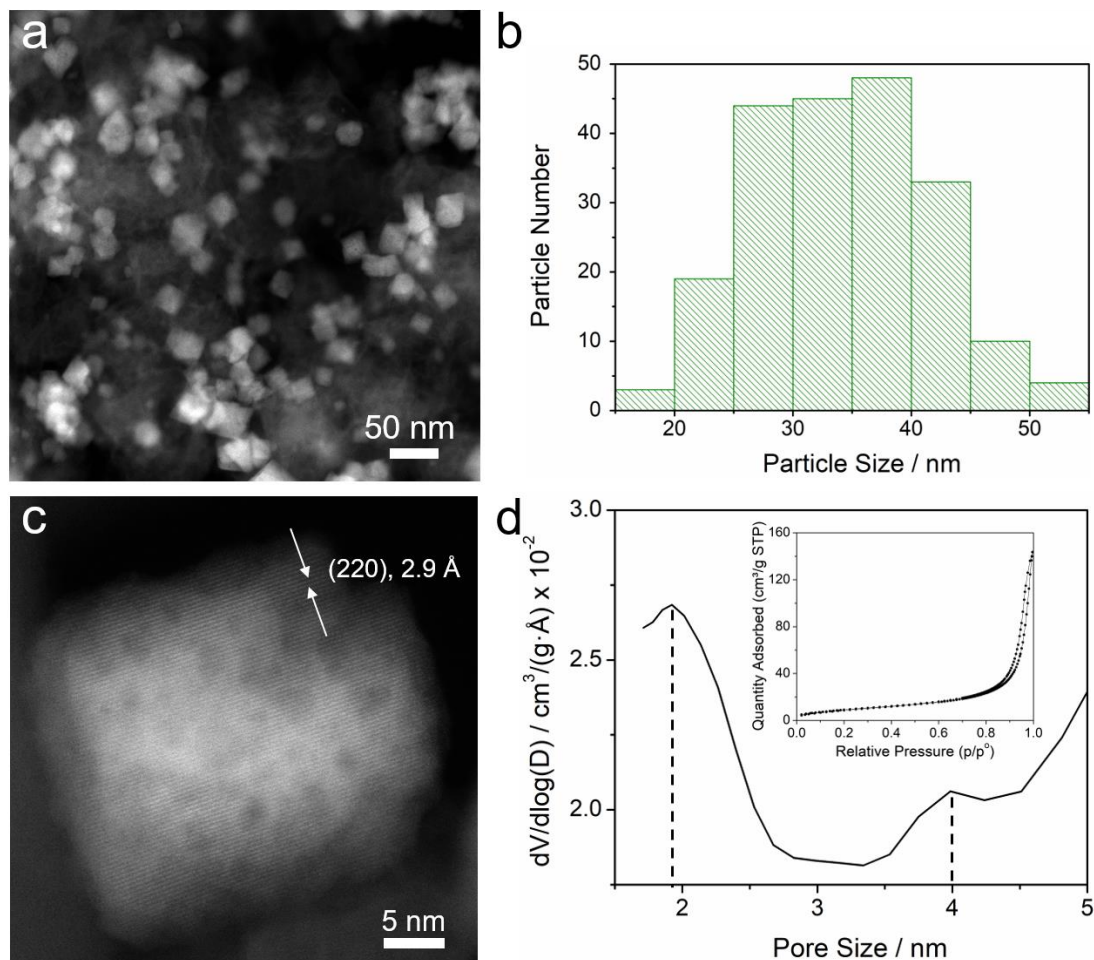


**Figure 4.2.** (a) HAADF-STEM image of  $\text{MnCo}_2\text{O}_4$  with 40 wt.% metal oxide loading on HSC KB. (b) Particle size distribution (PSD) histogram of  $\text{MnCo}_2\text{O}_4$  nanoparticles. (c) Atomic-scale STEM image of one  $\text{MnCo}_2\text{O}_4$  particle with (220) lattice d-spacings (2.9 Å). (d) Pore size distribution of  $\text{MnCo}_2\text{O}_4$  without carbon support, derived from the  $\text{N}_2$  adsorption-desorption isotherm in the inset. The y-axis represents the logarithmic differential pore volume distribution,  $dV/d\log(D)$ , derived from the BJH method. Dashed lines indicate the existence of micropores (1.9 nm) and small mesopores (4.0 nm) in the porous  $\text{MnCo}_2\text{O}_4$  NPs.

#### 4.4 Porosity and Conductivity Studies of Co-Mn Oxides

To quantify the porosity of  $\text{MnCo}_2\text{O}_4$  without the influence of the mesoporous carbon substrate,  $\text{MnCo}_2\text{O}_4$  metal oxides were also synthesized without adding HSC

KB. The pore size distribution was derived from the N<sub>2</sub> adsorption-desorption isotherm using the Barrett-Joyer-Halenda (BJH) method (Figure 4.2d). It shows major micropores of 1.9 nm as well as minor small mesopores of 4.0 nm, which are consistent with the pore sizes indicated from previous STEM images (Figures 4.2c). The specific surface area was estimated to be 34 m<sup>2</sup>/g based on the BET analysis (Figure 4.2d, inset). The electrical conductivity of porous MnCo<sub>2</sub>O<sub>4</sub>, without carbon support, was estimated to be 19 mS/m, when compared to typical values of Si (1.6 mS/m) and amorphous carbon (10<sup>2</sup>-10<sup>3</sup> S/m, Figure 4.3). Given the fact that bulk MnCo<sub>2</sub>O<sub>4</sub> is an insulator with a band gap of 2.11 eV,<sup>46</sup> the electronic conductivity of MnCo<sub>2</sub>O<sub>4</sub> NPs may come from crystal defects and small particle sizes, leading to a smaller ohmic resistance for the ORR. CoMn<sub>2</sub>O<sub>4</sub> NPs (40 wt.%) exhibited a similar octahedral morphology with an average particle size of 22 nm, which also indicated the existence of sub-domains and nm-sized pores, give the XRD domain size of 15 nm and the STEM image contrast variation.



**Fig. 4.3.** Two-point conductivity measurements. Sample holder was made of Aluminum with a resistance less than 0.2 Ohm. The length and diameter of the same column was measured using a Vernier calipers. The calculated conductivity represents a lower bound, relative to the true value since the sample may be further compressed under a bigger pressure. More accurate measurements could be obtained if using the standard

four-point conductivity measurements.

#### 4.5 RDE Measurements of Co-Mn Oxides at Various Oxide Loadings

After thorough structural examination, the Mn-Co spinel oxides with various metal oxide loadings were employed as electrocatalysts for the ORR in alkaline media. ORR polarizations profiles were acquired in O<sub>2</sub>-saturated 1M KOH at a rotation rate of 1600 rpm and a scan rate of 5 mV/s with a catalyst loading of 0.25 mg/cm<sup>2</sup>. While the metal oxide loadings increased from 40 to 60 and finally 80 wt.%, CoMn<sub>2</sub>O<sub>4</sub>/C showed a similar ORR activity with a high half-wave potential ( $E_{1/2}$ ) of around 0.84 V vs. RHE and  $\Delta E_{1/2} < 3$  mV (Figure 4.4a). Noticeable changes only appeared when the potential was lower than 0.8 V vs. the reversible hydrogen electrode (RHE). CoMn<sub>2</sub>O<sub>4</sub>/C with an 80 wt.% metal oxide loading achieved the desired diffusion-limited current density at a more positive potential, relative to samples with 60% and 40% loadings. When compared to CoMn<sub>2</sub>O<sub>4</sub>/C, MnCo<sub>2</sub>O<sub>4</sub> also exhibited a similar ORR activity with changes in  $E_{1/2}$  less than 5 mV as the metal oxide loading increased from 40 to 80 wt.% (Figure 4.4b).

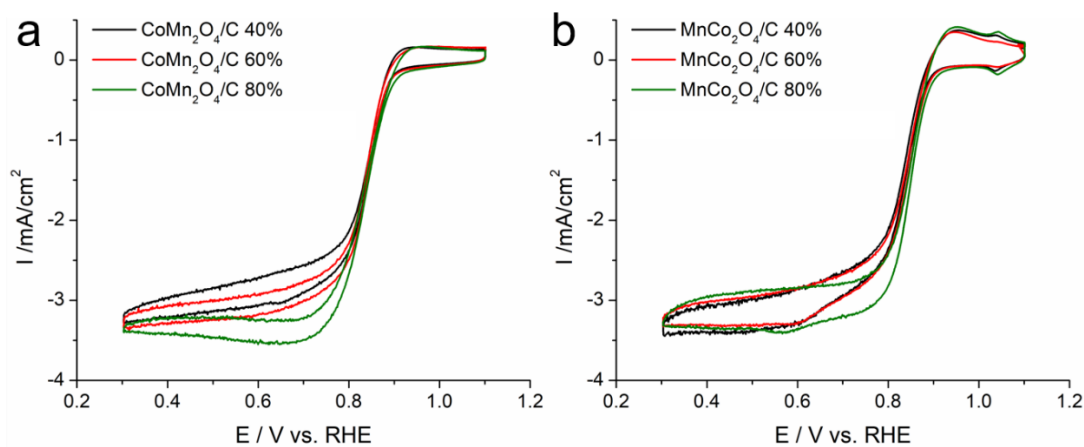


**Figure 4.4.** (a) ORR polarization profiles for MnCo<sub>2</sub>O<sub>4</sub> and (b) CoMn<sub>2</sub>O<sub>4</sub> with 40, 60

and 80 wt.% metal oxide loading on HSC KB in O<sub>2</sub>-saturated 1M KOH at a rotation rate of 1600 rpm and a scan rate of 5 mV/s with a catalyst loading of 0.25 mg/cm<sup>2</sup>.

Similar improvement in the high-polarization region was also observed at higher loading despite the small differences between 40% and 60 wt.%. The minor redox peaks of MnCo<sub>2</sub>O<sub>4</sub> at 1.05V were assigned to monolayer active species on the surface with highly reversible reaction process (Figure 2.8). The less smooth changes in the current density at around 0.6 V were ascribed to the influence of MnCo<sub>2</sub>O<sub>4</sub> reduction peaks at 0.6 V (Figure 2.8). One may conclude that MnCo<sub>2</sub>O<sub>4</sub>/C and CoMn<sub>2</sub>O<sub>4</sub>/C with high loading (60 and 80 wt.%) do not present significant advantages as ORR electrocatalysts, relative to the 40 wt.%, which is commonly reported as the metal oxide loading for both RDE and MEA measurements in the literature.<sup>19-24</sup> However, later practical MEA tests of Mn-Co oxides demonstrated the unexpected difference in performance with various metal oxide loadings on carbon (vide infra).

#### **4.6 MEA Measurements of Co-Mn Oxides at Various Oxide Loadings and Fuel Cell Test Conditions**

The H<sub>2</sub>-O<sub>2</sub> cell performance was tested using the quaternary ammonium poly(N-methyl-piperidine-co-p-terphenyl) (QAPPT, IEC=2.58 mmol/g), which was developed early in our group for stable cell operation at 80 °C as the alkaline membrane (thickness of 30 ± 5 μm) and ionomer binder in MEA measurements.<sup>40</sup> 60 wt.% PtRu/C (0.4 mg<sub>PtRu</sub>/cm<sup>2</sup>) was used as the anode catalyst and Mn-Co spinel oxides as the cathode catalyst. The cell was operated at 60 or 80°C with or without 0.1 MPa back-pressure. Both CoMn<sub>2</sub>O<sub>4</sub>/C and MnCo<sub>2</sub>O<sub>4</sub> exhibited an impressive enhancement in peak power density (PPD) at 80°C with 0.1 MPa back-pressure, as the metal oxide loading increased

from 40 to 60 and 80 wt.% (Figures 4.5a-b). The PPD of  $\text{CoMn}_2\text{O}_4/\text{C}$  showed a two-fold enhancement from  $0.63 \text{ W/cm}^2$  at 40 wt.% to  $1.2 \text{ W/cm}^2$  at 80 wt.% while the PPD of  $\text{MnCo}_2\text{O}_4/\text{C}$  was also boosted from  $0.46 \text{ W/cm}^2$  at 40 wt.% to  $1.1 \text{ W/cm}^2$  at 80 wt.% (Figures 4.5a-b and Tables 4.2-4.3). To the best of our knowledge, this performance of  $>1 \text{ W/cm}^2$  at a current density of  $>2.5 \text{ A/cm}^2$  represents the highest PPD ever achieved by non-precious ORR electrocatalysts in APEFCs,<sup>15,19, 35-38</sup> and is comparable to the state-of-the-art MEA results of Pt/C (Figure 4.6).

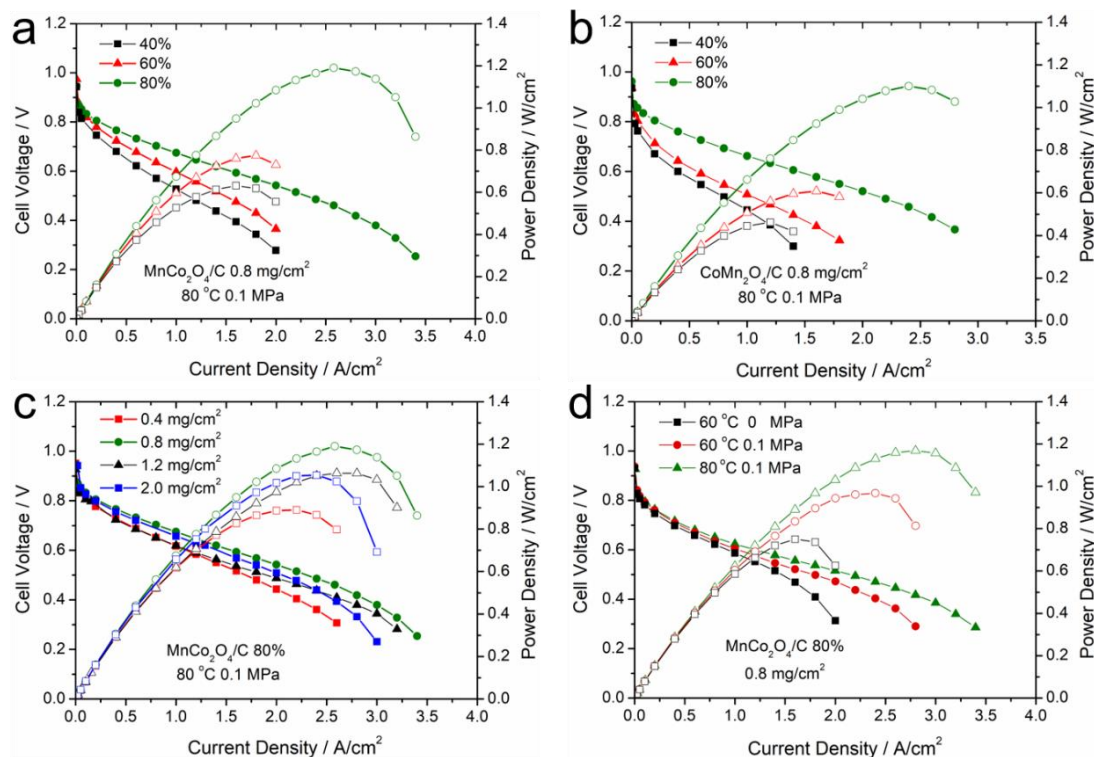


**Figure 4.5.** MEA measurements of AEMFCs using Co-Mn spinel oxides in the cathode, 60 wt.% PtRu/C ( $0.4 \text{ mg}_{\text{PtRu}}/\text{cm}^2$ ) in the anode, and QAPTT as the alkaline membrane ( $30 \pm 5 \mu\text{m}$ ) and ionomer binder (20 wt.% in the catalyst layers). Fully humidified  $\text{H}_2$  and  $\text{O}_2$  gas were fed into the cell at a flow rate of  $1000 \text{ mL/min}$ . (a-b) MEA results of  $\text{MnCo}_2\text{O}_4/\text{C}$  and  $\text{CoMn}_2\text{O}_4/\text{C}$  with 40, 60, and 80 wt.% metal oxide loadings on HSC KB. The catalyst loadings in the cathode were all controlled to be  $0.8 \text{ mg}_{\text{metal oxide}}/\text{cm}^2$  and the cell operating conditions were  $80 \text{ }^\circ\text{C}$  with  $0.1 \text{ MPa}$  back-pressure. (c) MEA results of  $\text{MnCo}_2\text{O}_4/\text{C}$  (80 wt.%) with a series of catalyst loadings from 0.4 to  $2.0 \text{ mg/cm}^2$  in the cathode with operating conditions of  $80 \text{ }^\circ\text{C}$  and  $0.1 \text{ MPa}$  back-pressure.

(d) MEA results of  $\text{MnCo}_2\text{O}_4$  at different operating conditions (60 or 80 °C; with or without 0.1 MPa back-pressure). Metal oxide loadings on carbon were controlled to be 80 wt.% and catalyst loadings in the cathode were  $0.8 \text{ mg}_{\text{metal oxide}}/\text{cm}^2$ . All the monotonic cell voltage-current density profiles correspond to the left y-axes while all the parabolic power density-current density profiles correspond to the right y-axes.

80% $\text{MnCo}_2\text{O}_4/\text{C}$	60°C 0MPa	60°C 0.1MPa	80°C 0.1MPa
0.4 $\text{mg}/\text{cm}^2$	700	840	890
0.8 $\text{mg}/\text{cm}^2$	920	1040	1190
1.2 $\text{mg}/\text{cm}^2$	560	780	1080
2.0 $\text{mg}/\text{cm}^2$	970	970	1050
60% $\text{MnCo}_2\text{O}_4/\text{C}$			
0.8 $\text{mg}/\text{cm}^2$	540	610	780
40% $\text{MnCo}_2\text{O}_4/\text{C}$			
0.8 $\text{mg}/\text{cm}^2$	470	N/A	630

**Table 4.2.** Peak powder density summary of  $\text{MnCo}_2\text{O}_4/\text{C}$  with different metal oxide loading on carbon and different catalyst loadings in the cathode under different operating conditions. Optimized conditions are marked in blue.

80% $\text{CoMn}_2\text{O}_4/\text{C}$	60°C 0MPa	60°C 0.1MPa	80°C 0.1MPa
0.8 $\text{mg}/\text{cm}^2$	780	960	1100
2.0 $\text{mg}/\text{cm}^2$	700	840	900
60% $\text{CoMn}_2\text{O}_4/\text{C}$			
0.8 $\text{mg cm}^{-2}$	420	490	580
40% $\text{CoMn}_2\text{O}_4/\text{C}$			
0.8 $\text{mg cm}^{-2}$	340	N/A	460

**Table 4.3.** Peak powder density summary of  $\text{CoMn}_2\text{O}_4/\text{C}$  with different metal oxide loading on carbon and different catalyst loadings in the cathode under different operating conditions. Optimized conditions are marked in blue.

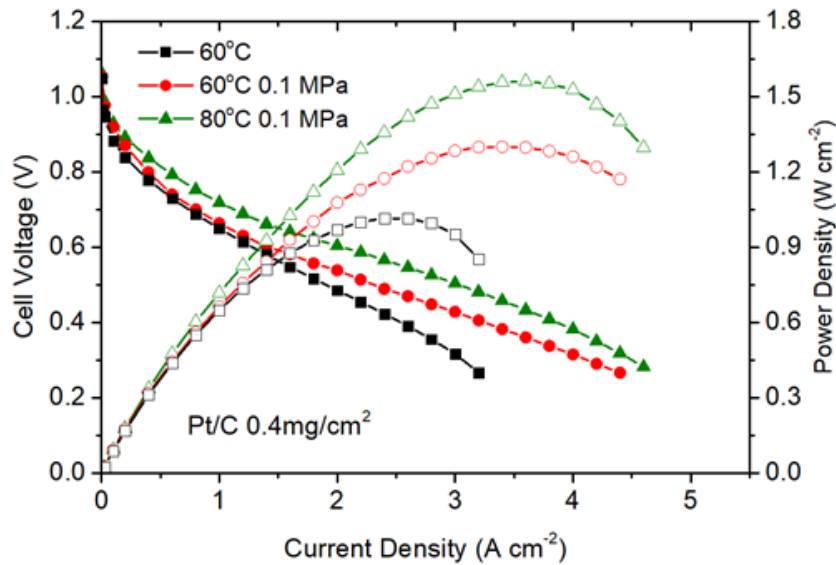


**Figure 4.6.** MEA measurements of Pt/C in APEFCs. Pt/C was used as both the cathode and anode with same Pt loading of 0.4 mg/cm<sup>2</sup> on both sides (H<sub>2</sub>/O<sub>2</sub> at 100/100% RH). All the monotonic cell voltage-current density profiles correspond to the left y-axis while all the parabolic power density-current density profiles correspond to the right y-axis.

This significant performance enhancement from 40wt.% to 80 wt.% Co-Mn oxides was ascribed to the enhanced mass transport efficiency at higher metal oxide loadings. The catalyst loadings in MEA were fixed at 0.8 mg<sub>metal oxide</sub>/cm<sup>2</sup>, so that the carbon loadings in MEA were 1.2 mg/cm<sup>2</sup>, 0.53 mg/cm<sup>2</sup> and 0.20 mg/cm<sup>2</sup> at metal oxide loadings of 40, 60 and 80 wt.%, respectively. SEM images of the cross section showed that the thickness of the catalyst layer decreased from 38 at 40 wt.% to 16 at 60 wt.% and finally to 8  $\mu\text{m}$  at 80 wt.% (Figure 4.7). A thinner catalyst layer of <10  $\mu\text{m}$  at 80 wt.% is more efficient for O<sub>2</sub>, H<sub>2</sub>O and OH<sup>-</sup> transport, which could more effectively supply reactants specially for high current densities (>2 A/cm<sup>2</sup>), leading to a higher PPD performance.

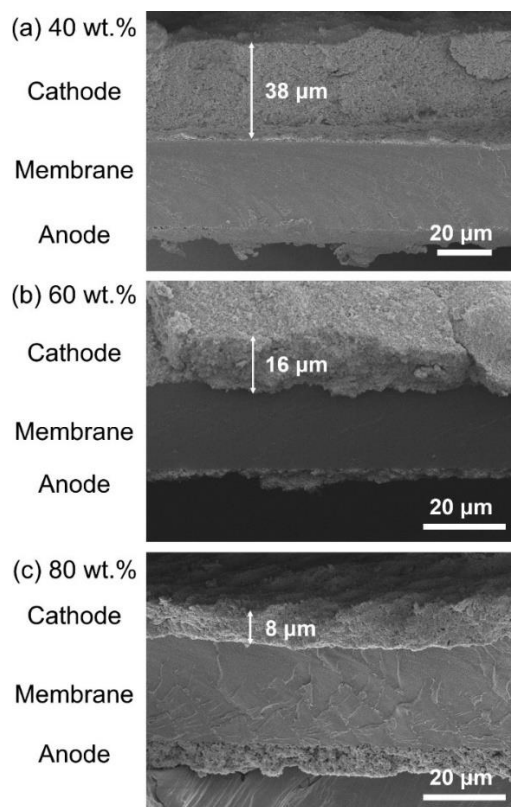


**Figure 4.7.** Cross-sectioned SEM images of the catalyst coated membrane (CCM) with metal oxide loadings of 40, 60 and 80 wt.% (a-c) with a fixed catalyst loading of  $0.8 \text{ mg}_{\text{metal oxide}}/\text{cm}^2$  in the MEA. The cathode catalyst layer decreased from  $38 \text{ }\mu\text{m}$  at 40 wt.% to  $16 \text{ }\mu\text{m}$  at 60 wt.% and  $8 \text{ }\mu\text{m}$  at 80 wt.% as the carbon loading decreased from 1.2 to 0.53 and  $0.20 \text{ mg}/\text{cm}^2$ , respectively. The thickness of the alkaline membrane in the middle is  $30 \pm 5 \text{ }\mu\text{m}$  and the thickness of the anode (PtRu/C, 60 wt.% with a loading  $0.4 \text{ mg}_{\text{PtRu}}/\text{cm}^2$ ) is around  $5 \text{ }\mu\text{m}$ . The as-prepared CCM was assembled in a fuel cell device and later taken out for cross-section SEM imaging, so that the thickness of the catalyst layer can represent the situation inside a fuel cell more accurately since the assembly process can compress the CCM to a certain degree.

The impact of the catalyst loading in the cathode was investigated from  $0.4$  to  $2.0 \text{ mg}_{\text{metal oxide}}/\text{cm}^2$  (Figure 4.5c). The cell PPD performance improved significantly, from  $0.89$  to  $1.2 \text{ W}/\text{cm}^2$  when the catalyst loadings increased from  $0.4$  to  $0.8 \text{ mg}/\text{cm}^2$ , which was attributed to the increased amount of catalyst active sites. However, further increases in the catalyst loading from  $0.8$  to  $2.0 \text{ mg}/\text{cm}^2$ , resulted in a noticeable decrease in the PPD from  $1.2$  to  $1.0 \text{ W}/\text{cm}^2$ . With catalyst loadings higher than  $0.8 \text{ cm}^2$ , the mass transport

limitation became dominant, relative to the increase in the amount of active sites. Different cell operating conditions were also systematically studied, including cell temperatures and operation with or without back-pressure (Figure 4.5d). The MEA with  $\text{MnCo}_2\text{O}_4/\text{C}$  (80 wt.%) exhibited a PPD enhancement from  $0.92 \text{ W/cm}^2$  to  $1.0 \text{ W/cm}^2$  by applying a  $0.1 \text{ MPa}$  back-pressure to both  $\text{H}_2$  and  $\text{O}_2$  and a further PPD increase from  $1.0$  to  $1.2 \text{ W/cm}^2$  when the temperature increased from  $60$  to  $80 \text{ }^\circ\text{C}$  with a  $0.1 \text{ MPa}$  back-pressure.  $\text{CoMn}_2\text{O}_4$  showed a similar PPD increase from  $0.78 \text{ W/cm}^2$  at  $60 \text{ }^\circ\text{C}$  with no back-pressure to  $1.1 \text{ W/cm}^2$  at  $80 \text{ }^\circ\text{C}$  with back-pressure. (Figure 4.8) This suggests that Co-Mn spinel oxides have an excellent temperature-tolerant performance at both  $60$  and  $80 \text{ }^\circ\text{C}$ , which is critical to maintain the high energy efficiency of fuel cells.<sup>2-4</sup> Few precious<sup>14,40</sup> or non-precious<sup>18</sup> ORR electrocatalysts can work at such a high temperature of  $80 \text{ }^\circ\text{C}$  at a PPD above  $1 \text{ W/cm}^2$ . This high power density was attributed to the combination of the high-loading active Co-Mn oxide electrocatalysts and stable QAPPT membrane/ionomers.

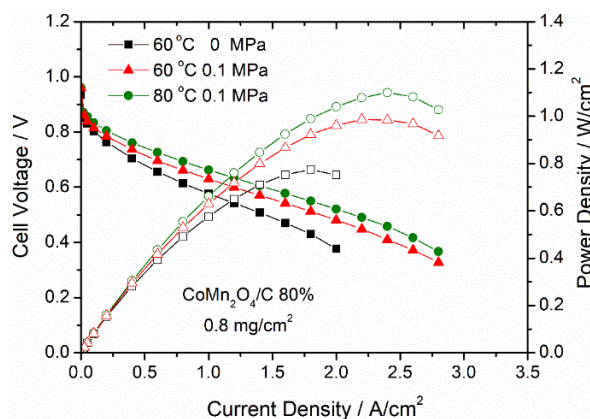


**Figure 4.8.** MEA measurements of  $\text{CoMn}_2\text{O}_4$  at different operating conditions ( $60$  and  $80 \text{ }^\circ\text{C}$ ; with or without  $0.1 \text{ MPa}$  back-pressure). Metal oxide loadings on carbon were controlled to be  $80 \text{ wt.}\%$  and catalyst loadings in the cathode were  $0.8 \text{ mg}_{\text{metal oxide}}/\text{cm}^2$ . All the monotonic cell voltage-current density profiles correspond to the left y-axis while all the power density-current density profiles correspond to the right y-axis.

## 4.7 Conclusion

In summary, we describe Co-Mn spinel oxide electrocatalysts with metal oxide loadings of up to 80 wt.% on carbon supports. Despite little variation in ORR activity derived from rotating disk electrode (RDE) measurements, practical membrane electrode assembly (MEA) tests exhibited significant enhancement in power density when loadings increased from 40 to 80 wt.%. This was ascribed to the enhanced mass transport through the thin catalyst layer at 80 wt.% (< 10  $\mu\text{m}$ ). This work highlights the importance of incorporating MEA tests, even in early-stage catalyst development. APEFCs with a record peak performance of over  $1\text{ W/cm}^2$  power density were achieved for both non-precious  $\text{MnCo}_2\text{O}_4/\text{C}$  ( $1.2\text{ W/cm}^{-2}$  at  $2.6\text{ A/cm}^{-2}$ ) and  $\text{CoMn}_2\text{O}_4/\text{C}$  ( $1.1\text{ W/cm}^{-2}$  at  $2.4\text{ A/cm}^{-2}$ ) with a high metal oxide loading of 80 wt.% at  $80^\circ\text{C}$  with 0.1 MPa back-pressure. This work suggests that MEA performance of Co-Mn spinel oxides is generally high even as the Co mole fraction of the cations varies from 2/3 to 1/3 from  $\text{MnCo}_2\text{O}_4/\text{C}$  to  $\text{CoMn}_2\text{O}_4/\text{C}$ . Consequently, even when Mn-Co oxide nanoparticles have variations in Mn and Co contents after large-scale synthesis, it will be less challenging to achieve the desired performance in practical fuel cell applications.

## 4.8 References

1. Debe, M. K. Electrocatalyst Approaches and Challenges for Automotive Fuel Cells. *Nature*. **2012**, 486, 43-51.
2. Xiong, Y.; Yang, Y.; Jorress, H.; Padgett, E.; Gupta, U.; Yarlagadda, V.; Agyeman-Budu, D. N.; Huang, X.; Moylan, T. E.; Zeng, R.; Kongkanand, A.; Escobedo, F. A.; Brock, J. D.; DiSalvo, F. J.; Muller, D. A.; Abruña, H. D. Revealing the Atomic Ordering of Binary Intermetallics Using in Situ Heating Techniques at Multilength Scales. *Proc. Natl. Acad. Sci. U.S.A.* **2019**, 116, 1974-1983.
3. Gasteiger, H. A.; Kocha, S. S.; Sompalli, B.; Wagner, F. T. Activity Benchmarks and Requirements for Pt, Pt-alloy, and Non-Pt Oxygen Reduction Catalysts for PEMFCs. *Appl. Catal. B: Environ.* **2005**, 56, 9-35.

4. Kongkanand, A.; Mathias, M. The Priority and Challenge of High-Power Performance of Low-Platinum Proton-Exchange Membrane Fuel Cells. *J. Phys. Chem. Lett.* **2016**, *7*, 1127-1137.
5. Xiong, Y.; Yang, Y.; DiSalvo, F. J.; Abruña, H. D. Pt-Decorated Composition-Tunable Pd–Fe@Pd/C Core–Shell Nanoparticles with Enhanced Electrocatalytic Activity toward the Oxygen Reduction Reaction *J. Am. Chem. Soc.* **2018**, *140*, 7248-7255.
6. Wang, D.; Xin, H. L.; Hovden, R.; Wang, H.; Yu, Y.; Muller, D. A.; DiSalvo, F. J.; Abruña, H. D. Structurally Ordered Intermetallic Platinum-Cobalt Core-Shell Nanoparticles with Enhanced Activity and Stability as Oxygen Reduction Electrocatalysts. *Nat. Mater.* **2012**, *12*, 81-87.
7. Xiong, Y.; Xiao, L.; Yang, Y.; DiSalvo, F. J.; Abruña, H. D. High-Loading Intermetallic Pt<sub>3</sub>Co/C Core–Shell Nanoparticles as Enhanced Activity Electrocatalysts toward the Oxygen Reduction Reaction (ORR). *Chem. Mater.* **2018**, *30*, 1532-1539.
8. Wang, G.; Huang, B.; Xiao, L.; Ren, Z.; Chen, H.; Wang, D.; Abruña, H. D.; Lu, J.; Zhuang, L. Pt Skin on AuCu Intermetallic Substrate: A Strategy to Maximize Pt Utilization for Fuel Cells. *J. Am. Chem. Soc.* **2014**, *136*, 9643-9649.
9. Lu, S.; Pan, J.; Huang, A.; Zhuang, L.; Lu, J. Alkaline Polymer Electrolyte Fuel Cells Completely Free from Noble Metal Catalysts. *Proc. Natl. Acad. Sci. U. S. A.* **2008**, *105*, 20611-20614.
10. Varcoe, J. R.; Atanassov, P.; Dekel, D. R.; Herring, A. M.; Hickner, M. A.; Kohl, P. A.; Kucernak, A. R.; Mustain, W. E.; Nijmeijer, K.; Scott, K.; Xu, T.; Zhuang, L. Anion-Exchange Membranes in Electrochemical Energy Systems. *Energy Environ. Sci.*, **2014**, *7*, 3135-3191.
11. Lima, F. H. B.; Zhang, J.; Shao, M. H.; Sasaki, K.; Vukmirovic, M. B.; Ticianelli, E. A.; Adzic, R. R. Catalytic Activity-d-Band Center Correlation for the O<sub>2</sub> Reduction Reaction on Platinum in Alkaline Solutions. *J. Phys. Chem. C* **2007**, *111*, 404-410.
12. Slanac, D. A.; Hardin, W. G.; Johnston, K. P.; Stevenson, K. J. Atomic Ensemble and Electronic Effects in Ag-Rich AgPd Nanoalloy Catalysts for Oxygen Reduction in Alkaline Media. *J. Am. Chem. Soc.* **2012**, *134*, 9812-9819.
13. Omasta, T. J.; Peng, X.; Miller, H. A.; Vizza, F.; Wang, L.; Varcoe, J. R.; Dekel, D. R.; Mustain, W. E. Beyond 1.0Wcm<sup>-2</sup> Performance without Platinum: The Beginning of a New Era in Anion Exchange Membrane Fuel Cells. *J. Electrochem. Soc.* **2018**, *165*, J3039-J3044.
14. Wang, L.; Bellini, M.; Millner, H. A.; Varcoe, J. R. A high conductivity ultrathin anion-exchange membrane with 500+ h alkali stability for use in alkaline membrane fuel cells that can achieve 2 W/cm<sup>2</sup> at 80 °C. *J. Mater. Chem. A* **2018**, *6*, 15404-15412.
15. Ren, H.; Wang, Y.; Yang, Y.; Tang, X.; Peng, Y.; Peng, H.; Xiao, L.; Lu, J.; Abruña, H. D.; Zhuang, L. Fe/N/C Nanotubes with Atomic Fe Sites: A Highly Active Cathode Catalyst for Alkaline Polymer Electrolyte Fuel Cells. *ACS Catal.* **2017**, *7*, 6485-6492.
16. Yang, Y.; Wang, Y.; Xiong, Y.; Huang, X.; Shen, L.; Huang, R.; Wang, H.; Pastore, J. P.; Yu, S.-H.; Xiao, L.; Brock, J. D.; Zhuang, L.; Abruña, H. D. In Situ X-ray Absorption Spectroscopy of a Synergistic Co–Mn Oxide Catalyst for the Oxygen Reduction Reaction. *J. Am. Chem. Soc.* **2019**, *141*, 1463–1466.
17. Xiong, Y.; Yang, Y.; Feng, X.; DiSalvo, F. J.; Abruña, H. D. A Strategy for Increasing the Efficiency of the Oxygen Reduction Reaction in Mn-Doped Cobalt Ferrites. *J. Am. Chem. Soc.* **2019**, *141*, 4412-4421.
18. Wang, Y.; Yang, Y.; Jia, S.; Wang, X.; Lyu, K.; Peng, Y.; Zheng, H.; Wei, X.; Ren, H.; Xiao, L.; Wang, J.; Muller, D. A.; Abruña, H. D.; Hwang, B. J.; Lu, J.; Zhuang, L.

- Synergistic Mn-Co Catalyst Outperforms Pt on High-Rate Oxygen Reduction Reaction for Alkaline Polymer Electrolyte Fuel Cells. *Nat. Commun.* **2019**, *10*, 1506.
19. Peng, X.; Omasta, T. J.; Magliocca, E.; Wang, L.; Varcoe, J. R.; Mustain, W. E. N-doped Carbon CoO<sub>x</sub> Nanohybrids: The First Precious Metal Free Cathode to Achieve 1.0 W/cm<sup>2</sup> Peak Power and 100 h Life in Anion-Exchange Membrane Fuel Cells. *Angew. Chem. Int. Ed.* **2019**, *58*, 1041-1051.
  20. Liang, Y.; Li, Y.; Wang, H.; Zhou, J.; Wang, J.; Regier, T.; Dai, H. Co<sub>3</sub>O<sub>4</sub> Nanocrystals on Graphene as a Synergistic Catalyst for Oxygen Reduction Reaction. *Nat. Mater.* **2011**, *10*, 780-786.
  21. Liang, Y.; Wang, H.; Zhou, J.; Li, Y.; Wang, J.; Regier, T.; Dai, H. Covalent Hybrid of Spinel Manganese–Cobalt Oxide and Graphene as Advanced Oxygen Reduction Electrocatalysts. *J. Am. Chem. Soc.*, **2012**, *134*, 3517-3523.
  22. Li, C.; Han, X.; Cheng, F.; Hu, Y.; Chen, C.; Chen, J. Phase and Composition Controllable Synthesis of Cobalt Manganese Spinel Nanoparticles towards Efficient Oxygen Electrocatalysis. *Nat. Commun.*, **2015**, *6*, 7345.
  23. Meng, Y.; Song, W.; Huang, H.; Ren, Z.; Chen, S.; Suib, S. Structure–Property Relationship of Bifunctional MnO<sub>2</sub> Nanostructures: Highly Efficient, Ultra-Stable Electrochemical Water Oxidation and Oxygen Reduction Reaction Catalysts Identified in Alkaline Media *J. Am. Chem. Soc.*, **2014**, *136*, 11452-11464.
  24. Indra, A.; Menezes, P.; Sahraie, N.; Bergmann, A.; Das, C.; Tallarida, M.; Schmeißer, D.; Strasser, P.; Driess, M. Unification of Catalytic Water Oxidation and Oxygen Reduction Reactions: Amorphous Beat Crystalline Cobalt Iron Oxides. *J. Am. Chem. Soc.*, **2014**, *136*, 17530-17536.
  25. Wu, J.; Zhang, J.; Peng, Z.; Yang, S.; Wagner, F. T.; Yang, H. Truncated Octahedral Pt<sub>3</sub>Ni Oxygen Reduction Reaction Electrocatalysts. *J. Am. Chem. Soc.* **2010**, *132*, 4984–4985.
  26. Carpenter, M. K.; Moylan, T. E.; Kukreja, R. S.; Atwan, M. H.; Tessema, M. M. Solvothermal Synthesis of Platinum Alloy Nanoparticles for Oxygen Reduction Electrocatalysis. *J. Am. Chem. Soc.* **2012**, *134*, 8535–8542.
  27. Gan, L.; Cui, C.; Heggen, M.; Dionigi, F.; Rudi, S.; Strasser, P. Element-Specific Anisotropic Growth of Shaped Platinum Alloy Nanocrystals. *Science* **2014**, *346*, 1502–1506.
  28. Chen, C.; Kang, Y.; Huo, Z.; Zhu, Z.; Huang, W.; Xin, H. L.; Snyder, J. D.; Li, D.; Herron, J. A.; Mavrikakis, M.; et al. Highly Crystalline Multimetallic Nanoframes with Three-Dimensional Electrocatalytic Surfaces. *Science* **2014**, *343*, 1339–1343.
  29. Huang, X.; Zhao, Z.; Cao, L.; Chen, Y.; Zhu, E.; Lin, Z.; Li, M.; Yan, A.; Zettl, A.; Wang, Y. M.; et al. High-Performance Transition Metal–doped Pt<sub>3</sub>Ni Octahedra for Oxygen Reduction Reaction. *Science* **2015**, *348*, 1230–1234.
  30. Strasser, P.; Koh, S.; Anniyev, T.; Greeley, J.; More, K.; Yu, C.; Liu, Z.; Kaya, S.; Nordlund, D.; Ogasawara, H.; Toney, M. F.; Nilsson, A. Lattice-Strain Control of the Activity in Dealloyed Core-Shell Fuel Cell Catalysts. *Nat. Chem.* **2010**, *2*, 454–460.
  31. Wang, C.; Chi, M.; Li, D.; Strmcnik, D.; Van Der Vliet, D.; Wang, G.; Komanicky, V.; Chang, K. C.; Paulikas, A. P.; Tripkovic, D.; Pearson, J.; More, K. L.; Markovic, N. M.; Stamenkovic, V. R. Design and Synthesis of Bimetallic Electrocatalyst with Multilayered Pt-Skin Surfaces. *J. Am. Chem. Soc.* **2011**, *133*, 14396–14403.
  32. Caldwell, K. M.; Ramaker, D. E.; Jia, Q.; Mukerjee, S.; Ziegelbauer, J. M.; Kukreja, R. S.; Kongkanand, A. Spectroscopic in Situ Measurements of the Relative Pt Skin Thicknesses and Porosities of Dealloyed PtMn (Ni, Co) Electrocatalysts. *J. Phys. Chem. C* **2015**, *119*, 757–765.

33. Han, B.; Carlton, C. E.; Kongkanand, A.; Kukreja, R. S.; Theobald, B. R.; Gan, L.; O'Malley, R.; Strasser, P.; Wagner, F. T.; Shao-Horn, Y. Record Activity and Stability of Dealloyed Bimetallic Catalysts for Proton Exchange Membrane Fuel Cells. *Energy Environ. Sci.* **2015**, *8*, 258–266.
34. Jia, Q.; Li, J.; Caldwell, K.; Ramaker, D. E.; Ziegelbauer, J. M.; Kukreja, R. S.; Kongkanand, A.; Mukerjee, S. Circumventing Metal Dissolution-Induced Degradation of Pt-Alloy Catalysts in Proton Exchange Membrane Fuel Cells: Revealing the Asymmetric Volcano Nature of Redox Catalysis. *ACS Catal.* **2016**, *6*, 928–938.
35. Lu, Y.; Wang, L.; Preuß, K.; Qiao, M.; Titirici, M.; Varcoe, J.; Cai, Q. Halloysite-Derived Nitrogen Doped Carbon Electrocatalysts for Anion Exchange Membrane Fuel Cells. *J. Power Sources* **2017**, *372*, 82-90.
36. Hossen, M.; Artyushkova, K.; Atanassov, P.; Serov, A. Synthesis and Characterization of High Performing Fe-N-C Catalyst for Oxygen Reduction Reaction (ORR) in Alkaline Exchange Membrane Fuel Cells. *J. Power Sources* **2018**, *375*, 214-221.
37. Sa, Y.; Seo, D.; Woo, J.; Lim, J.; Cheon, J.; Yang, S.; Lee, J.; Kang, D.; Shin, T.; Shin, H. et al. A General Approach to Preferential Formation of Active Fe–Nx Sites in Fe–N/C Electrocatalysts for Efficient Oxygen Reduction Reaction. *J. Am. Chem. Soc.* **2016**, *138*, 15046-15056.
38. Kim, O.; Cho, Y.; Chung, D.; Kim, M.; Yoo, J.; Park, J.; Choe, H.; Sung, Y. Facile And Gram-Scale Synthesis Of Metal-Free Catalysts: Toward Realistic Applications For Fuel Cells. *Sci. Rep.* **2015**, *5*: 8376.
39. Wang, Y.; Wang, G.; Li, G.; Huang, B.; Pan, J.; Liu, Q.; Han, J.; Xiao, L.; Lu, J.; Zhuang, L. Pt–Ru Catalyzed Hydrogen Oxidation in Alkaline Media: Oxophilic Effect or Electronic Effect? *Energy Environ. Sci.* **2015**, *8*, 177-181.
40. Peng, H.; Li, Q.; Hu, M.; Xiao, L.; Lu, J.; Zhuang, L. Alkaline Polymer Electrolyte Fuel Cells Stably Working at 80 °C. *J. Power Sources* **2018**, *390*, 165-167.
41. Wang, L.; Brink, J.; Liu, Y.; Herring, A.; Ponce-González, J.; Whelligan, D.; Varcoe, J. Non-Fluorinated Pre-Irradiation-Grafted (Peroxidated) LDPE-Based Anion-Exchange Membranes with High Performance And Stability. *Energy Environ. Sci.* **2017**, *10*, 2154-2167.
42. Maurya, S.; Noh, S.; Matanovic, I.; Park, E.; Narvaez Villarrubia, C.; Martinez, U.; Han, J.; Bae, C.; Kim, Y. Rational Design of Polyaromatic Ionomers for Alkaline Membrane Fuel Cells with > 1 W cm<sup>-2</sup> Power Density. *Energy Environ. Sci.* **2018**, *11*, 3283-3291.
43. Wang, L.; Brink, J.; Varcoe, J. The First Anion-Exchange Membrane Fuel Cell to Exceed 1 W cm<sup>-2</sup> at 70 °C with a Non-Pt-Group (O<sub>2</sub>) Cathode. *Chem. Commun.* **2017**, *53*, 11771-11773.
44. Li, Q.; Peng, H.; Wang, Y.; Xiao, L.; Lu, J.; Zhuang, L. The comparability of Pt to Pt-Ru in Catalyzing the Hydrogen Oxidation Reaction for Alkaline Polymer Electrolyte Fuel Cells Operated at 80 °C. *Angew. Chem. Int. Ed.* **2019**, *131*, 1456-1460.
45. Ren, D.; Shen, Y.; Yang, Y.; Shen, L.; Levin, B. D. A.; Yu, Y.; Muller, D. A.; Abruña, H. D. Systematic Optimization of Battery Materials: Key Parameter Optimization for the Scalable Synthesis of Uniform, High-Energy, and High Stability LiNi<sub>0.6</sub>Mn<sub>0.2</sub>Co<sub>0.2</sub>O<sub>2</sub> Cathode Material for Lithium-Ion Batteries. *ACS Appl. Mater. Interfaces* **2017**, *9*, 41, 35811-35819.
46. Shibli, S. M. A.; Arun, P. S.; Raj, A. V. Exploration of Octahedrally Shapes MnCo<sub>2</sub>O<sub>4</sub> Catalyst Particles for Visible Light Driven Photocatalytic Water Splitting Reaction. *RSC Adv.* **2015**, *5*, 19393-19399.

## CHAPTER 5

### ***Operando* X-ray Absorption Spectroscopy Investigation of Synergistic Reaction Mechanism of Spinel Oxide Catalysts**

#### **5.1 Introduction**

Our Previous work demonstrates that Co-Mn bimetallic spinel oxides are significantly superior to monometallic spinel oxides,  $\text{Co}_3\text{O}_4/\text{C}$  and  $\text{Mn}_3\text{O}_4/\text{C}$  and show impressive performance in MEA measurements. *Ex situ* measurements using STEM-EELS, XRD, XAS and XPS have provided a good baseline understanding of as-synthesized catalysts. However, the catalytic mechanism of the ORR using metal oxides remains unclear and catalysts, characterized *ex situ*, may not maintain the same properties under real-time electrochemical conditions, which calls for *in situ/operando* techniques to identify the true catalytically active sites for ORR catalysis. Synchrotron-based X-ray absorption spectroscopy (XAS) is a powerful *in situ* technique to study electrocatalytic mechanisms because the beam characteristics (energy and flux) can be managed so as to not influence the electrochemical reactions. The high penetration of high energy X-rays enables the *operando* study of electrochemical interfaces.<sup>1</sup>

---

\*Reproduced and modified with permission from the following publications

**Yao Yang**, Ying Wang, Yin Xiong, Xin Huang, Luxi Shen, Rong Huang, Hongseng Wang, James P. Pastore, Seung-Ho Yu, Li Xiao, Joel Brock, Lin Zhuang, Héctor Abruña, In Situ X-ray Absorption Spectroscopy of a Synergistic Co–Mn Oxide Catalyst for the Oxygen Reduction Reaction. *J. Am. Chem. Soc.* 2019, 141, 1463. © ACS

Yin Xiong,<sup>#</sup> **Yao Yang**,<sup>#</sup> Xinran Feng, Francis DiSalvo, Héctor Abruña, A Strategy for Increasing the Efficiency of the Oxygen Reduction Reaction in Mn-Doped Cobalt Ferrites. *J. Am. Chem. Soc.* 2019, 141, 4412. © ACS (Note: Y.X. conducted material synthesis and electrochemical tests. Y.Y. performed *operando* XAS measurements with the help of X.F.)

Recently, *operando* XAS has been extensively used to study structural and electronic properties of precious metal ORR catalysts, such as d-band vacancy, interatomic distances in Pt and Pt-based alloys<sup>2-4</sup> and surface oxide formation at the Pt-electrolyte interface.<sup>5-7</sup> This method has also been employed to follow the structural changes of manganese oxide,<sup>8</sup> cobalt oxide<sup>9</sup> and cobalt phosphate<sup>10</sup> as electrocatalysts for water oxidation. Previously, we demonstrated that Co-Mn oxide is a highly effective electrocatalyst towards the ORR and proposed that Co and Mn serve as co-active sites to catalyze the reduction of oxygen in alkaline media. To the best of our knowledge, this work represents the first study using *operando* XAS to study the synergistic effects of bimetallic and trimetallic oxide with high ORR activity. *Operando* X-ray absorption near edge structure (XANES) was employed to probe structural changes of Co and Mn in both steady state (constant applied potential) and non-steady state (dynamic cyclic voltammetry).

## 5.2 Experimental Methods

Synthesis of Mn-Co and Mn-Co-Fe spinel oxides adapted the same procedures in Chapters 2 and 3. Details can be found in corresponding publications.

***Operando* Electrochemical Cell Fabrication and Operation:** 20 mg of Co<sub>1.5</sub>Mn<sub>1.5</sub>O<sub>4</sub>/C (40% mass loading) was dispersed in 50 mL of a Nafion (0.05% mass fraction) ethanol solution. Carbon paper (200  $\mu$ m thick) was used as the substrate for the catalyst layer and the skeleton of the carbon paper was filled with carbon powder to increase the surface area and its mechanical strength for later device assembly. Carbon paper was later tailored into 1 $\times$ 5 cm<sup>2</sup> pieces as catalyst support. The catalyst-ionomer

mixture was sprayed on one end of the carbon paper ( $1 \times 1 \text{ cm}^2$ ) using an airbrush and the rest,  $1 \times 4 \text{ cm}^2$ , served as a non-active conductor with negligible effects on the catalytic current, compared with the active metal oxide catalysts. The thickness for the  $6 \text{ mg/cm}^2$  loading was estimated to be about  $40 \text{ }\mu\text{m}$  by SEM.

As described in the cell design in [Figs. 5.1 and 5.2](#), the electrochemical cell includes two pieces of Teflon, which is chemically inert in the strong base conditions of  $1 \text{ M KOH}$ . The two Teflon pieces could be tightly sealed using six screws. A Teflon U-shaped sealing ring was placed between the two Teflon pieces and the gap between them could be adjusted to make the electrolyte thickness less than  $200 \text{ }\mu\text{m}$ . On top of the electrochemical cell, a Teflon cap with one gas inlet and another gas outlet was used to seal the cell using another six screws to minimize the influence of trace amounts of  $\text{O}_2$  during electrochemical testing. Inside the electrochemical cell, the section of the carbon paper with the catalyst layer was immersed into the electrolyte near the window for X-ray transmission. A carbon rod was used as the counter electrode (CE) and placed near the working electrode (WE).  $\text{Ag/AgCl}$  (sat.  $\text{KCl}$ ) was used as the reference electrode (RE) and was placed at the bottom of the cell so that the distance between the WE and RE could be minimized. This, in turn, minimized the IR drop during electrochemical testing.  $1 \text{ M KOH}$  was used as the electrolyte and saturated with  $\text{N}_2$  gas to exclude dissolved  $\text{O}_2$ .

***Operando X-ray Absorption Measurements:*** Mn and Co K-edge X-ray absorption near edge structure (XANES) spectra were acquired at the F-3 beamline of the Cornell High Energy Synchrotron Source (CHESS). Each X-ray data point acquisition took two seconds and then the X-ray beam was blocked for one second (via shutter) to minimize

potential beam damage. All spectra were calibrated and aligned using the spectra of Mn and Co metal foil. XANES spectra and linear combination fitting (LCF) for valence analysis were performed using the ATHENA software package.

### 5.3 Device Design and Methodology for *Operando* XAS measurements

Co-Mn oxide particles, supported on carbon, were synthesized via a hydrothermal method and their crystal structure was examined by X-ray diffraction (XRD) (Fig. 3.5). The superior ORR activity of the bimetallic  $\text{Co}_{1.5}\text{Mn}_{1.5}\text{O}_4/\text{C}$ , over monometallic  $\text{Co}_3\text{O}_4/\text{C}$  and  $\text{Mn}_3\text{O}_4/\text{C}$ , suggests an underlying catalytic mechanism involving both Co and Mn to catalyze the reduction of oxygen. Synchrotron-based XAS was employed to investigate the catalytic mechanism of  $\text{Co}_{1.5}\text{Mn}_{1.5}\text{O}_4/\text{C}$  under real-time *operando* electrochemical conditions. As part of this study, we designed a new electrochemical cell for *operando* XAS measurements (Fig. 5.1). Details of the cell design can be found in the photo of the actual cell in Fig. 5.2.

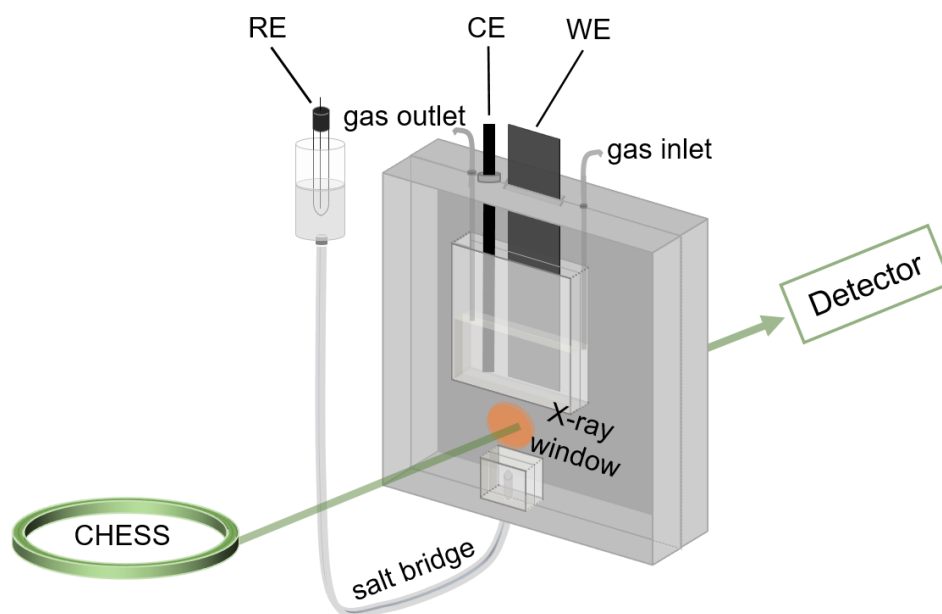


**Figure 5.1.** Schematic of the *operando* XAS electrochemical cell. Working electrode (WE, catalyst on carbon paper) and counter electrode (CE, carbon rod) were immersed in 1M KOH solution. Reference electrode (RE, Ag/AgCl in saturated KCl) was connected to the cell by a salt bridge and the distance between RE and catalysts at the end of carbon paper was minimized to reduce IR drops caused by the resistance in the thin electrolyte layer ( $< 200 \mu\text{m}$ ) in X-ray window. X-rays come from the Cornell High Energy Synchrotron Source (CHESS).

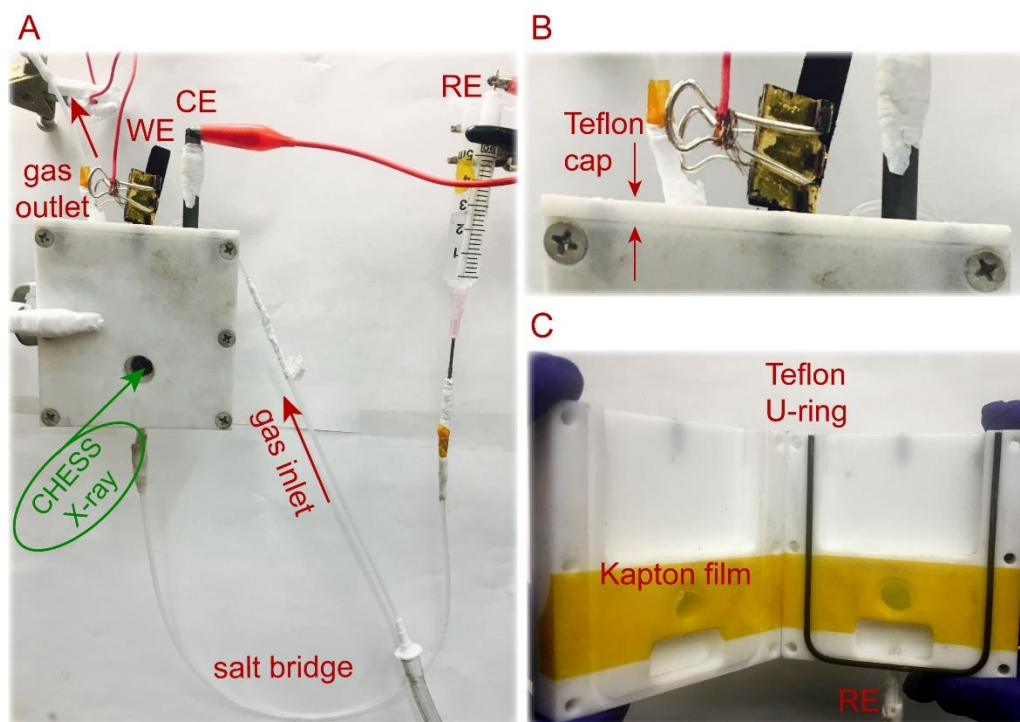


**Figure 5.2.** (A) *Operando* electrochemical cell for X-ray absorption spectroscopy experiments. (B) Magnified cell shows the Teflon cap for  $\text{N}_2$ -filled environment. (C) Inner structure of the *operando* cell. The electrolyte thickness can be controlled to be less than  $200 \mu\text{m}$  by six screws. WE, CE and RE represent working electrode (catalyst on carbon paper), counter electrode (carbon rod) and reference electrode (Ag/AgCl in saturated KCl), respectively.

The electrochemical cell was made of chemically inert Teflon and the thickness of the electrolyte, for XAS in transmission mode could be controlled to be less than  $200 \mu\text{m}$ . The working electrode (WE) consisted of a  $40 \mu\text{m}$  catalyst layer sprayed on  $200 \mu\text{m}$  thick carbon paper, as shown in a scanning electron microscopy (SEM) image (Fig. 5.3). The reference electrode (Ag/AgCl) was connected to the cell by a salt bridge and

placed right underneath the carbon paper working electrode to minimize IR drops in electrochemical tests. Prior to the *operando* XAS measurements, cyclic voltammetry (CV) of the  $\text{Co}_{1.5}\text{Mn}_{1.5}\text{O}_4/\text{C}$  electrode was carried out in both the *operando* XAS home-made cell and a conventional three-neck electrochemical cell to verify device performance. (Fig. 5.4) Compared to the CV profile of the catalyst on a glassy carbon, the CV of the catalyst on carbon paper exhibited virtually the same characteristic behavior of the Co-Mn oxide with one pair of oxidation/reduction peaks at 0.95V/0.55V vs. RHE. The oxidation/reduction peaks of the CV on carbon paper were slightly shifted to the left, compared with those on the glassy carbon electrode because the mass transport is slower in the thin layer of electrolyte in the home-made XAS cell.

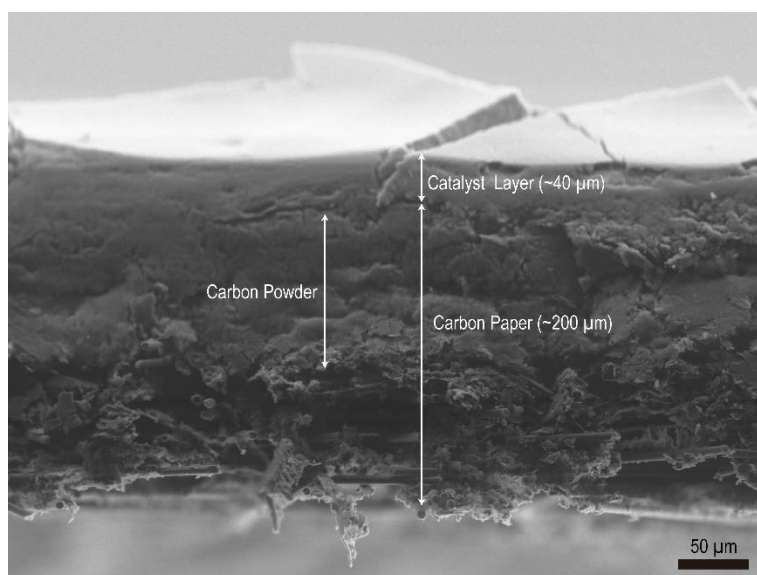


**Figure 5.3.** SEM image of  $\text{Co}_{1.5}\text{Mn}_{1.5}\text{O}_4/\text{C}$  (about 40  $\mu\text{m}$ ) on carbon paper (about 200  $\mu\text{m}$ ). Note that the carbon paper skeleton was filled with carbon powder to increase the surface area for catalyst loading and to enhance mechanical strength for device fabrication.

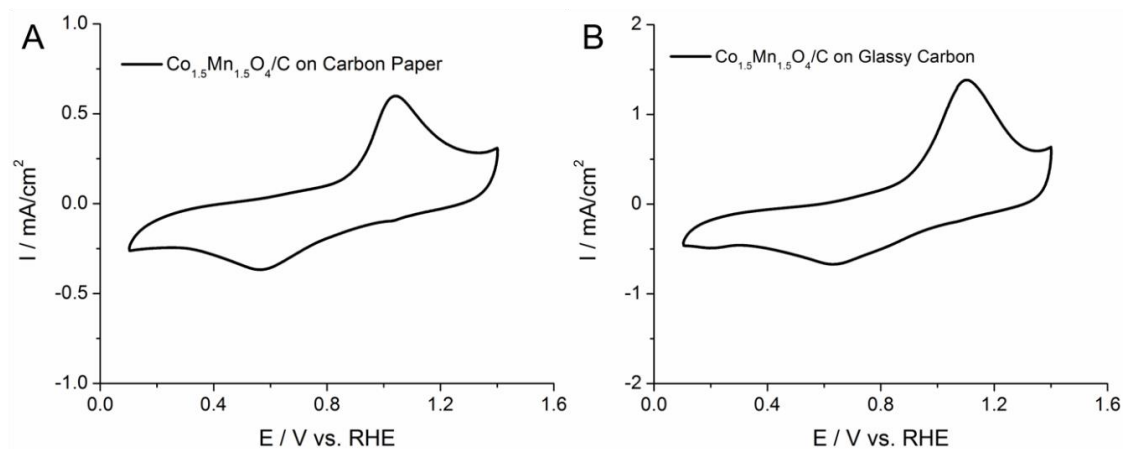


**Figure 5.4.** (A) CV of  $\text{Co}_{1.5}\text{Mn}_{1.5}\text{O}_4/\text{C}$  sprayed on carbon paper electrode in the *operando* electrochemical cell. (B) CV of  $\text{Co}_{1.5}\text{Mn}_{1.5}\text{O}_4/\text{C}$  deposited on a glassy carbon electrode in a conventional three-neck electrochemical cell. During tests in both (A) and (B), sweep rate, sweep range and catalyst loading were set to be 10 mV/s, 0.1-1.4 V vs. RHE and  $0.5\text{mg}/\text{cm}^2$ , respectively.

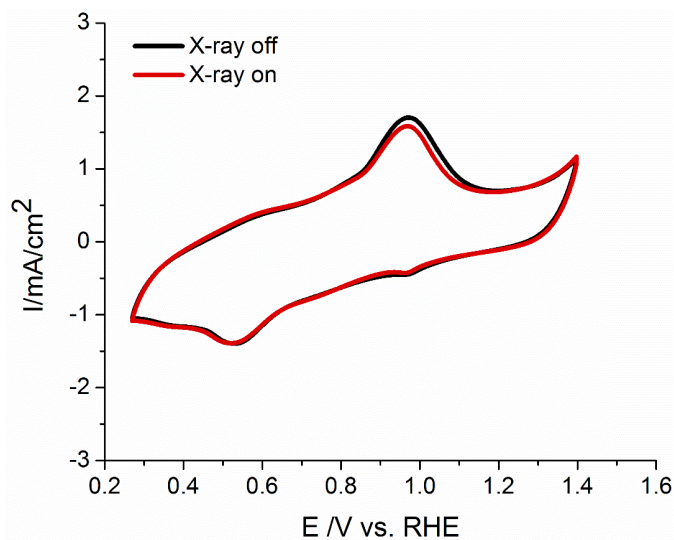


**Figure 5.5.** Control Experiment for CV of catalysts when X-ray beam was turned off and on.

The CV of the catalysts was then tested with the X-ray beam on and off to assess potential beam damage. (Fig. 5.5) The CV profile of the catalyst with the X-ray beam on exhibited nearly the same electrochemical behavior as the CV with the beam off when the CV was run at a sweep rate of 1 mV/s, which indicates that the studies of the

electrocatalytic mechanism will not be affected by the X-ray beam for the time interval of the in situ X-ray experiments.

To investigate the steady-state electrochemical response of the Co-Mn oxide catalysts, the applied potential was held constant while in situ XANES spectra were acquired, after the current had dropped to background levels. Based on the CV response of the catalysts at a sweep rate of 1 mV/s in the home-made cell (Fig. 5.5), constant applied potentials of 0.95 V, 1.15 V and 0.75 V correspond to the oxidation peak and its two onset potentials while potentials of 0.55 V, 0.75 V and 0.4 V correspond to the reduction peak and its two onset potentials. (These were arbitrarily chosen to be 200 mV above and below the peak.)

#### **5.4 Operando XANES of Mn-Co Oxides under Steady State (Constant Potentials)**

The XANES spectra around the Mn K-edge exhibit systematic changes in the local electronic structure of the  $\text{Co}_{1.5}\text{Mn}_{1.5}\text{O}_4$  crystal (Fig. 5.6). Mn XANES spectra were calibrated against the characteristic absorption edge of elemental Mn (metal foil) at 6539 eV, which corresponds to the ejection of electrons from the Mn 1s orbital. The magnified inset on the left of the shoulder peak at 6553.0 eV shows a gradual increase in the peak intensity and a small shift to lower energies when the applied potential decreases from 1.15 V to 0.4 V, indicating a lower Mn valence at the more negative electrochemical potentials. The most intense peak, near 6559 eV, originates from an electronic transition from 1s to 4p orbitals, since the 4p are the lowest allowed unoccupied orbitals. In the pre-edge region, the peak at 6540 eV arises from the electronic transition from 1s to 3d orbitals. Although 1s→3d transition is generally not

allowed due to the dipole selection rule  $\Delta l = \pm 1$ , it can be observed if the absorber coordinates in a non-centrosymmetric geometry, allows for hybridization of dipole-forbidden d orbitals and dipole-allowed p orbitals, which indicates that the  $\text{MnO}_6$  octahedra are slightly distorted due to Jahn-Teller effect.

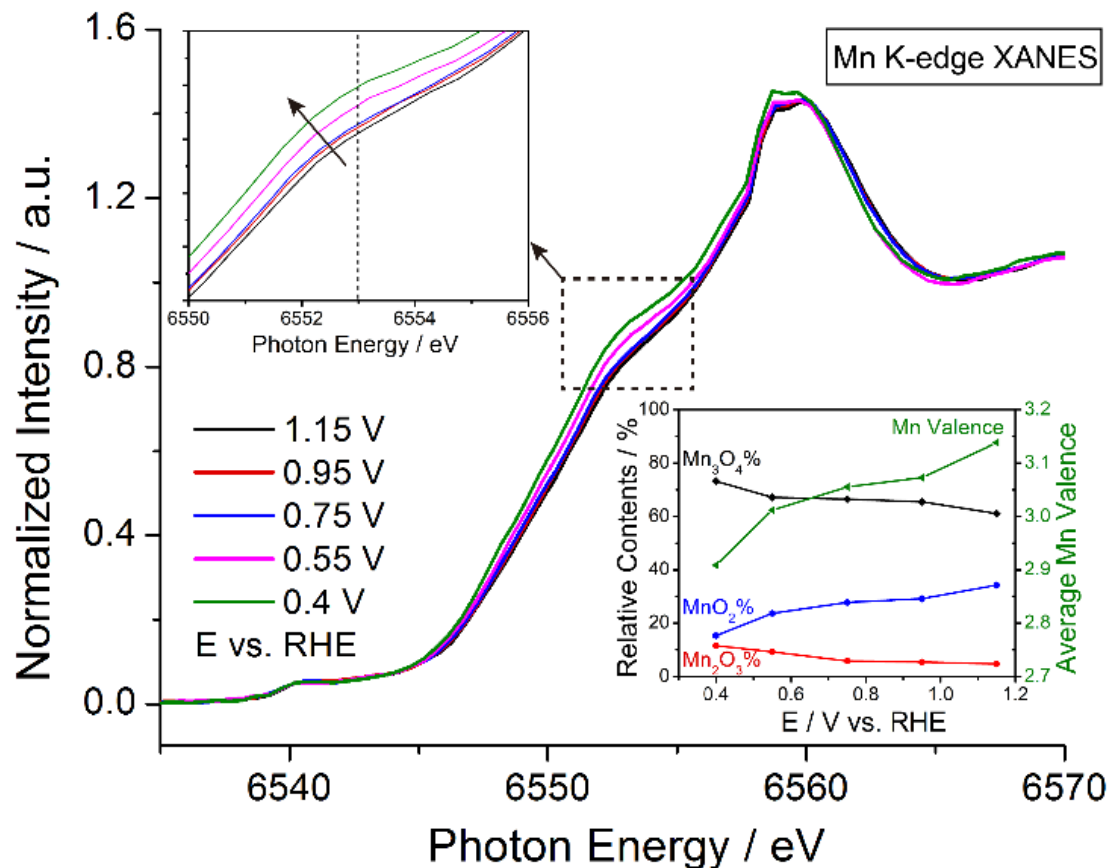


**Figure 5.6.** *Operando* XANES spectra of the Mn K-edge at a series of applied potentials. Inset on the right side shows the result of the Mn valence analysis by using the linear combination fitting (LCF) method and  $\text{MnO}(\text{II})$ ,  $\text{Mn}_3\text{O}_4(\text{II,III})$ ,  $\text{Mn}_2\text{O}_3(\text{III})$ , and  $\text{MnO}_2(\text{IV})$  as references.

In order to study the Mn valence changes more quantitatively, we used the linear combination fitting (LCF) method with pure manganese oxides including  $\text{MnO}(\text{II})$ ,  $\text{Mn}_3\text{O}_4(\text{II,III})$ ,  $\text{Mn}_2\text{O}_3(\text{III})$  and  $\text{MnO}_2(\text{IV})$  as references. As shown in Fig. 5.7, the LCF is able to fit well the experimental Mn XANES spectra and allows calculating the

relative contributions in terms of the different Mn oxide references. The magnified inset on the right in Fig. 5.6 shows the relative contents of Mn oxide references at a series of constant applied potentials as derived from the LCF fitting. When the applied potential decreases from 1.15 V to 0.4V, MnO<sub>2</sub>% decreases by 19% while Mn<sub>3</sub>O<sub>4</sub>% and Mn<sub>2</sub>O<sub>3</sub>% increase by 12% and 7%, respectively. Overall, the average Mn valence drops from 3.15 to 2.91. This systematic valence conversion of Mn(III,IV) to Mn(II,III) indicates that various Mn species can serve as the active site to catalyze oxygen reduction.

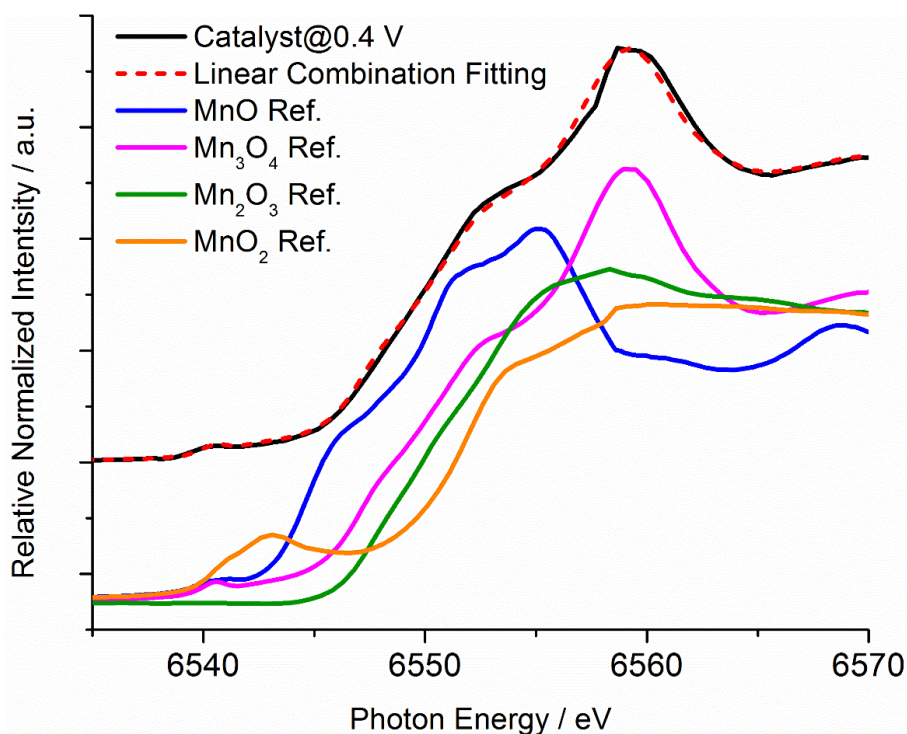


**Figure 5.7** (A) Valence analysis of Mn K-edge at 0.4 V vs. RHE. Linear combination fitting (LCF) indicates the relative content of MnO (0%), Mn<sub>3</sub>O<sub>4</sub> (73.2%), Mn<sub>2</sub>O<sub>3</sub> (11.5%) and MnO<sub>2</sub> (15.3%).

Similar to Mn valence changes at a series of applied potential, XANES spectra around the Co K-edge also show the regular changes in the local electronic structure of Co atoms in the Co<sub>1.5</sub>Mn<sub>1.5</sub>O<sub>4</sub>/C catalyst (Fig. 5.8). Co XANES spectra were calibrated against the characteristic absorption edge of elemental Co (metal foil) at 7709 eV. The

magnified inset of Co XANES spectra around 7722.5 eV reveals a gradual increase in the peak intensity and a small shift to lower energies when the applied potential decreases from 1.15 V to 0.4 V, indicating lower Co valence at lower applied potentials. LCF was also employed to quantitatively analyze Co valence with  $\text{Co(OH)}_2(\text{II})$ ,  $\text{Co}_3\text{O}_4(\text{II,III})$  and  $\text{CoOOH}(\text{III})$  as cobalt oxide references (Fig. 5.9). When the applied potential varied from 1.1 V to 0.4 V,  $\text{CoOOH}\%$  decreases by 14% while  $\text{Co(OH)}_2$  increases by 19%. In contrast to changes for  $\text{Mn}_3\text{O}_4\%$ , the  $\text{Co}_3\text{O}_4\%$  remained relatively stable under different applied potentials. Overall, the average Co valence decreased from 2.75 to 2.57, indicating a valence conversion from Co(III) to Co(II). Given the fact that Co valence changes with the applied potential took place at the same time as Mn suggest that, Co and Mn could serve as co-active sites to catalyze the oxygen reduction reaction.

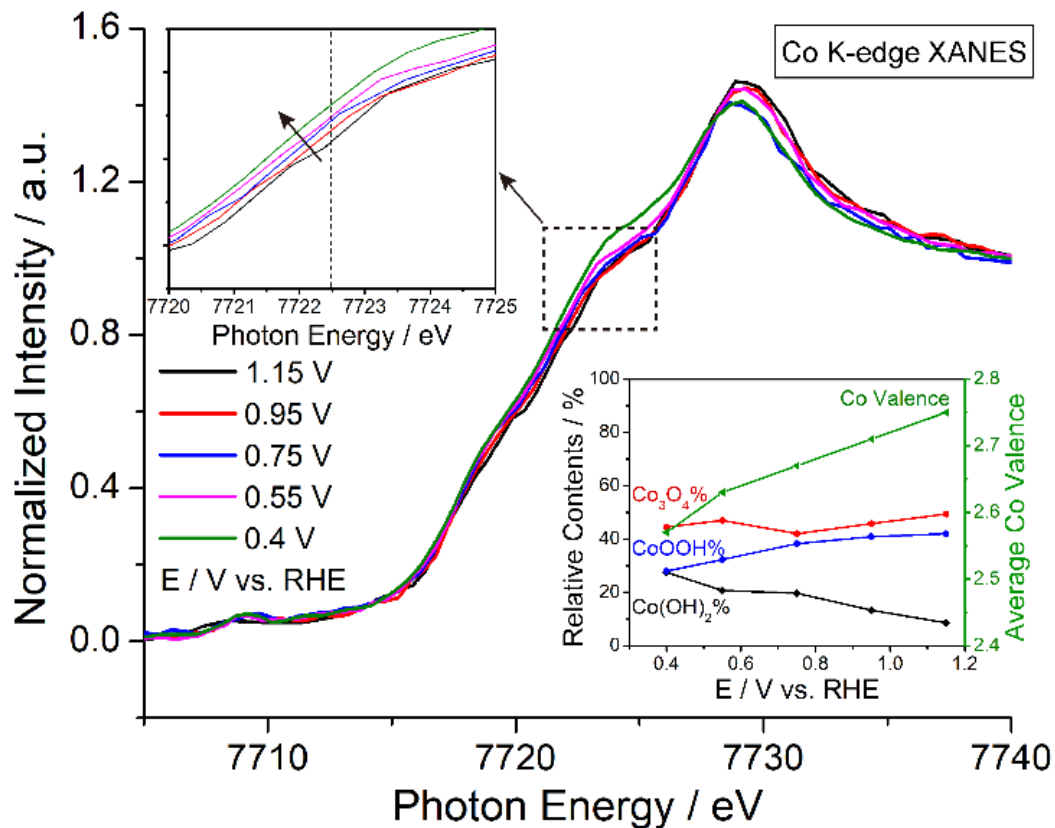


**Figure 5.8.** *Operando* XANES spectra of the Co K-edge at a series of applied potentials. Inset on the right side shows the result of the Co valence analysis, using the LCF method with  $\text{Co(OH)}_2(\text{II})$ ,  $\text{Co}_3\text{O}_4(\text{II,III})$  and  $\text{CoOOH}(\text{III})$  as references.

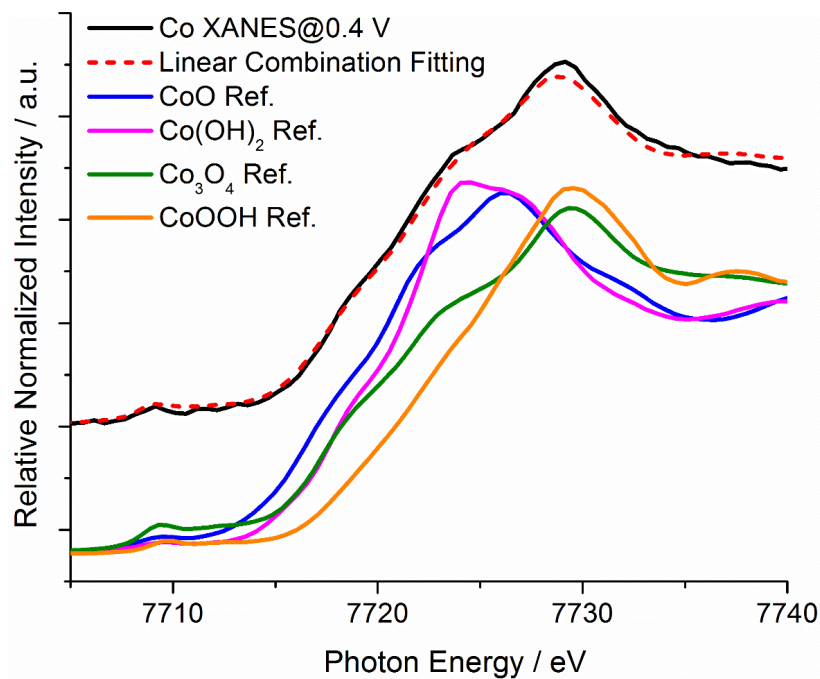


**Figure 5.9.** Valence analysis of Co K-edge at 0.4 V vs. RHE. Linear combination fitting (LCF) indicates the relative content of Co(OH)<sub>2</sub> (27.5%), Co<sub>3</sub>O<sub>4</sub> (44.5%), and CoOOH (15.3%).

### 5.5 *Operando* XANES of Mn-Co Oxides under Non-Steady State (Dynamic CV)

While Co and Mn valence changes could be monitored under steady state, it would be much more interesting and informative if we could also track the dynamic change of Co and Mn at the same time under non steady conditions. However, a typical high-quality XANES spectrum takes 20-30 min to acquire, making it impossible to acquire one XANES spectrum while the potential is being scanned in a cyclic voltammogram (CV). Alternatively, characteristic photon energy values corresponding to the Co, Mn valence changes can be used as probes to track the dynamic valence changes during a CV scan. Co XANES at 7722.5 eV and Mn XANES at 6553.0 eV were used as the characteristic  $E$  values since the largest changes in the X-ray intensities occurred at those  $E$  values. In order to quantify the speed at which a non-steady state could be tracked, a new concept we call “electrode potential resolution” was defined as the potential interval over which a single X-ray data point could be acquired. In this work, the electrode potential resolution = potential sweep rate  $\times$  X-ray acquisition time = 1 mV/s  $\times$  3 s = 3 mV, which means that the X-ray signal is averaged over a 3 mV potential range, closely approximating a non-steady measurement. We divided the cyclic voltammogram into two regions, based on the sign of the current (upper inset of [Fig. 5.10](#)). The positive current from 0.42 to 1.25 V (clockwise) indicates oxidation currents where Mn, Co are converted into higher valence species, during the negative

currents from 1.25 to 0.42 V the oxidized Co and Mn are converted back to the lower valence species.

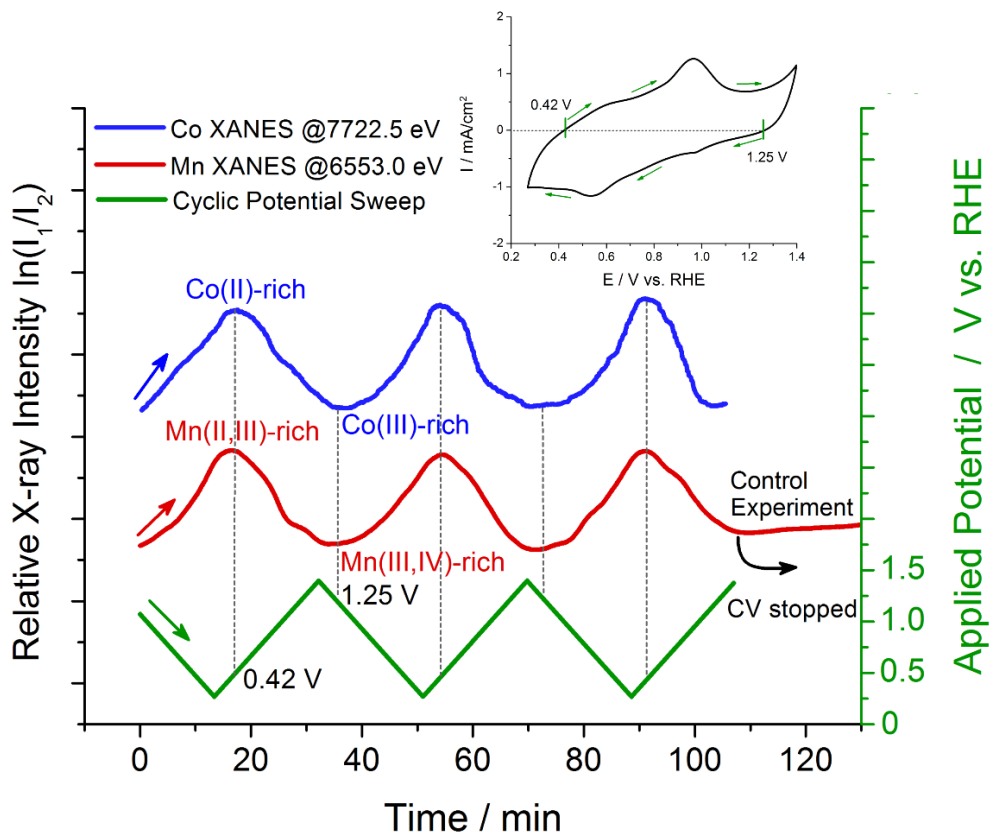


**Figure 5.10.** Periodic changes in the relative X-ray intensities ( $\ln(I_1/I_2)$ ) at 7722.5 eV (Co K-edge) and 6553.0 eV (Mn K-edge) as a function of the cyclic potential sweep. Intensity variations at 7722.5 eV and 6553.0 eV reflect the conversion between Co(II) and Co(III), Mn(II,III) and Mn(IV), respectively. The upper inset shows the corresponding CV at 1 mV/s over the potential range of 0.3-1.4 V vs. RHE. Oxidation and reduction currents in the CV are divided by two boundary potentials, 0.42V and 1.25V vs. RHE.

As shown in Fig. 5.10, the relative X-ray intensities of Co and Mn changed with the same periodic pattern as the cyclic potential sweep was applied. The relative X-ray intensity was calculated by  $\ln(I_1/I_2)$  where  $I_1$  and  $I_2$  are the incident and transmitted X-ray beam intensities, respectively. When the electrode potential goes from the upper limit (1.4 V) to the lower limit (0.3 V) (reductive current), the relative X-ray intensities

go from minimum (higher Co, Mn valence) to maximum values (lower Co, Mn valence), which indicates that  $\text{Co}_{1.5}\text{Mn}_{1.5}\text{O}_4$  is reduced and Co(III) is converted into Co(II) and Mn(III,IV) is converted into Mn(II,III). Co(II), Mn(II,III) reach their maxima at 0.42 V, instead of at the lower potential limit (0.3 V) while Co(III), Mn(III,IV) reach their maxima at 1.25 V, instead of at the higher potential limit (1.4 V). This is fully consistent with the boundary potentials (0.42V, 1.25V) of oxidation and reduction currents in the CV discussed above. The exact minimum and maximum of the relative X-ray intensities were determined from the first derivatives. The periodic patterns of Co,Mn valence changes are in sync with each other, which strongly indicates a synergistic catalysis mechanism between Co and Mn towards oxygen reduction reaction. Furthermore, dynamic changes in the Co and Mn valences were reversible over the time period of two hours, meaning that the catalyst is relatively stable. To rigorously evaluate the effect of the applied cyclic potential sweep, a control experiment was performed by acquiring the X-ray signal over the Mn XANES region without an applied potential. No change in the X-ray intensity was observed, indicating the dynamic changes of Co and Mn valences must primarily arise from the applied potential sweep, and not from possibly generated photoelectrons by the incident X-ray. In summary, the periodic changes of Co, Mn valences unambiguously establish the synergistic effect of Co and Mn towards the ORR. The superior activity of  $\text{Co}_{1.5}\text{Mn}_{1.5}\text{O}_4/\text{C}$  when compared to  $\text{Co}_3\text{O}_4/\text{C}$  and  $\text{Mn}_3\text{O}_4/\text{C}$  may come from the fact that  $\text{Co}^{+2/3}$  and  $\text{Mn}^{+2/3/4}$  redox couples serve as co-active sites to catalyze the oxygen reduction reaction.

In summary, *operando* X-ray absorption spectroscopy (XAS) has been employed to identify the active sites of a bimetallic  $\text{Co}_{1.5}\text{Mn}_{1.5}\text{O}_4/\text{C}$  catalyst, which exhibits impressive activity towards the ORR in APEFCs. To explore the mechanism, we used *operando* XANES to track the oxidation state changes of Co and Mn not only under constant applied potential (steady state), but also during dynamic cyclic voltammetry (CV, non-steady state). The periodic conversion between Mn(III,IV), Co(III) and Mn(II,III), Co(II) during the CV indicates that Co and Mn work together to catalyze oxygen reduction. The discovery of this synergistic catalytic mechanism may be the reason for the high activity of the Co-Mn oxide electrocatalyst.

## 5.6 Design Trimetallic Mn-Co-Fe Oxides with Improved Durability

Aiming for a practical, Pt-free, cathode for AEMFCs for automotive applications, non-precious ORR electrocatalysts need to not only fulfill the requirements of high initial ORR activity, but also address durability concerns. We designed a family of Mn-Co-Fe trimetallic oxides to effectively improve the durability of our first-generation Mn-Co catalysts.

A family of MCF was prepared using a facile hydrothermal method followed by a high-temperature treatment. Their crystal structures were examined by powder XRD, as presented in [Fig. 5.11](#). All of the prepared samples, named as  $\text{CoFe}_2\text{O}_4$  (MCF-0),  $\text{Mn}_{0.3}(\text{CoFe}_2)_{0.9}\text{O}_4$  (MCF-0.3),  $\text{Mn}_{0.6}(\text{CoFe}_2)_{0.8}\text{O}_4$  (MCF-0.6),  $\text{Mn}_{0.8}(\text{CoFe}_2)_{0.73}\text{O}_4$  (MCF-0.8),  $\text{Mn}_1(\text{CoFe}_2)_{0.66}\text{O}_4$  (MCF-1), and  $\text{Mn}_{1.2}(\text{CoFe}_2)_{0.6}\text{O}_4$  (MCF-1.2), possess cubic spinel structures. The broad peak at around  $25^\circ$  in the XRD belongs to carbon, and the remaining of diffraction peaks matched well with the standard cubic spinel  $\text{CoFe}_2\text{O}_4$

(PDF#01-077-0426,  $a=b=c=8.401 \text{ \AA}$ ) and  $\text{MnFe}_2\text{O}_4$  (PDF # 01-073-3820,  $a=b=c=8.498 \text{ \AA}$ ). There is a progressive shift to lower  $2\theta$  angle at higher Mn contents, corresponding to the gradual substitution of Co and Fe by Mn with larger atomic size. The average domain size of all MCF samples, as estimated from XRD measurements, was found to be around 10-15 nm, which is consistent with STEM images.

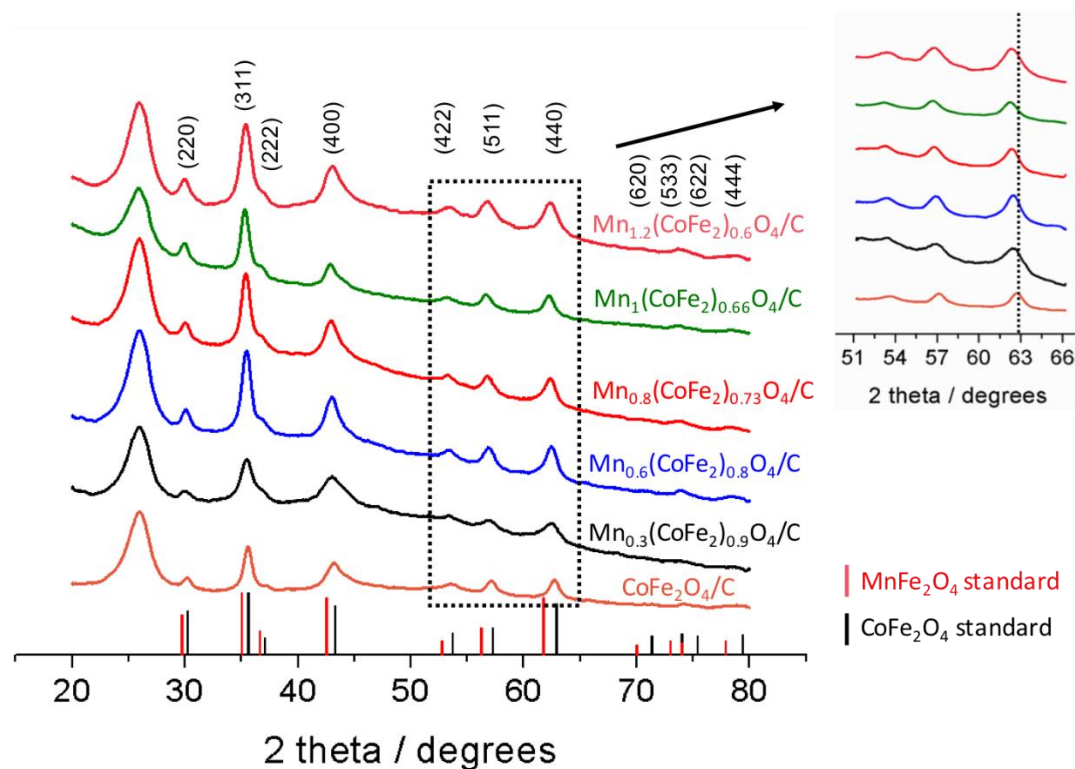


**Figure 5.11.** XRD patterns of as-synthesized MCF cubic spinel nanoparticles:  $\text{CoFe}_2\text{O}_4$ ,  $\text{Mn}_{0.3}(\text{CoFe}_2)_{0.9}\text{O}_4$ ,  $\text{Mn}_{0.6}(\text{CoFe}_2)_{0.8}\text{O}_4$ ,  $\text{Mn}_{0.8}(\text{CoFe}_2)_{0.73}\text{O}_4$ ,  $\text{Mn}_1(\text{CoFe}_2)_{0.66}\text{O}_4$  and  $\text{Mn}_{1.2}(\text{CoFe}_2)_{0.6}\text{O}_4$ . The red and black vertical lines correspond to standard  $\text{CoFe}_2\text{O}_4$  (PDF # 01-077-0426) and  $\text{MnFe}_2\text{O}_4$  (PDF # 01-073-3820) XRD patterns, respectively; inset represents the enlarged region of the  $\text{CoFe}_2\text{O}_4$  (440) diffraction peak.

The crystal structure of  $\text{Mn}_{0.8}(\text{CoFe}_2)_{0.73}\text{O}_4/\text{C}$  (MCF-0.8) with optimal activity was further examined at the atomic scale using high-angle annular dark-field (HAADF) scanning transmission electron microscopy (STEM) imaging at 100 keV (Cornell Nion UltraSTEM). Since  $\text{CoFe}_2\text{O}_4$  ( $a=8.401 \text{ \AA}$ ) shares a very similar cubic spinel crystal

structure to  $\text{MnFe}_2\text{O}_4$  ( $a=8.498 \text{ \AA}$ ), the crystal structure of MCF-0.8 from STEM imaging analysis can be built based on the structure of  $\text{CoFe}_2\text{O}_4$  (PDF # 01-077-0426). [Figs. 5.12A-B](#) present the atomic-scale lattice image of MCF-0.8 and the corresponding crystal model viewed along the  $[11\bar{2}]$  zone axis. Two perpendicular d-spacings were measured to be 4.9 and 3.0  $\text{\AA}$ , well consistent with the theoretical (111), 4.85  $\text{\AA}$  and ( $2\bar{2}0$ ), 2.97  $\text{\AA}$  lattice planes, respectively. Since the intensity of a HAADF-STEM image is proportional to the atomic number ( $I \propto Z^{1.7}$ ), it is intriguing to observe in [Figure 2A](#) that atom columns, **a**, at the corner, exhibit a higher intensity related to that of atom columns, **b**, on the side, even though they are supposed to be the same element, according to the 2D projected crystal model in [Figure 2B](#). This apparent inconsistency can be resolved by deliberately tilting the  $[11\bar{2}]$  zone axis to reveal the atom columns underneath. Despite being the same element, atom columns, **a**, clearly have a higher atom density than that of atom columns, **b**, resulting in a higher image intensity as observed in [Fig. 5.12A](#). It is also observed that atom columns, **c**, at the center of the lattice image in [Fig. 5.12A](#) seem to be elongated in the (111) direction, which, in fact, corresponds to an assembly of three atom columns next to each other. The distances among the three of them are too short and beyond the spatial resolution of STEM images.

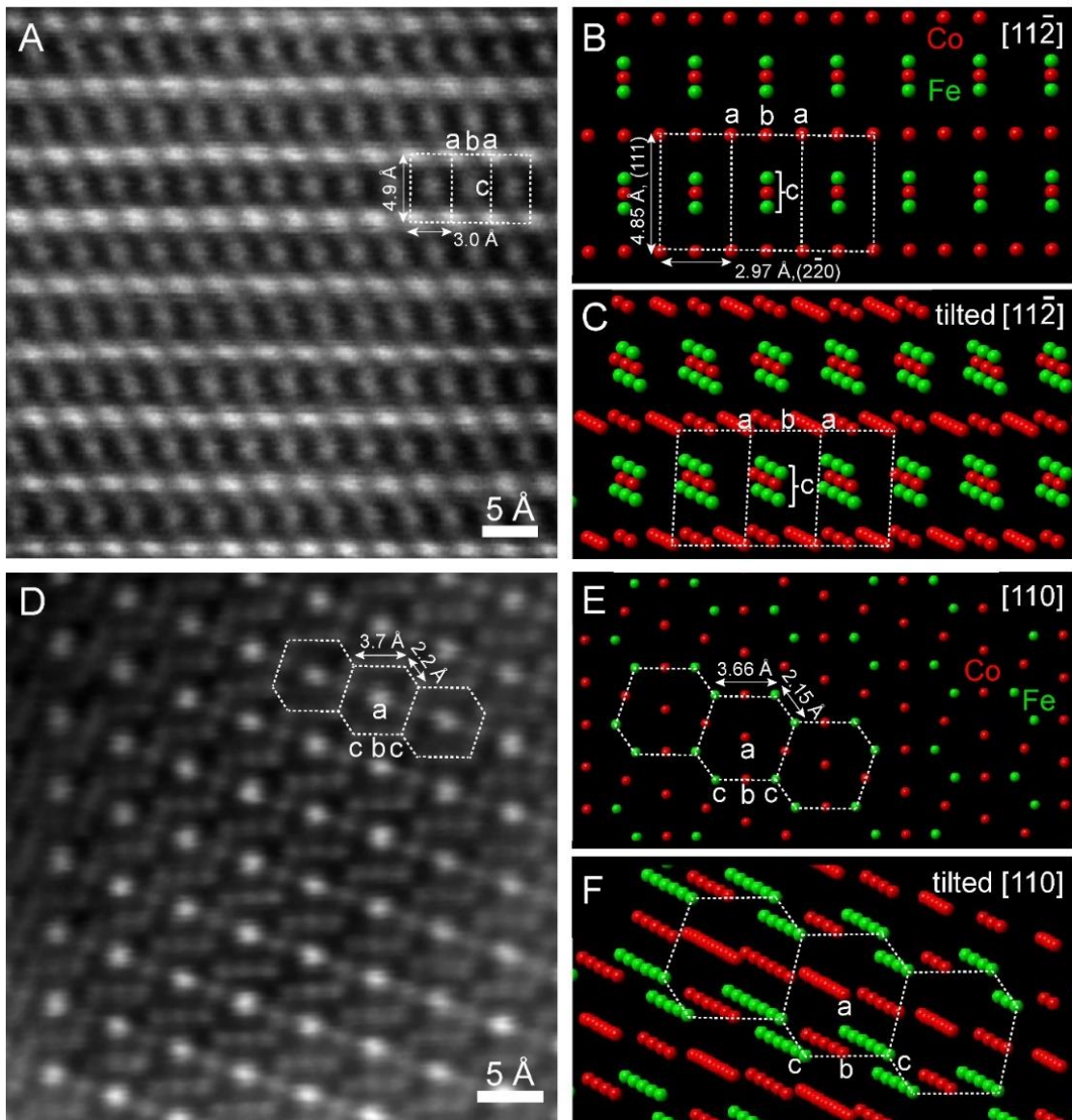


**Figure 5.12.** Atomic-scale HAADF-STEM images of MCF-0.8. (A-B) atomic-scale image and the corresponding crystal model on the  $[11\bar{2}]$  zone axis. Two lattice spacings were measured to be 4.9 and 3.0 Å, which matched well with the theoretical values of (111), 4.85 Å and  $(2\bar{2}0)$ , 2.97 Å, respectively. (C) The crystal model on the  $[11\bar{2}]$  zone axis slightly tilted to reveal the underneath atom columns. (D-E) Another atomic-scale image and the corresponding crystal model on the  $[110]$  zone axis. (F) The crystal model on the  $[110]$  zone axis was slightly tilted to reveal the underneath atom columns.

Figs. 5.12D-E exhibit another atomic-scale lattice image of MCF-0.8 and the corresponding crystal model on the more basic  $[110]$  zone axis. Hexagonal repeating

unit cells are indicated in the dashed boxes with two nearby sides of 3.7 and 2.2 Å with an angle of 125°, which are consistent with the theoretical values of 3.66 and 2.15 Å, respectively, with an angle of 126°. Similar to Fig. 5.12A, atom columns, **a**, at the center of the lattice image in Fig. 5.12D, exhibit a higher intensity than that of atom columns, **b** and **c**, on the side. The intensity variations also come from the fact that atom columns, **a**, have higher atoms density than that of **b** and **c**, as shown in the tilted [110] zone axis (Fig. 5.12F). Noticeably, atom columns **b** and **c**, exhibit no significant difference in image intensity, although they could be different element combinations, Co and Fe or Mn and Fe. Given that Mn, Fe and Co have very similar atomic numbers, the image intensity variations are likely below the noise level threshold of the electron detector. In summary, the aforementioned atomic-scale STEM imaging analysis directly visualized and confirmed the cubic spinel crystal structure of MCF-0.8.

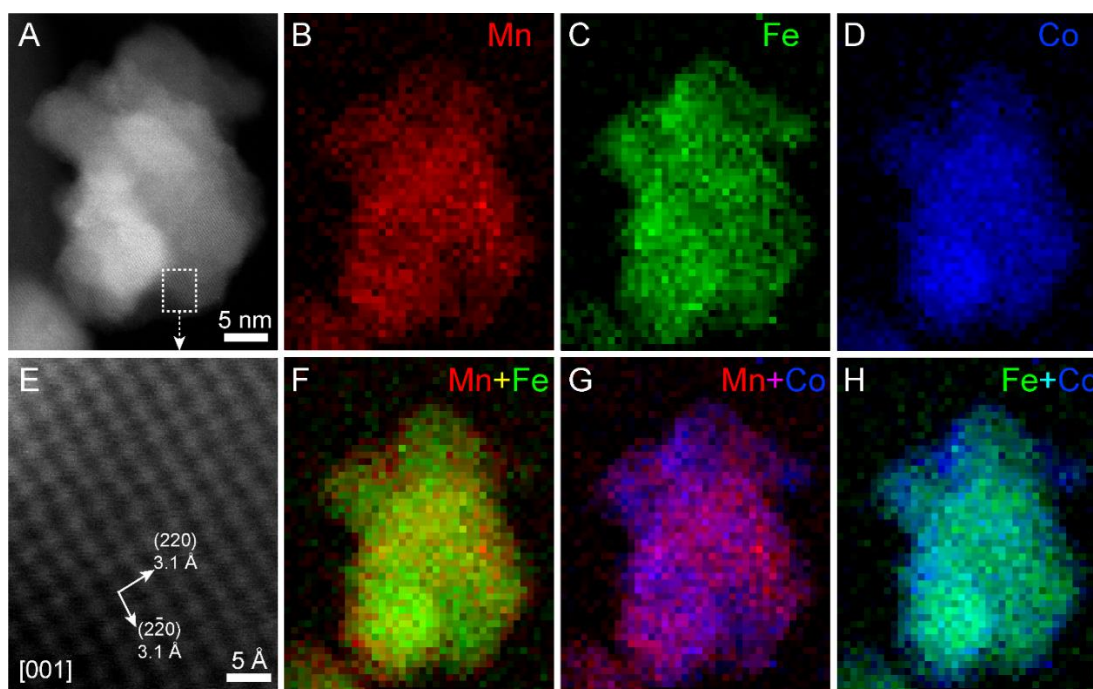


**Figure 5.13.** EELS elemental maps of MCF-0.8. (A) HAADF-STEM image of a typical nanoparticle composed of smaller sub-domains. The lattice image in the dashed box was magnified in (E) to show (220) and (2̄20) with same d-spacing values of 3.1 Å on the zone axis of [001]. (B-D) EELS elemental maps of Mn (red), Fe (green) and Co (blue), respectively. (F-H) EELS elemental composite maps of Mn vs. Fe, Mn vs. Co and Fe vs. Co, respectively.

The chemical composition of MCF-0.8 nanoparticles was investigated using electron energy loss spectroscopy (EELS) elemental mapping. Fig. 5.13A shows a typical MCF-0.8 nanoparticle composed of multiple sub-domains. The region in the dashed box was magnified in Figure 3E to show the lattice image, which is on the [001] zone axis with the perpendicular (220) and (2 $\bar{2}$ 0) lattice planes (3.1 Å). Figures. 3B-D present the EELS elemental maps of Mn (red), Fe (green) and Co (blue) for the particle in Fig. 5.13A. Figs. 5.13F-H show the composite EELS maps of Mn vs. Fe, Mn vs. Co and Fe vs. Co. The composite EELS map of Mn vs. Fe suggests a homogenous elemental distribution in which Mn and Fe are intimately mixed on a nearly atomic scale. The composite EELS maps of Mn vs. Co and Fe vs. Co exhibit a relatively homogenous elemental distribution with a local enrichment of Co at the edge of the particle. This EELS chemical mapping study combined with the previous analysis of atomic-scale STEM images in Fig 5.12, unambiguously demonstrate that MCF-0.8 has a cubic spinel crystal structure with a relatively homogenous elemental distribution of Mn, Co and Fe.

The cyclic voltammetric profiles (CVs) of all MCF NPs, with different Mn content were obtained in an Ar-saturated 1 M NaOH solution at a scan rate of 5 mV/s from 0.15 to 1.2 V vs. RHE (Fig. 5.14A). To identify the redox couples more accurately, the CVs of MCF, together with CoFe<sub>2</sub>O<sub>4</sub> and MnFe<sub>2</sub>O<sub>4</sub> were investigated and as presented in Figure S5. There are two redox couples in the 0.15-1.2V potential window for all Mn-containing oxides. Mn exhibits two oxidative peaks in the positive potential scanning direction, at around 0.68 and 0.91 V respectively, corresponding to the gradual evolution from Mn (II) to higher valence states (Mn (III, IV)). Conversely, two reductive peaks were observed at 0.72 and 0.6 V repeatedly indicating the conversion back to Mn (II).

Co (III) exhibited a single oxidative peak at around 0.97 V, which overlapped with the more pronounced features from Mn. With increasing Mn and decreasing Co contents, the first peak at higher potential shifts gradually from 0.97 to 0.91 V, which is consistent with the compositional variation. No redox couples from Fe were observed in the CV profiles, as its redox reactions typically occur at more negative potentials.<sup>11-12</sup>

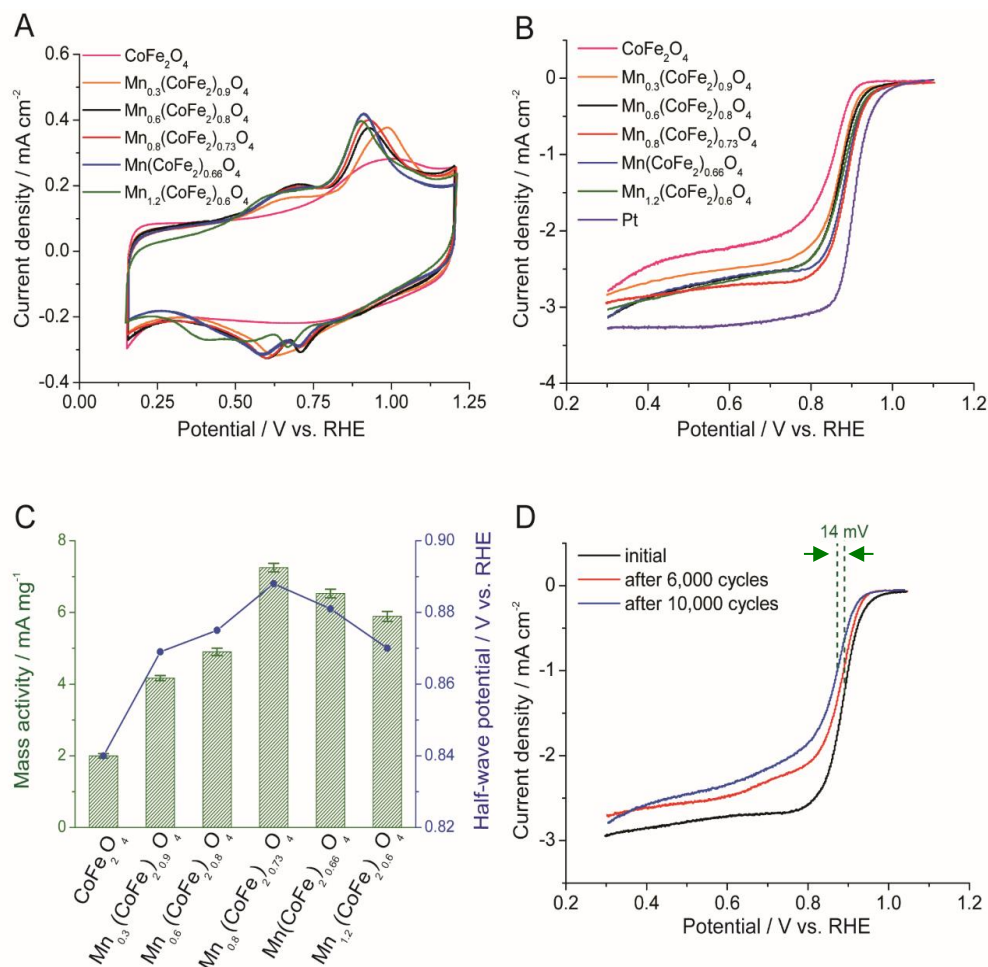


**Figure 5.14.** Electrocatalytic properties of as-synthesized MCF nanoparticles. (A) Cyclic voltammety (CV) profiles of synthesized MCF NPs in Ar-saturated 1 M NaOH solution, scanned at a rate of 5 mV/s at room temperature. (B) ORR polarization curves in O<sub>2</sub>-saturated 1 M NaOH at a scan rate of 5 mV/s and rotation at a rate of 1600 rpm. (C) Comparison of mass activity and half-wave potential of different MCFs at 0.9 V vs. RHE. (D) Polarization profiles of MCF-0.8 after 10,000 potential cycles.

Rotating disk electrode (RDE) voltammetry was employed to assess the ORR

activity of all MCF electrocatalysts. The polarization curves shown in Fig. 5.14B were obtained in 1 M O<sub>2</sub>-saturated NaOH solution, at 5 mV/s and 1600 rpm. The half-wave potential ( $E_{1/2}$ ) exhibited a correlation between the electrochemical activity and the Mn content following the order of MCF-0 (0.84 V) < MCF-0.3 (0.868 V) < MCF-0.6 (0.875 V) < MCF-1.2 (0.87 V) < MCF-1 (0.88 V) < MCF-0.8 (0.888 V), as shown in Fig. 5.14C (right Y-axis). With increased Mn content, the kinetics were enhanced at first, and then decreased to higher Mn content, with an optimal performance at MCF-0.8, suggesting a “volcano trend”. The mass-specific activity (MA) of the MCFs at 0.9V was calculated by normalizing the kinetic current to the catalyst mass from the Koutecky–Levich equation, (Fig. 5.14C, left Y-axis). MCF-0.8 exhibited the highest MA value of 7.25 mA mg<sub>oxide</sub><sup>-1</sup>, outperforming its counterparts with other Mn contents. To gain further insight into the long-term durability of MCF-0.8, a stability test was carried in Ar-saturated 1M NaOH solution for 6,000 and 10,000 cycles between 0.6 to 1.0 V, the typical working potential region of APEFCs. There was a progressive negative shift in the polarization curve after 6,000 and 10,000 cycles and the diffusion limiting current decreased slightly, especially in the high polarization region. The degradation of the electrocatalysts after 10,000 cycles was ascribed to the loss of active material upon extended cycling. This was further confirmed by comparing the CV profiles before and after potential cycles, where the Mn/Co redox peaks gradually faded and broadened as an indication of losing Mn and Co active sites in addition to possible particle aggregation. Despite this minor degradation after durability testing, the MCF-0.8 still exhibited a remarkable ORR electrocatalytic activity, with an  $E_{1/2}$  of 0.874 V and  $\Delta E_{1/2}$

of only 14 mV (Fig 5.14D).

To further understand the degradation mechanism(s), STEM imaging and EDX spectroscopy were employed to investigate the structural and chemical evolution after cycling. STEM image of MCF-0.8 nanoparticles, after electrochemical cycles, indicated particle aggregation/coalescence. STEM-EDX was used to quantitatively analyze the relative amounts of Co, Fe and Mn before and after electrochemical cycles. Relative amounts of Co, Fe and Mn were calculated from the EDX spectra, where the intensity of Fe was normalized to 1 for comparison (Fig. 5.15). It is clear that the Mn loss is nearly 50%, relative to its original content, Co lost around 30%, while the Fe content was stable during the cycling process. The quantitative results are shown in Tables 5.1 and 5.2. The relative atomic percentages of as synthesized MCF-0.8 were 29.2, 23.8 and 47.0 % for Mn, Co and Fe, respectively, which is quite consistent with the theoretical ratio of reactants of 27, 24 and 49 %. After electrochemical cycling, the relative amounts of Mn and Co dropped from 29.2 to 20.2 % and from 23.8 to 18.3 %, respectively, while the content of Fe increased from 47.0 to 61.5 %.

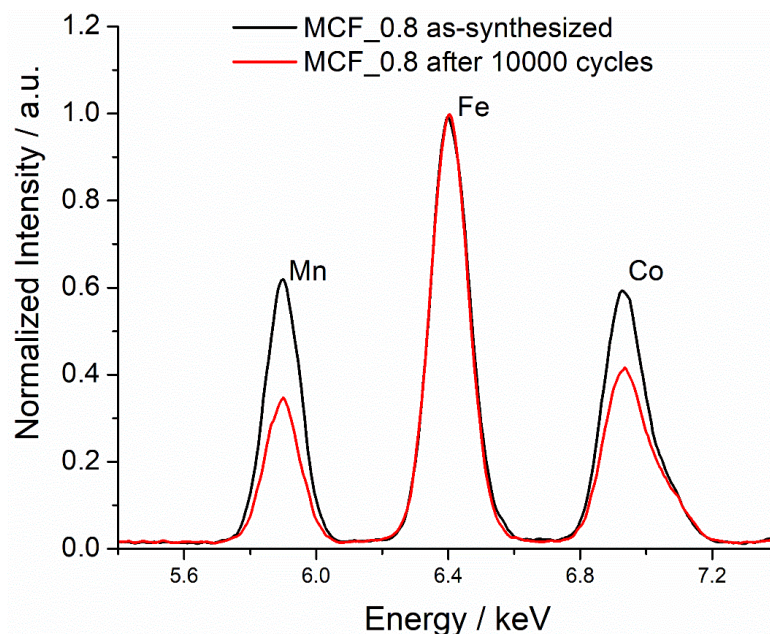


**Figure 5.15.** EDX spectra of MCF-0.8 before and after electrochemical cycles. The X-ray intensities were normalized to the value of Fe K $\alpha$  edge for comparisons. It should be noted that the Mn major K $\alpha$  edge is at 5.89 keV and the Mn minor K $\beta$  edge at 6.49 keV overlaps with Fe’s major K $\alpha$  edge(6.40 keV). Fe’s minor K $\beta$  edge at 7.05 keV overlaps with Co’s major K $\alpha$  edge at 6.93 keV, which explains why Fe and Co peaks have small shoulder peaks on the right side of their peaks.

Based on the Cliff-Lorimer thin-film criterion,<sup>13</sup> if the sample is assumed to be a thin foil so that the X-ray absorption or fluorescence can be safely ignored, the elemental concentration of two elements can be proportional to the X-ray intensity ratio (peak integral):  $\frac{c_1}{c_2} = k_{12} \frac{I_1}{I_2}$ , where  $k_{12}$  is a constant.

Mn, Co and Fe relative contents were calculated by integrating their K edge peaks and taking into account their k-factors. The results were summarized in the following table.

MCF_0.8	Mn at.%	Co at.%	Fe at.%
As-synthesized	26.4	28.2	45.4
After CV cycles	18.3	23.8	57.9

**Table 5.1.** EDX quantitative analysis of MCF\_0.8 catalysts before and after electrochemical cycles without considering the overlap between Mn K $\beta$  and Fe K $\alpha$  and between Fe K $\beta$  and Co K $\alpha$ .

Considering Mn K $\beta$  overlaps with Fe K $\alpha$  and Fe K $\beta$  overlaps with Co K $\alpha$ , the above table overestimates the relative contributions of Fe and Co. The intensity ratio of K $\beta$ /K $\alpha$  is 17/150 for Mn, Co and Fe.<sup>14</sup> Assuming the actual relative contents of Mn, Fe and Co are x at.%, y at.% and z at.%, three following equations were set to solve the actual relative contents.

$$1. x + y + z = 100$$

$$2. \frac{\frac{17}{150}x+y}{x} = \frac{45.4}{26.4}$$

$$3. \frac{\frac{17}{150}y+z}{y} = \frac{28.2}{45.4}$$

Solving equations results in the actual relative contents of Mn (29.2 at.%), Co (23.8 at.%) and Fe (47.0%), which is more consistent with the ideal relative contents of Mn (26.7% at.%), Co (24.3 at.%) and Fe (48.6 at.%) in Mn<sub>0.8</sub>(CoFe<sub>2</sub>)<sub>0.73</sub>O<sub>4</sub> catalysts (MCF\_0.8). The actual relative contents of MCF\_0.8 after electrochemical cycles were also calculated using the same strategy and summarized in the following table together with that of as-synthesized MCF\_0.8.

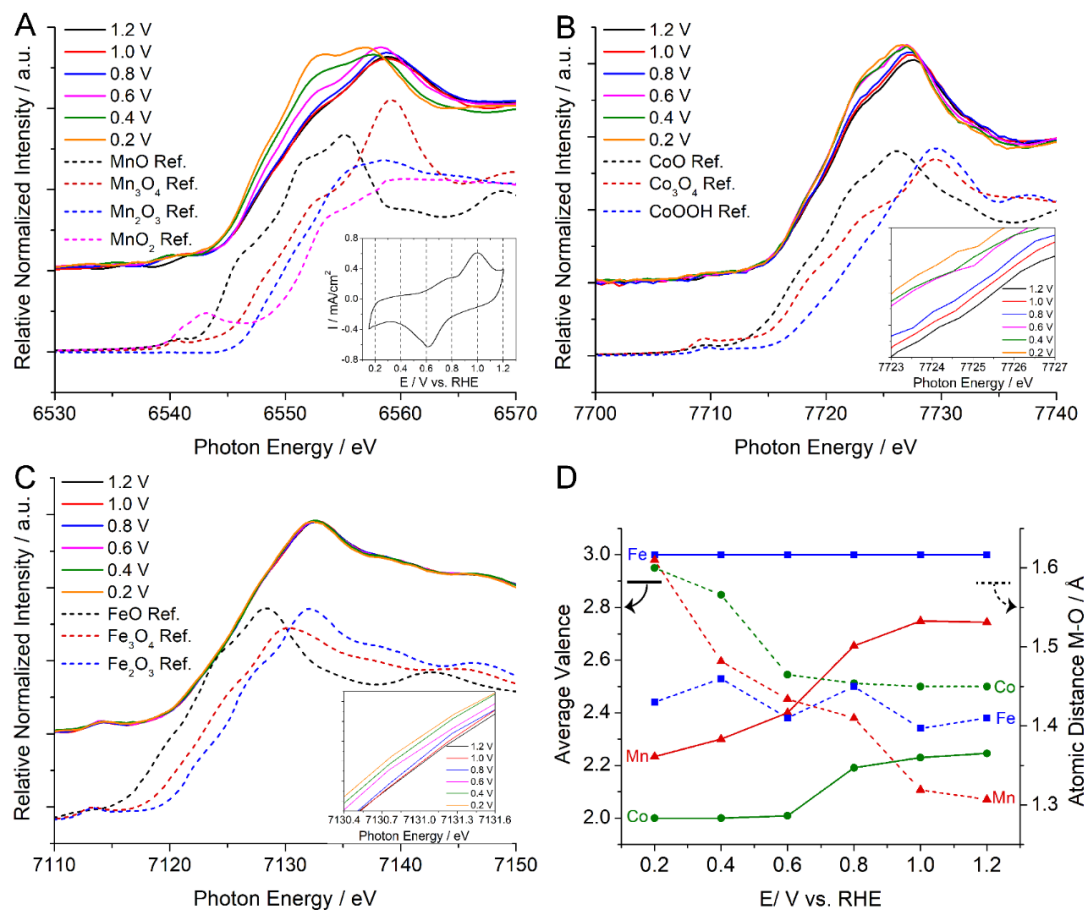
MCF_0.8	Mn at.%	Co at.%	Fe at.%
As-synthesized	29.2	23.8	47.0
After CV cycles	20.2	18.3	61.5

**Table 5.2.** More accurate EDX quantitative analysis of MCF\_0.8 catalysts before and after electrochemical cycles after considering the overlap between Mn K $\beta$  and Fe K $\alpha$  and between Fe K $\beta$  and Co K $\alpha$ .

## 5.7 *Operando* XANES of Trimetallic Mn-Co-Fe Oxides under Steady State

The superior ORR activity and durability of the trimetallic oxide MCF-0.8 over both CoFe<sub>2</sub>O<sub>4</sub>/C and MnFe<sub>2</sub>O<sub>4</sub>/C, suggest that the underlying catalytic mechanism involves multiple metal active sites catalyzing the reduction of oxygen. *Operando* synchrotron-based XAS was employed to investigate the catalytic mechanism of MCF-0.8 under real-time electrochemical conditions. We have designed a customized electrochemical cell for *operando* XAS measurements in our previous report (Figs. 5.1 and 5.2). The cell consisted of a working electrode of a MCF-0.8 catalyst loaded on porous carbon paper, a Ag/AgCl (1M KCl) reference electrode and a carbon rod counter electrode. Details of the cell design can be found in Figure S3. To investigate the structural evolution of the Co-Mn oxide catalysts at steady state, the applied potential was held constant while *operando* XAS spectra were acquired, after the current had dropped to background levels. According to the CV profile of the catalysts at a scan rate of 1 mV/s in the home-made cell (Fig. 5.16A, inset), constant applied electrochemical potentials (*E*) of 1.2 V, 1.0 V and 0.8 V vs. RHE correspond to the oxidation peak and its two onset potentials while values of 0.8 V, 0.6 V and 0.4 V vs. RHE correspond to the reduction peak and its two onset potentials. *E* value of 0.2 V vs. RHE was also included to investigate the electrochemical behavior of MCF-0.8 in a strongly reducing environment. Fig. 5.16A exhibits the *operando* XANES spectra of the Mn K-edge of MCF-0.8 at various applied potentials, suggesting systematic changes in the local electronic structure. Mn XANES spectra were calibrated, based on the characteristic absorption edge of elemental Mn (metal foil) at 6539.0 eV, which corresponds to the excitation of electrons from the Mn 1s orbital. The white line in these Mn spectra, near

6559 eV, originates from an electronic transition from 1s to 4p orbitals, since the 4p are the lowest allowed unoccupied orbitals of 3d transition metals based on the dipole



selection rule,  $\Delta l = \pm 1$ . The shoulder peak at 6553 eV shows a gradual increase in the peak intensity and a small shift to lower energies when the applied potential decreases from 1.2 to 0.2 V, indicating a lower Mn valence state at more negative potentials. More specifically, this peak at 6553 eV exhibited no significant changes when the potential varies from 1.2 to 0.8 V and became pronounced when  $E$  decreased from 0.8 to 0.6 V. When the potential was below 0.4V, it became more prominent and similar to the feature in the MnO (II) reference, qualitatively suggesting a larger contribution from a lower-valence Mn.

**Figure 5.16.** Operando XANES spectra of the Mn, Co and Fe K-edges of MCF-0.8 and

the evolution of the average metal valence and metal-oxygen atomic distance at a series of applied potentials. (A) *Operando* XANES spectra at the Mn K-edge of the MCF-0.8 (solid lines) and the reference manganese oxides (dashed lines). Inset shows the selected applied potential from the CV profile at a scan rate of 1mV/s in the home-made electrochemical cell at which signals were detected. (B) *Operando* XANES spectra at the Co K-edge of the MCF-0.8 (solid lines) and the reference cobalt oxides (dashed lines). Inset shows the gradual shift of the Co K-edge to lower photon energies with changing in intensity. (C) *Operando* XANES spectra at the Fe K-edge of the MCF-0.8 (solid lines) and the reference iron oxides (dashed lines). Inset shows the incremental shift of Fe K-edge to lower photon energies with a change in intensity. (D) Calculated average metal valence (solid lines, left Y-axis) as a function of potential based on the linear combination fitting using XANES spectra of reference metal oxides. Measured metal-oxygen (M-O) atomic distance as a function of potential (dashed lines, right Y-axis) based on the *operando* EXAFS analysis.

In order to study the gradual changes in the Mn valence more quantitatively, linear combination fitting (LCF) analysis was performed using pure manganese oxides, MnO (II), Mn<sub>3</sub>O<sub>4</sub> (II, III), Mn<sub>2</sub>O<sub>3</sub> (III) and MnO<sub>2</sub> (IV) as reference spectra. Details of peak fitting can be found in Fig. 5.17. When  $E$  decreased from 1.2 V to 0.8V, the relative contents of different metal oxides remained relatively unchanged, corresponding to the little change in the XANES spectra (Fig. 5.16A). When  $E$  continues to decrease from 0.8 V to 0.2 V, the relative contents of MnO<sub>2</sub> (IV) and Mn<sub>2</sub>O<sub>3</sub> (III) quickly dropped from 7%, 10%, respectively, to nearly 0 % and the relative contents of Mn<sub>3</sub>O<sub>4</sub> (II, III) dropped from 60% to 35%. Concomitantly, the relative contents of MnO (II) increased dramatically from 23% to 65%, corresponding to the more dominant features of MnO (II) in XANES spectra of MCF-0.8 at lower potentials. The calculated average valence of Mn decreased substantially and continuously from 2.58 to 2.23 when  $E$  decreased from 1.2 to 0.2 V (Figs. 5.17A-B). A lower Mn valence at lower applied potentials would suggest a longer Mn-O chemical bond and weaker binding strength to oxygen,

which are clearly confirmed by the corresponding *operando* EXAFS spectra in Fig. 5.18A. The Mn-O atomic distance increased continuously from 1.31 to 1.61 Å when  $E$  decreased from 1.2 to 0.2 V, as shown in Fig. 5.18A. This systematic evolution of the Mn valence and the M-O atomic distance strongly indicate that various Mn species can serve as the active site to catalyze the oxygen reduction reaction.

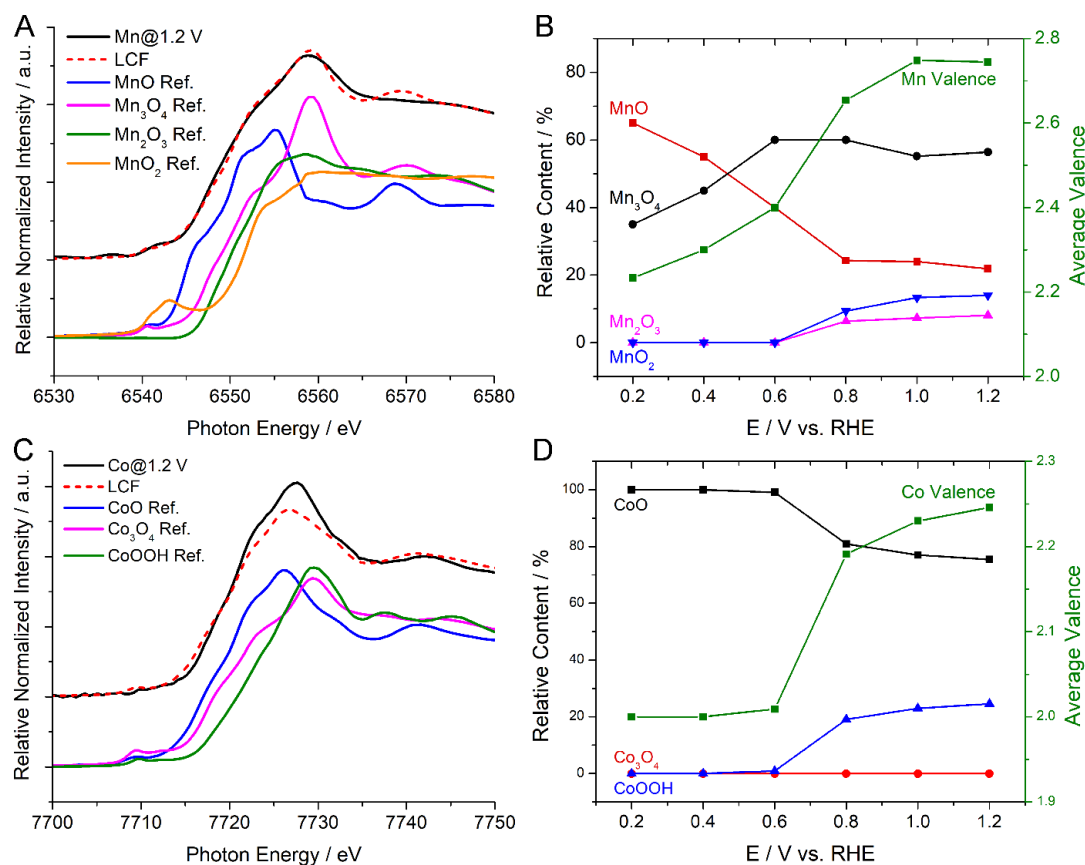


**Figure 5.17.** (A) Valence analysis of Mn K-edge at 1.2 V vs. RHE. Linear combination fitting (LCF) (red dashed line) indicates the relative content of MnO (22%), Mn<sub>3</sub>O<sub>4</sub> (56%), Mn<sub>2</sub>O<sub>3</sub> (8.1%) and MnO<sub>2</sub> (14%) at 1.2 V. This LCF has a small R-factor of 0.00276 and reduced  $\chi^2$  of 0.000710, indicating a good fitting quality. (B) Average Mn valence at a series of applied potential, which was calculated from the relative contribution of four manganese oxide references. (C) Valence analysis of Co K-edge at 1.2 V. Linear combination fitting (LCF) (red dashed line) indicates the relative content of CoO (75.5%), Co<sub>3</sub>O<sub>4</sub> (0%) and Co<sub>2</sub>O<sub>3</sub> (24.5%) at 1.2 V. This LCF has a small R-factor of 0.0179 and reduced  $\chi^2$  of 0.00517, indicating a reasonable fitting quality. (D)

Average Co valence at a series of applied potential, which was calculated from the relative contribution of three cobalt oxide references.

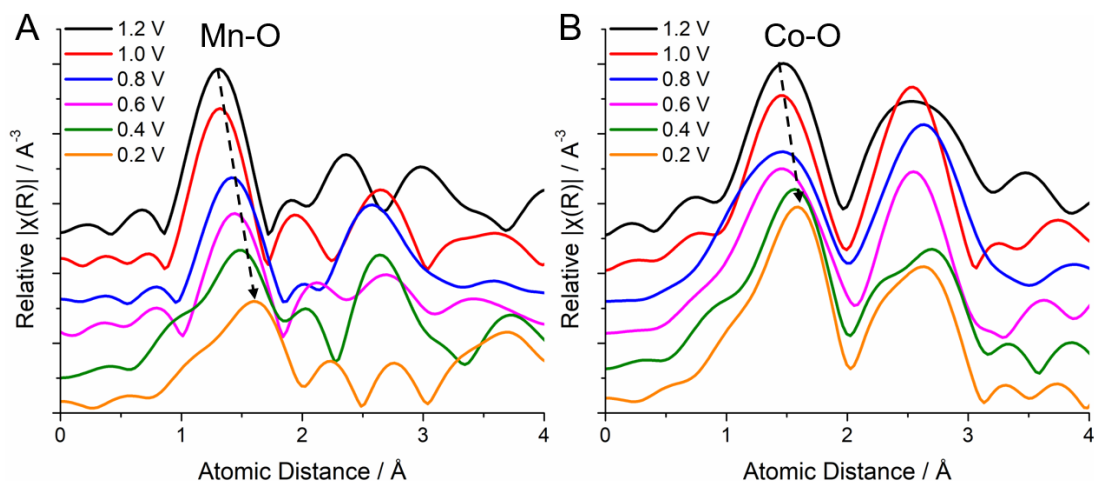


**Figure 5.18.** *Operando* EXAFS of Mn (A) and Co (B) at a series of applied potential. The Metal-oxygen (M-O) bond distance increases as the applied potential decreased from 1.2 to 0.2 V, corresponding to a lower metal valence and weaker binding strength to oxygen. EXFAS spectra were processed by setting the background value (Rbkg) to 1.2 in Athena software with the FT-window set to 3 to 10  $\text{\AA}^{-1}$  and no phase correction.

Co K-edge XANES spectra exhibited similar changes to those of Mn in the MCF-0.8 electrocatalyst. (Fig. 5.16B). Co XANES spectra were calibrated based on the characteristic absorption edge of elemental Co (metal foil) at 7709.0 eV. The *operando* Co XANES spectra and the magnified inset in Fig. 5.16B, exhibit a gradual increase in the peak intensity at around 7725 eV, and a continuous shift to lower energies when  $E$  decreased from 1.2 to 0.2 V, indicating lower Co valences at lower applied potentials. The absorption edge of Co had the most significant changes when  $E$  dropped from 0.8 to 0.6 V, indicating an abrupt change in its oxidation state and electronic environment. LCF analysis was also employed to quantitatively study the Co valence with CoO (II), Co<sub>3</sub>O<sub>4</sub> (II, III) and CoOOH (III) as cobalt oxide references (Figs 5.17C-D). When  $E$  varied from 1.2 V to 0.6 V, the relative contents of CoOOH decreased from 24% to

nearly 0% while that of CoO increased from 76% to nearly 100%, corresponding to the abrupt change in XANES spectra in Fig. 5.16B. The XANES spectra of Co remained essentially unchanged with 100 % CoO when the applied  $E$  further was decreased from 0.6 to 0.2 V. In contrast to changes of relative contents of  $Mn_3O_4$ , the relative contents of  $Co_3O_4$  were calculated to be consistently zero at various potentials, suggesting a negligible contribution from  $Co_3O_4$ . The calculated average valence of Co decreased from 2.246 to 2.0 when  $E$  varied from 1.2 to 0.6 V, and stayed at 2.0 from 0.6 to 0.2V, as shown in Fig. 5.17D (green line). *Operando* EXAFS of Co further revealed that the Co-O atomic distance gradually became longer, from 1.45 to 1.60 Å, when  $E$  shifted from 1.2 to 0.2 V, as shown in Fig. 5.18B (black dashed line). This is consistent with the lower Co valence at lower applied potentials, suggesting a weaker Co binding strength to oxygen. Although the gradual evolution of the average Co valence and Co-O atomic distance at various applied potentials were less pronounced than for Mn, the changes in the valence state of Co and Mn shared a similar pattern, suggesting that Co and Mn could serve as co-active sites to catalyze the reduction of oxygen.

Contrary to Co and Mn, the *operando* XANES of Fe at the K-edge indicated no significant changes during the entire potential range from 1.2 to 0.2 V (Fig. 5.16C). The magnified inset exhibits a small increase in the peak intensity at around 7131 eV and a slight shift to lower energies. Further LCF analysis of the Fe valence suggests a 100% contribution from  $Fe_2O_3$  (III) at 1.2 V. The Fe valence remained unchanged over the entire  $E$  range, from 1.2 to 0.2 V, when considering the small statistical error of the LCF analysis (reduced  $\chi^2 < 0.001$ ). The *operando* EXAFS spectra around the Fe K-edge in Fig. 5.19 suggest that the Fe-O atomic distance remained relatively stable at 1.43 Å with

no more than  $\pm 0.05 \text{ \AA}$  variation when  $E$  decreased from 1.2 to 0.2 V. Given the above analysis of the average Fe valence and the Fe-O inter atomic distance, unlike Co and Mn, the local electronic structure of Fe stays relatively unchanged over a wide potential range from 1.2 to 0.2 V, indicating that Fe can serve as a “stabilizing agent” in MCF-0.8, and at least in part, contribute to the remarkable durability of MCF-0.8 even after 10,000 electrochemical cycles.

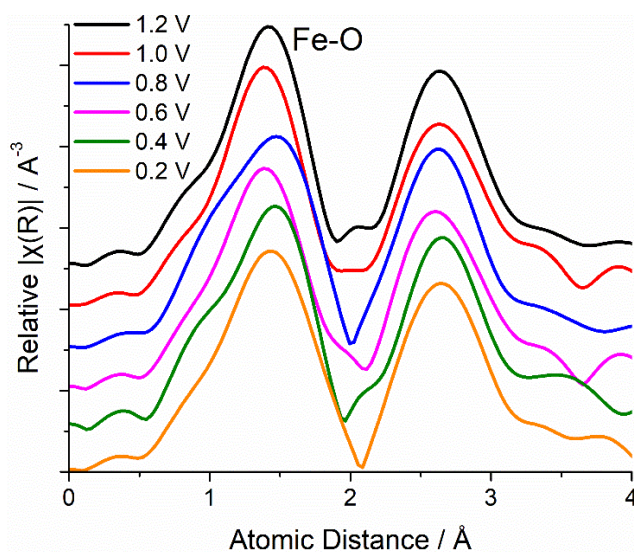


**Figure 5.19** *Operando* EXAFS of Fe at a series of the applied potential. The iron-oxygen (Fe-O) bond distance exhibits no significant variation as the applied potential decreased from 1.2 to 0.2 V, indicating a relatively stable Fe-O bond.

Fig. 5.16D serves as a compact summary of the dynamic evolution of average metal valence (solid lines, left Y-axis) and metal-oxygen (M-O) inter atomic-distance (dashed lines, right Y-axis) at various applied potentials. The average Mn and Co valences share a similar decreasing trend at lower applied potentials (red and green solid lines), but some differences in the details can be noted. The Mn-O distance continuously and dramatically decreased from 2.581 to 2.233  $\text{\AA}$  while the Co-O distance decreased from 2.246 to 2.000  $\text{\AA}$  when  $E$  varied from 1.2 to 0.6 V and remained at 2.000  $\text{\AA}$  even when

$E$  was below 0.6 V. Considering that the typical working voltages of the membrane electrode assembly (MEA) in alkaline fuel cells are from 0.6 to 1.0 V, the dynamic changes of the valence of Mn and Co suggested that both could serve as active sites and catalyze the reduction of oxygen. The Mn-O atomic distance increased at lower potentials which is consistent with the decrease of Mn valence at lower potentials, suggesting a weaker binding energy of Mn towards oxygen. Changes of the Co-O inter atomic distance followed a similar pattern through with less pronounced changes than for Mn at various potentials (dashed green line). The Co-O inter atomic distance continuously increased when  $E$  was below 0.6V while the Co valence mainly remained at 2.0, indicating that other factors in the electronic structure and local chemical environment may also influence the binding energy of Co towards oxygen. The lack of significant changes in the Fe valence and the Fe-O inter atomic distance (solid and dashed blue lines) suggest that Fe could serve as a stabilizing core element to maintain the integrity of the spinel structure and enhance the long-term durability.

### **5.8 *Operando* XANES of Trimetallic Mn-Co-Fe Oxides under Non-Steady State**

We investigated the evolution of the local electronic structures of Mn, Co and Fe using *operando* XANES and EXAFS under steady state, constant applied potential conditions. We then explored the dynamic changes in the valence state of the metal active sites during cyclic voltammetry (CV). Such experiments require a non-conventional strategy to enable fast recording of absorption differences, of transmitted X-rays, down to the level of seconds, so as to enable following the relatively potential fast changes during CV. This strategy was first reported in our previous study (Fig. 5.1). and employed in this work to enable understanding the synergistic effects of the multi-

active sites in MCF-0.8. Instead of acquiring a full XAS spectrum over a time long period (20-30 min). The absorbed X-ray intensity variations were recorded within seconds, at a characteristic energy where the largest changes in the intensity of absorption occurred in the above mentioned steady-state measurements (Figure 5A). The X-ray absorption intensity was calculated as  $\ln(I_1/I_2)$  where  $I_1$  and  $I_2$  are the incident and transmitted X-ray beam intensities, respectively. In this particular case, the characteristic energy values of Mn, Co and Fe were determined to be 6553, 7225 and 7131 eV, respectively. A scan rate of 1mV/s, combined with a X-ray acquisition time of 3s, indicates that the X-ray signal will be averaged over a 3mV potential range, closely approximating to non-steady (dynamic) measurements. From the CV profile at 1 mV/s in the upper inset of Fig. 5.20, we observed that the oxidation currents (positive values) and the reduction currents (negative values) were divided by two boundary potentials, 1.12 and 0.28V. One would expect that the oxidation/reduction currents will reflect metal active sites being converted into higher/lower valence states, and that a periodic change of the metal valence will follow the triangular potential scan (*vide infra*).

Fig. 5.20 reveals the periodic changes in the relative X-ray intensity,  $\ln(I_1/I_2)$ , as a cyclic potential scan is applied. When the applied potential starts at the upper boundary value, 1.12 V and is scanned to the lower limit, 0.15 V, the relative X-ray intensity of Mn increases dramatically, and keeps increasing to the maximum intensity until the potential passes the lower limit, 0.15 V and reaches the lower boundary potential, 0.28 V. Higher X-ray intensities, as shown in Figure 5A, indicate higher contents of lower Mn valence since the selected energy is closer to the Mn (II) white line energy. The

processes from 1.12 to 0.28 V represent the conversion from Mn (III, IV) to Mn (II, III). Symmetrically, when the potential varies from the lower boundary potential, 0.28 V to the upper limit, 1.2 V, the X-ray intensity keeps decreasing to the minimum values until the potential first passes the upper limit, 1.2 V and reaches the upper boundary potential, 1.12 V. The processes from 0.28 V to 1.12 V represent for the conversion from Mn (II, III) to Mn (III, IV). Mn valences change in a periodic fashion in the subsequent two cyclic potential scans. This is fully consistent with the boundary potentials (0.28 V, 1.12 V) of oxidation and reduction currents in the CV discussed before, unveiling a real-time glimpse of an intriguing electrocatalytic mechanism of Mn active sites in MCF-0.8.

Compared to the changes of Mn, the relative X-ray intensity of Co at 7225 eV also increases as the potential drops from 1.12 V, but reaches a relatively stable plateau at around 0.6 V, which is consistent with the dramatic changes in the Co XANES spectra from 1.2 to 0.6 V with little, if any, changes below 0.6 V (Fig. 5.16B). During the cyclic potential scan, the periodic behavior of the relative X-ray intensity of Co, corresponds to the reversible conversion between Co(III) at high  $E$  to Co(II) at lower  $E$ . In sharp contrast to the patterns of Mn and Co, the relative X-ray intensity of Fe at 7131 eV, remains essentially unchanged during the cyclic potential scan, suggesting no significant changes in the Fe valence. A smaller X-ray intensity variation of Fe evident at very negative potentials at around 0.15~0.28 V may suggest a slight reduction from Fe(III) to Fe(II), which is consistent with the incremental increase in the X-ray intensity of the Fe K-edge XANES (Fig. 5.16C). Such a small conversion from Fe(III) to Fe(II) may not be revealed in the change of Fe valence, considering the statistical error of LCF analysis.

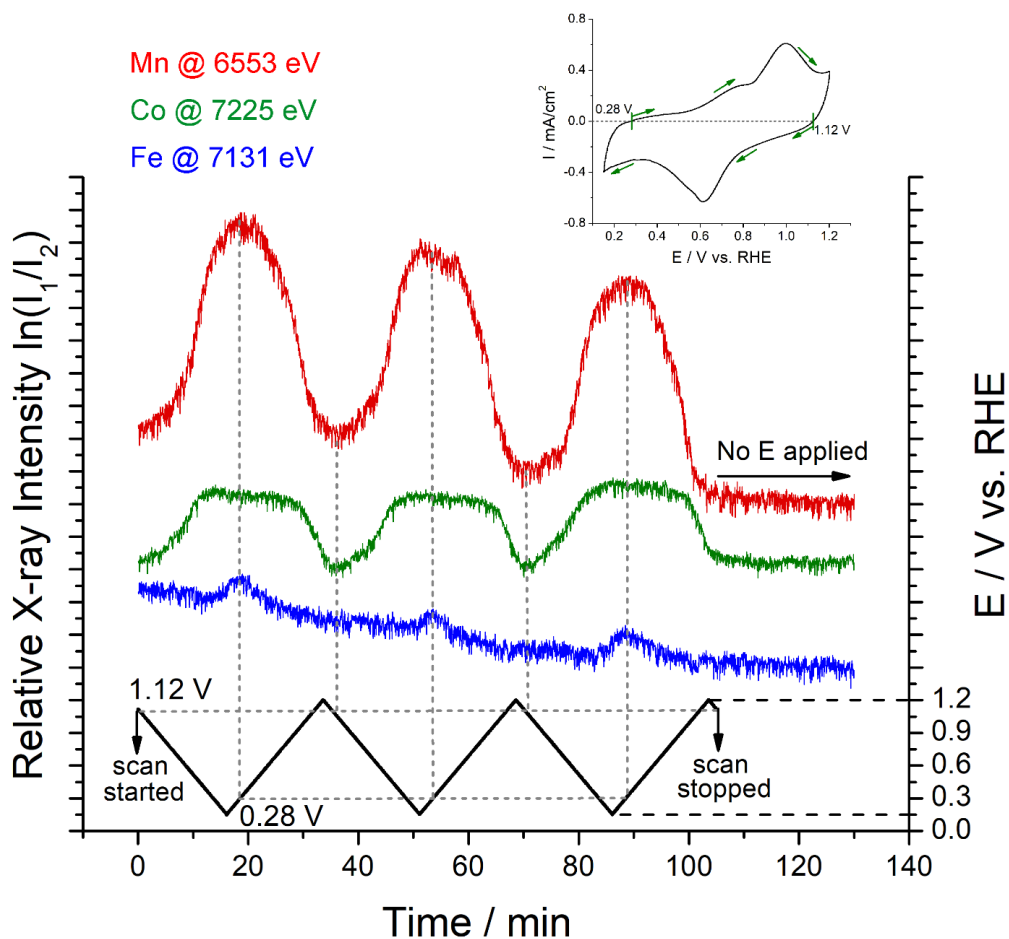


**Figure 5.20.** Periodic changes of the relative X-ray intensities ( $\ln(I_1/I_2)$ ) at 6553 eV (Mn K-edge, red lines), 7225 eV (Co K-edge, green lines) and 7131 eV (Fe K-edge, blue lines), respectively, as a function of the cyclic potential sweep at 1 mV/s from 1.2 to 0.15 V vs. RHE. Intensity variations at 6553, 7225 and 7131 eV reflect the conversion among Mn(IV), Mn(III) and Mn(II), between Co(III) and Co(II), and Fe(III) and Fe(II), respectively. Relative X-ray intensity increases, suggesting a conversion of the metal from higher valence to lower valence as the applied potential goes from 1.2 to 0.15 V, and reach a maximum value at 0.28 V. Concomitantly, the relative X-ray intensity decreased as the applied potential goes from 0.15 to 1.2 V and reach a maximum value at 1.12 V. The upper inset shows the corresponding CV at 1 mV/s over the potential range of 0.15-1.2 V vs. RHE. Oxidation and reduction currents in the CV are divided by two boundary potentials, 0.28V and 1.12 V vs. RHE.

The relative changing X-ray intensities of Mn, Co and Fe following repeating patterns during three continuous cyclic potential scans, suggest a reproducible and stable electrochemical behavior of the three metal active sites under electrochemical operating

conditions. To rigorously exclude other factors, such as X-ray generated photoelectrons, which may result in periodic patterns of X-ray intensity variations, a control experiment was performed by recording the X-ray signal without an applied potential. A stable background in the X-ray intensity indicates that the periodic changes of Mn and Co valences primarily arise from the applied cyclic potential scan.

## 5.9 Conclusion

In Summary, we have performed *Operando* synchrotron-based X-ray absorption spectroscopy (XAS) studies to investigate a synergistic Co-Mn oxide catalyst which exhibits impressive activity towards the ORR in alkaline fuel cells. X-ray absorption near edge structure (XANES) was used to track the dynamic structural changes of Co and Mn under both steady state (constant applied potential) and non-steady state (cyclic voltammetry, CV). Under steady state conditions, both Mn and Co valences decreased at lower potentials, indicating the conversion from Mn (III,IV), Co(III) to Mn(II,III), Co(II). Fast X-ray data acquisition, combined with slow sweep rate in CV, enabled a 3 mV resolution in potential change, approaching non steady state. Changes in the Co and Mn valence states are simultaneous with each other and exhibit periodic patterns that track the cyclic potential sweeps.

Furthermore, *operando* X-ray absorption spectroscopy (XAS) reveals that the superior performance of the trimetallic Mn-Co-Fe spinel oxides originates from the synergistic catalytic effect of Mn and Co, While Fe helps preserve the spinel structure during cycling to enhance durability. We employed *operando* XAS to track the evolution of the oxidation states and the metal-oxygen distances under not only constant applied potentials (steady state) but also during dynamic cyclic voltammetry (CV) (non-

steady state). The periodic conversion between Mn(III, IV)/Co(III) and Mn(II, III)/Co(II) as well as the essentially constant oxidation state of Fe during the CV suggest collaboration efforts among Mn, Co and Fe. Mn and Co serve as the synergistic co-active sites to catalyze the oxygen reduction, apparently resulting in the observed high activity, while Fe works to maintain the integrity of the spinel structure, likely contributing to the remarkable durability of the catalyst.

To the best of our knowledge, this represents the first study, using *operando* XAS, to resolve the synergistic catalytic mechanism of bimetallic and trimetallic oxides towards the ORR. Strategies and insights described herein can provide a promising approach to unveil the reaction mechanism for other multi-metallic electrocatalysts.

### 5.10 References:

1. Abruña, H. D. *Electrochemical Interface: Modern Techniques for In Situ Interface Characterization* VCH: New York, **1991**.
2. Mukerjee, S.; Srinivasan, S.; Soriaga, M. P.; McBreen, J. Role of Structural and Electronic Properties of Pt and Pt Alloys on Electrocatalysts of Oxygen Reduction. *J. Electrochem. Soc.* **1995**, *142*, 1409-1421.
3. Becknell, N.; Kang, Y.; Chen, C.; Resasco, J.; Kornienko, N.; Guo, J.; Markovic, N. M.; Somorjai, G. A.; Stamenkovic, V. R.; Yang, P. Atomic Structure of Pt<sub>3</sub>Ni Nanoframe Electrocatalysts by In Situ X-ray Absorption Spectroscopy. *J. Am. Chem. Soc.* **2015**, *137*, 15817-15824.
4. Friebel, D.; Viswanathan, V.; Miller, D.; Anniyev, T.; Ogasawara, H.; Larsen, A. H.; O'Grady, C. P.; Nørskov, J. K.; Nilsson, A. *J. Am. Chem. Soc.* Balance of Nanostructure and Bimetallic Interactions in Pt Model Fuel Cell Catalysts: In Situ XAS and DFT Study **2012**, *134*, 9664-9671.
5. Erickson, E. M.; Thorum, M. S.; Vasić, R.; Marinković, N. S.; Frenkel, A. I.; Gewirth, A. A.; Nuzzo, R. G. In Situ Electrochemical X-ray Absorption Spectroscopy of Oxygen Reduction Electrocatalysis with High Oxygen Flux. *J. Am. Chem. Soc.* **2012**, *134*, 197.
6. Imai, H.; Izumi, K.; Matsumoto, M.; Kubo, Y.; Kato, K.; Imai, Y. In Situ and Real-Time Monitoring of Oxide Growth in a Few Monolayers at Surfaces of Platinum Nanoparticles in Aqueous Media. *J. Am. Chem. Soc.* **2009**, *131*, 6293-6300.
7. Casalongue, H. S.; Kaya, S.; Viswanathan, V.; Miller, D. J.; Friebel, D.; Hansen, H. A.; Nørskov, J. K.; Nilsson, A.; Ogasawara, H. Direct Observation of the Oxygenated Species during Oxygen Reduction on a Platinum Fuel Cell Cathode. *Nat. Commun.* **2013**, *4*, 2817.

8. Gorlin, Y.; Lassalle-Kaiser, B.; Benck, J. D.; Gul, S.; Webb, S. M.; Yachandra, V. K.; Yano, J.; Jaramillo, T. F. In Situ X-ray Absorption Spectroscopy Investigation of a Bifunctional Manganese Oxide Catalyst with High Activity for Electrochemical Water Oxidation and Oxygen Reduction. *J. Am. Chem. Soc.* **2013**, 135, 8525-8534.
9. Risch, M.; Ringleb, F.; Kohlhoff, M.; Bogdanoff, P.; Chernev, P.; Zaharieva, I.; Dau, H. Water Oxidation by Amorphous Cobalt-Based Oxides: In situ Tracking of Redox Transitions and Mode of Catalysis. *Energy Environ. Sci.* **2015**, 8, 661.
10. Kanan, M. W.; Yano, J.; Surendranath, Y.; Dincă, M.; Yachandra, V. K.; Nocera, D. G. Structure and Valency of a Cobalt–Phosphate Water Oxidation Catalyst Determined by in Situ X-ray Spectroscopy. *J. Am. Chem. Soc.* **2010**, 132, 13692-13701.
11. Castro, P.; Vago, E.; Calvo, E. Surface Electrochemical Transformations on Spinel Iron Oxide Electrodes in Aqueous Solutions. *J. Chem. Soc. Faraday Trans.* **1996**, 92, 3371.
12. Zhou, Y.; Xi, S.; Wang, J.; Sun, S.; Wei, C.; Feng, Z.; Du, Y.; Xu, Z. J. Revealing the Dominant Chemistry for Oxygen Reduction Reaction on Small Oxide Nanoparticles. *ACS Catal.*, **2018**, 8, 673–677.
13. Cliff, G.; Lorimer, G. W. The quantitative analysis of thin specimens. *J. Microsc.* **1975**, 103, 203.
14. Bearden, J. A. X-ray wavelengths. *Rev. Mod. Phys.* **1967**, 39, 78.

## CHAPTER 6

### Non-Precious ORR Electrocatalysts beyond Spinel Oxides\*

#### 6.1 Introduction

In previous chapters 2-5, we showed that Mn-Co spinel oxides exhibited a promising ORR activity in RDE measurements and achieved a high peak power density of over 1 W/cm<sup>2</sup> in membrane electrode assembly (MEA) measurements.

In the first part of this chapter, we went one step further to explore Mn-Co bimetallic oxides with different crystal structures, in order to better understand the catalyst structure and the observed ORR activity. We discovered a new compound, MnCo<sub>2</sub>O<sub>3</sub>, or MnO(CoO)<sub>2</sub>/C, with a rock-salt-type structure, through a partial reduction of MnCo<sub>2</sub>O<sub>4</sub>/C under NH<sub>3</sub> treatment. MnCo<sub>2</sub>O<sub>3</sub>/C that exhibited an enhanced ORR activity, relative to MnCo<sub>2</sub>O<sub>4</sub>. The microstructure and chemical environment of newly discovered catalysts were examined by STEM and high-energy-resolution ELNES, a method intensively used for spinel oxides in chapter 2.

In the second part of this chapter, we aimed to develop a new family of non-precious catalysts, metal nitrides. Bulk metal oxides, such as cobalt and manganese oxides, have a low intrinsic electronic conductivity due to their large band gap (> 2 eV) and may only achieve a semi-conductor level conductivity even when they present as small nanoparticles with some levels of defects on carbon supports, which could partially mitigate their insulating character.<sup>1,2</sup>

---

\*Reproduced and modified with permission from the following publications

**Yao Yang**, Rui Zeng, Yin Xiong, Francis DiSalvo, Héctor Abruña, Rock-salt-type MnCo<sub>2</sub>O<sub>3</sub>/C as Efficient Oxygen Reduction Electrocatalysts for Alkaline Fuel Cells. *Chem. Mater.* 2019, 31, 9331. © ACS

**Yao Yang**, Rui Zeng, et al. Francis J. DiSalvo, Héctor Abruña. Cobalt-Based Nitride-Core Oxide-Shell Oxygen Reduction Electrocatalysts. *J. Am. Chem. Soc.* 2019, 141, 19241. ©ACS

It is thus important to develop novel conductive metal-based catalysts for the ORR. Benefiting from their conductive nature and, often, metallic behavior,<sup>3</sup> transition metal nitrides have emerged as a new family of electrocatalysts for the ORR. Previous reports include early 3d transition metal nitrides (TiN, VN, CrN),<sup>4</sup> Mn,<sup>5</sup> Co,<sup>6</sup> Fe,<sup>7</sup> Ni-based nitrides,<sup>8,9</sup> Cu<sub>3</sub>N,<sup>10</sup> MoN<sup>6</sup> and other bimetallic nitrides.<sup>4</sup> However, the reported activities are at best modest ( $E_{1/2} < 0.8$  V vs. reversible hydrogen electrode, RHE) and generally far lower than that of Pt/C. Cobalt-based nitrides, previously investigated mainly as magnetic materials,<sup>11</sup> have been reported to exhibit promising performance in a wide range of energy-related applications, like the oxygen evolution reaction (OER),<sup>3,12,13</sup> metal-air batteries<sup>13,14</sup> and supercapacitors.<sup>15</sup> Nevertheless, there have been scarce studies of using cobalt-based nitrides as effective electrocatalysts for the ORR in alkaline fuel cells. In this work, we have prepared a series of cobalt nitrides loaded on porous carbon supports (Co<sub>2</sub>N/C, Co<sub>3</sub>N/C and Co<sub>4</sub>N/C) by a facile nitridation process in NH<sub>3</sub> at controlled temperatures. Co<sub>4</sub>N/C exhibited the highest ORR activity among the three types of cobalt nitrides studied, an eight-fold improvement in mass activity at 0.85 V, when compared to cobalt oxide, Co<sub>3</sub>O<sub>4</sub>/C. The superior performance was ascribed to the formation of a conductive nitride core surrounded by a naturally formed thin active oxide shell (about 2 nm). The conductive nitride core effectively mitigated the low conductivity of the metal oxide catalysts and the thin oxide shell on the surface provided the active sites for the ORR. Strategies developed herein can represent a promising approach to for the design of other novel metal nitrides as electrocatalysts for fuel cells.

## 6.2 Experimental Methods

**Synthesis of Rock-salt-type  $\text{MnCo}_2\text{O}_3/\text{C}$ :**  $\text{Mn}(\text{Ac})_2 \cdot 4\text{H}_2\text{O}$  and  $\text{Co}(\text{Ac})_2 \cdot 4\text{H}_2\text{O}$ , were dissolved in 15 mL deionized (DI) water and sonicated for 15 min. 500  $\mu\text{L}$  concentrated  $\text{NH}_3 \cdot \text{H}_2\text{O}$  were diluted in 5 mL DI water and added to the metal precursor solution dropwise under vigorous stirring at 1200 rpm. The pH of the formed metal- $\text{NH}_3$  complex solution was tested and controlled to be around 11. Ethanol (20 mL) was later added to the metal- $\text{NH}_3$  complex solution with an  $\text{EtOH}/\text{H}_2\text{O}$  volume ratio of 1:1. Ketjen Black (KB) with a BET surface area of 900  $\text{m}^2/\text{g}$  was added to the resulting suspension/solution, which was kept stirring at 1200 rpm and 60  $^\circ\text{C}$  for 12 h. The solution was then transferred into a 50 mL autoclave for hydrothermal reaction at 150  $^\circ\text{C}$  for 3h.  $\text{Co}_3\text{O}_4$  and  $\text{MnCo}_2\text{O}_4$  supported on carbon (40 wt.%) were separated from the residual solution using a centrifuge at 6000 rpm and washed with  $\text{EtOH}/\text{H}_2\text{O}$  (vol. 1:1) three times and oven dried at 80  $^\circ\text{C}$  for 6h. Rock-salt-type  $\text{CoO}/\text{C}$  and  $\text{MnCo}_2\text{O}_3/\text{C}$  were formed by treating the as-synthesized  $\text{Co}_3\text{O}_4/\text{C}$  and  $\text{MnCo}_2\text{O}_4/\text{C}$  in  $\text{NH}_3$  at 300  $^\circ\text{C}$  for 3h with a temperature ramping rate of 5  $^\circ\text{C}/\text{min}$ .  $\text{NH}_3$  treatment at higher temperatures would introduce metallic or metal nitride impurity phases and  $\text{H}_2$  treatment at 300  $^\circ\text{C}$  would lead to the formation of metallic Co.  $\text{MnCo}_2\text{O}_3$  NPs with no carbon support were prepared from  $\text{MnCo}_2\text{O}_4$  NPs with no carbon support, which was synthesized using the same hydrothermal procedures except without adding carbon during the synthesis.

**Synthesis of Cobalt Nitrides ( $\text{Co}_2\text{N}$ ,  $\text{Co}_3\text{N}$  and  $\text{Co}_4\text{N}$ ):** In a typical synthesis, 95.18 mg  $\text{CoCl}_2 \cdot 6\text{H}_2\text{O}$  and 112.15 mg of hexamethylenetetramine (HMT) were dissolved in a 20 mL mixture of deionized water and ethanol (volume ratio of 1:1) in a 50 mL conical flask under magnetic stirring to form a transparent pink solution. 94.29 mg high surface

carbon Ketjen Black (HSC KB) were then added to the solution and sonicated for 30 min. The resulting suspension was then aged in an oil bath at 90 °C with a stirring rate of 900 rpm for 1.5 h. The precursor was separated from the solution by centrifuge at 7000 rpm for 10 min and washed with deionized water and ethanol three times. The sample was then dried in oven at 60 °C for 2 h. Cobalt nitrides ( $\text{Co}_2\text{N}/\text{C}$ ,  $\text{Co}_3\text{N}/\text{C}$  and  $\text{Co}_4\text{N}/\text{C}$ ) were formed by treating the as-synthesized precursor in a  $\text{NH}_3$  atmosphere at various temperatures, for 2 h with a temperature ramping rate of 8 °C/min. For samples used for electrochemical tests, the ammonia treatment was extended to 24 h. The unsupported  $\text{Co}_4\text{N}$  was synthesized at 460 °C for 24h and formed a mechanical mixture with HSC carbon by ball milling. An acid wash was performed by soaking  $\text{Co}_4\text{N}/\text{C}$  in 0.5 M  $\text{H}_2\text{SO}_4$  at 60 °C for 10 h.

Electrochemical measurements, STEM, EELS and XRD adapted same procedures in Chapter 2. Specific surface area and pore size distributions were analyzed based on Brunauer–Emmett–Teller (BET) and Barrett–Joyner–Halenda (BJH) methods from the  $\text{N}_2$  adsorption-desorption isotherms acquired at -195 °C (liquid  $\text{N}_2$ ) in a Micromeritics ASAP2020 instrument. XPS spectra were acquired using a Surface Science Instruments SSX-100 with an operating pressure of  $2 \times 10^{-9}$  Torr. Monochromatic Al  $K\alpha$  X-rays (1486.6 eV) with 1 mm diameter beam size were used. Photoelectrons were collected at a 55° emission angle. A hemispherical analyzer determined electron kinetic energy, using a pass energy of 150 V for wide/survey scans, and 50 V for high resolution scans.

### **6.3 Rock-Salt-Type $\text{MnCo}_2\text{O}_3/\text{C}$ derived from $\text{MnCo}_2\text{O}_4/\text{C}$ under $\text{NH}_3$ Treatment**

$\text{Co}_3\text{O}_4/\text{C}$  and  $\text{MnCo}_2\text{O}_4/\text{C}$  with cubic spinel structures were first synthesized through a facile hydrothermal method. Powder XRD patterns of  $\text{Co}_3\text{O}_4/\text{C}$  exhibited the typical

features of cubic spinel oxides with a major (311) peak (PDF # 01-071-1178) (Fig. 6.1a). The domain size of the  $\text{Co}_3\text{O}_4$  nanoparticles (NPs) was estimated to be 18 nm based on the Scherrer equation.  $\text{Co}_3\text{O}_4/\text{C}$  was then partially reduced to  $\text{CoO}/\text{C}$  under mild  $\text{NH}_3$  reduction at 300 °C for 3h (referred to  $\text{CoO}/\text{C-N300}$ ). The resulting  $\text{CoO}/\text{C-N300}$  exhibited a single-phase XRD pattern as the  $\text{CoO}$  XRD reference (PDF # 01-076-1802) with a slightly smaller domain size of 14 nm. As a fingerprint of the chemical environment of Co, ELNES spectra of  $\text{CoO}/\text{C-N300}$  exhibited nearly identical features as the  $\text{CoO}$  reference, indicating  $\text{CoO}/\text{C-N300}$  shared the same chemical environment of Co(II) as  $\text{CoO}$  (Fig. 6.1b). Comparisons in crystal structure of  $\text{Co}_3\text{O}_4$  and  $\text{CoO}$  are demonstrated in Fig. 6.2. During  $\text{NH}_3$  treatment, some of the oxygen atoms in the spinel  $\text{Co}_3\text{O}_4$  were removed to form the rock-salt-type  $\text{CoO}$ . Consequently, the coordination numbers (CN) of Co changed from the co-existence of tetrahedral  $[\text{CoO}_4]$  and octahedral  $[\text{CoO}_6]$  in  $\text{Co}_3\text{O}_4$  to all octahedral  $[\text{CoO}_6]$  in  $\text{CoO}$ .

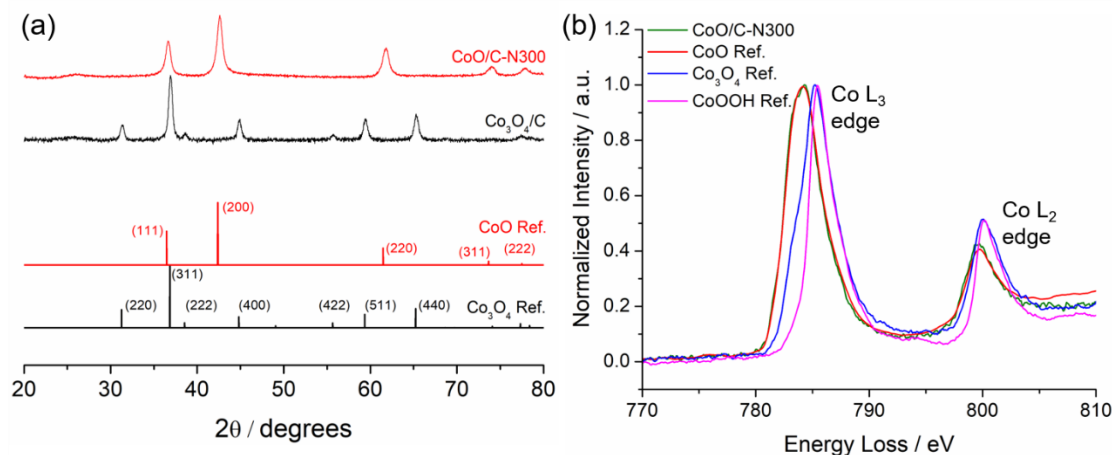


**Figure 6.1.** (a) Powder XRD patterns of  $\text{CoO}/\text{C}$  synthesized from  $\text{Co}_3\text{O}_4$  under  $\text{NH}_3$  treatment at 300 °C for 3h and standard XRD patterns of  $\text{CoO}$  (PDF # 01-071-1178) and  $\text{Co}_3\text{O}_4$  (PDF # 01-076-1802). N300 represents  $\text{NH}_3$  treatment at 300 °C. (b) ELNES spectra of  $\text{CoO}/\text{C-N300}$  compared to reference Co oxides,  $\text{CoO}$ ,  $\text{Co}_3\text{O}_4$  and  $\text{CoOOH}$ . The nearly identical features of  $\text{CoO}/\text{C-N300}$  and  $\text{CoO}$  Ref. (green and red lines) confirm that the synthesized  $\text{CoO}/\text{C-N300}$  nanoparticles have the same chemical

environment of Co as Co(+2) in rock-salt-type CoO.

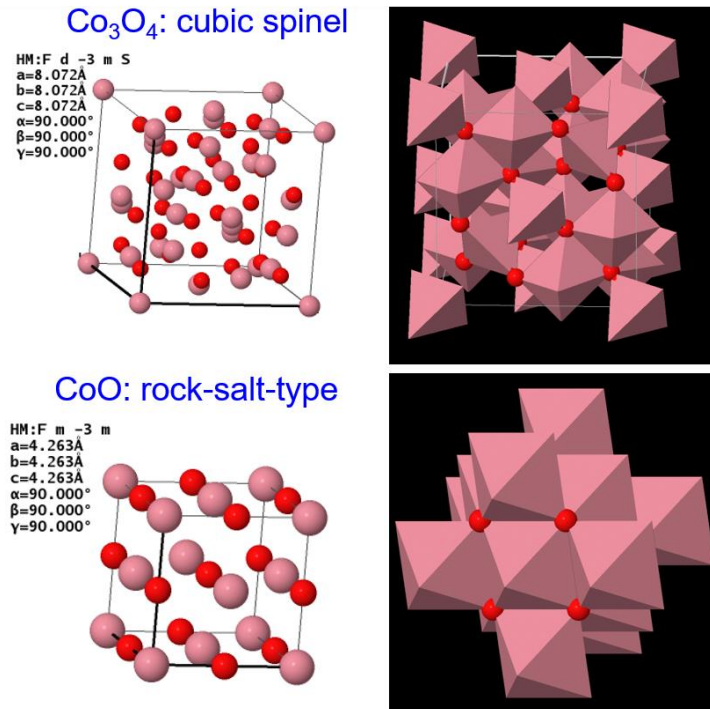


**Figure 6.2.** Crystal structures of spinel-type Co<sub>3</sub>O<sub>4</sub> and rock-salt-type CoO. Co<sub>3</sub>O<sub>4</sub> has Co with two different coordination numbers, Co(II) in tetrahedral sites (CN=4) and Co(III) in octahedral sites (CN=6). CoO has Co all in tetrahedral coordination (CN=4). Pink and Red atoms are Co and O, respectively. Crystal models were built based on Co<sub>3</sub>O<sub>4</sub> (PDF # 01-076-1802) and CoO (PDF # 01-071-1178).

Following the successful synthesis of CoO/C NPs, MnCo<sub>2</sub>O<sub>4</sub>/C spinel oxides were synthesized and used as precursors for further NH<sub>3</sub> treatment at 300 °C. As shown in Fig. 6.3a, Mn-Co bimetallic oxides exhibited a similar rock-salt-type structure to the CoO reference with a major (200) peak. Thus, we propose that this new compound has a chemical formula of MnO(CoO)<sub>2</sub>/C, or simply MnCo<sub>2</sub>O<sub>3</sub>/C. It has been reported that CoO and MnO could form a miscible solid solution, bulk-phase Co<sub>x</sub>Mn<sub>1-x</sub>O (0 < x < 1) under high-temperature (1100 °C) sintering.<sup>16</sup> The domain sizes of the nanoparticles were calculated to be 15 nm for MnCo<sub>2</sub>O<sub>4</sub>/C and 13 nm for MnCo<sub>2</sub>O<sub>3</sub>/C, respectively. The chemical composition of MnCo<sub>2</sub>O<sub>3</sub>/C was determined by X-ray energy-dispersive spectroscopy (EDX) (Fig. 6.3b), based on the Cliff-Lorimer equation.<sup>17</sup> MnCo<sub>2</sub>O<sub>3</sub>/C exhibited a relative content of 33.1 at.% Mn and 66.9 at.% Co, respectively, (relative error: 0.2% was defined as one standard deviation), which matched the theoretical

values of 33.3% and 66.6% in  $\text{MnCo}_2\text{O}_3$ , respectively.

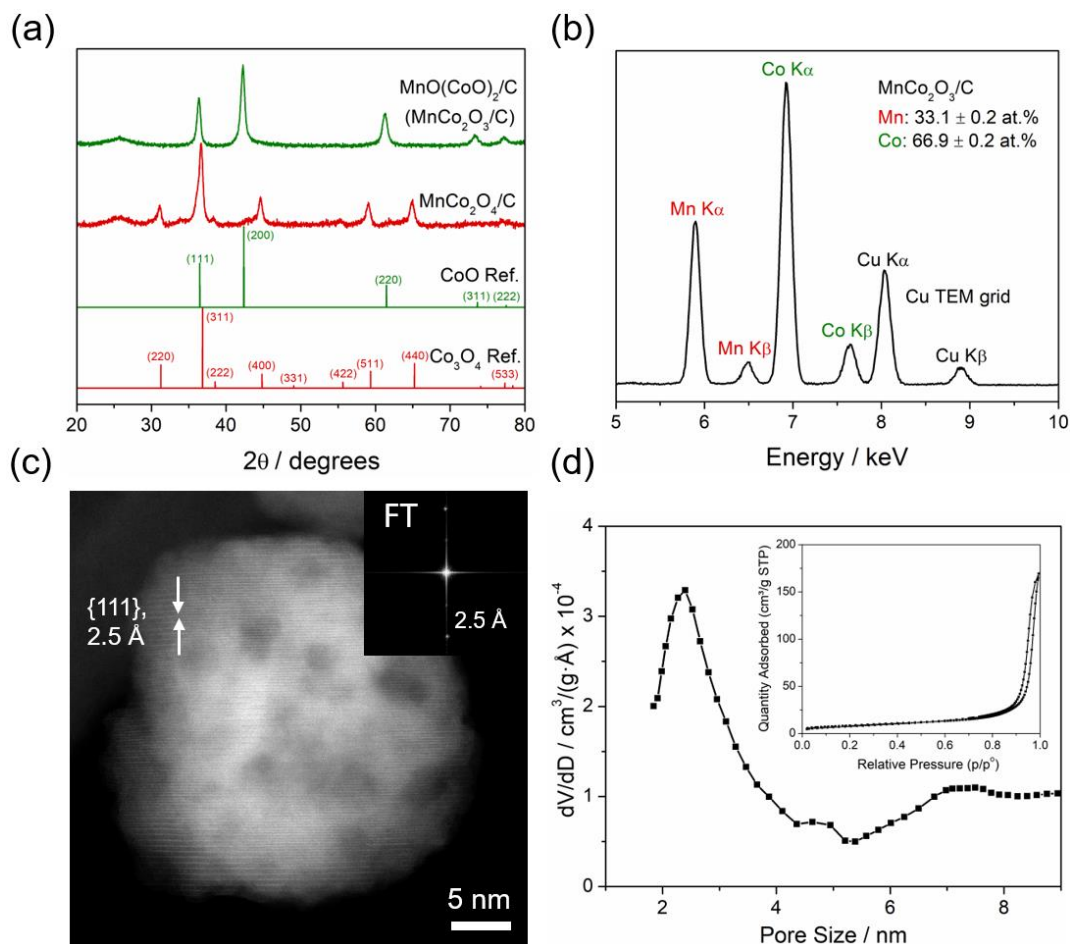


**Figure 6.3.** (a) Powder XRD patterns of  $\text{MnCo}_2\text{O}_3/\text{C}$ ,  $\text{MnCo}_2\text{O}_4/\text{C}$  compared to standard XRD patterns of  $\text{CoO}$  and  $\text{Co}_3\text{O}_4$ . (b) TEM-EDX spectrum of  $\text{MnCo}_2\text{O}_3/\text{C}$ , showing the relative Co/Mn atomic ratio of 2:1. (c) Atomic-scale STEM image of  $\text{MnCo}_2\text{O}_3/\text{C}$  with {111} d-spacings and the corresponding Fourier transform (FT). (d) Differential pore volume distribution ( $dV/dD$  profile) as a function of pore size, of  $\text{MnCo}_2\text{O}_3$  without carbon support and the corresponding  $\text{N}_2$  adsorption-desorption BET isotherm (inset).

Since  $\text{NH}_3$  was used as a mild reducing agent, it is important to know whether any N was introduced into the product during the synthesis. As shown in Fig. 6.4, no evidence of a N signal from  $\text{MnCo}_2\text{O}_3/\text{C}$  was found to be above the detection limit of EDX, electron energy loss spectroscopy (EELS) and X-ray photoelectron spectroscopy (XPS) characterizations.

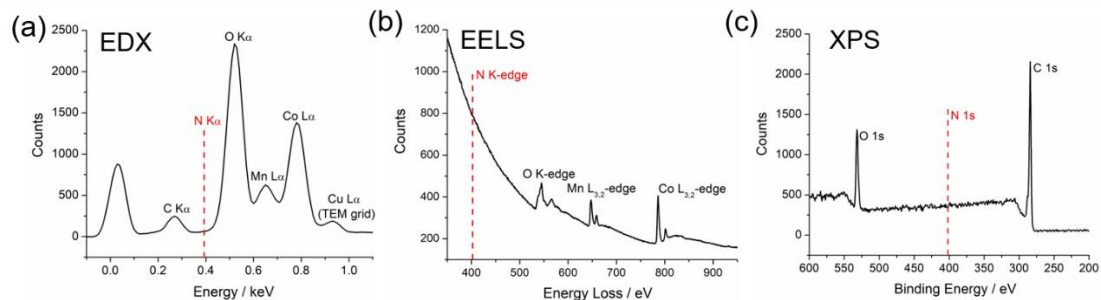


**Figure 6.4.** (a-c) EDX, EELS and XPS spectra of  $\text{MnCo}_2\text{O}_3/\text{C}$ . No evidence of a N signal above the detect limitation of techniques, was found here.

The morphology and crystal structure of  $\text{MnCo}_2\text{O}_3/\text{C}$  were examined using aberration-corrected high-angle annular dark-field scanning transmission electron microscopy (HAADF-STEM) imaging at 100 keV (Nion UltraSTEM).  $\text{MnCo}_2\text{O}_3/\text{C}$  exhibited a particle size of 30-50 nm embedded in a Ketjen black (KB) carbon matrix, indicating that the majority of particles have multiple sub-domains, given an XRD domain size of about 13 nm. Atomic-scale STEM images of individual  $\text{MnCo}_2\text{O}_3$  nanoparticles showed single-crystal features with d-spacings of 2.5 Å, as indicated by the diffraction spots in the Fourier transform, which are same as the {111} d-spacings of CoO (2.46 Å) within the STEM spatial resolution (Fig. 6.3c). The lattice images of  $\text{MnCo}_2\text{O}_3$  show a non-uniform image intensity, suggesting the existence of nm-scale mesoporous morphology, which was also found in other  $\text{MnCo}_2\text{O}_3$  NPs (Fig. 6.5).

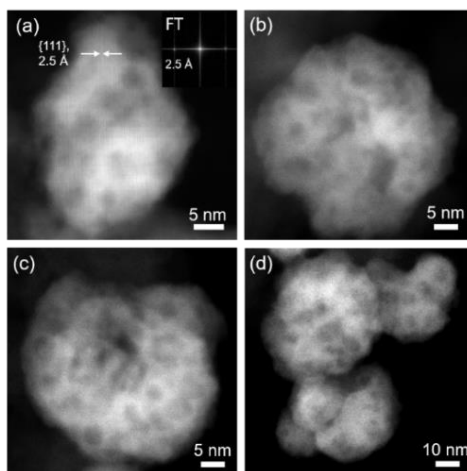


**Figure 6.5.** A collection of STEM images of  $\text{MnCo}_2\text{O}_3/\text{C}$  nanoparticles (NPs). Variation of image intensity suggests  $\text{MnCo}_2\text{O}_3$  NPs may have micropores and mesopores with pore sizes of 2-6 nm.

#### 6.4 Porosity and Microstructure of MnCo<sub>2</sub>O<sub>3</sub>/C

To quantify the porosity of MnCo<sub>2</sub>O<sub>3</sub> NPs, a N<sub>2</sub> adsorption-desorption test was performed on MnCo<sub>2</sub>O<sub>3</sub> without KB carbon support since the larger surface area of carbon (900 m<sup>2</sup>/g) would likely dominate the measured surface area in the catalyst/carbon composite. The specific surface area of MnCo<sub>2</sub>O<sub>3</sub> NPs was estimated to be 30 ± 0.1 m<sup>2</sup>/g by the Brunauer-Emmett-Teller (BET) method (Fig. 6.3d, inset). The pore size distribution of MnCo<sub>2</sub>O<sub>3</sub>, derived from the Barrett-Joyer-Halenda (BJH) method, suggested a narrow size distribution with an average pore size of 2.4 nm (Fig. 6.3d), which was consistent with the pore size in STEM images (Figs. 6.3c and 6.5). MnCo<sub>2</sub>O<sub>3</sub>/C exhibited a similar pore size distribution as the KB support which had undergone the same hydrothermal treatment and subsequent annealing in NH<sub>3</sub> gas. It indicates that MnCo<sub>2</sub>O<sub>3</sub> did not significantly change the porosity of KB. The spinel precursor, MnCo<sub>2</sub>O<sub>4</sub>, was found to have a similar BET surface area of 34.1 ± 0.3 m<sup>2</sup>/g, indicating no significant changes in the surface area during NH<sub>3</sub> treatment. (Fig. 6.6).

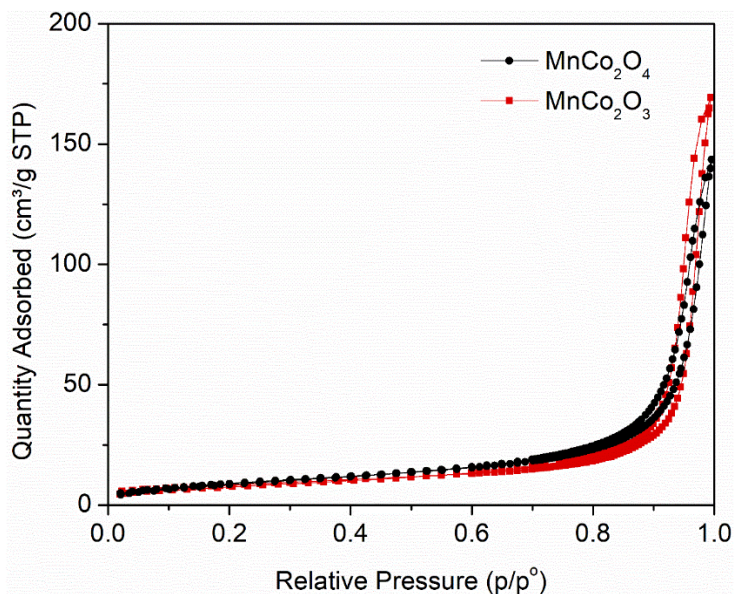


**Figure 6.6.** BET N<sub>2</sub> adsorption-desorption isotherms of MnCo<sub>2</sub>O<sub>4</sub> and MnCo<sub>2</sub>O<sub>3</sub> without KB carbon support. BET surface areas of MnCo<sub>2</sub>O<sub>4</sub> and MnCo<sub>2</sub>O<sub>3</sub> were calculated to be 34 and 30 m<sup>2</sup>/g, respectively.

The crystal structure of MnCo<sub>2</sub>O<sub>3</sub> was then directly visualized using atomic-scale STEM imaging and EELS mapping. As shown in Fig. 6.7a, MnCo<sub>2</sub>O<sub>3</sub> exhibited atom

columns with two perpendicular d-spacings of 4.3 and 3.0 Å on the [110] zone axis, which were consistent with the theoretical values of 4.26 and 3.01 Å, based on the crystal model of CoO (Fig. 6.7f). The [110] zone axis is proportional to the lattice plane indicated by the dashed rectangles in the unit cell of CoO (Fig. 6.7e). The d-spacing of 3.01 Å can be obtained by dividing the lattice parameter, 4.26 Å by  $\sqrt{2}$  due to a projection angle of 45°. The magnified image in Fig. 6.7c showed the characteristic hexagonal symmetry on the [110] zone axis of CoO. The corresponding fourier transform (FT) in Fig. 6.7d displayed the hexagonal arrangements of diffraction spots with {111} d-spacings of 2.5 Å, which matched well the theoretical values of 2.46 Å in the crystal model in Fig. 6.7f. Besides the imaging analysis on crystal structures, atomic-scale EELS mapping was employed to extract chemical composition using metal L<sub>3</sub> edges. An atomic-scale EELS map of Mn exhibited a clear layered structure, indicating the successful incorporation of Mn into the Co-based rock-salt-type structures at the atomic scale (Fig. 6.7b).

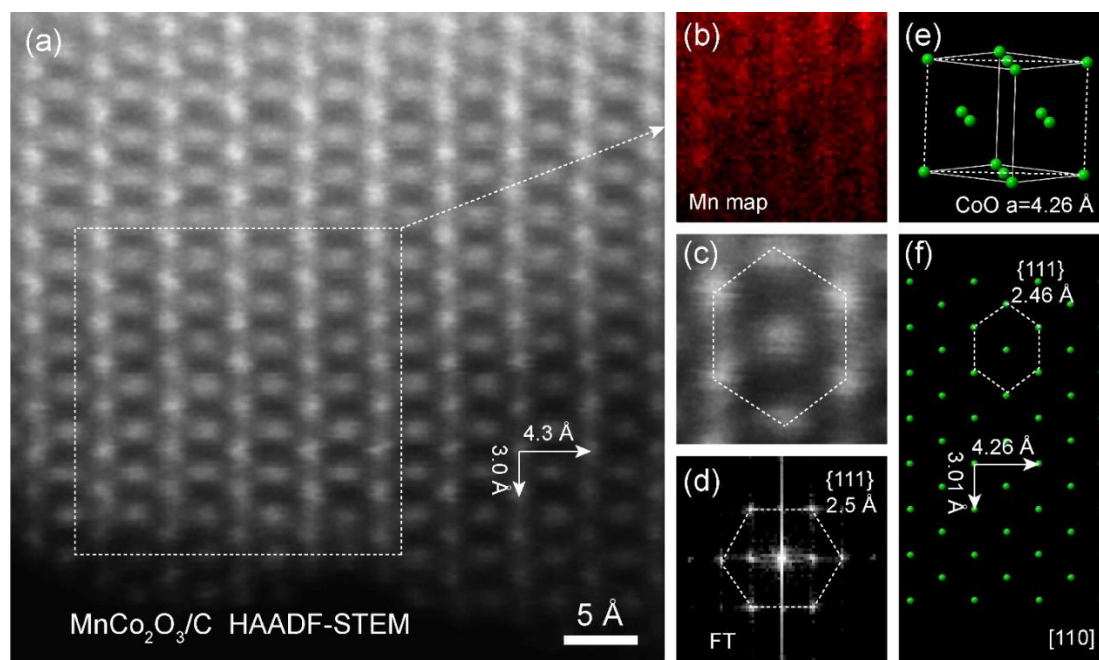


**Figure 6.7.** Atomic-scale HAADF-STEM image of rock-salt-type  $\text{MnCo}_2\text{O}_3/\text{C}$ . (a) Overall lattice image of  $\text{MnCo}_2\text{O}_3$  on the zone axis of [110]. (b) Atomic-scale EELS elemental map of Mn acquired from the dashed box in (a). (c) Magnified single unit cell of  $\text{MnCo}_2\text{O}_3$  showing the typical hexagonal symmetry. (d) Fourier transform (FT) of lattice image in (a) showing the corresponding hexagonal symmetry with {111} d-

spacing (2.5 Å). (e) Unit cell of rock-salt-type CoO (lattice parameter,  $a = 4.26$  Å), based on PDF # 01-071-1178. Dashed lines indicate the lattice planes proportional to the [110] zone axis. (f) 2D projection of the crystal model exhibiting the hexagonal symmetry with {111} d-spacings of 2.46 Å. Theoretical lattice spacings of 4.26 and 3.01 Å are consistent with experimental values of 4.3 and 3.0 Å in (a).

The chemical composition was investigated using electron energy loss spectroscopy (EELS). Figs. 6.8a-c present the STEM image of one  $\text{MnCo}_2\text{O}_3$  nanoparticle and the corresponding EELS elemental maps of Mn in red and Co in green. The composite map of Mn vs. Co in Fig. 6.8d suggests a Co-rich core with a thin Mn-rich shell of 1-3 nm, which was further evidenced by EELS maps of other  $\text{MnCo}_2\text{O}_3$  NPs (Fig. 6.9).

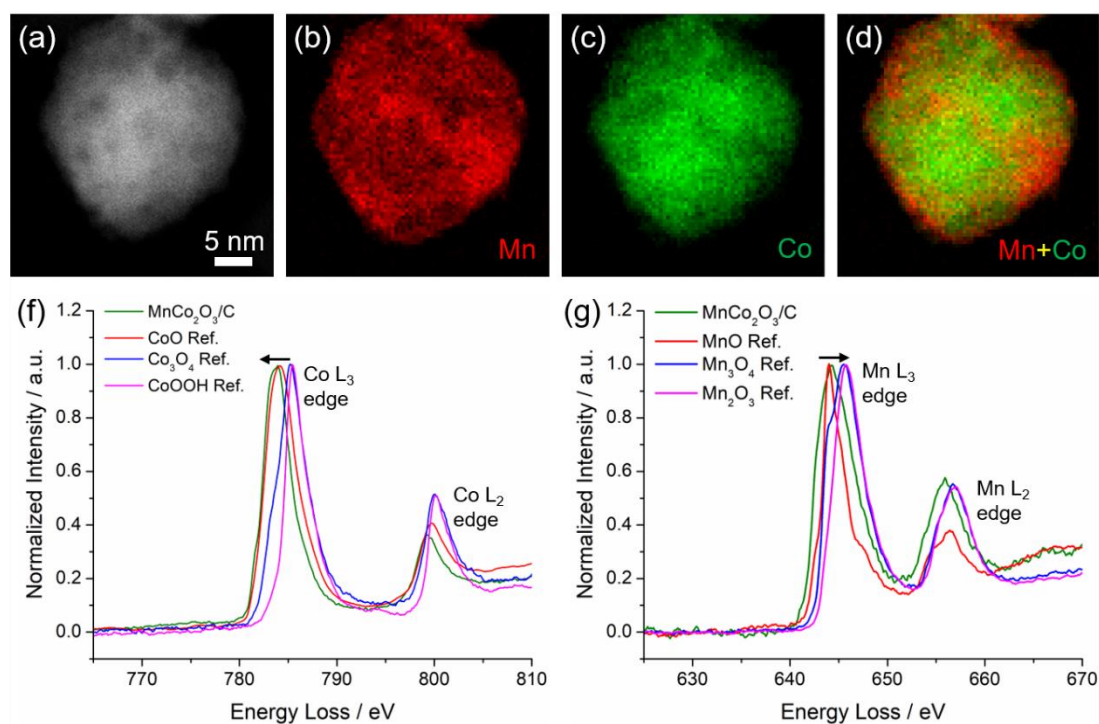


**Figure 6.8.** STEM-EELS elemental mapping and fine spectroscopic analysis of  $\text{MnCo}_2\text{O}_3/\text{C}$ . (a-d) STEM images of one  $\text{MnCo}_2\text{O}_3$  nanoparticle and the corresponding EELS elemental maps of Mn (red), Co (green) and composite map of Mn vs. Co. (f) Electron energy-loss near-edge structure (ELNES) of Co  $L_{3,2}$  edges of  $\text{MnCo}_2\text{O}_3/\text{C}$  and reference Co oxides, CoO,  $\text{Co}_3\text{O}_4$  and CoOOH. (g) ELNES spectra of Mn  $L_{3,2}$  edges of  $\text{MnCo}_2\text{O}_3/\text{C}$  and reference Mn oxides, MnO,  $\text{Mn}_3\text{O}_4$ ,  $\text{Mn}_2\text{O}_3$ . Black arrows in (f) and (g) indicate the negative and positive shift of Co and Mn  $L_3$  edges, relative to CoO and MnO references, respectively.

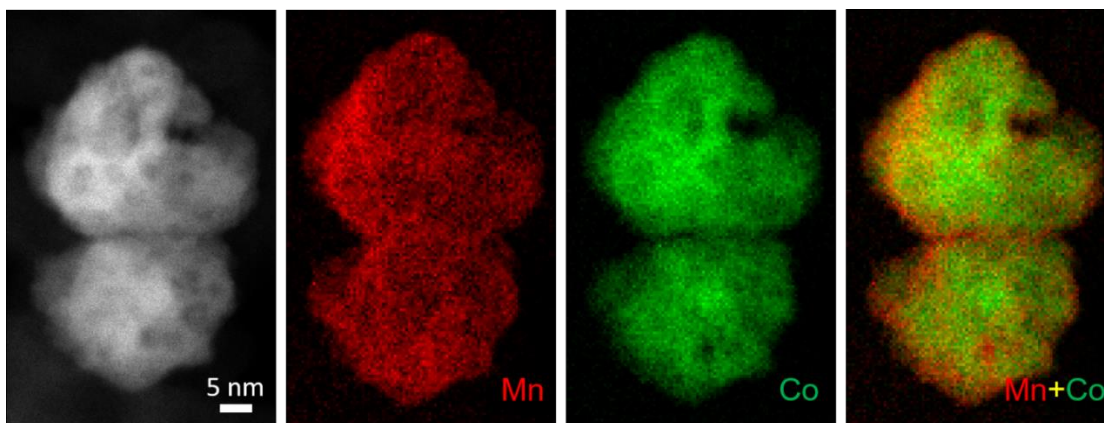


**Figure 6.9.** STEM images of  $\text{MnCo}_2\text{O}_3/\text{C}$  and the corresponding EELS elemental maps of Mn (red) and Co (green). Composite map of Mn vs. Co on the right side suggest a thin Mn-shell of 1-3 nm on the surface.

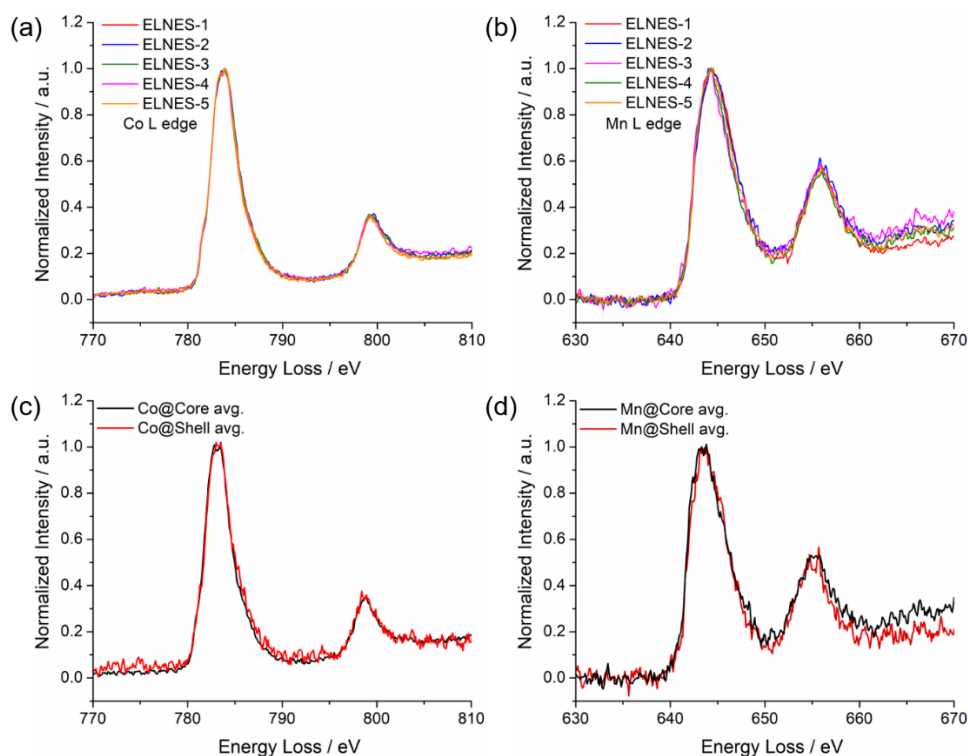


**Figure 6.10** (a-b) fine EELS (ELNES) spectra of Co and Mn  $L_{3,2}$  edges of  $\text{MnCo}_2\text{O}_3/\text{C}$  at five different regions on TEM grids. The highly reproducible profiles of both Co and Mn L edges indicate the high reliability of peak position and peak ratios of  $L_3$  to  $L_2$ . (c-d) average ELNES spectra of Co and Mn  $L_{3,2}$  edges in the core and shell section of the nanoparticle in Fig. 6.8. Features of Co and Mn remain basically the same in the core and shell, indicating a homogenous valence distribution despite of the heterogenous elemental distribution.

The electron energy-loss near-edge structure (ELNES) analysis offers microstructural analysis with atomic-scale spatial resolution and high energy resolution (0.5 eV) simultaneously. ELNES serves as a “fingerprint” to probe the local electronic structure, i.e., density of unfilled states (unfilled DOS) above the Fermi level ( $E_F$ ), which is particularly sensitive to the local atomic environment, such as valence state, chemical bonding and coordination environment. ELNES spectra of Co and Mn L edges were aligned against the zero loss peak (ZLP) and found to have high reproducibility among five different regions on the TEM grids. Given the existence of a thin Mn shell in  $\text{MnCo}_2\text{O}_3/\text{C}$ , ELNES spectra of Co and Mn in core and shell sections were extracted separately from spectrum images to identify any inhomogeneities of electronic structures between core and shell. As shown in Fig. 6.10, Co and Mn in core and shell sections shared nearly the same features in ELNES spectra, indicating a homogenous local valence distribution despite the heterogenous elemental distribution with Mn-rich shell.

To further identify the valence state of active sites of the electrocatalysts, ELNES spectra of  $\text{MnCo}_2\text{O}_3/\text{C}$  were compared to Co and Mn reference oxides (Figs. 6.8f-g). Co and Mn  $L_3$  edges of  $\text{MnCo}_2\text{O}_3/\text{C}$  exhibited similar features to CoO and MnO references (green and red lines in Figs. 6.8f-g) and were distinct from the ELNES spectra of  $\text{Co}_3\text{O}_4(\text{II,III})$ ,  $\text{Mn}_3\text{O}_4(\text{II,III})$ ,  $\text{CoOOH}(\text{III})$  and  $\text{Mn}_2\text{O}_3(\text{III})$ . It has been suggested that Co and Mn in  $\text{MnCo}_2\text{O}_3/\text{C}$  share the same rock-salt-type structures as CoO(II) and MnO(II), respectively. Furthermore, Co  $L_3$  edge showed a slightly negative shift, relative to CoO(II), while the Mn  $L_3$  edge had a slightly positive shift, relative to MnO(II). This symmetrical spectra shift indicated a local charge transfer from Mn to Co and a possible synergistic effect between the two of them, serving as co-active sites, which is consistent with our observation on Co-Mn spinel oxides using *operando* X-ray absorption spectroscopy (XAS) in Chapter 5. Besides the relative peak position, the intensity ratio of  $L_2/L_3$  edges also reveals the covalency of metal-oxygen bonds. A high  $L_2/L_3$  ratio indicates a more covalent bond, as shown by the difference between CoO(II) and CoOOH(III) and between MnO(II) and  $\text{Mn}_2\text{O}_3(\text{III})$  (Figs. 6.8f-g). Co in  $\text{MnCo}_2\text{O}_3/\text{C}$  exhibited an even lower  $L_2/L_3$  ratio than CoO(II) while Mn in  $\text{MnCo}_2\text{O}_3/\text{C}$  showed a

much higher  $L_2/L_3$  ratio than MnO (II), suggesting a less covalent (more ionic) Co-O bond and symmetrically a more covalent Mn-O, relative to CoO and MnO, respectively. Apart from the metal L edges, oxygen K edge can also provide a complementary picture of the metal-oxygen binding environment. The first and second peaks in ELNES spectra of the O K-edge represent the O-2p character in metal partially filled 3d bands and empty 4s,p bands, respectively (Fig. 6.11). The O K edge of  $\text{MnCo}_2\text{O}_3/\text{C}$  resembled the features of CoO and MnO rather than other reference oxides with higher valence (Figs. 6.11a-b). More specifically, the O K edge of  $\text{MnCo}_2\text{O}_3/\text{C}$  is more similar to CoO than MnO since Co is the majority metal in  $\text{MnCo}_2\text{O}_3/\text{C}$  (Fig. 6.11a).

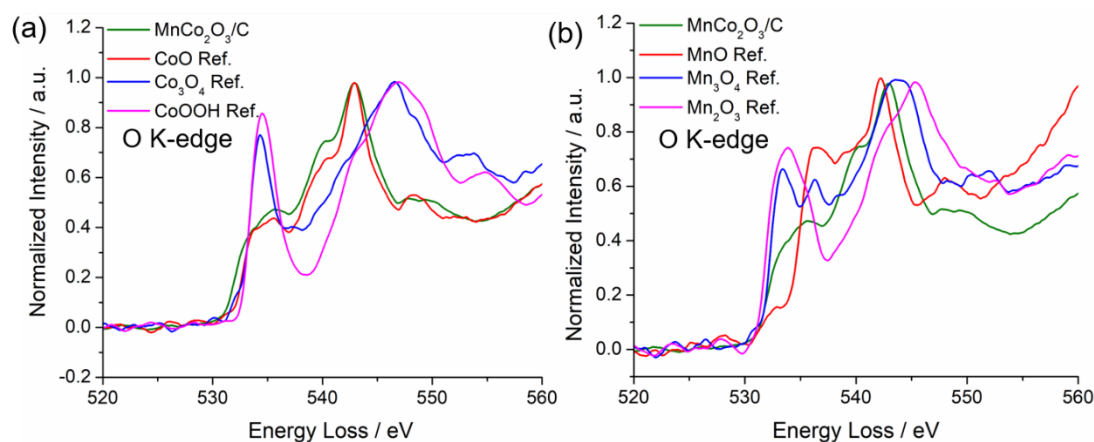


**Figure 6.11.** ELNES spectra of Oxygen K-edge of  $\text{MnCo}_2\text{O}_3/\text{C}$  compared to Co oxide references in (a) and Mn oxide references in (b). The similarity of O K-edge between  $\text{MnCo}_2\text{O}_3/\text{C}$  and CoO references indicates that the majority of the oxygen atoms share a chemical environment similar to CoO(+2).

### 6.5 ORR Activity and Durability of $\text{MnCo}_2\text{O}_3/\text{C}$

After thorough structural investigation, the well-defined rock-salt-type  $\text{MnCo}_2\text{O}_3/\text{C}$  as well as the spinel-type  $\text{MnCo}_2\text{O}_4/\text{C}$  materials were employed as oxygen reduction electrocatalysts in alkaline fuel cells. ORR polarization profiles were acquired in  $\text{O}_2$ -saturated 1M KOH at 1600 rpm and 5 mV/s using a rotating disk electrode (Pine Instruments).  $\text{MnCo}_2\text{O}_3/\text{C}$  with a loading of 0.1  $\text{mg}/\text{cm}^2$  exhibited a promising ORR activity with a half-wave potential ( $E_{1/2} = 0.86$  V vs. a reversible hydrogen electrode, RHE). This is 20 mV higher than that of the spinel  $\text{MnCo}_2\text{O}_4/\text{C}$  ( $E_{1/2} = 0.84$  V), corresponding to about two-fold enhancement in mass-specific activity (Fig. 6.12a). The  $E_{1/2}$  of  $\text{MnCo}_2\text{O}_3/\text{C}$  is only 30 mV away from the benchmark 20 wt.% Pt/C ( $E_{1/2} = 0.89$

V), making  $\text{MnCo}_2\text{O}_3/\text{C}$  a promising non-precious ORR electrocatalyst for alkaline fuel cells. It should be noted that the catalytic activities were preliminarily evaluated employing RDE measurements, while the more realistic MEA measurements are currently under investigation.  $\text{MnCo}_2\text{O}_3/\text{C}$  is able to reach the same diffusion-limited current density ( $-3.6 \text{ mA}/\text{cm}^2$ ),  $I_d$ , as  $\text{Pt}/\text{C}$ , suggesting a  $4e^-$  process of reducing  $\text{O}_2$  completely to  $\text{H}_2\text{O}$ . Additionally, as shown in Fig. 6.13,  $\text{MnCo}_2\text{O}_3/\text{C}$  and  $\text{MnCo}_2\text{O}_4/\text{C}$  have smaller Tafel slopes of 45 and 50 mV/dec, respectively, relative to  $\text{Pt}/\text{C}$  (60 mV/dec), suggesting a smaller overpotential to achieve the same kinetic current change. To investigate the catalyst surface, cyclic voltammetric (CV) profiles of  $\text{MnCo}_2\text{O}_3/\text{C}$  and  $\text{MnCo}_2\text{O}_4/\text{C}$  were acquired, which showed that  $\text{MnCo}_2\text{O}_3/\text{C}$  had a larger redox current than  $\text{MnCo}_2\text{O}_4/\text{C}$ , indicating the existence of more active sites in  $\text{MnCo}_2\text{O}_3/\text{C}$ . (Fig. 6.12b). Both  $\text{MnCo}_2\text{O}_4/\text{C}$  and  $\text{MnCo}_2\text{O}_3/\text{C}$  shared a similar redox peak position, indicating a similar catalyst surface, which actually matched our previous observation that spine-type  $\text{MnCo}_2\text{O}_4/\text{C}$  has a shell rich in  $\text{CoO}(\text{II})$  and a core rich in  $\text{Co}_3\text{O}_4$ . (Fig. S12) The small reduction peak at 1.1 V vs. RHE was separated from the main peak by changing the lower scan limit of the CV profile (Fig. S14). It was identified as monolayer species on the Mn-rich shell with a highly reversible redox process.

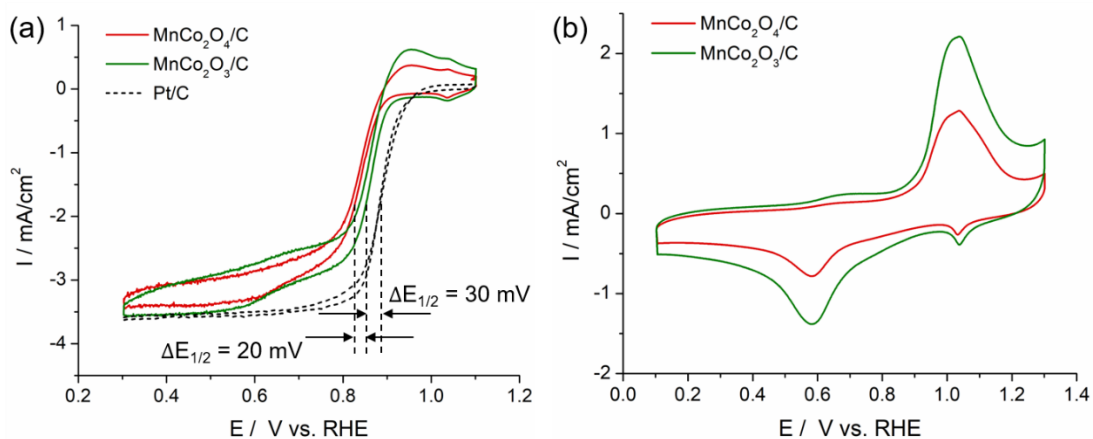


**Figure 6.12.** (a) ORR polarization profiles of  $\text{MnCo}_2\text{O}_4/\text{C}$ ,  $\text{MnCo}_2\text{O}_3/\text{C}$  and  $\text{Pt}/\text{C}$  in  $\text{O}_2$ -sat. 1M KOH at 1600 rpm and 5 mV/s. Metal oxides and Pt mass loadings are  $0.1 \text{ mg}/\text{cm}^2$  and  $25 \text{ }\mu\text{g}/\text{cm}^2$ , respectively. (b) CV profiles of  $\text{MnCo}_2\text{O}_4/\text{C}$  and  $\text{MnCo}_2\text{O}_3/\text{C}$  in Ar-sat. 1M KOH at 10 mV/s.

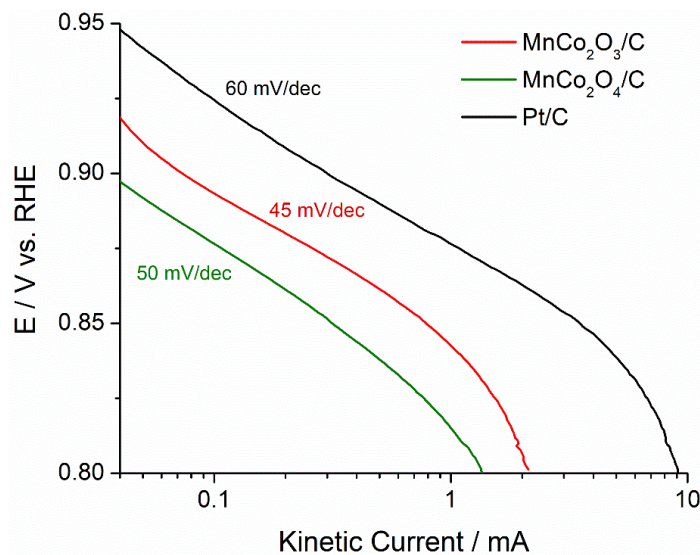


**Figure 6.13.** Tafel plots of MnCo<sub>2</sub>O<sub>3</sub>/C, MnCo<sub>2</sub>O<sub>4</sub>/C and Pt/C extracted from Fig. 4a based on the Koutecky-Levich equation.

In an attempt to implement a Pt-free cathode for AEMFCs, non-precious ORR electrocatalysts are required to not only satisfy the initial activity requirements, but also survive long-term durability tests. Catalyst durability was examined by following an accelerated aging protocol: continuous 10,000 CV cycles at 10 mV/s from 0.6 to 1.0 V vs. RHE in O<sub>2</sub>-sat. 1 M KOH (Fig. 6.14a). MnCo<sub>2</sub>O<sub>3</sub>/C exhibited a mild decay in ORR activity after 10K cycles as the  $E_{1/2}$  shifted from 0.86 V to 0.84 V. The activity decay of MnCo<sub>2</sub>O<sub>3</sub>/C is comparable to or slightly better than Pt/C ( $\Delta E_{1/2} = 25$  mV after 10K cycles) under same test conditions (Fig. 2.28). The activity decay of Pt/C was mainly ascribed to the loss of ECSA as shown in the CV profiles of Pt/C. Noticeably, The activity of MnCo<sub>2</sub>O<sub>3</sub>/C after 10K cycles was still comparable to the initial activity of MnCo<sub>2</sub>O<sub>4</sub>/C. A noticeable loss in the  $I_d$  was found in both MnCo<sub>2</sub>O<sub>3</sub>/C and MnCo<sub>2</sub>O<sub>4</sub>/C, suggesting a loss of surface area, possibly due to particle aggregation during cycles. Further strategies to enhance the catalyst-support interactions will be critical to mitigate the particle aggregation and extend the lifetime of non-precious metal oxide electrocatalysts. TEM-EDX spectra was used to quantitatively investigate the changes in chemical composition after durability tests. Mn and Co K $\alpha$  edges were used to quantify the relative contents of Mn and Co (Fig. 6.14b). They showed that the Mn content increased slightly from  $33.1 \pm 0.2$  at.% to  $35.9 \pm 0.4$  at.%.

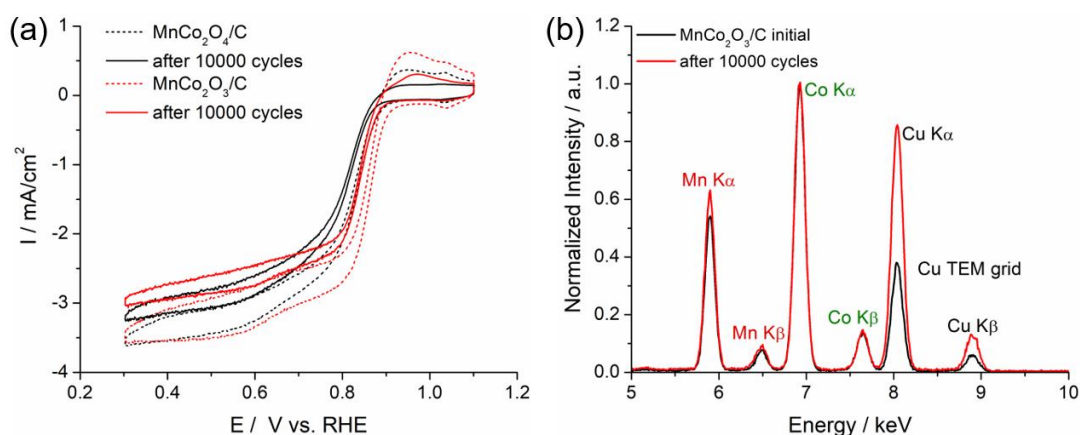


**Figure 6.14.** (a) ORR profiles before and after the accelerated ageing protocol: continuous 10000 cycles at a scan rate of 100 mV/s from 0.6 to 1.0 V vs. RHE in  $\text{O}_2$ -saturated 1M KOH. Metal oxide loading was controlled to be  $0.1 \text{ mg/cm}^2$ . ORR profile measurements after ageing protocol were performed in fresh 1M KOH solution to avoid the influence of possible contamination from the aging solution species. (b) TEM-EDX spectra of  $\text{MnCo}_2\text{O}_3/\text{C}$  before and after 10,000 potential cycles. Intensity was normalized to the Co  $\text{K}\alpha$  edge and the Cu signal was from Cu-made TEM grid.

## 6.6 Conclusion of $\text{MnCo}_2\text{O}_3/\text{C}$ Work

In this work, we designed a new Mn-Co bimetallic oxide,  $\text{MnCo}_2\text{O}_3/\text{C}$  with the rock-salt-type structure, derived from a spinel-type precursor,  $\text{MnCo}_2\text{O}_4/\text{C}$  under mild reduction using  $\text{NH}_3$  at  $300 \text{ }^\circ\text{C}$ . In-depth electron microscopic and spectroscopic investigations suggest that  $\text{MnCo}_2\text{O}_3/\text{C}$  predominantly has Mn(II) and Co(II) and can be written as  $\text{MnO}(\text{CoO})_2/\text{C}$ . Charge transfer between Mn and Co was probed by electron energy-loss near-edge structure (ELNES) analysis.  $\text{MnCo}_2\text{O}_3/\text{C}$  has a Co-rich core and a thin 1-3 nm Mn shell with a mesoporous morphology.  $\text{MnCo}_2\text{O}_3/\text{C}$  achieved a high ORR activity with a half-wave potential of 0.86 V in 1M KOH, which was ascribed to the microstructure and the synergistic effects between Mn and Co, serving as co-active sites for the ORR. This in-depth structural investigation will offer insightful strategies for materials design and developments in the renewable energy community,

in general, and in fuel cells, in particular.

It is worthwhile to mention that the table of contents of this work, published in Chem. Mater., featured the logo of Center for Alkaline-Based Energy Solutions, CABES (Fig. 6.15), an EFRC funded by U.S. DOE.

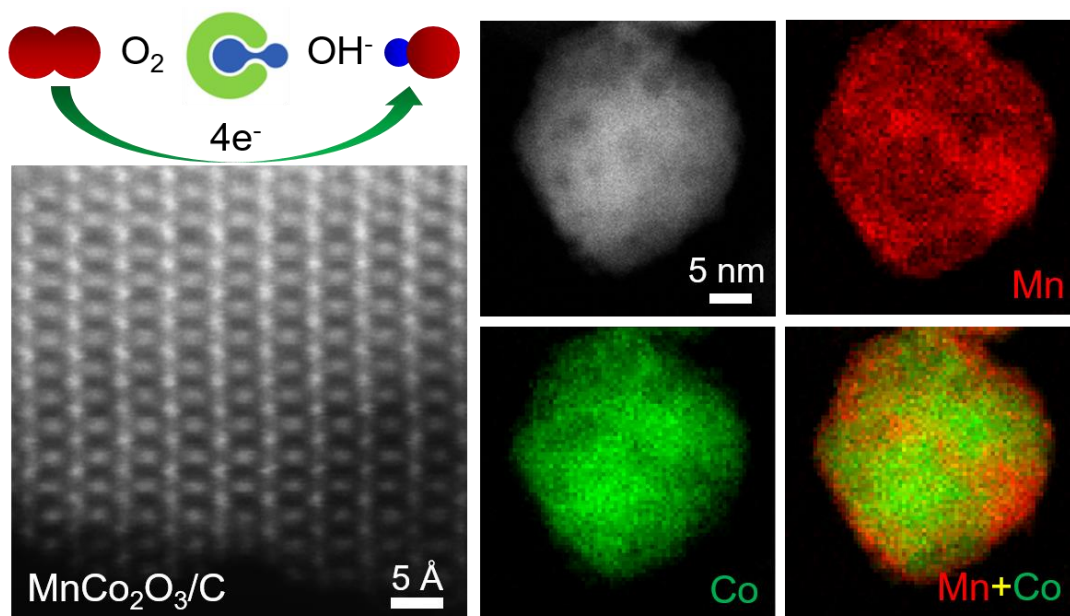


**Figure 6.15.** Table of Contents of this  $MnCo_2O_3/C$  work.

## 6.7 Synthesis of a Family of Cobalt Nitrides ( $\text{Co}_2\text{N/C}$ , $\text{Co}_3\text{N/C}$ and $\text{Co}_4\text{N/C}$ )

We have prepared a series of cobalt nitrides loaded on porous carbon supports ( $\text{Co}_2\text{N/C}$ ,  $\text{Co}_3\text{N/C}$  and  $\text{Co}_4\text{N/C}$ ) by a facile nitridation process in  $\text{NH}_3$  at controlled temperatures. The crystal structures of the as-synthesized cobalt nitrides were characterized by powder X-ray diffraction (XRD) (Fig. 6.16a). The XRD patterns of  $\text{Co}_2\text{N/C}$ ,  $\text{Co}_3\text{N/C}$  and  $\text{Co}_4\text{N/C}$  matched well with those of standard references,  $\text{Co}_2\text{N}$  (PDF # 04-004-4638),  $\text{Co}_3\text{N}$  (PDF # 04-021-6263) and  $\text{Co}_4\text{N}$  (PDF # 04-021-6262), respectively, indicating a successful synthesis of single-phase cobalt nitrides by treating the same Co precursors in  $\text{NH}_3$  at various precisely controlled temperatures. This finding highlights the key role of the treatment temperature in determining the Co/N ratio. As shown in Fig. 6.16b, increases in the temperature led to a monotonic increase of the Co/N ratio, indicating a gradual loss of nitrogen from the cobalt nitride crystals at higher temperatures. The characteristic temperatures for the formation of  $\text{Co}_2\text{N}$ ,  $\text{Co}_3\text{N}$  and  $\text{Co}_4\text{N}$  were 300, 360 and 460 °C, respectively, as indicated by the red marks in Fig. 6.16b. Mixed phases would co-exist when the annealing temperatures were in between the aforementioned characteristic temperatures, as indicated by the blue marks in Fig. 6.16b. XRD patterns of cobalt nitrides at various temperatures are summarized in Fig. 6.17. We propose the following temperature effects during  $\text{NH}_3$  treatment: the precursor is directly reduced by ammonia to  $\text{Co}_2\text{N}$  at 300 °C; further increases in the temperature lead to the partial decomposition of  $\text{Co}_2\text{N}$ , giving rise to  $\text{Co}_3\text{N}$  at 360 °C and further decomposition yielding in  $\text{Co}_4\text{N}$  at 460 °C. From the perspective of crystal structures (Fig. 6.16c),  $\text{Co}_4\text{N}$  exhibits a similar cubic structure to the cubic metallic Co and both show similar XRD patterns with just slight differences in d-spacings (Fig. 6.17g).

Further incorporation of N atoms into the lattice induces the transformation to new crystal structures. While  $\text{Co}_3\text{N}$  adopts a hexagonal structure with six cobalt and two nitrogen atoms in the unit cell,  $\text{Co}_2\text{N}$  exhibits an orthorhombic structure with a much lower symmetry.

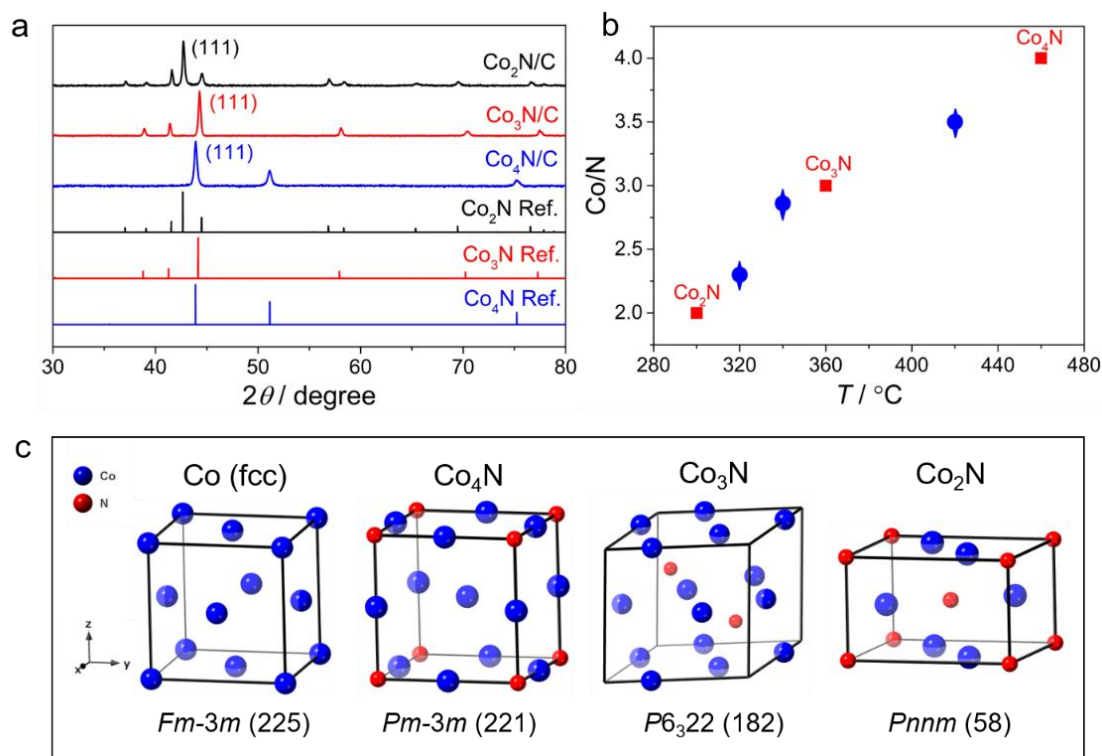


**Figure 6.16.** Crystal structure analysis of as-synthesized  $\text{Co}_x\text{N/C}$  ( $x = 2, 3, 4$ ). (a) XRD patterns of  $\text{Co}_2\text{N/C}$ ,  $\text{Co}_3\text{N/C}$  and  $\text{Co}_4\text{N/C}$ , synthesized under  $\text{NH}_3$  nitridation at 300, 360 and 460 °C, respectively and the corresponding standard XRD references. (b) Synthesis summary: Co/N atomic ratio vs. synthesis temperature. Red marks indicate the single phase  $\text{Co}_x\text{N/C}$  materials while blue marks suggest mixed phases of cobalt nitrides. (c) Crystal models of  $\text{Co}$ ,  $\text{Co}_4\text{N}$ ,  $\text{Co}_3\text{N}$  and  $\text{Co}_2\text{N}$  and the corresponding space groups.

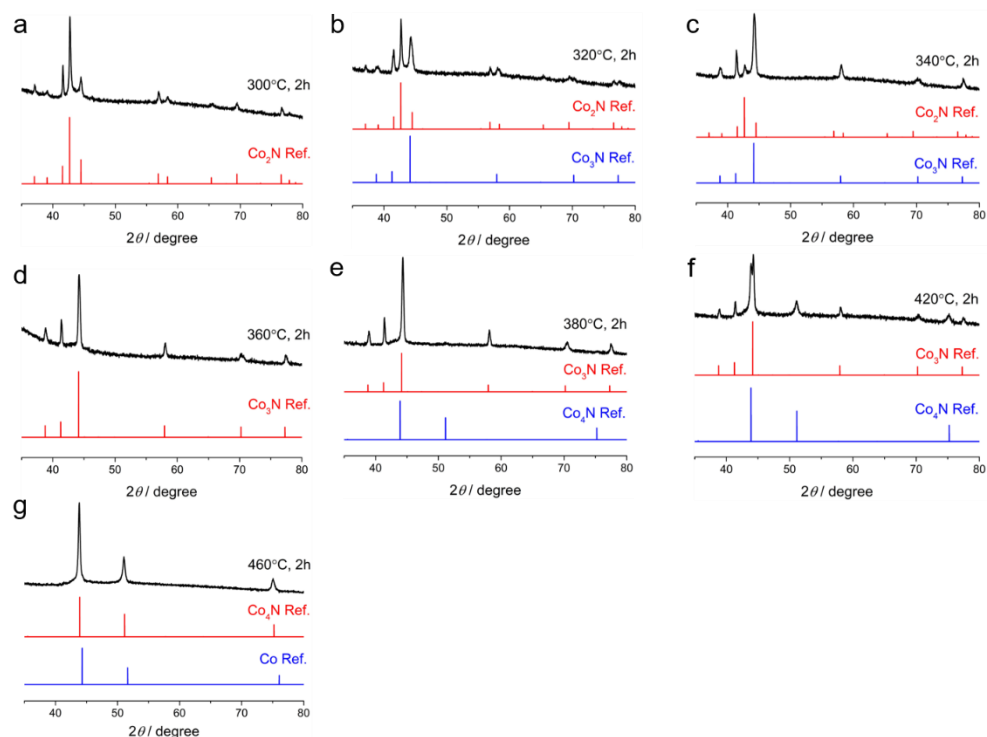


**Figure 6.17.** (a-g) XRD patterns of samples treated in  $\text{NH}_3$  for 2h under different temperatures.

### 6.8 STEM-EELS Mapping of $\text{Co}_4\text{N}/\text{C}$ with Nitride Core and Oxide Shell

The microstructure of the as-synthesized  $\text{Co}_4\text{N}/\text{C}$  was examined, at the atomic scale, using an aberration-corrected high-angle annular dark-field (HAADF) scanning transmission electron microscope (STEM) equipped with electron energy loss spectrometer (EELS). The chemical composition of  $\text{Co}_4\text{N}$  NPs were investigated using EELS analysis. The EELS spectrum exhibited the characteristic Co  $L_{3,2}$  edges and N K-edge (Fig. 6.18) from which the EELS elemental maps of Co and N were obtained Fig. 6.19. The as-synthesized  $\text{Co}_4\text{N}$  NPs exhibited a relatively homogenous elemental distribution of Co and N, which confirmed the uniform incorporation of N through the nanoparticles. Surprisingly, a pronounced O K-edge emerged in the EELS spectrum (Fig. 6.18) and resulted in an O elemental map with a clear surface enrichment (Fig.

6.19f). The composite map of O vs. N suggested a thin oxygen shell on the surface with a uniform thickness of  $\sim 2$  nm (i.e.,  $\sim$ six atomic layers). This intriguing finding indicated that the  $\text{Co}_4\text{N}$  NPs would naturally form a thin surface layer of cobalt oxide, upon exposure to air. Such a “native oxide layer” is also known as a passivation layer with a thickness of several atomic layers, which can prevent further oxidation and is particularly common in aluminum.<sup>18</sup>

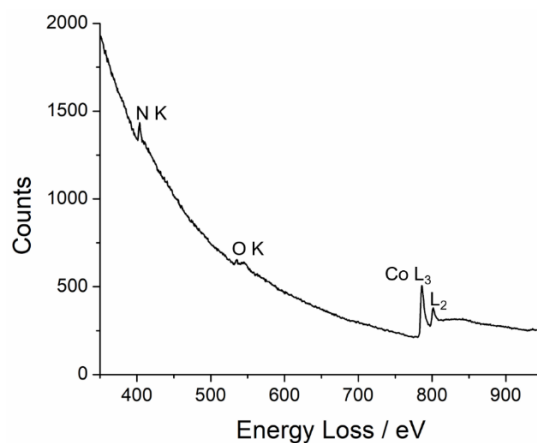


**Figure 6.18.** EELS spectrum of  $\text{Co}_4\text{N}/\text{C}$  corresponding to the following nanoparticle.

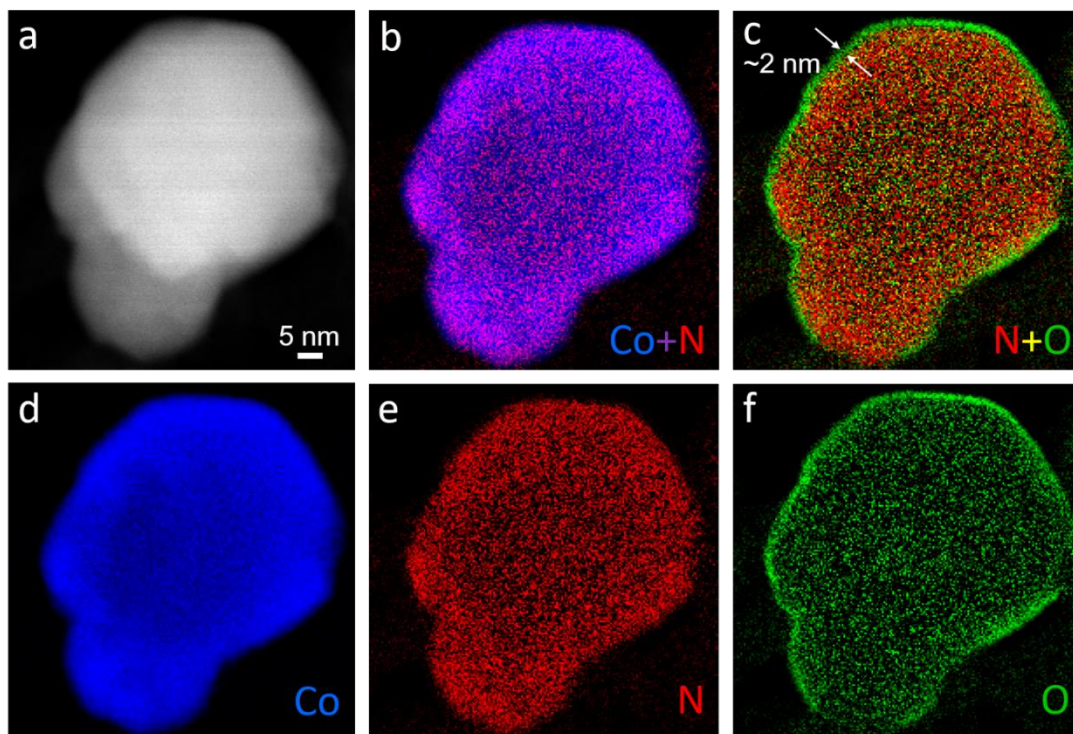


**Figure 6.19.** STEM-EELS analysis of the nitride-core and oxide-shell of Co<sub>4</sub>N/C. (a) HAADF-STEM image of one Co<sub>4</sub>N nanoparticle. (b-f) The corresponding EELS elemental maps of Co in green (d), N in red (e), O in green (f), and composite maps of Co vs. N (b) and O vs. N (c), respectively.

### 6.9 Surface-Sensitive XPS Analysis of Co<sub>4</sub>N/C

To elucidate the near-surface chemical environment, surface-sensitive X-ray photoelectron spectroscopy (XPS) was employed to study the surface oxide layer and near-surface nitride. Pronounced N and O 1s and Co 2p peaks appeared in the full XPS spectrum, indicating the presence of both cobalt oxide and nitride (Fig. 6.20a). The higher intensity of the O 1s peak, relative to the N 1s peak, is consistent with previous findings of the 2 nm surface oxide layer since the typical penetration depth of XPS is about 5 nm. By carefully fitting the high-resolution Co 2p spectrum (Fig. 6.20b), the peaks appearing at 778.0 eV and 793.0 eV were ascribed to the Co 2p<sub>3/2</sub> and Co 2p<sub>1/2</sub> of Co-Co coordination. The binding energies of 779.9 eV and 794.9 eV, corresponding to Co-N bonds, confirmed the formation of Co<sub>4</sub>N after the nitridation process. The co-existence of both Co-Co and Co-N suggests two distinct chemical environments of Co in the Co<sub>4</sub>N crystal structures with the Co atoms having nearest neighbors of two N atoms in a collinear geometry and twelve surrounding Co atoms, as shown in Fig. 6.16c.

The Co-O bond were evidenced by peaks located at 782.1 eV and 797.1 eV and further verified by the presence of Co-O coordination at 528.8 eV in the O 1s spectrum (Fig. 6.20c). Besides of the Co-O bond from the surface cobalt oxide shell, a significant amount of OH and H<sub>2</sub>O adsorbed on the surface were evident and identified by their distinct chemical shifts at 530.7 and 532.1 eV, respectively.

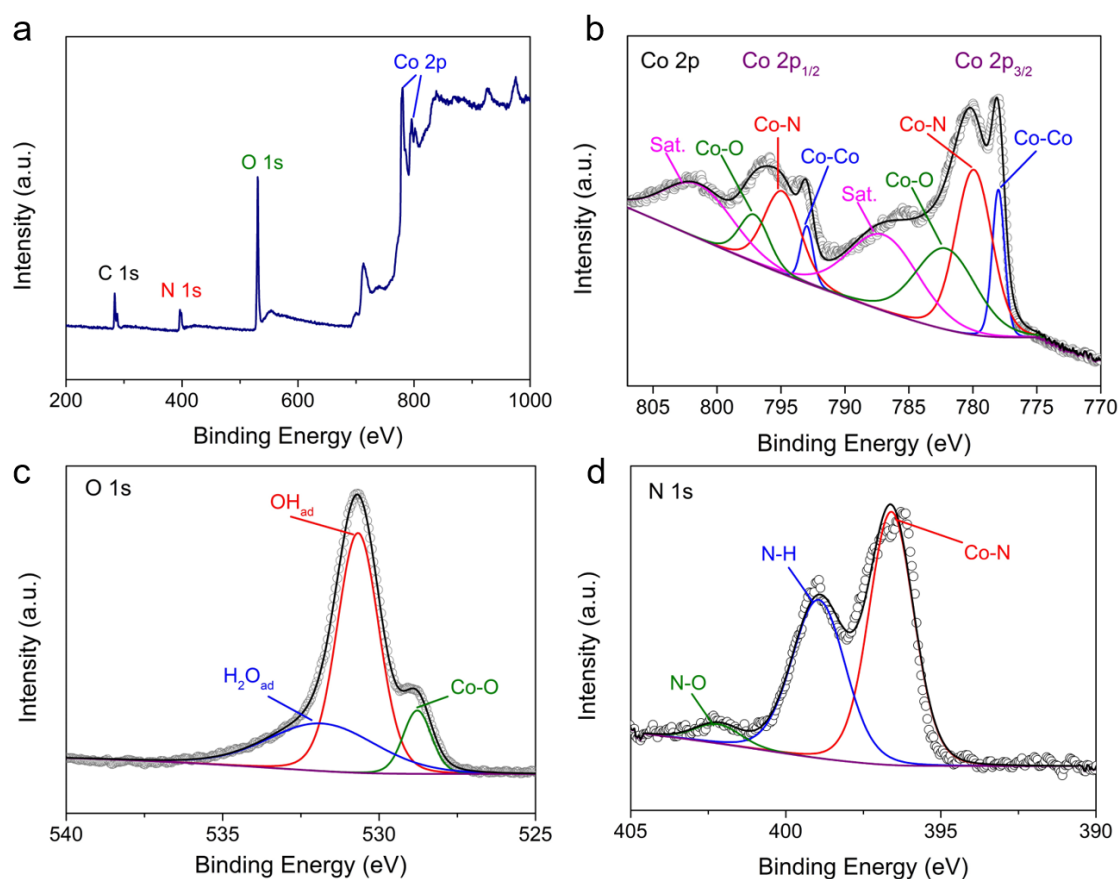


**Figure 6.20.** XPS spectra for Co<sub>4</sub>N. (a) full spectrum. (b-d) high-resolution spectra of (b) Co 2p region. (c) O 1s region. (d) N 1s region.

In a previous report in Chapter 3, we found that Co-OH<sub>ad</sub> and Co-OH<sub>2ad</sub> were able to activate water molecules on the surface and facilitate reduction of O<sub>2</sub>. Apart from the Co-N bond in Co<sub>4</sub>N, the peak at 399.0 eV in the N 1s spectrum could originate from the surface terminal group of N-H after NH<sub>3</sub> treatment<sup>19,20</sup> while the binding energy of 402.2 eV was assigned to the formation of N-O interactions<sup>21,22</sup> at the interface between cobalt oxide and Co<sub>4</sub>N (Fig. 6.20d). The combination of a conductive cobalt nitride core and an active cobalt oxide shell may serve as a rational design metric of heterogenous structures to mitigate the low conductivity of metal oxides yet remain as active sites on surface, and work as active ORR electrocatalysts.

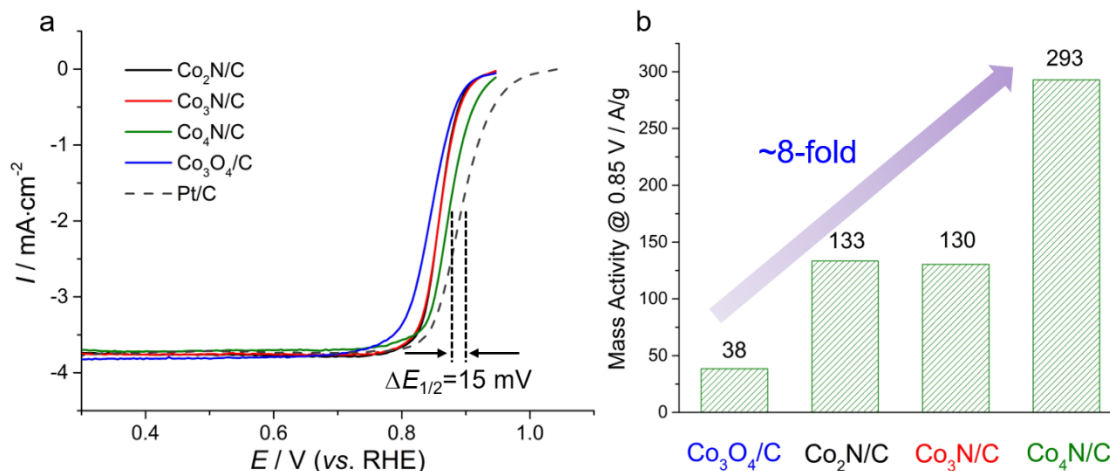


**Figure 6.21.** Evaluation of ORR activity of  $\text{Co}_x\text{N/C}$ . (a) ORR polarization profiles of  $\text{Co}_2\text{N/C}$ ,  $\text{Co}_3\text{N/C}$ ,  $\text{Co}_4\text{N/C}$ ,  $\text{Co}_3\text{O}_4/\text{C}$  and  $\text{Pt/C}$  in  $\text{O}_2$ -saturated 1M KOH at 5 mV/s and 1600 rpm. (b) Mass activity (MA) of  $\text{Co}_2\text{N/C}$ ,  $\text{Co}_3\text{N/C}$ ,  $\text{Co}_4\text{N/C}$ ,  $\text{Co}_3\text{O}_4/\text{C}$  at 0.85 V vs. RHE (normalized to the mass of Co).

### 6.10 ORR Activity and Durability of $\text{Co}_4\text{N/C}$ and Identification of Active Sites

The oxygen reduction activity of cobalt nitrides was evaluated with a rotating disk electrode (RDE) system in  $\text{O}_2$ -saturated 1M KOH at 1600 rpm. In addition to the as-prepared cobalt nitrides, control groups, including spinel oxide  $\text{Co}_3\text{O}_4/\text{C}$  and commercial  $\text{Pt/C}$  (Johnson Matthey), were also examined for comparison. As shown in Fig. 6.21a, all the catalysts displayed a similar diffusion-limiting current of  $\sim 3.8 \text{ mA/cm}^2$  in 1M KOH solution, indicating a 4-electron ORR process. The half-wave potential ( $E_{1/2}$ ) was then used as a metric to evaluate the initial activity of various catalysts. While  $\text{Co}_3\text{O}_4/\text{C}$  exhibited a high  $E_{1/2}$  value of 0.845 V, both  $\text{Co}_2\text{N/C}$  and  $\text{Co}_3\text{N/C}$  outperformed the spinel oxide by 15 mV in  $E_{1/2}$ , suggesting enhanced kinetics for the ORR. Surprisingly,  $\text{Co}_4\text{N/C}$  achieved a further enhancement in the activity with an  $E_{1/2}$  at 0.875 V, comparable to that of  $\text{Pt/C}$  (0.890 V), and the highest recorded performance when compared to the reports of other metal nitrides in the literature (Table

6.1). The enhanced activity was further evaluated in terms of the mass activity (MA) at 0.85 V vs. RHE (Fig. 6.21b). Compared to Co<sub>3</sub>O<sub>4</sub>/C, a significant enhancement, by more than a factor of 3, was observed for Co<sub>2</sub>N/C or Co<sub>3</sub>N/C. Furthermore, the mass activity of Co<sub>4</sub>N/C reached a remarkable MA of about 300 A/g, respectively, representing an eight-fold increase when compared to Co<sub>3</sub>O<sub>4</sub>/C and much higher than other reports in the literature (Table 6.1). The enhanced ORR performance was attributed to the unique nitride-core oxide-shell structure, which is consistent with previous theoretical predictions by Nørskov et al.<sup>23</sup>

Catalyst type	Loading* ( $\mu\text{g}/\text{cm}^2$ )	Solution	Test condition	$I_{dl}$ ( $\text{mA}/\text{cm}^2$ )	$E_{1/2}$ / V vs. RHE	MA@0.85 V (A/g)**
Co <sub>3</sub> N/C This work	50	1M KOH	1600 rpm 5 mV/s	3.8	0.860	130
Co <sub>2</sub> N/C This work	50	1M KOH	1600 rpm 5 mV/s	3.8	0.860	133
Co <sub>4</sub> N/C This work	50	1M KOH	1600 rpm 5 mV/s	3.8	0.875	293
JM Pt/C This work	25	1M KOH	1600 rpm 5 mV/s	3.8	0.890	900
ETEK Pt/C <sup>[3]</sup>	20	0.1M NaOH	1600 rpm 5 mV/s	5.3	0.88	550
TiN <sup>[4]</sup>	127	0.1M KOH	1600 rpm 10 mV/s	N/A	0.53	N/A
VN <sup>[4]</sup>	127	0.1M KOH	1600 rpm 10 mV/s	N/A	0.54	N/A
CrN <sup>[4]</sup>	127	0.1M KOH	1600 rpm 10 mV/s	N/A	0.53	N/A
CrN/GC <sup>[5]</sup>	N/A	0.1M KOH	1600 rpm 5 mV/s	3.93	0.66	N/A
Mn-O-N/C <sup>[6]</sup>	127	1M KOH	1600 rpm 5 mV/s	N/A	0.53	N/A
FeN <sub>x</sub> /NG <sup>[7]</sup>	163	0.1M KOH	1500 rpm 10 mV/s	3.65	0.64	N/A
Co-O-N/C <sup>[8]</sup>	700	0.1M KOH	2500 rpm 10 mV/s	5.4	0.65	N/A
Ti-Ni-N/C <sup>[9]</sup>	500	0.1M KOH	1600 rpm 10 mV/s	5.3	0.80	5.1
Ni <sub>3</sub> N/NiO <sup>[10]</sup>	152	0.1M KOH	1600 rpm 10 mV/s	4.7	0.76	5.2
Cu <sub>3</sub> N <sup>[11]</sup>	389	0.1M KOH	3025 rpm 5 mV/s	N/A	0.23	N/A
Cu <sub>3</sub> N/C <sup>[12]</sup>	7.5	0.1M KOH	1600 rpm 5 mV/s	5.5	0.68	N/A

$V_{0.95}Co_{0.05}N^{[4]}$	127	0.1M KOH	1600 rpm 10 mV/s	5.5	0.76	3.7
Mo-O-N/C <sup>[8]</sup>	700	0.1M KOH	2500 rpm 10 mV/s	4.0	0.61	N/A
MoCo-O-N/C <sup>[8]</sup>	700	0.1M KOH	2500 rpm 10 mV/s	4.8	0.76	0.39

**Table 6.1** Literature Summary of metal nitrides and oxynitrides as the ORR catalysts for alkaline fuel cells. \*Catalyst loading was based on the mass of active materials. \*\*Mass activity calculation is based on Koutecký–Levich equation assuming  $I_d = 5.5 \text{ mA/cm}^2$  and  $3.8 \text{ mA/cm}^2$  for 0.1M and 1.0M KOH, respectively. N/A in  $I_d$  means the catalysts have not reached diffusion limited behavior. N/A in MA means the current at 0.85V is too low for calculating the kinetic current.

The stability of  $Co_4N/C$  was assessed by potential cycling between 0.60 and 0.95 V for 10,000 cycles (U.S. DOE protocols).  $Co_4N/C$  exhibited significant stability with an  $E_{1/2}$  decay of only 14 mV (Fig. 6.22a), close to that of Pt/C (17 mV) (Fig. 6.22b).

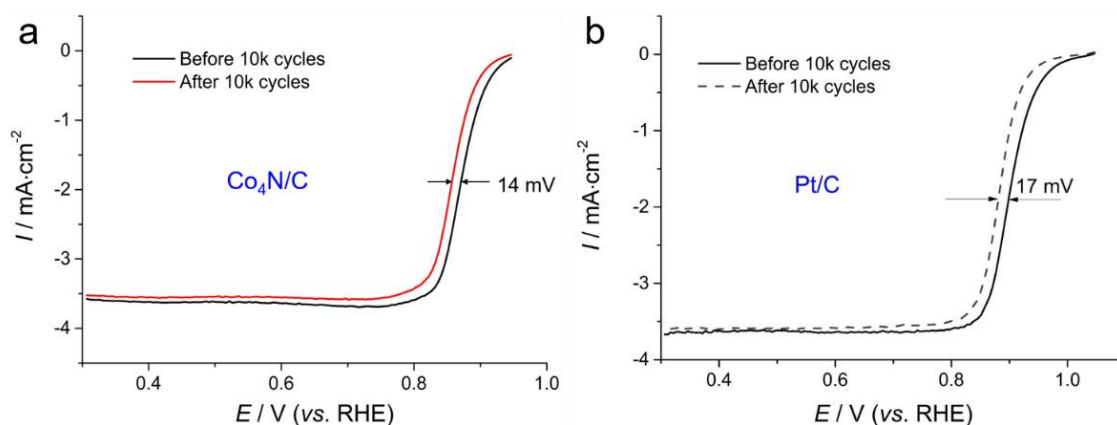


**Figure 6.22.** ORR polarization profiles of  $Co_4N/C$  (a) and Pt/C (b) before and after 10,000 (10k) cycles in  $O_2$ -saturated 1M KOH. Scan rate: 5 mV/s. The 10k-cycle test (0.60-0.95 V) was done in  $O_2$ -saturated 1M KOH, at a sweep rate of 100 mV/s.

### 6.11 *Operando* XAS Studies of the Stability of Cobalt Nitrides under Oxidation Potentials

*Operando* synchrotron-based XAS was employed to understand the activity and structural stability of a similar  $Co_3N/C$  under real-time electrochemical conditions in

alkaline media. Constant potentials from 0.2 to 1.6 V vs. RHE were applied in order to investigate the Co<sub>3</sub>N/C, under steady state in both reduction and oxidation environments in alkaline media (Fig. 6.23). When the potential was increased from 1.0 to 1.2 V vs. RHE, the Co K-edge showed a significant shift to higher energy along with a higher intensity of the absorption peak, and the broad pre-edge changed to a sharper feature like those in cobalt oxide references, which correspond to a valence increase from ~0.82 to ~2.16 (Fig. 6.23a). Further increases in potentials to 1.4 and 1.6 V led to average Co valences of 2.23 and 2.39, respectively. *Operando* EXAFS spectra of Co<sub>3</sub>N/C at 1.0 V (OCP) showed the characteristic Co-N bond at an R value of 1.5 Å, pronounced Co-Co bond at 2.2 Å (nearest neighbors) and an additional peak at 4.2 Å (further coordination shells) (Fig. 6.23b). When the potential was increased to 1.2 V, the amplitude of the EXAFS signal,  $|\chi(R)|$  decreased dramatically from 1.8 to less than 0.6 Å<sup>-3</sup>. This indicates that the structure of Co<sub>3</sub>N/C has been dramatically perturbed under oxidation at 1.2 V becoming significantly more disordered. Further oxidation at 1.4 and 1.6 V showed a new feature emerging at 4.4 Å, with an increasing magnitude to 0.6 and 0.9 Å<sup>-3</sup>, respectively. This suggests the formation of more ordered cobalt oxides at very high oxidation potentials. In contrast to the dramatic changes at oxidation potentials above 1.0 V, *operando* XANES and EXAFS showed a much more stable behavior at lower potentials (Figs. 6.2c-d). When the potential decreased from 1.0 V (OCP) to 0.8 V, both XANES and EXAFS showed little change. Only when the potential was decreased to the lower limit of 0.2 V, was a slight negative shift of the edge energy in XANES was observed, which is likely due to the reduction of surface oxide layer. As shown in the schematic in Fig. 6.23b, the results unambiguously demonstrate that oxidizing potentials

above 1.2 V will destroy the original structure of  $\text{Co}_3\text{N}$  and generate new species of Co oxides, while reducing potentials, down to 0.2 V, have minimal impact on the structural stability.  $\text{Co}_3\text{N}/\text{C}$  has a safe “potential threshold” of 1.0 V but is not suitable to catalyze the OER at high oxidizing potentials in alkaline media. However, several reports have employed Co-based nitride materials for the OER in alkaline solution,<sup>25,26</sup> which contradicts our *operando* XAS observations. The nitride catalysts exhibited a tendency towards complete oxidation with the collapse of the conductive-core-active-shell structure, leading to dramatic performance deterioration. Further treatment of the catalyst surface with a passivation layer could help mitigate the core from oxidizing under oxidative conditions and thus improve the durability and structural stability of TMNs for the ORR in alkaline media.<sup>27</sup>

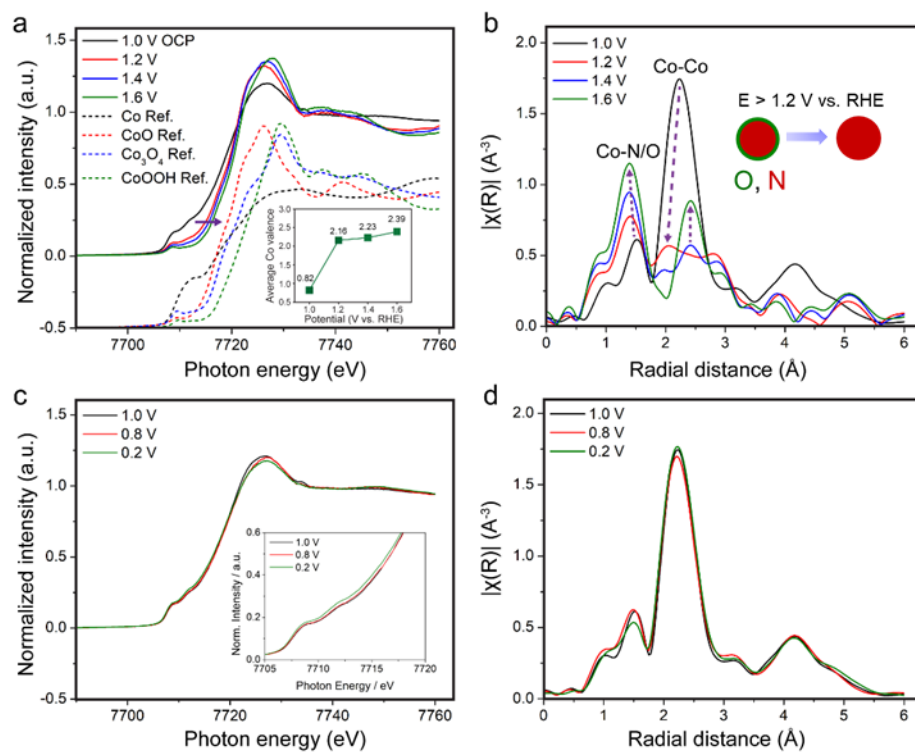


**Figure 6.23** *Operando* XAS studies of the stability of cobalt nitrides under electrochemical conditions. (a) *Operando* XANES spectra of  $\text{Co}_3\text{N}/\text{C}$  under steady state

at 1.0 V (open circuit potential, OCP) followed by applied oxidative potentials from 1.2-1.6 V vs. RHE, and comparison with XANES reference spectra (a Y-offset of 0.5 was applied to better show the differences). Purple arrows show the progressive positive shift of the Co K-edge, indicating higher Co valences at higher potentials. The inset shows the average Co valences at 1.2-1.6 V based on a linear combination fitting analysis. (b) *Operando* EXAFS spectra of Co<sub>3</sub>N/C at 1.0-1.6 V with  $k^3$ -weighting Hanning window and no phase correction, showing the dramatic changes of Co-N/O and Co-Co bonds at different applied oxidative potentials. (c) *Operando* XANES and EXAFS spectra of Co<sub>3</sub>N/C at reducing potentials from 1.0 V down to 0.2 V. The inset in (c) shows the slight negative shift of the Co edge energy, suggesting the overall good stability of Co<sub>3</sub>N/C at potentials lower than 1.0 V.

## 6.12 Conclusions

In summary, we report on a novel family of cobalt nitrides (Co<sub>x</sub>N/C, x=2, 3, 4) as ORR electrocatalysts in alkaline fuel cells. Co<sub>4</sub>N/C exhibited the highest ORR activity among the three types of cobalt nitrides studied, with a half-wave potential ( $E_{1/2}$ ) of 0.875 V vs. RHE in 1M KOH, rivaling that of commercial Pt/C (0.89 V). Moreover, Co<sub>4</sub>N/C showed an eight-fold improvement in mass activity at 0.85 V, when compared to cobalt oxide, Co<sub>3</sub>O<sub>4</sub>/C, and a negligible degradation ( $\Delta E_{1/2} = 14$  mV) after 10,000 potential cycles. The superior performance was ascribed to the formation of a conductive nitride core surrounded by a naturally formed thin active oxide shell (about 2 nm). The conductive nitride core effectively mitigated the low conductivity of the metal oxide catalysts and the thin oxide shell on the surface provided the active sites for the ORR. Our work may shed light upon the development of new transition metal nitrides not only for alkaline fuel cells but also for other electrocatalysis system. *Operando* XAS shows that cobalt nitrides are stable for the ORR at potentials below 1.0 V vs. RHE and undergo irreversible oxidation at potentials above 1.2 V, which can occur during fuel

cell start-up/shut down procedures as well as the OER in water electrolyzers.

### 6.13 References

1. Shibli, S. M. A.; Arun, P. S.; Raj, A. V. Exploration of Octahedrally Shaped  $\text{MnCo}_2\text{O}_4$  Catalyst Particles for Visible Light Driven Photocatalytic Water Splitting Reaction. *RSC Adv.* **2015**, *5*, 19393–19399.
2. Yang, Y.; Peng, H.; Xiong, Y.; Li, Q.; Lu, J.; Xiao, L.; DiSalvo, F. J.; Zhuang, L.; Abruña, H. D. High-Loading Composition-Tolerant Co–Mn Spinel Oxides with Performance beyond  $1 \text{ W}/\text{cm}^2$  in Alkaline Polymer Electrolyte Fuel Cells. *ACS Energy Lett.* **2019**, *4*, 1251–1257.
3. Chen, P.; Xu, K.; Fang, Z.; Tong, Y.; Wu, J.; Lu, X.; Peng, X.; Ding, H.; Wu, C.; Xie, Y. Metallic  $\text{Co}_4\text{N}$  Porous Nanowire Arrays Activated by Surface Oxidation as Electrocatalysts for the Oxygen Evolution Reaction. *Angew. Chem. Int. Ed.* **2015**, *54*, 14710–14714.
4. Luo, J.; Tian, X.; Zeng, J.; Li, Y.; Song, H.; Liao, S. Limitations and Improvement Strategies for Early-Transition-Metal Nitrides as Competitive Catalysts toward the Oxygen Reduction Reaction. *ACS Catal.* **2016**, *6*, 6165–6174.
5. Miura, A.; Rosero-Navarro, C.; Masubuchi, Y.; Higuchi, M.; Kikkawa, S.; Tadanaga, K. Nitrogen-Rich Manganese Oxynitrides with Enhanced Catalytic Activity in the Oxygen Reduction Reaction. *Angew. Chem. Int. Ed.* **2016**, *55*, 7963–7967.
6. Cao, B.; Veith, G. M.; Diaz, R. E.; Liu, J.; Stach, E. A.; Adzic, R. R.; Khalifah, P. G. Cobalt Molybdenum Oxynitrides: Synthesis, Structural Characterization, and Catalytic Activity for the Oxygen Reduction Reaction. *Angew. Chem. Int. Ed.* **2013**, *52*, 10753–10757.
7. Varga, T.; Vásárhelyi, L.; Ballai, G.; Haspel, H.; Oszkó, A.; Kukovecz, Á.; Kónya, Z. Noble-Metal-Free Iron Nitride/Nitrogen-Doped Graphene Composite for the Oxygen Reduction Reaction. *ACS Omega* **2019**, *4*, 130–139.
8. Tian, X.; Luo, J.; Nan, H.; Fu, Z.; Zeng, J.; Liao, S. Binary Transition Metal Nitrides with Enhanced Activity and Durability for the Oxygen Reduction Reaction. *J. Mater. Chem. A* **2015**, *3*, 16801–16809.
9. Zhang, H.; Liu, M.; Cheng, W.; Li, Y.; Zhou, W.; Su, H.; Zhao, X.; Yao, P.; Liu, Q. Metallic  $\text{Ni}_3\text{N}$  Quantum Dots as a Synergistic Promoter for NiO Nanosheet toward Efficient Oxygen Reduction Electrocatalysis. *J. Phys. Chem. C* **2019**, *123*, 8633–8639.
10. Wu, H.; Chen, W. Copper Nitride Nanocubes: Size-Controlled Synthesis and Application as Cathode Catalyst in Alkaline Fuel Cells. *J. Am. Chem. Soc.* **2011**, *133*, 15236–15239.
11. Oda, K.; Yoshio, T.; Oda, K. Preparation of Co-N Films by Rf-Sputtering. *J. Mater. Sci.* **1987**, *22*, 2729–2733.
12. Zhang, Y.; Ouyang, B.; Xu, J.; Jia, G.; Chen, S.; Rawat, R. S.; Fan, H. J. Rapid Synthesis of Cobalt Nitride Nanowires: Highly Efficient and Low-Cost Catalysts for Oxygen Evolution. *Angew. Chem. Int. Ed.* **2016**, *55*, 8670–8674.

13. Zhu, X.; Jin, T.; Tian, C.; Lu, C.; Liu, X.; Zeng, M.; Zhuang, X.; Yang, S.; He, L.; Liu, H.; Dai, S. In Situ Coupling Strategy for the Preparation of FeCo Alloys and Co<sub>4</sub>N Hybrid for Highly Efficient Oxygen Evolution. *Adv. Mater.* **2017**, *29*, 1–6.
14. Meng, F.; Zhong, H.; Bao, D.; Yan, J.; Zhang, X. In Situ Coupling of Strung Co<sub>4</sub>N and Intertwined N-C Fibers toward Free-Standing Bifunctional Cathode for Robust, Efficient, and Flexible Zn-Air Batteries. *J. Am. Chem. Soc.* **2016**, *138*, 10226–10231.
15. Yoon, K. R.; Shin, K.; Park, J.; Cho, S. H.; Kim, C.; Jung, J. W.; Cheong, J. Y.; Byon, H. R.; Lee, H. M.; Kim, I. D. Brush-Like Cobalt Nitride Anchored Carbon Nanofiber Membrane: Current Collector-Catalyst Integrated Cathode for Long Cycle Li-O<sub>2</sub> Batteries. *ACS Nano* **2018**, *12*, 128–139.
16. Seetharaman, S.; Abraham, K. P. Activity Measurements in CoO-MnO Solid Solutions *Scripta Metallurgica*, **1969**, *3*, 911-916.
17. Cliff, G.; Lorimer, G. W. The Quantitative Analysis of Thin Specimens. *J. Microsc.* **1975**, *103*, 203-207.
18. Fehlner; F.P. Low Temperature Oxidation: The Role of Vitreous Oxides. A Wiley-Interscience Publication, John Wiley & Sons, New York, 1986.
19. Grunze, M.; Brundle, C. R.; Tománek, D. Adsorption and Decomposition of Ammonia on a W(110) Surface: Photoemission Fingerprinting and Interpretation of the Core Level Binding Energies Using the Equivalent Core Approximation. *Surf. Sci.* **1982**, *119*, 133–149.
20. Egawa, C.; Naito, S.; Tamaru, K. Adsorption and Decomposition of Ammonia on W(100); XPS and UPS Studies. *Surf. Sci.* **1983**, *131*, 49–60.
21. Stańczyk, K.; Dziembaj, R.; Piwowarska, Z.; Witkowski, S. Transformation of Nitrogen Structures in Carbonization of Model Compounds Determined by XPS. *Carbon* **1995**, *33*, 1383–1392.
22. Davis, R. E.; Horvath, G. L.; Tobias, C. W. The Solubility and Diffusion Coefficient of Oxygen in Potassium Hydroxide Solutions. *Electrochim. Acta* **1967**, *12*, 287–297.
23. Abroshan, H.; Bothra, P.; Back, S.; Kulkarni, A.; Nørskov, J. K.; Siahrostami, S. Ultrathin Cobalt Oxide Overlayer Promotes Catalytic Activity of Cobalt Nitride for the Oxygen Reduction Reaction. *J. Phys. Chem. C* **2018**, *122*, 4783–4791.
24. Gewirth, A. A.; Varnell, J. A.; DiAscro, A. M. Nonprecious Metal Catalysts for Oxygen Reduction in Heterogeneous Aqueous Systems. *Chem. Rev.* **2018**, *118*, 2313–2339.
25. Chen, P. *et al.* Metallic Co<sub>4</sub>N porous nanowire arrays activated by surface oxidation as electrocatalysts for the oxygen evolution reaction. *Angew. Chem. Int. Ed.* **2015**, *54*, 14710–14714.
26. Zhang, Y. *et al.* Rapid synthesis of cobalt nitride nanowires: Highly efficient and low-cost catalysts for oxygen evolution. *Angew. Chem. Int. Ed.* **2016**, *55*, 8670–8674.
27. Yuan, W. *et al.* Interfacial engineering of cobalt nitrides and mesoporous nitrogen-doped carbon: Toward efficient overall water-splitting activity with enhanced charge-transfer efficiency. *ACS Energy Lett.* **2020**, *5*, 692–700.

## CHAPTER 7

### **High-Throughput Combinatorial Studies of Palladium-based Oxygen Reduction Electrocatalysts for Alkaline Fuel Cells\***

#### **7.1 Introduction**

Developing Pt-free ORR catalysts has been a longstanding challenge for the implementation of fuel cell technologies. Among the alternatives for Pt, Pd has gained increasing attentions since Pd is the only element which shows comparable ORR activity to Pt in alkaline media, despite its much lower activity in acidic media.<sup>1</sup> In addition, alloying Pd with lower-cost 3d-transition metals, has been reported as an effective strategy to tune the lattice parameter and electronic structure of Pd so as to boost its ORR activity.<sup>2-6</sup> For example, Pd-Cu disordered alloys (solid solutions) were reported as active ORR catalysts in acidic media. While alloying a precious metal with a non-noble metal (e.g. PdCu) increases activity, the non-noble metal often leaches during cycles, which could contaminate and decrease the performance of the polymer membrane in fuel cells.<sup>7,8</sup> In contrast, based on the Pourbaix diagram of Cu, Pd-Cu alloys can be thermodynamically more stable in alkaline media (pH = 13~14), when compared to acidic media.<sup>9</sup> Despite extensive studies on Pd-based electrocatalysts, the electrocatalytic mechanism for the ORR has remained elusive.

---

\*Reproduced with permission from the following publications

**Yao Yang**, Guanyu Chen, Rui Zeng, Andrés Molina Villarino, Francis DiSalvo, R. Bruce van Dover, Héctor Abruña. Combinatorial Studies of Palladium-based Oxygen Reduction Electrocatalysts for Alkaline Fuel Cells. *J. Am. Chem. Soc.* 2020, 142, 3980-3988.

The fact that ORR electrocatalytic activity depends on particle composition, size, morphology, and surface and crystal structures, makes this task monumentally difficult. Additionally, nanoparticle studies often involve time-consuming trial-and-error synthetic procedures. Therefore, a systematic high-throughput combinatorial approach, with well-controlled morphology and structure, would be particularly beneficial for assessing and evaluating promising Pd-based candidate catalysts in a time-efficient manner.

Combinatorial synthesis and screening methods have enabled the efficient preparation of solid-state material libraries. Previous developments have contributed to the discovery of new functional materials with dielectric,<sup>10</sup> magnetic,<sup>11</sup> superconducting,<sup>12</sup> and luminescent properties,<sup>13</sup> among others. Over the past two decades, significant progress has been made in screening electrocatalysts for fuel cell and water splitting applications. The pioneering work of Mallouk et al. employed inkjet printing and a subsequent borohydride reduction method to screen a broad range of binary, ternary and quaternary precious metal electrocatalysts.<sup>14</sup> They developed a fluorescent acid-base indicator method to detect the concentration of protons, which were generated during the methanol oxidation reaction, and identified a composition of Pt<sub>44</sub>Ru<sub>41</sub>Os<sub>10</sub>Ir<sub>5</sub> with optimal activity. We recently employed a similar fluorescent-based method, and synchrotron-based X-ray fluorescence (XRF) spectroscopy to screen Pt-M binary alloys (M included 18 different metals) and selected promising catalysts, such as Pt<sub>65</sub>Ru<sub>35</sub>.<sup>15-17</sup> Hillier et al. proposed scanning electrochemical microscopy (SECM) as a reliable technique to screen PtRu-based catalysts for hydrogen and methanol oxidation.<sup>18,19</sup> Bard et al. designed a piezo-based microarray dispenser to

prepare Co-M binary alloy (M: Pd, Ag, Au) catalyst arrays for the ORR in acidic media and Fe<sub>2</sub>O<sub>3</sub>-based bimetallic oxide arrays for water oxidation and assessed their activity using SECM.<sup>20,21</sup> Russel et al. developed addressable multi-channel array electrodes to study Pt-Ru alloys for CO-tolerant methanol oxidation<sup>22,23</sup> and Pt-Pd-Au alloys for the ORR in acidic media.<sup>24</sup> Recently, Berlinguette et al. developed a photochemical metal-organic deposition (PMOD) method to prepare various amorphous Fe-Co-Ni trimetallic oxides for water oxidation.<sup>25,26</sup>

For the development of PEMFCs, the rotating disk electrode (RDE) technique has been widely used as a standard tool to evaluate electrocatalytic activity. In contrast, the aforementioned fluorescent-based and SECM techniques only provide indirect predictions of potential activity. On the other hand, multi-channel array electrodes require delicate device fabrication and few of those results have translated into realistic activities in RDE measurements. There is clearly a need for a standard and reliable RDE platform for catalyst screening. Here, we report on a facile catalyst screening method using replaceable glassy carbon disk electrodes as the substrate, which enables the rapid and reliable evaluation of ORR activity using standard RDE measurements. We employed a high-throughput magnetron sputtering chamber to prepare 36 kinds of binary Pd-M thin-film alloy electrocatalysts for the ORR in alkaline fuel cells (M: Fe, Co, Ni and Cu). Among all those thin-film catalysts, Pd<sub>50</sub>Cu<sub>50</sub> (i.e. 1:1 molar ratio, or just PdCu) was found to be the most promising candidate. Following this guidance, and using an impregnation method, we further synthesized Pd<sub>50</sub>Cu<sub>50</sub> nanoparticles which showed promising activity and durability in alkaline fuel cells.

## 7.2 Experimental section

**Thin-film preparation by magnetron sputtering:** The sputtering chamber consists of three 2-in. 90° off-axis magnetron sputtering guns (radio frequency, RF mode) on the side of the chamber (Angstrom Sciences Onyx-2). A 2-in. on-axis sputtering gun (AJA, Inc.) on the top (direct current, DC mode) allows for the deposition of a uniform adhesion layer, such as Ti or Ta. Sputtering targets of Pd and Cu metals were purchased from ACI Alloys, Inc. with a purity of 99.99%. The sputtering rate of each metal was measured as a function of sputtering power and calibrated based on the thickness measurements obtained using a profilometer (Tencor AlphaStep 500). Ti adhesion layers were sputtered at 125 W (0.5 A, 250 V) for 60 s. The Pd-Cu thin films were sputtered with the Pd target at 25 W and the Cu target at 35 W for 10 min. The sputter rate of Pd and Cu was measured to be around 2.5 Å/s in the center of the substrate. A glassy carbon (GC) rod was purchased from HTW GmbH (Germany) and cut into columns (D = 5mm, H = 5 mm); one side was mirror polished and thoroughly cleaned with ethanol and H<sub>2</sub>O. A ceramic electrode holder was custom built to hold up to 9 GC electrodes for co-sputtering of binary alloys. After Pd and Cu metal targets were mounted into the sputtering guns, the system was pumped down to a high vacuum condition ( $2 \times 10^{-6}$  Torr). The sputtering occurred in a  $3 \times 10^{-2}$  Torr Ar gas environment and the Ti adhesion layer was deposited on the GC first, followed by co-sputtering of the Pd and M elements (M: Mn, Fe, Co, Ni, Cu). The sputtering parameters of different Pd-M alloys were summarized in [Table 7.1](#).

Binary Catalysts	Pd-Cu	Pd-Ni	Pd-Co	Pd-Fe	Pd-Mn
Pd gun (RF) /W	25	25	25	25	25
3d metal gun (RF)	35	50	50	60	56

/W					
Top gun (DC) / W	125	125	125	125	125

**Table 7.1.** Sputtering power of Pd, 3d metal and Ti guns. The sputter rate of all metals was estimated to be around 2.5 Å/s. The RF bias was set at 7W for all Pd-M films. The top Ti gun was run at 0.5 A and 250 V. The Ti adhesion layer was sputtered for 1min and Pd-Cu thin films was sputtered for 10min

**Structural characterizations:** Scanning electron microscopy (SEM) images and energy dispersive spectroscopy (EDX) were performed using a ZEISS Gemini 500 SEM. SEM images were acquired at 3 kV and 1 nA and EDX spectra were acquired at 20kV and 38 nA to maximize the X-ray signal output for elemental quantification while maintain reasonable spatial resolution for elemental mapping. EDX images were obtained with a size of 256×256 pixels and a dwell time of 2.5 ms/pixel. EDX elemental mapping of Pd and 3d metals were processed using Pd  $L_{\alpha,\beta}$  and 3d metal  $K_{\alpha}$  edges in ImageJ. The thin-film XRD patterns were acquired using a Bruker D8 General Area Detector Diffraction System (GADDS) with a Vanter 2D large-area detector. Diffraction patterns were collected at a step size of 10°/frame and an acquisition time of 1 min/frame from 20° to 80°. A laser pointer guided the sample height alignment precisely to ensure the reproducibility among different batches of thin films. Since a GC electrode would have large diffraction peaks of graphite in the background, the Pd-based films used for XRD analysis were deposited on a single-crystal Si wafer (University Wafer, p-type doped, (100) orientation, 380 μm thick).

**Electrochemical measurements:** A replaceable disk electrode system (Pine Instrument, E4TQ) was employed as the standard RDE platform for evaluating the ORR activity of the Pd-based thin films. The thin-film coated GC working electrode (WE) was loaded into the electrode holder with Teflon tape on the side for tight sealing to

prevent electrolyte leakage. The GC was pushed against the internal Au spring-loaded pin to ensure a reliable electrical contact. Ag/AgCl in saturated KCl solution served as the reference electrode (RE) and connected to the WE through a salt bridge. A large-surface-area graphite rod was used as the counter electrode (CE). The potential difference between Ag/AgCl in saturated KCl and a reversible hydrogen electrode (RHE) in 1 M KOH was calculated to be 1.0258 V based on the Nernst equation. Electrochemical measurements were performed using a Solartron potentiostat. All potential values in this work are referenced against RHE unless otherwise stated. ORR measurements were carried out in oxygen-saturated 1 M KOH at 1600 rpm and 5 mV/s at room temperature (23 °C). The relative activity was calculated by normalizing the kinetic current, extracted from the Koutecky-Levich equation, to the relative Pd contents of Pd in the binary alloys. Cyclic voltammograms (CVs) were obtained in Ar-bubbled 1 M KOH at a scan rate of 10 mV/s.

**Pd-Cu Nanoparticle synthesis:** Pd and PdCu (Pd/Cu molar ratio, 1:1) were synthesized using an impregnation-reduction method. In a typical synthesis, 2.354 mL of 50 mM  $\text{H}_2\text{PdCl}_4$  mixed with 2 M HCl and 15.8 mg of  $\text{CuCl}_2$  were dissolved into a mixture of 15 mL  $\text{H}_2\text{O}$  and 5 mL EtOH, followed by the addition of 80 mg of high-surface area carbon (HSC) Ketjen Black (KB). The mass fraction of PdCu on carbon was 20% and the synthesis rendered a maximum of 100 mg of catalyst per batch. The suspension was sonicated for 30 min and then stirred at 1500 rpm for 10 h at room temperature (23°C). The mixture was then heated to 60 °C while stirring, on the same heating/stirring plate, to allow for the solvent to slowly evaporate and the suspension to form a uniform slurry. The slurry was then dried in an oven at 60 °C for ~10 h to form a powder

precursor. This precursor was crushed in an agate mortar and heated in a crucible under forming gas at 800 °C for 12h to form the PdCu nanoparticles. Pd nanoparticles on carbon were synthesized under identical conditions with the exception of using 3.758 mL H<sub>2</sub>PdCl<sub>4</sub> and no CuCl<sub>2</sub> to achieve the same mass fraction of 20% Pd/C. The crystal structure of all the synthesized electrocatalysts was examined by powder X-ray diffraction (XRD) using a Rigaku Ultima IV Diffractometer. Diffraction patterns were collected at a scan rate of 2°/min at 0.02° steps from 20° to 80°.

**Electrochemical measurements of Pd-Cu nanoparticle catalysts:** 5.0 mg of electrocatalyst (Pd/C or PdCu/C) were mixed with 1.0 mL of 0.05 wt.% Nafion/ethanol solution and subsequently sonicated for approximately 30 min to form a uniform catalyst ink. 5 µL of the resulting catalyst ink were loaded onto a glassy carbon (GC) electrode (D = 5.0 mm, Pine Instruments) as the working electrode (WE), achieving a metal loading of 25 µg/cm<sup>2</sup>, followed by thermal evaporation of the solvent under an infrared light. Ag/AgCl in saturated KCl solution was used as the reference electrode (RE), and a graphite rod with a large surface area was used as the counter electrode (CE). Electrochemical measurements were performed on the same Solartron potentiostat as before. ORR measurements were performed with a rotating disk electrode (RDE, Pine Instruments) in oxygen-saturated 1 M KOH at room temperature (23°C). Reproducible experiments suggested that the relative error of E<sub>1/2</sub> was less than 2 mV. CVs were obtained at 20 mV/s from 0.05 to 1.2 V in Ar-saturated 1 M KOH. ORR polarization profiles were obtained at 5 mV/s and 1600 rpm after 10 CV cycles at 20 mV/s to clean the surface and activate the catalyst. CO stripping experiments were performed by adsorbing the CO at 0.1 V vs. RHE for 10 min and subsequently bubbling

Ar gas for 20 min to remove the residual CO in the solution so that only the CO adsorbed on the surface would be analyzed. CO stripping profiles were acquired at 10 mV/s from 0.1 to 1.2 V vs. RHE. Accelerated durability tests were carried out by potential cycling from 0.6 V to 1.0 V at 100 mV/s from 10,000 to 100,000 cycles. The ORR profiles after potential cycles were measured in a fresh 1 M KOH solution to avoid the contamination accumulating in the solution.

### **7.3 Magnetron Sputtering of Pd-based thin-film electrodes**

Magnetron sputtering has been employed as a powerful tool to prepare various Pd-based binary thin films (Fig. 7.1). Sputtering is a physical vapor deposition (PVD) method in which the positively charged ions from an Ar plasma strike a negatively charged metal target(s) with enough kinetic energy to sputter surface atoms from the target(s). In magnetron sputtering, a localized magnetic field under the target guns aids in controlling the electron trajectory in space and concentrating the Ar plasma over the target. Thus, higher plasma densities and improved deposition rates are achieved. The ejected target atoms re-deposit on a substrate to form a thin film. In this work, a custom-built magnetron sputtering system was used for the combinatorial preparation of Pd-based thin films (Fig. 7.1a).<sup>27</sup>

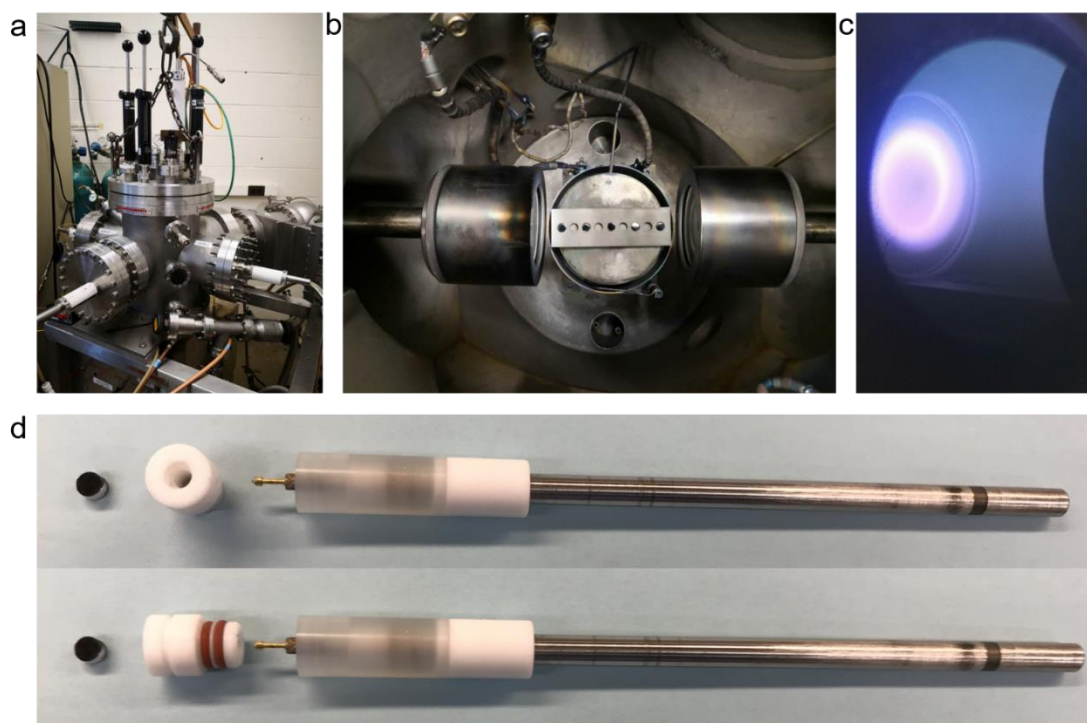


**Figure 7.1** Methodology for the preparation and activity evaluation of thin-film electrodes. (a) Custom-built magnetron sputtering chamber with two sputter guns on the side for preparing Pd-M binary thin films and one Ti gun on the top for sputtering adhesion layers. (b) View inside the chamber showing the home-made sample holder with glassy carbon electrodes between the two sputter guns (Pd and Cu targets). (c) Plasma glow on Pd target during sputtering process. (d) Top and side view of the glassy carbon disk holder along with the replaceable rotating disk electrode (RDE).

The sputtering chamber is composed of a sputtering gun on top, for depositing Ti adhesion layers, and three sputtering guns on the side for co-depositing binary or ternary thin films. The sputtering chamber is pumped to high vacuum conditions ( $< 2 \times 10^{-6}$  Torr) before film deposition. Single-crystal Si wafers were used as the substrate for depositing films for XRD measurements. Polished glassy carbon (GC) electrodes (5 mm diameter) were loaded onto a home-made sample holder, and used as substrates for electrochemical measurements (Pd-M/Ti/GC, [Figs. 7.1b-c](#)). A maximum of nine electrodes could be loaded per batch and were labeled No. 1 to No. 9 from the position

closer to the Pd and M targets, respectively. After film deposition, the Pd-M/Ti/GC electrodes were mounted into a replaceable disk set-up for rotating disk electrode (RDE) measurements (Fig. 7.1d).

#### 7.4 Chemical Composition and Surface Morphology of Pd-Based Thin-Film Alloys

Scanning electron microscopy (SEM) and energy dispersive X-ray (EDX) spectroscopy were employed to assess the chemical composition and surface morphology of Pd-M thin films. As shown in Figure 7.2a, the EDX spectra of a series of Pd-Cu thin films exhibited a progressive compositional change from sample No. 1 to No. 9. The Pd  $L_{\alpha,\beta}$  edges at around 2.8 keV showed a gradual decrease in the intensity while the Cu  $K_{\alpha,\beta}$  edges at 8.0 and 8.9 keV increased, showing the inverse proportionality of the Pd and Cu at.% at different sample positions. The Ti  $K_{\alpha}$  edge at 4.5 keV was also detected due to presence of the Ti adhesion layer under the films. The relative Pd at.% and Cu at.% were quantified based on the Pd L and Cu K edges using the Cliff-Lorimer equation.<sup>28</sup> The total elemental contents of Pd and Cu were set to 100% and the relative errors (one standard deviation) were estimated to be 1-2%. As shown in Figure 7.2b, the Pd at.% smoothly decreased from 95% in sample No. 1 to 7% in sample No. 9. With the sputtering powers of the targets properly calibrated, one could achieve a Pd<sub>50</sub>Cu<sub>50</sub> (Pd/Cu atomic ratio, 1:1) in sample No. 5 (indicated by dashed lines in Figure 7.2b). We observe a Pd or Cu concentration gradient of about 1 at.% per mm across the substrate, although the change was not perfectly linear (Figure 7.2b).

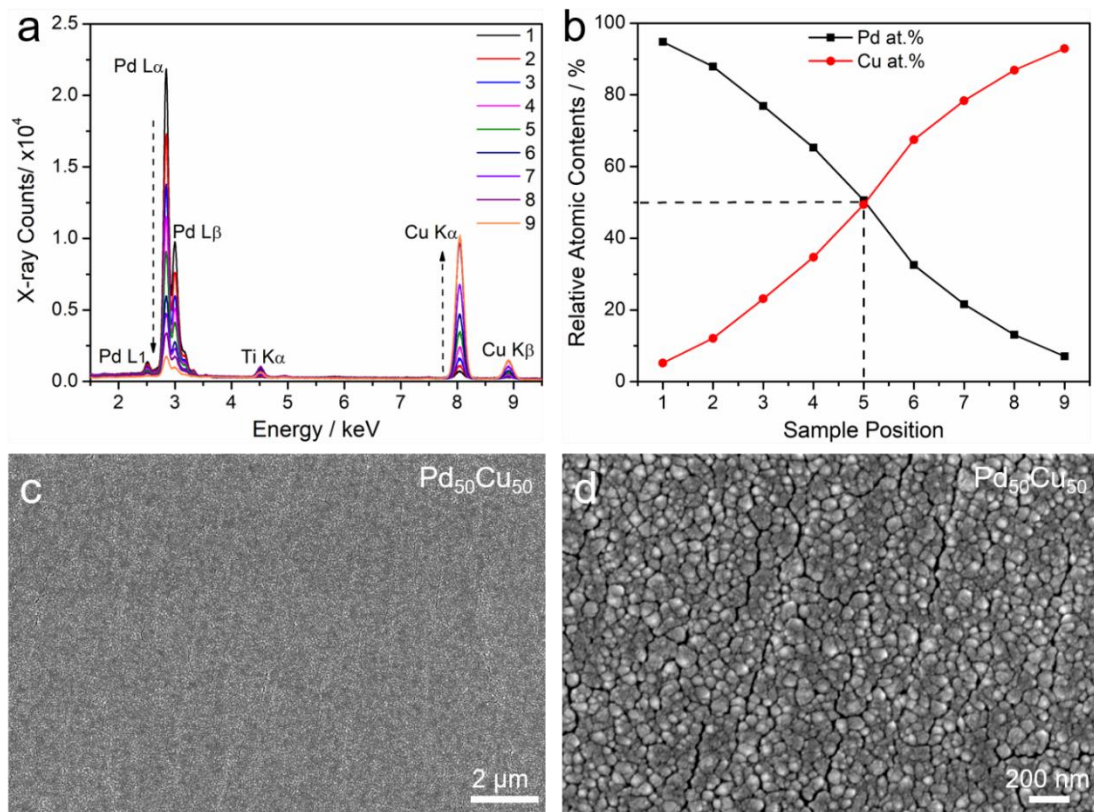


**Figure 7.2 Elemental quantification of Pd-Cu thin-films.** (a) EDX spectra of Pd-Cu thin films with sample position from 1 to 9 (Pd-rich to Cu-rich). Pd L<sub>α,β</sub> and Cu K<sub>α</sub> edges were used for elemental quantification. Ti signal came from the Ti adhesion layer. (b) Relative atomic contents of Pd and Cu (at.%) as a function of the sample position, which covers the range of Pd at.% from ~95% to ~5% with Pd<sub>50</sub>Cu<sub>50</sub> in the middle. (c-d) SEM images of Pd<sub>50</sub>Cu<sub>50</sub> showing a uniform film morphology and a domain size of around 100 nm.

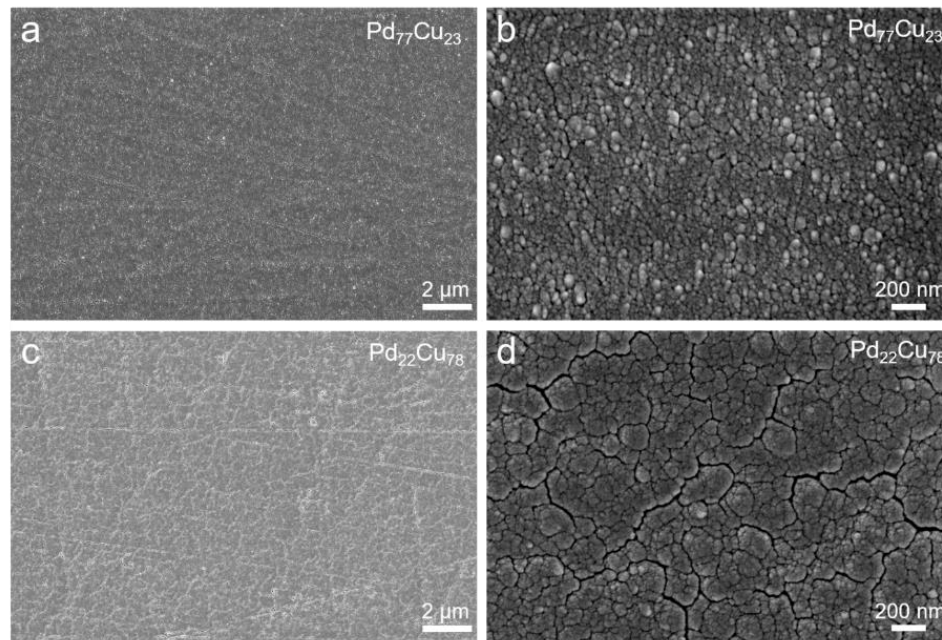


**Figure 7.3** SEM images of Pd-rich Pd<sub>77</sub>Cu<sub>23</sub> (a-b) and Cu-rich Pd<sub>22</sub>Cu<sub>78</sub> (c-d) thin films, respectively, showing a uniform film morphology and a domain size of about 100 nm.

The surface morphology of the thin films was characterized using SEM (Figure 7.2c). Over the field of view of 16 μm or larger, Pd<sub>50</sub>Cu<sub>50</sub> showed highly uniform surface morphology without noticeable μm-sized agglomeration. The magnified SEM image of Pd<sub>50</sub>Cu<sub>50</sub> in Figure 7.2d showed that the smooth surface was composed of metallic clusters with a size of approximately 100 nm. The surface morphologies of Pd-rich and Cu-rich films were also examined under SEM (Figure 7.3). Pd<sub>77</sub>Cu<sub>23</sub> and Pd<sub>22</sub>Cu<sub>78</sub> (estimated as Pd<sub>3</sub>Cu and PdCu<sub>3</sub>) exhibited a homogenous surface morphology over the μm-sized field of view (Figures 7.3a,c). When compared to Pd<sub>50</sub>Cu<sub>50</sub>, Pd<sub>77</sub>Cu<sub>23</sub> and Pd<sub>22</sub>Cu<sub>78</sub> exhibited a similar surface morphology with metallic clusters of around 100 nm (Figures S7.3b,d). Pd<sub>22</sub>Cu<sub>78</sub> showed a smoother surface morphology and larger domain sizes, possibly due to the higher mobility of Cu atoms, relative to Pd atoms, during sputtering.

After examining the surface morphology and bulk compositions, we also characterized the structure and chemical composition of cross sections of the thin films. EDX mapping was employed to evaluate the elemental distribution in the cross section (Figure 7.4). The L edge of Pd and K edges of C, Ti and Cu were used to construct the elemental maps. The elemental maps of C, Ti, Pd and Cu provided a direct visualization of the layered structure of Pd<sub>50</sub>Cu<sub>50</sub>/Ti/C along the cross section (Figures 7.4b-e). In particular, the EDX map of Ti suggested a Ti adhesion layer with a thickness of around 50 nm (Figure 7.4c). The EDX maps of Pd and Cu indicated a catalyst layer of around 350 nm (Figures 7.4d-e). The composite map of Pd + Cu in Figure 7.4f showed a homogenous elemental distribution of Pd and Cu, indicating the successful formation of a binary alloy at the nanometer scale. The EDX map of PdCu on another region also confirmed the same observation of ~50 nm Ti and ~350 nm PdCu film thicknesses, respectively.

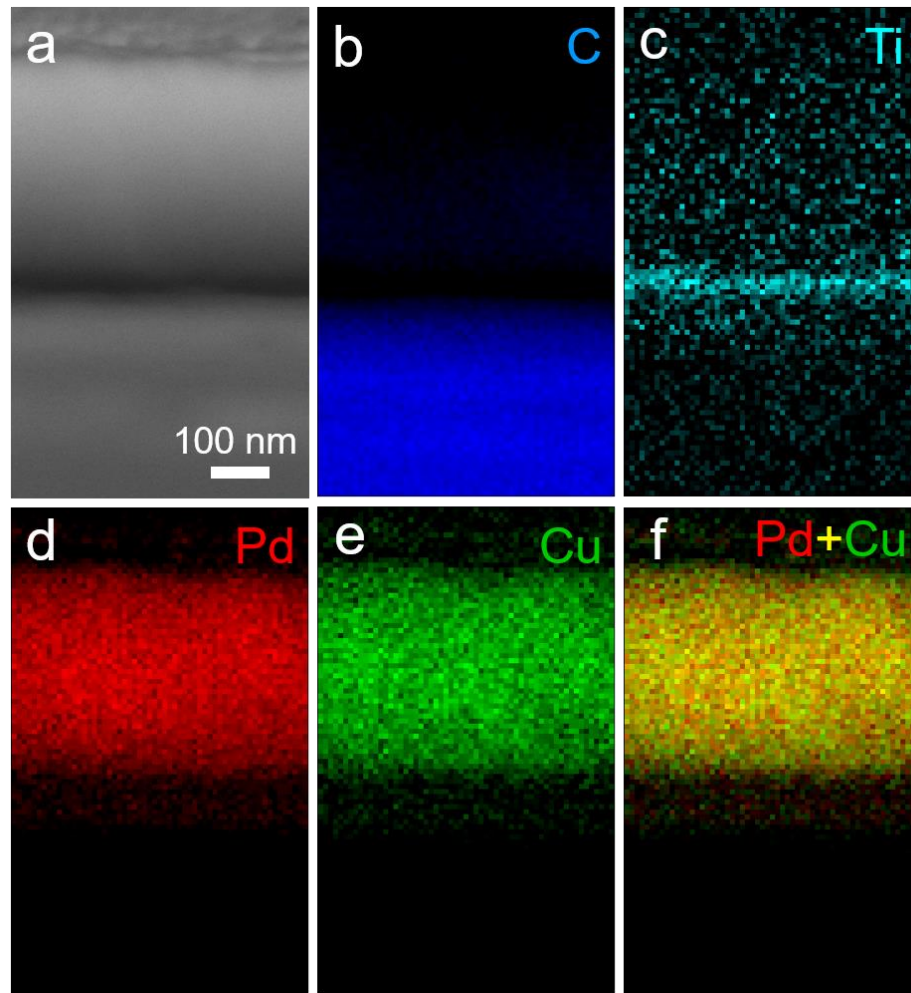


**Figure 7.4** SEM image (a) and the corresponding EDX elemental maps of C (b), Ti (c), Pd (d), Cu (e) and the composite map of Pd + Cu (f) for a Pd<sub>0.5</sub>Cu<sub>0.5</sub> thin film. The thickness of Pd-Cu thin films and Ti underlayer were estimated to be 350 nm and 50 nm, respectively. The uniform false color map in yellow in (f) suggested a homogenous elemental distribution of Pd and Cu.

SEM-EDX was further used to examine the structure and composition of other Pd-based binary thin films (Pd-Co, Pd-Ni and Pd-Fe). Fig. 7.5a presents the EDX spectra of Pd-Co thin films with Ti as the adhesion layer. The intensity was normalized to Co K<sub>α</sub> edges to better show the changes in Pd at.%. Pd-Co thin films exhibited a continuous decay in the intensity of Pd L edges from the sample No.1 to No.9,

corresponding to a higher Pt at.%. As shown in Fig. 7.5b, relative contents of Pd at.% monotonically decreased from 95% in sample No.1, to 48% in sample No.5 and finally to 5% in sample No.9. SEM images of Pd<sub>48</sub>Co<sub>52</sub> exhibited a highly uniform surface morphology (Fig. 7.5c) and metal clusters with sizes of ~100 nm (Fig. 7.5d).

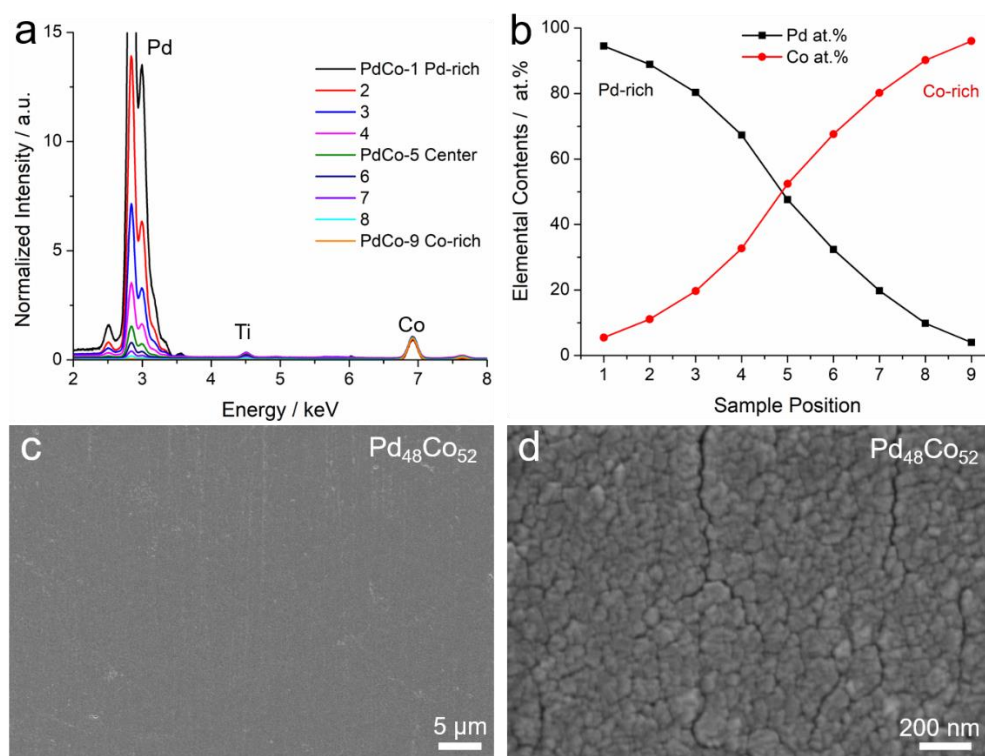


**Figure 7.5 Elemental quantification of Pd-Co thin-film electrodes.** (a) EDX spectra of Pd-Co thin films with sample position from 1 to 9 (Pd-rich to Co-rich). Pd  $\alpha$ , $\beta$  and Co K $\alpha$  edges were used for elemental quantification. (b) Relative atomic contents of Pd and Co (at.%) as a function of sample position, which covers the range of Pd at.% from ~95% to ~5% and Pd<sub>50</sub>Co<sub>50</sub> in sample No.5 (c-d) SEM images of Pd<sub>50</sub>Co<sub>50</sub> showing a uniform film morphology and a domain size of around 100 nm.

Pd-Ni and Pd-Fe also exhibited similar regular patterns in the composition variation from Pd-rich composition in sample No.1 to Ni or Fe-rich composition in sample No.9, with Pd<sub>55</sub>Ni<sub>45</sub> or Pd<sub>48</sub>Fe<sub>52</sub> in sample No.5 (Fig. 7.6). In summary, four families of Pd-based binary thin films (Pd-Cu, Co, Ni and Fe) were examined to have well-controlled compositions and uniform surface morphology. EDX quantification suggested that Pd-

based thin films were able to cover the entire composition range from 95% to 5% with a step size of around 10% among nine continuous samples. SEM images of selected samples indicated that Pd-based thin films were highly homogenous in the surface morphology and exhibited metal cluster with sizes of around 100 nm.

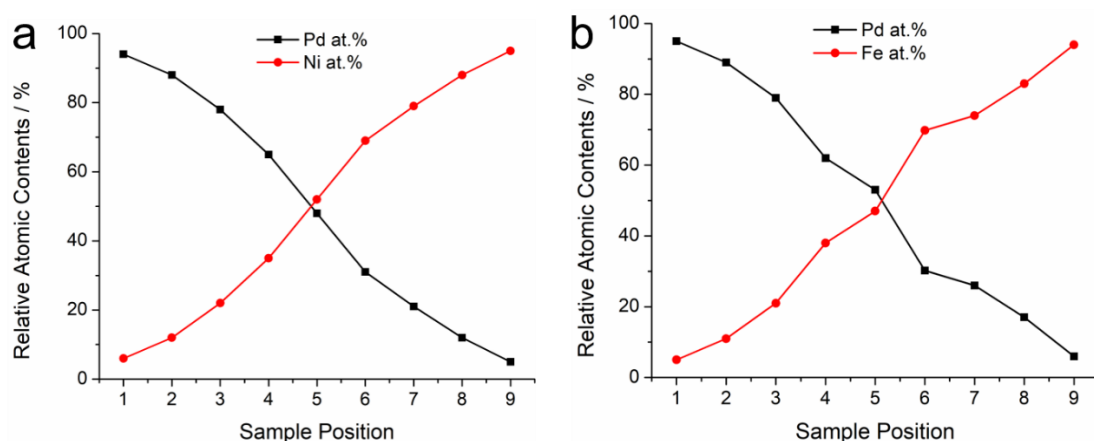


**Figure 7.6** (a-b) Relative atomic contents of Pd-Ni and Pd-Fe thin films.

### 7.5 Crystal Structure of Pd-Based Thin-Film Alloys

The crystal structure of Pd-based thin films was examined using X-ray diffraction (XRD). The XRD patterns of Pd-based thin films would be introduced following the orders of Pd-Cu, Ni, Co, Fe and Mn. All nine Pd-Cu samples exhibited single-phase face centered cubic (fcc) solid solutions with characteristic peaks such as, (111), (200) and (220) (Fig. 7.7). As the thin film compositions changed from Pd-rich sample No. 1 to Cu-rich sample No. 9, the diffraction peaks progressively shifted to higher  $2\theta$  angles due to the incorporation of Cu, with a smaller atomic size, into the Pd lattice. The Pd-Cu (111) peaks shifted to higher angles at higher Cu at.% with Pd<sub>50</sub>Cu<sub>50</sub> (green lines) located right at the middle. Extra diffraction peaks were examined to origin from the background rather than impurity phase of the binary thin films.

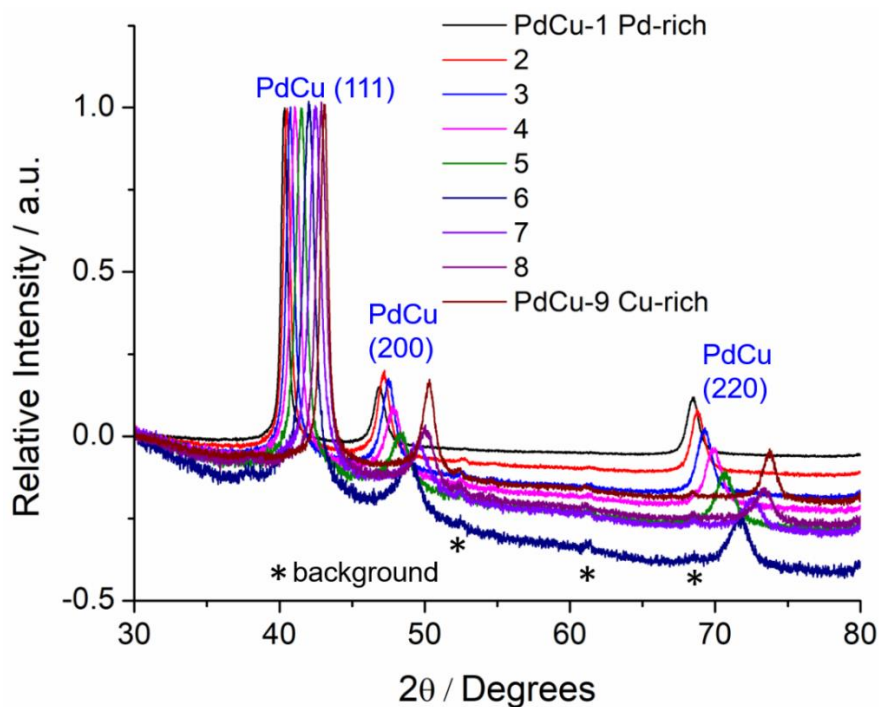


**Figure 7.7** XRD patterns of 9 Pd-Cu thin films with the characteristic (111), (200) and (220) peaks of face centered cubic (fcc) type Pd-Cu binary alloys. The background artifact was labeled as “\*”.

To quantitatively study the formation of solid solutions between Pd and 3d metals, the major diffraction peak, (111) in fcc phase and (110) in bcc phase were summarized in Fig. 7.8 and analyzed using Bragg’s law in Fig. 7.9. The crystal structures and lattice parameters of Pd and 3d metals were summarized in Table 7.2. The (111) peaks of Pd-Cu and Pd-Ni exhibited strong trends as (111) peaks shifting to higher angles with Pd<sub>50</sub>Cu<sub>50</sub> and Pd<sub>50</sub>Ni<sub>50</sub> (green lines) locating in the middle (Figs. 7.8a-b). Pd-Co thin films exhibited similar patterns except the existence of hcp-Co in very Co-rich sample (Pd<sub>5</sub>Co<sub>95</sub>) (indicated by the arrow in Fig. 7.8c). Pd-Fe thin films exhibited a gradual transition from fcc-type to bcc-type PdFe alloys with the existence of a mixed phase at Pd<sub>31</sub>Fe<sub>69</sub> in Fig. 7.8d. For a solid solution, Vegard’s law states that the lattice parameter of a binary alloy will be a weighted average of the two components’ lattice parameters

at the same temperature. The lattice parameters of Pd-based thin films were calculated based on the diffraction angles of the major peaks shown in Fig. 7.8 and plotted as a function of Pd at.% (Fig. 7.9).

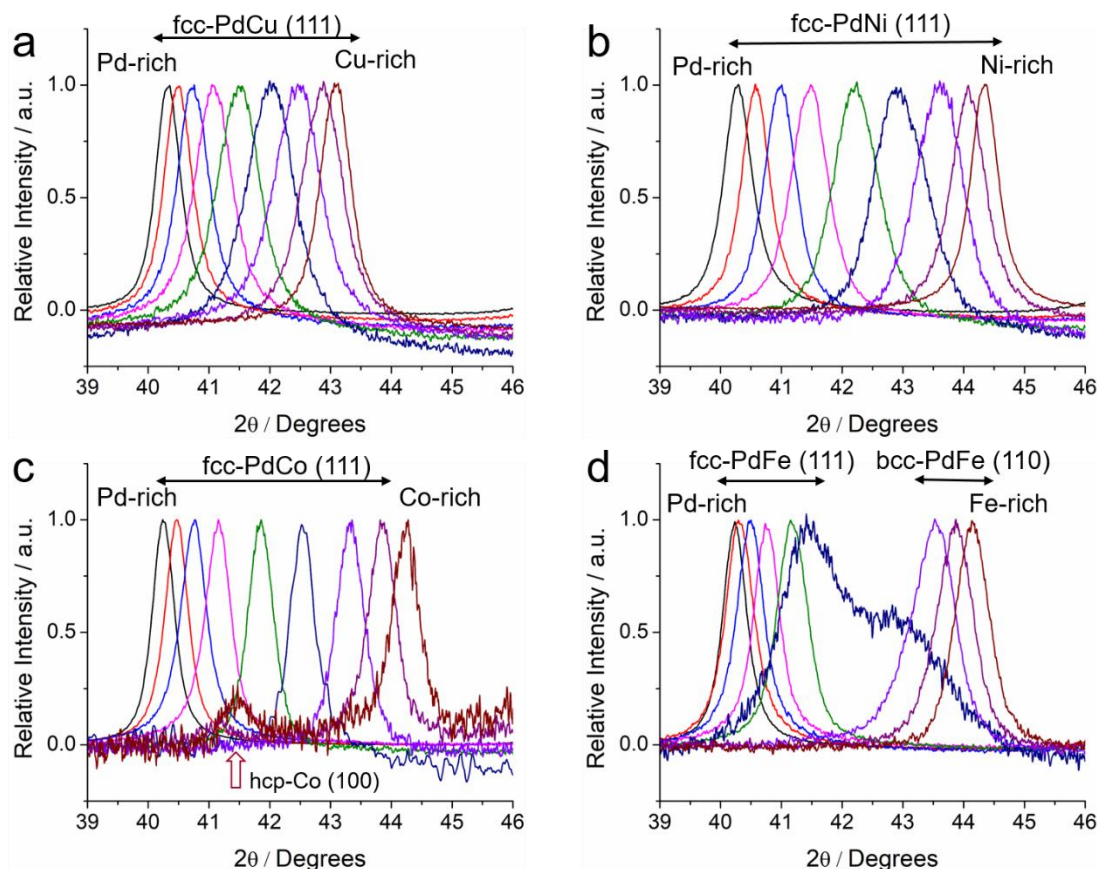


**Figure 7.8** Summary of XRD patterns of Pd-M binary alloys (M: Cu, Ni, Co and Fe). (a-b) XRD patterns of the (111) facets of the 9 Pd-Cu and Pd-Ni thin-film electrodes, respectively. The composition progressively changed from Pd-rich to Cu-rich or Ni-rich compositions, leading to the gradual peak shift to higher angles due to the incorporation of Cu or Ni atoms with small atomic sizes into the Pd lattice. (c) XRD patterns of Pd-Co thin films, which showed similar patterns as the Pd-Cu and Pd-Ni thin films. The noticeable peak at around  $41.5^\circ$  was ascribed to the formation of hcp-Co at very Co-rich  $\text{Pd}_5\text{Co}_{95}$  films. (d) XRD patterns of Pd-Fe thin films. The first five Pd-rich samples from  $\text{Pd}_{95}\text{Fe}_5$  (black) to  $\text{Pd}_{50}\text{Fe}_{50}$  (green) exhibited a fcc-type PdFe alloys. The Fe-rich films from  $\text{Pd}_{26}\text{Fe}_{74}$  (purple) to  $\text{Pd}_6\text{Fe}_{94}$  (brown) showed the body centered cubic (bcc) structure.  $\text{Pd}_{31}\text{Fe}_{69}$  films showed the mixed phase of fcc and bcc structures.

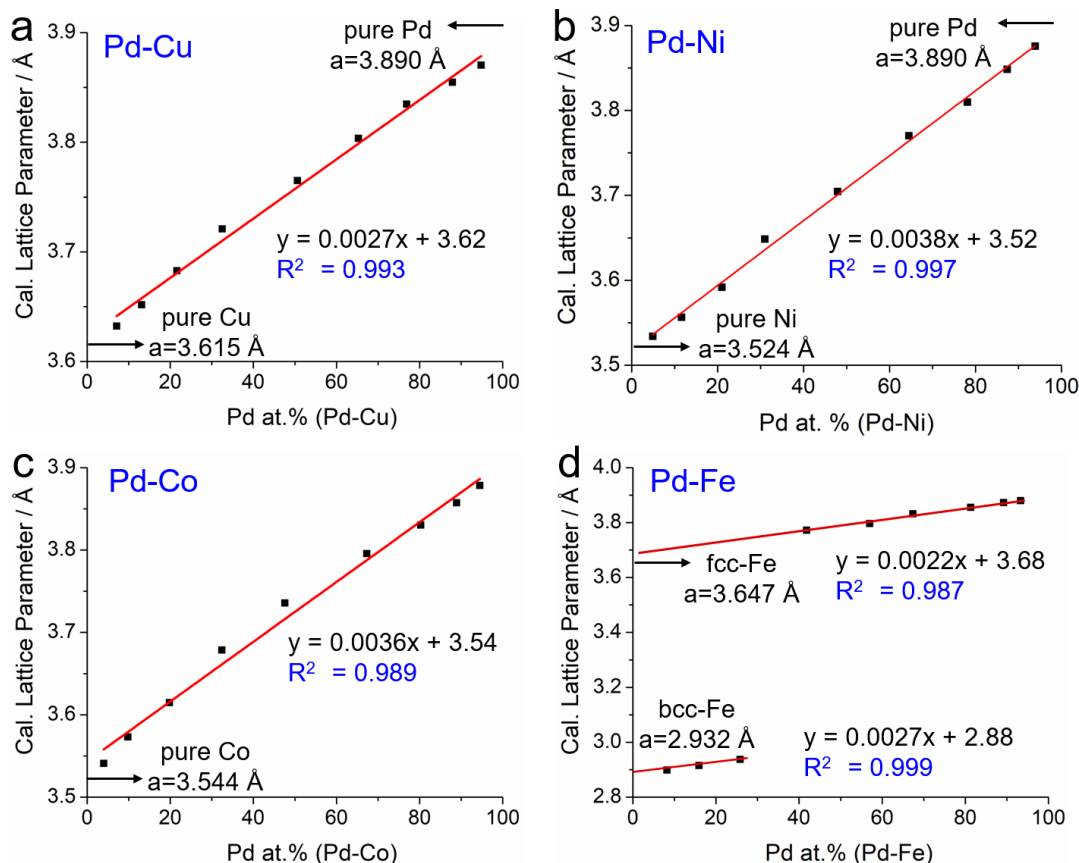


**Figure 7.9** Linear relation of calculated lattice parameters and relative Pd at.% in Pd-M thin films, following the prediction of Vegard's law. (a) The lattice parameter of Pd-Cu thin films, calculated from (111) peaks as a function of the Pd at.%. The scattered plot was fitted into a linear expression of  $y = 0.0027x + 3.62$  with a high quality of  $R^2 = 0.993$ . The y-intercept is the lattice parameter of Cu and the slope is the lattice parameter difference between Pd and Cu divided by 100. (b-c) The lattice parameter of Pd-Ni and Pd-Co thin films as a function of Pd at.%, showing good linear relationship. (d) The lattice parameter of Pd-Fe as a function of Pd at.%, which was divided into two regions: the Pd-rich films (samples 1-6) and the Fe-rich regions (samples 7-9).

Pd-Cu thin films exhibited an excellent linear relation of the calculated lattice parameter as a function of Pd at.% with a linear fitting coefficient  $R^2 = 0.993$  (Fig. 7.9a). The fitted linear equation was calculated as  $y = 0.0027x + 3.62$ . The y-intercept (3.62 Å) at 0% of Pd is consistent with the lattice parameter of pure Cu (3.615 Å). The slope (0.0027 Å) is consistent with the theoretical percentage difference in the lattice

parameters between Pd and Cu ( $(3.890 \text{ \AA} - 3.615 \text{ \AA})/100 = 0.00275 \text{ \AA}$ ). Those results strongly suggested Pd-Cu thin films formed complete solid solutions. Pd-Ni exhibited a similar linear relation with a remarkable  $R^2$  value of 0.997. The Y-intercept (3.52) and slope (0.0038) matched well with the theoretical values of 3.524 and 0.00366, respectively (Fig. 7.9b). Pd-Co showed a reasonably good linear relation with a  $R^2$  value of 0.989 (Fig. 7.9c). The last point corresponding to the hcp-type Pd<sub>5</sub>Co<sub>95</sub> is slightly off from the fitted line, which was possibly due to the difference in crystal structure between hcp-Co and fcc-Co (Table 7.2). Pd-Fe showed two distinct categories of linear relations in Pd-rich fcc-type alloys and Fe-rich bcc-type alloys (Fig. 7.9d). Both of them exhibited a linear relation with  $R^2$  values of  $\geq 0.99$ , and Y-intercepts and slopes matched well with the theoretical values. The formation of bcc-type Fe-rich films (Fe at.% from 74% up to 94%) was possibly ascribed to the significant difference in crystal structures between fcc-type Pd and bcc-type Fe.

Elements	Pd, fcc	Cu, fcc	Ni, fcc	Co, fcc/hcp	Fe, fcc/bcc	Mn, bcc	Cr, bcc	V, bcc
Lattice Parameters / $\text{\AA}$	3.890	3.605	3.524	3.544/ a=b=2.505, c=4.089	3.647/ 2.932	3.081	2.885	3.028

**Table 7.2.** Summary of lattice parameters of Pd and 3d metals. Co and Fe can exist in two phases. fcc, hcp and bcc represent face centered cubic, hexagonal close packed and body centered cubic, respectively.

In addition, Pd-Mn thin films were prepared and examined using XRD (Fig. 7.10). Pd-Mn exhibited mixed phases of fcc-Pd and bcc-Mn across the whole composition range from sample No.1 to No.9. Little peak shift of (111) from sample No.1 to No.5, despite of the composition changing from Pd<sub>95</sub>Mn<sub>5</sub> to Pd<sub>50</sub>Mn<sub>50</sub>, suggested that little amount of Mn was incorporated into the Pd lattice to cause a noticeable lattice

contraction.

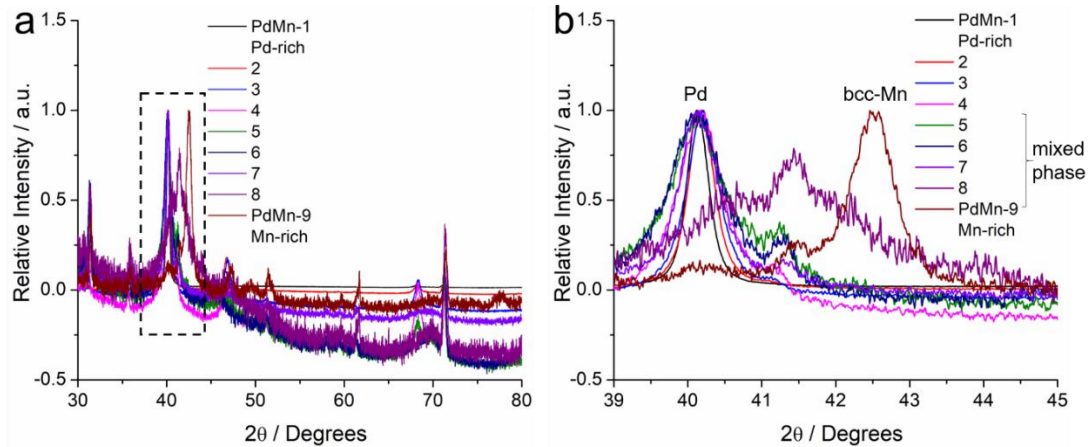


**Figure 7.10** (a) XRD patterns of Pd-Mn thin films. As shown in the magnified region in (b), The (111) peaks at around  $40^\circ$  showed little peak shift despite the composition changed from  $\text{Pd}_{95}\text{Mn}_5$  to  $\text{Pd}_{50}\text{Mn}_{50}$ , indicating little Mn was incorporated into the Pd lattice. Further increase the Mn contents from  $\text{Pd}_{50}\text{Mn}_{50}$  to  $\text{Pd}_5\text{Mn}_{95}$  resulted in the mixed phases of bcc-type Mn or Mn-rich alloys with Pd-rich alloys. The XRD patterns suggested that Pd-Mn single-phase binary alloys were not achieved under the current sputtering conditions.

To some extents, crystal structures and lattice parameters of Pd and 3d metals can help us rationalize the similarity and difference among different families of Pd-M thin films (Table 7.2). In general, in order to form a single-phase solid solution, two components should have same or similar crystal structures and lattice constants. The relative differences in lattice parameters of Pd and Cu, Pd and Ni are about 6% and 9%, which were moderate to cause lattice contractions but not induce phase segregation. The formation of Pd-Ni and Pd-Cu solid solutions can also be understood from the phase diagram (Figs. 7.11a-b). Despite of some multi-phase regions (white) in the Pd-Cu phase diagram, Pd-Cu still showed a complete solid solution among the whole composition range. This was possibly due to the formation of metastable binary alloys over those multi-phase regions during magnetron sputtering in which gas-phase

sputtered atoms into solid-phase metal films at an ultrafast cooling rate. The formation of Pd-Co fcc-type solid solutions were mostly successful except the very Co-rich alloys ( $\text{Pd}_5\text{Co}_{95}$ , which was a single-phase hcp-type alloy with similar crystal symmetry to the fcc-type alloys. This was noticeable in the miscible phase diagram of Pd-Co (Fig. 7.11c). In Pd-Fe alloys, a certain amount of Fe (up to around 50%) was able to be incorporated into the Pd lattice to form fcc-type PdFe alloys. Further increase in Fe at.% to 69% or higher would induce the formation of bcc-type PdFe alloys with a much smaller lattice parameter of 2.932 Å. Those observation in XRD was consistent with the phase distribution in the Pd-Fe phase diagram (Fig. 7.11d). When Fe at.% is larger than 50%, thermodynamically, Fe prefers not to form a solid solution with Pd. The formation for bcc-type PdFe alloys was probably due to the sputtering process forcing Pd atoms into the bcc-type lattice of Fe to form metastable alloys.

When an enormous lattice mismatch was introduced, such as in the case of Pd-Mn thin films. The difference in lattice parameters of Pd and Mn was as large as 21% (Fig. 7.12a), which would not allow for the formation of single-phase solid solutions, even metastable compositions under current sputtering conditions. Other metals like V, Cr or Ti may also have the similar challenges to form single-phase alloys with Pd. The lattice mismatch between Pd and Mn, V, Cr or Ti is consistent with the large multi-phase regions in their phase diagrams. (Figs. 7.12b-d).

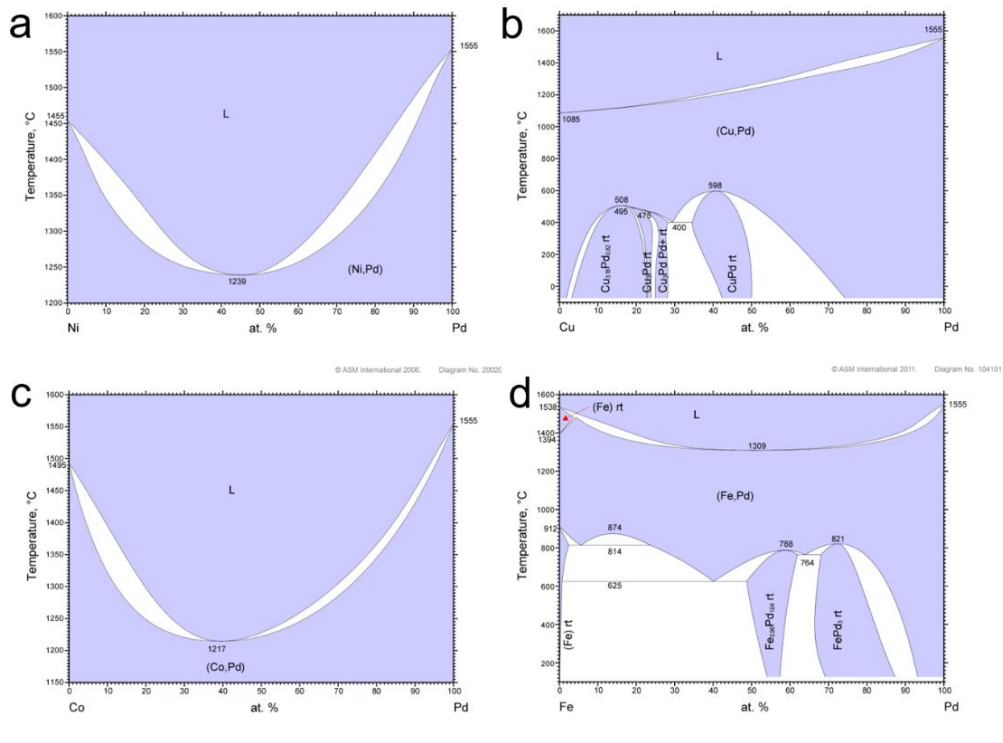


Figure 7.11 Phase diagrams of Pd-Ni, Pd-Cu, Pd-Co and Pd-Fe. Copyright © ASM

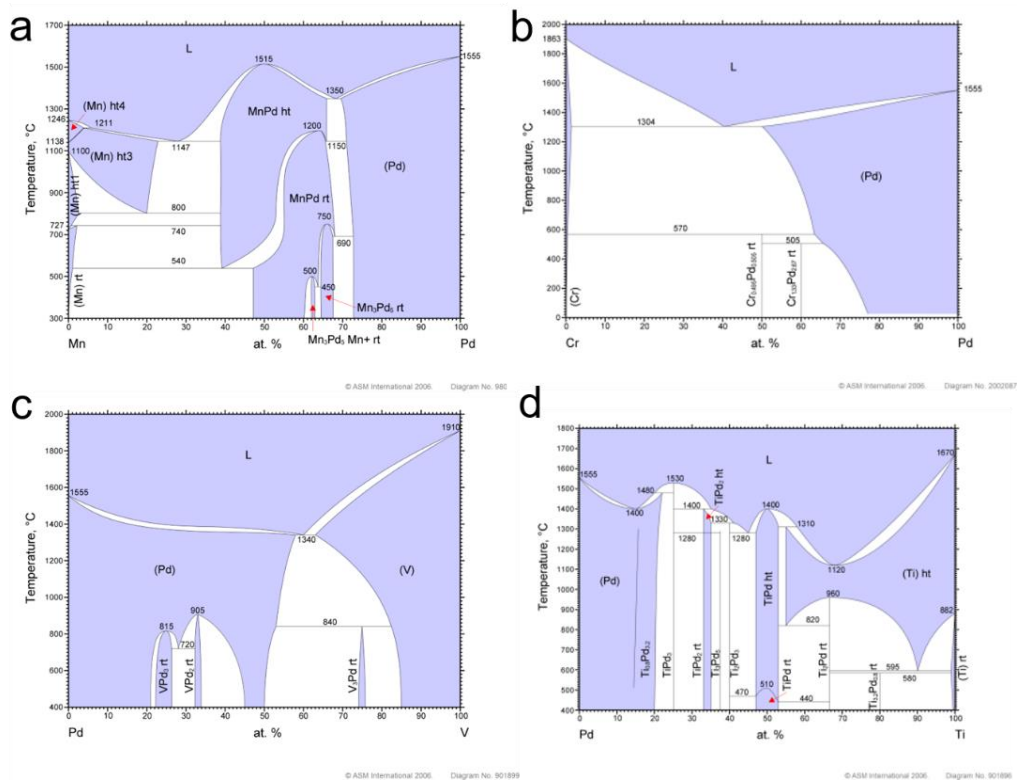
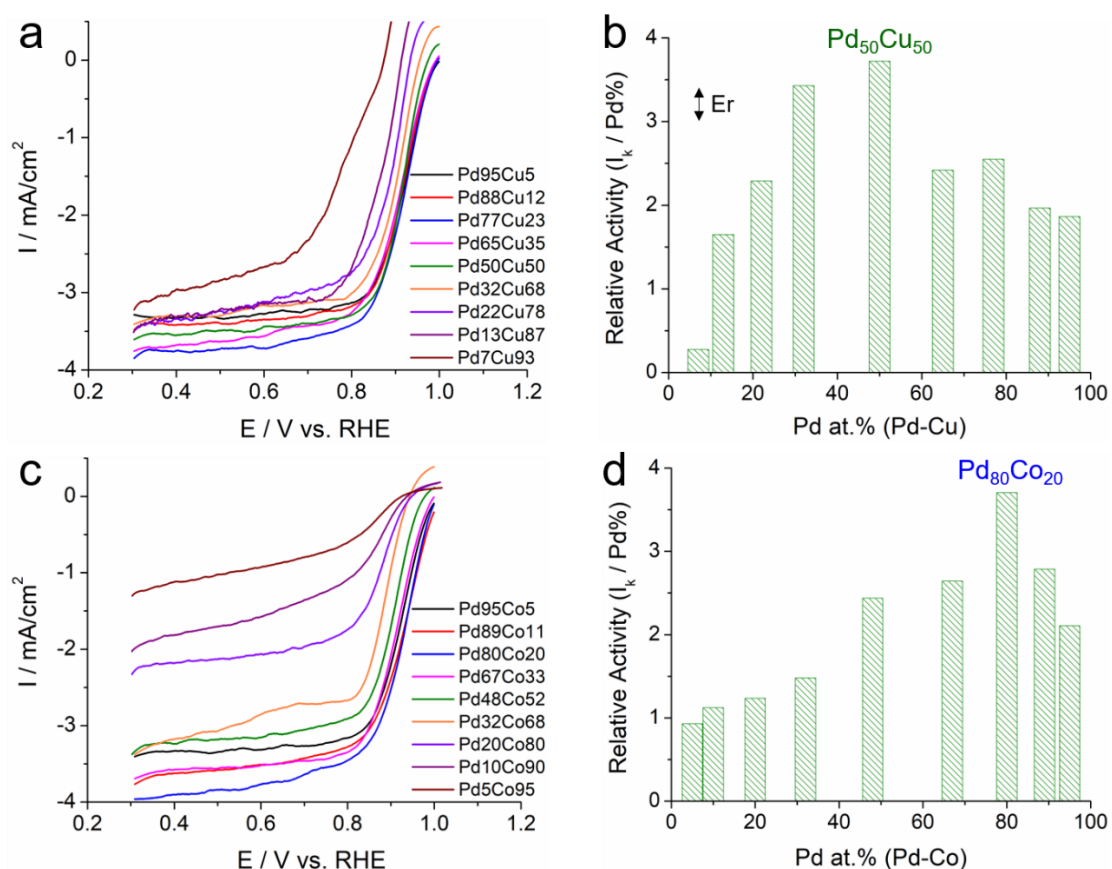


Figure 7.12 Phase diagrams of Pd-Mn, Pd-Cr, Pd-CV and Pd-Ti. Copyright © ASM

## 7.6 ORR Activity of Pd-Based Thin-Film Alloys

The Pd-Cu thin films were subsequently tested as electrocatalysts for the ORR in alkaline media. Pd-Cu/Ti/GC electrodes were loaded into the described replaceable disk electrode assembly for RDE measurements in 1 M KOH at a scan rate of 5 mV/s and a rotation rate of 1600 rpm. As shown in Fig. 7.13a, Pd-Cu thin films were able to achieve a  $I_d$  of around  $-3.5 \text{ mA/cm}^2$ , suggesting the preponderance of the  $4e^-$  process of reducing  $O_2$  completely to  $H_2O$ , instead of the  $2e^-$  process leading to hydrogen peroxide formation. Pd-Cu thin films with Pd at.% from 32% to 7% (Cu-rich alloys) exhibited  $I_d$  values lower than  $-3.5 \text{ mA/cm}^2$ , indicating a larger contribution of hydrogen peroxide formation. Lowering the Pd at.% from 32% to 7% also caused a noticeable decrease in the half-wave potential ( $E_{1/2}$ ) of 31 mV. To quantitatively assess the activity of the various Pd-Cu thin films, the kinetic current ( $I_k$ ) at 0.9 V was calculated, based on the Koutecký-Levich equation, and normalized to the relative Pd at.%. As previously shown, the Pd-Cu thin films were homogeneously mixed on the surface, as evidenced by the SEM-EDX maps (Fig. 7.4). Therefore, the relative Pd at.% can be used as representing the relative coverage of Pd on the surface.



**Figure 7.13** (a) ORR polarization profiles of Pd-Cu thin films at 5 mV/s and 1600 rpm, and (b) the corresponding the relative activity ( $I_k$  @ 0.9 V vs. Pd at.%), with an optimal value at Pd<sub>50</sub>Cu<sub>50</sub> (c) ORR polarization profiles of Pd-Co thin films at 5 mV/s and 1600 rpm, and (d) the corresponding the relative activity ( $I_k$  @ 0.9 V vs. Pd at.%), with an optimal value at Pd<sub>80</sub>Co<sub>20</sub>.

Normalizing the  $I_k$  to Pd at.% can, thus, represent the relative intrinsic activity per Pd site. As shown in Fig. 7.13b, the relative activity of various Pd-Cu thin films followed a volcano plot with an optimal activity at Pd<sub>50</sub>Cu<sub>50</sub>. The relative activity of Pd<sub>50</sub>Cu<sub>50</sub> was about twice that of the nearly pure Pd film (Pd<sub>95</sub>Cu<sub>5</sub>). Further increases of the Cu at.% above 50% caused a gradual decay of the relative activity and, eventually, a significantly low activity at Pd<sub>7</sub>Cu<sub>93</sub> (only 15% of the relative activity of Pd<sub>95</sub>Cu<sub>5</sub>). Cyclic voltammetry (CV) profiles of Pd-Cu thin films suggested that lowering the Pd

content from Pd<sub>88</sub>Cu<sub>12</sub> to Pd<sub>50</sub>Cu<sub>50</sub> and Pd<sub>13</sub>Cu<sub>87</sub> caused the hydrogen region (0.1-0.2 V) to be suppressed as a result of fewer Pd sites on the surface. (Fig. 7.14). Lower Pd content (i.e. higher Cu at.%) was also associated with larger reduction peaks near 0.7 V, which was presumably due to the formation of larger amount of Cu oxide during the previous positive scan. In summary, the RDE measurements indicated that Pd<sub>50</sub>Cu<sub>50</sub> is as a promising composition for PdCu nanoparticles for the ORR in alkaline media.

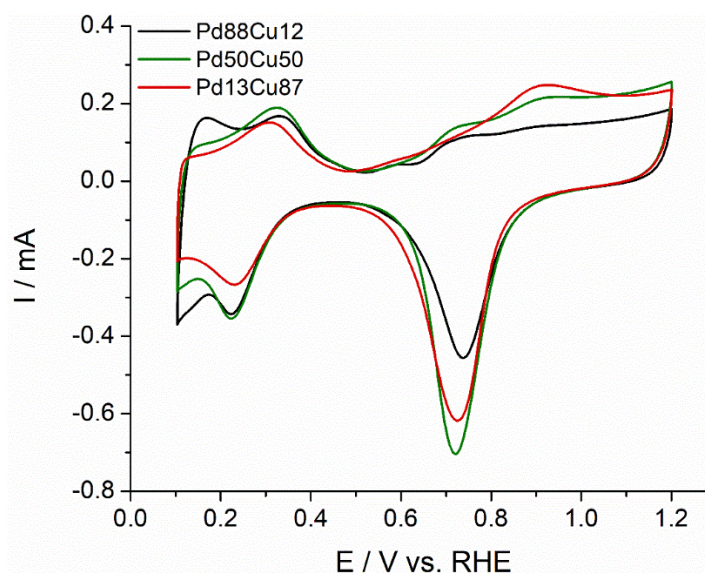


**Figure 7.14** CV profiles of 3 types of Pd-Cu films at 20 mV/s in Ar-sat. 1 M KOH.

RDE measurements of Pd-Co were performed under same test conditions in 1M KOH (Fig. 7.13c). Reducing Pd at.% from 95% to 67% did not result in a significant change in the early kinetic-controlled region (0.9-1.0 V). Further lowering the Pd at.% from 48% to 5% caused a dramatic decrease in both the half-wave potential ( $E_{1/2}$ ) as well as the  $I_d$ , suggesting Pd at.% (<50%) would induce a larger contribution from the  $2e^-$  peroxide formation, especially for Pd at.% less than 20%. The relative activity increased from Pd<sub>95</sub>Co<sub>5</sub> to Pd<sub>80</sub>Co<sub>20</sub> and then continuously decreased from Pd<sub>80</sub>Co<sub>20</sub> to Pd<sub>5</sub>Co<sub>95</sub> (Fig. 7.13d).

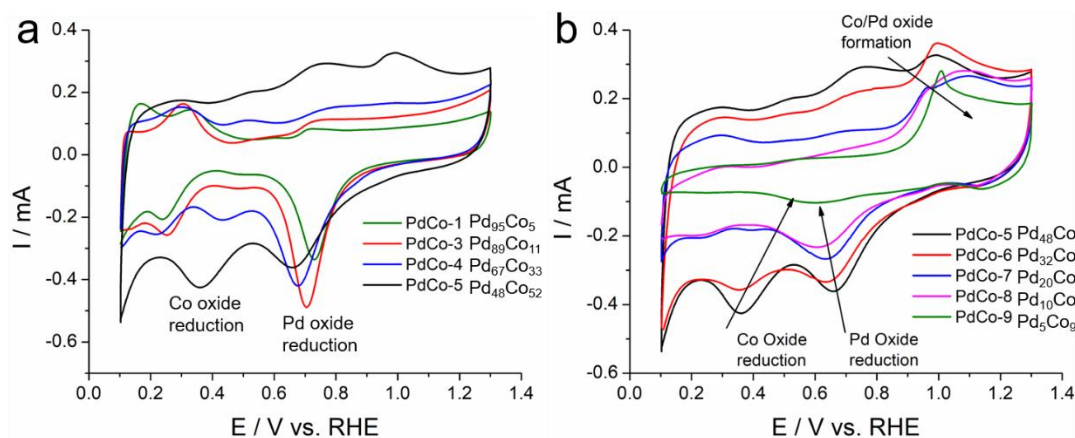


**Figure 7.15** CV profiles of Pd-rich Pd-Co films (a) and Co-rich Pd-Co films (b) at 20mV/s in Ar-sat. 1M KOH.

CV profiles of Pd-Co thin films showed the involvement of the co-existence of two redox couples (Pd/Pd oxides and Co/Co oxides, Fig. 7.15). Pd<sub>95</sub>Co<sub>5</sub> and Pd<sub>89</sub>Co<sub>11</sub> showed the characteristic hydrogen regions of Pd with the peak near 0.2V corresponding to the underpotential deposition of hydrogen atoms (H<sub>UPD</sub>) (Fig. 15a). Further increase Pd at.% to Pd<sub>67</sub>Co<sub>33</sub> and Pd<sub>48</sub>Co<sub>52</sub> showed the noticeable reduction peak at around 0.4 V, which corresponded to the reduction of Co oxide and suggested Pd and Co co-existed on the surface of thin films (Fig. 15a). In the Co-rich films, the reduction peak of Pd oxide gradually decreased from Pd<sub>48</sub>Co<sub>52</sub> to Pd<sub>10</sub>Co<sub>90</sub> with less pronounced hydrogen regions (Fig. 15b). Very Co-rich Pd<sub>5</sub>Co<sub>95</sub> films almost only showed the redox couple of Co (1.1V/0.6V) given the little amount of Pd. In summary, those results indicate Pd<sub>80</sub>Co<sub>20</sub> (i.e., Pd<sub>4</sub>Co) could be a potential composition for further nanoparticle synthesis.

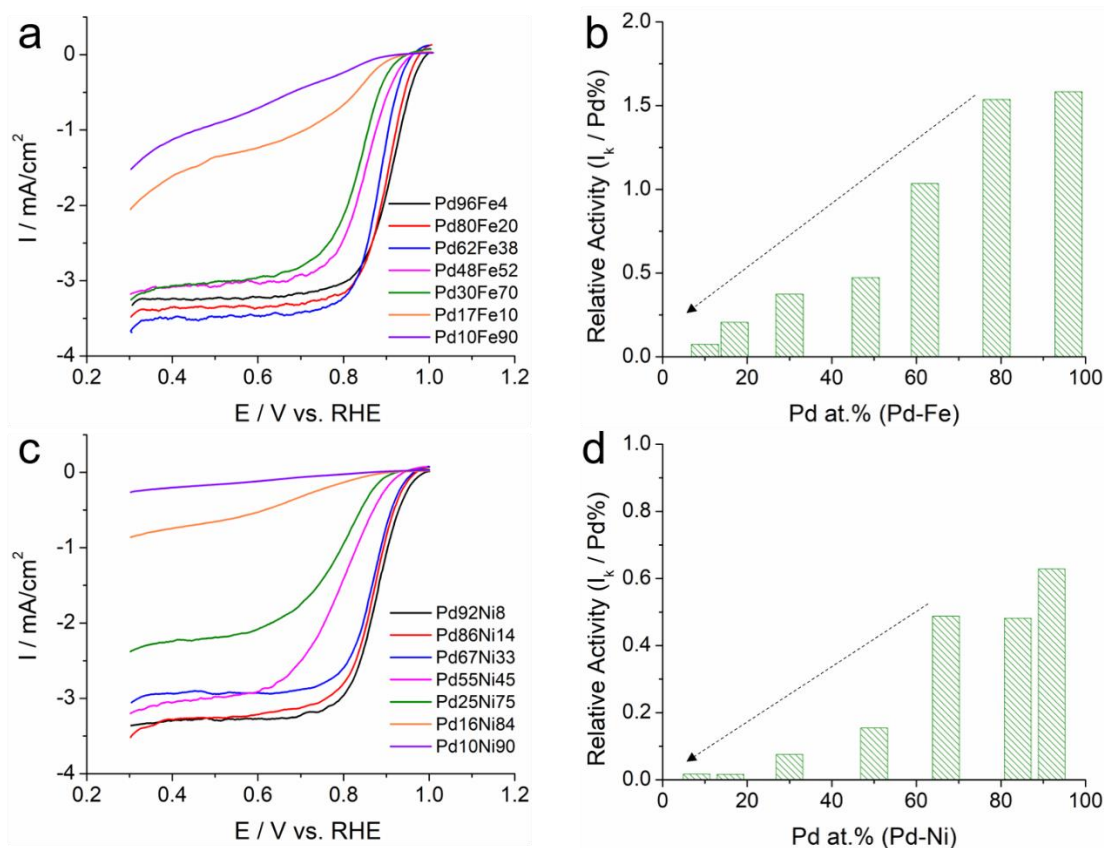


**Figure 7.16** (a) ORR polarization profiles of Pd-Fe thin films at 5 mV/s and 1600 rpm in O<sub>2</sub>-sat. 1M KOH , and (b) the corresponding the relative activity ( $I_k$  @ 0.9 V vs. Pd at.%), with a monotonic activity decay at less Pd at.% (c) ORR polarization profiles of Pd-Co thin films at 5 mV/s and 1600 rpm, and (d) the corresponding the relative activity ( $I_k$  @ 0.9 V vs. Pd at.%), with an optimal value at Pt<sub>80</sub>Cu<sub>20</sub>, with the similar trend as Pd-Fe system.

ORR activities of Pd-Fe and Pd-Ni were also measured under same test conditions in 1M KOH (Fig. 7.16). When Pd at.% decreased from Pd<sub>96</sub>Fe<sub>4</sub> to Pd<sub>30</sub>Fe<sub>70</sub>, Pd-Fe thin films exhibited a near-4e<sup>-</sup> process with a gradual decay in the  $E_{1/2}$  (Fig. 7.16a). Further decrease of Pd at.% from Pd<sub>30</sub>Fe<sub>70</sub> to Pd<sub>10</sub>Fe<sub>90</sub> caused a significant loss in the  $I_d$ , indicating a larger contribution from 2e<sup>-</sup> peroxide formation. The calculated relative activity of Pd-Fe thin films showed an monotonic decay as Pd at.% decreased from 96% to 10% (Fig. 7.16b). When the Pd at.% in Pd-Ni films decreased from Pd<sub>92</sub>Ni<sub>8</sub> to

Pd<sub>10</sub>Ni<sub>90</sub>. Pd-Ni thin films showed a similar trend in the ORR polarization profiles (Fig. 7.16c) and calculated relative activity (Fig. 7.16d). CV profiles of Pd-Fe and Pd-Ni films suggested a gradual loss of H<sub>UPD</sub> regions from Pd<sub>96</sub>Fe<sub>4</sub> to Pd<sub>17</sub>Fe<sub>83</sub> and from Pd<sub>86</sub>Ni<sub>14</sub> to Pd<sub>16</sub>Ni<sub>84</sub> (Fig. 7.17).

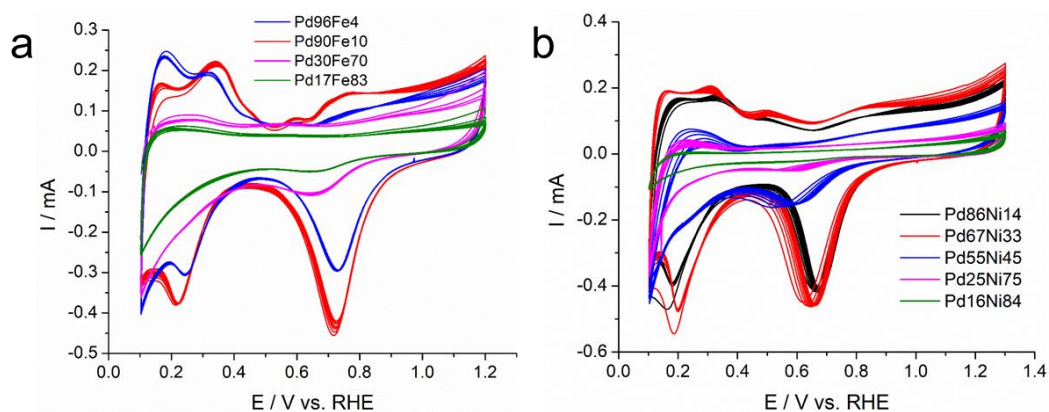


**Figure 7.17** CV profiles of Pd-Fe (a) and Pd-Ni (b) films at 20mV/s in Ar-sat. 1M KOH.

In summary, ORR activities of four families of Pd-Cu, Co, Fe and Ni binary alloys were examined using replaceable disk electrodes in RDE measurements. Pd<sub>50</sub>Cu<sub>50</sub> and Pd<sub>80</sub>Co<sub>20</sub> showed optimal activities among Pd-Cu and Pd-Co thin film electrodes. In contrast, Pd-Fe and Pd-Ni showed a monotonic activity decay as a result of the decrease of Pd at.%. The composition of Pd<sub>50</sub>Cu<sub>50</sub> would be used as a guideline to design PdCu nanoparticles for practical fuel cell applications.

## 7.7 Synthesis of the Nanoparticle Form of Pd<sub>50</sub>Cu<sub>50</sub>, the Optimal Composition from Thin-Film Studies

Following the thin-film screening, Pd and PdCu nanoparticles, supported on carbon, were synthesized by an impregnation-reduction method using either metal chlorides or nitrates as precursors (Figure 7.26).

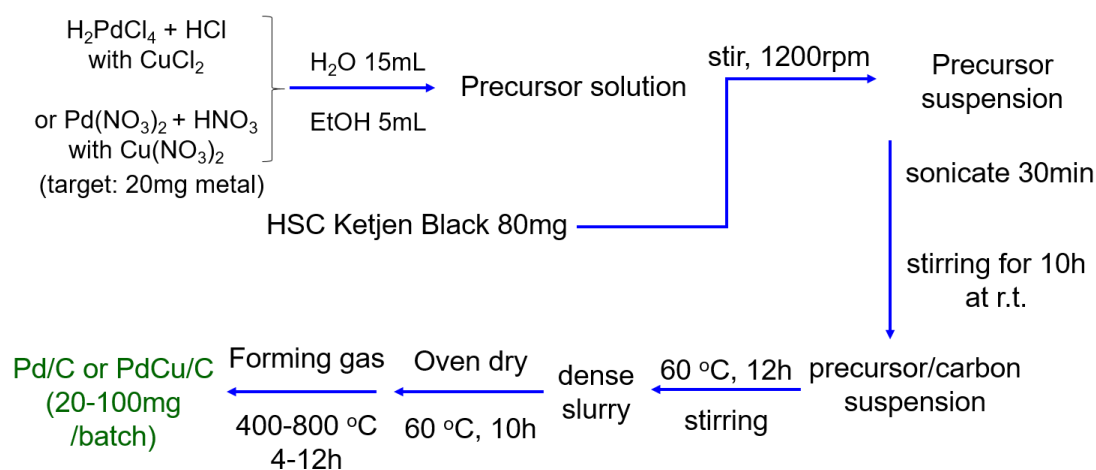


**Figure 7.18** Synthesis of Pd/C and PdCu/C using Pd and Cu chloride or nitrate precursors. The slurry was prepared using the described impregnation method and reduced to nanoparticle catalysts under forming gas (5% H<sub>2</sub> and 95% N<sub>2</sub>). HSC Ketjen Black is one type of high surface area carbon with a BET surface area of ~800 m<sup>2</sup>/g.

As shown in the phase diagram of PdCu (Fig. 7.11b), PdCu with a molar ratio of 1:1 is located at the edge between the single-phase PdCu and a multi-phase region, indicating that its chemical synthesis requires a delicate control of the precursor types and reaction conditions. When Pd and Cu chlorides were used as precursors and reduced at 800 °C for 12 h in forming gas, the synthesized PdCu/C exhibited a single-phase ordered structure (o-PdCu/C, CsCl-type, Pm-3m) with characteristic diffraction peaks of (100), (110), etc. (Fig. 7.19). The domain size of the PdCu nanoparticles was estimated to be around 25 nm based on the Scherrer equation. Lowering the reaction

time or temperature caused a significant phase segregation.

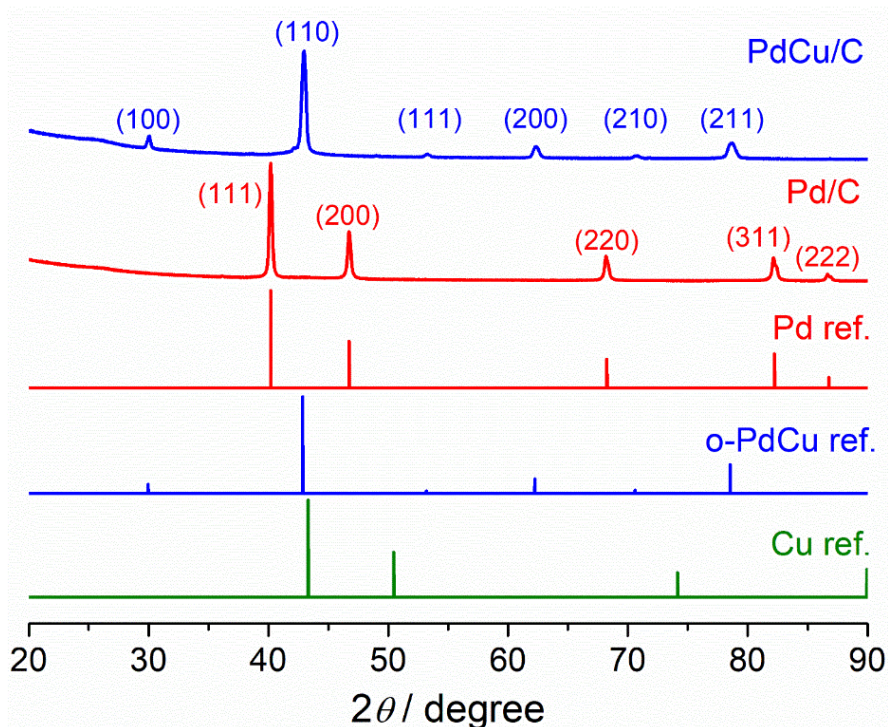


**Figure 7.19** XRD patterns of PdCu and Pd nanoparticles supported on carbon with the references of Pd, Cu and o- PdCu (o-PdCu, PDF # 04-015-2413).

As a comparison, Pd/C, with a face centered cubic (fcc) phase, was synthesized at 800 °C for 4 h to achieve a similar particle size and surface area, relative to PdCu/C (Figure 7.19). When Pd and Cu nitrates were employed to synthesize PdCu alloy nanoparticles, the XRD patterns showed a dramatic difference in the crystal structure, when compared to o-PdCu/C (Figure 7.20). Too low reaction temperatures under forming gas (e.g., 400 °C) resulted in the formation of a mixture of elemental Pd and Cu as well as Pd-Cu disordered alloys. However, too high reaction temperatures (e.g. 900 °C) resulted in mixed phases of Pd-rich and Cu-rich alloys (green lines). Even the optimized reaction conditions of 800 °C for 12 h still led to the formation of asymmetrical diffraction peaks in the PdCu disordered alloys (cyan lines), indicating

multi-phase nanoparticles. To this end, single-phase ordered PdCu/C was synthesized from Pd and Cu chloride precursors at 800 °C for 12h. It has been reported that Pd and Pt-based intermetallics, or ordered alloys, can effectively mitigate the leaching problem of 3d metals and exhibit enhanced durability, relative to their disordered counterparts.<sup>29-31</sup> Therefore, we focused on the synthesized o-PdCu/C for further structural and electrochemical characterization.

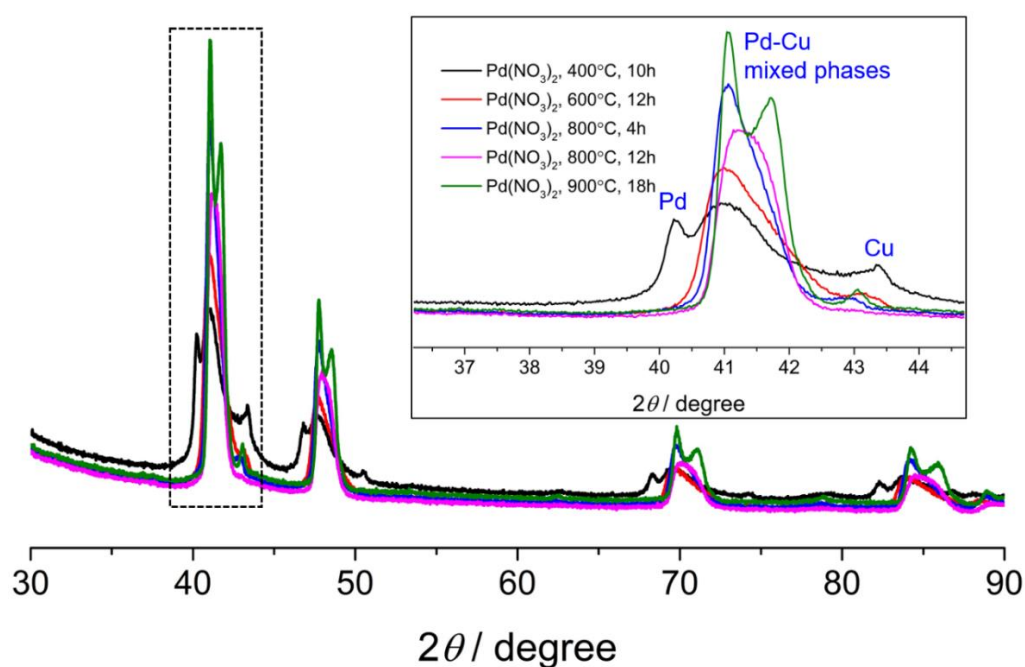


**Figure 7.20** XRD patterns of a variety of mixed phased of Pd-Cu disordered alloys using Pd and Cu nitrate as precursors at different annealing conditions. The inset shows the peak splitting or broadening due to phase segregation at the peak position corresponding to the (111) peak of the PdCu disordered alloys. The chloride-precursor-optimized condition of annealing of 800 °C for 12 h still resulted in asymmetrical diffraction peaks (magenta profile in the inset), indicating a mixture of two phases.

### 7.8 Microstructure and Chemical Composition of Pd<sub>50</sub>Cu<sub>50</sub> Nanoparticles

The microstructure of o-PdCu/C was analyzed using a high-angle annular dark-field scanning/transmission electron microscope (HAADF-S/TEM). o-PdCu/C exhibited a

uniform size distribution of PdCu nanoparticles on the carbon (Fig. 7.21a). Statistical analysis of around 500 PdCu nanoparticles resulted in a particle size distribution (PSD) of  $40 \pm 7$  nm (Fig. 7.21b). This differs from the average domain size of 25 nm calculated from the XRD, suggesting that these nanoparticles have multiple domains. As a comparison, Pd/C, synthesized at 800 °C for 4 h, showed a similar narrow PSD of  $50 \pm 9$  nm. The atomic-scale bright field (BF) TEM image and the corresponding Fourier transform of the o-PdCu showed a single-crystal structure on the [110] zone axis with two perpendicular d-spacings of 3.0 and 2.1 Å, respectively (Figs. 7.21c-d). The enlarged TEM image in Fig. 7.21e directly visualized the ordered structure with periodic rectangular 2D unit cells and the same d-spacings as anticipated. The d-spacings of 3.0 and 2.1 Å were assigned to the (100) and (110) lattice planes, consistent with the theoretical values of 2.98 and 2.11 Å in the crystal model on the same zone axis of ordered PdCu (PDF # 04-015-2413, Fig. 7.21f).

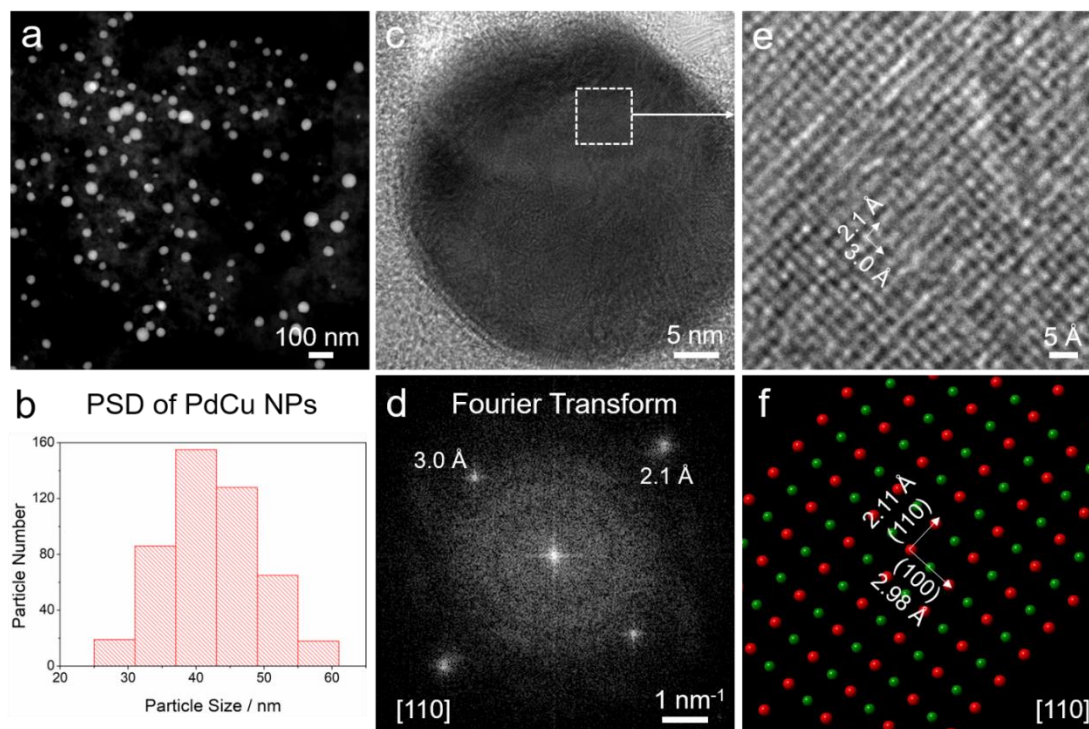


**Fig. 7.21** S/TEM images of PdCu nanoparticles supported on carbon. (a-b) HAADF-STEM images of PdCu/C and particle size distribution of around 500 PdCu nanoparticles. (c-d) A single crystal PdCu nanoparticle with the corresponding Fourier transform on the [110] zone axis. (e-f) Atomic-scale TEM image of PdCu nanoparticles showing the periodic rectangular 2D unit cells with the same d-spacings of 3.0 and 2.1 Å, which is consistent with the theoretical values of (110) and (100) facets, respectively, based on the crystal model of ordered PdCu in (f) (PDF # 04-015-2413).

The chemical composition of o-PdCu/C was examined using STEM equipped with electron energy loss spectroscopy (EELS). As shown in Figs. 7.22a-d, EELS elemental maps of Pd (red), Cu (green) and composite map of Pd + Cu indicated that the PdCu core (yellow) was surrounded by a thin Pd shell (red) on the surface. The EELS line profile in Fig. 7.22e, extracted from dashed box in Fig. 6d, suggested a Pd shell of 0.6-0.8 nm, corresponding to 2-3 atomic layers. Such a thin Pd-rich shell, on the surface of PdCu, may serve as a protection layer to effectively mitigate possible Cu leaching, enhance catalytic activity, and improve catalyst durability.

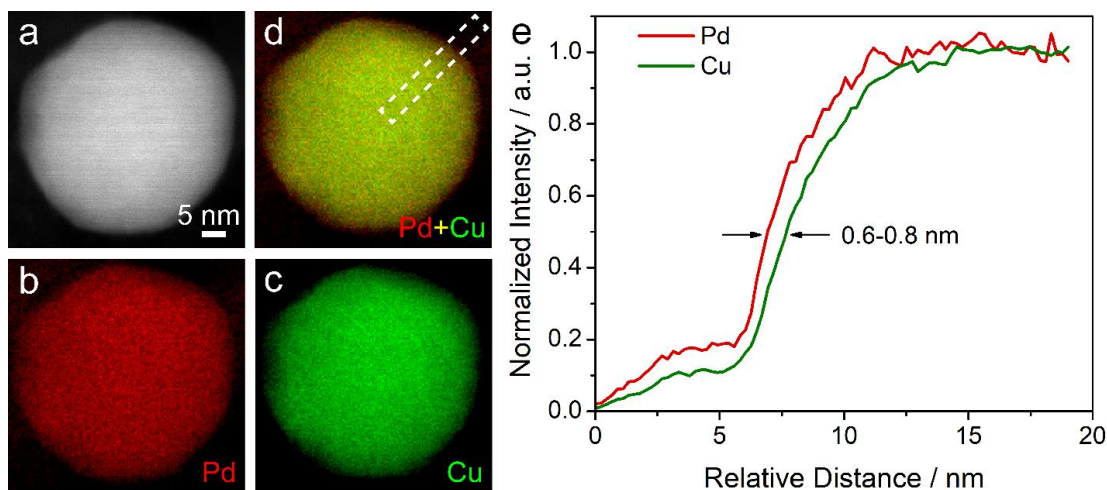


**Figure 7.22** (a) STEM image of a PdCu nanoparticle and (b-d) the corresponding EELS elemental maps of Pd (b), Cu (c) and Pd + Cu, showing a thin Pd shell (red) on the surface (d). (e) EELS line scan profile extracted from the dashed box in (d), indicating a 0.6-0.8 nm Pd shell (2-3 atomic layers).

### 7.9 ORR Activity and Durability of PdCu Nanoparticles

After detailed structural investigations, the ORR activities of PdCu/C and Pd/C were evaluated with a catalyst ink deposited on a GC electrode in an RDE system in O<sub>2</sub>-sat. 1 M KOH. The ORR polarization profiles in Fig. 7.23 showed that the  $E_{1/2}$  of PdCu/C was 0.886 V, 18 mV more positive than that of Pd/C (0.868 V), corresponding to a significant increase in ORR activity. Tafel plots of PdCu/C exhibited a smaller Tafel slope of 36 mV/dec in the early kinetic-controlled region (0.96-0.94 V), relative to Pd/C (42 mV/dec), indicating a smaller over potential required to achieve the same kinetic current change (Fig. 7.23b). The mass-specific activity (MA) and surface-specific activity (SA) at 0.9 V were calculated to quantitatively assess electrocatalytic activity, by normalizing the kinetic current to the mass loading of Pd and electrochemical surface area (ECSA) calculated from CO stripping measurements, respectively (Fig. 7.23c-d). The MA of PdCu/C at 0.9 V was 0.13 mA/ $\mu\text{g}_{\text{Pd}}$ , 3 times as high as Pd/C. The SA of

PdCu/C at 0.9 V was  $2.3 \text{ mA/cm}^2_{\text{Pd}}$ , 2.5 times as high as Pd/C (Fig. 7.32c).

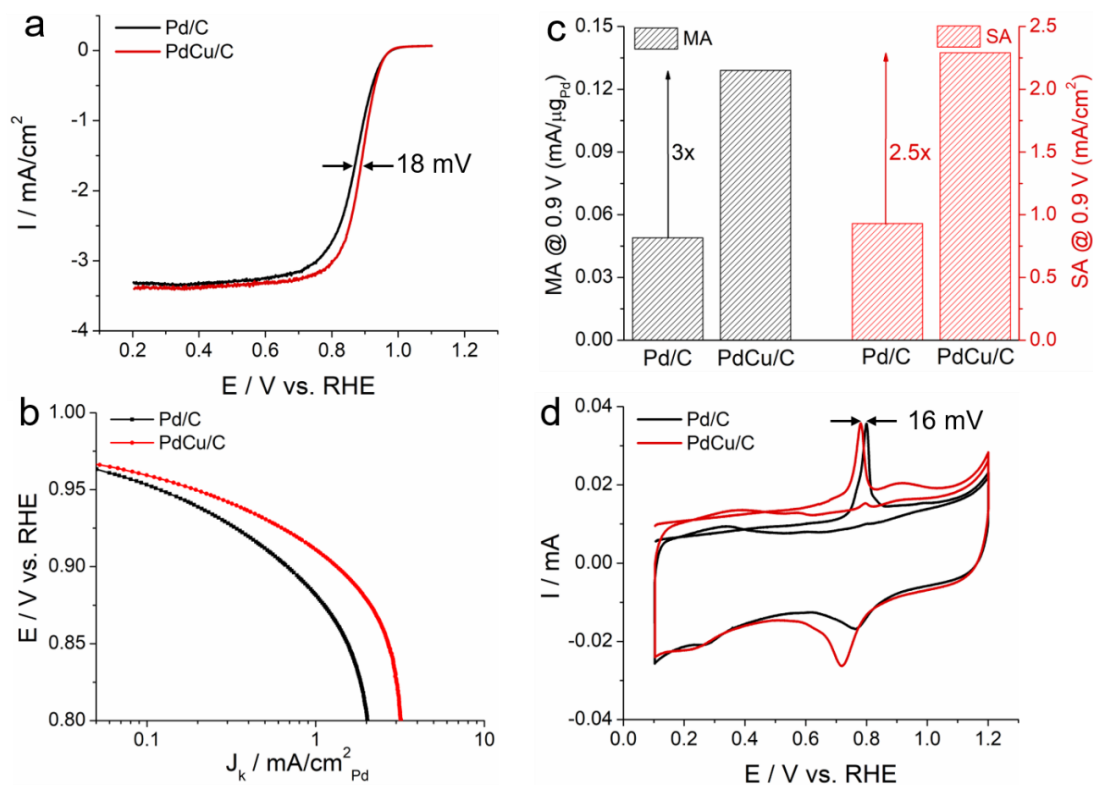


**Figure 7.23** ORR activity of PdCu/C and Pd/C. (a) ORR polarization profiles of Pd/C and PdCu/C in  $\text{O}_2$ -sat. 1 M KOH at 1600 rpm and 5 mV/s. (b) Tafel plots of Pd/C and PdCu/C. (c) MA and SA of Pd/C and PdCu/C at 0.9 V vs. RHE. MA was normalized to the Pd loading and SA was normalized to the ECSA from CO stripping results. (d) CO stripping measurements of Pd/C and PdCu/C at 10 mV/s. The dosing potential for CO was 0.1 V.

The superior ORR activity of PdCu/C, relative to Pd/C, was likely due to the lattice contraction and weakened oxygen adsorption energy on the Pd lattice caused by the incorporation of Cu. CO stripping measurements showed that PdCu/C had an ECSA of  $54 \text{ cm}^2/\text{mg}_{\text{Pd}}$ , comparable to that of Pd/C ( $50 \text{ cm}^2/\text{mg}_{\text{Pd}}$ ) (Fig. 7.23d), which matched well with their similar particle sizes from TEM images. PdCu/C showed a CO stripping peak potential of 0.781 V, which represents a 16 mV negative shift, relative to Pd/C, indicating a more CO-tolerant behavior, which would benefit the practical fuel cell

applications under operation in air.

Finally, in order to implement a Pt-free cathode for practical alkaline fuel cells, ORR electrocatalysts need to not only achieve high initial ORR activity, but also achieve long term durability. Benefiting from the stable ordered structure and enhanced stability of Cu in alkaline media (Fig. 7.24), PdCu/C exhibited remarkable durability during prolonged potential cycles (Fig. 7.25). PdCu/C showed a negligible activity decay with  $\Delta E_{1/2}$  of only 3 and 8 mV after 20,000 and 50,000 cycles, respectively (Figs. 7.25a-b). Concomitantly, the MA of PdCu/C at 0.9 V decreased only by 15% and 25%, respectively, after the same number of scans (Fig. 7.25b). After extended testing (100,000 cycles, about 220 hours), the PdCu/C catalyst showed an unprecedentedly low  $\Delta E_{1/2}$  of 13 mV and a MA retention of 57%, which still surpassed the initial performance of Pd/C ( $\Delta E_{1/2}$  of 18 mV, MA marked in the grey histogram in Fig. 7.25b). The progressive decay in activity during CV cycles was likely due to the decrease of ECSA from particle aggregation over long-term tests as evidenced by CO stripping (Fig. 7.26).

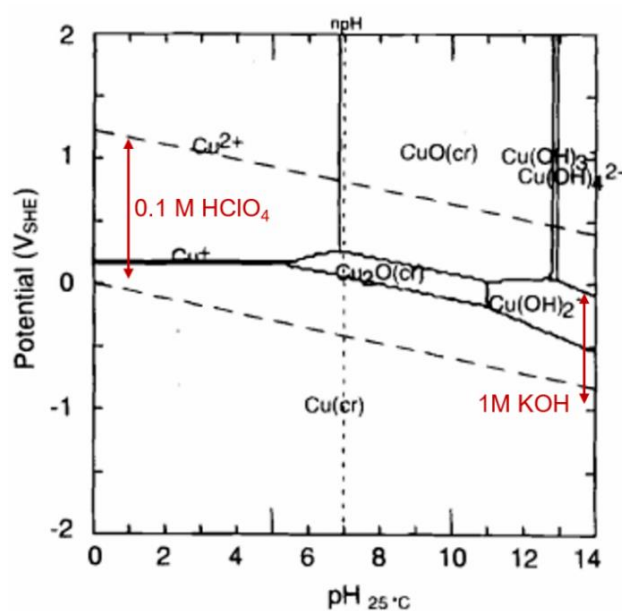


**Figure 7.24** Pourbaix diagram of Cu at 25°C with  $[Cu(aq)] = 10^{-6}$  mol/kg. [2] Copyright @ECS. A typical potential range (0.05-1.2 V vs. RHE) was marked in red for both acidic (0.1 M HClO<sub>4</sub>) and alkaline media (1 M KOH).

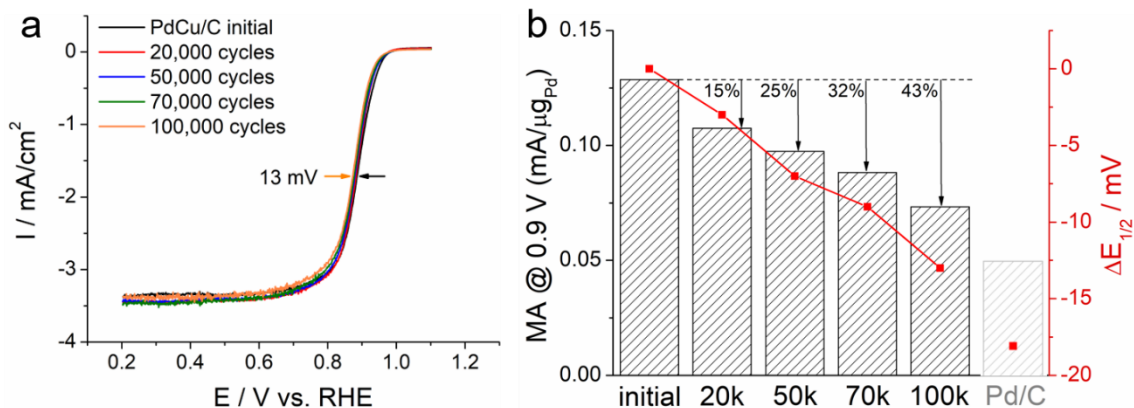


**Figure 7.25** Durability tests of PdCu/C in O<sub>2</sub>-sat. 1 M KOH following the accelerated aging protocol: 0.6-1.0 V at 100 mV/s. (a) ORR polarization profiles of PdCu/C at the initial state and after 20,000 to 100,000 accelerated cycles. The  $E_{1/2}$  shifted to lower potentials by only 13 mV after 100,000 cycles. (b) MA at 0.9 V (left Y-axis) and  $\Delta E_{1/2}$  (right y-axis) at the initial state and after durability cycles.  $\Delta E_{1/2}$  was calculated based on the difference from the  $E_{1/2}$  of PdCu/C at the initial state (0.886 V). The MA of PdCu/C only showed a 15% loss after 20k cycles and still surpassed the performance of Pd/C (at the initial state) after 100k cycles.

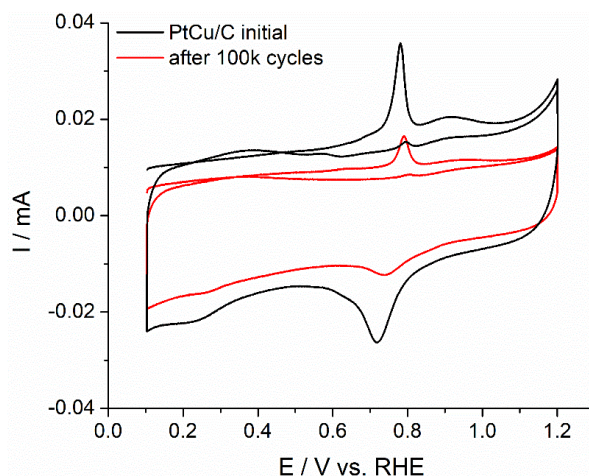


**Figure 7.26** CO stripping measurements of PdCu/C before and after 100,000 accelerated cycles, at a CO dosing potential of 0.1 V and a scan rate of 10 mV/s. The ECSA of PdCu/C decreased from 54 to about 20  $\text{cm}^2/\mu\text{g}_{\text{Pd}}$ . The double layer of PdCu/C was also significantly smaller after 100k cycles, suggesting the carbon support possibly lost some of its porosity.

## 7.10 Conclusion

In summary, we present a high-throughput combinatorial study of 36 kinds of Pd-M thin-film electrodes with well-defined composition and structures, prepared by magnetron sputtering (M: Fe, Co, Ni and Cu). Thin-film RDE has been developed as a standard tool to assess the ORR activity of binary alloys. Among all those thin-film alloy catalysts, Pd<sub>50</sub>Cu<sub>50</sub> was identified as the most promising composition for the ORR, and employed as a target for nanoparticle synthesis. The PdCu nanoparticles, supported on carbon, achieved a mass-specific and surface-specific activity, 3 and 2.5 times, respectively, as high as a Pd/C reference in 1 KOH. PdCu/C further exhibited an impressive durability with only 3 and 13 mV negative shifts in the half-wave potential after 20,000 and 100,000 potential cycles, respectively. The combinatorial approach guiding the nanoparticle synthesis, described herein, provides an optimized high-throughput screening method for other binary or ternary alloys as fuel cell electrocatalysts. Improvements on the synthesis of ordered Pd-based alloys, with smaller particle sizes under lower reaction temperature, is also important to further improve the mass activity of these nanoscale catalysts for fuel cells.

## 7.11 References

1. Lima, F.; Zhang, J.; Shao, M.; Sasaki, K.; Vukmirovic, M.; Ticianelli, E.; Adzic, R. Catalytic Activity–d-Band Center Correlation for the O<sub>2</sub> Reduction Reaction on Platinum in Alkaline Solutions. *J. Phys. Chem. C* **2007**, 111, 404-410.
2. Yang, Y.; Xiao, W.; Feng, X.; Xiong, Y.; Gong, M.; Shen, T.; Lu, Y.; Abruña, H. D.; Wang, D. Golden Palladium Zinc Ordered Intermetallics as Oxygen Reduction Electrocatalysts. *ACS Nano* **2019**, 13, 5968-5974.
3. Jiang, G.; Zhu, H.; Zhang, X.; Shen, B.; Wu, L.; Zhang, S.; Lu, G.; Wu, Z.; Sun, S., Core/Shell Face-Centered Tetragonal FePd/Pd Nanoparticles as an Efficient Non-Pt Catalyst for the Oxygen Reduction Reaction. *ACS Nano* **2015**, 9, 11014-11022.
4. Wang, D.; Xin, H. L.; Wang, H.; Yu, Y.; Rus, E.; Muller, D. A.; DiSalvo, F. J.; Abruña, H. D., Facile synthesis of carbon-supported Pd–Co core–shell nanoparticles as

- oxygen reduction electrocatalysts and their enhanced activity and stability with monolayer Pt decoration. *Chem. Mater.* **2012**, *24*, 2274-2281.
5. Xiao, W.; Cordeiro, M. A. L.; Gong, M.; Han, L.; Wang, J.; Bian, C.; Zhu, J.; Xin, H. L.; Wang, D. Optimizing the ORR activity of Pd based nanocatalysts by tuning their strain and particle size. *J. Mater. Chem. A*, **2017**, *5*, 9867-9872.
  6. Luo, L.; Zhu, F.; Tian, R.; Li, L.; Shen, S.; Yan, X.; Zhang, J. Composition-Graded Pd<sub>x</sub>Ni<sub>1-x</sub> Nanospheres with Pt Monolayer Shells as High-Performance Electrocatalysts for Oxygen Reduction Reaction. *ACS Catal.* **2017**, *7*, 5420-5430.
  7. Shao, M.; Shoemaker, K.; Peles, A.; Kaneko, K.; Protsailo, L. Pt Monolayer on Porous Pd-Cu Alloys as Oxygen Reduction Electrocatalysts. *J. Am. Chem. Soc.* **2010**, *132*, 9253-9255.
  8. Wang, X.; Kariuki, N.; Vaughey, J. T.; Goodpaster, J.; Kumar, R.; Myers, D. J. Bimetallic Pd-Cu Oxygen Reduction Electrocatalysts. *J. Electrochem. Soc.* **2008**, *155*, B602-609.
  9. Xu, C.; Zhang, Y.; Wang, L.; Xu, L.; Bian, X.; Ma, H.; Ding, Y. Nanotubular Mesoporous PdCu Bimetallic Electrocatalysts toward Oxygen Reduction Reaction. *Chem. Mater.* **2009**, 3110-3116.
  10. Beverskog, B.; Puigdomenech, I. Revised Pourbaix Diagrams for Copper at 25 to 300 °C. *J. Electrochem. Soc.* **1997**, *144*, 3476-3483.
  11. van Dover, R. B. Schneemeyer, L. F. & Fleming, R. M. Discovery of a Useful Thin-Film Dielectric Using a Composition-Spread Approach. *Nature* **1998**, *392*, 162-164.
  12. Briceno, G.; Chang, H.; Sun, X.; Schultz, P. G.; Xiang, X.-D. A Class of Cobalt Oxide Magnetoresistance Materials Discovered with Combinatorial Synthesis. *Science* **1995**, *270*, 273-275.
  13. Xiang, X.-D.; Sun, X.; Briceno, G.; Lou, Y.; Wang, K.-A.; Chang, H.; Wallace-Freedman, W. G.; Chen, S.-W.; Schultz, P. G. A Combinatorial Approach to Materials Discovery. *Science* **1995**, *268*, 1738-1740.
  14. Danielson, E.; Golden, J. H.; McFarland, E. W.; Reaves, C. M.; Weinberg, W. H.; Wu, X.-D. A Combinatorial Approach to the Discovery and Optimization of Luminescent Materials. *Nature* **1997**, *389*, 944-948.
  15. Reddington, E.; Sapienza, A.; Gurau, B.; Viswanathan, R.; Sarangapani, S.; Smotkin, E. S.; Mallouk, T. E. Combinatorial Electrochemistry: A Highly Parallel, Optical Screening Method for Discovery of Better Electrocatalysts. *Science* **1998**, *280*, 1735-1737.
  16. Tague, M. E.; Gregoire, J. M.; Legard, A.; Smith, E.; Dale, D.; Hennig, R.; DiSalvo, F. J.; van Dover, R. B.; Abruña, H. D. High Throughput Thin Film Pt-M Alloys for Fuel Electrooxidation: Low Concentrations of M (M = Sn, Ta, W, Mo, Ru, Fe, In, Pd, Hf, Zn, Zr, Nb, Sc, Ni, Ti, V, Cr, Rh) *J. Electrochem. Soc.* **2012**, *159*, F880-F887.
  17. Gregoire, J. M.; Tague, M. E.; Cahen, S.; Khan, S.; Abruña, H. D.; DiSalvo, F. J.; van Dover, R. B. Improved Fuel Cell Oxidation Catalysis in Pt<sub>1-x</sub>Ta<sub>x</sub>. *Chem. Mater.* **2010**, *22*, 1080-1087
  18. Prochaska, M.; Jin, J.; Rochefort, D.; Zhuang, L.; DiSalvo, F. J.; Abruña, H. D.; van Dover, R. B. High Throughput Screening of Electrocatalysts for Fuel Cell Applications. *Rev. Sci. Instrum.* **2006**, *77*, 054104.

19. Jayaraman, S.; Hillier, A. C. Screening the Reactivity of  $Pt_xRu_y$  and  $Pt_xRu_yMo_z$  Catalysts toward the Hydrogen Oxidation Reaction with the Scanning Electrochemical Microscope. *J. Phys. Chem. B* **2003**, 107, 5221-5230.
20. Jayaraman, S.; Hillier, A. C. Construction and Reactivity Screening of a Surface Composition Gradient for Combinatorial Discovery of Electro-Oxidation Catalysts. *J. Comb. Chem.* **2004**, 6, 27-31.
21. Fernandez, J. L.; Walsh, D. A.; Bard, A. J. Thermodynamic Guidelines for the Design of Bimetallic Catalysts for Oxygen Electroreduction and Rapid Screening by Scanning Electrochemical Microscopy. M-Co (M: Pd, Ag, Au). *J. Am. Chem. Soc.* **2005**, 127, 357-365
22. Lee, J.; Ye, H.; Pan, S.; Bard, A. J. Screening of Photocatalysts by Scanning Electrochemical Microscopy. *Anal. Chem.* **2008**, 80, 7445-7450.
23. Strasser, P.; Fan, Q.; Devenney, M.; Weinberg, W. H.; Liu, P.; Nørskov, J. K. High Throughput Experimental and Theoretical Predictive Screening of Materials – A Comparative Study of Search Strategies for New Fuel Cell Anode Catalysts. *J. Phys. Chem. B* **2003**, 107, 11013.
24. Smotkin, E. S.; Jiang, J.; Nayar, A.; Liu, R. High-Throughput Screening of Fuel Cell Electrocatalysts. *Appl. Surf. Sci.* **2006**, 252, 2573-2579
25. Guerin, S.; Hayden, B. E.; Lee, C. E.; Mormiche, C.; Russell, A. E. High-Throughput Synthesis and Screening of Ternary Metal Alloys for Electrocatalysis. *J. Phys. Chem. B* **2006**, 110, 14355-14362.
26. Smith, R. D. L.; Prévot, M. S.; Fagan, R. D.; Zhang, Z.; Sedach, P. A.; Siu, M. K. J.; Trudel, S.; Berlinguette, C. P. Photochemical Route for Accessing Amorphous Metal Oxide Materials for Water Oxidation Catalysis. *Science* **2013**, 340, 60-63.
27. Gregoire, J. M.; van Dover, R. B.; Jin, J.; DiSalvo, Abruña, H. D. Getter Sputtering System for High-Throughput Fabrication of Composition Spreads. *Rev. Sci. Instrum.* **2007**, 78, 072212.
28. Cliff, G.; Lorimer, G. W. The Quantitative Analysis of Thin Specimens. *J. Microsc.* **1975**, 103, 203-207.
29. Cable, R. and Schaak, R. Solution Synthesis of Nanocrystalline M-Zn (M: Pd, Au, Cu) Intermetallic Compounds via Chemical Conversion of Metal Nanoparticle Precursors. *Chem. Mat.* **2007**, 19, 4908-4104.
30. Wang, D.; Liu, S.; Wang, J.; Lin, R.; Kawasaki, M.; Rus, E.; Silberstein, K. E.; Lowe, M. A.; Lin, F.; Nordlund, D.; Liu, H.; Muller, D. A.; Xin, H. L.; Abruña, H. D., Spontaneous Incorporation of Gold in Palladium-Based Ternary Nanoparticles Makes Durable Electrocatalysts for Oxygen Reduction Reaction. *Nature Commun.* **2016**, 7, 11941.
31. Zhu, J.; Yang, Y.; Chen, L.; Xiao, W.; Liu, H.; Abruña, H. D.; Wang, D. Copper-Induced Formation of Structurally Ordered Pt-Fe-Cu Ternary Intermetallic Electrocatalysts with Tunable Phase Structure and Improved Stability. *Chem. Mater.* **2018**, 30, 5987-5995.

## PART II *Operand/In Situ* TEM for Atomic-Scale Mechanistic Understanding of Electrochemical Reactions at Interfaces

### CHAPTER 8

#### Revealing the Atomic Ordering of Binary Intermetallics Using *In Situ* Heating STEM and XRD\*

##### 8.1 Introduction

Pt-based intermetallics display superior electrocatalytic activity for the normally sluggish oxygen reduction reaction (ORR), as well as enable a decrease in Pt loading, compared to Pt/C, in proton exchange membrane (PEM) fuel cells.<sup>1-6</sup> As-synthesized, Pt-based alloy (Pt-M; M=Mn, Fe, Co, Ni, etc.) nanoparticles (NPs) generally form as a disordered solid solution in which the occupancy of a given site by Pt or M atoms is random and without local preference. The probability of occupancy by Pt or M is determined only by the stoichiometric ratio of Pt and M in a particular particle. These alloys generally suffer from a rapid loss of activity during electrochemical cycling due to the oxidation and dissolution of the M element and subsequent changes in both the particle morphology and the crystal structures.<sup>7</sup>

---

\*Yin Xiong<sup>†</sup>, Yao Yang<sup>†</sup>, Howie Jorress<sup>†</sup>, Elliot Padgett, Unmukt Gupta, Venkata Yarlagadda, David N. Agyeman-Budu, Xin Huang, Thomas E. Moylan, Rui Zeng, Anusorn Kongkanand, Fernando A. Escobedo, Joel D. Brock, Francis J. DiSalvo, David A. Muller, and Héctor D. Abruña. Revealing the Atomic Ordering of Binary Intermetallics Using *in situ* Heating Techniques at Multilength Scales. *Proc. Natl. Acad. Sci.* 2019, 116, 1974.  
(<sup>†</sup>Equal Contributions) © NAS

This work has been a result of two-year extensive collaborations among multiple research groups at Cornell as well as GM Fuel Cell R&D. Y.X., Y.Y., E.P., and H.J. conceived and designed the experiments under the guidance of H.D.A, D.A.M, F.J.D, and J.D.B. Y.X., H.J. and Y.Y. performed *in situ* heating XRD experiments with the help of X.H. and D.A.B. Y.Y. and E.P. performed *in situ* heating TEM experiments with the help of Y.X. U.P. performed Monte Carlo simulations under the guidance of F.A.E. V.Y. and T.E.M. performed MEA measurements under the guidance of A.K. at GM. Y.Y., Y.X. and E.P. wrote the manuscript. All authors discussed the results and commented on the manuscript.

In some systems, such as the Pt-Sn system, partially ordered intermetallic particles can be obtained at room temperature and further improved to fully ordered phase by low temperature annealing (200 °C).<sup>8</sup> However, in most other cases, post-synthesis annealing at high temperatures is required to transform the disordered solid solution phase into the ordered intermetallic phase. These intermetallic NPs show significantly better durability and improved electrocatalytic activity.<sup>9-29</sup> The enhanced durability of ordered intermetallics can be attributed to a more stable structure, which arises from the stronger heteroatomic Pt-M bond and a greater enthalpy of formation relative to its disordered counterpart. Ordered Pt<sub>3</sub>M intermetallics normally have a primitive cubic crystal structure (AuCu<sub>3</sub>-type, Pm-3m), while ordered PtM intermetallics typically have a tetragonal crystal structure (tcs) of the AuCu-type, P4/mmm. Because ordered intermetallics of Pt<sub>3</sub>M and PtM have different crystal symmetry and additional atomic ordering, compared with their disordered counterparts, they show extra peaks in X-ray diffraction (XRD), which are usually referred to as superlattice ordering peaks.

In studies of ordered intermetallic catalysts, there are two related questions that are of particular interest: Is the ordered intermetallic phase present and what is the phase fraction of the intermetallic? The first question can be quantitatively determined by the existence of superlattice ordering peaks in powder XRD.<sup>11-29</sup> By measuring the relative intensity of the superstructure peaks, information that is important but often neglected, the degree of ordering can be quantified. Having a measure of the degree of ordering is important to understand the intermetallic phase's contribution to catalyst performance and is necessary for understanding and optimizing the synthesis and annealing conditions.

After performing a systematic literature survey on ordered intermetallic nanoparticles, which included the most common Pt-M and Pd-M intermetallics, we realized that most of these studies only qualitatively described the formation of ordered intermetallics, and further quantitative understanding of the degree of ordering was required (Table 9.1).<sup>11-29</sup> For example, in our previous studies on Pt<sub>3</sub>Co<sup>2</sup> and PdFe<sup>6</sup>, intermetallic nanoparticles were found to be only partially ordered, despite our attempts to optimize the post-synthesis annealing conditions. In our other studies on PtSn<sup>8</sup> and PdZn<sup>20</sup>, intermetallic nanoparticles were measured to be fully in the ordered phase. This suggests that it is likely that some claims of “ordered” intermetallic electrocatalysts may, in fact, be mixed phases of ordered intermetallic and disordered solid solution particles. It is possible that, due to high strain and surface energy, for some NP systems, and from a thermodynamic standpoint, only partial order can be achieved, even if a pure phase can be obtained at equilibrium in the bulk. In either case, the synthesized, disordered alloy needs to overcome energetic barriers and kinetics to nucleate and grow the more stable, ordered intermetallic phase through the annealing treatment. However, the annealing process must be carefully designed/controlled. The newly formed ordered intermetallic phase can revert back to the disordered phase if the temperature surpasses a critical, order-disorder, phase transition (ODPT) temperature ( $T_c = 750$  °C for bulk Pt<sub>3</sub>Co).<sup>30</sup> The ODPT represents an intriguing process, coupling both kinetic and thermodynamic aspects. Further, nucleation and growth may also be (and likely are) influenced by the composition, morphology and size of each nanoparticle.

Ref.	Claimed ordered intermetallic catalysts	Crystal Structure	Synthesis/annealing conditions	XRD database PDF number
11	Pt <sub>3</sub> Ti	AuCu <sub>3</sub> , Pm-3m	Pt <sub>3</sub> Ti alloy annealed at 600 °C, 12h	03-065-3259
12	Pt <sub>3</sub> V	AuCu <sub>3</sub> , Pm-3m	Pt <sub>3</sub> V alloy annealed at 650-700 °C, 24h	01-072-3016
13	Pt <sub>3</sub> Cr	AuCu <sub>3</sub> , Pm-3m	Pt <sub>3</sub> Cr alloy annealed at 700 °C, 24h	01-071-7609
14	Pt <sub>3</sub> Mn	AuCu <sub>3</sub> , Pm-3m	Pt(acac) <sub>2</sub> +Mn(acac) <sub>2</sub> OAm/OAc at 200 °C, 0.5h	01-071-9674
15	Pt <sub>3</sub> Fe	AuCu <sub>3</sub> , Pm-3m	Pt-Fe alloy annealed at 700 °C	01-071-5031
				01-089-2051
2	Pt <sub>3</sub> Co	AuCu <sub>3</sub> , Pm-3m	Pt <sub>3</sub> Co alloy annealed at 700 °C, 2h	01-071-7410
16	PtNi	AuCu, P4/mmm	Pt(acac) <sub>2</sub> +Ni(acac) <sub>2</sub> KBH(Et) <sub>3</sub> in THF r.t.	01-072-2524
17	PtCu <sub>3</sub>	AuCu <sub>3</sub> , Pm-3m	PtCu <sub>3</sub> alloy annealed at 1000 °C, 10h	03-065-3247
18	Pt <sub>3</sub> Zn	AuCu <sub>3</sub> , Pm-3m	Pt(acac) <sub>2</sub> +Zn(acac) <sub>2</sub> PVP in DMF, 180°C, 9h	01-072-3028
19	Pt <sub>3</sub> Zn	AuCu <sub>3</sub> , Pm-3m	Pd(acac) <sub>2</sub> +Zn(acac) <sub>2</sub> OAm/OAc at 350°C, 1h	01-072-3028
20	PtZn	AuCu, P4/mmm	Pt/C +Zn chip heated at 500 °C, 8h	01-072-3027
21	Pt <sub>3</sub> Sn	AuCu <sub>3</sub> , Pm-3m	H <sub>2</sub> PtCl <sub>6</sub> +SnCl <sub>2</sub> , DDA+HDD, 300°C, 0.5h	01-072-2977
6	PdFe	AuCu, P4/mmm	PdFe alloy annealed at 500 °C, 2h	01-089-2051
22	Au <sub>10</sub> Pd <sub>40</sub> Co <sub>50</sub>	AuCu, Fm-3m	Au <sub>10</sub> Pd <sub>40</sub> Co <sub>50</sub> alloy annealed at 800 °C, 0.5h	01-071-7394 (PdCo)
23	PdCu	CsCl, Pm-3m	PdCu annealed at 400 °C	01-080-4575
24	PdCu	CsCl, Pm-3m	PdCu alloy, annealed at 375 °C, 1h	01-080-4575
25	PdZn	AuCu, P4/mmm	Pd <sub>2</sub> (dba) <sub>3</sub> +Et <sub>2</sub> Zn OAm at 250 °C, 1h	01-072-2936
26	Pd <sub>3</sub> Pb	AuCu <sub>3</sub> , Pm-3m	Pd/C + Pb(Ac) <sub>2</sub> , EG microwave 300W, 6min	01-089-2062
27	AuCu <sub>3</sub>	Pm-3m	Cu(Ac) <sub>2</sub> +Au NPs OAm/OAc at 300 °C	01-088-1731
28	AuCu	P4/mmm	HAuCl <sub>4</sub> +CuCl <sub>2</sub> glycerol at 300 °C, 5h	01-089-2037
29	AuCu	P4/mmm	AuCu alloy annealed at 500 °C, 12h	01-089-2037

**Table 9.1:** All of the above reported catalysts are nanoparticles supported on carbon substrate. Pt-M and Pd-M ordered intermetallic compounds: M can be: Ti, V, Cr, Mn, Fe, Co, Ni, Cu, Zn, Sn, Pb, Bi Abbreviations: OAm: oleylamine; OAc: oleic acid; acac: acetylacetonate Ac: acetate; dba: dibenzylideneacetone; Et: ethyl. r.t.: room temperature. DDA: dodecylamine; HDD: 1,2-hexadecandiol; EG: ethylene glycol

It is critical to understand the ODPT behavior of nanoparticles, which will, in turn, enable us to develop better annealing processes to increase the degree of ordering of NP electrocatalysts and, by extension, enhance fuel cell performance. However, mechanistic studies of such processes have been challenging due to the lack of suitable *in situ* techniques capable of tracking the dynamic phase transition and structural changes of metastable intermediates under real-time annealing conditions. Previous studies have only involved *in situ* heating, during XRD, to study the lattice strain of Pt-Cu intermetallics,<sup>31</sup> or have employed microscopic-level, *in situ* heating TEM, to investigate morphological changes of Pt<sup>32</sup> and Pt-based alloys.<sup>33-37</sup> However, to the best of our knowledge, none of them has attempted to quantitatively study the degree of ordering using X-ray diffraction and correlate it with the evolution of particle morphology and the formation of ordered intermetallics, at the atomic scale, using electron microscopy.

In this study, we have investigated the ODPT of Pt<sub>3</sub>Co nanoparticles during a temperature annealing treatment, using both *in situ* heating synchrotron-based XRD and *in situ* heating TEM. We have studied, quantitatively, the effects of annealing and cooling conditions (temperature and time) on the degree of ordering. We further employed *in situ* heating TEM to directly visualize the morphological and structural transition at the atomic-scale, during the thermal annealing treatment. Finally, we have systematically correlated catalyst durability to the degree of ordering, where a higher degree of ordering led to enhanced durability. This mechanistic study, involving both *in situ* heating XRD and *in situ* heating TEM, provides a microscopically detailed picture of post-synthesis processing.

## 8.2 Experimental Methods

**Preparation of Pt<sub>3</sub>Co/C catalysts:** The Pt<sub>3</sub>Co/C catalysts were prepared by an impregnation method. In a typical synthesis, 0.1 mmol (51.8 mg) H<sub>2</sub>PtCl<sub>6</sub>·6H<sub>2</sub>O and 7.9 mg (0.034 mmol) CoCl<sub>2</sub>·6H<sub>2</sub>O were dissolved in deionized water, with 86 mg of Vulcan XC-72 carbon support dispersed later to make the mass loading of Pt<sub>3</sub>Co nanoparticles to be 20%. After ultrasonic mixing for 30 min, the suspension was heated under magnetic stirring to evaporate extra moisture and form a smooth and thick slurry. The slurry was then dried in an oven at 60 °C. After being ground in an agate mortar, the resulting dark and free-flowing powder was heated in a tube furnace at 300 °C under flowing forming gas (5% H<sub>2</sub>, 95% N<sub>2</sub>) for 2 h. The high-temperature treated samples were prepared by annealing the as-synthesized Pt<sub>3</sub>Co/C alloy at specific temperatures for 2 h under forming gas. Powder XRD of Pt<sub>3</sub>Co/C was performed using a Rigaku Ultima VI X-ray diffractometer, which was measured from 10° to 90° at a scan rate of 2°/min.

**Electrochemical characterizations:** Electrochemical activity and durability were measured at room temperature in a 0.1M HClO<sub>4</sub> solution using a Solartron potentiostat. 5 mg of the 20 wt.% Pt<sub>3</sub>Co/C intermetallic catalyst were mixed with 2 mL of 0.05 wt.% Nafion/ethanol solution and sonicated subsequently to form a well-dispersed catalyst ink. 10 μL of the resulting catalyst ink were loaded onto a glassy carbon electrode (D = 5.0 mm), followed by the thermal evaporation of the ethanol solvent. The mass loading of Pt<sub>3</sub>Co on the electrode was calculated to be 22 μg/cm<sup>2</sup>. A coiled Pt wire was used as the counter electrode and a Ag/AgCl in saturated KCl served as the reference electrode. ORR measurements were carried out using a rotating disk electrode (RDE, Pine

Instruments) in an oxygen-saturated 0.1M HClO<sub>4</sub> solution at a rotation rate of 1600 rpm and a sweep rate of 5 mV/s. ORR polarization profiles were obtained after 50 cycles over the potential range from 0.05 to 1.1 V at 50 mV/s in 0.1M HClO<sub>4</sub> to remove surface contamination. Cyclic voltammetry (CV) was performed to obtain the electrochemical surface area (ECSA) by integrating the charge over the hydrogen adsorption/desorption region from 0.05 V to +0.4 V vs RHE. We used a conversion factor of 200 μC/cm<sup>2</sup>, according to recent results from Feliu. Durability tests were carried out by continuous CV scanning for 2,000 cycles over the potential range between 0.6 to 1 V vs RHE. ECSA measurements and ORR profiles were also obtained after cycling to evaluate the electrocatalytical durability.

**MEA measurements:** Fuel cell evaluations of each catalyst were done in a membrane-electrode assembly (MEA) with the electrocatalyst of interest at the cathode. The active area of the fuel cell single cell was 53 cm<sup>2</sup>. The metal weight percent on carbon black-supported electrocatalysts was approximately 25%. 2.8 g of catalyst were mixed with 3.4 g of perfluorosulfonic acid (PFSA) ionomer (900 equivalent weight) in a 60 g water-propanol solution, then coated on a gas-diffusion carbon paper to fabricate a gas-diffusion electrode (GDE). The electrode Pt loadings were 0.1 and 0.025 mgPt/cm<sup>2</sup> for the cathode and anode, respectively. The MEA was then fabricated by hot pressing an 18 μm thick PFSA-based membrane between the cathode and anode GDEs at 146°C, 3 MPa for 4 min. Detailed fabrication procedures have been discussed elsewhere. Catalyst accelerated stability tests (AST) recommended by the U.S. Department of Energy (DOE) were used in this study ([https://www.energy.gov/sites/prod/files/2017/05/f34/fcto\\_myrrdd\\_fuel\\_cells.pdf](https://www.energy.gov/sites/prod/files/2017/05/f34/fcto_myrrdd_fuel_cells.pdf)). The

AST consisted of 30,000 trapezoidal voltage cycles between 0.6 and 0.95 V, at 80°C, 100% relative humidity, and ambient pressure. The dwell time at each voltage was 2.5 s and the ramp time was 0.5 s and each cycle took 6 s. The fuel cell performance, electrochemically active surface area (ECSA), and oxygen reduction reaction (ORR) mass activity were measured after 0, 10,000 and 30,000 cycles during the AST. ORR activity was reported at 0.9 VRHE at 80°C, 100% relative humidity, and 1 bar of O<sub>2</sub>. Pt ECSA was measured by CO stripping in an MEA. Fuel cell current-voltage and power density characteristics were evaluated under the following operating conditions in the order of anode/cathode: H<sub>2</sub>/air, 94°C, 65/65% RH, 250/250 kPaabs, outlet, reactant stoichiometries of 1.5/2.

***In situ* heating synchrotron-based X-ray diffraction (XRD) setup.** The *in situ* X-ray diffraction measurements were performed at the A1 station of the Cornell High Energy Synchrotron Source (CHESS) using a customized setup. The sample was heated, *in-situ*, using a SabreTube furnace (Absolute Nano, Wixom, MI) which consists of a resistively heated strip of single crystal Si inside a quartz tube. The furnace was fitted with a customized quartz tube with two Kapton windows to allow the incident X-ray beam to reach the sample and the diffracted beam to reach the detector. The furnace was continually purged with forming gas (5% H<sub>2</sub>, 95% N<sub>2</sub>) to prevent the oxidation of the sample. Sample holders were lithographically fabricated from a double side polished Si wafer by etching 200 μm deep wells using KOH. The holder had a nitride coating to prevent current from passing through the sample holder. The sample powder was mixed with acetone before being pressed into the well to help in forming a stable powder compact. The furnace temperature was measured by a thermo couple pushed up

against the bottom of the heating element. During diffraction, the sample was held at a fixed angle to the incident beam.

***In situ* heating synchrotron-based XRD measurements:** XRD experiments were performed at the A1 station (X-ray energy = 19.6 keV,  $\lambda = 0.63 \text{ \AA}$ ) in CHESS. A Pilatus 100K (Dectris, Switzerland) pixel array detector was used to collect the X-ray signal, and the temperature calibration of the setup was conducted by measuring the melting point of metal powders (Al, Sn and Zn) with a purity > 99.99% by tracking their changes in the XRD pattern with increasing temperature. The temperature difference between the measured and real values was 4 °C (Fig. S1). Directly measured d-spacing data were converted to the standard  $2\theta$  values when using Cu K $\alpha$  radiation ( $\lambda=1.5406\text{\AA}$ ). The  $2\theta$  values of the XRD were calibrated based on a CeO<sub>2</sub> reference sample. The  $2\theta$  resolution was also measured using CeO<sub>2</sub> powder and was found to be at least 0.1°.

**Monte-Carlo simulation:** Monte Carlo (MC) simulations, using N-body potentials, provide an efficient means to quickly simulate the equilibrium and kinetic properties of large atomic systems (~10,000 particles). We employ a commonly used semi-empirical atomistic potential derived in the framework of the second moment approximation of the density of states in a tight-binding model (TB-SMA). More MC simulation details can be found in our PNAS paper.

**Electron Microscopy Characterizations:** *Ex situ* atomic-scale STEM images were recorded using an aberration-corrected FEI Titan Themis STEM operated at 300 keV with a convergence angle of 30 mrad. *In situ* heating STEM experiments were conducted in a FEI Tecnai F20 with a Schottky field emission gun at 200 keV with a convergence angle of about 9.8 mrad. An annular, dark field detector was used to collect

the image signal with high collection angles to achieve better atomic number sensitivity. The temperature was controlled using a Protochips Aduro heating holder with the sample powder dispersed on a model E-AHA21 Protochips E-chip, which has an amorphous carbon film that covered the viewing window. The temperature was pre-calibrated before use. The particle size distribution was calculated from STEM images using an automated procedure implemented in MATLAB. A light Gaussian smoothing was applied to each image to reduce noise, and the uneven background of the carbon support was estimated and removed using a gray-scale morphological opening operation with a 30 nm radius, spherical, structure element. The Pt<sub>3</sub>Co particles were then segmented using an active contour with the Chan-Vese method.<sup>54</sup> The active contour segmentation began with an initial estimate from threshold segmentation and operated on the square root of the background-subtracted STEM image to reduce the impact of thickness variations from particles of different sizes. After the Pt<sub>3</sub>Co nanoparticles were segmented, their size distribution was calculated using a procedure that estimated the local radius of particle sub-regions. This provided a more robust estimate of size than a simple spherical-particle approximation for particles that had irregular shapes or were overlapping in the STEM images. Particles were separated into sub-regions using a watershed transform, and the local radius for each sub-region was calculated as the maximum distance from the particle edge in that sub-region. The sub-regions were weighted according to their projected area in the image for inclusion in the particle size distribution and for estimation of the specific surface area (SSA).

### **8.3 *In situ* Heating Synchrotron-Based X-ray Diffraction**

Pt<sub>3</sub>Co/C disordered alloys were synthesized using an impregnation method<sup>2</sup> in which

precursors were reduced under forming gas at 300 °C and the as-synthesized Pt<sub>3</sub>Co/C catalysts were subsequently annealed further at high temperatures under forming gas. The XRD patterns of the as-synthesized Pt<sub>3</sub>Co/C and Pt<sub>3</sub>Co/C annealed at 700 °C in a conventional tube furnace were first measured in the *in situ* heating XRD stage to verify the reliability of the set-up (Fig. 8.1A). After annealing, the sample exhibited multiple superlattice ordering peaks: (100) at 23°, (110) at 32.5°, (210) at 53.5°, (211) at 59°, (300) at 74.3° and (310) at 79°, which match well with the XRD reference of ordered intermetallic Pt<sub>3</sub>Co (PDF #01-071-7410), confirming the formation of ordered phase. (Fig. 8.1B) In this experiment, the orientation of the crystallites should be random both at the nanoparticle (NP) level, and within the NP/C mixture. Beyond this assumption, the data itself provide assurance that the orientations of the crystallites are sufficiently random. First, data were collected using a 2D detector and integrated to generate the 1D data sets. The detector image of the as-prepared Pt<sub>3</sub>Co intermetallic NPs collects a portion of the ring (Fig. 8.2B). It can be seen, particularly in the smallest ring, that there is no change in intensity as a function of position along the ring, indicating a random orientation of grains. The sample temperature was calibrated by the melting point of several metals (Fig. 8.2A).

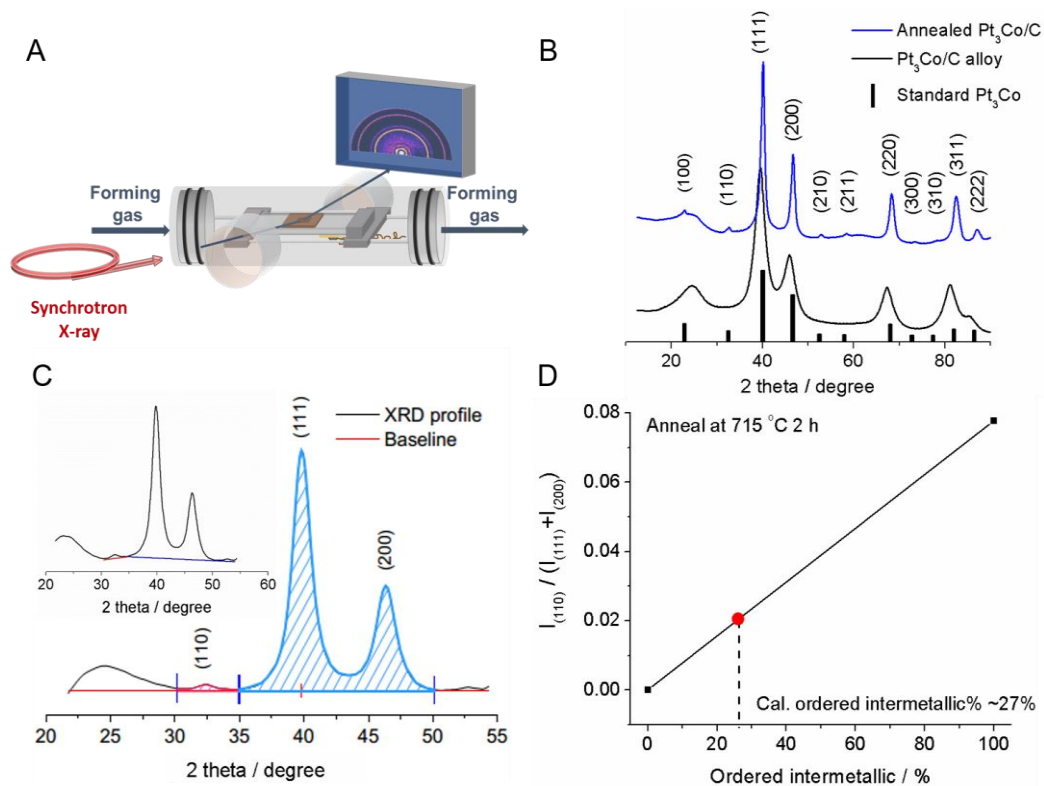


**Figure 8.1.** (A) Schematic illustration of the home-made device for the *in situ* synchrotron-based, X-ray diffraction (XRD) study. (B) XRD patterns of the as-synthesized  $\text{Pt}_3\text{Co}/\text{C}$  alloy and  $\text{Pt}_3\text{Co}/\text{C}$  after further annealing at  $700^\circ\text{C}$  in the *in situ* heating cell. (C) Quantitative analysis of the peak integral of the (110) ordering peak, and the (111) and (200) major peaks. Inset: illustration of background subtraction. (D) Quantitative calculations of the relative content of ordered intermetallic based on the assumption of a linear relationship between the ratio of the integrated areas of the ordered intermetallic peak at (110) to the sum of the (111) and (200) peaks.

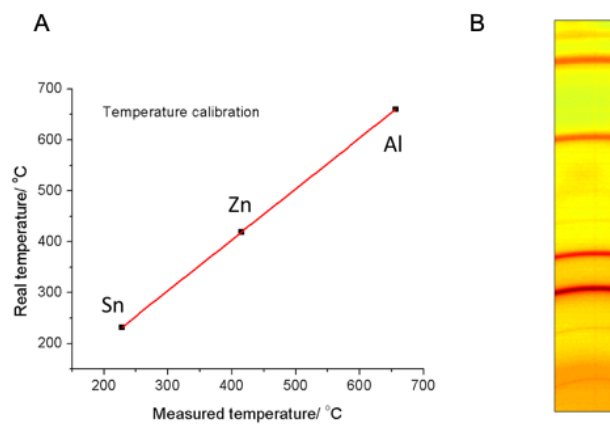


**Figure 8.2.** (A) Temperature calibration of the *in situ* heating stage (Si substrate). The

Y axis is the theoretical melting temperature of metals and the X axis is the measured melting temperature from the heating stage. The plot shows a linear offset between the measured temperature and the actual temperature (B) XRD pattern of as-synthesized annealed Pt<sub>3</sub>Co collected from 2D detector.

After subtracting the background, by selecting three points to form the baseline (Fig. 8.2C, inset), the XRD pattern was analyzed further to quantify the relative content of the ordered phase. We employed the intermetallic peak (110) at 32.5° for analysis. It is the second strongest intermetallic peak, yielding a sufficient signal-to-noise ratio for further analysis. While the strongest intermetallic peak is the (100), it is located within the diffuse scattering ring from the carbon support, making it difficult to accurately extract the integrated intensity of this peak, precluding an accurate intensity analysis. Because there was some overlap between the (111) and (200) peaks, due to the broadening of the peaks by the relatively small domain/crystallite size, the ratio of the integrated area under the (110) peak (red) to that of the sum of the areas under the (111) and (200) peaks (blue),  $I_{(110)}/(I_{(111)}+I_{(200)})$ , was used so as to yield a more accurate quantitative evaluation. The theoretical value of  $I_{(110)}/(I_{(111)}+I_{(200)})$ , based on the structure factor, for Pt<sub>3</sub>Co is 0.078, as calculated using the XRD database of ordered Pt<sub>3</sub>Co. This corresponds to a 100 % of fully ordered intermetallic Pt<sub>3</sub>Co particles (Fig. 8.2D). The relative fraction of the ordered phase exhibits a linear relationship with  $I_{(110)}/(I_{(111)}+I_{(200)})$ . This approach is valid since the intensity of the (111) and (200) peaks, the fundamental reflections, are constant for both ordered and disordered phases since the average electron density for these planes is fixed, assuming a fixed composition. For example, we found that Pt<sub>3</sub>Co/C annealed at 715 °C had a peak ratio of 0.020, and therefore we calculated that the phase fraction of nanoparticles adopting the ordered

phase was approximately 26%.

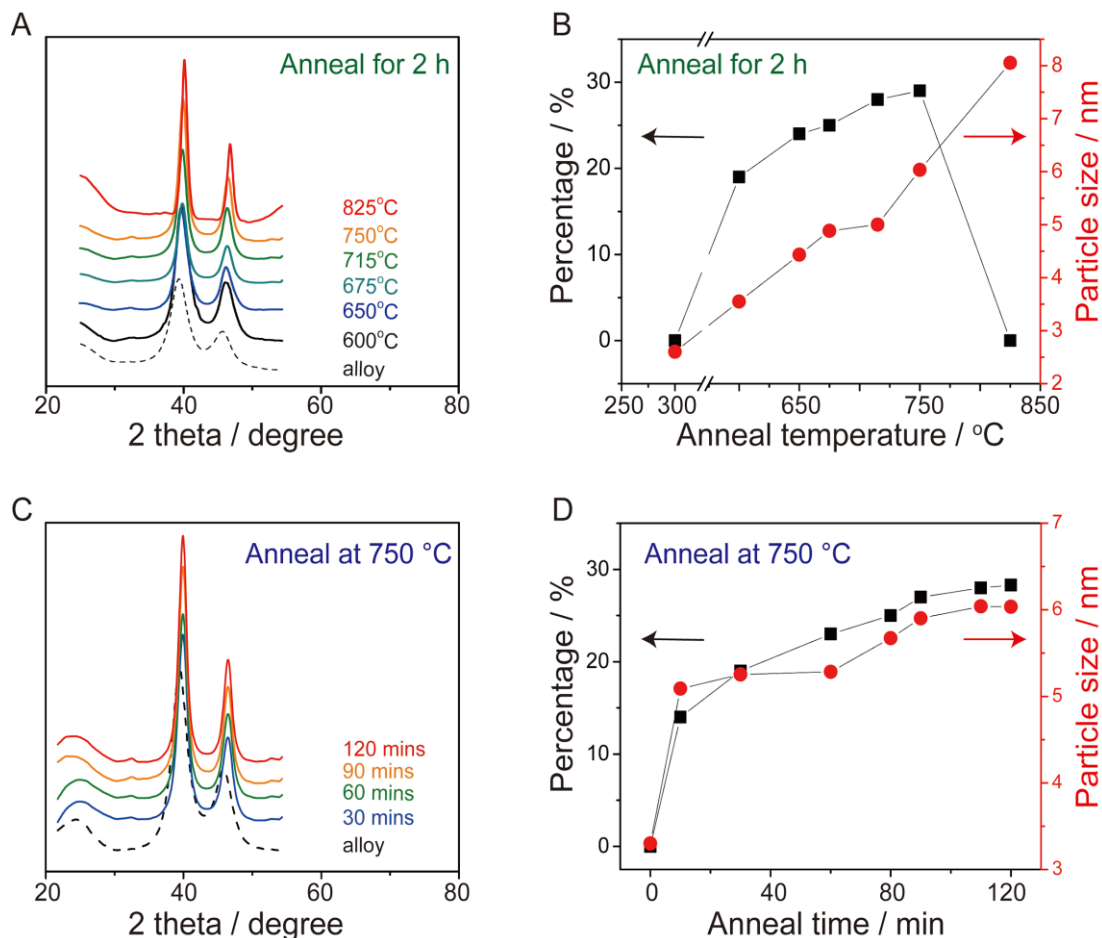


**Figure 8.3.** (A) *In situ* heating XRD patterns of Pt<sub>3</sub>Co/C annealed at various temperatures. The dashed line represents the as-synthesized Pt<sub>3</sub>Co/C alloy. (B) Calculated relative content of ordered intermetallic Pt<sub>3</sub>Co/C formed and particle size (calculated from the width of the (111) peak). (C) *In situ* heating XRD patterns of Pt<sub>3</sub>Co/C at 750 °C, the optimal temperature, as a function of annealing time. (D) Calculated relative content of ordered Pt<sub>3</sub>Co/C formed, and particle size.

To better understand the changes in XRD patterns as a function of the annealing temperature, the as-synthesized Pt<sub>3</sub>Co/C alloy catalysts were annealed at different temperatures, for 2 h each, in flowing forming gas (Fig. 8.3A). After the two-hour anneal, the intensity of the (110) superstructure peak at ~33° was compared to the fundamental (111) reflections. We found that the ratio,  $I_{(110)}/(I_{(111)}+I_{(200)})$ , increased

with annealing temperature over the 600 °C to 750 °C range. The increased ordering is likely due to the enhanced ability to overcome the nucleation and diffusion barriers with increasing temperature. The maximum relative superstructure peak intensity at 750 °C was 0.023, corresponding to an ordered intermetallic phase fraction of about 30%. When annealed at 825 °C for 2 h, the relative fraction of the ordered phase went to zero, within the signal to noise level, consistent with the presence of only the disordered phase which is stable when  $T > T_c$  (750 °C) in the bulk Pt-Co phase diagram. Similar changes at different temperatures were also observed in the powder XRD under the same conditions during the post-synthesis annealing treatment in a traditional tube furnace (Fig. 8.4).

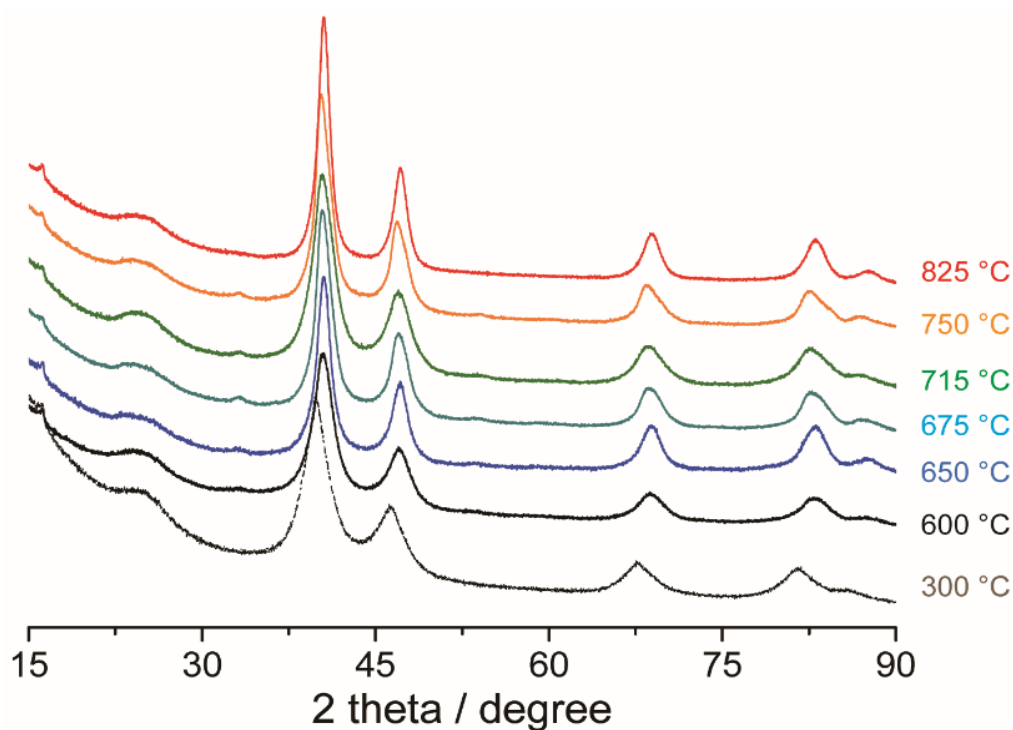


**Figure 8.4.** Powder XRD patterns of Pt<sub>3</sub>Co/C annealed at various temperatures for 2h in a flow furnace in the lab. The change in ordering peak at ~33° is fairly consistent with Figure 9.3A.

There are several factors that may influence the behavior of an ensemble of particles during annealing. The first is the diffusion rate, both intra- and inter-particle, which increases with increasing temperature. Overall, diffusion will drive the composition to be spatially uniform. After sufficient time, all particles will be alike. Concomitantly, the average particle size will grow. Further, higher diffusion rates will allow the NP's to reach their equilibrium state faster. During the cooling process, the driving force for nucleation increases and the diffusion rate decreases as the temperature falls below the phase transition temperature. The next consideration is the stoichiometric ratio of the components (Pt to M). The stoichiometric ratio may vary from particle to particle due to the randomness of aggregation of Pt and M to a growing particle. The average ratio, of course, will be determined by the ratio of reagents used in a particular synthesis procedure. Particle size and morphology may also play a factor in the overall behavior. Finally, even at thermodynamic equilibrium, the degree of ordering will likely be less than 100 % due to strain and finite size effects. Since thermal equilibrium is reached by diffusion, low temperature anneals may not result in nucleation nor subsequent growth.

We observed a sharper (111) peak at the higher annealing temperatures (Fig. 8.3A). The average domain size of each ensemble of particles was estimated by the Scherrer equation using the full width at half maximum (FWHM) of the (111) peak, which is fairly consistent with the particle size determined from our TEM analysis (*vide infra*). After a 2 h annealing process, the average domain size of Pt<sub>3</sub>Co/C increased from 3.5 nm to 6 nm with increasing annealing temperature from 600 °C to 750 °C, and it became as large as 8 nm when the temperature was 825 °C. The (111) diffraction peak also

shifted gradually to higher angles, indicating that the corresponding lattice d-spacing decreased from 2.29 Å, before annealing, and reached a value as low as 2.24 Å after a 2h anneal at 825 °C. The d-spacing approached the theoretical value of ordered bulk Pt<sub>3</sub>Co, 2.21 Å, (Fig. 8.5A). The relative content of the ordered phase and the particle size, both increased with increasing temperatures when the temperature was 600~750 °C (Fig. 8.3B). The above behavior is similar to that of bulk AuCu<sub>3</sub> and PtCo nanoparticles.<sup>38-42</sup>

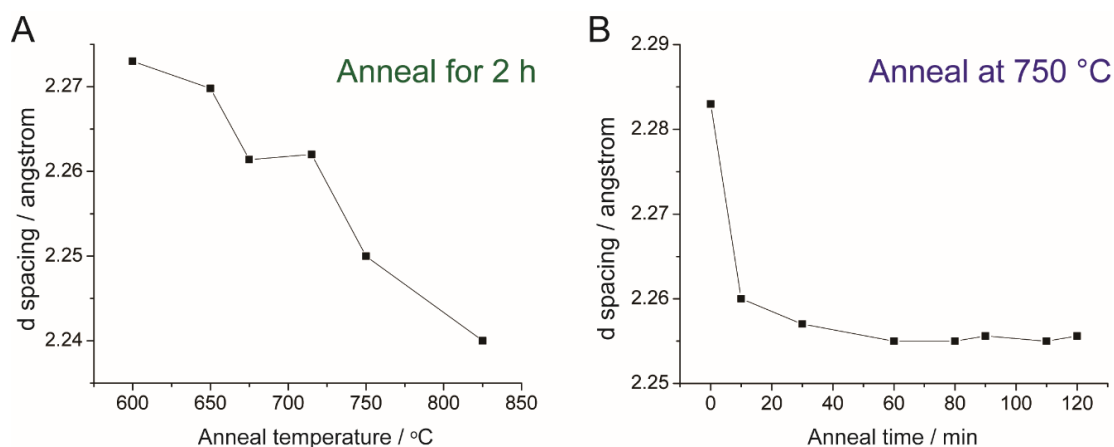


**Figure 8.5** (A) Measured d-spacings of Pt<sub>3</sub>Co/C (A) after 2 h annealing at various temperatures and (B) at different annealing times at 750 °C.

At 750 °C, which was the optimal annealing temperature for the highest degree of ordering achieved in this experiment, the XRD patterns were tracked dynamically as a function of annealing time (Fig. 8.3C). The (110) ordering peak became more pronounced, and the (111) peak became sharper and shifted to higher angles with longer annealing times. The calculated phase content of ordered Pt<sub>3</sub>Co/C and domain sizes exhibited a similar trend: They both increased rapidly during the first half hour, and gradually approached a relatively stable plateau (Fig. 8.3D). This suggested that 2 h was sufficient time to achieve a steady state (or possibly equilibrium) and optimal contents

of the ordered phase at such temperatures. After 2 h of annealing at 750 °C, Pt<sub>3</sub>Co/C had an average domain size of 6 nm and a (110) ordered peak intensity of 30% relative to the maximum possible, if ordering was complete. In addition, the d-spacing decreased during the first 30 mins and approached a plateau (Fig. 8.5B), indicating that the lattice contracted during annealing as the average order increased.

To investigate quantitatively the influence of Pt<sub>3</sub>Co particle size (3~8 nm) on the onset of disorder, we used Monte-Carlo simulations to calculate the degree of substitutional ordering at thermodynamic equilibrium at various temperatures from the average atomic occupation of the lattice sites.<sup>38-42</sup> The order-disorder transition (ODT) was characterized by both the (long-range order parameter) LROP and the (short-range order parameter) SROP and plotted as a function of temperature in Fig. 8.6A for two NP sizes (2.9 and 5.2 nm) and the bulk system (see calculation details in the supporting information). For each system, the temperature at which the LROP and SROP curves exhibit inflexion points is roughly the same and marks the ODT temperature,  $T_{\text{ODT}}$ . At  $T_{\text{ODT}}$ , the system undergoes a transition from the L1<sub>2</sub> phase (Fig. 8.6B) to a disordered phase via an intermediate, transient D0<sub>22</sub> phase (Fig. 8.6C). The D0<sub>22</sub> phase also possesses global long-range order with lower crystal symmetry, but is not captured by the LROP used (Figs. 8.6B-9.6C). The  $T_{\text{ODT}}$  of the NPs is significantly lower than that of the bulk system (750 °C), and there is a clear trend of a decrease in  $T_{\text{ODT}}$  with a decrease in NP size. This indicates that for a certain range of temperatures (below the bulk  $T_{\text{ODT}}$ ) one could observe larger NPs maintaining higher degree of substitutional order than smaller NPs, which is consistent with our observations in Fig. 8.6B.

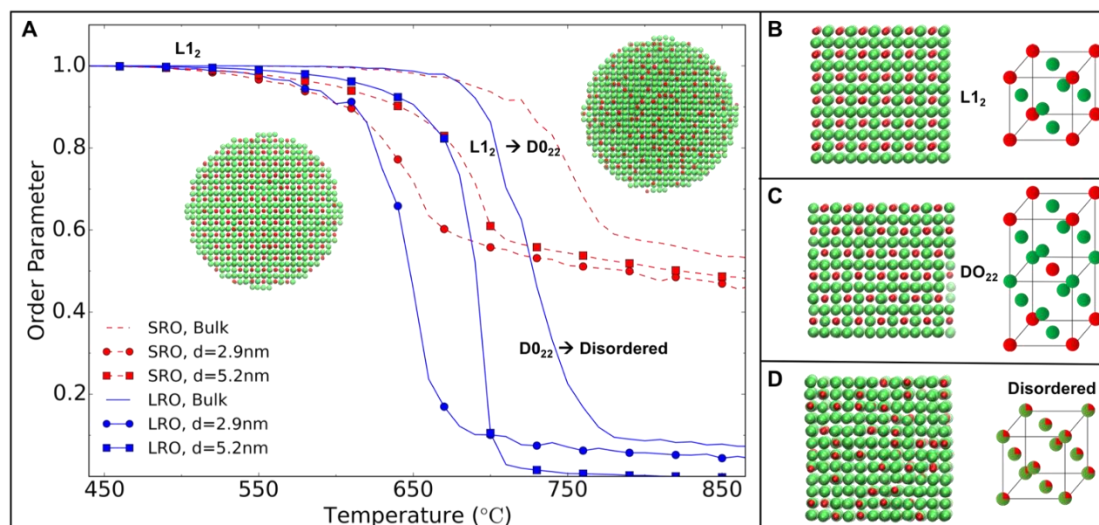


**Figure 8.6** (A) Simulation results for the SROP (red, dashed line) and LROP (blue, solid line) as a function of temperature for bulk ( $N=864$ , no marker) and spherical NPs with diameter  $d=2.9$  nm ( $N=800$ , circles) and  $d=5.2$  nm ( $N=4800$ , squares, with snapshots shown at temperatures just before the ODT on the left, and just after the ODT on the right). The temperatures are rigidly shifted so as to match the simulation results to the experimental Bulk order-disorder transition (ODT) temperature. As the size of the NP is reduced, the ODT temperature for the NPs also decreases. Snapshots of the bulk trajectory taken at increasing temperatures showing (B) ordered intermetallic phase,  $L1_2$ , (C)  $DO_{22}$  state with global long-range order and lower crystal symmetry, and (D) disordered solid solution phase. The green and red atoms represent Pt and Co, respectively.

To dynamically track the evolution of the superlattice ordering peaks during the annealing process, the XRD patterns of  $Pt_3Co/C$  were obtained by increasing the temperature at a very slow rate of  $0.5$  °C/min from  $620$  °C to  $830$  °C (Fig. 8.7A). Because each diffraction scan took less than 2 min, the temperature resolution was within  $1$  °C. With higher annealing temperatures, the (110) peak became more pronounced and attained a maximum at  $720$ - $750$  °C, while the absolute intensity of the (111) peak decreased, due to additional disordering in the lattice above the transition temperature as well as to Debye-Waller effects.<sup>43-44</sup> The relative magnitude of the peak intensity ratio of (110) to (111), with the maximum ratio normalized to 100%, was

employed as a simple (and reliable) metric to represent the relative amount of the ordered phase( (Fig. 8.7B).

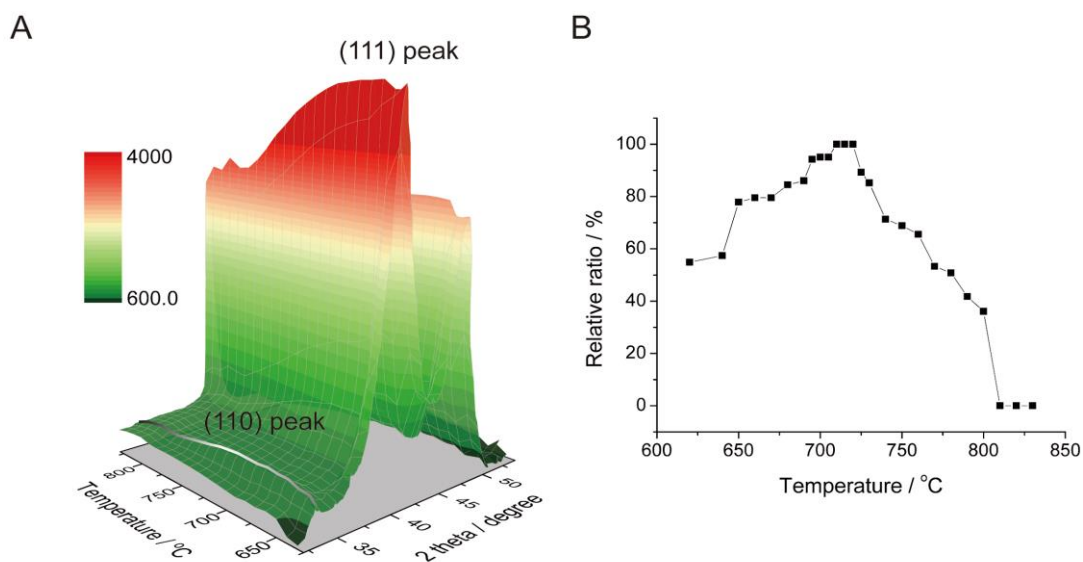


**Figure 8.7.** (A) *In situ* heating XRD patterns of Pt<sub>3</sub>Co/C annealed from 620 °C to 830 °C at a slow temperature ramping rate of 0.5 °C/min (B) Relative peak integral ratio of the (110) to (111) peaks (with the maximum ratio normalized to 100%) at a series of temperatures.

Because the annealing treatment of binary intermetallics during synthesis must be accompanied by cooling of the catalysts down to room temperature, the cooling procedure, after the *in situ* annealing process, was also investigated. Pt<sub>3</sub>Co/C powders, annealed at 715 °C for 2 h were used as a baseline to measure the effect of different cooling rates (Fig. 8.8A). After annealing at 715 °C for 2 h, and cooling to room temperature, the (111) peak shifted to higher angle, indicating that the lattice had contracted further. Cooling experiments were conducted at two different cooling rates after 2 h of annealing (Fig. 8.8B). The first was a slow rate of 6 °C/min, and in the second, the sample was cooled by turning off the electric heater and allowing the gas in the device to cool naturally at a rate of ~30 °C/min. At the slower cooling rate, the

relative contents of the ordered Pt<sub>3</sub>Co/C phase increased, which was ascribed to the extended period for the atomic rearrangement to the thermodynamically-favored state. The sample cooled at a higher rate showed only a slight increase in ordered phase content.

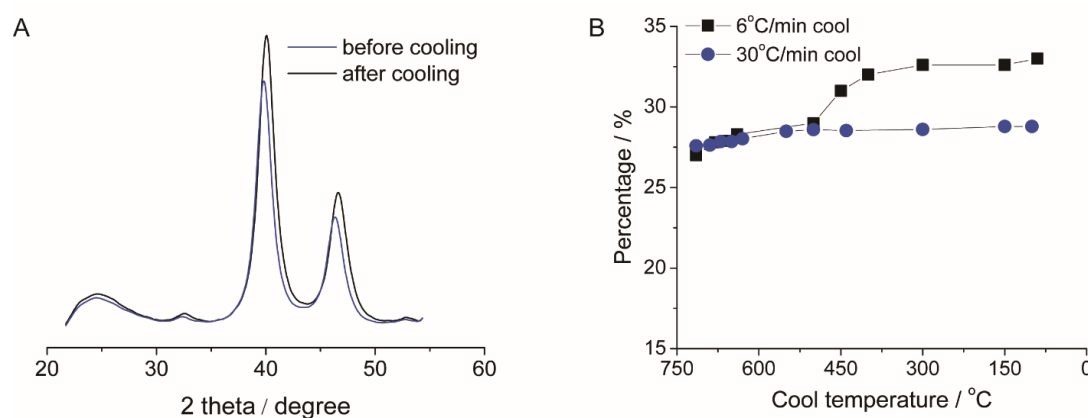


**Figure 8.8.** (A) XRD patterns of Pt<sub>3</sub>Co after annealing at 715 °C for 2 h, and after cooling down to room temperature. (B) Relative contents of ordered intermetallic Pt<sub>3</sub>Co/C under two different cooling rates. X-axis represents the monitored temperatures during the cooling process.

In summary, the effects of the annealing and cooling processes at different annealing temperatures and times on the ordered intermetallic content, were investigated. We conclude that the optimal annealing conditions were to anneal Pt<sub>3</sub>Co/C at 750 °C for 2 h and then to cool to room temperature at a slow rate (e.g., 6 °C/min). Other cooling procedures may lead to an even larger fraction of ordered particles. Such processing parameters are used to manufacture heat-resistant CorningWare glass, and in toughening metals by age precipitation hardening, for example.

#### 8.4 *In situ* Heating STEM Imaging

In addition to enabling structured ordering, the thermal annealing process can also alter the morphology of the Pt<sub>3</sub>Co nanoparticles. The most important morphological change

was coarsening of the Pt<sub>3</sub>Co particles, which increased their size and decreased the catalysts' active surface area. To observe these morphological changes, we conducted *in situ* annealing experiments in a scanning transmission electron microscope (STEM).

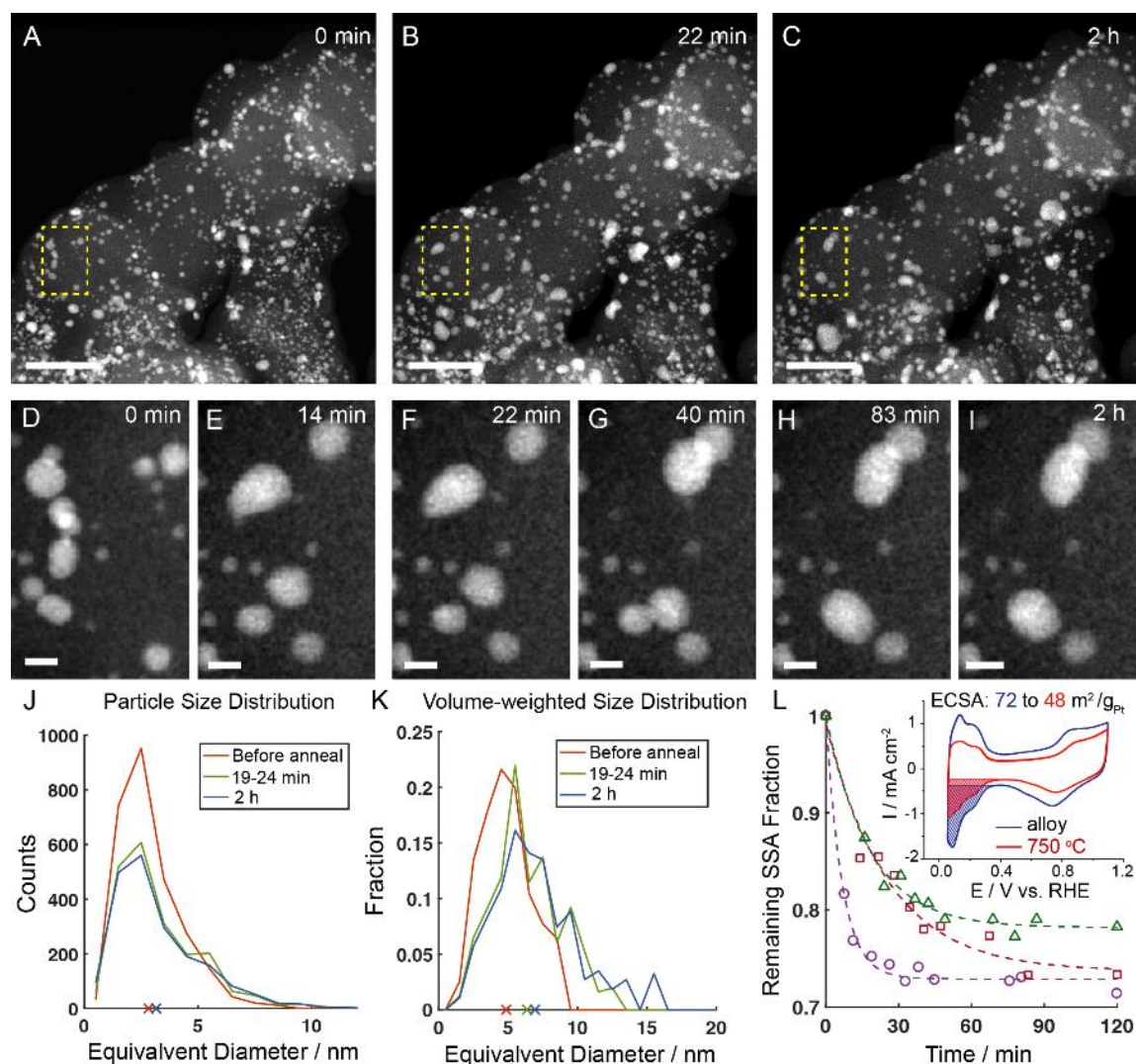


**Figure 8.9.** *In situ* heating STEM enabling tracking of the morphological changes of Pt<sub>3</sub>Co/C annealed at 750°C. (A-C) Pt<sub>3</sub>Co/C before annealing, annealed for 22 min, and annealed for 2h, respectively. (D-I) A specific region was magnified to illustrate particle migration and coalescence during a continuous 2 h annealing process. (J) Measured distribution of particle sizes of thousands of particles from Fig. 4A at different annealing times at 750°C. Cross marks on the X-axis represent the corresponding average particle sizes. (K) Volume-weighted, particle size distribution, which reflects the relative contribution of larger particles more clearly, as shown by the more pronounced tails for

particle sizes above 8 nm. Cross marks on the X-axis represent the corresponding volume-weighted, average particle sizes. (L) Specific surface area (SSA) ( $\text{m}^2/\text{g}_{\text{Pt}}$ ) estimated from STEM images of three different regions at different annealing times. Inset: Electrochemical surface area (ECSA) for  $\text{Pt}_3\text{Co}/\text{C}$  before and after annealing at  $750\text{ }^\circ\text{C}$  for 2 h, measured from the coulometric charge associate with hydrogen adsorption ( $\text{H}_{\text{ads}}$ ) regions in the cyclic voltammograms. Details of statistical analysis of particle sizes and SSA calculations can be found in the experimental section. Scale bars in Figures A-C are 50 nm, and scale bars in Fig. D-I are 5 nm.

A  $\text{Pt}_3\text{Co}/\text{C}$  alloy specimen was annealed at  $750^\circ\text{C}$  for 2 hours in an *in situ* STEM specimen holder in vacuum to approximate the conditions of a typical annealing protocol. Images were acquired alternately in three separate regions of the specimen to provide a more robust and representative measurement of changes in the specimen (Fig. 8.9). Figs. 8.9A-C show a broad area of the sample before the annealing procedure and after 22 minutes and 2 hours of heating at  $750\text{ }^\circ\text{C}$ , respectively. An overall coarsening of the particles was evident throughout the region, especially during the first 22 minutes. Figs. 8.9D-I show a smaller sub-region, in detail, to highlight the observed particle coalescence, which appeared to be the primary coarsening mechanism. Significant particle mobility on the carbon support was also observed, with some particles moving more than 10 nm and growing significantly in size from collisions and coalescence with other particles. Note that several  $\sim 2$  nm particles remained fixed near their initial positions throughout the experiment with no noticeable change in size. This observation argues against Ostwald ripening as being a significant contributor to the particle coarsening.

Additional insights can be gained by calculating the statistical distribution of particle sizes and considering their change during the experiment (Fig. 8.9J). The particle size distribution approximately followed a lognormal form, with smaller 2-3 nm

particles being the most common with a substantial tail of larger particles. After annealing, the count of smaller particles decreased, while the distribution tail of larger particles grew more pronounced. This change in the shape of the distribution is also consistent with coarsening by particle coalescence, when a subset of smaller particles merge to form larger particles.<sup>45,46</sup> By contrast, an Ostwald ripening mechanism would have resulted in a more uniform shift in the distribution. The most significant change in the distribution occurred prior to the end of 19-24 min frame, though more subtle changes in the distribution occurred during the remainder of the annealing process. The growth in the number of large particles is more readily observed in the volume-weighted size distribution (Fig. 8.9K), which shows that larger particles, formed by coalescence, accounted for a significant fraction of the Pt<sub>3</sub>Co volume, even though large particles were relatively few in number.

The consequences of coarsening that occurred during the annealing process, on the electrochemical surface area (ECSA) of the Pt<sub>3</sub>Co particles were examined by estimating the specific surface area (SSA) of the particles from the images in each region of the specimen (Fig. 8.9L). The overall estimated SSA loss was approximately 20-30% and it varied among the three different locations in the specimen. This was similar in magnitude to the 33% loss in ECSA that we calculated from the cyclic voltammograms (CV) of Pt<sub>3</sub>Co/C annealed for 2 h at 750°C in forming gas as discussed below. (Fig. 8.9L, inset) In each specimen region, the SSA tended to decrease in approximately an exponential manner, and decayed towards a lower (but non-zero) value with a time-constant that varied from 7-25 min among the three different regions. This confirmed previous observations that the most significant changes in the distribution of particle

sizes occurred very early in the annealing process. The variation between the total SSA loss and the decay rate likely reflect differences in the strength of the bonding between Pt<sub>3</sub>Co particles and the carbon support, suggesting that the structure of the carbon support can be quite heterogeneous.

### 8.5 Atomic-Scale *Ex Situ* HAADF-STEM Imaging

To directly observe the crystal structure of ordered intermetallics at the atomic-scale, we employed aberration-corrected scanning transmission electron microscopy (STEM) to study the Pt<sub>3</sub>Co/C after the annealing and cooling processes. We used the high-angle annular dark-field (HAADF) STEM imaging mode, which provides intensities that scale with the atomic number ( $I \propto Z^{1.7}$ ) so that Pt atoms appear much brighter than Co atoms. L<sub>12</sub> intermetallic ordering in Pt<sub>3</sub>Co nanoparticles can be recognized by the presence of unique, superlattice-ordered unit cells. The atomic-scale STEM image of a Pt<sub>3</sub>Co particle along the [100] zone axis exhibits a periodic square array of dimmer Co atom columns at the center, surrounded by brighter Pt columns at the corners (Fig. 8.10A). The square symmetry is consistent with the projected crystal model along the same [100] zone axis in ordered Pt<sub>3</sub>Co intermetallics, where four pure Pt atom columns (red), at the corners, surround the pure Co atom columns (green) at the center (Fig. 8.10C). However, another single-crystal Pt<sub>3</sub>Co nanoparticle (Fig. 8.10B), which was viewed along the [100] zone axis, exhibited only a partially ordered intermetallic phase, as only parts of the NP showed a similar variation in the intensity as the crystal model suggested (Fig. 8.10C). Other parts of the NP showed atoms at the center that were as bright as atoms at the corners, indicating that only a short-range, atom ordering existed in such Pt<sub>3</sub>Co nanoparticles. Figs. 8.10A-B indicate that both fully and partially ordered

intermetallics exist in the Pt<sub>3</sub>Co nanoparticles after the annealing process.

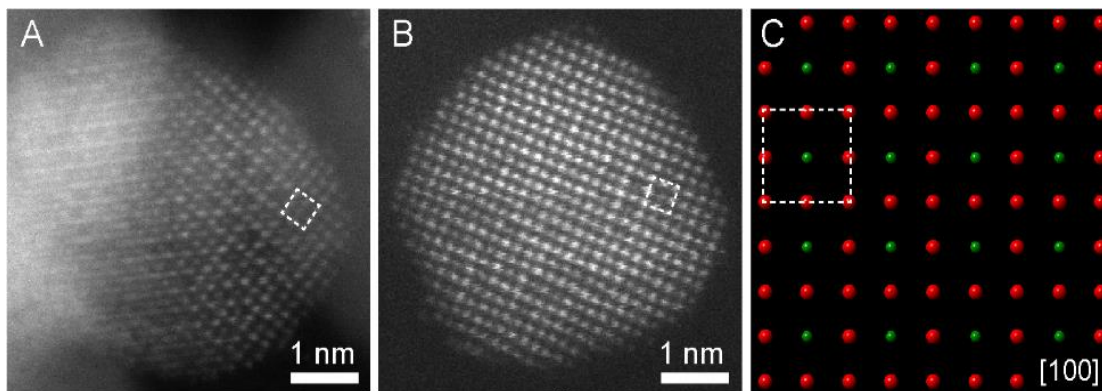


**Figure 8.10.** Atomic-scale *ex situ* HAADF-STEM images of Pt<sub>3</sub>Co/C after annealing. (A) An ordered intermetallic Pt<sub>3</sub>Co particle on the [100] zone axis. Brighter atoms at corners of squares are Pt, and dimmer atoms at the center are Co. (B) A partially ordered intermetallic particle on the [100] zone axis. Both brighter and dimmer atoms exist at the center of the squares. (C) Corresponding projected crystal model along [100]. Red and green atoms are Pt and Co, respectively. Crystal models were built based on the ordered intermetallic Pt<sub>3</sub>Co (PDF # 01-071-7410).

### 8.6 Correlation of the Degree of Ordering to Catalyst Durability

The above mechanistic studies involving both *in situ* heating XRD and *in situ* heating TEM yield a fuller picture of the order- disorder phase transition, and provide further practical guidance for the design of ORR catalysts with enhanced durability. The electrochemical properties of the electrocatalysts annealed at different temperatures in a tube furnace were studied systematically to correlate the degree of ordering to the catalyst's durability (Fig. 8.11). The powder XRD patterns of annealed Pt<sub>3</sub>Co/C (Fig. 8.4) exhibited a similar trend as the *in situ* heating XRD patterns in Fig. 8.3. The mass-specific activity (MA), the surface area-specific activity (SA), and the electrochemical surface area (ECSA) of the Pt<sub>3</sub>Co/C alloy electrocatalysts, that were annealed at different temperatures, were measured and calculated initially and after stability cycling, which involved potential cycling at 50 mV/s in 0.1M HClO<sub>4</sub> over the potential

range of 0.6 to 1.0 V vs. the reversible hydrogen electrode (RHE). The relative retentions of ECSA, MA (mass activity) and SA (specific activity) of Pt<sub>3</sub>Co/C annealed at various temperatures were calculated from the ratio between the initial activity/surface areas to that after the durability tests (Figs. 8.11B and Table 8.2). With increasing annealing temperature, the retention of the SA and MA improved continuously until reaching the highest values of 94% and 95%, respectively, at 750 °C. However, they dramatically decreased when the annealing temperature was increased to 825 °C. The trends in retention of SA and MA were quite consistent with the degree of ordering of the intermetallics, which indicated that the more ordered atomic structure improved the durability of the Pt<sub>3</sub>Co/C nanoparticles. ECSA retention reached a maximum plateau at 725-750 °C with nearly no decay, with respect to its initial value, suggesting that a higher degree of ordering suppressed the loss of Pt surface area. It should be noted that the as-synthesized Pt<sub>3</sub>Co/C (reduced at 300 °C) had a slightly higher ECSA than Pt<sub>3</sub>Co/C that was annealed at 600 °C, likely because the as-synthesized Pt<sub>3</sub>Co/C contained particles that were smaller than those annealed at 600 °C. This may have counteracted, or even surpassed, the benefit of the higher degree of ordering at 600 °C.

The shift in the half-wave potential ( $E_{1/2}$ ), which is considered as an indicator of the intrinsic electrocatalytic activity in a more straightforward way, was also evaluated for its stability. The  $E_{1/2}$  exhibited a trend similar to the SA and MA, with the least negative shift (< 5mV) observed at the optimal annealing temperature of 750 °C. The improvement in the stability of the Pt<sub>3</sub>Co with the highest ordered degree, comes from the stable intermetallic Pt, Co arrangement in the core and the Pt rich shell. In the

stability test of Pt<sub>3</sub>Co alloy or intermetallics, the degradation of the electrocatalyst comes mainly from the loss of Co and the leached Co ions in the electrolyte, in turn contaminating the Pt surface. The intermetallic nanoparticle with the highest ordered degree had the most uniform and regular atomic structure, so the Co was mostly bonded and surrounded by Pt. Also, the stable and ordered structure maintained the robust atomic structure, retaining the highest ECSA after the cycling process. As a result, it yielded a large improvement in the E<sub>1/2</sub> during the stability test. This enhancement is not only observed from the RDE experiments, but also demonstrated in the membrane electrode assembly results (see below). To the best of our knowledge, this study represents the first successful attempt to systematically correlate the degree of ordering of binary alloy catalysts to the durability of electrocatalysts towards the oxygen reduction reaction in fuel cells, which will provide valuable insights and strategies in the future design of novel, ordered intermetallic electrocatalysts.

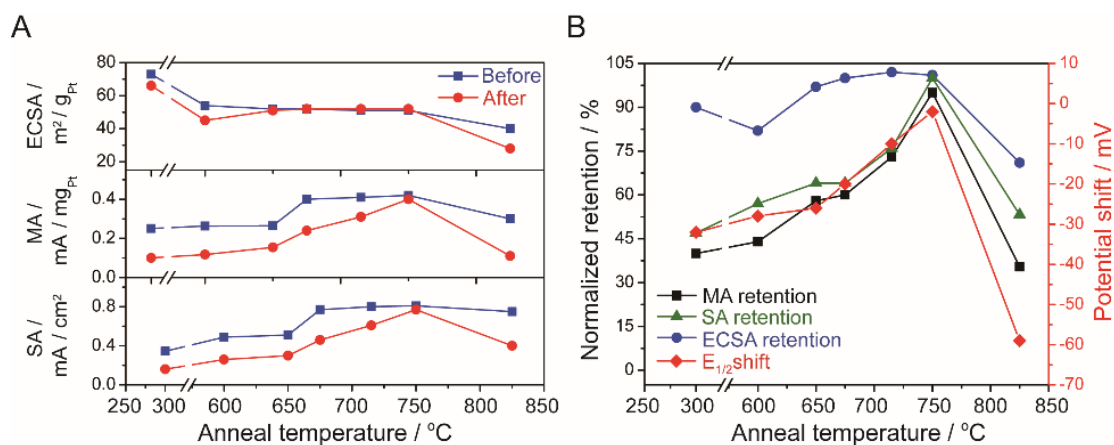


**Figure 8.11.** (A) Calculated ECSA, mass-specific activity (MA) and surface-specific activity (SA) at 0.9V vs. RHE of Pt<sub>3</sub>Co/C before and after stability tests, after a series of annealing temperatures for 2h. (B) Normalized retention of mass-specific activity (MA), surface area-specific activity (SA), and electrochemical surface area (ECSA) on the left axis, and half-wave potential shift on the right axis of Pt<sub>3</sub>Co/C after annealing at different temperatures. Normalized retention was calculated based on the ratio of the initial activity/surface areas to that after durability tests (2000 cycles in cyclic

voltammetry at 100 mV/sec in 0.1M HClO<sub>4</sub> over the potential at the range from 0.6 to 1.0 V vs RHE). The best durability was achieved at around 750 °C, corresponding to the optimal degree of ordering.

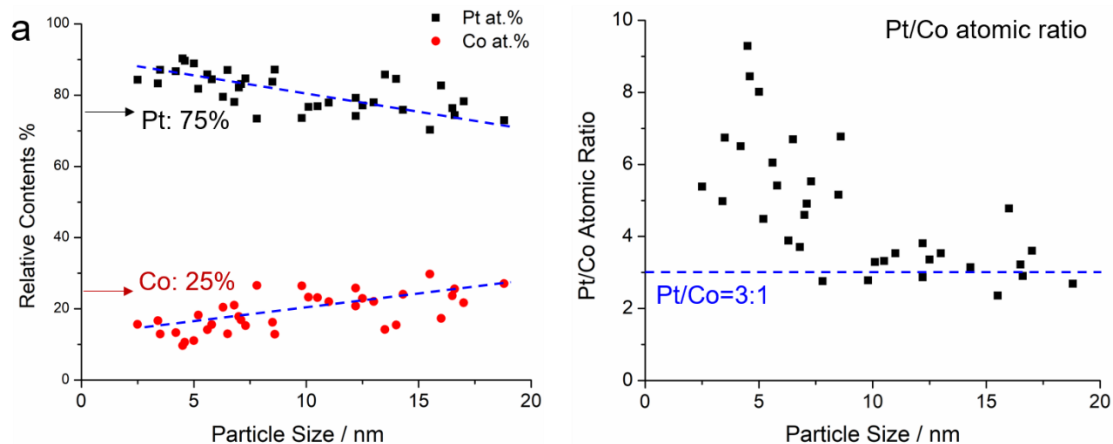
Temp. (°C)	ECSA (m <sup>2</sup> /g <sub>Pt</sub> )		ECSA retention (%)	MA (mA/μg <sub>Pt</sub> )		MA Retention (%)	SA (mA/cm <sup>2</sup> <sub>Pt</sub> )		SA Retention (%)	E <sub>1/2</sub> (V vs. RHE)		E <sub>1/2</sub> Shift (mV)
	Before	After		Before	After		Before	After		Before	After	
300	73	66	90	0.251	0.1	40	0.344	0.16	47	0.886	0.854	-32
600	54	45	82	0.263	0.117	44	0.488	0.26	53	0.899	0.871	-28
650	52	51	97	0.265	0.154	58	0.51	0.30	59	0.902	0.876	-26
675	52	52	100	0.4	0.24	60	0.77	0.46	60	0.909	0.89	-19
715	51	52	102	0.41	0.31	73	0.80	0.61	76	0.912	0.904	-8
750	51	52	102	0.42	0.4	95	0.82	0.77	94	0.915	0.912	-3
825	40	28	70	0.3	0.11	36	0.75	0.40	53	0.904	0.845	-59

**Table 8.2.** The calculated ECSA, MA, SA at 0.9 V and half-wave potential (E<sub>1/2</sub>) for different Pt<sub>3</sub>Co/C samples before and after stability tests. ECSA and Mass activity retentions were calculated from the ratio of hydrogen adsorption region between its initial values to that after stability test. Since all the catalysts have the same mass loading of Pt<sub>3</sub>Co, SA will have a value of MA divided by ECSA.

### 8.7 STEM-EDX Analysis of Pt and Co Contents of Individual Pt<sub>3</sub>Co Nanoparticles as a Function of Particle Sizes

Pt<sub>3</sub>Co/C was examined to have a 2-3 atomic-layer Pt shell on the surface after high-temperature annealing process in forming gas.<sup>2</sup> Therefore, The chemical compositions of as-synthesized Pt<sub>3</sub>Co in this work may depend on particle sizes since smaller nanoparticles will have larger shell-to-core volume ratios. To quantitatively study the effect of particle size, STEM-EDX was used to analyze relative Pt and Co contents of individual Pt<sub>3</sub>Co nanoparticles after optimized annealing process at 750 °C for 2h. A ideal Pt<sub>3</sub>Co nanoparticle without Pt shell will have 75% Pt and 25 Co%). Particle sizes were measured from STEM images with an average particle size of 7-8 nm. Relative Pt

and Co contents were calculated from EDX spectra of individual particles using Pt  $L\alpha$  edges and Co  $K\alpha$  edges.



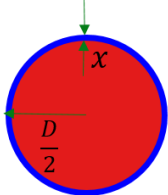
**Figure 8.12** Quantitative EDX Analysis of Pt and Co contents of individual  $Pt_3Co$  NPs as a function of particle sizes.

Fig. 8.12a shows that Pt% contents increased from 75% to about 90% while Co contents decreased from 25% to about 10%, as particle sizes decreased from 20 nm to 3 nm. Fig. 8.12b shows that Pt/Co ratios increased significantly from around 3:1 to about 9:1 as a result of the same change in particle sizes. A 20 nm  $Pt_3Co$  nanoparticle would have the vast majority contribution of chemical composition from  $Pt_3Co$  core (Pt/Co: 3:1) since 2-3 atomic-layer Pt shell (<1 nm) is negligible when compared to 20 nm core. However, a 3 nm  $Pt_3Co$  nanoparticle would have significant contributions from both  $Pt_3Co$  core and 2-3 atomic-layer Pt shell, leading to an overall much higher Pt/Co ratio of 9:1.

In order to calculate the theoretical Pt/Co mole ratio from a given particle size and shell thickness, we performed a geometric analysis (Fig. 8.13). Overall, all experimental STEM-EDX results (green dots) fall in the region between monolayer and three-atomic-layer Pt shells (black and blue curves, respectively). This indicates that the majority of

Pt<sub>3</sub>Co/C annealed at 750 °C for 2h have a Pt shell thickness of 1-3 atomic layers.

Additionally, all three curves with different layers of Pt shell exhibited that Pt/Co atomic ratio increased significantly as particle decreased from 20 nm (close to bulk level) to 2-3 nm (lower boundary in synthesized Pt<sub>3</sub>Co nanoparticles), which is due to larger contribution from the shell in smaller particles sizes. Forming a thicker Pt shell requires a higher Pt/Co ratio in reaction precursors, as indicated from black to red and blue curves. For example, Pt<sub>3</sub>Co/C annealed at 750 °C for 2h, with an average size of 7.5 nm (purple dashed line), requires Pt/Co atomic ratios of 4:1, 5:1 and 7:1 in order to achieve monolayer, two and three-atomic-layer Pt shells on Pt<sub>3</sub>Co core materials, respectively. This may be a useful guide for chemical synthesis of Pt<sub>3</sub>Co nanoparticles with tunable chemical composition and shell thickness.



Mole ratio: 
$$\frac{core}{shell} = \frac{\rho_{core}}{M_{core}} \times \frac{\left(\frac{D}{2} - x\right)^3}{\left(\frac{D}{2}\right)^3 - \left(\frac{D}{2} - x\right)^3}$$

Pt/Co atomic ratio: 
$$\frac{n_{core} + n_{shell}}{1/3(n_{core})}$$

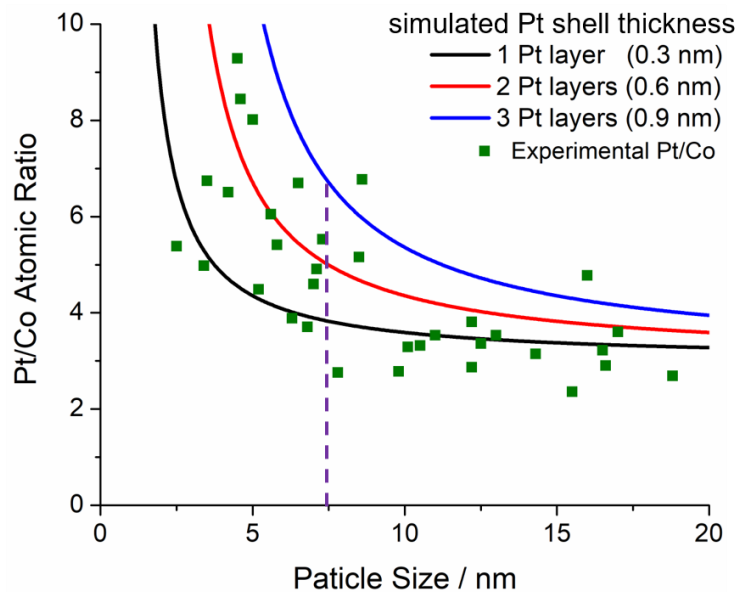


**Figure 8.13** Theoretical Calculation of Pt/Co mole ratio from a given particle size and shell thickness and comparison to STEM-EDX results. Dashed line indicates a particle size of 7.5 nm, which is the average size of Pt<sub>3</sub>Co NPs annealed at 750 °C for 2h.

### 8.8 Activity and Durability Evaluation of Pt<sub>3</sub>Co/C in MEA Measurements

For practical applications in PEMFCs, it is important to confirm that the findings in the laboratory can be translated to real-world (practical) improvement. The annealed, ordered, Pt<sub>3</sub>Co/C electrocatalysts prepared in this work were evaluated in a fuel cell membrane-electrode assembly (MEA) and compared to one of the most active and durable state-of-the-art PtCo/C catalysts (Fig. 8.14).<sup>47-48</sup> The disordered Pt<sub>3</sub>Co/C used for comparison was made by chemically dealloying a PtCo/C precursor. The disordered Pt<sub>3</sub>Co/C had already exhibited excellent activity and stability in MEA results and had surpassed the U.S. Department of Energy (DOE) targets (initial ORR mass activity >0.44 A/mg<sub>Pt</sub> and <40% loss after stability test) (Fig. 8.14B). In this study, the disordered Pt<sub>3</sub>Co was further processed through the aforementioned optimal annealing conditions to achieve a maximum degree of ordering. The annealed Pt<sub>3</sub>Co/C showed comparable initial ORR activity and Pt ECSA to the disordered catalyst, however, it had about a 40% lower loss after the stability test (Fig. 8.14B middle plot). This is an impressive achievement over an already-very-stable, high performing electrocatalyst. These results support the findings of the above-described *in situ* experiments on Pt<sub>3</sub>Co, that ordered intermetallic phases represent a promising path to develop stable, high performance fuel cell electrocatalysts. The initial high-current-density (HCD) performance (Fig. 8.14B lower plot) of the ordered catalyst, although quite respectable by industry standards, is still slightly lower than our well-optimized baseline disordered Pt<sub>3</sub>Co/C catalyst. The development of MEA electrodes for HCD for new catalysts

generally takes several months and large amount of materials to optimize the ionomer, catalyst, and pore distribution within the electrode. Taking the mass activity and ECSA of the ordered catalyst into account, we predict that once optimized, the initial performance of the ordered phase Pt<sub>3</sub>Co electrocatalyst will surpass that of the disordered Pt<sub>3</sub>Co/C catalyst.<sup>49</sup>

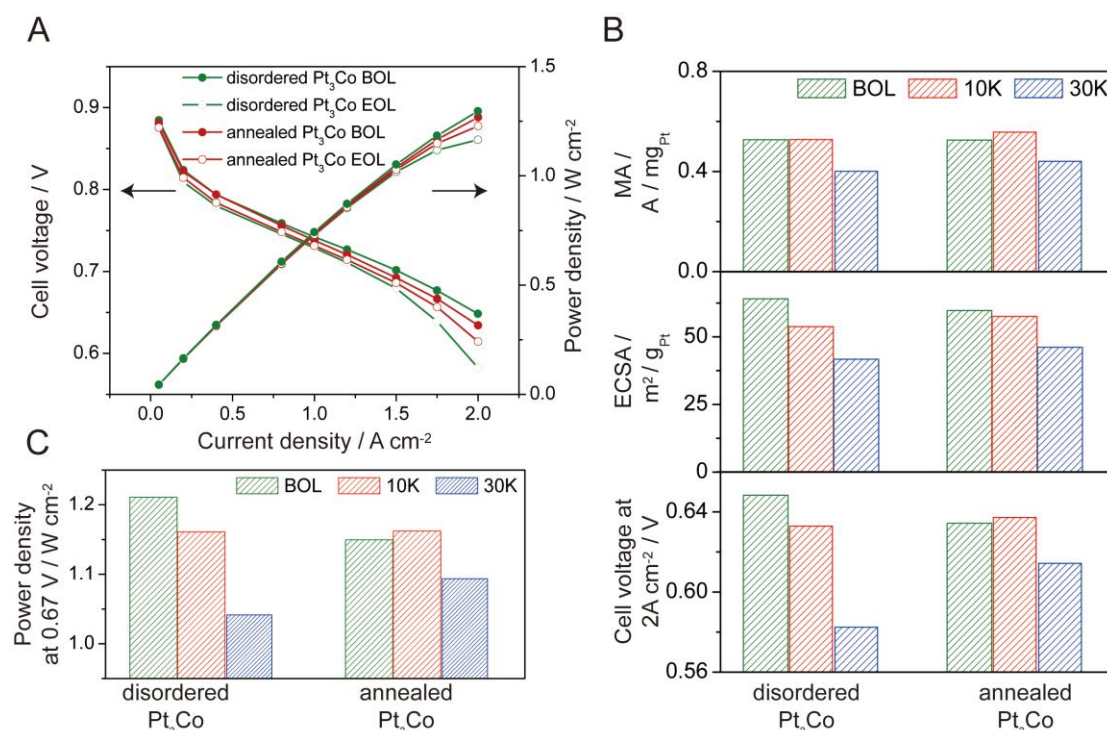


**Figure 8.14.** MEA performance comparison of disordered and annealed Pt<sub>3</sub>Co/C before and after stability testing. BOL and EOL represent beginning-of-life (initial performance) and end-of-life (after 30,000 cycles), respectively. (A) MEA performance at Pt loadings of 0.025 and 0.10 mg<sub>Pt</sub>/cm<sup>2</sup> on anode and cathode, respectively. Cell operation conditions are in the order of anode/cathode: H<sub>2</sub>/air, 94 °C, 65/65%RH, 250/250 kPa<sub>abs,outlet</sub>, stoichiometries of 1.5/2. (B) Mass-specific activity (MA) measured at 0.9 V vs. RHE; ECSA of Pt measured by CO stripping in MEA; Voltage measured at a high current density of 2 A/cm<sup>2</sup>. (C) Power density at 0.67 V under the same condition as (A).

The greatest value of the stability improvement of this catalyst is especially evident at HCD, as the durability under HCD performance is the leading factor determining the

cost of a fuel cell stack.<sup>49</sup> The annealed Pt<sub>3</sub>Co/C catalyst showed significantly smaller losses compared to the disordered catalyst after 30,000 cycles; only 20 mV vs. 66 mV (Fig. 8.14B lower plot). This is due to the better retention of ORR activity and ECSA of the ordered catalysts as discussed above. To practically meet the U.S. DOE heat rejection target ( $Q/\Delta T$  of  $<1.45$ ), the voltage must be higher than the 0.67 V under the operating conditions used in this work (94 °C).<sup>48</sup> As shown in Fig. 8.14C, the annealed Pt<sub>3</sub>Co/C exhibited only a 5% loss in power density at 0.67 V after 30,000 cycles, relative to a 14% loss for the disordered Pt<sub>3</sub>Co/C electrocatalyst. To the best of our knowledge, these results represent a cathode catalyst in PEMFCs with the highest performance and stability published to date. While we employed an accelerated stability test and yet require performing a long-term durability validation in this study, the advancement projects progress toward meeting the US DOE durability target of less than 10% performance loss after 8,000 h of automotive drive cycle.

## 8.9 Conclusion

In summary, this work represents the first time that both *in situ* heating synchrotron-based XRD for large ensembles of nanoparticles and *in situ* heating TEM at microscopic level have been used to quantitatively study the dynamics of the order-disorder phase transition and morphological and structural changes of binary intermetallics during a thermal annealing treatment. We have studied the impact of the annealing temperature and cooling conditions (temperature and time) comprehensively, on the degree of ordering, particle size, and lattice strain of Pt<sub>3</sub>Co intermetallics. Through Monte Carlo simulations, we have also found that Pt<sub>3</sub>Co nanoparticles have a lower order-disorder phase transition temperature than their bulk counterpart (by up to ~100 °C for 3-5 nm

nanoparticles). At the optimal annealing temperature (750 °C), the total content of ordered intermetallic phase peaks at about 30%, reflecting the presence of both fully and partially ordered nanoparticles and a correlation between intermetallic order and particle size. To directly visualize the morphological and structural transitions during the annealing treatment, we further employed *in situ* heating STEM to study the mechanism of nanoparticle migration and growth, and we quantitatively investigated the evolution of particle size distribution and the specific surface area during the annealing process. We achieved a direct visualization of both fully ordered and partially ordered individual Pt<sub>3</sub>Co nanoparticles at the atomic scale. Finally, we have built a structure-activity correlation in which the Pt<sub>3</sub>Co/C catalysts, with a higher degree of ordering, exhibited significantly enhanced durability. We further demonstrated that the annealed Pt<sub>3</sub>Co/C with optimal degree of ordering exhibited remarkable long-term durability in practical MEA measurements in PEMFCs. This systematic and in-depth study, which involved both *in situ* heating XRD and *in situ* heating TEM, will have a broad impact on the further development of ordered intermetallic electrocatalysts for fuel cell applications.

## 8.10 References

1. Cano, Z. P.; Banham, D.; Ye, S., Hintennach, A., Lu, J.; Fowler, M. & Chen, Z. Batteries and fuel cells for emerging electric vehicle markets. *Nat. Energy* **3**, 279-289 (2018).
2. Wang, D., Xin, H., Hovden, R., Wang, H., Yu, Y., Muller, D., DiSalvo, F. & Abruña, H. Structurally ordered intermetallic platinum–cobalt core–shell nanoparticles with enhanced activity and stability as oxygen reduction electrocatalysts. *Nat. Mater.* **12**, 81-87 (2013).
3. Stamenkovic, V., Mun, B., Arenz, M., Mayrhofer, K., Lucas, C., Wang, G., Ross, P. & Markovic, N. Trends in electrocatalysis on extended and nanoscale Pt-bimetallic alloy surfaces. *Nat. Mater.* **6**, 241-247 (2007).

4. Cui, C., Gan, L., Heggen, M., Rudi, S. & Strasser, P. Compositional segregation in shaped Pt alloy nanoparticles and their structural behaviour during electrocatalysis. *Nat. Mater.* **12**, 765-771 (2013).
5. Shao, M., Chang, Q., Dodelet, J. & Chenitz, R. Recent advances in electrocatalysts for oxygen reduction reaction. *Chem. Rev.* **116**, 3594-3657 (2016).
6. Xiong, Y.; Yang, Y.; DiSalvo, F. J. & Abruña, H. D. Pt-Decorated Composition-Tunable Pd-Fe@Pd/C Core-Shell Nanoparticles with Enhanced Electrocatalytic Activity toward the Oxygen Reduction Reaction. *J. Am. Chem. Soc.* 10.1021/jacs.8b03365 (2018).
7. Han, B., Carlton, C., Kongkanand, A., Kukreja, R., Theobald, B., Gan, L., O'Malley, R., Strasser, P., Wagner, F. & Shao-Horn, Y. Record activity and stability of dealloyed bimetallic catalysts for proton exchange membrane fuel cells. *Energy Environ. Sci.* **8**, 258-266 (2015).
8. DeSario, D. Y. & DiSalvo, F. J., Ordered intermetallic Pt-Sn nanoparticles: Exploring ordering behavior across the bulk phase diagram. *Chem. Mater.* **26**, 2750-2757 (2014).
9. Yan, Y., Du, J., Gilroy, K., Yang, D., Xia, Y. & Zhang, H. Intermetallic nanocrystals: syntheses and catalytic applications. *Adv. Mater.* **29**, 1605997 (2017).
10. Luo, M., Sun, Y., Wang, L. & Guo, S. Tuning multimetallic ordered intermetallic nanocrystals for efficient energy electrocatalysis. *Adv. Energy Mater.* **7**, 1602073 (2017).
11. Abe, H., Matsumoto, F., Alden, L., Warren, S., Abruña, H. & DiSalvo, F. Electrocatalytic performance of fuel oxidation by Pt<sub>3</sub>Ti nanoparticles. *J. Am. Chem. Soc.* **130**, 5452-5458 (2008).
12. Cui, Z., Chen, H., Zhao, M., Marshall, D., Yu, Y., Abruña, H. & DiSalvo, F. Synthesis of structurally ordered Pt<sub>3</sub>Ti and Pt<sub>3</sub>V nanoparticles as methanol oxidation catalysts. *J. Am. Chem. Soc.* **136**, 10206-10209 (2014).
13. Ghosh, T., Leonard, B., Zhou, Q. & DiSalvo, F. Pt alloy and intermetallic phases with V, Cr, Mn, Ni, and Cu: synthesis as nanomaterials and possible applications as fuel cell catalysts. *Chem. Mater.* **22**, 2190-2202 (2010).
14. Kang, Y. & Murray, C. Synthesis and electrocatalytic properties of cubic Mn-Pt nanocrystals (nanocubes). *J. Am. Chem. Soc.* **132**, 7568-7569 (2010).
15. Chung, D., Jun, S., Yoon, G., Kwon, S., Shin, D., Seo, P., Yoo, J., Shin, H., Chung, Y., Kim, H., Mun, B., Lee, K., Lee, N., Yoo, S., Lim, D., Kang, K., Sung, Y. & Hyeon, T. Highly durable and active PtFe nanocatalyst for electrochemical oxygen reduction reaction. *J. Am. Chem. Soc.* **137**, 15478-15485 (2015).
16. Leonard, B., Zhou, Q., Wu, D. & DiSalvo, F. Facile synthesis of PtNi intermetallic nanoparticles: influence of reducing agent and precursors on electrocatalytic activity. *Chem. Mater.* **23**, 1136-1146 (2011).
17. Wang, D., Yu, Y., Xin, H., Hovden, R., Ercius, P., Mundy, J., Chen, H., Richard, J., Muller, D., DiSalvo, F. & Abruña, H. Tuning oxygen reduction reaction activity via controllable dealloying: a model study of ordered Cu<sub>3</sub>Pt/C intermetallic nanocatalysts. *Nano Lett.* **12**, 5230-5238 (2012).

18. Chen, Q., Zhang, J., Jia, Y., Jiang, Z., Xie, Z. & Zheng, L. Wet chemical synthesis of intermetallic Pt<sub>3</sub>Zn nanocrystals via weak reduction reaction together with UPD process and their excellent electrocatalytic performances. *Nanoscale* **6**, 7019-7024 (2014).
19. Kang, Y., Pyo, J., Ye, X., Gordon, T. & Murray, C. Synthesis, shape control, and methanol electro-oxidation properties of Pt–Zn alloy and Pt<sub>3</sub>Zn intermetallic nanocrystals. *ACS Nano* **6**, 5642-5647 (2012).
20. Miura, A., Wang, H., Leonard, B., Abruña, H. & DiSalvo, F. Synthesis of intermetallic PtZn nanoparticles by reaction of Pt nanoparticles with Zn vapor and their application as fuel cell catalysts. *Chem. Mater.* **21**, 2661-2667 (2009).
21. Wang, X., Altmann, L., Stöver, J., Zielasek, V., Bäumer, M., Al-Shamery, K., Borchert, H., Parisi, J. & Kolny-Olesiak, J. Pt/Sn intermetallic, core/shell and alloy nanoparticles: colloidal synthesis and structural control. *Chem. Mater.* **25**, 1400-1407 (2013).
22. Kuttiyiel, K., Sasaki, K., Su, D., Wu, L., Zhu, Y. & Adzic, R. Gold-promoted structurally ordered intermetallic palladium cobalt nanoparticles for the oxygen reduction reaction. *Nat. Commun.* **5**, 5185 (2014).
23. Li, G., Kobayashi, H., Kusada, K., Taylor, J., Kubota, Y., Kato, K., Takata, M., Yamamoto, T., Matsumura, S. & Kitagawa, H. An ordered bcc CuPd nanoalloy synthesised via the thermal decomposition of Pd nanoparticles covered with a metal–organic framework under hydrogen gas. *Chem. Commun.* **50**, 13750-13753 (2014).
24. Jiang, K., Wang, P., Guo, S., Zhang, X., Shen, X., Lu, G., Su, D. & Huang, X. Ordered PdCu-based nanoparticles as bifunctional oxygen-reduction and ethanol-oxidation electrocatalysts. *Angew. Chem. Int. Ed.* **55**, 9030-9035 (2016).
25. Cable, R. & Schaak, R. Solution synthesis of nanocrystalline M-Zn (M: Pd, Au, Cu) intermetallic compounds via chemical conversion of metal nanoparticle precursors. *Chem. Mat.* **19**, 4098-4104 (2007).
26. Gunji, T., Noh, S., Tanabe, T., Han, B., Nien, C., Ohsaka, T. & Matsumoto, F. Enhanced electrocatalytic activity of carbon-supported ordered intermetallic palladium–lead (Pd<sub>3</sub>Pb) nanoparticles toward electrooxidation of formic acid. *Chem. Mater.* **29**, 2906-2913 (2017).
27. Chen, W., Yu, R., Li, L., Wang, A., Peng, Q. & Li, Y. A seed-based diffusion route to monodisperse intermetallic CuAu nanocrystals. *Angew. Chem. Int. Ed.* **49**, 2917-2921 (2010).
28. Wang, G., Huang, B., Xiao, L., Ren, Z., Chen, H., Wang, D., Abruña, H., Lu, J. & Zhuang, L. Pt skin on AuCu intermetallic substrate: a strategy to maximize Pt utilization for fuel cells. *J. Am. Chem. Soc.* **136**, 9643-9649 (2014).
29. Sra, A. & Schaak, R. Synthesis of atomically ordered AuCu and AuCu<sub>3</sub> nanocrystals from bimetallic nanoparticle precursors. *J. Am. Chem. Soc.* **126**, 6667-6672 (2004).
30. Okamoto, H. Co-Pt (cobalt-platinum). *J. Phase Equilib.* **22**, 591 (2001).
31. Oezaslan, M., Hasché, F. & Strasser, P. *In situ* observation of bimetallic alloy nanoparticle formation and growth using high-temperature XRD. *Chem. Mater.* **23**, 2159-2165 (2011).

32. Avanesian, T., Dai, S., Kale, M., Graham, G., Pan, X. & Christopher, P. Quantitative and atomic-scale view of CO-induced Pt nanoparticle surface reconstruction at saturation coverage via DFT calculations coupled with *in situ* TEM and IR. *J. Am. Chem. Soc.* **139**, 4551-4558 (2017).
33. van der Vliet, D., Wang, C., Tripkovic, D., Strmcnik, D., Zhang, X., Debe, M., Atanasoski, R., Markovic, N. & Stamenkovic, V. Mesostructured thin films as electrocatalysts with tunable composition and surface morphology. *Nat. Mater.* **11**, 1051-1058 (2012).
34. Dubau, L., Nelayah, J., Moldovan, S., Ersen, O., Bordet, P., Drnec, J., Asset, T., Chattot, R. & Maillard, F. Defects do catalysis: CO monolayer oxidation and oxygen reduction reaction on hollow PtNi/C nanoparticles. *ACS Catal.* **6**, 4673-4684 (2016).
35. Dai, S., You, Y., Zhang, S., Cai, W., Xu, M., Xie, L., Wu, R., Graham, G. & Pan, X. In situ atomic-scale observation of oxygen-driven core-shell formation in Pt<sub>3</sub>Co nanoparticles. *Nat. Commun.* **8**, 204, (2017).
36. Chi, M., Wang, C., Lei, Y., Wang, G., Li, D., More, K., Lupini, A., Allard, L., Markovic, N. & Stamenkovic, V. Surface faceting and elemental diffusion behaviour at atomic scale for alloy nanoparticles during *in situ* annealing. *Nat. Commun.* **6**, 8925 (2015).
37. Xin, H., Alayoglu, S., Tao, R., Genc, A., Wang, C., Kovarik, L., Stach, E., Wang, L., Salmeron, M., Somorjai, G. & Zheng, H. Revealing the atomic restructuring of Pt–Co nanoparticles. *Nano Lett.* **14**, 3203-3207 (2014).
38. Alloyeau, D., Ricolleau, C., Mottet, C., Oikawa, T., Langlois, C., Le Bouar, Y., Braidy, N. & Loiseau, A. Size and shape effects on the order–disorder phase transition in CoPt nanoparticles. *Nat. Mater.* **8**, 940-946 (2009).
39. Keating, D. T. & Warren B. E., Long-range order in beta-brass and Cu<sub>3</sub>Au *J. Appl. Phys.* **33**, 286-290 (1951).
40. Yasuda, H. & Mori, H. Effect of cluster size on the chemical ordering in nanometer-sized Au-75at%Cu alloy clusters. *Z. Phys. D* **37**, 181-186 (1996).
41. Rossi, G., Ferrando, R. & Mottet, C. Structure and chemical ordering in CoPt nanoalloys. *Faraday Discuss.* **138**, 193-210 (2008).
42. Rosato, V., Guillope, M. & Legrand, B. Thermodynamical and structural properties of f.c.c. transition metals using a simple tight-binding model. *Phil. Mag. A* **59**, 321-336 (1989).
43. Warren, B. E. X-Ray Diffraction; Dover Publications: New York, 2014
44. Flinn, P., McManus, G. & Rayne, J. Effective X-ray and calorimetric Debye temperature for copper. *Phys. Rev.* **123**, 809-812 (1961).
45. Granqvist, C. G. & Buhrman, R. A. Size Distributions for supported metal catalysts: Coalescence growth versus Ostwald ripening. *J. Catal.* **42**, 477–479 (1976).
46. Xin, H. L.; Mundy, J. A.; Liu, Z.; Cabezas, R.; Hovden, R.; Kourkoutis, L. F.; Zhang, J.; Subramanian, N. P.; Makharia, R.; Wagner, F. T. & Muller, D. A. Atomic-resolution spectroscopic imaging of ensembles of nanocatalyst particles across the life of a fuel cell. *Nano Lett.* **1**, 490-497 (2012).

47. Han B.; Carlton C. E.; Kongkanand A.; Kukreja R. S.; Theobald B. R.; Gan L.; O'Malley R.; Strasser P.; Wagner F. T. & Shao-Horn Y. Record activity and stability of dealloyed bimetallic catalysts for proton exchange membrane fuel cells. *Energy Environ Sci* **8**, 258–266 (2015).
48. Yarlagadda V.; Carpenter M. K.; Moylan T. E.; Kukreja R. S.; Koestner R.; Gu W.; Thompson L. & Kongkanand A. Boosting fuel cell performance with accessible carbon mesopores. *ACS Energy Lett* **3**, 618-621 (2018).
49. Kongkanand A. & Mathias M. F. The priority and challenge of high-power performance of low-platinum proton-exchange membrane fuel cells. *J Phys Chem Lett* **7**, 1127–1137 (2016).
50. Vidal-Iglesias, F., Arán-Ais, R., Solla-Gullón, J., Herrero, E. & Feliu, J. Electrochemical characterization of shape-controlled Pt nanoparticles in different supporting electrolytes. *ACS Catal.* **2**, 901-910 (2012).
51. Chen, Q., Solla-Gullón, J., Sun, S. & Feliu, J. The potential of zero total charge of Pt nanoparticles and polycrystalline electrodes with different surface structure: the role of anion adsorption in fundamental electrocatalysis. *Electrochim. Acta* **55**, 7982–7994 (2010).
52. Gasteiger H. A., Kocha S. S., Sompalli B. & Wagner F. T. Activity benchmarks and requirements for Pt, Pt-alloy, and non-Pt oxygen reduction catalysts for PEMFCs. *Appl Catal B Environ* **56**, 9–35 (2005).
53. Garrick T. R., Moylan T. E., Carpenter M. K. & Kongkanand A. Electrochemically active surface area measurement of aged Pt alloy catalysts in PEM fuel cells by CO stripping *J Electrochem Soc* **164**, F55–F59 (2017).
54. Chan, T. & Vese, L. Active contours without edges. *IEEE Trans. Image Process.* **10**, 266-277 (2001).

## CHAPTER 9

### ***Operando* EC-STEM to Resolve the Electrochemical Double Layer at Solid/Liquid Interfaces**

#### **9.1 Introduction**

Most energy-related chemical reactions involve electro(chemical) processes at solid/liquid interfaces, in general, and electrode-electrolyte, in particular. *Operando/in situ* electrochemical liquid-cell STEM (EC-STEM) can shed light on the fundamental understanding of electrocatalytic processes and catalyst degradation mechanisms under native environments without alternating, by freezing or drying, the samples. This chapter presents preliminary progress employing *operando* EC-STEM to tackle the grand challenge of the electrochemical double layer (EDL) at solid/liquid interfaces, a central question at the heart of physical chemistry in general, and electrochemistry in particular. Resolving the EDL is key to advance our fundamental understanding of interfacial electrocatalysis, electron transfer as well as ionic and potential gradients at charged interfaces.<sup>1</sup> The potential profile of the EDL depends on the applied potential, electrolyte type and concentration (ionic strength) and type. While the EDL on flat thin-film surfaces has been explored by *operando* X-ray methods,<sup>2</sup> its nature on practical nanoparticle electrocatalysts has remained largely unknown due to the heterogeneity in structures and surface compositions as well as strong particle-particle interactions when they are in close proximity.<sup>3</sup> The central question is: what is the nature of the EDL of a nanoparticle when its size is comparable to the length scale of the EDL? With small, finite sizes, nanoparticles can have different/distinct local electric field distributions at terraces, steps, edges and corners which can exhibit an increased field concentration relative to their

bulk counterparts. The local electric field largely determines the concentration gradient of solution species at and near the surface, and thus, has a significant impact on electrochemical reaction kinetics and mechanisms. Since the EDL exists only near the electrode surface at a length scale of around 0-10 nm (Fig. 9.1A), atomic/molecular-level understanding of the double layer requires nanometer (or higher) spatial resolution in liquids. Such high spatial resolution in liquids makes *operando* EC-STEM an indispensable tool to investigate the EDL. *Operando* EC-STEM imaging has the potential to directly monitor potential-induced changes of the ionic distribution at electrolyte/electrode interfaces (Fig. 9.1B). At potentials above the potential of zero charge ( $pzc$ ), the electrode surface attracts anion and repels cations. At potentials below the  $pzc$ , the electrode surface attracts cations and repels anions.

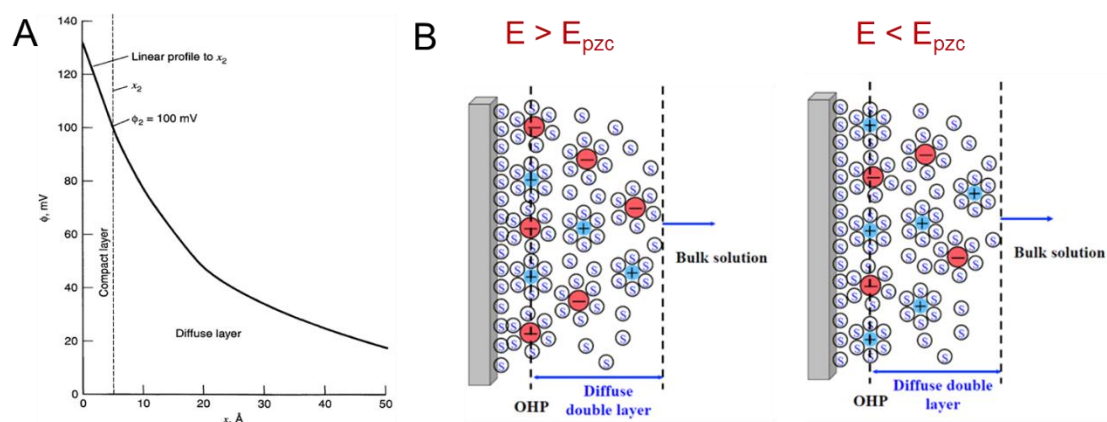


**Figure 9.1.** (A) Potential profile through the electrochemical double layer calculated based on the Gouy-Chapman-Stern (GCS) model for 0.01 M 1:1 electrolyte in water at 25 °C. Reproduced from page 552 of the book by A. Bard and L. Faulkner.<sup>1</sup> (B) Schematics of ionic distributions at charged interfaces in non-adsorbing electrolytes.

## 9.2 Resolving Ionic Distributions at Charged Interfaces with Halide Probes

In order to employ *operando* EC-STEM to visualize the ionic distributions at charged interfaces, the chemical probes need to meet the following requirements.

A. 1 mM 1:1 electrolyte is selected as the suitable electrolyte concentration to give a theoretical EDL width of ~10 nm. This is because a higher concentration, such as 0.1 M, results in too narrow an EDL of 0.3 nm, below the typical spatial resolution of EC-STEM (2-5 nm) while a lower concentration, such as 1  $\mu$ M, despite giving a much wider EDL of 300 nm, is too diluted to induce measurable changes in STEM image intensity.

B. Chemical probes should contain heavy elements to induce significant changes in image intensity as surface ionic distributions change. Using heavy anion, iodide (I<sup>-</sup>), as an example, the theoretical STEM image intensity ratio of iodide to water can be estimated using the formula: Intensity  $\propto Z^{1.5} \times C$  in which Z is the atomic number, C is the concentration. Thus, [I]/[O]  $\approx (53/8)^{1.5} \times 0.001/56 \approx 0.03\%$ . To detect such a small intensity variation, the beam dose needs to be sufficiently high to accumulate enough counting statistics. However, too high a beam dose often gives rise to beam-induced damage.

C. Given the strong beam-liquid interaction, control experiments are required to examine the beam dose threshold below which the chemical probes are stable over the time periods of acquiring STEM images. Thus, heavy halides and alkali cations represent potential candidates, while many other transition metals are unstable under the electron beam.

With the above constraints in mind, NaBr, NaI, CsBr, CsI and CsClO<sub>4</sub> were selected as potential candidates of heavy chemical probes. Au nanocubes with {100} facets are chosen as electrochemically inert electrodes to provide a double-layer behavior with a wide potential window. To minimize faradaic processes, including Au oxidation (~1.5 V vs. SHE) and halide oxidation (e.g. Br<sub>2</sub>/Br<sup>-</sup> of ~1.3 V vs. SHE) as well as HER (below

0 V vs. SHE) and OER (above 1.6 V vs. RHE), we identified a potential window of 0 to 1.3 V vs. SHE in which all solution species are theoretically stable. Considering that the potential of a pseudo-Pt RE is  $\sim 0.8$  V vs. SHE, the experimental applied potentials were set from -0.6 to +0.6 V vs. Pt (i.e. a potential window of 1200 mV), so as to leave 0.1 V margin at both lower and upper potential limits, considering the instability drift of pseudo-Pt RE. Experimental details of assembling the liquid-cell holder and TEM instruments can be found in APPENDIX III.

STEM images of 1 mM NaBr solution near a carbon working electrode (WE) showed no evidence of beam-induced damage during continuous image acquisition for 5 min at a beam dose of  $\sim 640$  e/nm<sup>2</sup> (Fig. 9.2A). When positive potentials above the open circuit potential (OCP) were applied, no significant changes, corresponding to possible halide anionic attraction, were observed (Figs. 9.2B-C). However, noticeable features began to grow in solution as the potential decreased from -0.2 to -0.6 V vs. Pt. This undesirable potential-induced growth was further evidenced by the noticeable beam-induced deposition on Au nanocubes near the carbon WE (Figs. 9.3A-D). At -0.6 V, the deposition was so thick that the STEM image contrast was reversed, as indicated by the darker contrast of Au cubes (Fig. 9.3D). It was at first counterintuitive to observe the unstable behavior of halide anions under reducing potentials. The CV profiles of 1 mM NaBr with Au cubes explained the puzzle. Instead of the anticipated double-layer capacitive behavior, multiple redox couples emerged during CV cycles and exhibited diffusion-like behavior. The presence of bromide possibly formed Au-Br coordination complexes in solution, which significantly lowered the Au oxidation potential from AuO<sub>x</sub>/Au ( $\sim 1.5$  V vs. SHE) to AuBr<sub>4</sub><sup>-</sup>/Au (0.85 V vs. SHE) and induced the corrosion

of Au cubes at  $\sim 0.1$  V vs. Pt. The electroreduction of soluble Au-Br species in the negative-going scan possibly explains the potential-induced deposition in Figs. 9.2-9.3 under reducing potentials.

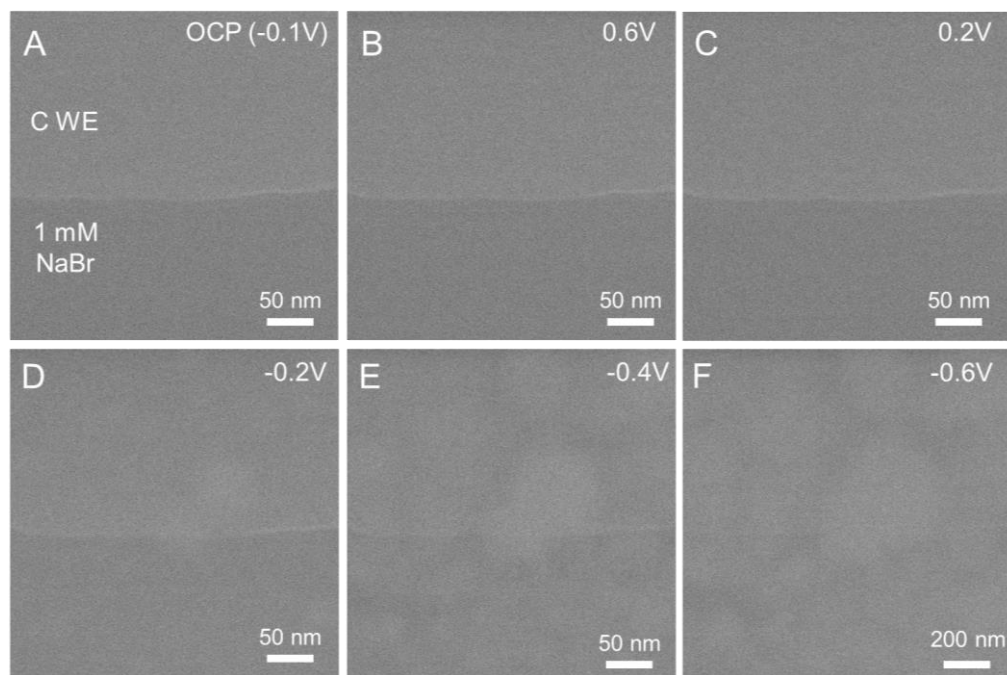


**Figure 9.2** STEM images of 1mM NaBr near a carbon WE under applied potentials. Beam dose was estimated to be  $\sim 640$   $e/\text{nm}^2$  ( $\sim 16$   $e/(\text{nm}^2 \cdot \text{s})$ ) during acquiring STEM images with  $2048 \times 2048$  pixels (field of view: 363 nm) at a dwell time of 8  $\mu\text{s}/\text{pixel}$  and frame time of 40 s/frame under a beam current of  $\sim 4$  pA.

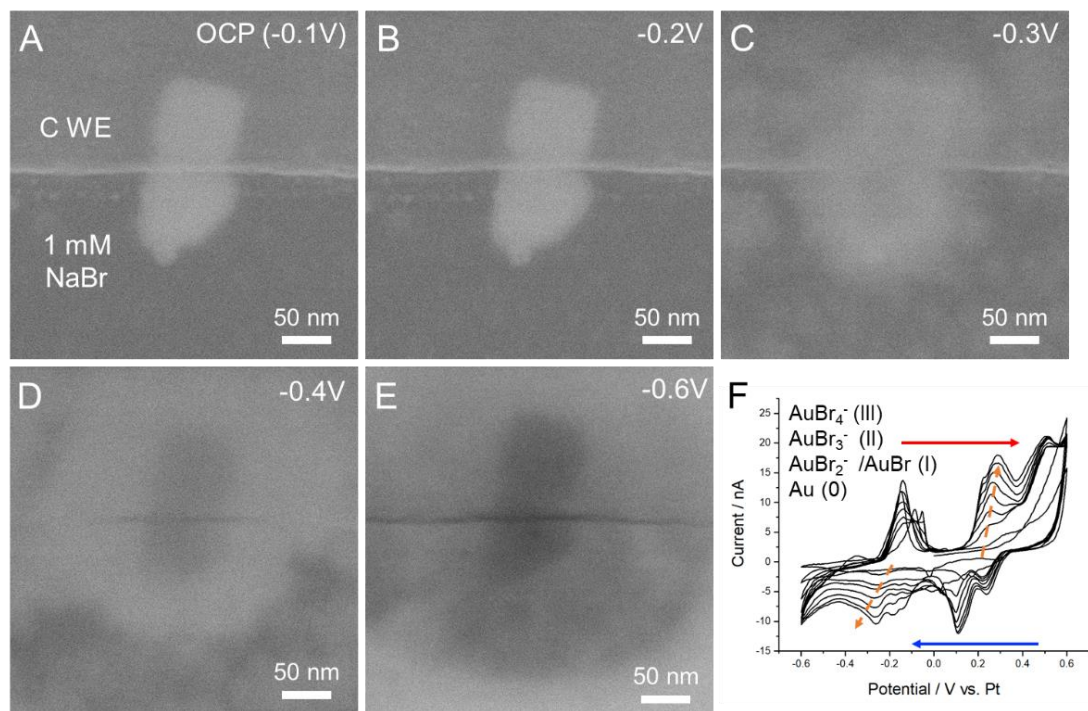


**Figure 9.3** (A-E) STEM images of Au nanocubes in 1mM NaBr near a carbon WE under applied potentials under a beam dose of  $\sim 640$  e/nm<sup>2</sup>. (F) The corresponding CV profiles at 100 mV/s with dashed orange lines indicating the growth of redox couples during 10 CV cycles. Red and blue arrows point to the oxidation and reduction of Au species in the presence of halides.

Given the instability of Au nanocubes in the presence of halides, bulk poly-crystalline Pt WE was then employed to study the ionic distribution in iodide solution. As shown in Fig. 9.4, no beam nor potential-induced artifacts were observed over the time period of STEM imaging. Given that the HER occurs below -0.6 V and iodide oxidation happens above 0.2 V vs. Pt, three potential values of -0.6, -0.3 and +0.2 V vs. Pt were selected to explore the potential-induced changes in iodide distribution. The Epzc of poly-Pt is around +0.3 V vs. SHE,<sup>4</sup> close to the middle potential of -0.3 V vs. Pt. Line profiles were extracted from the regions as indicated by the dashed line in Fig. 9.4D to quantify the STEM image intensity. As shown in Fig. 9.4E, STEM images drifted by  $\sim 3$  nm every 5 min when using the edge position of the Pt WE as a reference point. After

correcting the sample drift, no evident changes of STEM image intensity profiles, corresponding to iodide repulsion, were observed as the potential was increased from -0.6 to 0 V (Fig. 9.4 F). Further examination of the intensity profile at +0.2 V also showed no noticeable changes, which would otherwise indicate possible iodide attraction.

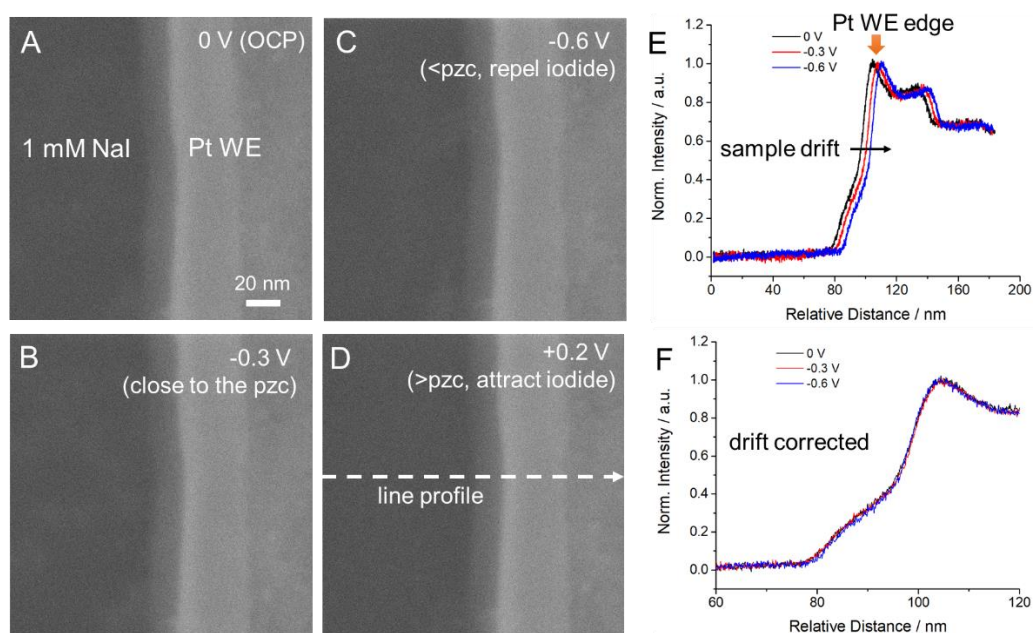


**Figure 9.4** STEM images of 1mM NaI near a polycrystalline Pt working electrode (WE) under applied potentials. Beam dose was estimated to be  $\sim 2500$   $e/nm^2$ .

Since neither NaBr nor NaI exhibited evident potential-induced changes in ionic distributions, CsI, containing both heavy cations and heavy anions, was studied as the next chemical probe (Fig. 9.5). However, CsI exhibited significant beam-induced damage at a beam dose of  $40$   $e/nm^2$ , which is two orders of magnitude lower than the previous studies on NaI and NaBr. Figs. 9.5A-D shows the growth of bulk-like precipitation during continuous STEM imaging for 2 min. At a very low beam dose of  $4$   $e/nm^2$ , the growth of dendritic-like features was observed during STEM imaging for 8 min, indicating a typical diffusion-controlled behavior (Figs. 9.5E-H). Given the highly unstable nature of CsI under the  $e^-$  beam, the slightly less heavier CsBr was then

investigated. At a low beam dose of  $30 \text{ e/nm}^2$ , the electron beam triggered the homogenous nucleation and growth of small nanocrystals with sizes of 10-20 nm during STEM imaging for 6 min (Figs. 9.6A-B). From 6 to 9 min, large crystals of 20-200 nm emerged with a pattern resembling a diffusion-limited aggregation (LDA) process<sup>5</sup> in which nanoparticles undergo a random walk due to Brownian motion prior to particle aggregation (Figs. 9.6C-F). From 9 to 14 min, large crystals continued to grow at the expense of small nanocrystals, suggesting an Ostwald Ripening process under electron beam illumination (Figs. 9.6F-H). We hypothesize that the beam-induced growth in CsI and CsBr is possible due to the formation of polyhalogen complexes with lower solubility, such as  $\text{CsI}_3$  or  $\text{Cs}_2\text{I}_8$ .<sup>6,7</sup>

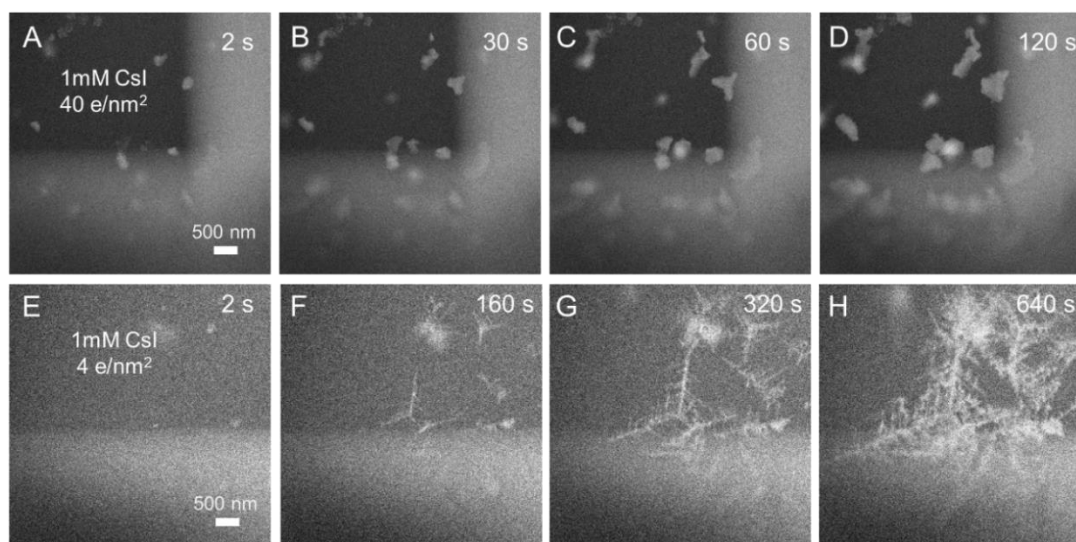


**Figure 9.5** STEM images showing beam-induced damage in 1mM CsI without applied potentials at beam doses of  $\sim 40$  and  $4 \text{ e/nm}^2$ , respectively.

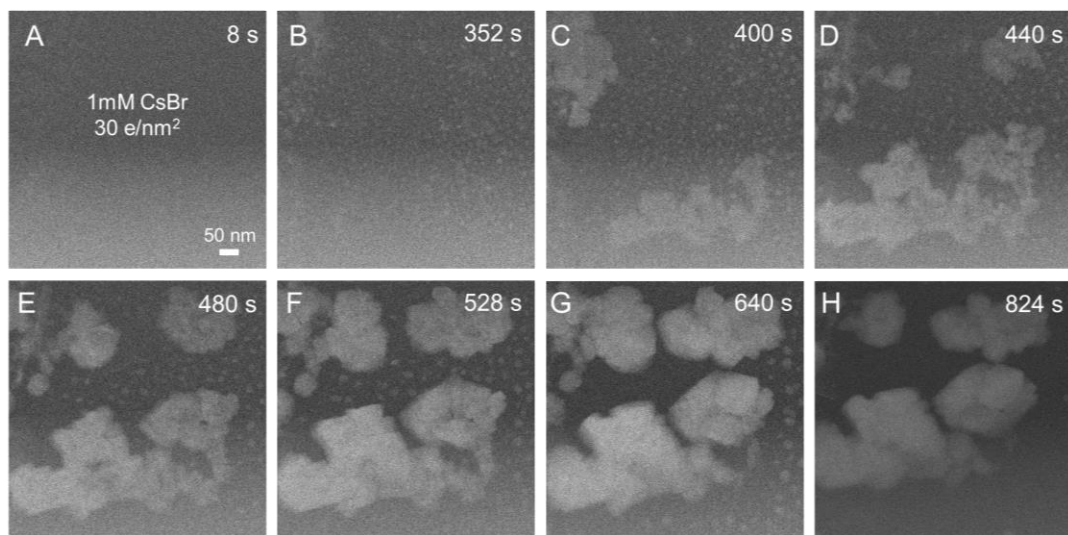


**Figure 9.6** STEM images showing beam-induced damage in 1mM CsBr without applied potentials at a beam dose of  $\sim 30$  e/nm<sup>2</sup>.

### 9.3 Resolving Ionic Distributions at Charged Interfaces with Alkali Cation Probes

Besides the above four halide candidates, which can display specific adsorption on Pt or Au electrodes, CsClO<sub>4</sub> was studied as an example of a heavy non-adsorbing cation as well as non-adsorbing anion. One of the challenges facing liquid-cell STEM imaging is the compromised spatial resolution due to  $\sim 500$  nm thick liquid layer. When potentials were sufficiently negative (below -1.2 V vs. Pt or -0.4 V vs. SHE), a hydrogen bubble could be triggered to create a thin-liquid layer at the solid-liquid-gas interface (Fig. 9.7A). Thus, the liquid thickness can be minimized while the electrode is still immersed in the native electrolyte with the same or similar composition, relative to the thick electrolyte. Figs. 9.7C-F present the 1 mM CsClO<sub>4</sub>/Pt WE interface as potentials increased from -0.6 to +0.2 V vs. Pt. Average line profiles, extracted from the regions shown in Fig. 9.7D, show no evident changes of STEM image intensity at different potentials (Fig. 9.7B). It should be noted that the line profiles in the thin liquid (Fig. 9.7B) were much sharper than those in the regular thick electrolyte (Fig. 9.4F).

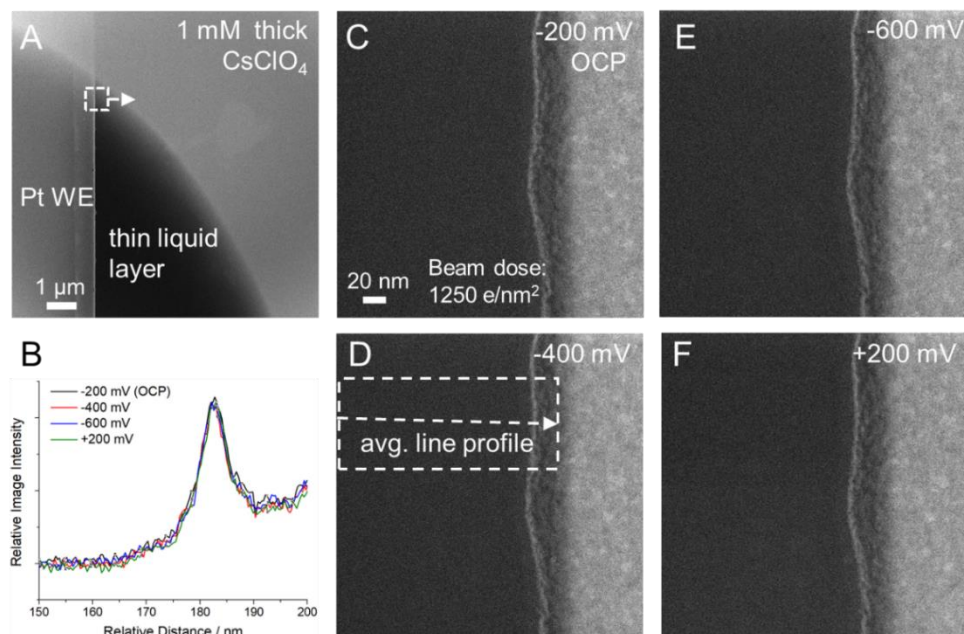


**Figure 9.7** (A) STEM images of a thin-liquid 1 mM CsClO<sub>4</sub> near a poly-Pt WE after triggering a H<sub>2</sub> bubble by scanning potentials to -1.2 V vs. Pt. (C-F) STEM images of the 1 mM CsClO<sub>4</sub>/Pt WE interface magnified from the dashed box in (A) under a beam dose of 1250 e/nm<sup>2</sup> at various applied potentials. Line profiles in (B) were extracted from the dashed box regions in STEM images in (C-F).

Finally, a 1 mM CsClO<sub>4</sub> solution enabled the study of ionic distributions near individual Au nanocubes. Fig. 9.8A presents Au nanocube clusters deposited on the Pt WE immersed in a thin-layer solution of CsClO<sub>4</sub>. Four Au cubes, with flat surfaces, were selected to study the ionic distributions at various applied potentials (Figs. 9.8B-D). Line profiles, extracted from the regions in Fig. 9.8A, showed the sharp interface near the Au cube surfaces (Figs. 9.8F-I) in thin liquid. Those profiles exhibit no significant evidences of variations in STEM image intensity, which would otherwise correspond to the repulsion and attraction of Cs<sup>+</sup> at positive and negative potentials, respectively. Notably, applying a potential of +0.3 V vs. Pt for ~3 min brought back the thick electrolyte (Fig. 9.8E), which is likely due to the gradual consumption of the H<sub>2</sub> bubble under a positive potential, indicating the electrode surface was still in contact

with the electrolyte and was capable of driving the hydrogen oxidation reaction (HOR).

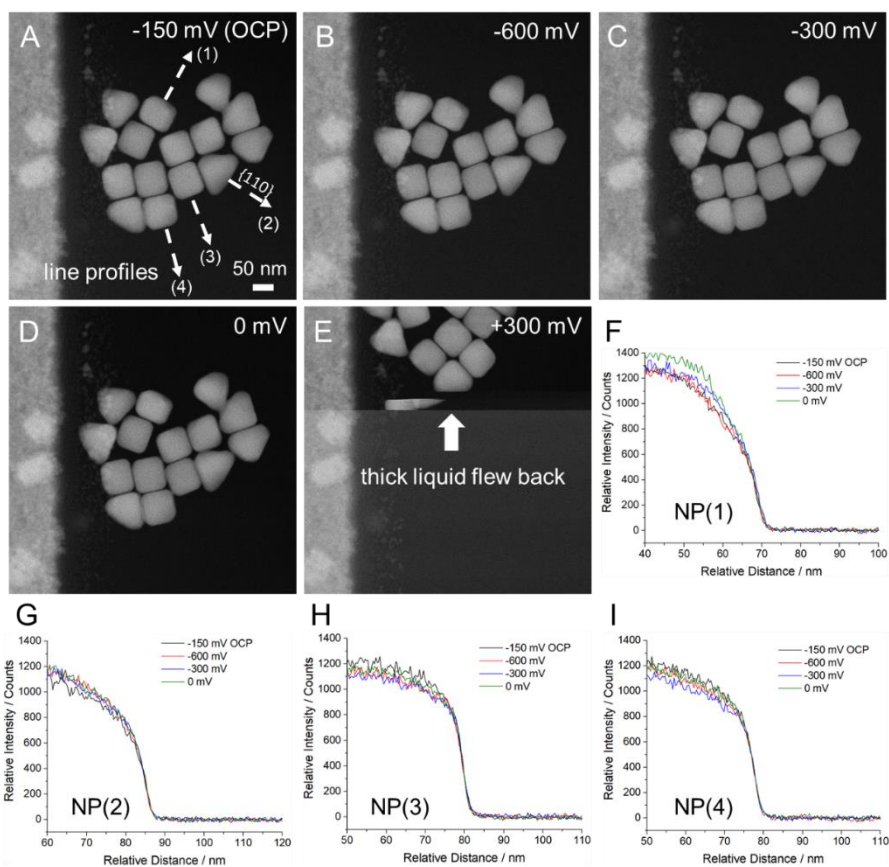


**Figure 9.8** STEM images of a thin-liquid 1 mM CsClO<sub>4</sub> solution near Au nanocubes attached to poly-Pt WE after triggering a H<sub>2</sub> bubble under a beam dose of 220 e/nm<sup>2</sup> at various applied potentials. Line profiles in (F-I) were extracted along the dashed lines as shown in STEM images in (A-D).

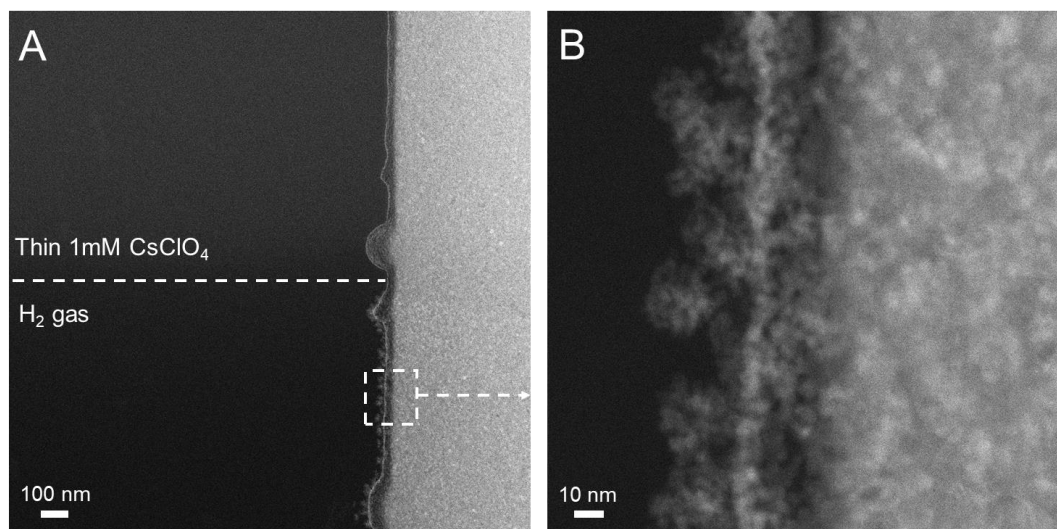


**Figure 9.9.** STEM images of thin liquid/gas interfaces after generating a H<sub>2</sub> bubble by scanning potentials from 0 to -1.5 V at 100 mV/s.

#### 9.4 Conclusions

In summary, *operando* EC-STEM offers a platform for systematic investigations of the electrochemical double layer, specifically ionic distributions, at charged electrode/electrolyte interfaces at the nm-scale. No significant evidence of changes in ionic distributions were observed when using NaBr, or NaI near bulk poly-Pt electrodes and CsClO<sub>4</sub> near Au nanocube surfaces. This is possibly due to the intrinsically low STEM intensity of 1 mM chemical probes, relative to the 56 M H<sub>2</sub>O, and the compromise between spatially resolving the nm-scale EDL and the electrolyte concentration. In addition, CsI and CsBr were unstable under the electron beam and exhibit interesting beam-induced growth patterns at relatively low beam doses. While this preliminary study has yet to provide the anticipated potential-induced ionic distribution in the double layer, it echoes the common philosophy during scientific adventures, “The absence of evidence is not the evidence of absence”. Other chemical probes may provide additional opportunities, if the EDL is out of reach by present *operando* EC-STEM techniques, for examples, the μm-wide diffuse layer during redox reactions can be another interesting research objective. Besides using electrons as probes, other *operando* methods, such as synchrotron-based X-ray standing waves,<sup>2</sup> offer new possibilities to investigate the ionic distribution of alkali cations near well-defined Pt electrodes, which can provide important insights on the effects of cations on the ORR electrocatalysis in alkaline media, as well as numerous other processes.

The pursuit of the EDL at nm-scale led to an intriguing observation, after creating a

thin-liquid layer by electrochemically generating a H<sub>2</sub> bubble (Fig. 9.9). Noticeably, mossy structures were grown near the Pt electrode surfaces after a potential scan to the very negative potential at -1.5 V vs. Pt (about -0.7 V vs. SHE), indicating that the Pt electrode could be corroded under sufficiently negative potentials. Preliminary EDX and electron diffraction analysis suggested that those mossy structures are highly polycrystalline Pt. The observation of bulk Pt disintegration, under very negative potentials inspired an important discovery on cathodic corrosion presented in the following chapter (*vide infra*).

## 9.5 References

1. A. Bard, L. Faulkner, *Electrochemical Methods: Fundamental and Applications*, 2nd Ed. 2001, p552.
2. Abruña, H. D.; Bommarito, G. M.; Acevedo, D. The Study of Solid/Liquid Interfaces with X-ray Standing Waves. *Science* 1990, *250*, 69–74.
3. Dong, J.; Zhang, X.-G.; Briega-Martos, V.; Jin, X.; Yang, J.; Chen, S.; Yang, Z.-L.; Wu, D.-Y.; Feliu, J. M.; Williams, C. T.; Tian, Z.-Q.; Li, J.-F. In situ Raman Spectroscopic Evidence for Oxygen Reduction Reaction Intermediates at Platinum Single-Crystal Surfaces. *Nat. Energy* **2019**, *4*, 60-67.
4. Chen, Q.-S.; Solla-Gullón, J.; Sun, S.-G.; Feliu, J. M.; The Potential of Zero Total Charge of Pt Nanoparticles and Polycrystalline Electrodes with Different Surface Structure: The Role of Anion Adsorption In Fundamental Electrocatalysis. *Phys. Chem. Chem. Phys.* **2008**, *10*, 1359-1373.
5. Witten, T. A.; Sander, L. M. Diffusion-Limited Aggregation, a Kinetic Critical Phenomenon. *Phys. Rev. Lett.* **1981**, *47*, 1400-1403.
6. Finney, J. T. The Structure and Stability of Simple Tri-Iodides. Thesis (University of Tasmannia), 1973.
7. Havinga, E. E.; Boswijk, K. H.; Wiebenga, E. H. The Crystal Structures of Cs<sub>2</sub>I<sub>8</sub> (CsI<sub>4</sub>). *Acta Cryst.* **1954**, *7*, 487.

## CHAPTER 10

### **Elucidating Cathodic Corrosion Mechanisms with *Operando* Electrochemical Transmission Electron Microscopy**

#### **10.1 Introduction**

Corrosion is a ubiquitous process in nature and daily life that causes the spontaneous degradation of materials, often metals, by (electro)chemical reactions with their environment.<sup>1</sup> Corrosion processes have a significant economic impact and it is estimated to cost 3~4% of the gross domestic product of countries.<sup>2-4</sup> Cathodic protection has been widely adapted as an effective strategy to prevent metal corrosion by applying a negative potential or using a sacrificial anode which thermodynamically suppresses the metal oxidation.<sup>1</sup> Conventional wisdom would suggest that metals can stay indefinitely stable in their state under negative potentials. However, it is counterintuitive to observe that corrosion processes emerge again at sufficiently negative potentials, a process that is referred to as *cathodic corrosion*. Originally reported by Fritz Haber in the late 19<sup>th</sup> century, cathodic corrosion was described as the formation of “metallic dust” from bulk Pt electrodes under cathodic polarization.<sup>5,6</sup> Although cathodic corrosion was briefly studied by Soviet electrochemists in late 1900s to prepare alloys,<sup>7,8</sup> it remained mostly as empirical observations during the 20<sup>th</sup> century. Recently, our understanding of cathodic corrosion processes has been revived by the advent of new experimental techniques, especially the application of Pt single crystals and scanning/transmission electron microscopy (S/TEM).<sup>9</sup> In 2011, Koper *et al.* reported on the generation of metallic NPs by cathodic corrosion with an alternating

current (AC).<sup>10,11</sup> Inspired by this pioneering work, extensive efforts have been devoted to examining the effects of different metals, applied potential/current, and electrolyte type and concentration.<sup>12,13</sup> Cathodic corrosion has emerged as a facile surfactant-free top-down method, relative to elaborate colloidal synthesis,<sup>14</sup> to “disintegrate” bulk electrodes for nanoparticle (NP) synthesis of alloys<sup>15-17</sup> and metal oxides,<sup>18</sup> which can be driven by renewable electricity. Those electrogenerated catalysts exhibit enhanced activity and/or selectivity for many renewable energy applications, such as the oxygen reduction/evolution reactions (ORR/OER) for fuel cells,<sup>15</sup> solar-driven water splitting,<sup>18</sup> the reduction of CO<sub>2</sub><sup>16</sup> and nitrite<sup>11,19,20</sup> and the oxidation of alcohols and NH<sub>3</sub>.<sup>10,19</sup>

Despite encouraging progresses, most studies have employed cathodic corrosion of bulk electrodes for NP synthesis, while few studies have attempted to quantitatively study the cathodic corrosion processes and investigate the reaction mechanisms. Although previous “post-mortem” S/TEM studies provide a baseline understanding of the effects of cathodic corrosion,<sup>10-19</sup> They cannot provide real-time changes at electrode-electrolyte interfaces. Furthermore, in contrast to extensive studies of bulk electrodes, the cathodic corrosion of nanocrystals has remained unexplored, due to the lack of *operando/in situ* microscopic methods. The cathodic corrosion of nanocrystals can provide important insights into structural evolution of nanosized electrocatalysts under reducing potentials, as present in CO<sub>2</sub> and N<sub>2</sub> reduction, for their potential to lower carbon emissions and produce valuable chemicals.<sup>21-26</sup> For instance, cathodic corrosion is likely present during CO<sub>2</sub> reduction, which often requires applied potentials lower than -0.5 V vs. reversible hydrogen electrode (RHE), under which poly-Cu reconstructs to (100)-oriented Cu nanocubes, resulting in a drastic increase in selectivity

of ethylene over methane.<sup>21-24</sup>

The cathodic corrosion processes make it extremely challenging to employ *in situ* vibrational spectroscopy, *operando* X-ray methods, or scanning electrochemical microscopy<sup>27</sup> since the vigorously formed H<sub>2</sub> bubbles can cause severe fluctuations in the spectroscopic or imaging background. Although liquid-cell TEM has been widely used to study morphological changes during chemical reactions,<sup>27,28</sup> few studies have shown reliable electrochemical measurements in liquid-cell TEM,<sup>29-31</sup> when compared to standard electrochemical measurements. Conventional EC-TEM employs a liquid thickness of ~500 nm or above, which hinders/precludes quantitative elemental analysis with energy dispersive spectroscopy (EDX) or electron energy loss spectroscopy (EELS) as well as crystallographic structural analysis with electron diffraction.<sup>27</sup> There have been several reports on electron diffraction under TEM mode achieved in thin liquids by irradiating the liquid at very high beam doses to form gas bubbles,<sup>32,33</sup> such processes lead to significant changes in pH and compositions of the liquid and thus likely alter the (electro)chemical processes.<sup>34</sup>

Here, we have investigated two model systems, Pt(111) and Au nanocubes on bulk Pt, in an effort to quantitatively characterize cathodic corrosion mechanisms. While Pt(111) showed well-defined anisotropic growth during corrosion, Au nanocubes exhibited significantly higher levels of structural degradation (than bulk Pt) with the formation of Au-Pt alloy NPs. We employed *operando/in situ* EC-STEM to track dynamics changes in morphology, elemental composition and crystal structures. In contrast to previous strategies, we took advantage of naturally generated H<sub>2</sub> bubbles, during cathodic corrosion, to form a thin liquid without inducing undesirable beam

damage. This enabled STEM imaging, EDX elemental mapping, and 4D scanning electron nanodiffraction (SEND) analysis<sup>35,36</sup> in a native electrolyte environment. With this thin-liquid-film strategy, we have been able to carry out, for the first-time, a comprehensive investigation of the dynamic structural and compositional evolution of nanocrystals at nm-scale, relative to bulk electrodes, during cathodic corrosion. *Ex situ* atomic-scale STEM imaging and EELS analysis in a H<sub>2</sub>-filled gas cell confirmed the structural and compositional information at the same locations as in the *in situ* measurements. Guided and informed by those microscopic insights, we employed cathodic corrosion as a top-down synthetic method to prepare Au-Pt alloy NPs, which are essentially immiscible, based on the phase diagram. We proposed a cathodic corrosion reaction mechanism involving the formation of Au and Pt hydrides in the presence of adsorbed hydrogen and alkali cations.

## 10.2 Experimental Methods

**Electrochemical measurements in standard electrochemical cells.** The Pt (111) electrode was fabricated from a Pt wire by the Clavilier method. The geometric surface area of the electrode was measured as 3.274 mm<sup>2</sup> based on its high-resolution optical image. Prior to each experiment, the electrode was annealed in a propane flame for 15 s. The hot electrode was then cooled down in a 5% hydrogen balance argon gas atmosphere, quenched in ultrapure water, and immediately transferred to the electrochemical cell, protected by an ultrapure water droplet on top of the electrode surface. The electrochemical cell and all the other glassware used in the experiment were soaked in KMnO<sub>4</sub>/H<sub>2</sub>SO<sub>4</sub> solution overnight. The remaining KMnO<sub>4</sub>/H<sub>2</sub>SO<sub>4</sub> solution on the glassware was removed by reacting with H<sub>2</sub>O<sub>2</sub> before the experiment.

The glassware was then rinsed with ultrapure water, followed by boiling in ultrapure water 3 times. CV profiles of Pt(111) were performed at room temperature using a Pine potentiostat in a three-electrode electrochemical cell with glass frits between the working electrode with the reference electrode and counter electrode. A coiled Pt wire was used as the counter electrode, and a Ag/AgCl in 1 M KCl (0.235 V vs. SHE) was used as the reference electrode. The Pt (111) working electrode was in contact with the electrolyte in the hanging meniscus configuration. The cathodic corrosion of Pt(111) was performed in 0.1 M NaOH at -0.5 V vs. RHE for 2 min and rinsed in ultrapure water before measuring CV profiles in 0.1 M HClO<sub>4</sub>. Then, the Pt(111) electrode was annealed in a propane flame for 15 s to eliminate the effects of cathodic corrosion at -0.5 V vs. RHE, which was verified by the flat hydrogen region of the CV profile in 0.1 M HClO<sub>4</sub>. The cathodic corrosion was then performed at -1.0 V vs. RHE in 0.1 M NaOH followed by CV measurements in 0.1 M NaOH. This cycle of cathodic corrosion and CV measurement was repeated for cathodic corrosion at more negative potentials (-1.5~-4.0 V vs. RHE). Thus, each CV profile of Pt(111) after corrosion started from the same pristine Pt(111) rather than accumulating effects from previous cathodic corrosion experiments. CV profiles of Au nanocubes on poly-Pt film were measured in 0.1 M HClO<sub>4</sub> after activation between 0.05 and 1.6 V vs. RHE for 20 cycles. The cathodic corrosion of Au nanocubes/Pt film was performed in 0.05 M CsClO<sub>4</sub> for 30 min.

**Electrochemical measurements in EC-STEM.** A Protochips Poseidon liquid-cell holder was used for electrochemical measurements in EC-STEM. The electrochemical chip encapsulates a liquid pocket within two electron-transparent SiN<sub>x</sub> windows, which can withstand the ultrahigh vacuum (10<sup>-8</sup> Torr) inside the TEM chamber. To

demonstrate that *operando/in situ* EC-STEM is capable of delivering reliable electrochemical measurements, we performed CV measurements of a Pt WE in 0.1 M HClO<sub>4</sub> and Cu electrodeposition, with both the RE and CE made of Pt for its chemical stability. The distance between the RE and WE is small to minimize the iR-drop in a sub- $\mu\text{m}$  electrolyte while the CE has a large surface area to enable rapid polarization. The cathodic corrosion of Au nanocubes on Pt WE was performed in EC-STEM with a non-adsorbing neutral electrolyte (CsClO<sub>4</sub>) since thin SiN<sub>x</sub> windows are not stable in alkaline solution, such as NaOH, KOH often used for cathodic corrosion studies. A 1 mM CsClO<sub>4</sub> was used to prevent the potential precipitation after generating H<sub>2</sub> bubble (which consumes water) given the low solubility of CsClO<sub>4</sub> in H<sub>2</sub>O (~85 mM at 25 °C).

***Operando/in situ/ex situ* EC-STEM measurements of cathodic corrosion.** *Operando* EC-STEM imaging was performed in 1 mM CsClO<sub>4</sub> with a regular liquid thickness (~500 nm) at a beam dose of ~8 e/nm<sup>2</sup> in a Tecnai F-20 STEM. A STEM image acquisition time of 8 s/frame (1024×1024 pixels with a dwell time of 6  $\mu\text{s}$ /pixel) and a slow CV scan rate at 20 mV/s enabled an electrochemical potential resolution of 0.16 V per frame while maintaining a good STEM imaging quality. A beam dose control experiment was performed at a dose of 15 e/nm<sup>2</sup> showing no evidence of beam damage except the rotation of a Au nanocube. Non-local means (NLM) algorithm and Gaussian blur were adapted to denoise the STEM images for better resolving morphological changes of nanoparticles. *In situ* EC-STEM was enabled by the electrochemical generation of a H<sub>2</sub> bubble by performing CV cycles from 0 to -1.6 V vs. Pt for 20 cycles or from 0 to -2.0 V vs. Pt for 4 cycles. To achieve high-quality STEM-EDX elemental maps, a scanning electron beam was required to illuminate the sample constantly for 1

h at a high beam dose of  $\sim 8500$  e/nm<sup>2</sup>. Minimal beam damage was observed after EDX elemental mapping of this low-magnification STEM image. However, STEM-EDX of individual alloy NPs in thin liquid at a higher beam dose of  $10^4$  e/nm<sup>2</sup>, exhibited noticeable particle rotation drifts, precluding a high-resolution STEM-EDX elemental mapping in thin liquid. SEND experiments were performed using an electron microscope pixel array detector (EMPAD), by recording a 2D diffraction pattern at each probe position, resulting in 4D datasets. The SEND was performed in the nearby region with a probe size of  $\sim 1.3$  nm in the full-width at half-maximum,  $256 \times 256$  scan over an area of  $1100 \times 1100$  nm<sup>2</sup>. To enhance the signal-to-noise ratio in the diffraction patterns for further analysis, the 4D dataset was segmented into clusters based on the watershed segmentation of virtual BF image. *Ex situ* on-site atomic-scale HAADF-STEM imaging and EELS were performed in an H<sub>2</sub> gas cell in a Titan STEM at 300 keV with an convergence angle of 21.4 mrad and a collection angle of  $\sim 43$  mrad.

**Cathodic corrosion for Au-Pt bimetallic nanoparticle synthesis.** Au and Pt nanowires were melted together in a methane flame (2000 °C) and subjected to cathodic corrosion in 10 M KOH. An AC square wave potential was applied between -10 and 0 V at 100 Hz with a DC offset to ensure a reducing (cathodic) process employing a Hewlett-Packard 3312 function generator. SEM imaging was performed with a ZEISS Gemini 500 SEM at 1 keV.

### **10.3 Cathodic Corrosion of Pt(111) and Au Nanocubes on poly-Pt Electrode**

Pt single crystals and Au nanocubes on a polycrystalline Pt film were designed to investigate the dynamic structural evolution during cathodic corrosion. Pt single

crystals, prepared by the flame annealing technique (Clavilier method),<sup>37</sup> enable a direct correlation between structural changes on atomically flat surfaces and the cathodic corrosion conditions. The cyclic voltammetry (CV) profile of Pt(111) exhibits a well-defined hydrogen region (0.05-0.45 V) and OH ad/desorption regions (0.55-0.9 V), separated by a double-layer region in 0.1 M HClO<sub>4</sub> (Fig. 10.1a, black curve).

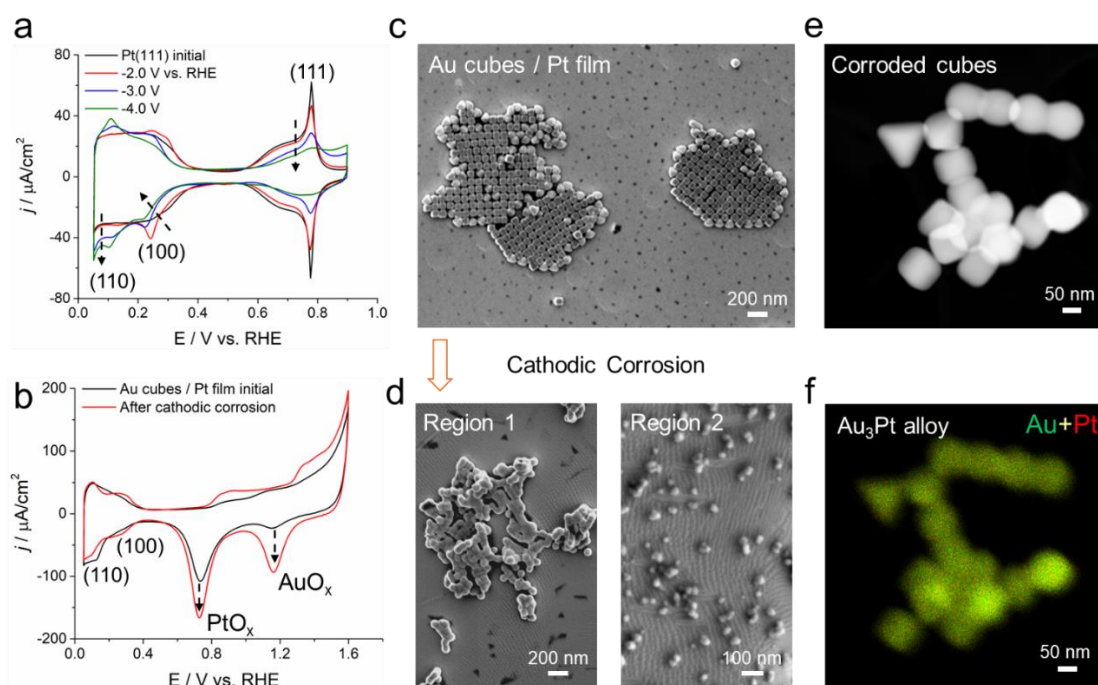


**Figure 10.1** Cathodic corrosion of Pt(111) and Au nanocubes on poly-Pt electrode. (a) CV profiles of Pt(111) in Ar-sat. 0.1 M HClO<sub>4</sub> at 50 mV/s before and after cathodic corrosion. The cathodic corrosion was performed in 0.1 M NaOH at given potentials vs. RHE for 2 min. (b) CV profiles of Au nanocubes on a poly-Pt film in Ar-sat. 0.1 M HClO<sub>4</sub> at 50 mV/s before and after cathodic corrosion. The cathodic corrosion was performed in 0.05 M CsClO<sub>4</sub> at -3 V vs. SHE for 30 min. (c) SEM images of pristine Au nanocubes (~100 nm) on a Pt film (d) SEM images of Au cubes/Pt film after cathodic corrosion in (b). Region 1 exhibits the formation of deformed/aggregated Au cube clusters and concave pits on the Pt film while Region 2 shows the formation of newly generated smaller NPs (NPs, 20-50 nm) and pronounced stepped etch features on the Pt film. (e-f) STEM-EDX elemental composite maps of Au-Pt alloy NPs with Au in green and Pt in red and an atomic ratio of Au/Pt of 3:1.

CV profiles of Pt(100) and Pt(110) exhibit the characteristic hydrogen underpotential

deposition ( $H_{UPD}$ ) peaks at  $\sim 0.3$  and  $\sim 0.1$  V vs. reversible hydrogen electrode (RHE), respectively (Fig. 10.2). Given the flat and featureless plateau of the  $H_{UPD}$  of Pt(111), the emergence of any traces of (100) or (110) steps will be evident and unambiguous. The cathodic corrosion of Pt(111) was performed in 0.1 M NaOH at corrosion potentials from -0.5 to -4.0 V vs. RHE for 2 min. CV profiles of Pt(111) after corrosion at -0.5 to -1.5 V exhibited negligible changes in the hydrogen region, indicating little or no surface structural changes (Fig. 10.3a). After cathodic corrosion at -2.0 V, the emergence of a pronounced  $H_{UPD}$  peak at  $\sim 0.3$  V, corresponding to (100) steps, indicated that the onset potential of cathodic corrosion of Pt(111) in 0.1 M NaOH was at around -2.0 V vs. RHE (Fig. 10.1a, red curve). At increasingly negative potentials (-3.0 and -4.0 V), the (100) steps gradually diminished, accompanied by the progressive increase of (110) steps at  $\sim 0.1$  V (Fig. 10.1a, blue/green curves). The well-defined Pt single crystals enable the accurate and precise quantification of the relative step density by calculating the  $H_{UPD}$  charge (Fig. 10.3c).

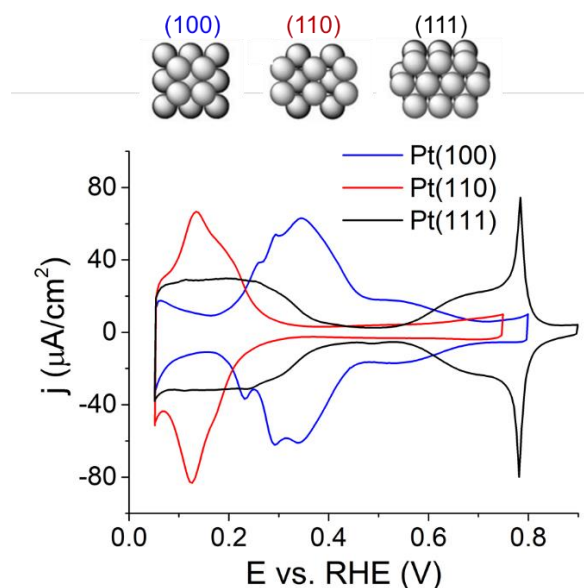


**Figure 10.2.** CV profiles of (111), (110) and (100) planes of single-crystal Pt electrodes

in Ar-sat. 0.1 M HClO<sub>4</sub> at 50 mV/s. The upper panels show the corresponding atomic models of those three basal planes. The surface atomic density decreases in the order: Pt(111) > Pt(100) > Pt(110). Pt(111) has the highest atomic density while Pt(110) has the lowest atomic density (the most open structure), which is also a naturally stepped surface [2(111) × (111)]. Pt(111), (100) and (110) have a hydrogen underpotential deposition (H<sub>UPD</sub>) charge constant of 241, 208 and 147 μC/cm<sup>2</sup>, respectively.

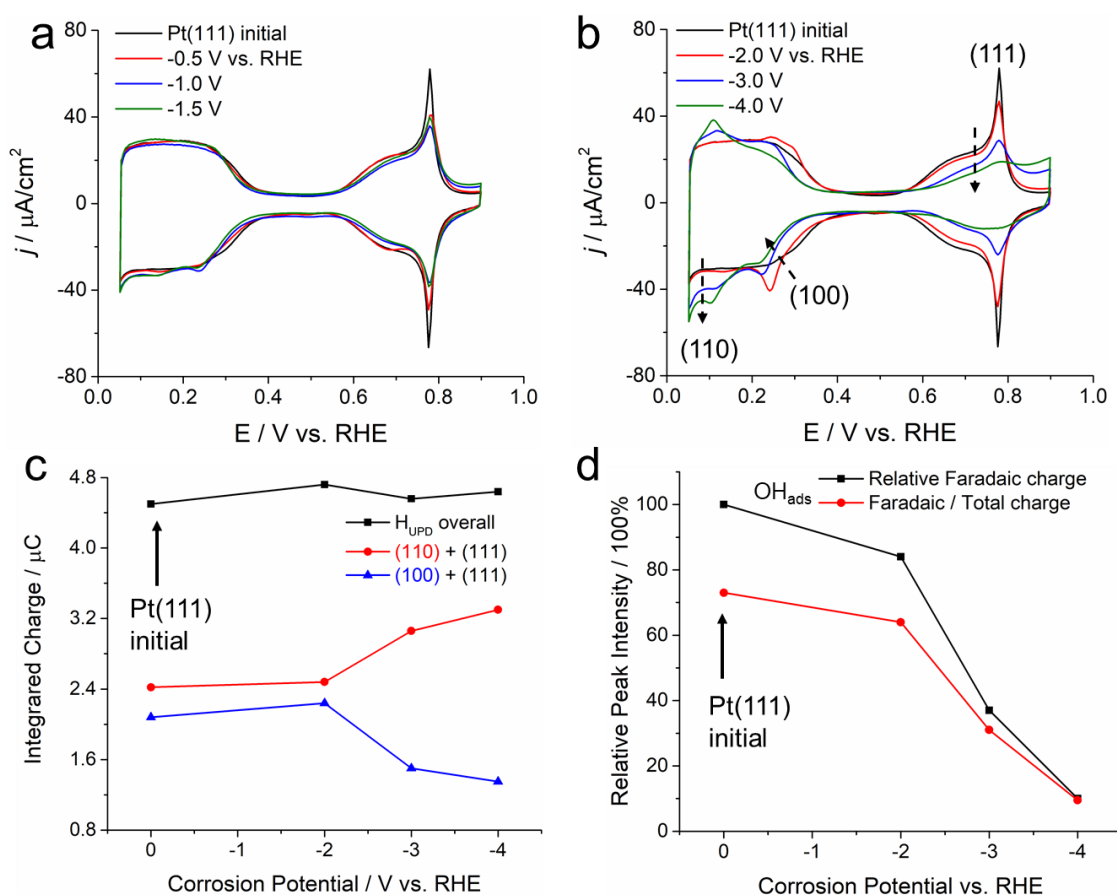


**Figure 10.3.** CV profiles of Pt(111) (a) before and (b) after cathodic corrosion, in Ar-sat. 0.1M HClO<sub>4</sub> at 50 mV/s. The cathodic corrosion was performed in 0.1M NaOH at given potentials (-0.5 to -4.0 V) vs. RHE for 2 min. (c) Charge integrals of the overall H<sub>UPD</sub> region (0.05-0.45 V vs. RHE), (110) step/(111) terrace region (0.05-0.19 V) and (100) step/(111) terrace region (0.19-0.45 V), before and after cathodic corrosion at -2, -3 and -4 V vs. RHE in 0.1M NaOH. (d) The Faradaic charge, relative to pristine Pt(111) (black curve) and the Faradaic / total charge ratio between 0.5 and 0.9 V vs. RHE in (b) before and after cathodic corrosion.

The (100) step density exhibited a significant decrease at -3.0 and -4.0 V while the (110)

step density exhibited a symmetrical increase (Fig. 10.3c). Interestingly, the overall  $H_{\text{UPD}}$  charge remained relatively unchanged, indicating a gradual conversion from (100) to (110) steps at more negative corrosion potentials, while the total integrated amount of step density remained stable. To rationalize this trend, the  $H_{\text{UPD}}$  charge constants of Pt(111), (100) and (110) were calculated to be 241, 208 and 147  $\mu\text{C}/\text{cm}^2$  (Fig. 10.2), which are consistent with literature values.<sup>38</sup> The constant  $H_{\text{UPD}}$  charge constant values suggest that Pt(111) is the most stable facet with the highest surface atomic density while Pt(110) is the least stable facet with the lowest atomic density. This can explain the trend in anisotropic growth from the most stable Pt(111) to intermediate Pt(100) steps and finally to the most energetically unstable Pt(110) steps, at increasingly negative corrosion potentials. In addition to the changes in the  $H_{\text{UPD}}$ , the  $\text{OH}_{\text{ads}}$  peak at  $\sim 0.8$  V vs. RHE in Fig. 10.1a is a characteristic feature of Pt(111) surface, exhibiting a continuous decay of the  $\text{OH}_{\text{ads}}$  Faradaic charge at increasingly more negative corrosion potentials (Fig. 10.3d). This is consistent with the increasing step density revealed from the  $H_{\text{UPD}}$  measurements and suggests a higher level of surface roughening. SEM images were acquired to visualize the morphological changes during cathodic corrosion. After corrosion at -2.0 V, the Pt(111) electrode changed from a smooth surface to steps and ridges (Figs. 10.4), which, from the CV profiles, corresponds to the formation of (100) steps (Fig. 10.1a). At the very negative corrosion potential of -4.0 V vs. RHE, the Pt(111) electrode exhibited sharp stepped features and noticeable concave pits.

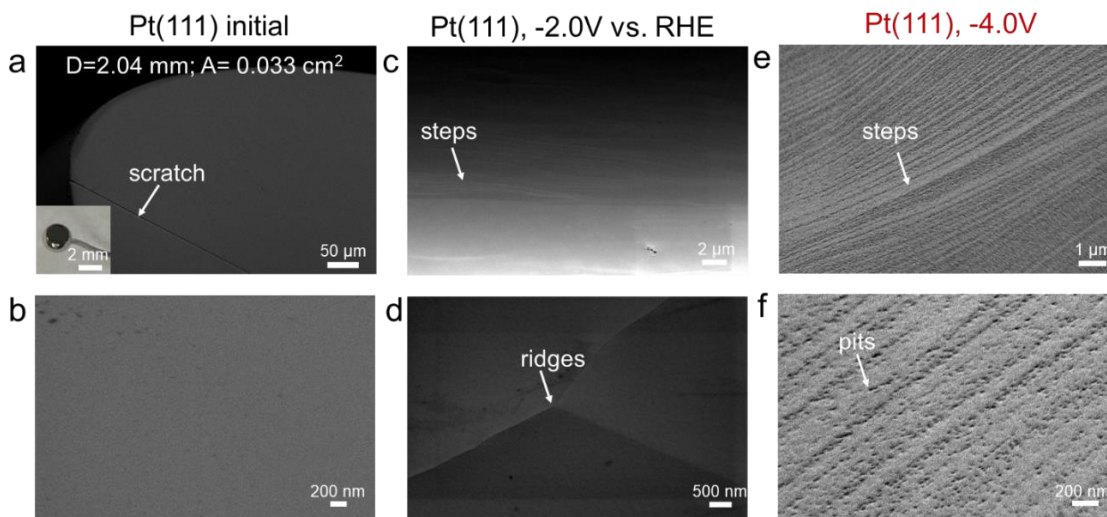


**Figure 10.4** SEM images of Pt(111) before and after cathodic corrosion in Figure 10.3b. (a) SEM images of the pristine Pt(111) surface (Inset in (a), optical images of a 2 mm diameter single-crystal Pt(111) bead). The scratch was used as a marker for SEM imaging alignment. (b) High-resolution SEM image of pristine Pt(111) shows a very smooth surface. (c-d) SEM images of Pt(111) after cathodic corrosion at -2.0 V vs. RHE in 0.1M NaOH show the onset formation of steps and ridges. (e-f) SEM images of Pt(111) after cathodic corrosion at -4.0 V vs. RHE in 0.1M NaOH show the pronounced formation of steps and pits on Pt(111) surface.

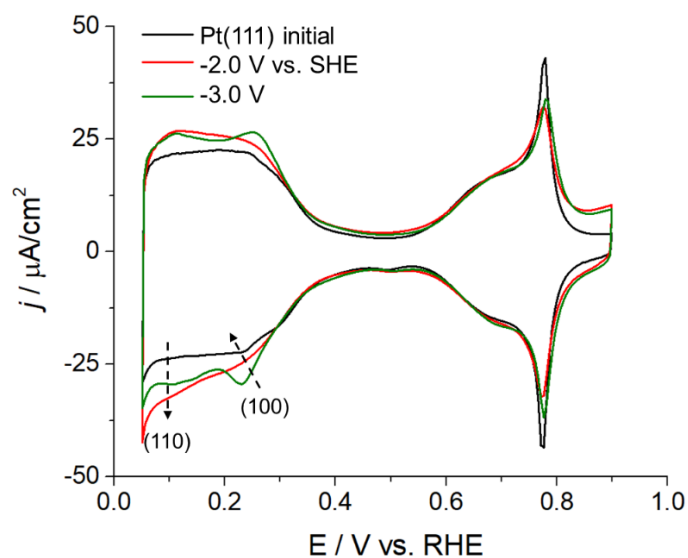


**Figure 10.5** CV profiles of Pt(111), before and after cathodic corrosion, in Ar-sat. 0.1M HClO<sub>4</sub> at 50 mV/s. The cathodic corrosion was performed in 0.05 M CsClO<sub>4</sub> at given potentials for 2 min.

The cathodic corrosion of the Pt(111) single crystal was also examined in a non-adsorbing neutral electrolyte, CsClO<sub>4</sub> (Fig. 10.5), since it would be suitable for *operando/in situ* EC-STEM study due to the instability of SiN<sub>x</sub> window in the alkaline media. The Pt(111) used above experienced a similar growth of (100) feature after corrosion at -2.0 V, and conversion to (110) after corrosion at -3.0 V in CsClO<sub>4</sub>, although the changes were less pronounced than those in NaOH, which is possibly due to the weaker interaction between Cs<sup>+</sup> and Pt, relative to Na<sup>+</sup>.<sup>13</sup> A corrosion onset potential of around -2.0 V vs. RHE was found in both 0.05 M CsClO<sub>4</sub> and 0.1 M NaOH. A recent study by Koper *et al.* found that the onset potentials of cathodic corrosion of Pt(111) are less negative, at around -0.6 V and -0.4 V vs. RHE in 1 and 10 M NaOH, respectively, indicating a lower energy barrier for cathodic corrosion at higher concentrations of hydroxide solutions.<sup>39,40</sup> The cathodic corrosion of Pt single crystals in (Fig. 10.1a) has important implications for tuning electrocatalyst activity. For instance, the ORR activity of Pt(111) in acid was doubled, relative to pristine Pt(111), after cathodic corrosion, which was ascribed to the formation of concave etching features.<sup>39</sup>

The single-crystal Pt(111) study above lays the foundation for investigating the cathodic corrosion of well-defined nanocrystals on a bulk poly-Pt film. Au nanocubes (~100 nm) with {100}-oriented single-crystal surface facets were selected as an example of inactive electrocatalysts for the hydrogen evolution reaction (HER), in contrast to Pt. The CV profile of pristine Au cubes/Pt film showed a PtO<sub>x</sub> reduction peak at ~0.8 V and a smaller AuO<sub>x</sub> reduction peak of the Au nanocubes (Fig. 10.1b). The CV profile after cathodic corrosion in 0.05 M CsClO<sub>4</sub> at -3.0 V vs. SHE exhibited

a 5.4-fold increase in the reduction peak area of  $\text{AuO}_x$  and a 1.3-fold increase in that of  $\text{PtO}_x$  (Fig. 10.6a). These changes suggest that Au nanocrystals, with a high surface energy, are subjected to a significantly higher level of structural changes and surface roughening, relative to the bulk Pt electrode. A control experiment of cathodic corrosion of a bulk Au film in  $\text{CsClO}_4$  under same conditions exhibited negligible morphological changes based on SEM images, confirming the faster corrosion kinetics of Au nanocrystals than bulk Au counterparts. The  $H_{\text{UPD}}$  charge revealed a slight increase in Pt(100) steps accompanied by a slight decrease in Pt(110) sites (Fig. 10.6b). Early reports on a poly-Pt wire also showed a similar enrichment of (100) steps after cathodic corrosion.<sup>12,13</sup>

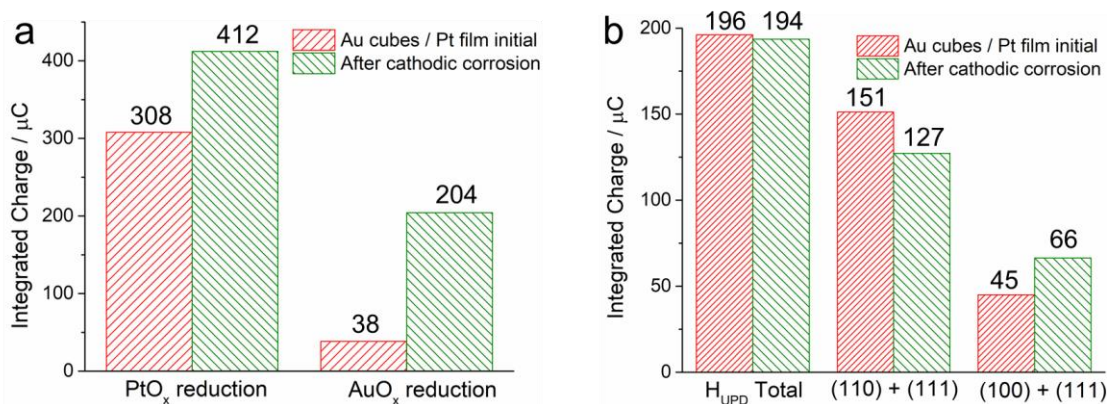


**Figure 10.6** (a) Charge integral of the  $\text{PtO}_x$  reduction peaks and  $\text{AuO}_x$  reduction peaks of Au cubes on Pt film after cathodic corrosion based on CV profiles in Fig. 10.1b. (b) Charge integrals of the overall  $H_{\text{UPD}}$  region (0.05-0.45 V vs. RHE), (110) step/(111) terrace region (0.05-0.19 V) and (100) step/(111) terrace region (0.19-0.45 V), before and after cathodic corrosion based on CV profiles in Fig. 10.1b. Given that Au has no hydrogen peaks between 0 and 0.5 V vs. RHE, the  $H_{\text{UPD}}$  charge calculation revealed a slight increase in Pt(100) steps accompanied by a slight decrease in Pt(110) while the total  $H_{\text{UPD}}$  charge remained nearly unchanged.

SEM images of the Au cubes/Pt film exhibit striking morphological changes after

cathodic corrosion (Figs. 10.1c,d). Pristine Au nanocrystals exhibited a well-defined cubic morphology and are self-assembled in a periodic pattern/arrangement (Fig. 10.1c). After cathodic corrosion in CsClO<sub>4</sub>, the Au cubes experienced drastic morphological changes while the bulk Pt electrode showed only mild changes with wrinkle-like stepped edges (Figs. 10.1d). Region 1 represents an intermediate state of many cubic particles, which deform and aggregate into clusters, as well as the formation of triangular, square and rectangular pits on the Pt film, which were suggested to preferentially form on (111), (100) and (110) facets, respectively, based on studies on those low-index Pt single crystals.<sup>40</sup> Region 2 represents a final state of much smaller newly generated, small NPs (10-50 nm) and the co-existence of pronounced stepped etching features on the Pt film (Fig. 10.1d). STEM-EDX elemental maps of corroded Au nanocubes and newly generated NPs (~20 nm) show homogenous elemental distributions of Au and Pt, indicating the formation of single-phase Au<sub>3</sub>Pt alloy NPs (Figs. 10.1e-f). In summary, during cathodic corrosion, Pt films and Au nanocubes were “atomized” so that highly mobile Pt atoms were injected into the Au cubes to form Au-Pt alloy NPs. It is possible that the disintegration of bulk Pt and the deformation/aggregation of Au nanocubes occur simultaneously, and are strongly modulated by the local electrical field, interfacial pH and concentration of alkaline cations. Although it is challenging to quantify the corrosion rate, nanocrystals experienced a significantly higher level of structural destruction than the bulk electrodes.

#### **10.4 *Operando/In Situ* Electrochemical Liquid-Cell STEM (EC-STEM) Studies of Dynamic Structural Evolution during Cathodic Corrosion**

To elucidate the structural and elemental evolution of nanocrystals and bulk electrodes, we employed *operando/in situ* EC-STEM, including STEM imaging, EDX elemental mapping and SEND diffraction imaging. Fig. 10.7a presents a cross section of the *operando/in situ* EC-STEM cell with a three-electrode configuration, including working, reference and counter electrodes (WE, RE and CE). The SEND works by using an electron microscope pixel array detector (EMPAD) to record the 2D electron diffraction pattern over a 2D grid of probe positions, resulting in 4D datasets,<sup>41</sup> which can dramatically reduce beam dose while retrieving temporal and spatially resolved structural information in liquids. We designed strategy to enable *operando*, *in situ* and *ex situ* EC-STEM operation in the same cell, and at identical locations to enable reliable electrochemical measurements and simultaneously probe real-time interfacial changes across multiple scales, by generating H<sub>2</sub> bubble to reversibly control the liquid thickness (Fig. 10.7b). *Operando* EC-STEM was employed to track the morphological changes under similar reaction conditions to standard electrochemical measurements in Figs. 10.1a-b but not able to perform EDX nor SEND analysis in thick electrolytes. The thin liquid, naturally formed by H<sub>2</sub> bubble during cathodic corrosion, drastically improves spatial resolution and enables nm-scale *in situ* STEM-EDX and SEND in a native electrolyte, which nonetheless, deviates from optimal electrochemical conditions. To resolve atomic-scale lattice structures, H<sub>2</sub> gas was flowed to remove completely the liquid while preserving the corroded electrode in a reducing environment. *Ex situ* EC-STEM, despite the lack of real-time information, serves as an identical-location STEM to perform on-site characterization before and after cathodic corrosion. *Ex situ* STEM also improves the spatial resolution of EDX and EELS elemental analysis by

circumventing the undesirable beam damage and sample drift in liquids.

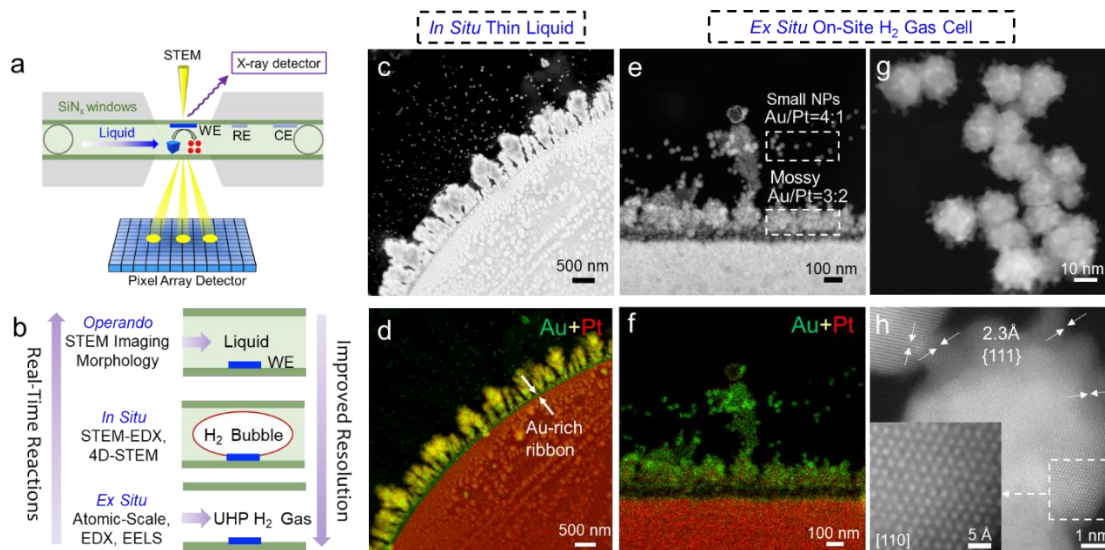


**Figure 10.7. Operando/in situ electrochemical liquid-cell STEM (EC-STEM) studies of cathodic corrosion.** (a) Schematic of *operando/in situ* EC-STEM cell with the capability to enable reliable electrochemical measurements and simultaneously track morphological, compositional and structural changes under operating conditions. WE, RE and CE stand for working, reference and counter electrodes, respectively. Scanning electron nanodiffraction (SEND) based on 4D STEM datasets acquired on an electron microscope pixel array detector (EMPAD). (b) Overview of characterization methodology: *Operando* EC-STEM for visualizing morphological changes in regular thick electrolyte; *In situ* EC-STEM for STEM-EDX elemental analysis and SEND for resolving crystal structures. The thin-liquid is naturally formed by electrochemically generating a H<sub>2</sub> bubble during cathodic corrosion; *Ex situ* on-site STEM imaging at the atomic scale, in ultrahigh purity (UHP) H<sub>2</sub> gas cell. (c-d) *In situ* thin-liquid EC-STEM image and EDX composite maps of Au-Pt alloy nanostructures grown on an Au-rich ribbon (~100 nm) at the bulk Pt electrode after cathodic corrosion of Au cubes on the Pt WE. (e-f) *Ex situ* high-resolution STEM-EDX, in H<sub>2</sub> gas cell, showing the co-existence of small Au-Pt alloy NPs (Au/Pt = 4:1) and mossy structures (Au/Pt = 3:2). (g) *Ex situ* HAADF-STEM image, clearly resolving “nano-spikes” at the particle surface. (h) *Ex situ* atomic-scale lattice image of an Au-rich Au-Pt alloy NP with multiple {111}-oriented domains along different crystal orientations (white arrows). Inset, one Au-alloy domain oriented near the [110] zone axis, magnified from the dashed box.

In an effort to demonstrate that *operando* EC-STEM is capable to deliver reliable electrochemical measurements, we performed CV measurements of Pt in acid and Cu

electrodeposition (Fig. 10.8). CV profiles of Pt in the acid in the EC-STEM cell match well the standard electrochemical measurements of Pt in Fig. 1a and show no evidence of beam damage at a dose of  $\sim 300$  e/nm<sup>2</sup>. The potential of the Pt pseudo-RE was estimated to be about +0.8 V vs. SHE based on the H<sub>UPD</sub> peak position of Pt. CV profiles in CuSO<sub>4</sub> show the well-defined Cu electrodeposition and stripping peaks at around -0.65 V vs. Pt, which is consistent with the potential (-0.648 V) at which the largest amount of deposited Cu nanoclusters occurred (Fig. 10.8). The onset potential of Cu electrodeposition was estimated to be 0.25 V vs. SHE in the *operando* EC-STEM study, which matches well with the theoretical value of E<sup>o</sup> (Cu<sup>2+</sup>/Cu) in 10 mM CuSO<sub>4</sub> (0.22 V vs. SHE).

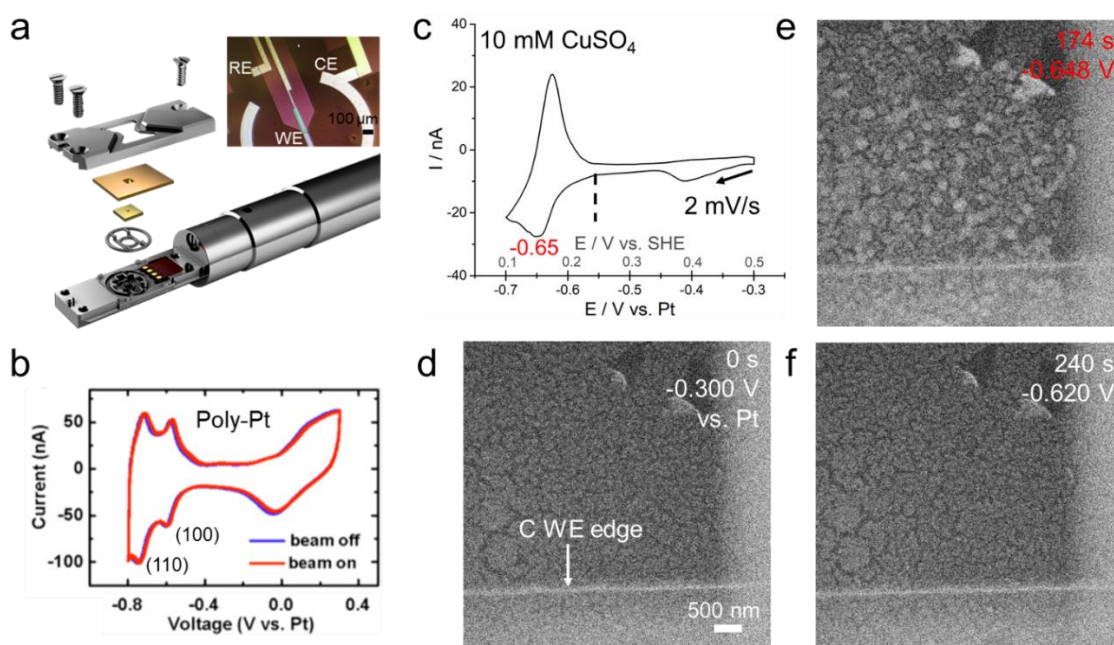


**Figure 10.8** Potential calibration of the reference electrode of Electrochemical liquid-cell chips. (a) Schematic of the layered structure of a Protochips Poseidon liquid-cell holder. Inset: optical image of the three-electrode microchip loaded with Pt/C nanoparticles. (b) CV profiles of polycrystalline Pt films in 0.1 M HClO<sub>4</sub> when the electron beam is on and off at a beam dose of  $\sim 300$  e/nm<sup>2</sup>, acquired previously by our group.<sup>30</sup> (c) CV profiles of Cu electrodeposition on carbon WE in 10 mM CuSO<sub>4</sub> at 2

mV/s when electron beam is turned on at a dose of  $35 \text{ e/nm}^2$ . An amorphous carbon WE was selected to enable the electron beam to image metallic nanoparticles with minimal background scattering. **(d-f)** The dynamic electrodeposition and stripping of Cu on the carbon WE. The potential, at which the largest amount of Cu nanoclusters electrodeposits, is highly consistent with the Cu deposition peak at  $-0.65 \text{ V vs. Pt}$ , indicating that the STEM imaging is highly synchronized to the electrochemical measurements. Based on the  $0.8 \text{ V}$  difference between Pt pseudo RE and SHE, the onset potential of Cu deposition was estimated to be  $\sim 0.25 \text{ V vs. SHE}$ , as indicated by the dashed line in [Fig. 10.8c](#). That matches well with the theoretical values of  $E^\circ (\text{Cu}^{2+}/\text{Cu})$  at  $0.22 \text{ V vs. SHE}$  in  $10 \text{ mM Cu}^{2+}$ .

With a rigorous electrochemical protocol established, we performed *operando* EC-STEM studies of cathodic corrosion of Au nanocrystals on a bulk Pt electrode. The cathodic corrosion was first performed on a bare Pt WE as a control study ([Fig. 10.9](#)). After applying sufficiently negative potentials ( $-1.5 \text{ V vs. Pt}$ ), noticeable mossy features appeared on the bulk Pt electrode surface, while no mossy features were evident in the absence of alkaline cations, indicating the important role of alkaline cations to initiate cathodic corrosion.

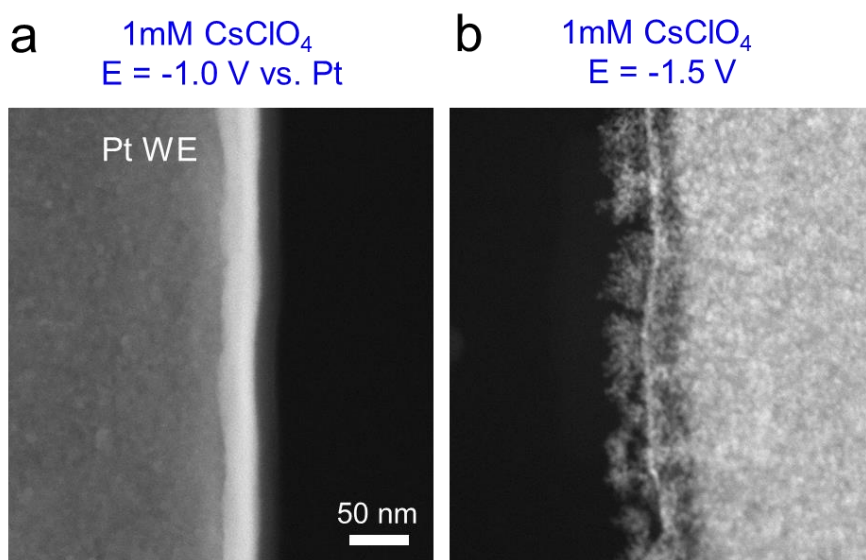


**Figure 10.9** STEM images of Pt working electrode (WE) in thin liquid after electrochemically generated  $\text{H}_2$  bubble repelling most of the electrolyte in  $1 \text{ mM CsClO}_4$  at constant potentials of  $-1.0$  and  $-1.5 \text{ V vs. Pt}$ . **(a)** No features were grown after applying

-1.0 V while (b) noticeable mossy features were grown after -1.5 V. *Operando* EC-STEM was then employed to investigate the cathodic corrosion of Au nanocubes on bulk Pt working electrodes (Au cubes/Pt WE) in 1 mM CsClO<sub>4</sub>. CV profiles of Au cubes/Pt WE exhibited the characteristic oxidation peaks of both Au and Pt at ~0.6 V vs. Pt (~1.4 V vs. SHE) (Fig. 10.10), which matched the standard electrochemical measurements in Fig. 1b.

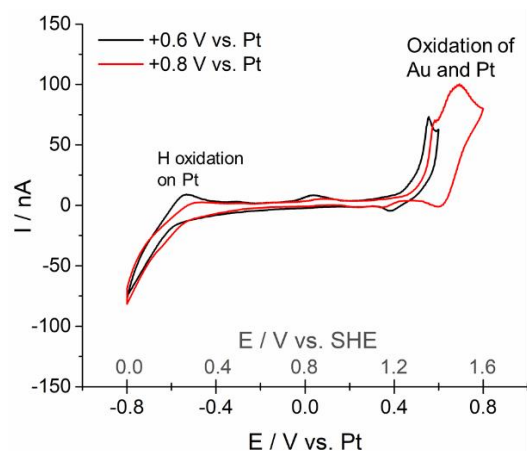


**Figure 10.10** CV profiles of Au cubes on the Pt WE in 1 mM CsClO<sub>4</sub> with different upper potential limits at a scan rate of 100 mV/s.

To explore the effects of corrosion potentials, the lower potential limit was systematically lowered from -1.0 to -2.0 V (Figs. 10.11a-b). As the lower potential limit was lowered from -1.0 to -1.6 V, the peak current density of the redox couple gradually increased (Fig. 10.11a). 10 continuous CV cycles from 0 to -1.6 V vs. Pt at 100 mV/s are plotted as an example, to show the progressive growth of well-defined redox couples with shoulder peaks at -1.0 V vs. Pt. When the lower potential limit was further decreased to very negative values of -1.8 and -2.0 V, a rapid current drop to nearly zero was observed at around -1.5 V vs. Pt, corresponding to the formation of H<sub>2</sub> bubbles, which created a native thinner liquid layer (Fig. 10.11b). The gradual increase of peak

currents at more negative potentials and during continuous CV cycles is possibly due to the accumulation of higher concentrations of soluble  $\text{H}_2$  and other reaction intermediates during cathodic corrosion in the presence of alkali cations. Once the  $\text{H}_2$  concentration in the electrolyte reaches a critical saturation concentration, a  $\text{H}_2$  bubble forms instantaneously. A recent study by White *et al.* reported that  $\text{H}_2$  bubble nucleation on Pt nanoelectrodes follows first-order kinetics and the nucleation rate can increase by four orders of magnitude over a very small relative change in the  $\text{H}_2$  concentration at the electrode surface.<sup>42</sup>

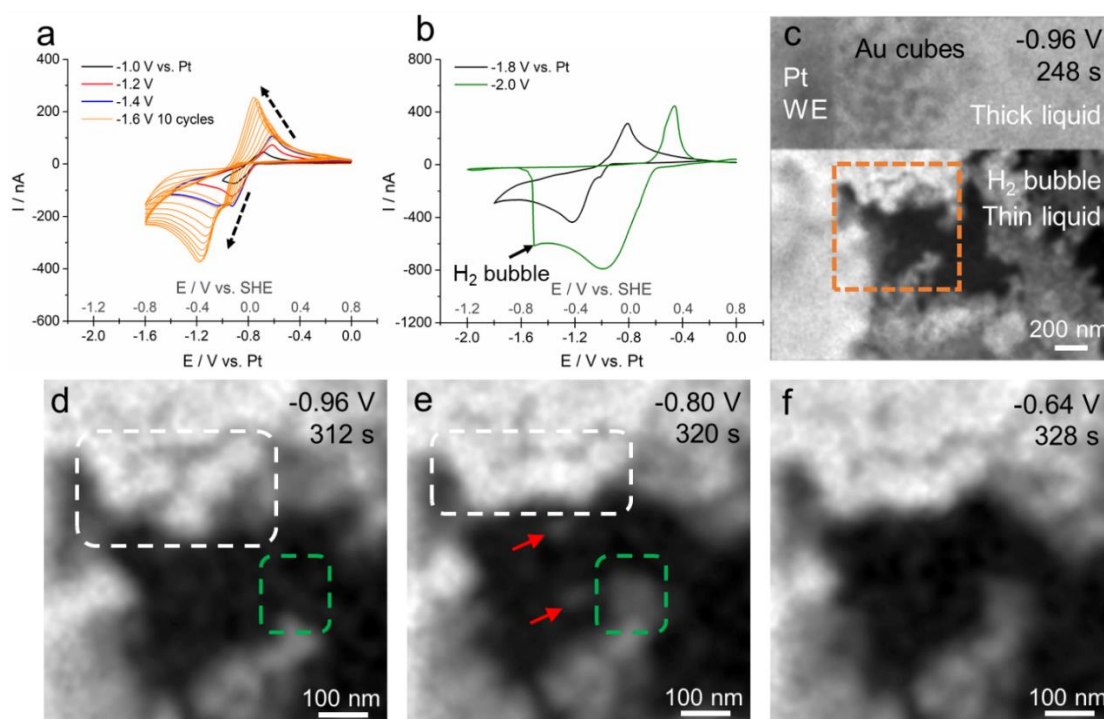


**Figure 10.11** Operando EC-STEM studies of dynamic morphological changes during cathodic corrosion. (a) CV profiles of Au cubes on Pt WE in 1 mM  $\text{CsClO}_4$  in EC-STEM in a regular thick electrolyte with various lower potential limits from -1 to 1.6 V vs. Pt at 100 mV/s. 10 continuous cycles from -1.6 to 0 V (orange profiles) are shown to demonstrate the process of accumulating soluble  $\text{H}_2$  and other reaction intermediates. (b) CV profiles with lower limits at -1.8 and -2.0 V vs. Pt. At -2.0 V, the  $\text{H}_2$  concentration in the electrolyte reaches saturation and generates a  $\text{H}_2$  bubble, which caused a sharp current drop to nearly zero. (c) A representative example of the

dramatically enhanced spatial resolution enabled by the formation of H<sub>2</sub> bubble. **(d-f)** Three continuous STEM imaging frames from the orange box in (c) showing the dynamic morphological changes during cathodic corrosion. The dashed white boxes mark the reconstruction of two large NP clusters into a longer particle chain. The red arrows point the migration of two clusters of small NPs and the green boxes mark the growth of new NPs.

*Operando* EC-STEM imaging was employed to track the morphological changes during cathodic corrosion. *Operando* EC-STEM images showed little morphological changes during the first 200 second cycling between 0 and -1.6 V vs. Pt at 20 mV/s. After 248 s, a H<sub>2</sub> bubble emerged and pushed away the electrolyte, leading to a dramatically improved spatial resolution (Figs. 10.11c). The upper part of the STEM image in Fig. 10.11c illustrates that the Au nanocubes are barely visible in the thick liquid film. Once a H<sub>2</sub> bubble is electrochemically generated, the STEM image of the NPs can be clearly resolved. *Operando* EC-STEM images in Figs. 10.11d-f exhibits the dynamic morphological changes during cathodic corrosion over three continuous frames (magnified from the orange box in Fig. 10.11c. Two large NP clusters of 100-200 nm experienced particle agglomeration into one longer particle chain (white dashed boxes in Figs. 10.11d-e). In addition, two small new particles of ~30 nm emerged and migrated in between those large particle clusters (red arrows, Fig. 10.11e). Individual particle growth was also observed (green boxes in Figs. 10.11d-e). Those particle reconstruction/migration/growth were captured at a very low beam dose of ~8 e/nm<sup>2</sup>, which was caused by cathodic corrosion rather than beam-induced artifacts, as verified by the beam dose control experiment at a higher dose of 15 e/nm<sup>2</sup> over longer-time STEM imaging. A static STEM image in Fig. 10.12 exhibited the co-existence of reacted Au cubes (~100 nm) and newly generated small NPs (20-50 nm) at the solid-

liquid-gas interface reproducing the formation of small alloy NPs in Fig. 10.1d.

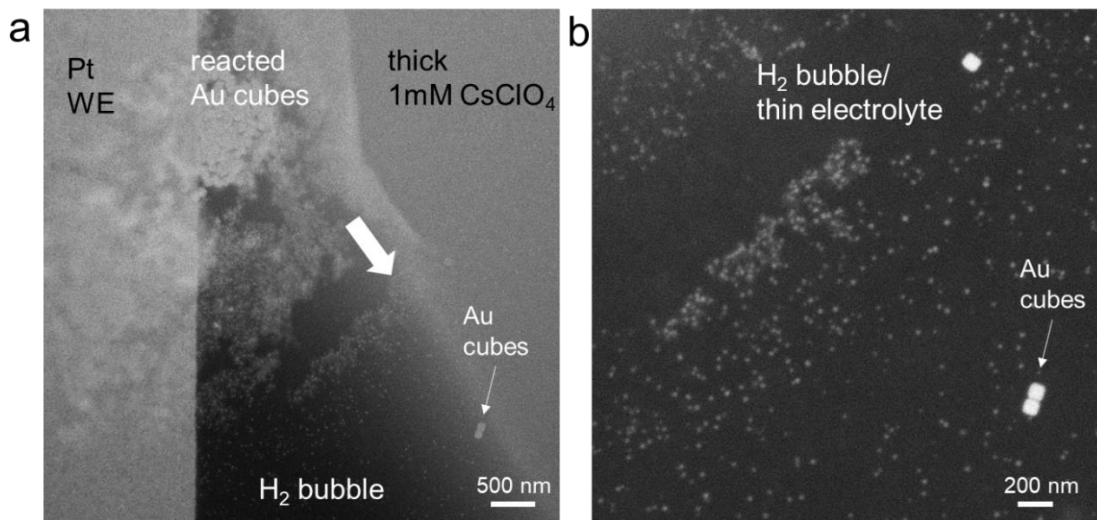


**Figure 10.12** (a) STEM images of a snapshot of the cathodic corrosion of Au cubes (~100 nm reactants) and the generation and repulsion of numerous small alloy NPs (20-50nm). Significant resolution improvement can be noticed when comparing the small NPs in thin liquid (white arrow) enabled by the H<sub>2</sub> bubble repelling strategy with the regular thick electrolyte on the upper right side. This is also a direct visualization of a gas-solid-liquid triphase interface near an electrode. (b) A magnified region showing the co-existence of unreacted (or partially reacted) Au cubes and many newly generated small NPs.

*In situ* EC-STEM in thin liquid films, enabled carrying out STEM-EDX elemental analysis in an electrolyte (Figs 10.7c-d). After pushing away most of the bulk electrolyte, newly grown nanostructures were clearly observed at the Pt electrode surface (Fig. 10.7c). *In situ* STEM-EDX composite elemental mapping at a dose of ~8,500 e/nm<sup>2</sup> exhibited a striking inhomogeneous elemental distribution of Au and Pt where Au-Pt alloy nanostructures were grown on an Au-rich ribbon (~100 nm, green) on the bulk Pt electrode (red) (Fig. 10.7d). The drastic changes from Au nanocubes to Au-Pt alloy nanostructures suggest a much higher level of structural degradation for nanocrystals during corrosion, relative to the mild changes of bulk electrodes.

Quantification of STEM-EDX spectra yielded a Au/Pt atomic ratio of ~1:1 for those alloy nanostructures, and ~5:1 for newly formed Au-rich alloy NPs (~30 nm) located in the upper left corner. The presence of a thin liquid film was indicated by the significantly higher intensity of O signals in the EDX as well as the rapid flow of NPs. Although minimal beam damage was observed after EDX mapping at low magnification, STEM-EDX in thin liquid film at a higher dose of  $10^4$  e/nm<sup>2</sup>, exhibited noticeable beam damage and sample drift, precluding high-resolution STEM-EDX mapping of individual Au-Pt alloy NPs in thin liquid layers.

In addition to morphological and elemental information obtained by *in situ* EC-STEM, crystallographic structural information was derived from 4D STEM datasets by performing *in situ* SEND in the thin liquid film (Fig. 10.13). For example, Fig. 10.13a shows an HAADF image of reacted Au nanocubes and newly generated Au-Pt alloy NPs. A virtual bright field (BF) image (Fig. 10.13b) was reconstructed from the SEND dataset by integrating the transmitted (000) spot, which revealed additional mossy particles of 20-50 nm in the left region of the image. The crystallographic orientation of each NP was retrieved by indexing the diffraction patterns for each cluster using an fcc structure model. Fig. 10.13c shows the reconstructed crystallographic orientation map, where the color represents the superposition of three corners ( $\{100\}$ ,  $\{110\}$ ,  $\{111\}$  as R, G, B, respectively) in the inverse pole figure. Figs. 10.13d-f show representative diffraction patterns from labeled regions in Fig. 10.13c with orientations near the zone axes of  $[100]$ ,  $[110]$ ,  $[110]$ , respectively. The left region in Fig. 10.13c exhibits the crystal orientation of highly polycrystalline mossy structures. The SEND analysis and molecular dynamic simulations enabled quantification of the thickness of the thin liquid

film as xx nm. In addition, the SEND illustrates the polycrystalline nature of newly generated Au-Pt alloys (Fig. 10.14) after corroding Au nanocubes on Pt film in Fig. 10.1d. In summary, this study is the first demonstration that *in situ* SEND diffraction analysis, in thin liquids, serves as a powerful tool to provide structural insights beyond morphological and compositional changes.

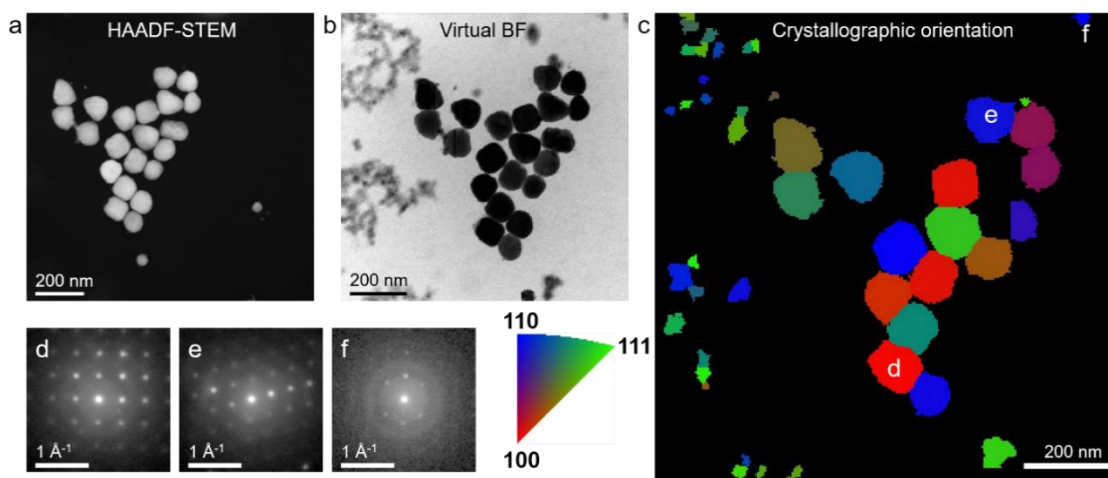


**Figure 10.13.** *In situ* scanning electron nanodiffraction (SEND) of reacted Au nanocubes and Au-Pt NPs in thin liquid. (a) HAADF-STEM image of reacted Au nanocubes near the Pt WE in a thin layer of 1mM CsClO<sub>4</sub>. The SEND, based on a 4D dataset, was acquired by recording a 2D diffraction pattern at each probe position in a 2D grid. (b) Virtual bright-field (BF) image reconstructed from the SEND dataset, showing larger Au cubes (~100 nm) and smaller Au-Pt NPs (20-50 nm). (c) Crystallographic orientation map obtained by careful indexing of each clustered diffraction pattern using an fcc structure model. (d-f) Representative diffraction patterns shown in logarithmic scale from labeled regions in (c), respectively.

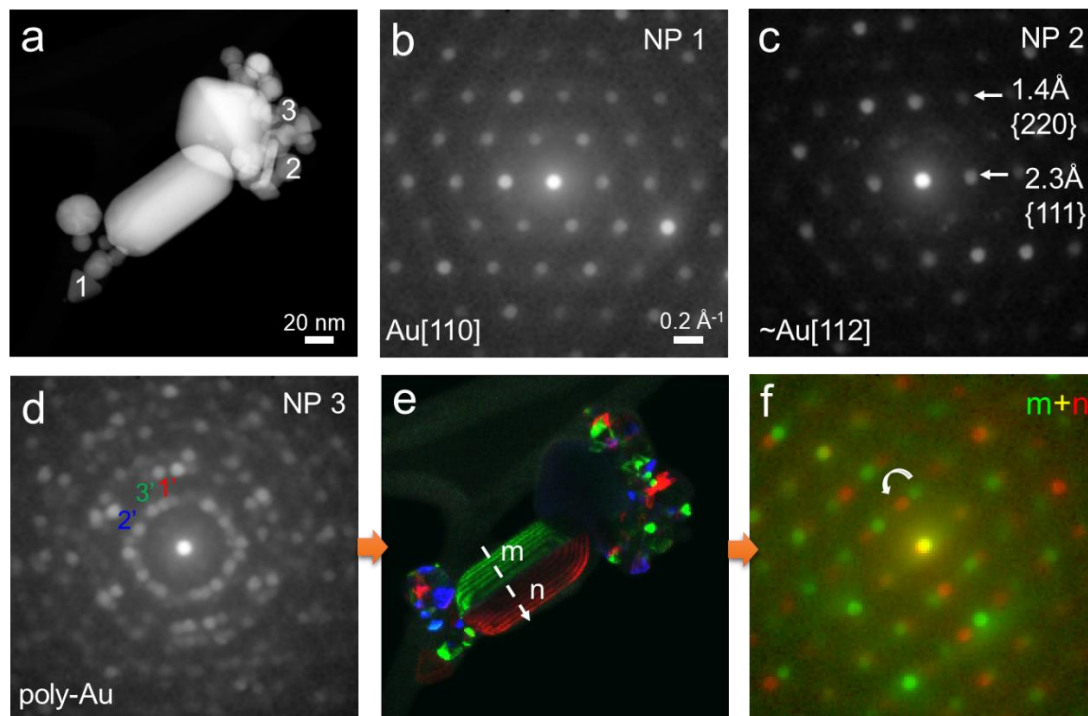


**Figure 10.14.** SEND analysis of nanoparticles in Fig. S8 after the cathodic corrosion of Au nanocubes on Pt film in CsClO<sub>4</sub> at -3 V vs. RHE. (a) STEM image (b-d) Representative electron diffraction patterns of three selected small NPs. (e) False color overlay of three dark-field images from three diffraction spots labeled in (d). (f) False color overlay of electron diffraction patterns across a twin boundary in (e).

*Ex situ* EC-STEM in the H<sub>2</sub> gas cell was employed to resolve the atomic lattice structure of individual alloy NPs (Figs. 10.7e-h). A significant improvement of the spatial resolution was demonstrated in the H<sub>2</sub> gas cell by resolving the subtle features of Au-Pt NPs and mossy structures (Fig. 10.7e), which were not accessible in the thin-liquid-film images. STEM-EDX in the H<sub>2</sub> gas cell showed that, in general, the small NPs were Au-rich alloys with Au/Pt atomic ratios of 4~5:1, while the mossy structures near the Pt WE had Au/Pt atomic ratios of 1.5~1:1 (Figs. 10.7e,f, 10.15).

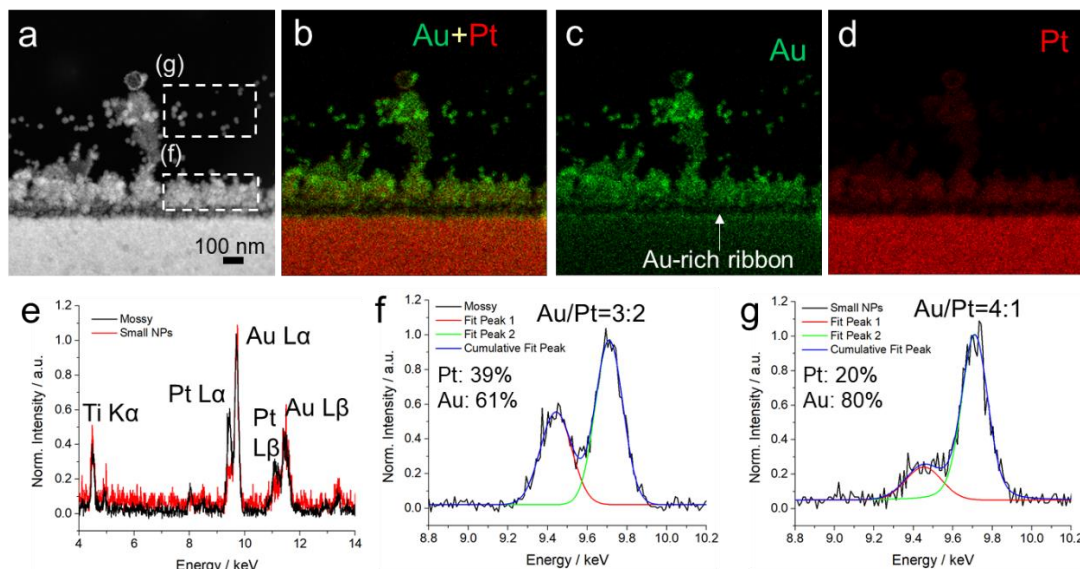


**Figure 10.15.** *Ex situ* STEM-EDX mapping and quantitative analysis in H<sub>2</sub> gas cell. (a) High-magnification STEM image of Au cubes on the Pt WE after cathodic corrosion. (b-d) STEM-EDX elemental maps of Au/Pt composite map (b), Au map in green (c) and Pt map in red (d). (e) EDX spectra from the dashed box in (a). Pt and Au L $\alpha$  edges were deconvoluted and employed to extract elemental maps in (b-d) from EDX hyperspectral imaging dataset. (f-g) EDX peak deconvolution of Pt and Au L $\alpha$  edges from the dashed box in (a) based on the Voigt peak fitting function. Ti signal is from the Ti adhesion layer under the Pt WE.

The above STEM-EDX analysis has provided unique insights into the locally heterogeneous elemental distributions of Au-Pt alloys after cathodic corrosion. It should be noted that the Ti peaks in the EDX spectra (Fig. 10.15), are from the Ti adhesion layer under the Pt WE. *Ex situ* STEM-EELS in the H<sub>2</sub> gas cell showed the presence of Au and Pt and the absence of Ti, confirming that the alloy NPs contained only Au and Pt (Fig. 10.16). The absence of Cs also rules out the formation of Cs-intercalation compounds after corrosion. Valence EELS, based on the relative intensity of the plasma peak,<sup>43</sup> allowed estimating the thickness of the SiN<sub>x</sub> window, Au-Pt alloy NPs and corroded Pt WE as 116, 50 and 100 nm, respectively (Fig. 10.17).

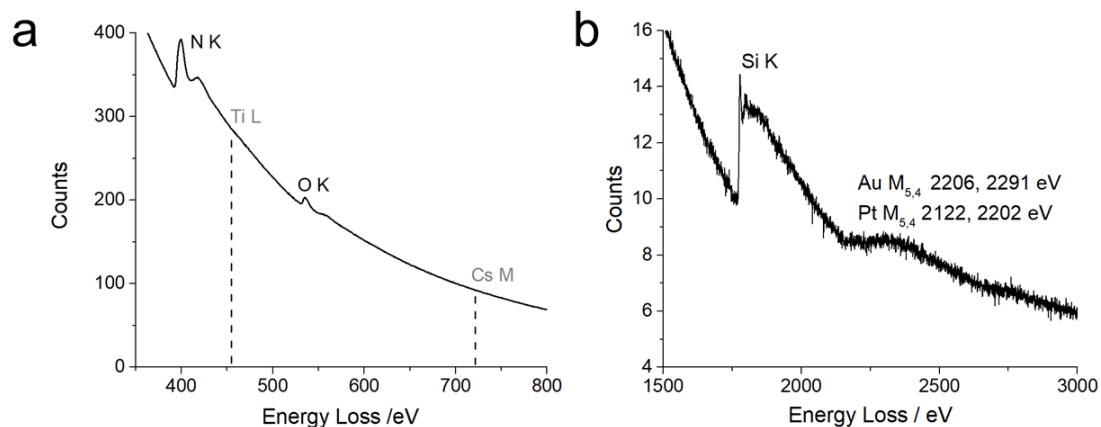


**Figure 10.16** *Ex situ* STEM-EELS analysis of Au-Pt alloy NPs generated from Au cubes on the Pt WE after cathodic corrosion reaction in the H<sub>2</sub> gas cell. (a) EELS spectrum showing the presence of N and O owing to the oxidized SiN<sub>x</sub> window and the absence of Ti and Cs signals. (b) EELS spectrum showing the Si K edge from SiN<sub>x</sub> window and the overlapped Au and Pt M edges.

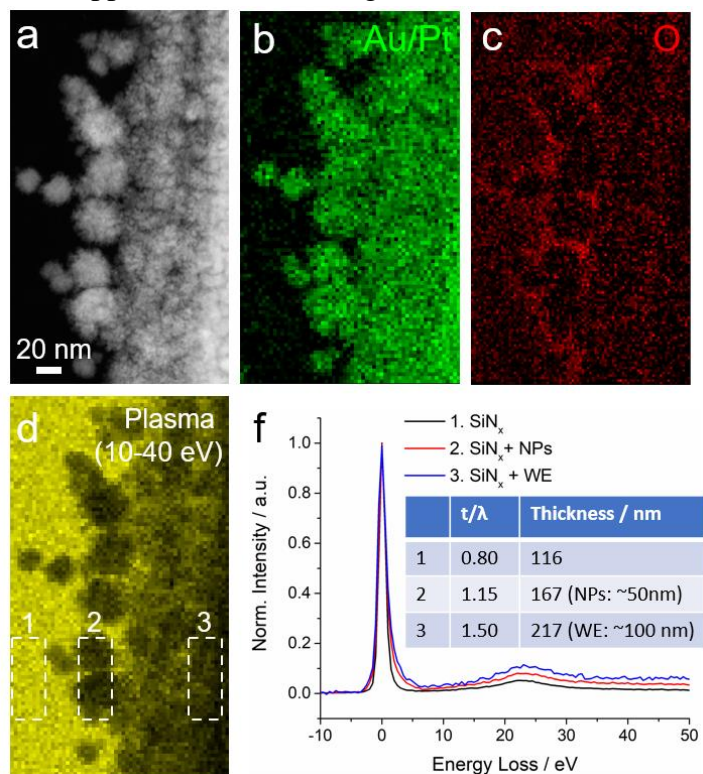


**Figure 10.17** *Ex situ* STEM-EELS analysis of Au-Pt alloy NPs generated from Au cubes on the Pt WE after cathodic corrosion reaction in the H<sub>2</sub> dry cell. (a-c) STEM image and EELS elemental maps based on the combined Au and Pt M edges and O K edge. The feature in the O map matches the contour of NPs in (b), indicating residual O-containing species at the nanoparticle surface. (d-f) Thickness analysis based on the

peak ratio of plasma peak to the zero loss peak (ZLP). The inelastic mean free path ( $\lambda$ ) was estimated to be 145 nm at 300 keV with a collection angle of  $\sim 40$  mrad.<sup>43</sup> The total thickness of two layers of SiN<sub>x</sub> window was calculated to be around 116 nm, which matches well with the estimated thickness of each SiN<sub>x</sub> window ( $\sim 50$  nm) from the chip manufacturer. It should be noted that the pristine electrode is composed of 25 nm Ti under 50 nm Pt.

*Ex situ* EC-STEM also enabled the direct visualization of crystal structures at the atomic scale (Figs. 10.7g-h). Small Au-Pt alloy NPs exhibited “nano-spikes” on the particle surface (Fig. 10.7g), which are not readily visible in the thin liquid. An atomic-scale high-angle annular dark-field (HAADF) STEM image exhibited the polycrystalline nature of the small alloy NPs (Fig. 10.7h). Given the Au-rich composition of the small alloy NPs, and the close values of lattice parameters ( $a_{\text{Au}}=4.078$  Å,  $a_{\text{Pt}}=3.923$  Å), it is reasonable to use the d-spacing values of pure Au to index the lattice images of those Au<sub>3</sub>Pt alloy NPs. Multiple {111}-oriented domains of a few nm were visualized along different crystal orientations. The domain magnified from the dashed box in Fig. 10.7h exhibited an fcc lattice domain oriented near the [110] zone axis.

### 10.5 Cathodic Corrosion for the synthesis of Au-Pt bimetallic NPs

Cathodic corrosion can serve as an effective top-down synthetic method to “disintegrate” bulk electrodes into alloy NPs. Au and Pt intertwined wires were subjected to cathodic corrosion in 10 M KOH with an AC square wave (-10~0 V) at 100 Hz with a direct current (DC) offset of -5 V to ensure a reduction process (Fig. 10.18a, inset). After corrosion for 2 h, the CV profiles of the Au-Pt wires exhibited a five-fold increase of the AuO<sub>x</sub> reduction peak and an evident PtO<sub>x</sub> reduction peak, relative to pristine electrodes (Fig. 10.18a). After cathodic corrosion, the CV profiles of the Au-Pt

wires exhibited the  $H_{UPD}$  features of polycrystalline Pt, indicating that Au was subjected to a higher level of corrosion relative to Pt. SEM images of Au-Pt wires after 2 h of corrosion indicated that the electrode had cracked into  $\mu\text{m}$ -sized domains generating new NP clusters of 10-100nm (Figs. 10.18b). After a longer corrosion time of 20 h, the Au-Pt wires further disintegrated into a highly porous surface (Figs. 10.18c).

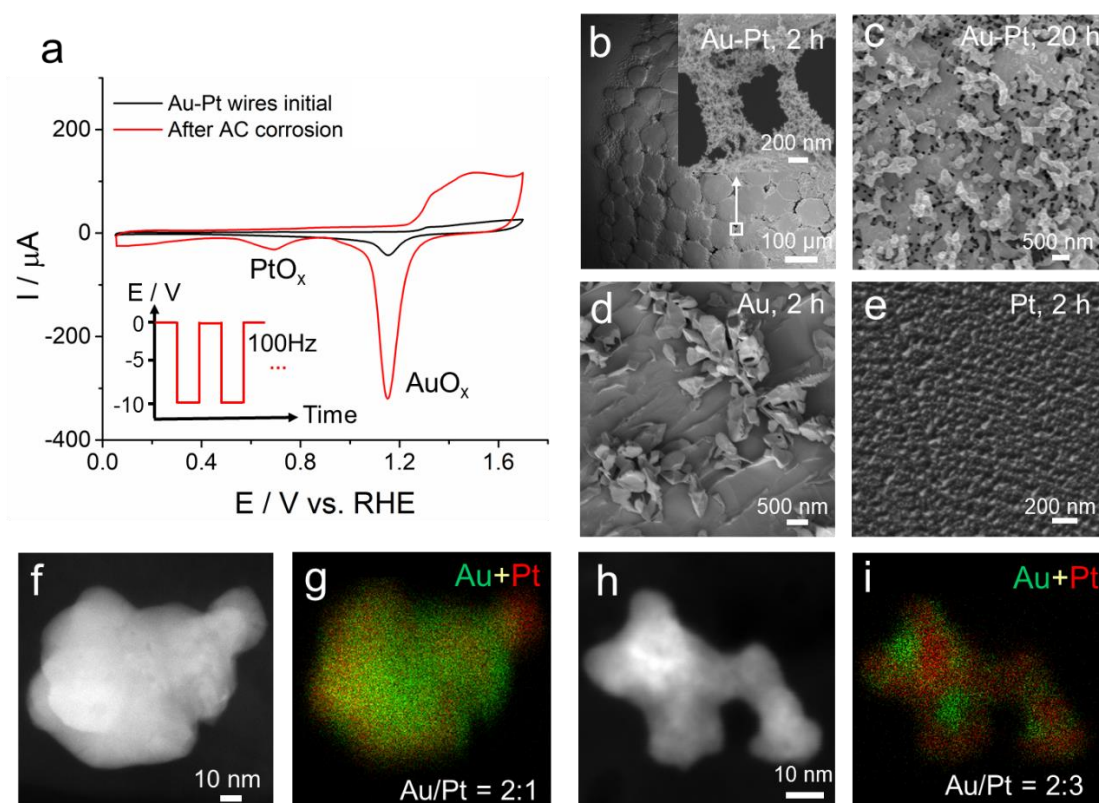


**Figure 10.18** Cathodic corrosion for the synthesis of Au-Pt bimetallic NPs. (a) CV profiles of Au-Pt mixed wires in Ar-sat. 0.1 M  $\text{HClO}_4$  at 50 mV/s before and after cathodic corrosion in 10 M KOH for 2 h. The inset shows the corrosion conditions with an AC square wave between 0 and -10 V with a DC offset at -5 V at a frequency of 100 Hz. (b) SEM images of Au-Pt wires after corrosion for 2 h showing the cracking of bulk electrodes and generation of numerous small NPs. (c) SEM image of Au-Pt wires after corrosion for 20 h showing a much higher level of surface roughening, relative to 2 h in (b). (d-e) SEM images of Au wire (d) and Pt wire (e) under the same cathodic corrosion conditions after 2 h. (f-i) STEM images and EDX elemental maps of newly generated Au-Pt bimetallic particles from Au-Pt wires after cathodic corrosion processes in (a).

In order to deconvolute the morphological changes of Au from Pt, cathodic corrosion of individual Au and Pt wires were performed under the same conditions. SEM images of the Au wire after corrosion, exhibited the formation of needle-shaped nanocrystals and noticeable etching steps on the electrode surface (Fig. 10.18d), which corresponded to a 10-fold increase of the AuO<sub>x</sub> reduction peak (Fig. 10.19a). In comparison, SEM images of Pt showed much milder etching features (Fig. 10.18e) and only a ~15% increase of the ECSA (Fig. 10.19b).

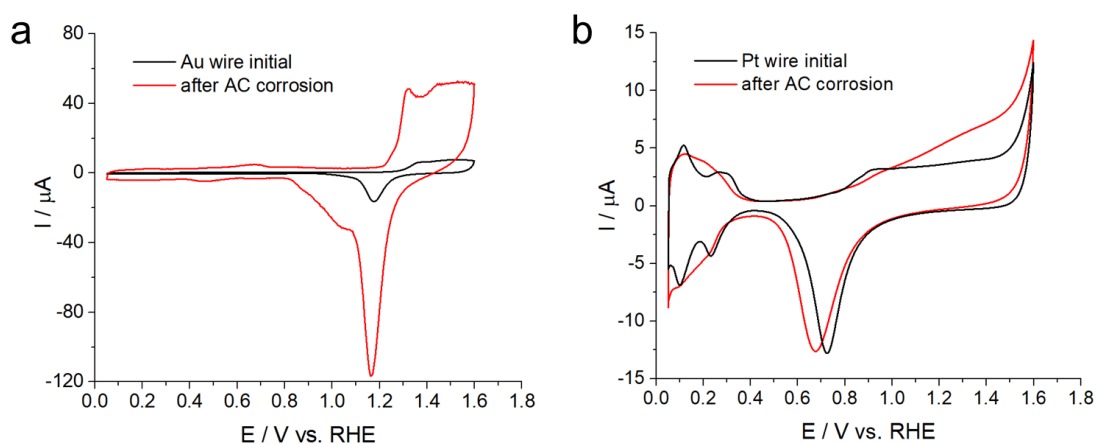


**Figure 10.19.** CV profiles of (a) Au and (b) Pt wires in Ar-sat. 0.1 M HClO<sub>4</sub> at 50 mV/s before and after cathodic corrosion in 10 M KOH with an AC square-wave potential scan between 0 and -10 V and DC offset of -5 V at a frequency of 100 Hz for 2 h.

Such differences between Au and Pt can be rationalized by the competition between cathodic corrosion and their HER activities. The HER kinetics on Au are so sluggish that the strongly reducing potentials mainly drive the corrosion of the bulk Au into nanocrystals. In contrast, the HER occurs readily on Pt below 0 V vs. RHE, which makes the very negative potentials primarily drive the HER while causing milder morphological changes as a result of the corrosion. STEM-EDX maps of the as-

synthesized NPs showed the elemental distribution of Au-Pt alloy NPs with multiple Au-rich (green) and Pt-rich (red) domains of a few nm (Fig. 10.18) with average Au/Pt ratios ranging from 2:1 to 2:3. The disintegration of Au and Pt bulk wires into Au-Pt bimetallic NPs yielded a certain level of alloying at the nm scale but not a single phase as that formed by corrosion of the Au nanocubes on the Pt film (Figs. 10.1e-f). This is ascribed to the significantly higher corrosion rate of nanocrystals, relative to bulk electrodes in Fig. 10.18. Thus, cathodic corrosion shows the potential to overcome the thermodynamic solubility limitations of phase diagrams and enable the incorporation of Au into Pt lattices, which has been reported to enhance durability of Pd-based ORR electrocatalysts.<sup>44,45</sup> Cathodic corrosion of other largely immiscible alloys from bulk electrodes, such as Pt-M (M=Bi, Pb, Pr),<sup>15,17</sup> Au-Co<sup>11</sup> and Sn-Pb,<sup>16</sup> also show noticeable evidences of phase and/or elemental segregation of the synthesized alloy NPs. By optimizing cathodic corrosion conditions and environments, cathodic corrosion has the potential to enable preparation of single-phase alloys with tunable structures and compositions.

### **10.6 Proposed Cathodic Corrosion Mechanisms**

Although the exact cathodic corrosion mechanisms are still under investigation, based on this study and Koper's previous work,<sup>9</sup> we propose the following possible reaction pathways for the cathodic corrosion of Au nanocubes on bulk Pt electrodes (Fig. 10.20). At sufficiently negative potentials, atomic hydrogen is generated, together with alkali cations ( $\text{Cs}^+$ ,  $\text{K}^+$  or  $\text{Na}^+$ ), which adsorbs on the Au and Pt surfaces (Fig. 10.20a). Adsorbed hydrogen ( $\text{H}^*$ ) and alkali cations can induce a surface reconstruction and initiate the corrosion from flat terraces to roughened step edges. Au nanocubes, with a

larger surface energy, are subjected to faster corrosion kinetics, relative to bulk Pt. Mobile Au and Pt atoms, etched from electrode surfaces, are hypothesized to form metal hydrides (e.g.  $[\text{MH}_4]^-$ ) and diffuse to nearby electrolyte (Fig. 10.20b), potentially contributing to the redox peaks in Figs. 10.20a-b. Those metal hydride anionic species, while unconfirmed, can be stabilized by alkali cations in a locally strong reducing environment. When metal hydrides encounter water molecules at appropriate collision orientations, the negatively charged H in  $[\text{MH}_4]^-$  reacts instantaneously with the positively charged H in  $\text{H}_2\text{O}$  (Fig. 10.20b) and results in the formation of elemental Au and Pt atoms (Fig. 10.20c). Thus, those metal hydrides, once generated, have extremely short lifetime and are very challenging to isolate and analyze. Those newly generated Au and Pt atoms nucleate and grow into Au-Pt alloy NPs (Fig. 10.20d).

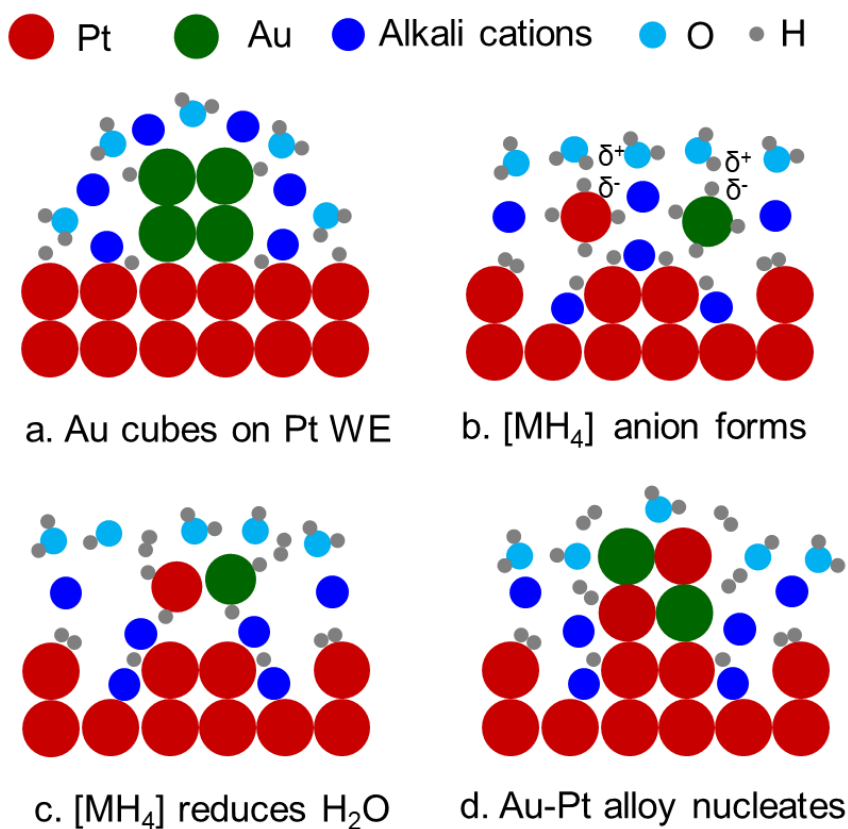


**Figure 10.20 Schematic of proposed cathodic corrosion mechanisms.** (a) Cathodic corrosion is initiated by the presence of atomic hydrogen and adsorbed alkali cations at sufficiently negative potentials. (b) Pt and Au atoms are electrochemically converted to metal hydrides (e.g.  $[\text{MH}_4]^-$ ), which are stabilized by alkali cations when in close proximity. (c) The highly reducing, negatively charged hydrogen (ostensibly hydride) in  $[\text{MH}_4]^-$  reacts with water, resulting in an extremely short-lifetime intermediate species. (d) Au and Pt atoms encounter and nucleate in the form of Au-Pt bimetal alloys, leading to the growth of alloy NPs. Note: only one Au and one Pt atom in (b) and (c) were drawn for the purpose of simplification.

At reducing potentials well below equilibrium, the cathodic corrosion process leads to the formation of highly active Au-Pt bimetallic anions and subsequent quenching and deposition of Au-Pt alloy NPs, which can achieve metastable phases that are normally immiscible in the phase diagram (Fig. 10.21).

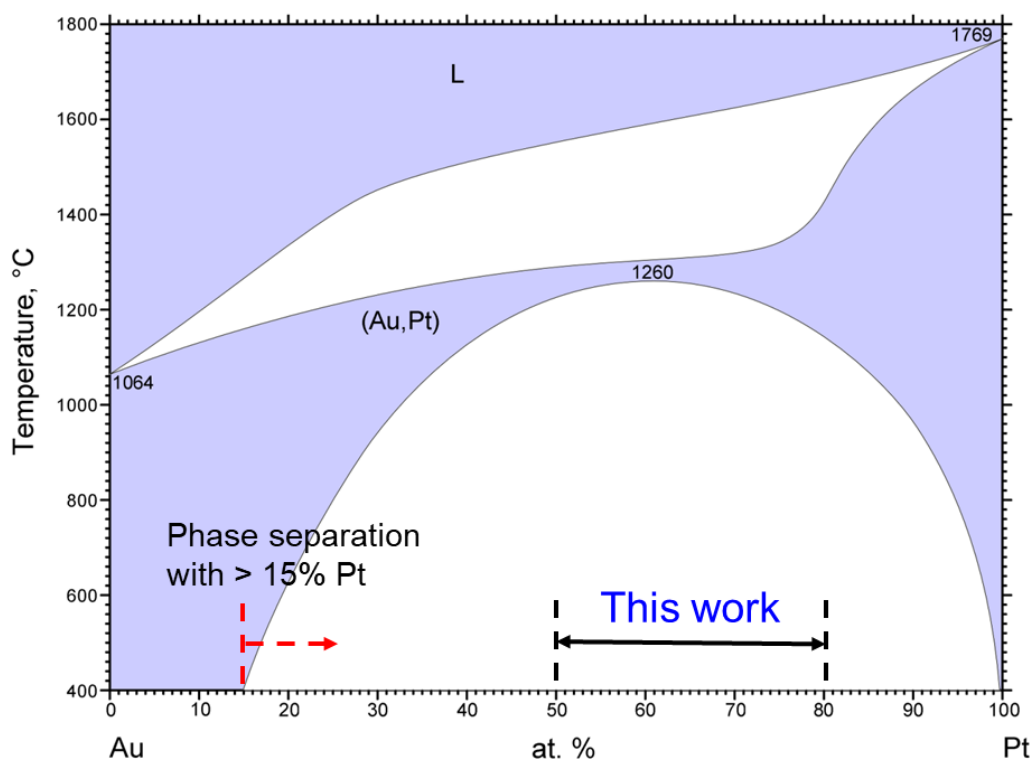


**Figure 10.21** Phase diagram of Au and Pt (ASM International Database No. 900242). This work demonstrates the formation of Au-Pt bimetallic alloy nanoparticles with Au/Pt ratios from 5:1 to 1:1.

The proposed Pt hydrides, such as  $\text{Na}_2[\text{PtH}_4]$  and  $\text{Cs}_2[\text{PtH}_4]$ , have been previously synthesized with Pt and alkali hydrides.<sup>46</sup> The presence of Au hydrides has been experimentally confirmed at ultralow temperatures.<sup>47</sup> A recent study by Hoffmann *et al.* predicted that ternary Au hydrides could be thermodynamically stabilized by alkali cations under ambient conditions.<sup>48</sup> Alkali cations and adsorbed hydrogen from water molecules are necessary to induce the cathodic corrosion since the corrosion process does not occur if the protons are the only cations in solution<sup>13</sup> and no corrosion process occurs in aprotic solvents.<sup>49</sup> In summary, cathodic corrosion mechanisms likely involve key intermediates, such as ternary metal hydrides, in the presence of alkali cations and adsorbed hydrogen.

## 10.7 Conclusions

In conclusion, this work reports on the anisotropic cathodic corrosion processes of Pt single crystals and reveals, for the first time, the dynamic corrosion process of nanocrystals, which have significantly faster corrosion kinetics than bulk electrodes. *Operando/in situ* EC-STEM in regular electrolyte and thin liquid films, as well as *ex situ* STEM in an  $\text{H}_2$  gas cell, have enabled the direct probing of morphological, compositional and structural changes at nm and atomic scales. Guided by microscopic insights from *operando* EC-STEM, we demonstrate that cathodic corrosion can serve as a top-down surfactant-free alloy NP synthetic method, which can overcome the thermodynamic limitations of phase diagrams. Cathodic corrosion of nanocrystals can provide valuable insights into the structural evolution of widely used nanosized electrocatalysts under reducing potentials, such as in  $\text{CO}_2$  and  $\text{N}_2$  reduction. Such unintentional structural changes of nanosized electrocatalysts occurring within the

potential window of cathodic corrosion, can have a great impact on electrocatalyst activity/selectivity and electrode stability. This study provides valuable insights to utilize cathodic corrosion to tailor the structures and compositions of nanosized electrocatalysts for enhanced activity and selectivity. A microscopic understanding of the cathodic corrosion of nanocrystals will help circumvent the undesirable corrosion under reducing potentials, so as to develop corrosion-resistant electrocatalysts. The *operando* EC-STEM offers a platform for advancing the microscopic understanding of cathodic corrosion, which can be extended to the study of other renewable energy-related electrochemical reaction mechanisms at electrode-electrolyte interfaces under realistic operating conditions.

## 10.8 References

1. von Baeckmann, W.; Schwenk, W.; Prinz, W. Handbook of Cathodic Corrosion Protection Elsevier, Amsterdam, ed. 3, 1997.
2. Koch, G. H.; Brongers, M. P. H.; Thompson, N. G.; Virmani, Y. P.; Payer, J. H. Corrosion Costs and Preventive Strategies in the United States. Federal Highway Administration (FHWA), 2002.
3. Biezma, M. V.; Schanack, F. Collapse of Steel Bridges. *J. Perform. Constr. Facil.* **2007**, *21*, 398-405.
4. Cole, I. S.; Marney, D. The Science of Pipe Corrosion: A Review of the Literature on the Corrosion of Ferrous Metals in Soils. *Corros. Sci.* **2012**, *56*, 5-16.
5. Haber, F. Über elektrolyse der Salisburj nebst mittheilungen über kathodische formation von blei. *Z. Anorg. Chem.* **1898**, *16*, 438-449.
6. Haber, F. The Phenomenon of the Formation of Metallic Dust from Cathodes. *Trans. Am. Electrochem. Soc.* **1902**, *2*, 189-196.
7. Kabanov, B. N.; Astakhov, I. I.; Kiseleva, I. G. Formation of Crystalline Intermetallic Compounds and Solid Solutions in Electrochemical Incorporation of Metals into Cathodes, *Electrochim. Acta.* **1979**, *24*, 167-171.
8. Salzberg, H. W.; Mies, F. Cathodic Disintegration of Tin. *J. Electrochem. Soc.* **1958**, *105*, 64-66.
9. Hersbach, T. J. P.; Koper, M. T. M. Cathodic Corrosion: 21st Century Insights into A 19th Century Phenomenon. *Curr. Opin. Electrochem.* **2021**, *26*, 100653.
10. Yanson, A. I.; Rodriguez, P.; Garcia-Araez, N.; Mom, R. V.; Tichelaar, F. D.; Koper, M. T. M. Cathodic Corrosion: A Quick, Clean, and Versatile Method for the Synthesis of Metallic NPs. *Angew. Chemie Int. Ed.* **2011**, *50*, 6346-6350.

11. Rodriguez, P.; Tichelaar, F. D.; Koper, M. T. M.; Yanson, A. I. Cathodic Corrosion as a Facile and Effective Method To Prepare Clean Metal Alloy NPs. *J. Am. Chem. Soc.* **2011**, *133*, 17626-17629.
12. Hersbach, T. J. P.; Yanson, A. I.; Koper, M. T. M. Anisotropic Etching of Platinum Electrodes at the Onset of Cathodic Corrosion, *Nat. Commun.* **2016**, *7*, 12653.
13. Hersbach, T. J. P.; McCrum, I. T.; Anastasiadou, D.; Wever, R.; Calle-Vallejo, F.; Koper, M. T. M. Alkali Metal Cation Effects in Structuring Pt, Rh, and Au Surfaces through Cathodic Corrosion, *ACS Appl. Mater. Interfaces.* **2018**, *10*, 39363-39379.
14. Xia, Y.; Xia, X.; Peng, H.-C. Shape-controlled synthesis of colloidal metal nanocrystals: thermodynamic versus kinetic products. *J. Am. Chem. Soc.* **137**, 7947-7966 (2015).
15. Fichtner, J.; Garlyyev, B.; Watzele, S.; El-Sayed, H. A.; Schwämmlein, J. N.; Li, W.-J.; Maillard, F. M.; Dubau, L.; Michalička, J.; Macak, J. M.; Holleitner, A.; Bandarenka, A. S. Top-Down Synthesis of Nanostructured Platinum–Lanthanide Alloy Oxygen Reduction Reaction Catalysts: Pt<sub>x</sub>Pr/C as an Example, *ACS Appl. Mater. Interfaces.* **2019**, *11*, 5129-5135.
16. Pavesi, D.; van de Poll, R. C. J.; Krasovic, J. L.; Figueiredo, M.; Gruter, G. -J. M.; Koper, M. T. M.; Schouten, K. J. P. Cathodic disintegration as an easily scalable method for the production of Sn and Pb-Based Catalysts for CO<sub>2</sub> Reduction, *ACS Sustain. Chem. Eng.* **2020**, *8* 15603–156.
17. Bennett, E.; Monzó, J.; Humphrey, J.; Plana, D.; Walker, M.; McConville, C.; Fermin, D.; Yanson, A.; Rodriguez, P. A Synthetic Route for the Effective Preparation of Metal Alloy NPs and Their Use as Active Electrocatalysts. *ACS Catal.* **2016**, *6*, 1533-1539.
18. Kromer, M. L.; Monzó, J.; Lawrence, M. J.; Kolodziej, A.; Gossage, Z. T.; Simpson, B. H.; Morandi, S.; Yanson, A.; Rodríguez-López, J.; Rodríguez, P. High-Throughput Preparation of Metal Oxide Nanocrystals by Cathodic Corrosion and their Use as Active Photocatalysts. *Langmuir* **2017**, *33*, 13295-13302.
19. Duca, M.; Rodriguez, P.; Yanson, A. I.; Koper, M. T. M. Selective Electrocatalysis on Platinum NPs with Preferential (100) Orientation Prepared by Cathodic Corrosion. *Top. Catal.* **2014**, *57*, 255-264.
20. Katsounaros, I.; Ipsakis, D.; Polatides, C.; Kyriacou, G. Efficient Electrochemical Reduction of Nitrate to Nitrogen on Tin Cathode at Very High Cathodic Potentials. *Electrochim. Acta.* **2006**, *52*, 1329-1338.
21. Li, Y.; Kim, D.; Louisia, S.; Xie, C.; Kong, Q.; Yu, S.; Lin, T.; Aloni, S.; Fakra, S.; Yang, P. Electrochemically Scrambled Nanocrystals are Catalytically Active for CO<sub>2</sub>-To-Multicarbon. *Proc. Natl. Acad. Sci. U. S. A.* **2020**, *117*, 9194-9201.
22. Aran-Ais, R. M.; Rizo, R.; Grosse, P.; Algara-Siller, G.; Dembele, K.; Plodinec, M.; Lunkenbein, T.; Chee, S. W.; Cuenya, B. R. Imaging Electrochemically Synthesized Cu<sub>2</sub>O Cubes and Their Morphological Evolution Under Conditions Relevant To CO<sub>2</sub> Electroreduction. *Nat. Commun.* **2020**, *11*, 3489.
23. Kim, Y.-G.; Javier, A.; Baricuatro, J. H.; Torelli, D.; Cummins, K. D.; Tsang, C. F.; Hemminger, J. C.; Soriaga, M. P. Surface Reconstruction of Pure-Cu Single-Crystal Electrodes under CO-Reduction Potentials in Alkaline Solutions: A Study by Seriatim ECSTM-DEMS. *J. Electroanal. Chem.* **2016**, *780*, 290-295.

24. Vavra, J.; Shen, T.-H.; Stoian, D.; Tileli, V.; Buonsanti, R. Real-Time Monitoring Reveals Dissolution/Redeposition Mechanism in Copper Nanocatalysts During the Initial Stages of The CO<sub>2</sub> Reduction Reaction. *Angew. Chem. Int. Ed.* **2021**, *60*, 1347-1354.
25. Chen, J. G.; Crooks, R. M.; Seefeldt, L. C.; Bren, K. L.; Bullock, R. M.; Darensbourg, M. Y.; Holland, P. L.; Hoffman, B.; Janik, M. J.; Jones, A. K.; Kanatzidis, M. G.; King, P.; Lancaster, K. M.; Lymar, S. V.; Pfromm, P.; Schneider, W. F.; Schrock, R. R. Beyond Fossil Fuel-Driven Nitrogen Transformations. *Science* **2018**, *360*, eaar6611.
26. Foster, S. L.; Bakovic, S. I. P.; Duda, R. D.; Maheshwari, S.; Milton, R. D.; Minteer, S. D.; Janik, M. J.; Renner, J. N.; Greenlee, L. F. Catalysts for Nitrogen Reduction to Ammonia. *Nat. Catal.* **2018**, *1*, 490-500.
27. Yang, Y.; Xiong, Y.; Zeng, R.; Lu, X.; Krumov, M.; Huang, X.; Xu, W.; Wang, H.; DiSalvo, F. J.; Brock, J. D.; Muller, D. A.; Abruña, H. D. *Operando* Methods in Electrocatalysis. *ACS Catal.* **2021**, *11*, 1136-1178.
28. Zeng, Z.; Zheng, W.; Zheng, H. Visualization of Colloidal Nanocrystal Formation and Electrode-Electrolyte Interfaces in Liquids Using TEM. *Acc. Chem. Res.* **2017**, *50*, 1808-1817.
29. Williamson, M.; Tromp, R.; Vereecken, P.; Hull, R.; Ross, F. Dynamic Microscopy of Nanoscale Cluster Growth at the Solid-Liquid Interface. *Nat. Mater.* **2003**, *2*, 532-536.
30. Holtz, M. E.; Yu, Y.; Gunceler, D.; Gao, J.; Sundararaman, R.; Schwarz, K. R.; Arias, T. A.; Abruña, H. D.; Muller, D. A. Nanoscale Imaging of Lithium Ion Distribution during In Situ Operation of Battery Electrode and Electrolyte. *Nano Lett.* **2014**, *14*, 1453-1459.
31. Karki, K.; Serra-Maia, R.; Stach, E.; Alsem, D. H.; Salmon, N. Realistic Bulk Electrochemistry in Liquid Cell Microscopy. *Micro. Microanal.* **2020**, *26*, 1458-1459.
32. Khelifa, A.; Byun, C.; Nelayah, J.; Wang, G.; Ricolleau, C.; Alloyeau, D. Structural Analysis of Single NPs in Liquid by Low-Dose STEM Nanodiffraction. *Micron* **2019**, *116*, 30-35.
33. Karakulina, O. M.; Demortiere, A.; Dachraoui, W.; Abakumov, A. M.; Hadermann, J. In Situ Electron Diffraction Tomography Using A Liquid-Electrochemical Transmission Electron Microscopy Cell for Crystal Structure Determination of Cathode Materials for Li-Ion Batteries. *Nano Lett.* **2018**, *18*, 6286-6291.
34. Schneider, N. M.; Norton, M. M.; Mendel, B. J.; Grogan, J. M.; Ross, F. M.; Bau, H. H. Electron-Water Interactions and Implications for Liquid Cell Electron Microscopy. *J. Phys. Chem. C* **2014**, *118*, 22373-22382.
35. Zuo, J. M.; Tao, J. Scanning Electron Nanodiffraction and Diffraction Imaging. In: S. Pennycook, P. Nellist (eds) Scanning Transmission Electron Microscopy, Springer, New York, 2011.
36. Ophus, C. Four-Dimensional Scanning Transmission Electron Microscopy (4D-STEM): From Scanning Nanodiffraction to Ptychography and Beyond. *Micro. Microanal.* **2020**, *25*, 563-582.
37. Clavilier, J.; Faure, R.; Guinet, G.; Durand, R. Preparation of Monocrystalline Pt

- Microelectrodes and Electrochemical Study of The Plane Surfaces Cut in the Direction of the {111} And {110} Planes. *J. Electroanal. Chem.* **1980**, *107*, 205-209.
38. Vidal-Iglesias, F. J.; Aran-Ais, R. M.; Solla-Gullon, J.; Herrero, E.; Feliu, J. M. Electrochemical Characterization of Shape-Controlled Pt NPs in Different Supporting Electrolytes. *ACS Catal.* **2011**, *2*, 901-910.
39. Hersbach, T. J. P.; Ye, C.; Garcia, A. C.; Koper, M. T. M. Tailoring the Electrocatalytic Activity and Selectivity of Pt(111) Through Cathodic Corrosion. *ACS Catal.* **2020**, *10*, 15104-15113.
40. Arulmozhi, N.; Hersbach, T. J. P.; Koper, M. T. M. Nanoscale Morphological Evolution of Monocrystalline Pt Surfaces During Cathodic Corrosion. *Proc. Natl. Acad. Sci.* **2020**, *117*, 32267-32277.
41. Jiang, Y.; Chen, Z.; Han, Y.; Deb, P.; Gao, H.; Xie, S.; Purohit, P.; Tate, M. W.; Park, J.; S. M. Gruner; V. Elser; D. A. Muller, Electron ptychography of 2d materials to deep sub-ångström resolution. *Nature* **2018**, *559*, 343-349.
42. German, S. R.; Edwards, M. A.; Ren, H.; White, H. S. Critical Nuclei Size, Rate, and Activation Energy of H<sub>2</sub> Gas Nucleation. *J. Am. Chem. Soc.* **2018**, *140*, 4047-4053.
43. Holtz M. E.; Yu, Y.; Gao, J.; Abruña, H. D.; Muller, D. A. *In Situ* Electron Energy-Loss Spectroscopy in Liquids. *Microsc. Microanal.* **2013**, *19*, 1027-1035.
44. Zhang, J.; Sasaki, K.; Adzic, R. R. Stabilization of platinum oxygen-reduction electrocatalysts using gold clusters. *Science* **2007**, *315*, 220-222.
45. Yang, Y.; Xiao, W.; Feng, X.; Xiong, Y.; Gong, M.; Shen, T.; Abruña, H. D.; Wang, D. Golden Palladium Zinc Ordered Intermetallics as Oxygen Reduction Electrocatalysts. *ACS Nano* **2019**, *13*, 5968-5974.
46. Auffermann, G.; Muller, P.; Bronger, W. Neutron Scattering as a Powerful Tool in Solid State Chemistry. Examples From the Investigations in Crystal Structures and Properties of Metal Hydrogen and Metal Chalcogen Compounds. *Z. Anorg. Allg. Chem.* **2004**, *630*, 2113-2124.
47. Wang, X.; Andrews, L. Gold is Noble but Gold Hydride Anions are Stable. *Angew. Chem. Int. Ed.* **2003**, *42*, 5201-5206.
48. Rahm, M.; Hoffmann, R.; Ashcroft, N. W. Ternary Gold Hydrides: Routes to Stable and Potentially Superconducting Compounds. *J. Am. Chem. Soc.* **2017**, *139*, 8740-8751.
49. Elnagar, M. M.; Hermann, J. M.; Jacob, T.; Kibler, L. A. Faceting and Nanostructuring of Gold Surfaces through Cathodic Corrosion: Role of Cationic Electrolyte Species and Water. *ECS Meet. Abstr.* **2020**, MA2020-01, 1011-1011.

## CHAPTER 11

### Conclusions

#### 11.1 Summary

This thesis has witnessed and contributed to the fast-growing field of alkaline fuel cells over the past decade. Opportunities and challenges co-exist ahead. Since the first AEMFC was reported in 2008,<sup>1</sup> significant progress has been made to address both fundamental scientific challenges and potential practical applications. AEMFCs enable the use of non-precious ORR catalysts at the cathode while bringing another challenge of slow HOR kinetics at the anode. We have also learned, from the history of developing PEMFCs since 1960, that advances in nanosized ORR electrocatalysts, in particular Pt<sub>3</sub>Co/C intermetallics, and proton exchange membrane (e.g. Nafion) have been two of the most important driving forces for PEMFC technologies.

This thesis has focused on a fundamental question; how can we better understand the design principles of non-precious electrocatalysts and elucidate their reaction mechanisms in alkaline media? We have developed a family of spinel oxides as ORR electrocatalysts, in particular Co-Mn spinels, elucidated their catalytic mechanisms and evaluated catalyst performance in realistic MEA devices. Despite their modest ORR activity in RDE measurements, Co-Mn spinels achieved a benchmark MEA performance of over 1 W/cm<sup>2</sup> with a PtRu/C anode, for high-power electric vehicle applications, and a record 200 mW/cm<sup>2</sup> with a Ni-based anode for medium-to-low power applications, such as low-cost backup/stationary power. *Operando* X-ray spectroscopic studies and theoretical simulations supported a synergistic ORR mechanism in which Mn prefers to bind O<sub>2</sub> while Co activates co-adsorbed H<sub>2</sub>O, which

is fundamentally different from the conventional wisdom of ORR mechanisms of Pt-based alloys based on lattice strain and electronic effects. The superior MEA performance of Co-Mn spinels in low relative humidity, relative to Pt/C, was ascribed to the Co sites with unique capability to maintain H<sub>2</sub>O under water-depletion condition. Those studies highlight a fundamental aspect of the ORR mechanisms; H<sub>2</sub>O is the reactant and proton donor for the ORR in alkaline media whereas H<sub>2</sub>O is the product and H<sup>+</sup> is the proton donor for the ORR in acidic media.

One of the key remaining challenges in alkaline fuel cell technologies is to evaluate and improve long-term durability of non-precious electrocatalysts in MEA measurements. The RDE/MEA discrepancy points out the necessity of MEA measurements, even at the early stages of catalyst development. Future research should focus on deconvolving the catalyst durability from membrane/ionomer stability and mass transport at high current densities. With continuous advances in alkaline fuel cell technologies, it is foreseeable to achieve the DOE AEMFC MEA milestones of performance  $\geq 600 \text{ mW/cm}^2$  with long-term durability under H<sub>2</sub>/air in PGM-free MEA in the next decade.<sup>3</sup>

The second part of this thesis introduced the *operando* EC-STEM studies of electrochemical reactions at electrode/electrolyte interfaces. We presented the preliminary progress on resolving the electrochemical double layer (EDL), i.e. the ionic distributions at charged nanocrystal surfaces with systematic investigations of several chemical probes. The pursuit of the EDL led to the surprising observation of cathodic corrosion at the nm-scale. We employed EC-STEM to reveal that cathodic corrosion led to a significantly higher level of structural destruction for Au nanocubes than bulk Pt

electrodes, accompanied by the unexpected formation of Au-Pt alloy nanostructures, which are thermodynamically immiscible in the Au-Pt phase diagram. Dynamic evolution in morphology, composition, and crystallographic information was retrieved by analytical and four-dimensional STEM techniques. We designed a strategy to enable *operando*, *in situ* and *ex situ* EC-STEM operation in the same cell, and at identical locations to enable reliable electrochemical measurements of cathodic corrosion and simultaneously probe real-time interfacial changes by generating H<sub>2</sub> bubbles to reversibly control the liquid thickness. This microscopic study of cathodic corrosion of nanocrystals underlies the structural evolution of nanoscale electrocatalysts during many electrochemical reactions under highly reducing potentials, such as CO<sub>2</sub> and N<sub>2</sub> reduction. The *operando* EC-STEM strategies designed here can serve as a generalized platform for understanding interfacial electrocatalysis across multiple scales, allowing for our initial work on cathodic corrosion to be extendable beyond to other important energy-related electrochemical reactions.

In summary, electrocatalysis lies at the interface between chemistry and physics and represents one of the most promising approaches for renewable energy technologies. This thesis has contributed to the design and understanding of non-precious electrocatalysts for alkaline fuel cells, a long-standing interest that bridges interfacial electrocatalysis and real-world energy applications. With the continuous advances in techniques, *operando* TEM and X-ray based methods may lead to ground-breaking advances in addressing fundamental challenges in sustainable energy.

## 11.2 Future work

### 11.2.1 Elucidate ORR mechanism on MBE-grown single-crystal metal oxides

Nanoparticle catalysts provide large surface areas with morphology, surface composition and structures to tune for performance optimization. However, the ORR activity of nanoparticle catalysts depends on the synthesis methods employed, particle size (and its distribution), morphology, as well as surface and crystal structures. Those factors present formidable challenges to control simultaneously, and complicate our understanding of the intrinsic activity of electrocatalysts. Thus, we are interested in using single-crystal spinel oxides, with well-defined surface structures, to better understand the structure-(re)activity relationship(s) and identify the ORR active site(s). They have the potential to advance our understanding of ORR electrocatalysis like single-crystal Pt studies have done for metals.

In order to perform standard electrochemical measurements on well-defined oxides on insulating substrates, a custom-built rotating disk electrode (RDE) holder assembly, made of polyether ether ketone (PEEK), was designed with a front electrical contact (Fig. 11.1A).<sup>4</sup> We further employed a (110)-oriented RuO<sub>2</sub> film grown on an insulating TiO<sub>2</sub> (110) substrate to examine the application of the custom-built RDE for MBE-grown metal oxides. CV profiles of RuO<sub>2</sub> exhibit two well-defined redox peaks of Ru<sup>+3/+4</sup> (OH adsorption) and Ru<sup>+4/+5</sup> (O adsorption),<sup>5,6</sup> indicating the high quality of MBE-grown single-crystal oxides (Fig. 11.1B).

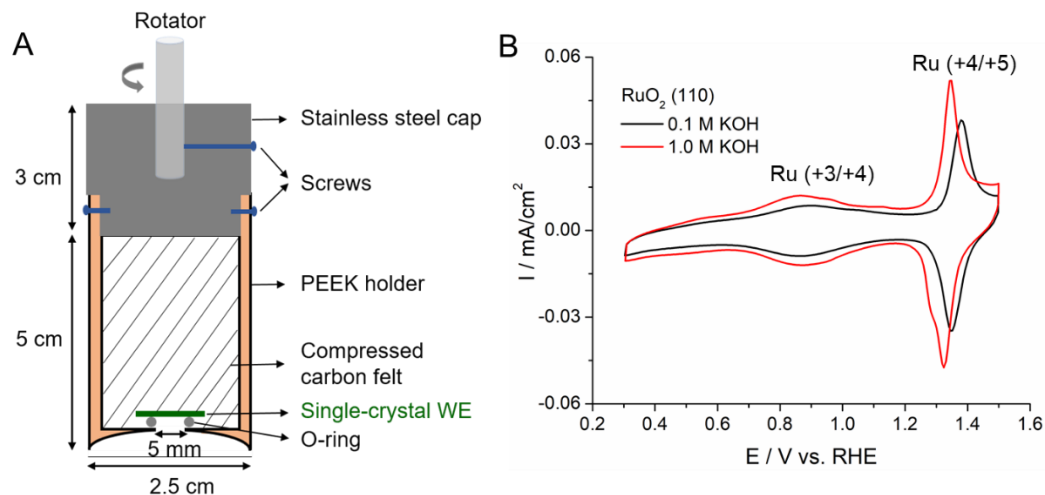


**Figure 11.1** (A) Customized RDE holder for MBE-grown single-crystal oxides. (B) CV profiles of  $\text{RuO}_2$  (110) at 50 mV/s in Ar-sat. 0.1 and 1 M KOH.

Preliminary experiments showed that MBE-grown  $\text{Co}_3\text{O}_4$  and  $\text{Mn}_3\text{O}_4$  single crystals are too resistive for electrochemical measurements and  $\text{Fe}_3\text{O}_4$  single crystals are semiconductors but not active for the ORR. In order to tackle this challenge, we designed Co-doped  $\text{Fe}_3\text{O}_4$  and revealed that a 15% Co-doping level achieved the optimal ORR activity in alkaline media (Figs. 11.2A-B). This was ascribed to the maximum number of Co active sites that could be incorporated without affecting the conductivity of the  $\text{Fe}_3\text{O}_4$  matrix. In an effort to search for conductive and active single-crystal metal oxides, perovskites,  $\text{LaMO}_3$  ( $\text{M}=\text{Ni}, \text{Mn}, \text{Co}$ ) have emerged as promising candidates. Conductive  $\text{LaNiO}_3$  was grown on a  $\text{LaAlO}_3$  substrate and showed an ORR activity higher than Co-doped  $\text{Fe}_3\text{O}_4$  by several orders of magnitude (Fig.11.2C). However,  $\text{LaNiO}_3$  is not stable at potentials lower than 0.7 V (Fig. 11.2D), which is possibly due to the unstable nature of  $\text{Ni}^{3+}$  in the structure.

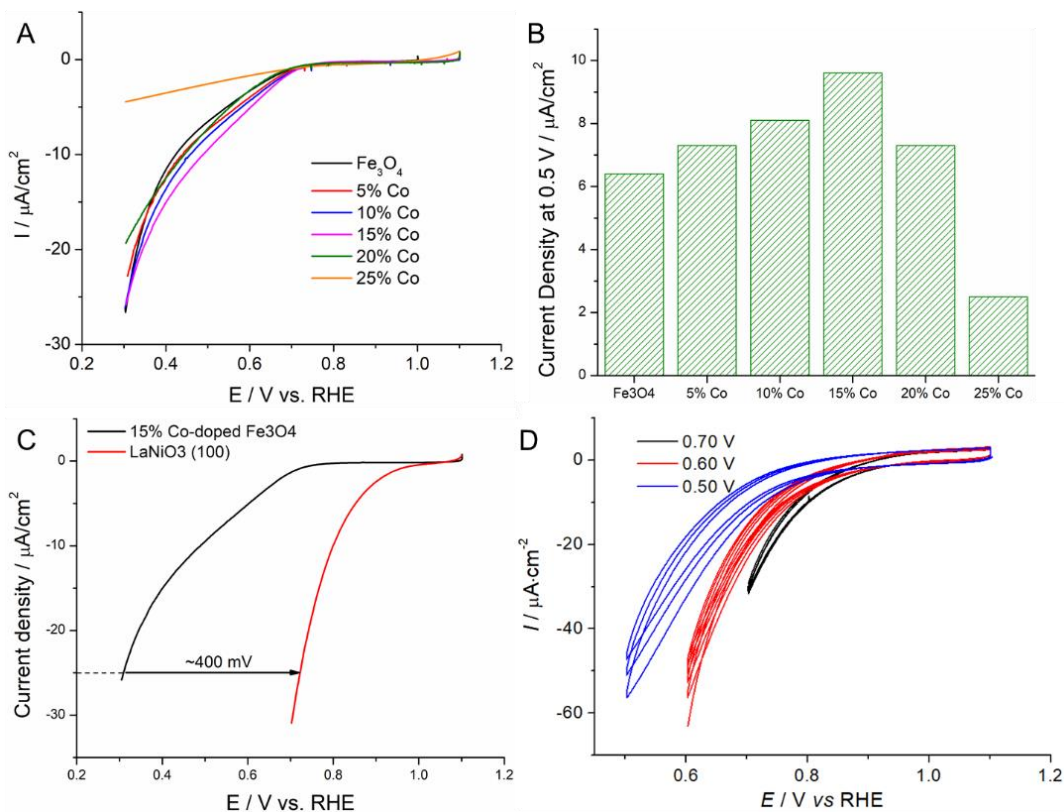


**Figure 11.2** (A) ORR polarization profiles of Co-doped Fe<sub>3</sub>O<sub>4</sub> single crystals on a MgO (100) substrate grown by MBE. (B) Kinetic current density at 0.5 V measured from (A) as a function of Co-doping level. (C) ORR profiles of 15% Co-doped Fe<sub>3</sub>O<sub>4</sub> and LaNiO<sub>3</sub> (100) on a LaAlO<sub>3</sub> substrate. (D) ORR profiles of LaNiO<sub>3</sub> (100) with different potential lower limits. All RDE measurements were conducted under the same conditions: O<sub>2</sub>-sat. 1M KOH at 1600 rpm and 5 mV/s.

RDE measurements of LaMO<sub>3</sub> (M=Ni, Mn, Co) nanoparticle catalysts showed that LaCoO<sub>3</sub> and LaMnO<sub>3</sub> are more active than LaNiO<sub>3</sub>. More interestingly, LaMnO<sub>3</sub> exhibited better ORR activity than LaCoO<sub>3</sub> in the kinetically-controlled regions (0.82-1 V vs. RHE) while LaCoO<sub>3</sub> showed higher ORR selectivity than LaMnO<sub>3</sub> in the mass transport-controlled regions (0.4-0.6 V vs. RHE). This intriguing finding shows a great potential to prepare single-crystal LaCo<sub>x</sub>Mn<sub>1-x</sub>O<sub>3</sub> with tuneable ORR activity and selectivity (Figure 11.3).

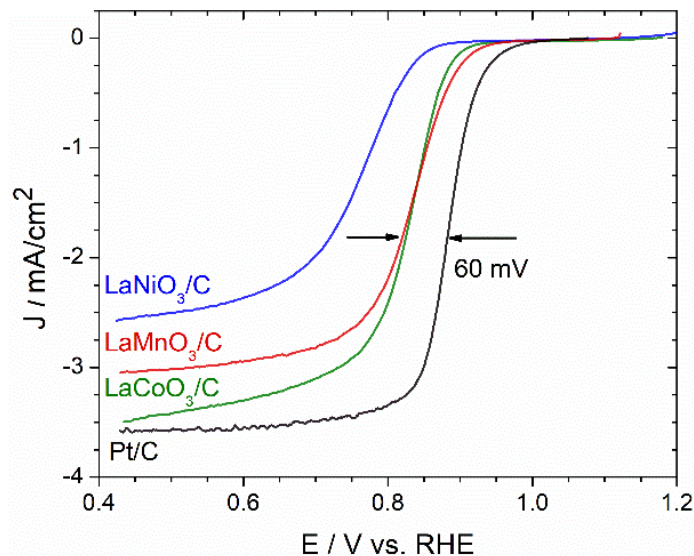


**Figure 11.3** ORR Polarization Profiles in O<sub>2</sub>-saturated 1M KOH at 1600rpm and 5mV/s. The E<sub>1/2</sub> values of LaMnO<sub>3</sub> and LaCoO<sub>3</sub> are only 60 mV away from that of Pt/C.

We proposed to first prepare pure LaMnO<sub>3</sub>/LaCoO<sub>3</sub> layered perovskites and examined their structure-(re)activity correlations (Fig. 11.4A-B). Given bulk LaCoO<sub>3</sub> is semiconductive, LaMnO<sub>3</sub> is insulating while LaNiO<sub>3</sub> is conductive, we plan to first epitaxially grow LaNiO<sub>3</sub> (100) films on single-crystal LaAlO<sub>3</sub> (100) substrates with a lattice mismatch of 1.3% and examine their ORR activity and stability (Fig. 11.4A). Subsequently, we will grow two types of layered structures, (LCO)<sub>2</sub>/(LNO)<sub>4</sub> and (LMO)<sub>2</sub>/(LNO)<sub>4</sub> with two layers of LCO or LMO on top of four layers of LNO and a surface termination of LCO or LMO. The lattice mismatches between LCO, LMO and LNO are 0.8% and 2.8%, respectively (Figs. 11.4B-C). A previous study on MBE-grown (LMO)<sub>2</sub>/(LNO)<sub>4</sub> superlattices reported a noticeable charge transfer from LaMnO<sub>3</sub> to LaNiO<sub>3</sub> layers, leading to a transition from Mn<sup>3+</sup>/Ni<sup>3+</sup> to Mn<sup>4+</sup>/Ni<sup>2+</sup>.<sup>7</sup> Such a change in electronic structure shows the potential to tune the ORR activity by controlling the number of layers of LMO or LCO (1-2 layers) and LNO (n ≥ 4). Finally, following observations from nanoparticle studies (Fig. 11.3), we plan to grow layered

LCO/LMO and LMO/LCO on top of the LNO underlayer to investigate the interaction between Mn and Co layers (Figs. 11.4D-E). The Co/Mn ratios in the first and second layers, and Ni in the underlayer, enable the precise control of surface composition and tuneability of the electronic structure of the electrode surface, which are expected to significantly influence ORR activity and stability.

Previously, through collaboration with Brock and Schlom groups, we employed *operando* X-ray reflectivity to measure the crystal truncation rod (CTR) to study the surface reordering of MBE-grown SrTiO<sub>3</sub> under applied potentials with joint DFT simulations, and identified an anatase-like (TiO<sub>2</sub>) surface, which is responsible for significant activity increase after electrochemical treatment.<sup>8</sup> We intend to use the same *operando* X-ray method to detect the surface structure change under electrochemical reaction conditions. With the first-principles joint DFT simulations, it is possible to provide a molecular-level picture of the oxygen adsorption on the oxide surfaces, and help identify possible ORR intermediates and the rate-determining step (RDS) in alkaline media.

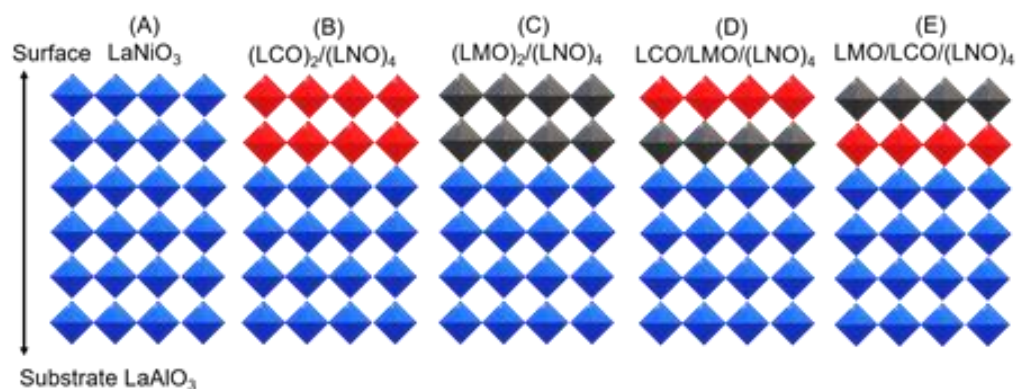


**Figure 11.4** Proposed epitaxial LaMO<sub>3</sub> films on LaAlO<sub>3</sub> (100) by MBE. (A) pure LaNiO<sub>3</sub>. (B-C) (LCO)<sub>2</sub>/(LNO)<sub>4</sub> and (LMO)<sub>2</sub>/(LNO)<sub>4</sub> layered structure (D-E) (LCO)/(LMO)/(LNO)<sub>4</sub> and (LMO)/(LCO)/(LNO)<sub>4</sub> layered structures

### 11.2.2 Spatially resolved local crystal structures of metal oxide nanoparticles

$\text{Co}_{1.5}\text{Mn}_{1.5}\text{O}_4/\text{C}$  has three different types of surface compositions, Co-rich shell (i.e. Mn-rich core), Mn-rich shell and Co, Mn evenly distributed, depending on the aging temperatures in the hydrothermal synthesis (Fig. 3.2).  $\text{Co}_{1.5}\text{Mn}_{1.5}\text{O}_4$  with homogenous distribution of Co and Mn showed the highest ORR activity in alkaline media. Synchrotron-based XRD patterns revealed that  $\text{Co}_{1.5}\text{Mn}_{1.5}\text{O}_4$  with a Co-rich or Mn-rich shell, exhibited tetragonal  $\text{CoMn}_2\text{O}_4$  and cubic  $\text{MnCo}_2\text{O}_4$  structures respectively, indicating that the dominant element in the core largely determined the overall crystal structure. However, why did  $\text{Co}_{1.5}\text{Mn}_{1.5}\text{O}_4$  with homogenous distribution of Co and Mn adapt the cubic and not the tetragonal spinel structure? This question can be addressed by spatially resolving the local crystal structures.

A recently developed electron microscope pixel array detector (EMPAD) provides STEM with a  $10^6:1$  dynamic range per frame, enabling the imaging of direct electron beam at the single electron sensitivity.<sup>9,10</sup> The EMPAD revolutionizes the scanning nanobeam electron diffraction (NBED) technique, which enables direct straining mapping of the local lattice structure at the atomic scale. The exit wave power cepstrum (EWPC) method has been developed by Padgett et al. as a robust data processing technique to decouple lattice information from the intensity variations in electron diffraction due to sample thickness variation and tilt.<sup>11</sup>

We used EMPAD to analyze  $\text{MnCo}_2\text{O}_4$  spinel oxide nanoparticles and were able to resolve the local variations of lattice structures, as shown in the color maps of lattice d-spacing differences ( $\sim 1\%$ ) in different lattice planes (Figure. 11.5). Those lattice planes in the tetragonal spinel structure would have slightly larger d-spacings than

corresponding cubic spinels, so that those regions in red are tetragonal while those in blue are cubic.

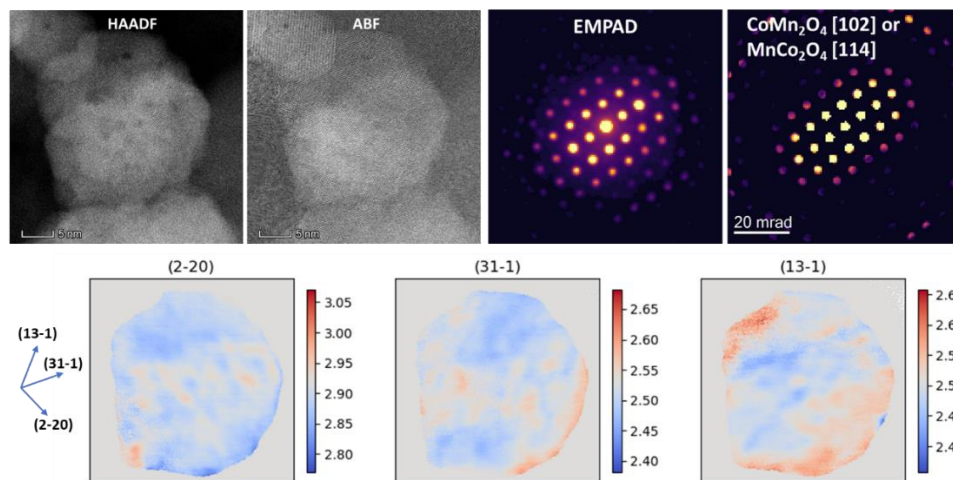


**Figure 11.5** Preliminary lattice map based on NBED of  $\text{MnCo}_2\text{O}_4$  nanoparticles.

However, those spinel particles, synthesized by hydrothermal methods, showed several challenges for obtaining high-quality NBED data, such as considerable sample inhomogeneity, large sample thickness (30-50 nm) and polycrystalline nature with defects. To tackle those challenges, we proposed to make small (less than 20 nm), highly crystalline metal oxide nanocrystals, which initiated a collaboration with the Fang group at Binghamton University, to make shape-controlled Mn-Co spinel oxides, which only expose certain facets of the surface. Early studies on octahedral and cubic  $\text{Co}_3\text{O}_4$  nanoparticles and DFT simulations by the Arias group suggested that octahedral  $\text{Co}_3\text{O}_4$  showed higher ORR activity than the cubic counterpart. Thus, we will focus on the synthesis of octahedral  $\text{MnCo}_2\text{O}_4$  and  $\text{CoMn}_2\text{O}_4$  nanocrystals, which requires the deliberate addition of surfactants in organic solvents. The removal of organic surfactant is essential for not only long-time NBED experiments but also electrochemical measurements. The strain mapping of nanocrystals will be critical for characterizing the

surface composition, distribution and structure for optimal ORR activities. This project will be carried out by Dasol Yoon from the Muller group in collaboration with the Fang group at CABES.

### 11.2.3 MEA measurements with long-term durability in H<sub>2</sub>-Air mode

CABES enables the close collaborations between fundamental studies of reaction mechanisms and realistic device evaluations. The assembly of fuel cell test stations and MEA testing protocols will be introduced in detail in **APPENDIX B**. The MEA studies at Cornell have really accelerated since we invited Qihao Li from the Zhuang group at WHU for an one-week training and dedicated collaborations with Zhifei from the Mallouk group at Penn ([Fig. 11.6](#)). We are now able to demonstrate peak power densities of 1.5 and 1 W/cm<sup>2</sup> for Pt and Mn-Co spinel cathodes in H<sub>2</sub>-O<sub>2</sub> mode ([Fig. 11.7](#)).

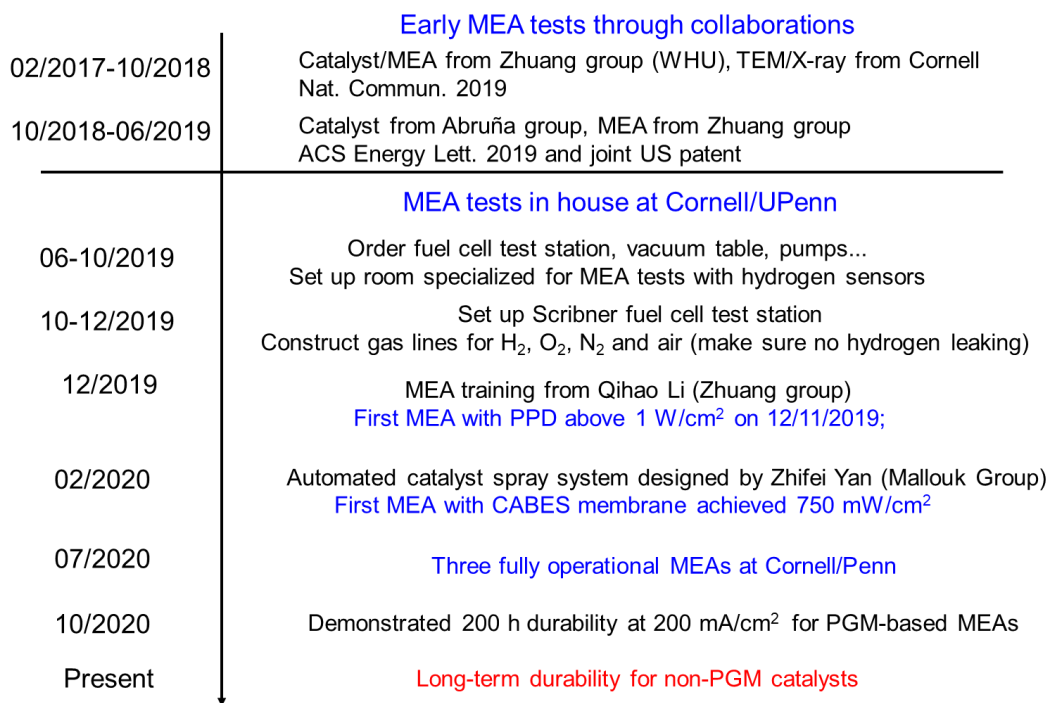


**Figure 11.6** Timeline of the progress of MEA studies at Cornell

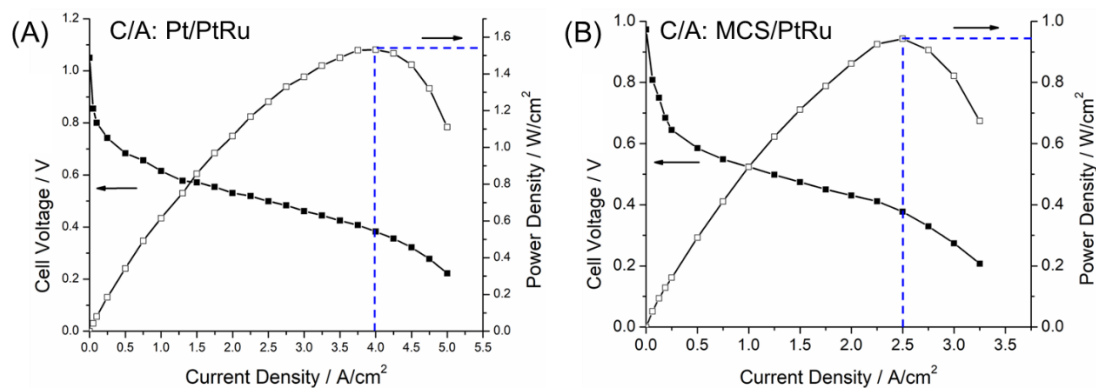


**Figure 11.7** MEA performance of Pt (A) and Mn-Co spinel (MCS) (B) as cathode catalysts. Mass loadings of Pt/C, PtRu/C and MCS/C are  $0.3 \text{ mg}_{\text{Pt}}/\text{cm}^2$ ,  $0.3 \text{ mg}_{\text{PtRu}}/\text{cm}^2$ ,  $0.8 \text{ mg}_{\text{oxide}}/\text{cm}^2$ , respectively. Test conditions are  $\text{H}_2\text{-O}_2$  mode with fully humidified gases at a flow rate of  $1000 \text{ mL}/\text{min}$  and backpressure of  $0.2 \text{ MPa}$  at a cell temperature of  $80 \text{ }^\circ\text{C}$ .

Besides the promising progress on non-precious ORR electrocatalysts, we also need to tackle the challenge of developing high-performance HOR electrocatalysts since the HOR in alkaline media is 100 times slower than in acidic media and requires a significant amount of Pt or Pt-Ru catalysts. We recently developed Ni-based HOR catalysts with a Ni core and a N-doped carbon shell,  $\text{CN}_x$ , in collaboration with the Zhuang group (Figures 11.8A-C).  $\text{CN}_x$  shell effectively suppressed the oxidation of Ni on the surface, which was the key to prevent the performance degradation of Ni at polarization potentials above  $0.2 \text{ V}$ . As a result,  $\text{Ni}@\text{CN}_x$  showed significantly enhanced activity and durability in MEA tests, relative to bare Ni nanoparticles.  $\text{Ni}@\text{CN}_x$  achieved a PPD of  $480 \text{ mW}/\text{cm}^2$  with Pt cathode at a current density of  $800 \text{ mA}/\text{cm}^2$  (Figure 11.8D). Furthermore,  $\text{Ni}@\text{CN}_x$  achieved a PPD of  $210 \text{ mW}/\text{cm}^2$  with Mn-Co spinel cathode, which is the highest among literatures of completely non-precious alkaline fuel cells published to date (Figure 11.8E).

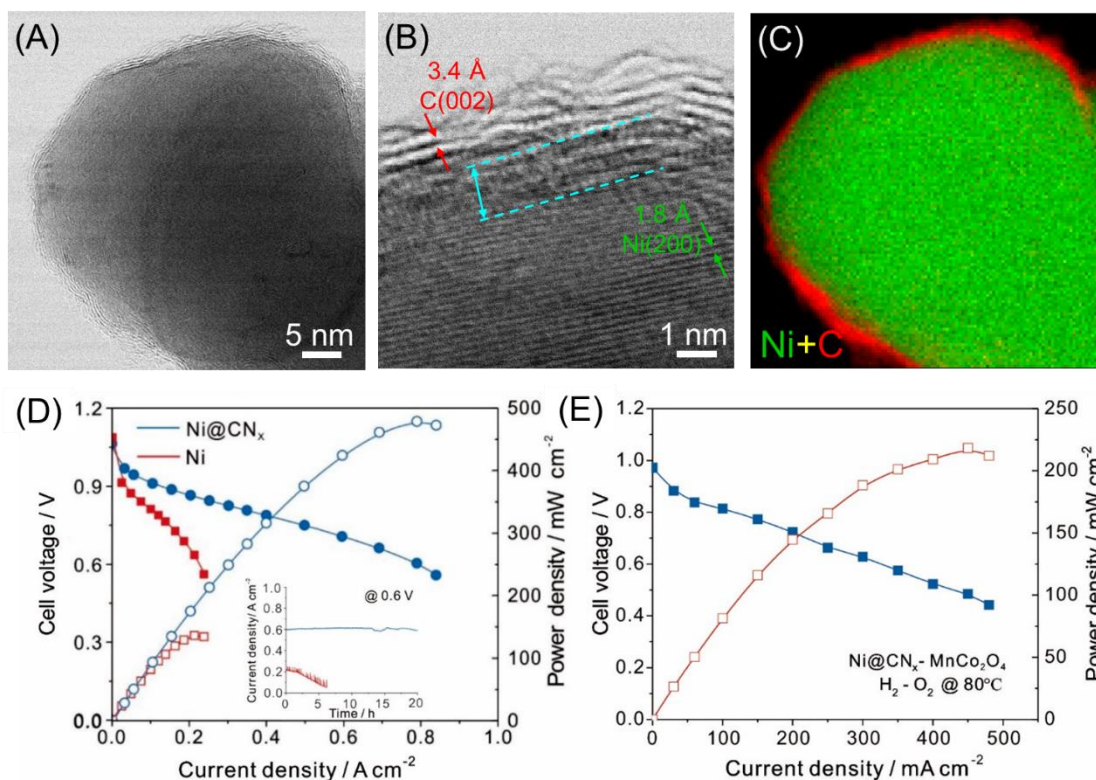


**Figure 11.8** Structure and MEA performance of Ni@CN<sub>x</sub> anode. (a-b) ADF-STEM images of Ni@CN<sub>x</sub> (c) EELS maps of Ni and C, showing the existence of a Ni core and 1-3 nm N-doped carbon shell. (d) MEA performance of Ni@CN<sub>x</sub> and Ni nanoparticles with a loading of 15 mg<sub>Ni</sub>/cm<sup>2</sup> and cathode catalysts of 60 wt.% Pt/C with a loading of 0.4 mg<sub>Pt</sub>/cm<sup>2</sup>. The inset describes stability test at a constant potential polarization at 0.6 V. (d) MEA performance using Ni@CN<sub>x</sub> as anode (15 mg<sub>Ni</sub>/cm<sup>2</sup>) and 80 wt.% MnCo<sub>2</sub>O<sub>4</sub> (1.5 mg<sub>oxide</sub>/cm<sup>2</sup>) as cathode catalysts. Fuel cell operation conditions: cell temperature of 80 °C, gas backpressure of 0.2 MPa on both sides of the cell. Fully humidified H<sub>2</sub> and O<sub>2</sub> were fed at a flow rate 500 ml/min.

Looking forward, we will continue to improve the MEA testing protocols and better understand the effects of relative humidity on flooding in the anode and water depletion in the cathode, gas pressure and flow rate, H<sub>2</sub>/O<sub>2</sub> reactant stoichiometries, and others. To really implement non-precious ORR catalysts for AEMFCs, we need to pay close attention to the long-term durability of the catalysts and AEM, which are often convolved. Non-precious catalysts experience mild particle aggregation, leading to smaller surface areas during accelerated durability tests in RDE, which needs to be

carefully examined in MEA tests. Non-precious catalysts, such as spinel oxides and Fe-N-C, often have a peroxide yield of 5-10%, higher than that of Pt/C (1-3%) and also potentially generate other radical species that can attack ionomers and membranes like nucleophilic reagents. During long-term durability tests,  $\text{OH}^-$  can also degrade the side chain and/or polymer backbone through  $\beta$ -elimination or Hofmann elimination. Analyzing degradation mechanism from just I-V curve measurements will be challenging and additional characterization techniques, such as impedance, NMR and cryo-TEM, will be particularly valuable to understand degradation mechanism(s).

Preliminary MEA measurements in  $\text{H}_2$ -air mode showed that the addition of  $\text{CO}_2$  (around 400 ppm in air) can cause a 50% performance loss. Several degradation mechanisms have been proposed and need to be verified by experimental evidence. For example,  $\text{CO}_2$  can react with  $\text{OH}^-$  and decrease the amount of accessible  $\text{OH}^-$  and lower the ionic conductivity. The origin of performance degradation, due to carbonation, is associated with the  $\text{CO}_2$  intake at the cathode and “self-purging” at the anode.<sup>12</sup> How to tackle this challenge remains an open question.

A recent DOE report proposed an AEMFC milestone of peak power performance of  $> 600 \text{ mW/cm}^2$  in  $\text{H}_2$ -air mode with PGM-free catalysts for the next decade.<sup>3</sup> With the approach of use-inspired research, I believe that our collaborative efforts at CABES will advance our understanding of the fundamental factors governing the activity and stability of catalysts and membranes/ionomers in alkaline media with the ultimate goal of achieving ultra-low Pt or precious-metal-free high-performance and durable alkaline fuel cells and related technologies. Electrocatalysis in alkaline media is a fast-growing community and I look forward to exciting research in this field in the near future.

### 11.3 References:

1. Lu S.; Pan J.; Huang A.; Zhuang L.; Lu J. Alkaline Polymer Electrolyte Fuel Cells Completely Free from Noble Metal Catalysts. *Proc. Natl. Acad. Sci.* **2008**, 105, 20611.
2. Xiong, Y.; Yang, Y.; Joress, H.; Padgett, E.; Gupta, U.; Yarlagadda, V.; Agyeman-Budu, D. N.; Huang, X.; Moylan, T. E.; Zeng, R.; Kongkanand, A.; Escobedo, F. A.; Brock, J. D.; DiSalvo, F. J.; Muller, D. A.; Abruña, H. D. Revealing the Atomic Ordering of Binary Intermetallics Using In Situ Heating Techniques at Multilength Scales. *Proc. Natl. Acad. Sci. U.S.A.* **2019**, 116, 1974-1983.
3. Tompson, S. T.; Peterson, D.; Ho, D.; Papageorgopoulos, D. Perspective—The Next Decade of AEMFCs: Near-Term Targets to Accelerate Applied R&D. *J. Electrochem. Soc.* **2020**, 167, 084514.
4. Yang, Y.; Zeng, R.; Paik, H.; Kuo, D.-Y.; Schlom, D.; DiSalvo, F.; Muller, D.; Suntivich, J.; Abruña, H. Epitaxial Thin-Film Spinel Oxides as Oxygen Reduction Electrocatalysts in Alkaline Media. *Chem. Mater.* **2021**, DOI: 10.1021/acs.chemmater.1c00388.
5. Goodenough, J. B.; Manoharan, R.; Paranthaman, M. Surface Protonation and Electrochemical Activity of Oxides in Aqueous Solution. *J. Am. Chem. Soc.* **1990**, 112, 2016-2082.
6. Kuo, D.-Y.; Paik, H.; Kloppenburg, J.; Faeth, B.; Shen, K. M.; Hautier, G.; Schlom, D. G.; Suntivich J. Measurements of Oxygen Electroadsorption Energies and Oxygen Evolution Reaction on RuO<sub>2</sub>(110): A Discussion of the Sabatier Principle and Its Role in Electrocatalysis. *J. Am. Chem. Soc.* **2018**, 140, 17597–17605.
7. Hoffman, J.; Tung, I. C.; Nelson-Cheeseman, B.; Liu, M.; Freeland, J. W.; Bhattacharya, A. Charge Transfer and Interfacial Magnetism in (LaNiO<sub>3</sub>)<sub>n</sub>/(LaMnO<sub>3</sub>)<sub>2</sub> Superlattices. *Phys. Rev. B* **2013**, 88, 144411.
8. Plaza, M.; Huang, X.; et al. Schlom, D. G.; Arias, T. A.; Brock, J. D.; Abruña, H. D. Structure of the Photo-catalytically Active Surface of SrTiO<sub>3</sub>. *J. Am. Chem. Soc.* **2016**, 138, 7816-7819.
9. Jiang, Y.; Chen, Z.; Muller, D. A. Electron Ptychography of 2D Materials to Deep Sub-ångström Resolution. *Nature*, **2018**, 559, 343-349.
10. Tate, M. W.; Purohit, P.; Chamberlain, D.; Nguyen, K. X.; Hovden, R.; Chang, C. S.; Deb, P.; Turgut, E.; Heron, J. T.; Schlom, D. G.; Ralph, D.; Fuchs, G. D.; Shanks, K. S.; Philipp, H. T.; Muller, D. A.; Gruner, S. M. High Dynamic Range Pixel Array Detector for Scanning Transmission Electron Microscopy. *Microsc. Microanal.* **2016**, 22, 237-249.
11. Padgett, E.; Holtz, M. E.; Cueva, P.; Langenberg, E.; Schlom, D. G.; Muller, D. A. The Exit-Wave Power-Cepstrum Transform for Scanning Nanobeam Electron Diffraction. Part 1: Robust Strain Mapping at Subnanometer Resolution and Subpicometer Precision. *Ultramicroscopy* **2020**, 214, 112994.
12. Zheng, Y.; Omasta, T. J.; Peng, X.; Wang, L.; Varcoe, J. R.; Pivovar, B. S.; Mustain, W. E. Quantifying and Elucidating the Effect of CO<sub>2</sub> on the Thermodynamics, Kinetics and Charge Transport of AEMFCs. *Energy Environ. Sci.* **2019**, 12, 2806-2819.

## 11.4 Publications and Patents during PhD Studies

### Publications (#Equal contributions)

#### Design and Understand Non-Precious Fuel Cell Electrocatalysts at the Atomic-Scale Using *Operando/In Situ* Scanning/Transmission Electron Microscopy (STEM)

1. **Y. Yang**, Y. Xiong, M. Holtz, X. Feng, R. Zeng, F. DiSalvo, D. Muller, H. Abruña. Octahedral Spinel Electrocatalysts for Alkaline Fuel Cells. *Proc. Natl. Acad. Sci.* 2019, 116, 244425.
2. **Y. Yang**, R. Zeng, Y. Xiong, F. DiSalvo, H. Abruña. Cobalt-Based Nitride-Core Oxide-Shell Oxygen Reduction Electrocatalysts. *J. Am. Chem. Soc.* 2019, 141, 19241.
3. **Y. Yang**, G. Chen, R. van Dover, H. Abruña, Combinatorial Studies of Palladium-Based Oxygen Reduction Electrocatalysts for Alkaline Fuel Cells, *J. Am. Chem. Soc.* 2020, 142, 8, 3980.
4. Y. Xiong,<sup>#</sup> **Y. Yang**,<sup>#</sup> H. Joress, E. Padgett, U. Gupta, V. Yarlagadda, A. Kongkanand, F. Escobedo, J. Brock, D. Muller, H. Abruña. Revealing the Atomic Ordering of Binary Intermetallics Using *In Situ* Heating Techniques at Multilength Scales. *Proc. Natl. Acad. Sci.* 2019, 116, 1974.  
**Y. Yang**, et al. H. Abruña, D. Muller. *Microsc. Microanal.* 2019, 25, 1488.
5. Y. Xiong,<sup>#</sup> **Y. Yang**,<sup>#</sup> F. DiSalvo, H. Abruña. Pt-Decorated Composition-Tunable Pd-Fe@Pd/C Core-Shell Nanoparticles with Enhanced Electrocatalytic Activity towards the Oxygen Reduction Reaction. *J. Am. Chem. Soc.* 2018, 140, 7248. (JACS Cover Story)
6. **Y. Yang**, H. Peng, Y. Xiong, Q. Li, J. Lu, L. Xiao, L. Zhuang, H. Abruña. High-loading Composition-Tolerant Co-Mn Spinel Oxides with Performance beyond 1W/cm<sup>2</sup> in Alkaline Polymer Electrolyte Fuel Cells. *ACS Energy Lett.* 2019, 4, 1251.
7. **Y. Yang**, W. Xiao, X. Feng, Y. Xiong, H. Abruña, D. Wang. Golden Palladium Zinc Ordered Intermetallics as Oxygen Reduction Electrocatalysts. *ACS Nano* 2019, 13, 5968.
8. **Y. Yang**, R. Zeng, Y. Xiong, F. DiSalvo, H. Abruña, Rock-salt-type MnCo<sub>2</sub>O<sub>3</sub>/C as Efficient Oxygen Reduction Electrocatalysts for Alkaline Fuel Cells. *Chem. Mater.* 2019, 31, 9331.
9. Y. Xiong,<sup>#</sup> **Y. Yang**,<sup>#</sup> H. Abruña. Metal–Organic-Framework-Derived Co–Fe Bimetallic Oxygen Reduction Electrocatalysts for Alkaline Fuel Cells. *J. Am. Chem. Soc.* 2019, 141, 10744.
10. **Y. Yang**, R. Zeng, H. Paik, D.-Y. Kuo, D. Schlom, F. DiSalvo, D. Muller, J. Suntivich, H. Abruña. Epitaxial Thin-Film Spinel Oxides as Oxygen Reduction Electrocatalysts in Alkaline Media. *Chem. Mater.* 2021, In Press.
11. Y. Xiong,<sup>#</sup> **Y. Yang**,<sup>#</sup> F. DiSalvo, H. Abruña. Synergistic Bimetallic MOF-Derived Pt-Co Oxygen Reduction Electrocatalysts. *ACS Nano* 2020, 14, 13069-13080.
12. Z. Li,<sup>#</sup> **Y. Yang**,<sup>#</sup> H. Abruña, L. Zhuang. Interface Enhanced Catalytic Selectivity on the C<sub>2</sub> Products of CO<sub>2</sub> Electroreduction. *ACS Catal.* 2020, 11, 2473-2482.
13. J. Zhu,<sup>#</sup> **Y. Yang**,<sup>#</sup> L. Chen, W. Xiao, H. Liu, H. Abruña, D. Wang. Copper-Induced Formation of Ordered Pt-Fe-Cu Ternary Intermetallic Electrocatalysts with Tunable Phase Structure and Improved Stability. *Chem. Mater.* 2018, 30, 5987.
14. H. Wang, **Y. Yang**, F. DiSalvo, H. Abruña, Multi-functional Electrocatalysts: Ru-M

- (M=Co, Ni, Fe) for Alkaline Fuel Cells and Electrolyzers. *ACS Catal.* 2020, 10, 4608.
15. Y. Xie, **Y. Yang**, D. Muller, H. Abruña, N. Dimitrov, J. Fang, Enhanced ORR Kinetics on Au-Doped Pt-Cu Porous Films in Alkaline Media. *ACS Catal.* 2020, 10, 9967.
  16. R. Zeng, **Y. Yang**, et al. H. Abruña, Methanol Oxidation Using Ternary Ordered Intermetallic Electrocatalysts: A DEMS Study. *ACS Catal.* 2020, 10, 770.
  17. H. Ren, Y. Wang, **Y. Yang**, H. Abruña, L. Zhuang, Fe/N/C Nanotubes with Atomic Fe Sites: A Highly Active Cathode Catalyst for Alkaline Polymer Electrolyte Fuel Cells. *ACS Catal.* 2017, 7, 6485.
  18. Y. Xiong, L. Xiao, **Y. Yang**, F. DiSalvo, H. Abruña, High-Loading Intermetallic Pt<sub>3</sub>Co/C Core-shell Nanoparticles as Enhanced Activity Electrocatalyst towards the Oxygen Reduction Reaction. *Chem. Mater.* 2018, 30, 1532.
  19. T. Shen, S. Chen, et al. **Y. Yang**, D. Wang, H. Xin, Héctor Abruña, Tailoring the Anti-Poisoning Performance of Pd for Formic Acid Electrooxidation via an Ordered PdBi Intermetallic. *ACS Catal.* 2020, 10, 9977.
- **Operando X-ray Absorption Spectroscopy of Fuel Cell Electrocatalysts**
    20. **Y. Yang**, Y. Wang, Y. Xiong, et al. J. Brock, L. Zhuang, H. Abruña, *In Situ* X-ray Absorption Spectroscopy of a Synergistic Co–Mn Oxide Catalyst for the Oxygen Reduction Reaction. *J. Am. Chem. Soc.* 2019, 141, 1463.
    21. Y. Xiong,<sup>#</sup> **Y. Yang**,<sup>#</sup> F. DiSalvo, H. Abruña, A Strategy for Increasing the Efficiency of the Oxygen Reduction Reaction in Mn-Doped Cobalt Ferrites. *J. Am. Chem. Soc.* 2019, 141, 4412.
    22. Y. Wang, **Y. Yang**, et al. D. Muller, H. Abruña, L. Zhuang, Synergistic Mn-Co Catalyst Outperforms Pt on High-Rate Oxygen Reduction for Alkaline Polymer Electrolyte Fuel Cells. *Nat. Commun.* 2019, 10, 1506.
  - **Cryogenic STEM Imaging and EDX Mapping for Reliable Characterizations of Sulfur Cathode in Lithium Sulfur Battery**
    23. **Y. Yang**, B. Levin, N. Zhang, H. Abruña, D. Muller, Cryo-STEM-EDX for Reliable Characterization of Sulfur Distribution and the Rational Design of Sulfur Hosts for Li-S Batteries. *Microsc. Microanal.* 2020, 26, 1654-1658.
    24. X.-C. Liu,<sup>#</sup> **Y. Yang**,<sup>#</sup> et al. D. Muller, H. Abruña, F.-S. Ke, Dynamic Hosts for High Performance Li-S Batteries Studied by Cryo-TEM and In Situ XRD. *ACS Energy Lett.* 2018, 3, 1325.
    25. N. Zhang,<sup>#</sup> **Y. Yang**,<sup>#</sup> X. Feng, S. Yu, J. Seok, D. Muller, H. Abruña, Sulfur Encapsulation by MOF-Derived CoS<sub>2</sub> Hosts for High-Performance Li–S Batteries. *J. Mater. Chem. A* 2019, 7, 21128. **(Hot Papers)**
    26. N. Zhang, B. Levin, **Y. Yang**, D. Muller, H. Abruña. Porous Fe<sub>3</sub>O<sub>4</sub> Nanospheres as Effective Sulfur Hosts for Li-S Batteries. *J. Electrochem. Soc.* 2018, 165, A1656.
  - **Electron Microscopy and Spectroscopy Characterizations of Electrode Materials in Advanced Lithium Ion Batteries and Functional Nanomaterials**
    27. D. Ren,<sup>#</sup> **Y. Yang**,<sup>#</sup> H. Abruña. Ni-Rich LiNi<sub>0.88</sub>Mn<sub>0.06</sub>Co<sub>0.06</sub>O<sub>2</sub> Cathode Interwoven by Carbon Fiber with Improved Rate Capability and Stability. *J. Power Sources.* 2019, 447, 227344.

28. D. Ren, E. Padgett, **Y. Yang**, B. Levin, et al. D. Muller, H. Abruña. Ultrahigh Rate Performance of a Robust Lithium Nickel Manganese Cobalt Oxide Cathode with Preferentially Orientated Li-Diffusing Channels. *ACS Appl. Mater. Interfaces* 2019, 11, 41178.
29. D. Ren, Y. Shen, **Y. Yang**, et al. D. Muller, H. Abruña. Systematically Optimization: Key Parameters to the Scalable Synthesis of Uniform, High-Energy and Highly Stable  $\text{LiNi}_{0.6}\text{Mn}_{0.2}\text{Co}_{0.2}\text{O}_2$  Cathode Material for Lithium-Ion Battery. *ACS Appl. Mater. Interfaces*. 2017, 9, 35811.
30. X. Xiao, P. Urbankowski, K. Hantanasirisakul, **Y. Yang**, et al. H. Abruña, Y. Gogotsi. Scalable Synthesis of Ultrathin  $\text{Mn}_3\text{N}_2$  Exhibiting Room-Temperature Antiferromagnetism. *Adv. Funct. Mater.* 2019, 1809001.
31. X. Xiao, H. Wang, W. Bao, P. Urbankowski, L. Yang, **Y. Yang**, et al. Y. Gogotsi. Two-Dimensional Arrays of Transition Metal Nitride Nanocrystals. *Adv. Mater.* 2019, 1902393.
32. Y. Huang, J. Ouyang, X. Tang, **Y. Yang**, J. Qian, J. Lu, L. Xiao, L. Zhuang,  $\text{NiGa}_2\text{O}_4/\text{rGO}$  Composite as Long-Cycle-Life Anode Material for Lithium-Ion Batteries. *ACS Appl. Mater. Interfaces*. 2019, 11, 8025.
33. X. Tang, X. Huang, Y. Huang, Y. Gou, **Y. Yang**, et al. H. Abruña, L. Zhuang. High-Performance  $\text{Ga}_2\text{O}_3$  Anode for Lithium-Ion Batteries. *ACS Appl. Mater. Interfaces*. 2018, 10, 5519.
34. S. Yu, A. Jin, X. Huang, **Y. Yang**, R. Huang, J. Brock, Y.-E. Sung, H. Abruña. SnS/C nanocomposites for high-performance sodium ion battery anodes. *RSC Adv.* 2018, 8, 23847.

● **Invited Reviews**

35. **Y. Yang**, C. Peltier, R. Zeng, R. Schimmenti, Q. Li, X. Huang, Z. Yan, G. Potsi, R. Selhorst, X. Lu, W. Xu, M. Tader, A. Soudackov, H. Zhang, M. Krumov, E. Murray, P. Xu, J. Hitt, L. Xu, H.-Y. Ko, B. Ernst, C. Bundschu, A. Luo, D. Markovich, M. Hu, C. He, H. Wang, J. Fang, R. DiStasio Jr., L. Kourkoutis, A. Singer, K. J. T. Noonan, L. Xiao, L. Zhuang, B. Pivovar, P. Zelenay, J. Feliu, E. Herrero, J. Suntivich, E. Giannelis, S. Hammes-Schiffer, T. Arias, M. Mavrikakis, T. Mallouk, J. Brock, D. Muller, F. DiSalvo, G. Coates, H. Abruña. Electrocatalysis in Alkaline Media and Alkaline-Based Energy Technologies. *Chem. Rev.* 2021, In Press.
36. **Y. Yang**, Y. Xiong, R. Zeng, X. Lu, M. Krumov, H. Wang, J. Brock, D. Muller, F. DiSalvo, H. Abruña, *Operando* Methods in Electrocatalysis. *ACS Catal.* 2021, 11, 1136-1178.
37. S. Lang, X. Feng, J. Seok, **Y. Yang**, M. Krumov, H. Abruña, Lithium Sulfur Redox: Challenges and Opportunities. *Curr. Opin. Electrochem.* 2021, 25, 100652.

**More information:** <https://scholar.google.com/citations?user=OiVZxMAAAAAAJ&hl=en>

**Patents**

- ❖ Titanium Disulfide-Sulfur Composites, *International Patent*, 2019, WO2019126499A1.
- ❖ Cobalt-Manganese Spinel Oxide Catalysts. *U.S. Patent*, 2019, No. 62/818,843.

## APPENDIX

### A. Testing Protocols for RDE Measurements

Rotating disk electrode (RDE) have been extensively used as a rapid screening tool to evaluate the catalyst activity before performing measurements in practical membrane electrode assembly (MEA) devices. Large variations in reported activity (sometimes up to orders of magnitude) are not uncommon for RDE measurements in the literature. To have a rigorous comparison among different research groups, we need to establish standard RDE testing protocols. Here, I will provide a practical guide for how to perform RDE measurements and evaluate ORR activity.

**Preparation of catalyst ink:** 5 mg catalysts are mixed with 1.0 mL 0.05 wt.% Nafion/ethanol solution (catalyst to ionomer ratio of 12.5:1) and sonicated for about 30 min to form a homogenous catalyst ink. 10  $\mu$ L of the resulting catalyst ink is loaded onto a glassy carbon (GC) electrode (diameter, 5 mm) as the working electrode (WE). If the catalyst is quite hydrophobic (e.g. carbon support is graphitized after high-temperature treatment), isopropanol (IPA) works better than ethanol for catalyst dispersion. If the catalyst is quite heavy, such as metal oxide without carbon support, a higher mass fraction (0.1-0.5%) of Nafion binder can mitigate particle precipitation from solvent too quickly before depositing on the GC. If the catalyst ink does not cover the GC uniformly, either the catalyst or the GC is hydrophobic and treating the GC in HNO<sub>3</sub> can make the GC surface more hydrophilic. The mass loading of catalyst on the GC (e.g. 20wt.% Pt/C) can be calculated as follows, and the mass loading can be easily adjusted by changing the volume of catalyst ink deposited onto the GC.

$$\frac{\frac{5 \text{ mg}}{1 \text{ mL}} \times 10 \mu\text{L} \times 20\%}{\pi(0.25 \text{ cm})^2} \approx 50 \mu\text{g}_{\text{Pt}}/\text{cm}^2$$

**Impact of catalyst loadings:** It should be noted that for each type of catalyst, the measured MA or SA is relatively independent of catalyst loadings within a certain range (e.g., 20-50  $\mu\text{g}/\text{cm}^2$  for Pt NPs). Catalysts with too low loadings will not fully cover the GC electrode, resulting in a diffusion-controlled limit current density,  $j_d$ , less than that for  $4e^-$  process and often a larger amount of peroxide. Catalysts with too high loadings will have too thick catalyst layers, which complicates the interpretation of mass transport-controlled region. For example, with a low carbon loading of 0.1-0.2  $\text{mg}/\text{cm}^2$ , Pt/C (0.025  $\text{mg}_{\text{Pt}}/\text{cm}^2$ ) and Co<sub>4</sub>N/C (0.05  $\text{mg}_{\text{Co}_4\text{N}}/\text{cm}^2$ ) both showed a  $j_d$  of 3.7  $\text{mA}/\text{cm}^2$ , which is the theoretical value expected for  $4e^-$  process in 1M KOH at 1600 rpm (Fig. A.1). Increasing the loading of Co<sub>4</sub>N/C, from 0.05 to 0.2  $\text{mg}/\text{cm}^2$ , increased the  $E_{1/2}$  from 0.875 to 0.9V, surpassing that of Pt/C, indicating a higher ORR activity. However, Co<sub>4</sub>N/C with higher metal loadings of 0.1 to 0.2  $\text{mg}_{\text{Co}_4\text{N}}/\text{cm}^2$  also increased the  $j_d$  to 4.8  $\text{mA}/\text{cm}^2$ , much higher than that of Pt/C. Based on the Levich equation,  $j_d = 0.62nFAD^{2/3}\omega^{1/2}\nu^{-1/6}C$  where electron number,  $n=4$ ,  $A$  is the electrode area,  $D$  is the diffusion coefficient,  $\omega$  is the angular rotation rate,  $\nu$  is the kinematic viscosity and  $C$  is the bulk O<sub>2</sub> concentration. At given testing conditions, it is very likely that the observed larger  $j_d$  was due to an increase in the effective electrode geometric area,  $A$ . As shown in Fig. A.1, Co<sub>4</sub>N/C with a metal loading of 0.2  $\text{mg}/\text{cm}^2$  and thus a carbon loading of 0.8  $\text{mg}/\text{cm}^2$  is as thick as 50  $\mu\text{m}$  and the side can contribute up to a 20% increase in the total electrode area, which explained why the  $j_d$  is larger than the theoretical values by 20% for  $4e^-$  process. Thus, we recommend that RDE measurements with various loadings are required to perform for each newly developed catalyst to assess the impact of loadings on measured activity. The same optimal loading then

should be selected for the same family of catalysts.

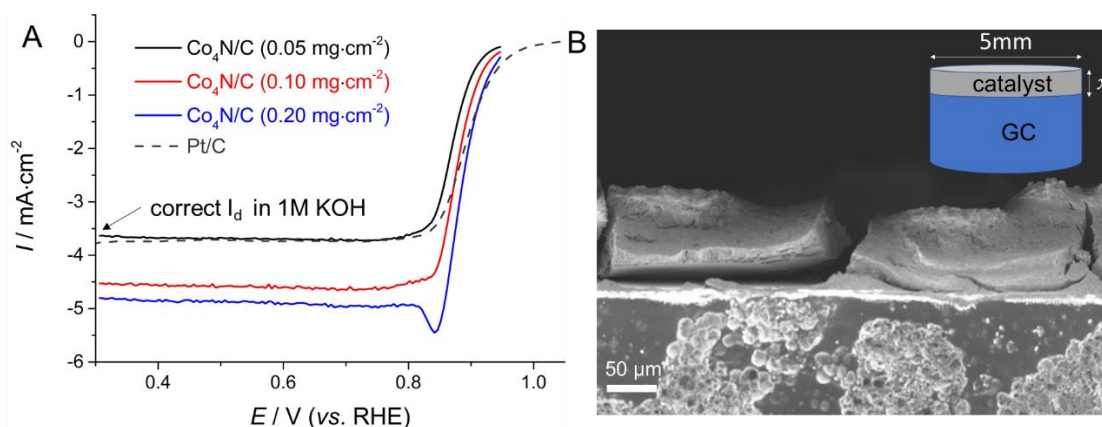


**Figure A.1** (A) RDE measurement of ORR polarization profiles of Pt/C (20 wt.%) and Co<sub>4</sub>N/C (20 wt.%) with various Co<sub>4</sub>N loadings at 1600 rpm and 5mV/s. Pt/C has a Pt loading of 0.025 mg/cm<sup>2</sup> and carbon loading of 0.1 mg/cm<sup>2</sup>. Co<sub>4</sub>N/C has a Co<sub>4</sub>N loadings of 0.05, 0.1 and 0.2 mg/cm<sup>2</sup>, corresponding to carbon loadings of 0.2, 0.4 and 0.8, respectively. (B) Cross-sectioned SEM image of Co<sub>4</sub>N/C (0.2 mg<sub>Co<sub>4</sub>N</sub>/cm<sup>2</sup> and 0.8 mg<sub>carbon</sub>/cm<sup>2</sup>).

**Impact of ionomers:** The main focus at the CABES will be devoted to developing catalysts in alkaline media, the use of Nafion, an ionomer designed for PEMFCs, seems to be problematic because it does not conduct OH<sup>-</sup>. While Nafion cannot be used as ionomers in AEMFCs, it generally works well as a polymer binder for RDE measurements in an ocean of hydroxide solution. As shown in [Figs. A.2A-B](#), Pt/C with Nafion or QAPPT alkaline ionomers (Pt/C to ionomer ratio is 4:1) exhibit nearly same ORR polarization profiles although Pt/C with Nafion ionomer shows a slightly smaller ECSA calculated from the H<sub>UPD</sub> region. Quantitative analysis in [Table A.1](#) shows that Pt/C with Nafion ionomer shows slightly lower E<sub>1/2</sub> and nearly same mass activity, relative to Pt/C with QAPPT ionomer. Those results suggest that the use of Nafion has a minimal impact on the ORR kinetics in alkaline media. However, alkaline ionomers, such as QAPPT, are recommended as the same ionomer in both RDE and MEA

measurements to better assess catalyst activity.

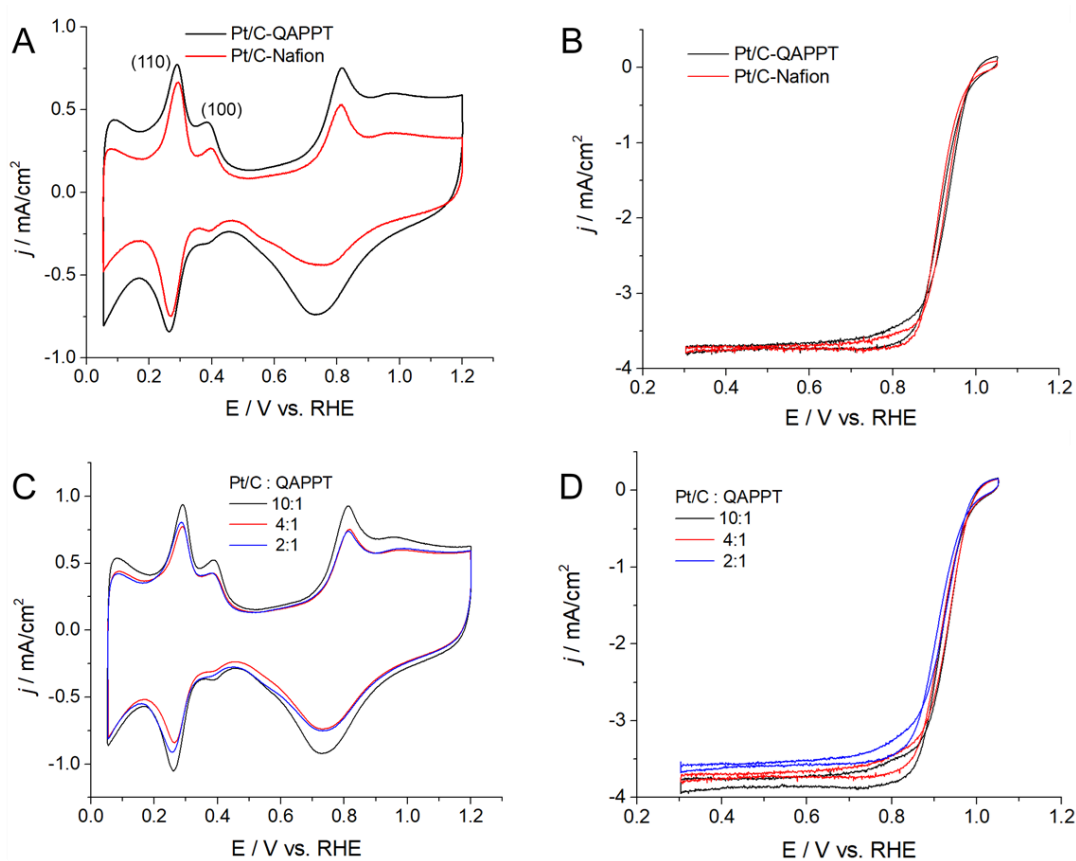


**Figure A.2** (A-B) CV and RDE measurements of Pt/C (60 wt.%) with a Pt/C to Nafion or QAPPT ionomer mass ratio of 4:1. Loadings of Pt/C, Pt and ionomer are 100, 60 and 25  $\mu\text{g}/\text{cm}^2$ , respectively. (C-D) CV and RDE measurements of Pt/C with catalyst to ionomer ratios of 10:1, 4:1 and 2:1. CV profiles were acquired in Ar-sat. 1 M KOH at 20 mV/s and RDE profiles were acquired in  $\text{O}_2$ -sat. 1 M KOH at 5 mV/s and 1600 rpm. Nafion ionomer is dispersed in ethanol while QAPPT alkaline ionomer is first dissolved in DMSO (2 wt.%) and then diluted in n-propanol. QAPPT stands for quaternary ammonium poly (N-methyl-piperidine-co-p-terphenyl).

Figure A.2C-D presents Pt/C with different catalyst to QAPPT ionomer mass ratios of 10:1, 4:1 and 2:1. Besides slight variations in the ECSA, Pt/C/QAPPT with a 10:1 mass ratio shows nearly same  $E_{1/2}$ , MA and SA as that with a 4:1 mass ratio (Table A.1). It should be noted that a 10:1 mass ratio has been widely adapted in literature for Nafion

as a binder in RDE tests while a 4:1 mass ratio is now the standard recipe in this group for QAPPT alkaline ionomer in MEA tests. Further increase Pt/C to QAPPT ratio to 2:1 leads to a negative shift in  $E_{1/2}$  by 13 mV, a decay of MA from 0.16 to 0.1 mA/g<sub>Pt</sub>, decay of SA from 0.34 to 0.22 mA/cm<sup>2</sup><sub>Pt</sub>, relative to that with 4:1 mass ratio (Table A.1). It indicates that a 2:1 Pt/C / QAPPT ratio has excess ionomer that blocks the active sites and impedes the ORR kinetics. In addition, a relatively larger amount of QAPPT ionomers also lowers the  $j_d$  slightly below the expected 3.7 mA/cm<sup>2</sup> for a 4e<sup>-</sup> ORR in 1 M KOH at 1600 rpm, which is possibly due to the effect of alkaline ionomers on the effective O<sub>2</sub> concentration in the catalyst layer or leading to a higher peroxide yield.

Catalysts/ionomers	H <sub>UPD</sub> ECSA/ m <sup>2</sup> <sub>Pt</sub> /g	E <sub>1/2</sub> / V vs. RHE	Mass Activity @ 0.9 V mA/g <sub>Pt</sub>	Surface Activity @ 0.9 V mA/cm <sup>2</sup> <sub>Pt</sub>
Pt/C / Nafion (4:1)	31	0.925	0.16	0.52
Pt/C / QAPPT (4:1)	46	0.930	0.16	0.34
Pt/C / QAPPT (10:1)	52	0.931	0.18	0.35
Pt/C / QAPPT (2:1)	47	0.918	0.10	0.22

**Table A.1** ECSA,  $E_{1/2}$ , MA and SA of Pt/C with Nafion and QAPPT ionomers with different catalyst to ionomer ratios.

In summary, we recommend a catalyst/alkaline ionomer ratio of about 10:1 to minimize the impact of ionomers on the ORR kinetics in RDE tests and a ratio of 4:1 for a sufficient amount of OH-conducting ionomer in MEA measurements. Such a conclusion has also been validated for Co-Mn metal oxides as ORR electrocatalysts in alkaline media.

**Three-electrode system:** Electrochemical measurements are performed in a three-electrode configuration, including working electrode (WE), reference electrode (RE) and counter electrode (CE) (Fig. A.3). The WE is often a glassy carbon (GC) electrode with one side mirror polished. Before depositing catalyst ink, the WE should be fine polished with 0.3 and 0.05  $\mu\text{m}$  alumina, respectively, rinsed and sonicated in ethanol and dried



**Figure A.3** Three-electrode RDE setup

under infrared light. It should be noted that one should only sonicate the PTFE-coated GC for a short period of time (5-10 s) and dry it at a medium temperature (60-100  $^{\circ}\text{C}$ ), to avoid damaging the PTFE by over-sonication or over-heating.

The type of the RE depends on the type of electrolyte. In acidic media, such as 0.1 M  $\text{HClO}_4$ , reversible hydrogen electrode (RHE) is an ideal reference electrode and can be easily prepared by sealing  $\text{H}_2$  gas in a glass tube with Pt/C or Pt black using the same electrolyte as that for testing catalysts. No salt bridge is required, and the raw data are collected directly versus RHE. However, one needs to be careful to ensure the purity of  $\text{H}_2$  gas (often done by multiple-time hydrogenation by water electrolysis). A trace amount of  $\text{O}_2$  in  $\text{H}_2$  can cause a positive shift of the RE potential. Additionally, the RHE reference electrode is not recommended for electrochemical measurements in alkaline media, especially for long-term tests since  $\text{CO}_2$  in air can react with KOH in the RE and change the RE potential.

Another widely used RE is Ag/AgCl in KCl solution. Benefiting from a stable solid/solid interface, It is the most widely used RE in literature (commercially available

from CHI or Pine) and can work at various pH environments. Since PGM electrocatalysts are sensitive to ppm-level  $\text{Cl}^-$  contamination, a salt bridge as well as a glass frit are necessary to slow down the diffusion of  $\text{Cl}^-$ . Additionally, running electrochemical tests over a long time will eventually cause a slow dilution of KCl by the testing electrolyte, which in turn will cause a positive shift in the RE potential. For example, Ag/AgCl in saturated KCl (4.8 M at 25 °C) has a potential of 0.197 V vs. SHE while Ag/AgCl in 1M KCl has a potential of 0.235 vs. RHE. We recommend that the Ag/AgCl RE should always be soaked in KCl if not being used. **Caution:** Home-made Ag/AgCl needs to make sure that the KCl solution is protected under  $\text{N}_2$  or Ar during the deposition of AgCl on Ag wire, in order to prevent the formation of  $\text{Ag}_2\text{O}$  (black vs. white AgCl). Hg/Hg $_2\text{Cl}_2$  in sat. KCl (saturated calomel electrode, SCE) has been widely used in early electrochemical studies and is gradually replaced by Ag/AgCl due to hazardous mercury. Other commonly used REs are Hg/Hg $_2\text{SO}_4$  in  $\text{H}_2\text{SO}_4$  for acidic media and Hg/HgO in KOH for alkaline media, Ag/AgNO $_3$  in acetonitrile (MeCN) for organic electrochemistry. Potentials of All REs are listed as follows with the SHE defined as 0 V (Fig. A.4).

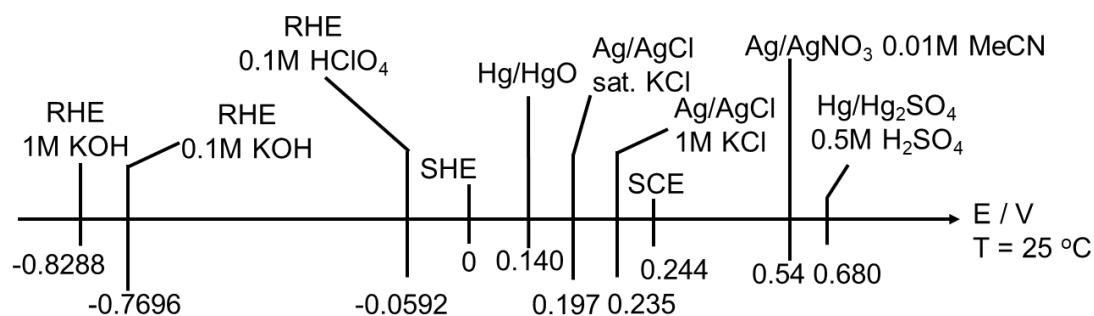


**Figure A.4** Potentials of various reference electrodes (REs).

**Electrochemical Testing Conditions:** The purity of solvent, chemicals and cleaning of

glassware are pivotal to ensure clean environment for rigorous electrochemical tests, especially for single-crystal metal electrodes. HClO<sub>4</sub> (Veritas Doubly Distilled, GFS chemical), when diluted to 0.1M, has trace amount of Cl<sup>-</sup> (1 ppb) and SO<sub>4</sub><sup>2-</sup> (10 ppb) while HClO<sub>4</sub> (ACS grade) has Cl<sup>-</sup> (100 ppb) and SO<sub>4</sub><sup>2-</sup> (100 ppb). KOH with a purity of 99.99% or 99.999% should be used for electrochemical measurements in alkaline media instead of KOH (ACS or AR grade), the latter has ppm-level impurity of Fe, Co, Mg, Al, etc. Ultrapure water should have a resistance of 18 MΩ·cm or higher. To avoid any potential contamination of precious metal for the measurements on non-precious electrocatalysts, the three-neck electrochemical cell can be washed using aqua regia (HCl/HNO<sub>3</sub>, mole ratio of 3/1) and followed by rinsing thoroughly using ultrapure water. Glassware can also be cleaned with KMnO<sub>4</sub>+H<sub>2</sub>O<sub>2</sub> followed by boiling in ultrapure water for three times to effectively remove possible organic impurity. Freshly prepared KOH solution can be stored for 1-2 weeks in plastic PE bottle for nanoparticle catalysts and should be freshly prepared right before use in single-crystal studies. The contamination from the slow reaction between glass and KOH is proven to be minimal for a short-term test within one day. PTFE cell works better than glass cell for long-term durability tests in alkaline media.

**Electrochemical data process and interpretation:** Catalyst activities are evaluated often with the following metrics including half-wave potential ( $E_{1/2}$ ), mass-specific activity (SA) and surface-specific activity (SA). The  $E_{1/2}$  is the potential at which measured current ( $I_m$ ) is half of the diffusion-limited current ( $I_d$ ). As shown in [Fig. A.5](#), Pt/C shows a  $E_{1/2}$  of 0.89 V vs. RHE at a loading of 25 μg/cm<sup>2</sup>. Pt/C exhibits a slightly lower  $E_{1/2}$  of 0.87 V vs. RHE in 0.1 M HClO<sub>4</sub> and 0.1 M KOH. It should be noted that

the  $E_{1/2}$  of Pt/C is a simplified activity metric and depends on the Pt loading and particle sizes. The  $E_{1/2}$  is straightforward to compare among different literatures and one can quickly assess if the literature reported a reasonable ORR activity of Pt/C. For example, a recent study<sup>1</sup> in Nat. Mater. claimed that the ORR activity of ZrN surpassed that of Pt/C, but the  $E_{1/2}$  of the Pt/C in this work is only 0.8 V vs. RHE, 90 mV lower than that of benchmark value despite a higher Pt loading of 50  $\mu\text{g}/\text{cm}^2$ . Unfortunately, many similar studies deliberately used a bad Pt/C reference to claim that their catalysts were “superior” to Pt/C, indicating a lack of basic electrochemical skills. We should do our best to avoid and discourage such an attempt.

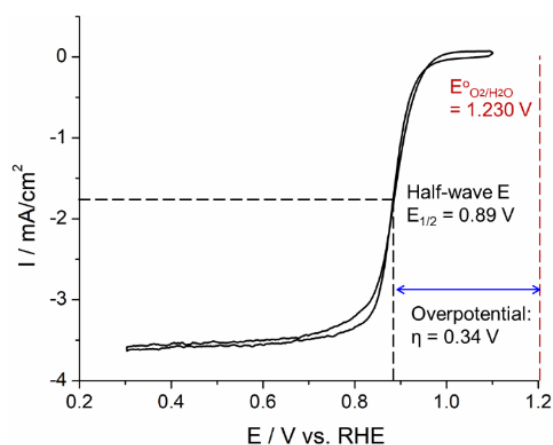


**Figure A.5** ORR polarization profiles of Pt/C in 1M KOH at 1600 rpm and 5 mV/s. 20 wt.% Pt has a Pt loading of 25  $\mu\text{g}/\text{cm}^2$  and particle size of 3 nm (Johnson-Matthey).

Compared to the  $E_{1/2}$ , the MA and SA represent more intrinsic activity metrics. The kinetic current is calculated based on the Koutecky-Levich equation ( $1/I_m = 1/I_d + 1/I_k$ ). The MA and SA at 0.9 V vs. RHE are standard metrics widely accepted for Pt-based catalysts in acidic media and recommended by the U.S. DOE. The MA and SA can be calculated by normalizing the kinetic current to the catalyst loading and electrochemical surface area (ECSA), respectively. The ECSA of Pt are measured from the  $H_{\text{UPD}}$  region

by integrating charge from 0.05 to 0.4 V vs. RHE in CV profiles and assuming a conversion factor of 200  $\mu\text{C}/\text{cm}^2$  measured by Feliu et al. It can also be calculated from the CO stripping method by integrating CO oxidation peak(s) with a conversion factor of 420  $\mu\text{C}/\text{cm}^2$ . The non-faradic double-layer contribution should be removed when calculating the total charge. Typical MA and SA values of Pt/C in acidic and alkaline media are summarized in [Table A.1](#). Those are the numbers one can refer to when evaluating the literature about ORR catalysts. In MEA studies<sup>2</sup>, Pt/C cathode in PEMFCs showed a MA of  $\sim 0.1 \text{ A}/\text{mg}_{\text{Pt}}$  and SA of  $\sim 0.2 \text{ mA}/\text{cm}^2_{\text{Pt}}$  at 0.9 V, which is relatively comparable to those values from RDE measurements in 0.1 M  $\text{HClO}_4$ . As we have learned from previous chapters, Pt-based alloy catalysts, such as our benchmark ordered  $\text{Pt}_3\text{Co}/\text{C}$  achieved a MA of  $0.52 \text{ A}/\text{mg}_{\text{Pt}}$  in MEAs ([Chapter 8](#)), representing a four-fold increase, relative to Pt/C, and surpassed the DOE 2020 target ( $0.44 \text{ A}/\text{mg}_{\text{Pt}}$ ).

Electrolyte	$E_{1/2} / \text{V vs. RHE}$	MA / $\text{A}/\text{mg}_{\text{Pt}}$	SA / $\text{mA}/\text{cm}^2_{\text{Pt}}$
0.1M $\text{HClO}_4$	0.87	0.06	0.09
0.1M KOH	0.87	0.07	0.10
1M KOH	0.89	0.09	0.13

**Table A.2** Summary of MA and SA of Pt/C from RDE measurements in acidic and alkaline media. MA and SA were calculated at 0.9 V vs. RHE by normalizing the  $I_d$  to the mass loading and ECSA of Pt, respectively. The ECSA was estimated to be around  $70 \text{ m}^2/\text{g}_{\text{Pt}}$  (Pt particle size of  $\sim 3 \text{ nm}$ ). The  $E_{1/2}$  has an error of 2-3 mV while MA and SA have relative errors of around 10%.

**IR-correction:** Although the DOE protocols recommend reporting ORR activity after IR correction, so-called “IR-free” measurements, in reality, the activity losses due to IR drops cannot be removed during fuel cell operation. All the electrochemical

measurements in this thesis are based on uncorrected RDE measurements and thus represent a lower limit of the ORR activity. After IR correction, the MA and SA would be even higher than what we reported. Using one example of Pt-Co catalysts, from electrochemical impedance spectroscopy (EIS) measurements, we estimated a total resistance of 25 Ohm for catalyst-loaded electrodes in 0.1 M HClO<sub>4</sub>, which would translate into about 10 mV loss in the  $E_{1/2}$  in RDE measurements. The IR-free (corrected) MA of PtCo was calculated to be close to 1 mA/g<sub>Pt</sub>, significantly higher than the reported value of 0.46 mA/gPt without IR correction. However, instead of making a claim that the activity of our catalyst is twice as high as the DOE 2020 target (0.44 mA/g<sub>Pt</sub>), we believe it is more appropriate (and realistic) to report values measured under real practical application conditions. The impact of IR-correction in MEA measurement will be more dramatic and will be discussed below (*vide infra*).

## **B. Testing protocols for MEA measurements**

MEA integrates electrocatalysts and membranes/ionomers into an operating fuel cell device. However, few research groups have reported high-performance MEA for PEMFCs or AEMFCs, which is mainly due to the complexity of MEA fabrication and testing protocols that involve meticulous engineering optimization. MEA studies in hydrogen fuel cells are so challenging that many papers developed ORR catalysts and then looked for applications such as Zn-Air or Li-Air batteries. Here, I will describe the basic aspects of MEAs and the impact of testing conditions. As shown in [Fig. B.1](#), MEAs are composed of two catalyst layers (cathode and anode), membrane (AEM) in between and gas diffusion layer (e.g. AvCard GDS3250 from fuel cell store), PTFE gasket and graphite bipolar plates. The key components are the catalyst coated

membrane (CCM) with a total thickness of  $\sim 100 \mu\text{m}$  or below. Pt/C and PtRu/C (60wt.%) can be purchased from Johnson-Matthey.

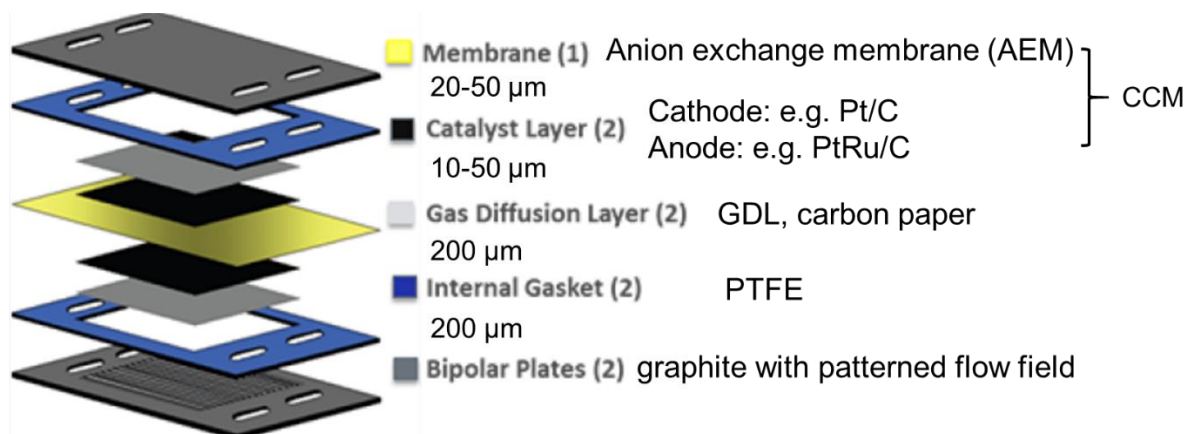


**Figure B.1** Schematic of MEA components. CCM represents catalyst coated membrane. Adapted from DOE Fuel Cell R&D overview, 2018.

**Catalyst ink preparation and spraying for CCM:** Catalyst ink for MEA tests are quite different that for RDE tests. Here, I will use an example of MEA, composed of Pt/C cathode and PtRu/C anode and QAPPT membrane, to illustrate the assembly process. Both 60wt.% Pt/C and 60 wt.% PtRu/C, instead of 20wt.% catalysts commonly used for RDE tests, are selected for MEA studies to minimize the catalyst layer thickness so as to enhance mass transport. Thus, we need to increase the mass fraction of Pt in Pt/C composite from 20% developed for RDE tests to 60-80% for MEA tests, which can be challenging for other alloy or metal oxide catalysts to maintain single-phase and desirable particle sizes at higher mass fractions. First, 200 mg QAPPT ionomer powder is dissolved in 10 mL DMSO at 60 °C to form a 2 wt.% ionomer solution (any undissolved residual particles need to be removed by a 0.2  $\mu\text{m}$  mesh Nylon syringe filter). 18 mg 60wt.% Pt/C are mixed with 225  $\mu\text{L}$  QAPPT/DMSO (2 wt.%) and 4.5 mL n-propanol. The catalyst/ionomer mass ratio is 4:1 and the resulting catalyst ink is

sonicated for 30 min. The catalyst/ionomer ratio needs to be optimized for each type of catalyst and ionomer and a proper amount of ionomer ensures sufficient local OH<sup>-</sup> conductivity while not blocking active sites of catalysts. After sonication, 1.5 mL of Pt/C catalyst ink is air sprayed on membrane and then PtRu/C is sprayed on another side of the membrane, which is heated at 80 °C in a vacuum table (Fig. B.2). Based on the reproducibility of a home-made automated air spray system, we estimated a yield of 50±7%. Therefore, the loading of Pt or PtRu is calculated as follows.

$$\frac{1.5\text{mL}\times 18\text{mg}\times 60\text{wt.}\%\times 50\%}{4.5\text{mL}\times 4\text{cm}^2} = 0.4 \pm 0.05 \text{ mg/cm}^2$$

Similarly, 28 mg 80% MnCo<sub>2</sub>O<sub>4</sub>/C are mixed with 350 μL QAPPT/DMSO and 4 mL n-propanol. 1mL catalyst ink is sprayed with a yield of 60% to achieve a metal oxide loading of 0.8 mg/cm<sup>2</sup>

$$\frac{1\text{mL}\times 28\text{mg}\times 80\text{wt.}\%\times 60\%}{4\text{mL}\times 4\text{cm}^2} = 0.8 \pm 0.1 \text{ mg/cm}^2$$

The catalyst loading can be adjusted by changing the volume of catalyst ink to be sprayed. Typically, a high Pt loading of 0.3-0.4 mg/cm<sup>2</sup> is used to examine the maximum MEA performance for a newly developed AEM while a minimal Pt loading (0.1-0.2 mg/cm<sup>2</sup>) should be used for well-established AEMs when considering the cost in practical applications. It should be noted that state-of-the-art PEMFCs use Pt loading of 0.1 and 0.025 mg/cm<sup>2</sup> in the cathode and anode, respectively (Chapter 9). 10% errors in PGM loadings varying from batch to batch result in about 10% errors in the final MEA performance in terms of the PPD of ~1.5 W/cm<sup>2</sup> (Fig. B.3). A PPD of ~1.5 W/cm<sup>2</sup> is a metric to keep in mind for benchmark MEA performance with present best AEM and PGM catalysts. The dry CCM in each batch is always weighted to accurately record

the catalyst loading, in order to assess its impact on the MEA performance.

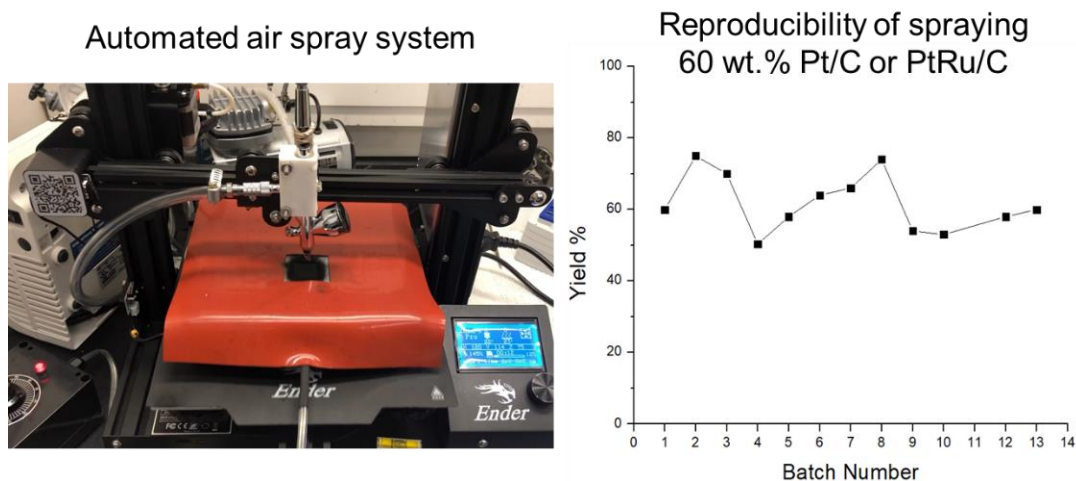


**Figure B.2** Home-made automated air spray system modified from a 3D printer. The white holder for air spray gun is 3D printed using polylactic acid (PLA). The reproducibility of spraying 14 batches of Pt/C or PtRu/C catalysts suggests a yield of 70%.

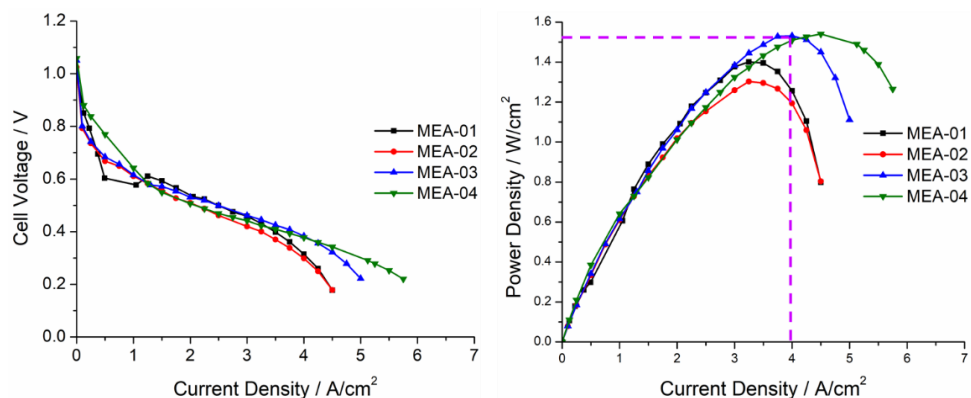


**Figure B.3** I-V and I-P curves of four MEA trials. Catalysts were sprayed using automated spray system with a PGM loading of  $0.3 \text{ mg}_{\text{Pt}}/\text{cm}^2$  at the cathode and  $0.3 \text{ mg}_{\text{PtRu}}/\text{cm}^2$  at the anode. Fuel cell test conditions: fully humidified  $\text{H}_2$  and  $\text{O}_2$  at a flow rate of 1000 mL/min and 0.2 MPa backpressure at a cell temperature of  $80^\circ\text{C}$ .

**Assembly of CCM in cell module:** The prepared dry CCM is in  $\text{Cl}^-$  form and will be exchanged to  $\text{OH}^-$  form by soaking it in 1 M KOH at  $60^\circ\text{C}$  for 6-8 h. The CCM in  $\text{OH}^-$  form will be rinsed by DI water to remove excess of mobile  $\text{OH}^-$  and only remain  $\text{OH}^-$  that is attached to the polymer. During the assembly process of CCM in cell module, it

is important to ensure that Pt/C catalyst is facing the cathode side and PtRu/C is facing the anode side of cell module, since Pt/C and PtRu/C electrodes look very similar unless they are clearly labeled (Fig. B.4). A torque screwdriver is required to apply a uniform pressure to eight screws in the cell module, in order to make a tight sealing to prevent H<sub>2</sub> or O<sub>2</sub> leaking. A typical torque force is controlled to be 6 N·m (4.4 lb·ft). Occasionally, the cell may have a gas leaking, stop both H<sub>2</sub> and O<sub>2</sub> gas immediately and increase the torque to 8 or 10 N·m to seal the cell again (don't panic!).

If gas leaking still occurs with a large torque, stop the test and examine the membrane and PTFE gasket to look for possible pinholes. Some novel membranes may not have desirable mechanical strength and too high torque may break the membrane and cause gas crossover and power failure.

Catalyst coated membrane (CCM)



Fuel Cell Test System

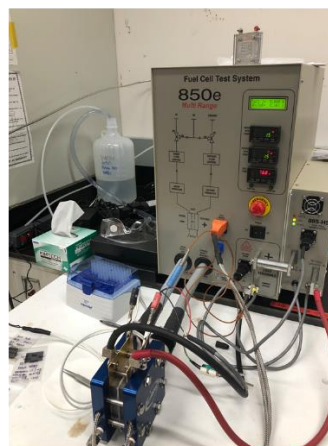


**Figure B.4** CCM with AEM (4 cm<sup>2</sup>) in the middle and catalysts on both sides and a single cell MEA connected to fuel cell test system (Scribner 850e).

**MEA test procedures:** It is necessary to go through the following checklist to ensure safety since MEA tests involve pure H<sub>2</sub> and O<sub>2</sub> in a sealed cell at elevated temperatures.

1. H<sub>2</sub> anti-flame arrestor and H<sub>2</sub> sensor are built in a room dedicated to MEA tests.

Absolutely no flame or chemical synthesis involving a hot plate is allowed in the room. H<sub>2</sub> gas tank should only be opened when a fuel cell test is performed, and should be closed once a fuel cell test is done. In case of gas leaking, shut down the fuel cell test immediately, fully open the sash and press the “exhaust” button of the fume hood, and the room can be ventilated with fresh air in several seconds.

2. Check pressure of H<sub>2</sub>, O<sub>2</sub> and N<sub>2</sub> tanks to make sure the tank pressure is above 500 psi and the second pressure gauge has a reading of above 50 psi to ensure enough gas pressure inside cell module. Test station does not allow fuel flow if the gas pressure of H<sub>2</sub>, O<sub>2</sub> and N<sub>2</sub> is below 50 psi. N<sub>2</sub> serves as purge gas to remove fuel from cell if needed. It's wise to have backup H<sub>2</sub>, O<sub>2</sub> and N<sub>2</sub> tanks available. Since H<sub>2</sub> outlet is inside the fume hood while O<sub>2</sub> outlet is in the room, the sash of the fume hood should remain closed during fuel cell tests to prevent H<sub>2</sub> from mixing with O<sub>2</sub>.
3. Scribner fuel cell test station has its own built-in safety precaution as the last defense line to prevent fuel leaking. It will automatically shut down fuels and purge the cell with N<sub>2</sub> if cell voltage drops below the shutdown voltage (often set as 0.1 V), which indicates a possible hydrogen crossover through broken membrane.
4. Open Scribner 850e test station and 885-HS fuel cell potentiostatic, and then Scribner fuel test software, set surface area (4 cm<sup>2</sup>), fuel and cell temperatures (60-80 °C), max. fuel and cell temperatures (90 °C), maximum current and power (50 A and 100 W), shutdown voltage (0.1 V) and gas flow rate (100-1000 mL/min). When the fuel temperature is same as cell temperature, the fuel is fully humidified (i.e. 100% RH). A more realistic operation condition would involve a lower RH to simulate the actual humidity when driving electric vehicles. For example, to achieve

a 50%RH at a gas pressure of 1 bar, the dewpoints of fuel temperatures need to be set at 63.8 °C for a cell temperature of 80 °C and 45.7 °C for a cell temperature of 60 °C. Calculation details can be found via: [VAISALA Humidity Calculator 5.0](#).

- Record the open circuit voltage (OCV) and save file with information about catalysts, membrane and test conditions. Set a small gas flow rate of 100 mL/min, Press the buttons of “Apply Fuel” and “Apply Temperature”, and it will take about 30 min for fuel and cell to achieve target temperatures. Then, make sure that the current is set at zero and press the button of “Apply Load”. As shown in [Fig. B.5](#), a stable OCV around 1.0 V, often indicates a successful preparation of MEA and good stability of AEM at elevated temperatures. If the membrane cannot survive at 80 °C, cell temperature should be set at 60 °C for a new MEA test.

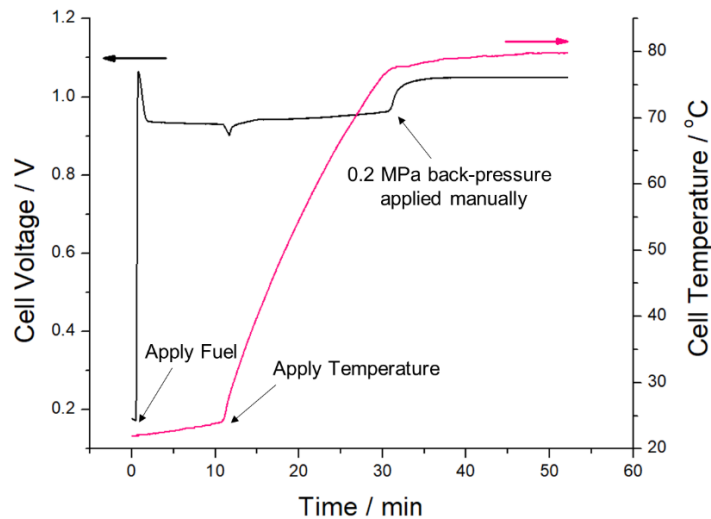


**Figure B.5** Open circuit voltage and Cell temperature as a function of time. Pt and PtRu loadings are both 0.3 mg/cm<sup>2</sup> with QAPPT membrane.

- Set the flow rate to be 500 mL/min, increased the backpressure to a desirable value (max. 0.2 MPa ) and begin the activation process. As shown in [Fig. B.6](#), the power

density is recorded as a function of applied current density ( $P = I \times E$ ) and the cutoff voltage is set at 0.2 V. The first cycle shows a sluggish P-I curve and power density abruptly increases at a current density of  $2 \text{ A/cm}^2$ , which is often described as “break-in procedure”<sup>3</sup> to activate the cell to reach its maximum performance and then remains stable. The following 2-5 cycles are intermediate process and then the cell achieves its maximum performance with a stable PPD of  $1.6 \text{ W/cm}^2$  at  $4 \text{ A/cm}^2$ . Current scanning mode is selected with a step size of 0.2-0.5 A/step and 5-10 s/step and voltage and power density are recorded in a steady-state mode.

7. After fuel test is finished, Stop “Apply Load” and then stop “Apply Fuel” and “Apply Temperature”. Close  $\text{H}_2$  and  $\text{O}_2$  tanks. It will take 0.5-1 h for the cell to cool down before dissembling it.

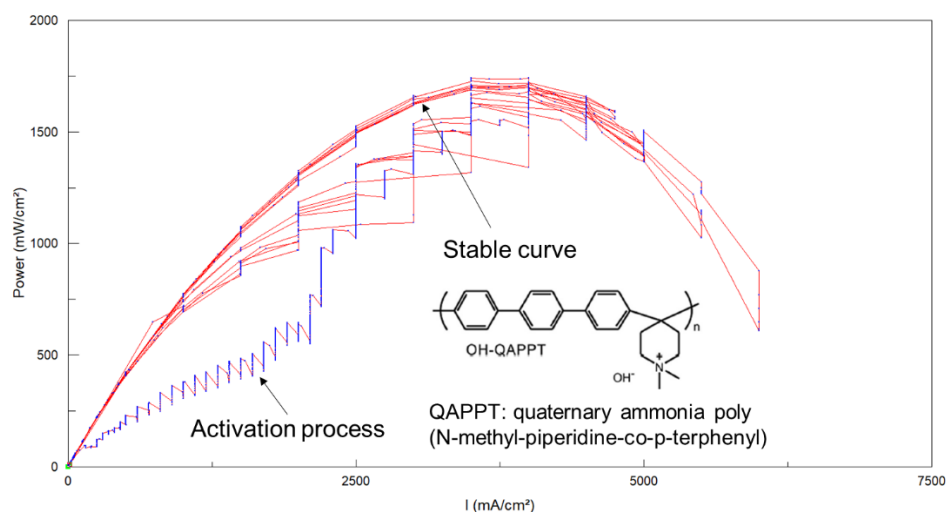


**Figure B.6** Cell performance with initial break-in procedure. Both Pt and PtRu loadings are  $0.3 \text{ mg/cm}^2$  and the AEM is QAPPT membrane. Fuel cell test conditions: fully humidified  $\text{H}_2$  and  $\text{O}_2$  at a flow rate of  $500 \text{ mL/min}$  and  $0.2 \text{ MPa}$  backpressure at a cell temperature of  $80 \text{ }^\circ\text{C}$ .

During fuel cell test, the high-frequency resistance (HFR) is recorded simultaneously as voltage and current. The HFR is recorded by EIS at a high frequency

of 10 kHz. The cell in Fig. B.6 shows a typical HFR of  $\sim 80 \text{ m}\Omega\cdot\text{cm}^2$  and varies slightly at different current densities. The HFR reflects ohmic resistance, which are mainly from three sources, electron transport within electrodes, GDL and flow field/current collectors; ion migration within the AEM; contact resistances.<sup>4</sup> Thus, catalysts with higher electronic conductivity and membranes with higher ionic conductivity and smaller thickness can lower the ohmic resistance (i.e., a lower HFR). Since the early stage of developing PEMFC, minimizing the HFR has been the key to optimize MEA performance. Fig. B.7 exhibits a 70 mV voltage loss due to ohmic resistance (HFR of  $50 \text{ m}\Omega\cdot\text{cm}^2$ ). Lowering the HFR is even more important for higher current density in AEFMCs. Using the data in Fig. B.6, voltage loss at  $4 \text{ A}/\text{cm}^2$  due to ohmic resistance will be:  $4 \text{ A}/\text{cm}^2 \times 80 \text{ m}\Omega\cdot\text{cm}^2 = 0.32 \text{ V}$ . Thus, it is very important to improve MEA to lower the HFR to be less than  $50 \text{ m}\Omega\cdot\text{cm}^2$ , a benchmark value for well-optimized PEMFCs. Additionally, it is crucial to know the HFR value of a MEA literature and whether the authors have applied IR-correction to remove the ohmic resistance. IR-corrected MEA performance is acceptable to report although such a voltage loss cannot be recovered in realistic fuel cell operation. However, the literature must honestly report the HFR value and provide the raw data without IR correction. For example, when a recent paper published in Science<sup>6</sup> reported an outrageous IR-corrected MEA performance of PEMFCs without mentioning the HFR value, the credibility of such work remains deeply questionable.

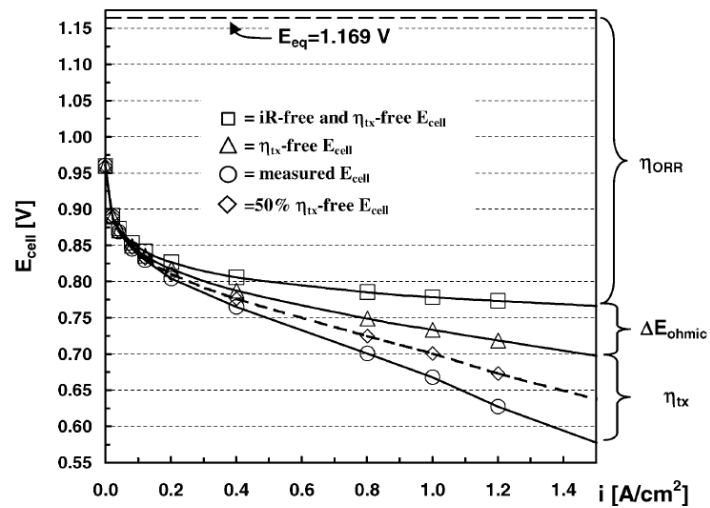


**Figure B.7** Performance loss break-down in an early study of PEMFCs.<sup>2</sup> 50 cm<sup>2</sup> single cell H<sub>2</sub>/air performance at T<sub>cell</sub> of 80 °C and 100 RH%, at a total pressure of 150 kPa. A HFR of 50 mΩ·cm<sup>2</sup> was estimated at 1 kHz.  $\eta_{tx}$  is the voltage loss due to mass transport.

Finally, long-term MEA durability for non-precious electrocatalysts are the key challenging facing the development of alkaline fuel cells, in order to meet the DOE AEMFC milestone of performance  $\geq 600$  mW/cm<sup>2</sup> with long-term durability under H<sub>2</sub>/air in PGM-free MEA. Fuel cells can operate over extended period of time at constant voltage of 0.6 V or constant current density of 600 mA/cm<sup>2</sup>. U.S. DOE established an accelerated stability test (AST) protocols for PEMFCs<sup>5</sup>: 30,000 trapezoidal voltage cycles between 0.6 V (3 s) and 0.95 V (3 s) with rise time of  $\sim 0.5$  s or less, at 80°C, 100% relative humidity, and ambient pressure. Such AST protocols emphasize on the stability of catalysts and may also be valuable for stability studies of AEMFCs. Fig. B.8 presents our recent progress on MEA durability at the CABES; a 200 h durability at 200 mA/cm<sup>2</sup> and a 50 h durability at 600 mA/cm<sup>2</sup> have been demonstrated with PGM electrocatalysts. Preliminary XPS measurements show the evidence of ionomer degradation catalyzed by Pt/C catalysts. This is an active area that

require tremendous collaborative efforts across electrocatalysts, membranes/ionomers and spectroscopic investigations, such as XPS, NMR, cryo-TEM, and theoretical simulations.

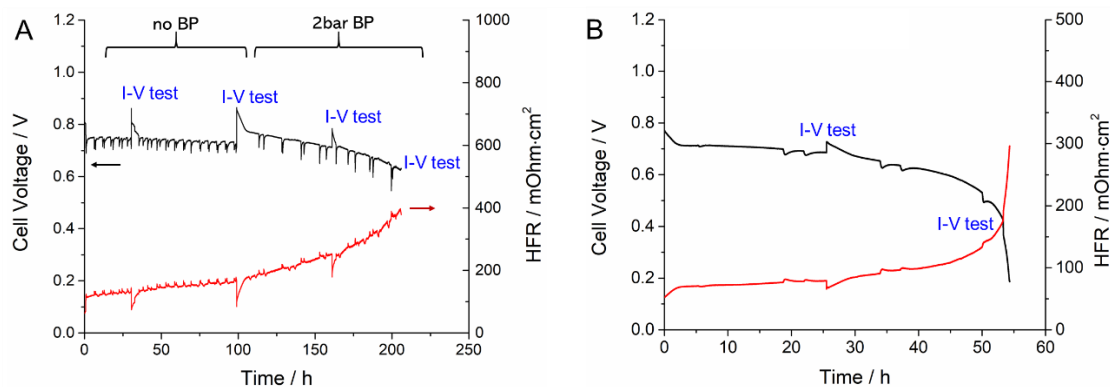


**Figure B.8** MEA durability tests at 200 (A) and 600 (B)  $\text{mA}/\text{cm}^2$  with Pt/C cathode ( $0.3 \text{ mg}_{\text{Pt}}/\text{cm}^2$ ) and PtRu/C anode ( $0.3 \text{ mg}_{\text{Pt}}/\text{cm}^2$ ). Fuel cell test conditions: fully humidified  $\text{H}_2\text{-O}_2$  at a flow rate of 500 mL/min at a cell temperature of 80 °C. The first 100 h test at 200  $\text{mA}/\text{cm}^2$  was at no backpressure and the second 100 h was at 0.2 MPa backpressure. The MEA test at 600  $\text{mA}/\text{cm}^2$  was at 0.2 MPa backpressure.

### C. Testing Protocols for *In situ* Electrochemical Liquid Cell TEM

The majority of my study on *in situ* liquid-cell TEM has benefited from Megan Holtz’s practical tutorial in her PhD thesis, publications,<sup>6-9</sup> and hands-on training sessions from Protochips engineers.

As-received electrochemical chips have a polymer coating, which can be removed by putting chips in acetone (>2 min) and methanol (>2 min). Cleaned chips then are plasma cleaned for 10s to make the surface partially hydrophilic. The first step involves a fast preliminary quality check of electrochemical chips in the Protochips “open cell” (Fig. C.1) before loading the chip in liquid-cell TEM holder. It is important to keep plasma clean time for 10-15 s, otherwise the chip surface will become too hydrophilic so that any drop of electrolyte will not only wet the electrode of the chip in open cell,

but also diffuse to three Au contact pins, which would cause short circuit. Once the chip passes the preliminary check in the open cell, the chip can be plasma cleaned for another 20 s for carbon electrode and 60 s for Pt electrode to make the surface fully hydrophilic for cell assembly in liquid-cell holder.



**Figure C.1** Protochips open cell with a plasma cleaned electrochemical chip in a drop of 0.1 M HClO<sub>4</sub> (~2 μL). This tiny drop can last for 3-5 min and needs to be refilled.

#### **Procedures for testing electrochemical chips in the open cell.**

1. Deposit catalyst nanoparticles (e.g. Pt NPs) on electrochemical chips and plasma clean chips for 30 s. Load chips in the open cell and add one drop of electrolyte (e.g. 0.1 M HClO<sub>4</sub>). Check connection to Gamry Potentiostatic and make sure the Gamry software recognizes the open cell.
2. Examine the open circuit potential (OCP) and single-frequency impedance (5 kHz) of the chip. A working chip should show a stable OCP of around 0 V ( $\pm$  0.1 V), a k $\Omega$ -level ohmic resistance (often in the range of 10-40 k $\Omega$ ) and a phase angle of 40-70°, indicating a mixed behavior of resistance and capacitance. Those three criteria need to be met at the same time before further electrochemical tests. An unstable OCP, a M $\Omega$ -level resistance or a phase angle close to 90° indicate the surface does not contact well with the electrolyte, and then the cell needs to be disassembled for further plasma process.

3. A series of “potential window opening” experiments are then performed with the potential range gradually opened from -0.1~0.1, -0.2~0.2..., ~-0.7-0.4 V vs. Pt. Despite Pt is a pseudo-stable RE relying on PtO<sub>x</sub>/Pt redox couple, it is relatively stable for a short-time test (potential stability is around 20 mV). The potential of Pt RE is about 0.8 V higher than that of RHE. Therefore, in order to perform a normal CV from 0.1-1.2 V vs. RHE, one needs to set the experimental potential window to be -0.7-0.4 V vs. Pt. As shown in Fig. C.2, well-defined hydrogen and oxygen regions of Pt suggest that the chip is able to deliver electrochemical results that can be compared to standard measurements. As discussed in detail in Fig. 10.8C, Cu electrodeposition is another routine experiment to evaluation the holder’s electrochemical function. The lower and upper potential limits should be kept within -0.8 V to 0.6 V to avoid the undesirable HER and OER, respectively. However, as illustrated in Chapter 10, the H<sub>2</sub> bubble formed under reduction potentials can significantly improve the spatial resolution in liquid if the HER naturally occurs as part of the electrochemical processes.

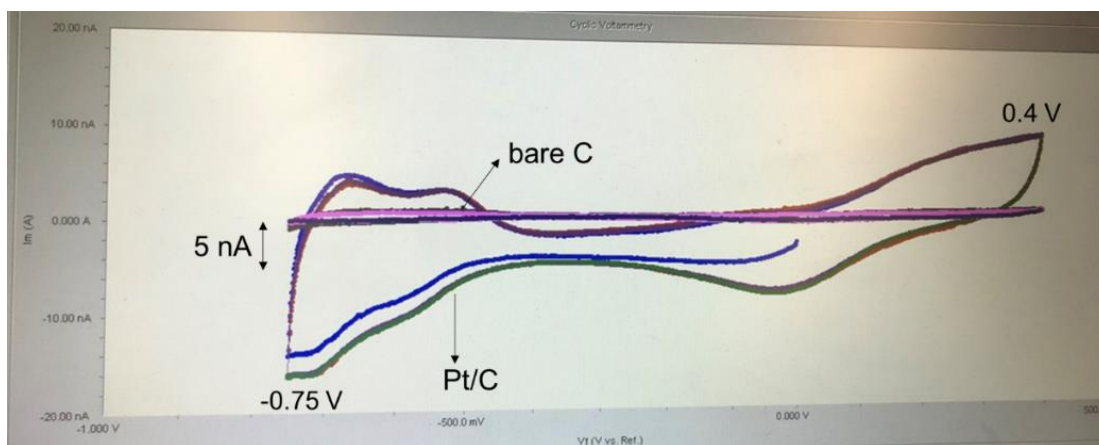


**Fig. C.2.** CV profiles of bare carbon WE and Pt/C loaded on carbon WE on electrochemical chip in the open cell in 0.1 M HClO<sub>4</sub> at 20 mV/s from -0.75V to 0.4 V vs. Pt RE (0.05-1.2 V vs. RHE).

## Procedures for testing electrochemical chips in liquid-cell TEM holder

Fig. C.3 shows an overview of assembly process of liquid-cell TEM holder. The assembly procedure is illustrated in Fig. C.3B: first insert the small chip into the O-ring in the holder tip with the membrane and spacer facing upwards. Then dispense a drop of electrolyte on the surface of the small chip, and put down the large chip with membrane side facing downwards. If the two chips are aligned properly, one should be able to see through the narrow SiN window under optical microscope. Gently close the lid and tighten the screws using torque driver. Verify again that the two chips are aligned properly and there should not be any gaps of uneven spacing between the holder tip and the lid. Use filter paper to absorb any visible water droplets outside of the holder tip.

Before inserting the liquid-cell holder into TEM, it is necessary to perform a “leak check” in a turbo pump. Observe the pressure and look for a steady pressure decrease without large oscillation in pressure reading. Typically, it takes 30min to 1h to reach the safety threshold of **5E-6 mbar** (3.8E-6 Torr) and will reach 2E-7 mbar after overnight pumping, which is similar to the column pressure of a typical TEM (~1E-7 mbar).

When the liquid-cell holder passes the safety threshold, syringe pump can control the liquid flow inside the holder (Fig. C.3.A). The electrolyte is purged with Ar and loaded in syringe. At a fast flow rate of 300  $\mu\text{L/h}$  and a force level of 50%, it will take about 1 h to completely remove the residual gas inside the long tubing and TEM holder. Then the flow rate is lowered to about 20-50  $\mu\text{L/h}$  to constantly supply fresh electrolyte.

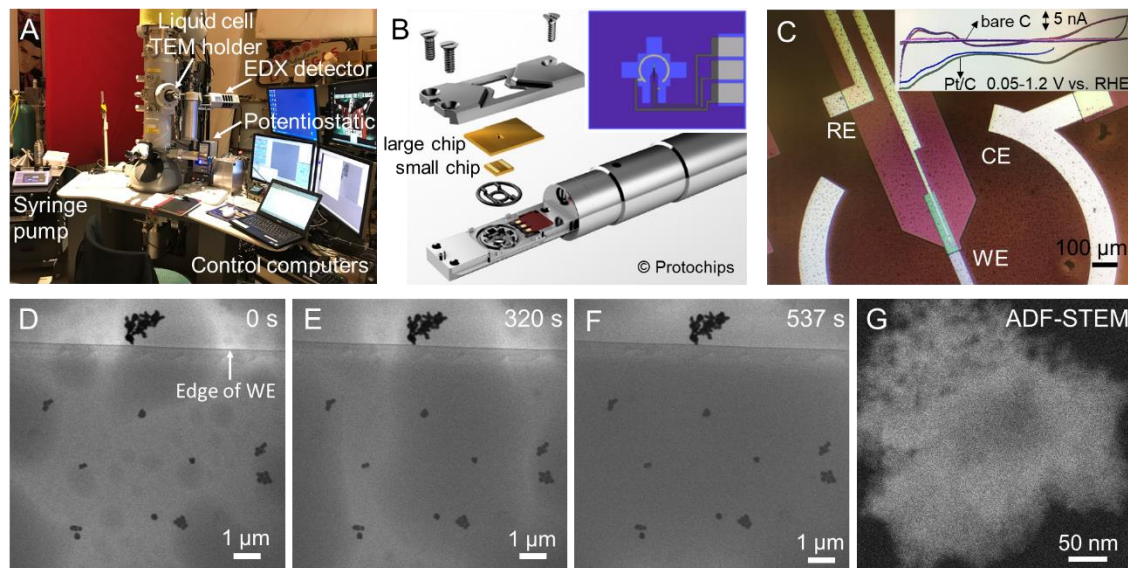


**Fig. C.3.** (A) *In Situ* liquid-cell TEM setup in F-20 STEM. (B) Schematic of Protochips Poseidon liquid-cell holder and three-electrode electrochemical chip (inset). (C) Optical image of three-electrode chip with WE (carbon), RE (Pt) and CE (Pt). (D-F) *In situ* BF-STEM image of surface wetting process of carbon during CV cycles between -0.5 and 0.5 vs. Pt at 20 mV/s in 0.1M HClO<sub>4</sub>. (G) ADF-STEM image of Pt nanoparticles in 0.1M HClO<sub>4</sub> at a beam dose of  $\sim 30$  e/(nm<sup>2</sup> s).

STEM (e.g. Tecnai F20) should be aligned before the liquid-cell holder is inserted. At lowest magnification, the position of view window can be found at middle right region of the search panel (Fig. C.4). The four corners of SiN window are labeled as 1-4 and the corners of carbon WE electrode are labeled as 5 and 6. Overall, the electron beam needs to penetrate SiN window (total 100 nm), electrolyte ( $\sim 500$  nm) and carbon WE (60 nm). The relative liquid thickness can be estimated from the plasma scattering in EELS.<sup>8</sup> Given the huge pressure differential between the cell and TEM vacuum, the SiN membrane will bulge in the center, and a spacer of 500 nm and 40  $\mu$ m wide windows can result in electrolyte in the center as thick as 800-1000 nm, relative to the corners ( $\sim 500$  nm). A smaller spacer of 250 nm and a narrower window of 25  $\mu$ m would result in a thinner electrolyte ( $\sim 650$  nm) in the center.

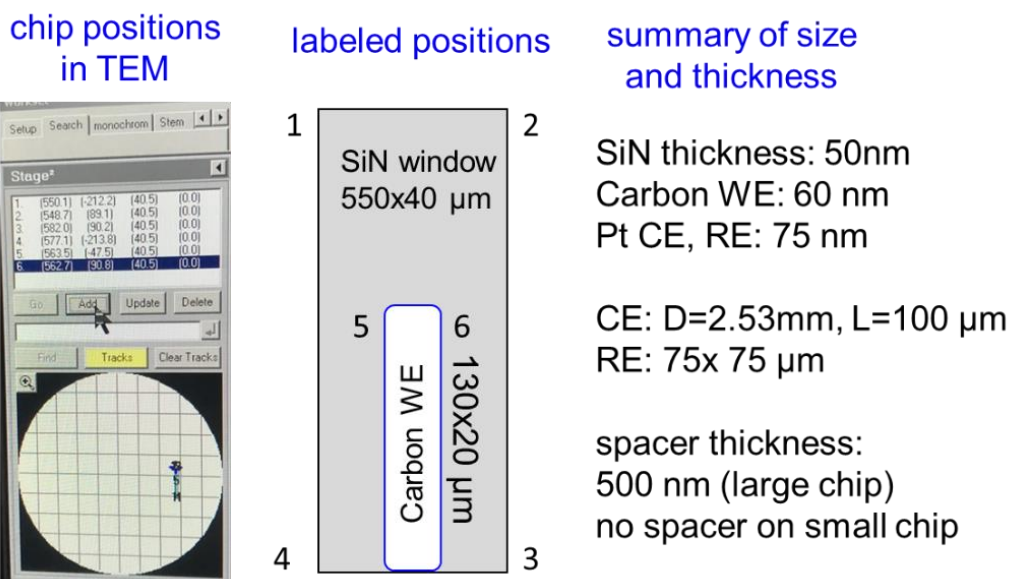


**Fig. C.4.** Relative chip positions in TEM and the summary of chip dimensions.

Thinner electrolyte will enhance spatial resolution while thicker electrolyte allows electrochemical reactions in TEM holder to better represent results of a conventional electrochemical cell. However, electrochemical cell with too thin electrolyte (<200 nm) suffers from larger ohmic drop in solution.<sup>7</sup> A spatial resolution of 2-5 nm can be achieved with an electrolyte thickness of ~500 nm (Fig. C.3.G). Octahedral PtNi particles can be visualized in STEM mode with a liquid thickness of 300 nm.<sup>9</sup> *In situ* TEM image can visualize the wetting process of carbon WE, suggesting the carbon surface changes from partially hydrophilic to fully hydrophilic after CV cycles. (Figs. C.3.D-F).

Beam dose control experiments need to be performed to determine a beam dose threshold for each electrochemical measurement. For example, Pt particles in 0.1M HClO<sub>4</sub> solution appear unaffected by the beam in STEM mode at a beam dose rate lower than 500 e<sup>-</sup>/(nm<sup>2</sup> s). However, 1 mM CuSO<sub>4</sub> is only stable under beam illumination at a

dose rate less than 10 e/(nm<sup>2</sup> s). The beam dose rate can be calculated from the following equation:  $D_{\text{beam}} = \frac{I \times \tau}{e \times t \times \left(\frac{\text{FOV}}{\text{Pixel number}}\right)^2}$  where I,  $\tau$ , t, e and FOV are beam current, dwell time (time/pixel), frame time (s/frame), elementary charge and the field of view (nm). For example, A STEM probe current of 2 pA with a dwell time of 12  $\mu$ s, a frame time of 3 s/frame, a FOV of ~500 nm and 512 by 512 pixels, would result in a beam dose rate of ~50 e/(nm<sup>2</sup> s), i.e. beam dose of 150 e-/nm<sup>2</sup>. Typically, soft materials, compounds with metallic cation, metal oxides and some organic solvent are particularly sensitive to beam damage.<sup>10</sup>

#### Reference:

1. Yuan, Y. et al. Attfield, J. P.; Yang, M. Zirconium Nitride Catalysts Surpass Platinum for Oxygen Reduction. *Nat. Mater.* **2020**, 19, 282-286.
2. Gasteiger, H. A., Kocha, S. S., Somali, B. & Wagner, F. T. Activity Benchmarks and Requirements for Pt, Pt-alloy, and non-Pt Oxygen Reduction Catalysts for PEMFCs. *Appl. Catal., B.* **2005**, 56, 9-35.
3. Break-in procedure from Scribner Inc. <http://www.scribner.com/wp-content/uploads/2017/06/Fuel-soft-32.pdf>
4. Cooper, K. R.; Smith, M. Electrical Test Methods for On-Line Fuel Cell ohmic Resistance Measurement. *J. Power Source* **2006**, 160, 1088-1095.
5. [https://www.energy.gov/sites/prod/files/2017/05/f34/fcto\\_myRDD\\_fuel\\_cells.pdf](https://www.energy.gov/sites/prod/files/2017/05/f34/fcto_myRDD_fuel_cells.pdf)
6. Chong, L. et al. Greeley, J.; Chan, M.; Barkholtz, H.; Ding, W.; Liu, D.J. Ultralow-Loading Platinum-Cobalt Fuel Cell Catalysts Derived from Imidazolate Frameworks. *Science*, **2018**, 362, 1276-1281.
7. Holtz, M.; Yu, Y. et al. Abruña, H. D.; Muller, D. A. Nanoscale Imaging of Lithium Ion Distribution During In Situ Operation of Battery Electrode and Electrolyte. *Nano Lett.* **2014**, 14, 1453-1459.
8. Holtz, M.; Yu, Y. et al. Abruña, H. D.; Muller, D. A. In Situ Electron Energy-Loss Spectroscopy in Liquids. *Microsc. Microanal.* **2013**, 19, 1027-1035.
9. Beermann, V.; Holtz, M. et al. Muller, D. A.; Strasser, P. Real-time Imaging of Activation and Degradation of Carbon Supported Octahedral Pt-Ni Alloy Fuel Cell Catalysts at the Nanoscale using In Situ Electrochemical Liquid Cell STEM. *Energy Environ. Sci.* **2019**, 12, 2476-2485.
10. de Jonge, N.; Dinin-Borkowski, R. E.; Ross, F. M. Resolution and aberration correction in liquid cell transmission electron microscopy. *Nat. Rev.* **2019**, 4, 61-78.